Thèse de doctorat

Présentée et soutenue publiquement pour l'obtention du titre de

DOCTEUR DE l'UNIVERSITÉ DE LORRAINE

Mention : Science des matériaux

par **Maïté FERNANDES TRONCO**

Electroactive polymer nanocomposites for energy harvesting applications

Thèse soutenue publiquement le 15 octobre 2025 à Nancy devant le jury composé de :

Directeur de thèse :	Didier ROUXEL	Professeur, Université de Lorraine, Nancy
Co-directeur de thèse :	Marc PONÇOT	Maître de conférences, HDR, Université de Lorraine, Nancy
Co-encadrant de thèse :	Nandakumar KALARIKKAL	Professeur, Mahatma Gandhi University, Inde
Examinateur :	Fabrice DOMINGUES DOS SANTOS	Docteur, Arkema Piezotech, Puteaux
Rapporteurs :	Aji P MATHEW	Professeure, Université de Stockholm, Suède
	Émilie PLANES	Professeure, Université de Savoie-Mont-Blanc, Chambéry, **Présidente du jury**
Membres invités :	Rafael JIMÉNEZ RIOBÓO	Docteur, Instituto de Ciencia de Materiales de Madrid, CSIC, Espagne
	Isabelle ROYAUD	Professeure, Université de Lorraine, Nancy
	Sabu THOMAS	Professeur, Mahatma Gandhi University, Inde

UNIVERSITÉ DE LORRAINE | BIBLIOTHÈQUES UNIVERSITAIRES

AVERTISSEMENT
DROIT D'AUTEUR

Ce document est le fruit d'un long travail approuvé par le jury de soutenance et mis à disposition de l'ensemble de la communauté universitaire élargie.

Il est soumis à la propriété intellectuelle de l'auteur. Ceci implique une obligation de citation et de référencement lors de l'utilisation de ce document. Toute contrefaçon, plagiat ou reproduction illicite encourt une poursuite pénale.

Contact bibliothèque : ddoc-theses-contact@univ-lorraine.fr
(Cette adresse ne permet pas de contacter les auteurs)

Code de la Propriété Intellectuelle. articles L 122. 4
Code de la Propriété Intellectuelle. articles L 335.2- L 335.10

UNIVERSITÉ DE LORRAINE
34 COURS LÉOPOLD — CS 25233
54052 NANCY CEDEX
TÉL : 03 54 50 54 00
CONTACT@UNIV-LORRAINE.FR
WWW.UNIV-LORRAINE.FR

À mon papa,

À la mémoire de Carlos Fernandes Tronco.

Acknowledgements

A PhD is never a work completed alone. I would like to express my gratitude to all the people who have been part of this journey.

I would like to thank my two thesis supervisors, Prof. Didier Rouxel and Dr. Ing. Marc Ponçot. You have welcomed me in your respective research teams, and guided me through all the steps of this thesis. We first met during my last year at EEIGM, when I got the opportunity to get a first glimpse at the world of research. Thank you for giving me the opportunity to explore it further, for real this time. Obviously, you helped me to improve as a researcher, and I have learned so much at your contact. But even more importantly, you have been of great support during the toughest periods, and have helped me to grow a lot as a person.

I am grateful to all the people in teams 304 (Physique, Mécanique et Plasticité) and 405 (Micro et Nanosystèmes). From training on the different elaboration and characterisation techniques, to data analyses and moral support, your contribution has been crucial to me. I would especially like to thank Stefan McMurtry, who in addition to providing training in the chemical rooms, was patient enough to help me become more confident, more attentive to my health and happiness, and explore my future career options. I would also like to thank Prof. Isabelle Royaud, you gave me my first internship opportunity at Institut Jean Lamour, and kept looking after me ever since. I also owe a lot to the help of all the doctoral students who have taught me so much, especially Sreelakshmi, Mouad and Hugo.

I owe a lot to all the people working in the different Competence Centres of Institut Jean Lamour. I want to thank Pauline Haraux from CC3M for the many hours spent trying to get SEM images of my fibrous materials, Emanuel Vatoux and the CCHéré for the amazing work on the custom-built tapping test bench, and all the adaptations to the Brillouin optical bench, Laurent Badie from CCMiNaLor for the clean room and polarisation training and Ghouti Medjahdi from CCXGamma for helping me with XRD measurements. A special thanks to Sébastien Hupont at CCOL. From your training and support, I went from a student scared to mess up during a FTIR measurement to an expert of Brillouin spectroscopy. The many hours spent at the CCOL have given me a unique opportunity to exchange with many students and researchers, develop an expertise in various vibrational spectroscopy techniques, and build my confidence as a researcher and a music DJ. I cannot mention the CCOL without expressing my gratitude to Rafael Jiménez Riobóo. Your guidance and patience truly helped me to get comfortable with the Brillouin spectroscopy, and realise one of the most exciting part of my thesis. I also want to thank David Pilloud for landing us the Linkam System and helping us set up the system. And of course, I keep in mind the work of CCErmione regarding all IT equipment. As team cooperation does not take place only in the CC, I would like to thank Lionel Aranda for helping me with the TGA measurements and result interpretation, and Cyril Noirel for his training on several characterisation techniques. I would also like to have a word for my CSI members, David Chapron and Etienne Tisserand, who I thank very much for his help regarding the electronical section of my work.

I am grateful for all the meetings with people from Mahatma Gandhi University. I want to thank Prof. Nandakumar Kalarikkal to have accepted to supervise my thesis, for his guidance and many words of encouragement. Of course, I want to express my gratitude to the post-doctoral researchers who came to Nancy to share with me their practical and scientific knowledge: Dr. Sathiyanathan, Dr. Bicy Kottathodi and Dr. Chitra Lekha. Your help has been fundamental to help me better understand the electrospinning process.

I want to thank all the students from the Mines of Nancy for their contribution in the elaboration and characterisation of PVDF materials, especially Nicolas Durey. I also want to thank all the students from the Master EEA-CIM (”Capteurs intelligents et micro-nanotechnologies”) that I co-supervised during the four years of my PhD (Alex, Dihia , Mourad, Alioune, Mounir, Aymane, Mourad, Sadrack, Flora, Amar, Sonia, Ousmane, Ibrahim and

Amal). A special thanks to Michael, Junfeng and Abdelkhalek, your dedication to the improvement of the tapping test machine and electric testing of the PVDF-based devices has been substantial to my work.

Last but not least, I want to thank all my friends and family for bearing with me during the ups and downs of these four last years. Thank you for supporting me, for believing in me, for taking me out for a beer or for a walk, when I needed it the most. I would not be the person I am today without you.

Abstract

Due to the growing concerns about energy consumption and environmental impacts of electronic devices, alternatives to batteries have become a huge topic of interest. For low power applications, energy harvesting through electroactive polymer based nanogenerators is one of the regarded routes. Among such polymers, polyvinylidene fluoride (PVDF) is the most widely studied due to its good electro-mechanical coupling properties, high chemical stability, flexibility and biocompatibility.

One of the major challenges regarding PVDF is the maximisation of its crystalline electroactive phases fraction, and especially the β phase. To precisely characterise the crystalline phase fractions of the produced PVDF samples, a multi-techniques approach has been developed, involving DSC, WAXS, FTIR and Raman spectroscopy. DSC and WAXS were mainly used for precise determination of the crystallinity ratio of the samples, while FTIR and Raman spectroscopy are better suited for phase identification. Additionally, a new Raman criterion for the precise quantification of the α, β and γ phase fractions was proposed, using a curve deconvolution approach.

A study of the influence of several electrospinning parameters highlighted that crystallinity ratio is very little influenced by the different sets of parameters, compared to the effect of stretching coming from the electrospinning technique. All produced fibres showed a negligible amount of crystalline α phase (<5%), and a proportion of β to γ crystalline phase of roughly 70/30%. However, higher solution flow rate, and an applied voltage either too low or to high have been demonstrated to lower the ratio of β/γ phase fractions, by causing the apparitions of defects. Addition of CNC and QC fillers did not notably impact the semi-crystalline microstructure of the electrospun fibres, showing that it is mainly controlled by the electrospinning process.

For the first time, micro-Brillouin spectroscopy was used for the mechanical characterisation of isolated electrospun fibres. The strong variation of mechanical properties observed comparing fibres elaborated with a 3:7 DMF:Acetone ratio compared to the fibres elaborated with a 4:6 DMF:Acetone ratio was attributed to the presence of mesoporosities within the fibres, originating from the difference in solvent evaporation speed. A study conducted on CNC composite fibres showed a slight reinforcement effect of a few percent of CNC fillers on the electrospun fibres, despite the disparities of c_{11} values observed within the same sample.

Another important result was obtained by exploring the evolution as a function of temperature of the mechanical properties of electrospun PVDF fibres. An unexpected elastic anomaly was evidenced, and the proposed explanation for this behaviour happening around 30°C is the reorientation of the crystalline region located at the amorphous-crystalline interface in mechanically oriented materials, preceding the melting of imperfect α crystals. A complementary study hints at the possibility of forming β phase in the sample with exposure to a 532 nm green laser.

The electric performances of the materials were evaluated using a tapping-test bench conceived in the lab. Using this setup, it was possible to test the performances of the PVDF-composite fibres, and ensure their sensitivity to applied force and frequency changes. The CNC5 sample device achieved the highest output performance while maintaining good signal stability, reaching 60 V of peak-to-peak voltage, and 60 µA of peak-to-peak current. After selecting an appropriate energy harvesting board, the EH300, a demonstrator application of the device was proposed. The PVDF proved its practical ability to function both as a pulse sensor, and as a mechanical energy harvesting nanogenerator, showing a potential for integration into low-power, wireless health monitoring systems.

Keywords:

1) Polyvinylidene fluoride (PVDF)
2) Energy harvesting
3) Electrospinning
4) Polymer nanocomposites
5) Vibrational spectroscopies
6) Brillouin spectroscopy

Résumé

Les préoccupations croissantes concernant la consommation d'énergie et l'impact environnemental des appareils électroniques mènent à étudier des alternatives aux piles. Pour les applications à faible consommation d'énergie, la récupération d'énergie à l'aide de nanogénérateurs à base de polymères électroactifs est une voie envisagée. Parmi ces polymères, le polyfluorure de vinylidène (PVDF) est le plus étudié, car il présente de bonnes propriétés de couplage électromécanique, une grande stabilité chimique, une bonne flexibilité et une bonne biocompatibilité.

L'un des principaux défis liés au PVDF est la maximisation de sa fraction de phases électroactives cristallines, en particulier la phase β. Pour caractériser avec précision les fractions de phases cristallines des échantillons de PVDF produits, une approche multi-techniques a été développée - DSC, WAXS, FTIR, spectroscopie Raman. La DSC et les WAXS ont été principalement utilisées pour déterminer avec précision le taux de cristallinité des échantillons, tandis que la FTIR et la spectroscopie Raman sont mieux adaptées à l'identification des phases. De plus, un nouveau critère Raman a été proposé pour quantifier avec précision les fractions des phases α, β et γ, en utilisant une approche de déconvolution de courbes.

Une étude de l'influence de plusieurs paramètres d'électrofilage a mis en évidence que le taux de cristallinité est peu influencé par les paramètres testés, par rapport à l'effet d'étirement provenant de la technique d'électrofilage. Toutes les fibres produites présentaient une quantité négligeable de phase cristalline α (<5 %) et une proportion de phases cristallines β et γ d'environ 70/30 %. Cependant, il a été démontré qu'un débit de solution plus élevé et une tension appliquée trop faible ou trop élevée réduisaient le rapport des fractions de phase β/γ, provoquant l'apparition de défauts. L'ajout de charges CNC et QC n'a pas eu d'impact notable sur la microstructure semi-cristalline des fibres électrofilées, confirmant qu'elle est principalement contrôlée par le processus d'électrofilage.

Pour la première fois, la spectroscopie micro-Brillouin a été utilisée pour la caractérisation mécanique de fibres électrofilées isolées. La forte variation des propriétés mécaniques observée entre les fibres élaborées avec un rapport DMF:acétone de 3:7 et avec un rapport DMF:acétone de 4:6 a été attribuée à la présence de mésoporosités dans les fibres, provenant de la différence de vitesse d'évaporation du solvant. Une étude menée sur des composites a montré un léger effet de renforcement de quelques pourcents de charges CNC sur les fibres électrofilées, malgré les disparités des valeurs c_{11} observées au sein d'un même échantillon.

Un autre résultat important a été obtenu en étudiant l'évolution des propriétés mécaniques des fibres de PVDF électrofilées en fonction de la température. Une anomalie élastique inattendue a été mise en évidence, et l'explication proposée pour ce comportement qui se produit autour de 30 °C serait la réorientation de la région cristalline située à l'interface amorphe-cristalline dans les matériaux orientés mécaniquement, précédant la fusion des cristaux α imparfaits. Une étude complémentaire suggère la possibilité de former une phase β dans l'échantillon exposé à un laser vert de 532 nm.

Grâce à un banc de test conçu au laboratoire, il a été possible de tester les performances des fibres composites PVDF et de vérifier leur sensibilité aux variations de force et de fréquence appliquées. L'échantillon CNC5 a atteint les performances de sortie les plus élevées tout en conservant une bonne stabilité du signal. Le dispositif a prouvé sa capacité pratique à fonctionner à la fois comme capteur de pouls et comme nanogénérateur de récupération d'énergie mécanique, montrant un potentiel d'intégration dans des systèmes de surveillance de la santé sans fil à faible consommation d'énergie.

Mots-clés :

1. Polyfluorure de vinylidène (PVDF)
2. Récupération d'énergie
3. Electrofilage
4. Nanocomposites polymère
5. Spectroscopies vibrationnelles
6. Spectroscopie Brillouin

Table of contents

General Introduction 1

Chapter 1: A review on electrospun PVDF-based nanocomposites - Recent trends and developments in energy harvesting and sensing applications 3

1. PVDF for sensor and energy harvesting applications 3

1.1. Semi-crystalline microstructure of PVDF 3

1.2. Elaboration of PVDF fibres through electrospinning 3

1.3. PVDF nanocomposite fibres 4

2. A review on electrospun PVDF-based nanocomposites: Recent trends and developments in energy harvesting and sensing applications 6

Chapter 2: Elaboration and characterisation of the nanocomposites 34

1. Materials of the study 34

1.1. Polyvinylidene fluoride (PVDF) 34

1.2. Cellulose nanocrystals (CNC) 34

1.3. Quasicrystals (QC) 34

1.4. Solvents 35

2. Elaboration of the nanocomposites 35

2.1. Solvent casting 35

2.2. Study of electrospinning parameters on pristine PVDF fibres 36

2.3. Electrospinning of nanocomposites 37

3. Experimental characterisation techniques 37

3.1. Differential scanning calorimetry (DSC) 37

3.2. Wide-angle X-ray scattering (WAXS) 39

3.3. FTIR 41

3.4. Raman spectroscopy 43

3.5. TGA 45

3.6. Brillouin spectroscopy 46

3.7. SEM 47

3.8. DMA 47

3.9. Electric characterisation and energy harvesting 48

Chapter 3: Crystalline characterisation of the electrospun fibres and influence of nanofillers addition 51

1. Introduction 51

2. New proposal for a Raman criterion for identification and quantification of PVDF crystalline phases 51

2.1. Crystalline phase identification using Raman spectroscopy 52

2.2. Calculation of the crystallinity ratio and determination of the different phase fractions 52

3. Optimisation of the electrospinning process: a study to optimise the parameters 55
3.1. Phase identification and qualitative analysis from FTIR spectra 56
3.1.1. Influence of the solvent ratio 56
3.1.2. Influence of the weight percentage of PVDF in solution 56
3.2. Crystallinity ratio from DSC thermograms 57
3.3. Crystallinity ratio from WAXS diffractograms 59
3.4. Phase identification, crystallinity ratio and phase fraction from Raman spectra 61
3.5. Additional characterisation from optical microscopy 64
4. Raman study of local crystallinity ratio and phase fraction within a sample 66
5. Study of the electrospun nanocomposites: effect of the filler addition on the fibre crystallinity 69
5.1. Phase identification and qualitative analysis from FTIR spectra 70
5.2. Crystallinity ratio from DSC thermograms 70
5.3. Phase identification and crystallinity ratio from WAXS diffractograms 71
5.4. Phase identification, crystallinity ratio and phase fraction obtained from Raman spectra 73
6. Conclusion 74
Chapter 4: Brillouin spectroscopy studies on single electrospun PVDF fibres 76
1. Introduction 76
2. Pristine PVDF nanofibres with different proportions of acetone and DMF solvents 76
2.1. Hypothesis of microstructural differences 81
2.2. Hypothesis of trapped solvent 82
2.3. Hypothesis of a topographic difference 82
3. Nanocomposite electrospun fibres with addition of cellulose nanocrystals (CNC) and Al-Cu-Fe-B quasicrystals (QC) 84
4. Brillouin scattering study in temperature: evidence of an elastic anomaly 86
4.1. Differentiation with the glass transition (Tg) 89
4.2. DMA and DSC analyses 91
4.3. Discussion 93
4.4. Conclusion 94
5. Influence of mechanical stretching and temperature cycles on the Brillouin response 94
6. Unexplained behaviour: discoloration of the sample 96
7. Conclusion 99
Chapter 5: Electric characterisation and energy harvesting performances of the electrospun PVDF-nanocomposites fibre mats 101
1. Introduction 101
2. Piezoelectric characterisation of a PVDF film: state of the art 102
2.1. Measurement of the piezoelectric coefficient (d33) 102
2.2. Tapping test 103
2.3. Bending test 106

3. Development of a testing bench in tapping mode 108
3.1. Design 108
3.2. Manufacturing and implementation 110
3.3. Electronic control system 111
3.4. Validation of the test bench 111
3.4.1. Parasitic effect of motor induction on current measurements 111
3.4.2. Frequency variation of the solicitation 113
4. Testing of the electrospun PVDF sensors: influence of the filler addition 115
4.1. Elaboration process of the electrospun PVDF based devices 115
4.2. Testing of the devices: voltage and current outputs 115
4.2.1. Pure PVDF electrospun fibres 116
4.2.2. PVDF fibres with addition of 1-5% CNC 117
4.2.3. PVDF fibres with addition of 1-5% QC 118
4.2.4. Conclusion and selection of the best sample 119
4.3. Electrical response analysis under applied loads 120
4.4. Validation of the PVDF nanogenerator using a full-bridge rectifier 121
5. Energy harvesting electronic circuits and optimisation 123
5.1. Comparison of commercially available energy harvesting circuits 123
5.1.1. LTC3588-1 (Analog Devices) 123
5.1.2. AEM30330 125
5.1.3. EH300 125
5.1.4. Experimental Comparison: EH300, EH300A, and passive diode bridge circuit 127
5.1.4.1. Reference: Passive Diode Bridge 127
5.1.4.2. Test with EH300 (1000 µF) 127
5.1.4.3. Test with EH300A (2 × 3300 µF) 127
5.1.5. Final choice of energy harvesting circuit 127
5.2. Energy Storage Experiment 128
5.2.1. Slope of the charging speed of capacitor 128
5.3. Optimising power output from the electroactive source 129
5.3.1. PZT buzzer 129
5.3.2. CNC5 device 130
6. Data transmission from a sensor: a low-power application for the PVDF devices 130
6.1. PVDF as energy harvesting nanogenerator 131
6.1.1. Charging of the EH300 capacitor 132
6.1.2. Discharge into a LED load 133
6.1.3. Conclusion of the experiment 134
6.2. Pulse sensor on an artery 134

6.2.1. First case: Human being at rest 135
6.2.2. Second case: Human being after a great effort 136
6.2.3. Third case: Laboratory rat after adrenaline injection 137
6.2.4. Conclusion 137
6.3. Powering and sending data via Bluetooth 137
6.3.1. Wireless Communication via Bluetooth Low Energy (BLE) 138
6.3.2. Theoretical assessment of the system capacity to power the BLE module 138
7. Conclusion: 139
Conclusion 141
Perspectives 144
Résumé en français de la thèse 146
References 154
Appendices i

List of figures

Figure 1: Solvent casted films with various DMF:Acetone ratio. From left to right: 5:5, 4:6, 3:7, 2:8, 1:9. 35
Figure 2: Schematic representation of the electrospinning setup [134]. 37
Figure 3: X-ray diffraction from a family of reticular planes inside a crystalline lattice [143]. 39
Figure 4: Deconvolution of a typical WAXS diffractogram of an electrospun PVDF sample. 41
Figure 5: FTIR spectra of PVDF films prepared by various methods. PVDF CP and PVDF NMP are solvent casted samples prepared with cyclopentanone and NMP as solvents respectively [134]. 43
Figure 6: Raman spectra of PVDF samples prepared by different methods. PVDF CP and PVDF NMP are solvent casted samples prepared with cyclopentanone and NMP as solvents respectively [134]. 44
Figure 7: Micro-Brillouin setup [171]. 47
Figure 8: Preparation steps of the PVDF devices A) the PET layer, B) the P-shaped electrode with the connecting wire, C) addition of the electrospun scaffold, D) the finished device. 49
Figure 9: A) Functional diagram and B) photograph of the tapping test bench. 49
Figure 10: Raman spectra of pristine PVDF electrospun fibres (black), and a PVDF solvent casted sample before (red), and after (blue) a heating ramp to 200°C. 52
Figure 11: Deconvolution of the Raman spectrum of molten PVDF. 53
Figure 12: Raman Spectra of A) pristine electrospun fibres and B) solvent casted PVDF sample and C) solvent casted sample cooled from melt. 54
Figure 13: Comparison between 3:7 and 4:6 DMF/acetone ratio for A) 15wt% PVDF and B) 16wt% PVDF in solution. 56
Figure 14: Comparison between 15wt% and 16wt% PVDF in solution for A) 3:7 and B) 4:6 DMF/acetone ratio. .. 57
Figure 15: Typical DSC thermograms of electrospun fibres A) full heating cycles B) zoom on the glass transition. 58
Figure 16: Thermograms of PVDF fibres elaborated with various electrospinning parameters: A) 15 wt.% PVDF – 3:7 D:A, B) 15 wt.% PVDF – 4:6 D:A, C) 16 wt.% PVDF – 3:7 D:A and D) 16 wt.% PVDF – 4:6 D:A. 59
Figure 17: WAXS diffractograms of the electrospun fibres elaborated with: A) 15 wt.% PVDF and B) 16 wt.% PVDF in solution. 60
Figure 18: Raman spectra of the electrospun fibres elaborated with: A) 15 wt.% PVDF and B) 16 wt.% PVDF in solution. 61
Figure 19: Optical micrographs of some electrospun fibres, A) ES15WT46DA 12_08_15, B) ES15WT37DA 13_1_12, C) ES16WT46DA 12_08_15 and D) ES16WT37DA 12_08_15. 64
Figure 20: Fibres elaborated with a FR of 1.2 mL/h: A) ES15WT46DA 13_12_12, B) ES15WT37DA 13_12_12, C) and D) ES16WT37DA 13_12_12 65
Figure 21: Fibres elaborated with an AP of 10 or 15 kV: A) ES15WT46DA 10_08_15, B) ES15WT46DA 15_08_15, C) ES16WT46DA 10_08_15 and D) ES16WT37DA 10_08_15. 66
Figure 22: Visible camera observation of where the Local Raman characterisation of the electrospun fibres were conducted: A1), A2) and A3 ES15WT37DA 10_08_15, B1), B2) and B3 are from ES16WT46DA 10_08_15, C1), C2) and C3) are from ES16WT37DA 10_08_15. 68
Figure 23 : FTIR spectra of: A) CNC and B) QC composite fibres. 70
Figure 24: DSC thermograms of the fibres composite with addition of A) CNC and B) QC. 70
Figure 25: WAXS diffractograms of the composite fibres with A) CNC and B) QC addition. 71
Figure 26: Raman spectra of the composite fibres with A) CNC and B) QC addition. 73
Figure 27: Optical micrographs of A) Type A fibres and B) Type B fibres. 77
Figure 28: Typical Brillouin spectrum of Type A fibres. 78
Figure 29: Example of fit on the Type A fibre spectrum. 78
Figure 30: Typical Brillouin spectrum of Type B fibres. 80

Figure 31 : Example of a Type B Brillouin spectrum fit. 80
Figure 32: TGA analysis of A) Type A fibres, and B) Type B fibres. 82
Figure 33: SEM micrographs of A) Type A and B) Type B fibres. 83
Figure 34: Calculated c_{11} values for the CNC samples, with sample average result. 85
Figure 35: Measures taken gradually closer to a QC cluster. 85
Figure 36: Fit and calculated Brillouin peak frequency gradually closer to the QC cluster (numerotation 1-4 corresponds to the points illustrated in Figure 35). 86
Figure 37: Optical micrograph showing the laser focused on a single Type A fibre. 87
Figure 38: Experimental spectra acquired at 0 and 110°C on a single PVDF fibre. 87
Figure 39: Evolution of the calculated c_{11} as a function of temperature. 88
Figure 40: Brillouin study of an oriented solvent-casted sample at high temperatures. 89
Figure 41: DSC determination of the glass transition of PVDF for various processing methods [214]. 89
Figure 42: Study of c_{11} as a function of temperature in the lower range (-73 to 13°C). 90
Figure 43: Static and dynamic properties determined at acoustic frequencies [215]. 90
Figure 44: Acoustic attenuation in the lower temperature range (-73 to 27°C). 91
Figure 45: Evolution of E' and tan δ as a function of temperature in DMA analysis of a solvent casted PVDF film. 91
Figure 46: Evolution of E' and tan δ as a function of temperature in DMA analysis of an electrospun PVDF film 92
Figure 47: DSC heating ramp at 10°C/min of A) Solvent casted PVDF and B) Electrospun PVDF fibres. 92
Figure 48: A) Second and C) Third heating cycles to 90°C on non-oriented PVDF. 94
Figure 49: DSC thermograms of the fibres heated to A) 90 and B) 110°C before full melting cycle. 95
Figure 50: Thermogram of the solvent-casted film submitted to three heating/cooling cycles 95
Figure 51: Discoloration on the PVDF film submitted to heating and laser beam. 96
Figure 52: TGA analysis of a solvent casted film. 97
Figure 53: Raman spectra taken in the brown region and discoloured white region of the sample. 97
Figure 54: Comparison on the spectra after definition of a baseline in A) the 780-920 cm^{-1} and B) the 1100-1600 cm^{-1} regions. 98
Figure 55: Brillouin frequency measured in the brown (1 and 4) and the white (2: centre and 3: off-centre) region of the sample. 98
Figure 56: Resulting Brillouin frequency shift due to laser exposure with a power of 3mW 99
Figure 57: Schematic diagram of a Berlincourt meter with 1) specimen, 2) probe, 3) electrode, 4) polarisation direction [231]. 102
Figure 58: Tapping test from human motion: A) Finger tapping [234], B) Foot tapping [235], C) Palm, wrist and elbow tapping [236] 103
Figure 59: Custom made tapping test setup [237]. 104
Figure 60: Effect of A) the contact area and B) the contact frequency on the output voltage and current [237]. 104
Figure 61: A) Schematic representation and B) photograph of the tapping test setup [239] 105
Figure 62: Peak-to-peak open-circuit voltage of A) non-encapsulated and B) PDMS-encapsulated devices made of poled PVDF, depoled PVDF, non-poled PVDF, Nylon and Teflon [239]. 105
Figure 63: A) Electrical testing setup and B) open-circuit voltage of the device as a function of the applied load [240] 106
Figure 64: A) Simple bending of a piezoelectric PVDF-based device and output voltage [241] and B) Output voltages of a PVDF-based membrane for monitoring the motions of body joints a) finger, b) wrist, c) elbow, d) ankle, e) toe, f) knee, g) cervical joint of hum and h) water flapping [242]. 107
Figure 65: A) Schematic illustration of the bending test, dependence of B) the open-circuit voltage and C) the short-circuit current on the bending angle, and D) an enlarged view showing the dependence of the open-circuit voltage on the bending angle [243]. 108
Figure 66: A) Functional diagram and B) photograph of the tapping test bench. 110

Figure 69: The force sensor mounted on the tapping test setup. 111
Figure 70: Short-circuit current of A) PZT, B) PVDF. 112
Figure 71: Measurement of motor-induced voltage A) without chassis connected to earth and B) with chassis connected to earth. 112
Figure 72: Short-circuit current of A) PZT, B) PVDF. 113
Figure 73: Voltage measurements for two different frequencies A) 3 Hz and B) 6 Hz. 113
Figure 74: Voltage measurement on a PZT buzzer with variating frequency from 1 to 5 Hz. 114
Figure 75: Current measurements for two different frequencies A) 1 Hz and B) 5 Hz. 114
Figure 76: Preparation steps of the PVDF devices A) the PET layer, B) the P-shaped electrode with the connecting wire, C) addition of the electrospun scaffold, D) the finished device. 115
Figure 77: A) Voltage and B) Current waveform of the pure PVDF nanogenerator under mechanical excitations from 1 to 5 Hz. 116
Figure 78: Zoomed view on the 5 Hz solicitation portion of A) Voltage and B) Current waveform of the pure PVDF nanogenerators. 117
Figure 79: A) Voltage and B) Current waveform of the PVDF-CNC devices under mechanical excitations at 5 Hz. 118
Figure 80: A) Voltage and B) Current waveform of the PVDF-QC devices under mechanical excitations at 5 Hz. 119
Figure 81: Voltage waveforms generated by the PVDF nanogenerator under increasing mechanical loads: A) 1.6 kg, B) 2.4 kg, C) 3.2 kg, D) 4.0 kg. 121
Figure 82: Energy harvesting and discharge circuit using a PVDF nanogenerator. 122
Figure 83: Estimated capacitor charging curve with PVDF and diode bridge. 122
Figure 84: Internal Functional Block Diagram of the LTC3588-1 piezoelectric energy harvesting power supply.. 123
Figure 85: Example of capacitor charge (from PZT buzzer). Each change in slope corresponds to a 1 Hz increment in the tapping frequency, here from 1 Hz to 5 Hz. 128
Figure 86: Capacitor charge from a CNC5 nanogenerator. Each 30s, a 1 Hz increment in the tapping frequency is applied, from 1 Hz to 5 Hz, and then back to 1 Hz. 129
Figure 87: Evolution of the PZT RMS power, voltage and current as a function of the load. 130
Figure 88: Evolution of the PVDF RMS power, voltage and current as a function of the load. 130
Figure 89: A schematic representation of the heart pulse sensing application. 131
Figure 90: Schematic diagram of the experimental setup. 131
Figure 91: Experimental setup for the PVDF-based energy harvesting test. 132
Figure 92: Charging profile of the 1000 µF capacitor obtained from experimental data recorded by the DMM 6500. 132
Figure 93: Voltage drop of the 1000 µF capacitor measured by the DMM 6500 during discharge into the LED load. 133
Figure 94: Current profile during the discharge of the 1000 µF capacitor into the LED, measured with the Power Profiler Kit II (PPK II). 133
Figure 95: Schematic representation of the pulse test bench. 135
Figure 96: A) No-load voltage of the oscilloscope probe (b) spectrum of the observed signal obtained after FFT. 135
Figure 97: A) voltage at the sample terminals in black, voltage filtered at a frequency of 5 Hz in red, B) spectrum of the signal filtered at 5 Hz after FFT. 136
Figure 98: A) voltage at the sample terminals in black, voltage filtered at a frequency of 10 Hz in red, B) spectrum of the signal filtered at 10 Hz after FFT. 136
Figure 99: A) voltage at the sample terminals in black, voltage filtered at a frequency of 20 Hz in red, B) spectrum of the signal filtered at 20 Hz after FFT. 137
Figure 100: Powering of the BLE module with a CNC5 device. 137

Figure 101: DLS results on CNC after 30 minutes of stirring. i
Figure 102: DLS results on CNC after sonication. i
Figure 103: DLS results on QC after 30 minutes of stirring. ii
Figure 104: DLS results on QC after sonication. ii
Figure 105: Overview of the tapping test machine. iii
Figure 106: Exploded view of the tapping test machine. iv
Figure 107: Connecting rod and weights assembly. iv
Figure 108: Zoomed view of A) the removable weights and B) the cell force and sample holder. v
Figure 109: NEMA 34 stepper motor datasheet [253]. vi
Figure 110 : Full torque curve of the NEMA 34 motor [254]. vi
Figure 111 : DM860T driver datasheet [255]. vii
Figure 112: Representation of an impulse signal [256]. ix
Figure 113: The Arduino Uno x
Figure 114: Impulse signal generated for a motor rotation at A) 1 Hz, B) 10 Hz. xi
Figure 115: Complete schematic wiring diagram of the tapping test bench. xi
Figure 116: Graphical diagram of the program execution sequence. xv
Figure 117: Serial port selection. xv
Figure 118: The test setting window. xvi
Figure 119: Voltage and current responses of CNC1 under mechanical excitation from 1 to 5 Hz. xvii
Figure 120: Voltage and current responses of CNC3 under mechanical excitation from 1 to 5 Hz. xvii
Figure 121: Voltage and current responses of CNC5 under mechanical excitation from 1 to 5 Hz. xvii
Figure 122: Voltage and current responses of QC1 under mechanical excitation from 1 to 5 Hz. xviii
Figure 123: Voltage and current responses of QC3 under mechanical excitation from 1 to 5 Hz. xviii
Figure 124: Voltage and current responses of QC5 under mechanical excitation from 1 to 5 Hz. xviii

List of tables

Table 1: DLS results on CNC after 30 minutes of stirring and after sonication. 34
Table 2: DLS results on QC after 30 minutes of stirring and after sonication. 35
Table 3: Pristine PVDF fibres electrospinning parameters for optimisation study. 36
Table 4: PVDF-based nanocomposites fibres. 37
Table 5: Correspondence of PVDF crystalline phases with corresponding planes and 2θ value [22,144–150]..... 40
Table 6: FTIR band assignation for phase identification in PVDF [138,155–160]. 42
Table 7: Characteristic Raman Bands of PVDF, with associated crystalline phase and vibration mode [158,162–166]. 44
Table 8: Name and composition of the devices. 48
Table 9: Area ratios between the Gaussian bands. 53
Table 10: Calculated values of crystallinity ratio and phase fraction using Raman spectroscopy and DSC. 54
Table 11: Pristine PVDF fibres electrospinning parameters for optimisation study. 55
Table 12: Calculated crystallinity ratio values and melting temperatures obtained from DSC analyses. 58
Table 13: Calculated crystallinity ratio values from WAXS diffractograms. (Introduce some evaluation of the precision on the values measured and calculated) 60
Table 14: Calculated crystallinity ratio and crystalline phase fractions values from Raman spectra. 63
Table 15: Crystallinity ratio and crystalline phase fractions from local Raman characterisation. 68
Table 16: Calculation of the crystallinity ratio of the fibres with addition of CNC and QC. 71
Table 17: Crystallinity ratios of the composite fibres with CNC and QC addition calculated from WAXS diffractograms. 73
Table 18: Crystallinity ratio and crystalline phase fractions from Raman characterisation of the composite fibres. 74
Table 19: Electrospinning parameters for the elaboration of the PVDF fibres. 77
Table 20: Calculated peak frequencies and corresponding c_{11} values for Type A fibres. 79
Table 21: Calculated peak frequencies and corresponding c_{11} values for Type B fibres. 81
Table 22: Crystallinity ratio (xc) and fraction in the crystalline phase of the three main crystalline phases observed in PVDF, α, β and γ, as measured by Raman spectroscopy. 81
Table 23: Name and composition of the devices. 115
Table 24: Comparative table of the PVDF-Based Nanogenerators electric performances. 120
Table 25: Comparison of the energy management modules. 126
Table 26: Pin definition of the DM860T [255]. viii
Table 27: Microstep resolution configurations of the DM860T [255]. ix

List of abbreviations

ATR: Attenuated Total Reflection

AV: Applied Voltage

BLE: Bluetooth Low Energy

CNC: Cellulose Nanocrystals

DLS: Dynamic Light Scattering

DMA: Dynamic Mechanical Analysis

DMF: Dimethylformamide

DSC: Differential Scanning Calorimetry

d_{33}: Piezoelectric Coefficient

EH: Energy Harvesting

FR: Flow Rate

FTIR: Fourier Transform Infrared Spectroscopy

IJL: Institut Jean Lamour

IoT: Internet of Things

I_{pp}: Peak-to-Peak Current

LED: Light Emitting Diode

MEMS: Micro Electronic Mechanical Systems

MGU: Mahatma Gandhi University

Mw: Average Molar Mass

PDMS: Polydimethylsiloxane

PET: Poly(ethylene terephthalate)

PVDF: Polyvinylidene Fluoride

PZT: Lead Zirconate Titanate

QC: Quasicrystals

SEM: Scanning Electron Microscopy

TCD: Tip-to-Collector Distance

T_m: Melt Temperature

T_g: Glass Transition

TGA: Thermogravimetric Analysis

UI: User Interface

V_{peak}: Peak Voltage

V_{pp}: Peak-to-Peak Voltage

WAXS: Wide Angle X-ray Scattering

XRD: X-Ray Diffraction

χ_c: Crystallinity ratio

General Introduction

The rapid growth of the Internet of Things (IoT) is considered one of the major technological advancements of the twenty-first century. IoT devices are found in a multitude of applications, including but not limited to embedded electronics, MEMS (microelectromechanical systems), biomedical implants, wireless sensors, foldable and wearable devices. This technology has not only won over the general public, it has also become of great interest to the industry, which sees its potential in improving business processes and overall productivity, and to the world of research. However, most of these objects are currently powered using batteries. This solution poses a number of problems concerning size, weight, rigidity, limited lifespan, difficulty in replacing batteries in the event of malfunction, and difficulty in producing and recycling batteries [1–9].

An alternative would be to recover the energy needed to power the device from its immediate environment. This process is called energy harvesting. Various possible sources can be considered, such as wind, solar, vibration, movement, electromagnetism, thermal and biomass. The transduction mechanism studied in this thesis is piezoelectricity, which consists of converting deformation into electrical energy. It is a particularly promising route for applications requiring very low amounts of energy. One of the earliest and well-known piezoelectric material is quartz, and nowadays the materials exhibiting the highest piezoelectric coefficients are ceramics. Nonetheless, environmental concerns and technical limitations, such as bulkiness and rigidity, have led to the search for alternatives [10–14].

Although they possess lower d_{33} piezoelectric constants compared to ceramics, piezoelectric polymers offer a broad array of uses by exhibiting good mechanical and processing properties, and offering flexibility, light weight, low costs and biocompatibility. Piezoelectric polymers can be either synthetic like polyvinylidene fluoride (PVDF), polyacrylonitrile (PAN), poly(l-lactic acid) (PLLA), polyurethane (PU), and polyamides (PA) or natural such as collagen, cellulose or chitin. Among those, polyvinylidene fluoride (PVDF) is the most widely studied piezoelectric polymer, because of its good electro-mechanical coupling properties, high chemical stability, flexibility and biocompatibility [15–21].

PVDF can crystallise in five crystalline phases: α, β, γ, δ and ε, among which α, β and γ are the prominent ones. The α phase is the most thermodynamically stable crystalline phase, and is naturally obtained from the melt with a trans-gauche-trans-gauche conformation, which makes it non-electroactive. The β phase has a zigzag all-trans conformation which allows it to possess the highest electric dipole moment of all PVDF crystalline phases, and exhibit ferro-, piezo- and pyroelectric properties. Several processing methods can be used to achieve crystallisation in the β phase, such as mechanical stretching, poling (application of a strong electric field), heat treatments, mixing with other polymers and copolymerisation [22–31].

Among the elaboration methods of PVDF films, electrospinning is a particularly promising innovative technique. The equipment required consists of a high-voltage source, a syringe containing the polymer in solution fitted with a metal needle, and an electrode connected to earth. This method has the advantage of combining the high stretching and *in situ* poling stages. The nanofibrous scaffolds obtained *via* electrospinning have been demonstrated to show higher electric responses compared to plain PVDF films [32–36].

Another route commonly explored to improve the β phase fraction in PVDF films is the addition of nanofillers. Moreover, depending on the filler nature, several benefits can be achieved with their addition, such as enhanced dielectric, piezo- and triboelectric properties, increased mechanical strength, better thermal stability, or extra properties, like magnetic properties for example. Kept at lower weight fractions, the filler can be introduced in the polymeric solution and electrospun to benefit from the advantages of the electrospinning process [37–43].

The aim of this thesis is to develop an energy generator for harvesting mechanical energy. The first stage of the project consists of producing PVDF fibre mats by electrospinning, with the addition of various fillers: nanocellulose crystals and Al-Cu-Fe-B quasicrystals. The use of electrospinning and the addition of fillers aim to maximise the formation of electroactive crystalline phases in PVDF, which is a major challenge for the thesis. The electrospun PVDF-nanocomposite scaffolds are then characterised, and made into mechanical energy harvesting nanogenerators and sensors.

The first chapter of this thesis provides a state-of-the-art review of the development of PVDF and PVDF-nanocomposites fibres. It imparts the fundamental knowledge about PVDF, and an in-depth explanation of the electrospinning process and associated challenges. The recent developments in energy harvesting and sensing applications of such materials are also explored.

The second chapter focuses on the presentation of the used materials, elaboration techniques of the PVDF films and nanocomposite fibres, and techniques used during the thesis for the characterisation of the materials. The fabrication process of the nanogenerator devices is also detailed, along with an overview of the custom-built tapping test bench and instrumentation used to test the electric response of the devices.

As previously mentioned, maximising the electroactive phase content within the PVDF scaffolds is one of the key challenges of the subject. Hence, a routine aiming at characterising the crystallinity of the materials (crystallinity ratio and crystalline phase fractions) using results from four different techniques: DSC, WAXS, FTIR and Raman spectroscopy. A new simplified Raman criterion is also proposed. The routine including the four techniques is then used to analyse the results of an optimisation study of the electrospinning parameters, and choose the most appropriate set of parameters, regarding the goal of maximising the electroactive phase content. The routine is also applied to nanocomposite fibres, to evaluate the impact of filler addition on the fibre crystallinity.

Once the optimised parameters have been selected, it is necessary to make sure the scaffolds will withstand the mechanical solicitations linked to the mechanical energy harvesting. The fourth chapter shows how micro-Brillouin spectroscopy allowed to investigate the difference the DMF:Acetone ratio can make on the elastic response of electrospun fibres. It is noteworthy that none of characterisation techniques previously employed showed differences between fibres based on the solvent ratio employed. Moreover, a study was performed on nanocomposites fibres to investigate how filler addition could impact the mechanical properties of the fibres. Finally, by studying the evolution of mechanical properties of the fibres with temperature, an unexpected elastic anomaly is demonstrated and studied.

The last chapter of this thesis is dedicated to the electric characterisation of the PVDF devices. After showing that usual testing methods are not well suited to electrospun materials, the design and implementation of the custom-built tapping-test bench is introduced. This fully instrumented bench is then used to compare the performances of pristine and composite electrospun scaffolds. After the selection of a suitable energy harvesting circuit board, a demonstrator pulse-monitoring application showing the energy harvesting and sensor abilities of the devices is presented.

Chapter 1: A review on electrospun PVDF-based nanocomposites - Recent trends and developments in energy harvesting and sensing applications

This first chapter is based on a literature review article previously published in Polymer:

A review on electrospun PVDF-based nanocomposites: Recent trends and developments in energy harvesting and sensing applications. Sreelakshmi Moozhiyil Purushothaman, ***Maïté Fernandes Tronco****, Bicy Kottathodi, Isabelle Royaud, Marc Ponçot, Nandakumar Kalarikkal, Sabu Thomas, Didier Rouxel. Polymer, 2023, vol. 283, p. 126179. DOI: 10.1016/j.polymer.2023.126179*

Before proposing the review article, a first section sums the fundamental knowledge about the use of Polyvinylidene fluoride (PVDF) for sensor and energy harvesting applications. The first part is dedicated to the semi-crystalline microstructure of PVDF, which is of utmost importance in controlling the final electric response of PVDF-based devices. Then, the second part focuses on the elaboration methods of PVDF films. It provides an in-depth description of the electrospinning process and the importance of the optimisation of the process parameters. The interest of filler addition to PVDF materials is also discussed.

1. PVDF for sensor and energy harvesting applications

1.1. Semi-crystalline microstructure of PVDF

Polyvinylidene fluoride (PVDF) is a semicrystalline homopolymer of molecular formula $(-CH_2-CF_2-)_n$. Depending on the conditions of elaboration, PVDF exhibits five crystalline polymorphs: α, β, γ, δ and ε [30,44]. Among those crystalline phases, α, β and γ are the most prominent, hence they are also the most studied. The thermodynamically stable phase is the α phase, and is naturally obtained from direct melt crystallisation [45]. Unfortunately, due to its trans-gauche-trans-gauche conformation, this phase is non-polar and non-electroactive. The electroactive character of PVDF is mainly governed by the presence of the β and γ phases. With an all trans conformation, the β phase offers the largest dipole moment (8.10^{-3} C.m) [46] and piezoelectric coefficient out of all PVDF phases. In order to enhance the formation of this phase, the combination of mechanical stretching and poling (polarisation under the application of a high electrical field) is required [47]. In terms in electroactive properties, the γ phase can be considered as an intermediate between α and β phases, and possesses a T_3GT_3G conformation. It is usually obtained after crystallisation under high pressure or temperature, and annealing of α crystals [48–50].

1.2. Elaboration of PVDF fibres through electrospinning

The most commonly used fabrication techniques of PVDF films are solvent casting [24,51–54] and spin coating [55–57]. Lately, a new technique called electrospinning has gained a lot of traction for the obtention of highly-oriented nanosized fibres containing a high β phase content without requiring additional post-treatment steps. Basically, the equipment can be summed up as a high-voltage source, a syringe containing the polymer in solution fitted with a metal needle, and an earthed electrode. Through the application of a high voltage, a viscoelastic jet formed will be submitted through uniaxial stretching, and upon evaporation of the solvent, solidified fibres can be collected [33,35]. The outcome of the electrospinning process can be affected by various parameters, thus prompting the optimisation of said parameters. They can be classified in three categories: solution parameters (polymer concentration in the solution, type of solvent, solution viscosity and conductivity), process parameters (applied

voltage, tip-to-collector distance, flow-rate, type of collector), and ambient parameters (humidity, temperature) [58–64].

Among the solution parameters, the molecular weight and concentration of the used PVDF and solvent choice are the easiest to tune. With increase of the molecular weight the viscosity of the polymeric solution logically increases as well. Such solution generally lead to higher β phase fraction as it takes a higher time to reach the collector, allowing more stretching of the jet and better evaporation of the solvents [65–68]. Similarly, increasing the concentration of PVDF is solution improves the β phase formation by allowing better stretching of the jet. However, increasing the concentration in excess causes the solution to become so viscous it is harder to stretch, impeding the stretching effect [69–71]. Regarding the choice of solvents used for the dissolution of PVDF and elaboration of the polymeric solution, using polar solvents like DMF helps with the formation of the electroactive phases. A mix with a volatile solvent like acetone tends to lower the α phase fraction and formation of defects like beading. However, an excess of acetone can interfere with the electrospinning process, with solidification of the solution at the needle tip due to the accelerated evaporation rate [69,72–74]. Although the appropriate solvent ratio depends on other selected parameters, commonly used DMF:Acetone ratios are 4:6 and 3:7 [75–77].

Electrospinning process parameters also need careful tuning. The applied voltage is generally in the order of magnitude of 10-15 kV. Increasing the voltage helps to obtain higher β phase content through stretching, but excessively high values lead to the formation of defects and ultimately braking of fibres and electrospraying [78–80]. An aspect tied to the applied voltage is the question of the fibre *in situ* polarisation during the electrospinning process. As stated in the work of Lei *et al*. [81], some works have demonstrated high-output piezoelectric nanogenerators made of electrospun PVDF fibres, without extra poling required [82–86]. However, other authors claim that an extra poling treatment is necessary to achieve the dipole orientation [87,88]. Even, some authors propose that the electret behaviour of the electrospun fibres generated by a combination of the process and triboelectric effect is predominant compared to a possible piezoelectric effect [89,90]. As of today, it seems that a scientific consensus is yet to be reached.

The average tip-to-collector distance is located between 10-20 cm. A compromise has to be found between improved stretching and solvent evaporation time, and defect formation occurring at higher values [60,64,91–93]. The choice of the solution flow rate is again a matter of balance. Lower flow rates allow higher stretching and poling of the jet, and longer solvent evaporation times. A selected value too low can lead to the bubble formation inside the needle, however with higher flow rate there is a risk of needle clogging [60,64,91–94].

While ambient parameters might be more challenging to control precisely, they too affect the electrospinning outcome. At higher temperature the solvent evaporation rate in increased, and the solution viscosity tends to decrease, which will affect the crystalline phase formation following the same above-mentioned logic. Increasing the temperature can also help with achieving more uniform fibres, but in excess it will favour the apparition of beads. Low relative humidity is privileged in order to obtain smooth and thin fibres. A raise in the relative humidity can lead to the formation of pores, bumps and grooves in the fibres. The evaporation of the solvents can also be hindered [69,95–100].

1.3. PVDF nanocomposite fibres

In addition to the possibility of obtaining PVDF fibres displaying high electroactive phase fraction from a one-step process, electrospinning also allows the elaboration of composite fibres. Usually, the intended effect of nanofillers addition is the increase of the electroactive phases fractions, and more specifically the β phase, and ultimately the piezoelectric coefficient. This effect can be obtained through the interaction between the hydrogen atoms of PVDF and the negatively polarised surface of the fillers, or in the contrary, in the case of nanocellulose, through the

formation of hydrogen bonds between the fluorine atoms of PVDF and hydroxyl groups of cellulose [40,101]. Depending on the targeted application of the electrospun fibres, other interesting properties can be tailored via nanofiller addition, such as mechanical strength [37,101–106], thermal stability [107,108] or thermal and electrical conductivity [109–117] for example. As a complement to the mechanical energy harvesting possibilities of electrospun PVDF-based nanocomposites, hybrid nanogenerators can be fabricated by including nanoparticles that will add extra properties to the materials. The use of ferromagnetic fillers allows to use electromagnetic fields as a new power source that is not usable in the case of pristine PVDF fibres [118–120].

2. A review on electrospun PVDF-based nanocomposites: Recent trends and developments in energy harvesting and sensing applications

Polymer 283 (2023) 126179

Contents lists available at ScienceDirect

Polymer

journal homepage: www.elsevier.com/locate/polymer

A review on electrospun PVDF-based nanocomposites: Recent trends and developments in energy harvesting and sensing applications

Sreelakshmi Moozhiyil Purushothaman [a], Maïté Fernandes Tronco [a], Bicy Kottathodi [a,b], Isabelle Royaud [a], Marc Ponçot [a], Nandakumar Kalarikkal [b], Sabu Thomas [b], Didier Rouxel [a,*]

[a] Université de Lorraine, CNRS, IJL, F-54000, Nancy, France
[b] International and Interuniversity Centre for Nanoscience and Nanotechnology, Mahatma Gandhi University, Kerala, India

ARTICLE INFO

Keywords:
PVDF-Nanocomposites
Electrospinning
Piezoelectricity
Triboelectricity
Hybrid nanogenerators

ABSTRACT

Modern-day requirements for efficient, eco-friendly, and self-powered devices have resulted in a growing interest in piezoelectric polymers among the scientific community. Polyvinylidene fluoride (PVDF) is an excellent electroactive polymer that is flexible, with high mechanical strength, thermal stability, and biocompatibility. The relatively low cost and easiness to be fabricated into thin pliable films made PVDF one of the most studied polymers for the development of nanogenerators and wearable sensors. The piezoelectric properties and therefore the energy harvesting and sensing capabilities of PVDF are distinct characteristics of its electroactive polar phases, especially the β phase. Hence, several PVDF-based nanocomposites that could achieve a high β phase fraction have been widely explored. Electrospinning is one of the best methods for manufacturing such PVDF-based nanocomposite films. This article, therefore, highlights essential information about different electrospinning parameters which help to enhance the β phase in PVDF. The review then progresses into the recent developments and technological advances of electrospun PVDF-based nanocomposite devices in energy harvesting and sensing applications. The piezo-, pyro-, and triboelectric properties of PVDF allow the fabrication of conventional and hybrid nanogenerators. The later can harvest energy simultaneously from multiple sources, sense various fluctuations in their surroundings, and transmit the acquired data immediately when integrated with Bluetooth or wireless devices. They are fine models of self-powered, portable, multifunctional, and sustainable engineering. Finally, a peek into the other possible applications of electrospun PVDF-nanocomposite fibers is also made. Overall, the review aims to illustrate the innovative research and developments of PVDF fiber-based devices and the relevance and prospects they hold as future green sources of energy.

1. Introduction

Technological advances and rising global energy consumption have turned wireless and self-powered devices into one of the requirements of the 21st century. Compactness, flexibility, durability, portability, and the ability to be integrated with other devices are other features expected of such modern devices. A possible solution to satisfy all the aforementioned requirements is the use of electroactive materials. Hence, a wide variety of piezoelectric, pyroelectric, and triboelectric materials have been explored for the development of energy harvesters and self-powered sensors. The ability of these materials to electrically respond to the omnipresent energy sources of mechanical vibrations and heat makes them exceptionally suitable for sustainable energy harvesting.

Quartz is a well-known piezoelectric material and was one of the first to be identified [1]. Some of the later materials include zinc oxide (ZnO), barium titanate ($BaTiO_3$), and lead zirconate titanate ($Pb(ZrTi)O_3$) (PZT) [2–4]. These ceramic materials possess high piezoelectric coefficients and high electroactive potential but have poor flexibility and a high-cost preparation process. Their toxicity also questions their suitability as ideal clean and green sources of energy [5,6]. Hence, it became necessary to investigate another class of piezoelectric materials: polymers. Polymers are flexible, with enhanced mechanical strength, and are lightweight, affordable, and biocompatible [7–10]. Many piezoelectric polymers are available, whether synthetic such as polyvinylidene fluoride (PVDF), polyamides, and polyL-lactic acid (PLLA) [11,12], or natural like cellulose, keratin, collagen, or chitin [13]. Among these, PVDF is one of the most explored and efficient piezoelectric polymers, which

* Corresponding author.
E-mail address: didier.rouxel@univ-lorraine.fr (D. Rouxel).

https://doi.org/10.1016/j.polymer.2023.126179
Received 17 February 2023; Received in revised form 9 June 2023; Accepted 28 June 2023
Available online 10 July 2023
0032-3861/© 2023 Elsevier Ltd. All rights reserved.

also exhibits pyroelectric and triboelectric properties. The outstanding properties of this fluoro-polymer lead to its frequent selection for the development of energy generators and sensors. This claim is statistically justified by the increasing number of publications on topics such as "PVDF", "PVDF- Energy harvesting", "PVDF-Electrospinning" and "PVDF-Electrospinning-Energy harvesting" (as obtained from the Web of Science core database of the Université de Lorraine, France, https://www-webofscience-com.bases-doc.univ-lorraine.fr/wos/bci/analyze-results/ac23749a-4a75-4103-8d9a-160d7ffa07de-9034f4bb). This article provides a brief description of PVDF and explores a wide variety of PVDF-based nanocomposites. Because of the increasing use of electrospinning to manufacture PVDF films, it also details the effect of various electrospinning parameters on PVDF. The review then focuses on the energy harvesting applications of electrospun PVDF and explains the recent trends and technological advances in the field of piezoelectric, pyroelectric, and triboelectric nanogenerators and sensors. Moreover, a new and emerging technology for energy harvesting, the hybrid nanogenerators, is also detailed. These devices can simultaneously harvest energy using the piezo, -pyro, and triboelectric properties of PVDF and sense various fluctuations in the surrounding environment. When integrated with wireless data-transmitting devices, they have the potential to become a true example of portable, multipurpose, multifunctional, and sustainable engineering. The inspiration behind this paper is to highlight the potential of electrospun PVDF films, with a focus on these devices, and inspire their integration as innovative sustainable sources of energy. To the best of our knowledge, there are no recent reviews that focus on all the above-mentioned types of nanogenerators together, and the wide variety of energy sources they could detect as sensors or use in the process of energy harvesting. In addition, a brief overview of other applications of such films is also presented. The current review is also significant as a good reference for the scientific community to look forward to the real-life applications and perhaps the commercialization of PVDF-based multifunctional devices as depicted in Fig. 1.

1.1. Fundamentals of PVDF

PVDF $(-CH_2-CF_2-)_n$ is a semicrystalline thermoplastic homopolymer [15,16]. It is a promising electroactive polymer with wide frequency responses, exceptional sensitivity, high piezoelectric coefficient, high dipole moment in the polar phases, and high thermal stability [17–25]. Depending on the different processing parameters and post-treatments, PVDF is found to exist in five different crystalline phases (α, β, γ, δ, and ε) [26]. The three principle phases are represented in Fig. 2. In general, PVDF crystallizes in the non-polar α phase and is commonly obtained by crystallization from the melt. The polymer chains adopt a trans-gauche-trans-gauche (TGTG) conformation, which is the thermodynamically favorable form of PVDF due to the minimal steric strains [27–29]. Uni- or bi-axial stretching [30,31], poling under a high electric field [31,32], pressure quenching [33], or sample fabrication techniques such as electrospinning [34,35] or spin coating [36] align the polymer chains in the all-trans (TTTT) conformation called the β phase (also referred to as phase I) [29]. In this phase, the dipole moments of C–F and C–H bonds add up so that an effective dipole moment develops in the direction perpendicular to the carbon backbone. Hence, as the highly polar phase of PVDF, the β phase is the most widely studied [37–39]. A semipolar polymorph of PVDF known as the γ phase is obtained by annealing at high temperature and pressure, slow melting, and recrystallization from different solvents or using different surfactants. In the γ phase, the polymer chains take a TTTGTTTG or T3GT3G conformation [15,40]. Often, the β phase and γ phases are together called the electroactive phases of PVDF. The δ phase of PVDF is the polar analog of the α phase. The ε phase is the antipolar analog of the γ phase. The δ phase can be obtained through the transition of the α phase with apparently no change in the chain conformation, and by the application of electric fields near 1 MV/cm at room temperature. At high temperatures, the δ phase easily transforms into a mixture of polymorphs in which small amounts of the ε phase are obtained along with a higher amount of the γ

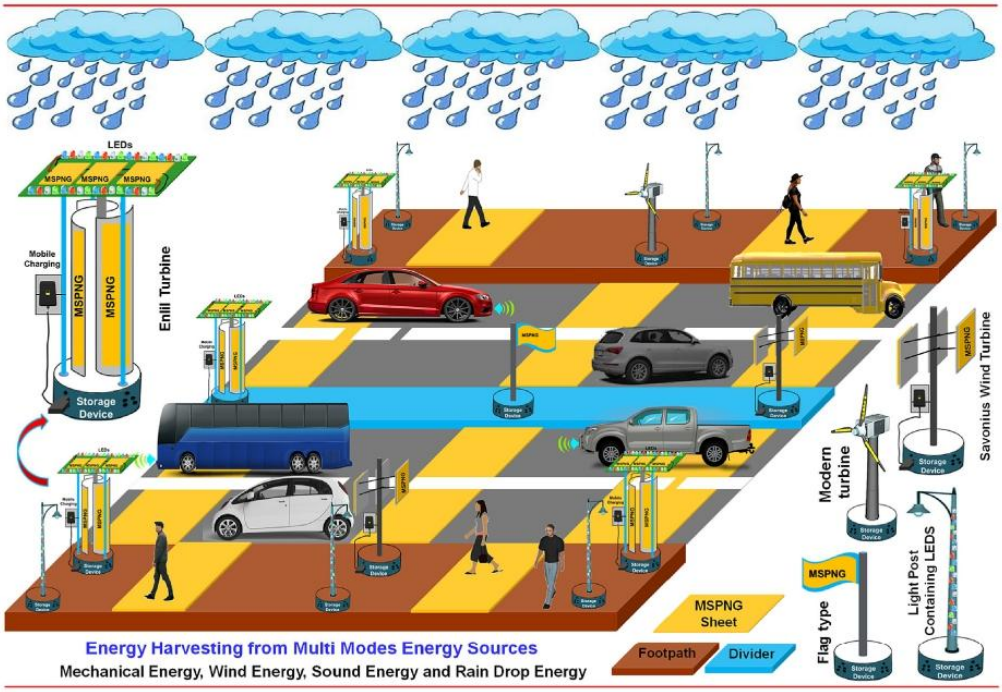

Fig. 1. Schematic visualization of the futuristic possible applications of PVDF-based multi-modes single piezoelectric nanogenerator devices (MSPNG) (reproduced with permission from Ref. [14]).

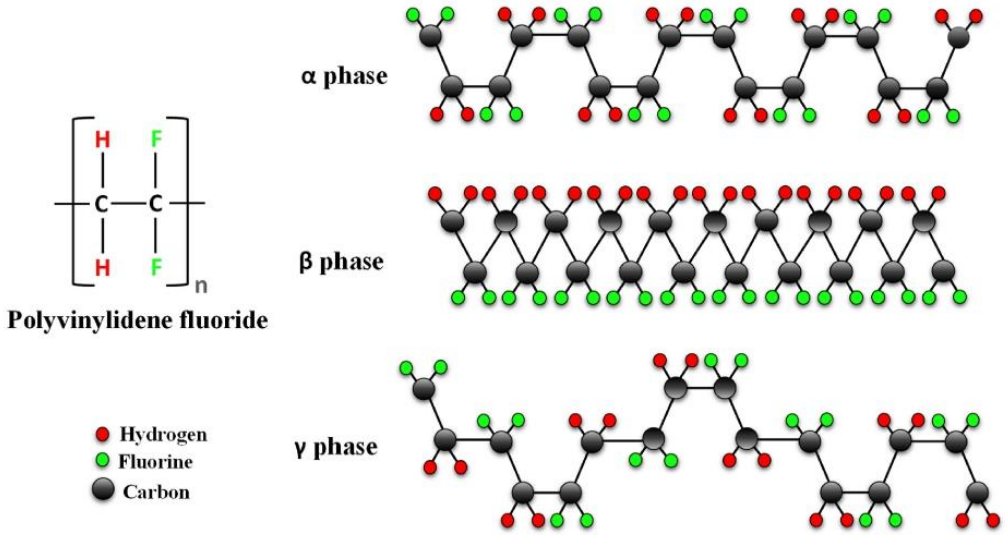

Fig. 2. Schematic representation of the α, β and γ phase of PVDF.

phase. [26,41–43].

The content of the three principle crystalline phases in PVDF is commonly investigated using Fourier Transform Infrared Spectroscopy (FT-IR). From the FT-IR spectra, the α phase can be identified from the bands at 1423, 1383, 1214, 1146, 976, 854, 796, 764, 615, and 532 cm^{-1} [44–50]. The characteristic band of the β phase which is not composed of other crystal modifications occurs at 1275 cm^{-1}, and the bands at 510 and 841 cm^{-1}, though initially considered to be characteristic of the β phase, are characteristic of both the β and γ phases. The characteristic bands of the γ phase occur at 813 cm^{-1}, 833 cm^{-1}, and 1232 cm^{-1} [37,44,45,48,51–65]. Apart from identifying the presence of different crystalline phases from the band positions, the fraction of the electroactive (EA) phases and α phase can be estimated as follows:

$$F_{EA} = \left(\frac{A_{EA}}{\frac{K_{840}}{K_{763}} * A_{763} + A_{EA}} \right) * 100\ \%$$

$$F(\alpha) = 100 - F_{EA}\ \%$$

where F represents the fraction of the corresponding phase; A_{EA} and A_{763} are the absorbance values at 840 and 763 cm^{-1}, respectively; K_{840} and K_{763} are the absorption coefficients at the respective wave numbers and are equal to $7.7x10^4$ and 6.1×10^4 cm^2 mol^{-1}, respectively.

Furthermore, the individual fraction of β and γ phases can be estimated as follows:

$$F(\beta) = F_{EA} * \left(\frac{\Delta H_{\beta'}}{\Delta H_{\beta'} + \Delta H_{\gamma'}} \right)$$

$$F(\gamma) = F_{EA} * \left(\frac{\Delta H_{\gamma'}}{\Delta H_{\beta'} + \Delta H_{\gamma'}} \right)$$

where $\Delta H_{\beta'}$ and $\Delta H_{\gamma'}$ are the height differences (absorbance differences) between the 1275 cm^{-1} peak and the nearest valley of 1260 cm^{-1}, and the 1234 cm^{-1} peak and the near valley of 1225 cm^{-1}, respectively [66].

X-ray diffraction (XRD) studies can also be used to distinguish the different phases in PVDF. XRD patterns show characteristic peaks of the α phase at 18.4° and 20.0° and two weak peaks at 26.6° and 35.9° corresponding to (020), (110), (021) and (200) reflections [43,66–69]. The peak at 20.6° due to the sum of the diffraction in the (110) and (200) planes and another one near 36.5° due to (020) reflections are the characteristic peaks of the β phase [61,66,69–73]. The characteristic peaks of the γ phase occur around 18.5 °, 20.3 °, and 39.0 ° because of the diffraction from the (020), (110/101), and (211) planes [66,67,70,74–76]. By curve deconvolution of the XRD spectra, the overall degree of crystallinity (χ_C), as well as crystallinity of β ($\chi_{C\beta}$) and γ ($\chi_{C\beta}$) phases can be calculated using the following equations:

$$\chi_C = \frac{\sum A_{CR}}{\sum A_{CR} + \sum A_{amr}} * 100\%$$

$$\chi_{C\beta} = \chi_C * \frac{\sum A_\beta}{\sum A_\beta + \sum A_\gamma}$$

$$\chi_{C\gamma} = \chi_C * \frac{\sum A_\gamma}{\sum A_\beta + \sum A_\gamma}$$

where, ΣA_{cr} and ΣA_{amr} represent the summation of the total integral areas of crystalline diffraction peaks and amorphous halo, respectively; ΣA_β and ΣA_γ are the area under crystalline β− and γ− peaks, respectively [77].

The determination of the fraction of each crystalline phase is important as the electroactive response of PVDF is determined by the content of the electroactive polar phases, especially the β phase. This fraction can vary under the influence of the electric field, temperature, or mechanical stress [30,38,45,77,78]. Considering the electric properties of PVDF is helpful to further understand the reasons behind this. In PVDF each monomer unit has an electric dipole moment directed perpendicular to the carbon backbone. Each monomer unit has a dipole moment of 8.10^{-30} *Cm* in the β phase and 5.10^{-30} *Cm* in the α phase. However, as these monomer units crystallize in anti-parallel orientation, the net dipole moment becomes zero in the α phase [79–83]. Dipole moments of PVDF can be permanently aligned to acquire considerable remnant polarization by the application of a high electric field, with or without applying temperature. Though polarization can take place upon heating, thus allowing the chains to rotate more easily [84], the application of higher temperatures can cause depolarization of the PVDF samples. The thermal depolarization of PVDF was studied by Eberle and Eisenmenger using a mechanically stretched and poled PVDF film with a

high fraction of β phase [85]. The β-PVDF which has high spontaneous polarization also exhibits the maximum ferroelectric response, highest remnant polarization, and coercive field [86–89]. In the study of Eberle and Eisenmenger, it was observed that with increased heating temperature, the remnant polarization of the PVDF film decreased slowly from 5.4 μC/cm^2 at 20°C and tended to zero at 180°C. Even after cooling down to 20°C, the values did not increase considerably except for an anomaly at 180°C. As the electroactive behavior of PVDF is associated with its absence of a centre of symmetry, high dielectric constant, and also the polarization of the material, depolarization of the film will significantly lower all its electroactive properties [82,90–92].

Though well-known as a potential dielectric material, extensive studies on the electroactive behavior of PVDF leaped with the discovery of piezoelectricity in PVDF by Kawai in 1969 [93]. The value of piezoelectric coefficients, such as d33 and d31 are often used to evaluate the piezoelectric properties of PVDF. Typically, PVDF exhibits d31 values between 8 to 22 pC/N and d33 values between -24 to –34 pC/N. However, these values can be significantly tailored through the modification of the polymer processing conditions, heat treatments, poling under high electric field, nano-confinement, formation of blends, formation of nanocomposites by the addition of fillers, electrospinning and creation of porous structures [94–97]. The discovery and detailed studies on the piezoelectricity in PVDF later lead to the exploration of the pyroelectric properties of PVDF which are related to the ferroelectric phase content of PVDF. The pyroelectric coefficient (p) of PVDF is typically observed to be between 0.27×10^{-4} and 0.357×10^{-4} C/m^2 K. However, the pyroelectric properties are also tunable like the piezoelectric properties [98–100].

1.2. PVDF based nanocomposites

There are different manufacturing methods to modify the properties of PVDF like copolymerization, blending, and addition of nanofillers. Compared to copolymers and blends, PVDF-based nanocomposites allow them to obtain distinct physicochemical properties that are otherwise difficult to tune. This is due to the higher surface-to-volume ratio and subsequent higher contact area of the fillers with the polymer matrix. The commonly used fillers can be classified as inorganic, organic, or bio-fillers, carbon-based fillers, and hybrid fillers. A few examples of inorganic fillers include metal nanoparticles like gold [55] or palladium [45], metal salts such as $CaCl_2$, $BaCl_2$ [101], several ferrites such as $ZnFe_2O_4$ [102], $CoFe_2O_4$ [103], and carbon-based materials like carbon nanotubes, graphene or graphene oxide [77,104]. Examples of organic include nanocellulose, chitin, and chitosan [105–107], and hybrid fillers include organometallic compounds, combination of fillers like multi-walled carbon nanotubes (MWCNT)-Cloisite 30B hybrid nanoparticles and titanium dioxide (TiO_2) nanoparticles-graphene oxide (GO) [108–110].

The selection of the fillers is often made to improve (or alter) the properties of the matrix and is specific to the final application of the polymer nanocomposite. However, a few of the basic properties to be considered are the chemical composition, shape, size, and aspect ratio of the fillers [111–113]. The synergic effect of the nanofillers is generally due to the interaction of the electronegative fluorine atom with the electropositive metal atom in a metallic compound or the positive surface charge of the fillers. It sometimes can be due to the interaction of the electropositive hydrogen atom with the effective negative surface charge of the fillers. But in the case of fillers like nanocellulose, a hydrogen bond is formed between the fluorine atoms of PVDF and hydrogen atoms of the filler [45,114]. Karan *et al.* suggested that in the case of composite fillers such as aluminum oxides decorated reduced graphene oxide (AlO-rGO) sheets, β-phase nucleation can occur through stress-induced polarization, in addition to surface charge-induced polarization. Here, external mechanical forces build a potential in the AlO-rGO nanosheets which aligns the PVDF dipoles in the direction of the applied force [115]. Just like the filler composition, the morphology of the fillers can also affect PVDF-filler interaction. For example, Fu *et al.* demonstrated this dependence by studying PVDF-$BaTiO_3$ spherical nanoparticles (BTNPs) and PVDF-$BaTiO_3$ nanorods (BTNRs) composites [116]. The higher interfacial area of the BTNRs/PVDF composite compared to the BTNPs/PVDF nanocomposites was found to enhance the interface polarization in the first configuration. Mendes *et al.*, from studies on PVDF-$BaTiO_3$ composite films, concluded that smaller nanoparticles act as nucleating agents for the β phase of PVDF during polymer phase crystallization. Larger particles, due to the reduced relative interaction area for a given volume concentration, can cause defect formation [117]. Apart from the type of fillers used, the properties of the nanocomposite will also depend on its filler dispersion, lattice matching, processing conditions, and, importantly, the relative fraction of the fillers. Every researcher chooses the most adequate fraction of fillers by studying the different films they prepared based on prior assumptions. This can be clearly understood from every research article illustrating the wide variety of applications of PVDF-based nanocomposites.

Very often, the primary intention behind the addition of fillers in the PVDF matrix is to increase the fraction of β phase, and piezoelectric coefficients in the case of piezoelectric applications. Indeed, the presence of nanofillers was observed to reduce the nucleation energy barrier and thus enhance the crystallization rate and the degree of crystallinity of PVDF [94]. For example, Thakur *et al.* observed that, by introducing ZnO NPs into a PVDF matrix, the β-phase content increased up to 84% (0.85 vol% of ZnO) and the piezoelectric coefficient d33 increased to 50 pC/N from 22.3 pC/N at 50 Hz [118]. The addition of fillers to PVDF can enhance its other properties as well, such as in the study of Elizalde *et al.* Here, they focused on altering the hydrophobicity and wettability of PVDF through the addition of chitosan. Similarly, Zhou focused on increasing the thermal conductivity of PVDF by adding core–shell-structured aluminum (Al) particles [119], while Ram et *al.* were working on both the thermal and electrical conductivity of PVDF-carbon black nanocomposite films [120]. The addition of such high electric conductivity fillers to PVDF increases the overall conductivity of PVDF-nanocomposite films, which also increases the d33 coefficient at lower concentrations of the fillers. It also leads to significant changes in the breakdown field, charge transport, charge distribution, and electric energy density of the material. In the case of highly conductive fillers, a drastic decrease in breakdown strength may occur due to high conductivity that limits the improvement of the piezoelectric performance of PVDF nanocomposites. The addition of fillers with high dielectric constants can significantly increase the dielectric permittivity of PVDF. However, on attaining the percolation threshold, the output of the piezoelectric devices is found to reduce drastically. The composites can also suffer from an abrupt variant in the dielectric loss. Sometimes, high filler loading might be necessary to achieve high dielectric permittivity, which weakens the processability, flexibility, and mechanical performance of the composites. Hence, there exists a certain threshold to provide an optimal balance [95,96,121–123]. Similar to increasing the conductivity of an insulator like PVDF, It is possible to impart other properties to the polymer nanocomposite that the polymer alone initially does not possess. For example, Durga Prasad, by the addition of ferromagnetic fillers like $ZnFe_2O_4$ and $CoFe_2O_4$ into ferroelectric PVDF, made multiferroic films [102,103].

With time, the number of fillers used with PVDF has increased considerably and their effect on the properties of PVDF is becoming very specific. Thus, a list addressing every filler and its applications will be quite long. However, it was attempted to cover a majority of the recent ones in different sections of the review.

2. Manufacturing of PVDF films

With advances in the field of material manufacturing, a variety of techniques are used for the fabrication of PVDF films. Solvent casting [124,125] and spin coating [126,127] are some of the simplest

techniques to obtain films, while melt spinning [128,129] and electrospinning are employed for fiber production. Hot-pressing and extrusion are also used for the production of PVDF films [39,130,131]. The latest addition to this list is an electric poling-assisted additive manufacturing (EPAM), which is a 3D printing process that incorporates electric poling, and allows simultaneous printing and poling of 3D free-form single structures [132,133].

Among these, one of the most promising techniques is electrospinning. It is used to produce highly oriented 2D nanofibrous films of PVDF with a high fraction of β phase without any post-treatment. The general trend observed within the literature about PVDF is the rapidly growing number of publications on electrospun PVDF films. This underlines that electrospinning is considered one of the best methods for manufacturing PVDF. Hence, this section proposes to discuss the preparation of electrospun PVDF nanofibers.

2.1. Electrospinning: basic principles and process

Electrospinning involves producing smooth and continuous fibers of different polymers with diameters down to the range of nanometers [134]. A viscoelastic jet derived from a polymer solution or melt is submitted through uniaxial stretching under the application of a high voltage. In general, an electrospinning setup consists of a high-voltage power supply, a spinneret, and a collector. When a high voltage is applied, the charge is induced at the surface of the polymer solution and as a result, a mutual charge repulsion opposing the cohesion and surface tension of the solution starts to develop. As the voltage increases, and because of the increasing charge repulsion, the solution droplets elongate into a conical shape called the Taylor cone. At a critical value of the voltage, the repulsive electric force overcomes the surface tension of the solution, and a charged jet of the polymer solution is ejected from the tip of the Taylor cone. As the jet extends, the solvent evaporates which results in its stretching and thinning.

The electrospinning process is influenced by a set of different parameters. These parameters are classified into three sets: the solution parameters, process parameters, and ambient parameters. The solution parameters include the type of material/polymer and solvents used, solution concentration, viscosity, conductivity, and surface tension. The process parameters include applied voltage, tip-to-collector distance (TCD), flow rate, spinneret choice, and the type of collector. Humidity and room temperature are the ambient parameters. Each of these parameters is chosen carefully to achieve efficient electrospinning [135–148].

2.2. Electrospinning of PVDF

To ensure the formation of PVDF fibers, optimization of the various sets of parameters plays an important and decisive role.

2.2.1. Effect of solvents and solution viscosity

The molecular weight, concentration of PVDF, and solvents used are the solution parameters that allow more tuning options over other parameters like viscosity, polarity, vapor pressure, and surface tension. An increase in the molecular weight of PVDF increases the viscosity of the solution. A more viscous solution will take longer to reach the collector and so the jet stretches more under the applied voltage and solvents evaporate better, enhancing the β phase content. Hence, higher molecular weight PVDF fibers generally have better piezoelectric and mechanical properties [149,150]. This was confirmed by the studies of Magniez *et al.* [151] and Zaarour *et al.* [152]. The weight percentage of PVDF also has a similar effect on the viscosity of the solution. With the increase in concentration, the uniformity and fraction of the β phase increase at first due to the improved stretching effects. If it increases beyond a critical limit, the solution becomes highly viscous and harder to stretch. As a result, the fraction of the β phase decreases [153]. Justifying this claim, Gade *et al.* reported that the β phase content decreased with an increase in concentration [154]. Baji also suggests that thinner fibers formed at lower concentrations will have higher β phase content [155].

In a similar study, Costa *et al.* suggested that adding a more volatile solvent (like acetone) to polar solvents like dimethylformamide (DMF) lowers the surface tension and increases the net evaporation rate of the solvents, thereby affecting the relative fraction of phases [156]. It also lowers the viscosity, α phase content, and formation of beads in PVDF fibers. However, too much acetone will speed up evaporation excessively and the solution may solidify at the tip of the needle [153,157,158]. Gee *et al.* studied the effects of different solvents on the electrospinning of PVDF. They used solvents like DMF, dimethyl sulfoxide (DMSO), and *N*-methyl-2-pyrrolidone (NMP) with a 6:4 vol ratio with acetone. They found DMF: acetone 6:4 v/v% to be the best combination to increase the fraction of β phase [159]. This solvent combination is often found in other works [108] but the ratio may vary from one to another. For example, Saha *et al.* suggested 7:3 [160] as the best ratio while 4:6 was preferred by Jiyong [161].

2.2.2. Effect of voltage

The applied voltage plays an irreplaceable role in altering the properties of PVDF fibers, especially the formation of the β phase. The fiber diameter is found to decrease and the fraction of β phase to increase with the increase of voltage. The excessive increase in voltage will result in the beading and eventually the breaking of the fibers [153,161,162]. This is clearly understood from the observation of Gade *et al.* [154]. A slightly different suggestion was put forward by Andrew and Clarke. They claim that the applied voltage has much less effect on the fraction of β phase for a less viscous solution and affects the solution with higher viscosity as mentioned above [163].

2.2.3. Effect of tip to collector distance (TCD)

The TCD affects the evaporation of the solvent and electric field intensity. As the TCD increases, the β phase content increases at first and then decreases, hence the most preferred TCD being between 10 to 20 cm [153,164]. Shao *et al.* reported that at a constant voltage, the average fiber diameter decreases with an increase in the TCD [165]. The studies of Motamedi *et al.* also support this observation [166]. Zaarour *et al.* reported that the pore size of porous fibers, groove size of grooved fibers, and roughness of rough fibers increased with an increase in the TCD [167].

2.2.4. Effect of flow rate

Finding the critical flow rate is necessary for the electrospinning of PVDF. Lower flow rates will cause a vacuum inside the needle, while at higher flow rates some polymer may deposit at the tip. A lower flow rate is preferred to ensure enough time to stretch and polarize the jet and the solvents to evaporate [153,164]. In general, the diameter of the PVDF fiber is found to increase with the increase in the flow rate [166,167]. On the contrary, Ghafari *et al.* did not find such sensitivity or change in fiber diameter with a change in flow rate [168]. Gade *et al.* observed that fiber diameter increased with flow rate, but β-phase content decreased from 92.5% at a flow rate of 2 ml/h to 85.5% at 8 ml/h [154]. Lei *et al.* reported the formation of the γ phase at a flow rate of 2000 μL/h at 30°C, and the formation of the α phase at 50°C [169].

2.2.5. Effect of collector type

The fraction of the β phase was found to improve as a static collector was replaced with a rotating one due to the additional stretching force. Fu *et al.* observed that the fraction of β phase increased to 93.2% at a speed of 2000 rpm for the rotating drum [150]. Along with the increase in β phase content, a decrease in fiber diameter is also observed with an increase in collector speed. However, an increase beyond an optimum value will result in wider, non-uniform, or broken fibers [153,154,158,166]. Zaarour *et al.* reported that by increasing the rotation speed of the drum collector, the macropores of the fiber changed into elliptical

shapes, grooves deepened, and roughness increased [167]. Thus, the collector speed has an intermediate optimum value which gives the best fibers.

2.2.6. Effect of temperature and humidity

The increase in the ambient temperature increases the solvent volatilization rate and reduces the surface tension and viscosity of the PVDF solution, thereby affecting the fiber morphology and fraction of β phase [153]. Huang *et al.* reported that with an increase in temperature, more uniform fibers with lesser beading were formed [170]. As the temperature increases, fiber diameter decreases but beading may occur. Mohamadi and Sanjani reported that with the temperature set to 40°C, the growth of the γ phase was seen. It was accounted for by the increase in thermal energy causing the rotation of the CF_2 group [171]. The relative humidity also affects solvent volatility and thus alters the surface morphology of the fibers. Szewczyk *et al.* observed that fibers spun at a relative humidity of 30% (PVDF-30) had a smooth surface and an average diameter of 0.92 μm while those spun at a relative humidity of 60% (PVDF-60) had a wrinkled surface and larger average diameter of 1.68 μm [172]. Zaarour *et al.* observed that smooth fibers were formed at 5% relative humidity, and macroporous, rough, and grooved fibers were produced at higher relative humidity [173]. Studies found that the relative humidity must not be increased beyond a critical value as this will inhibit the evaporation of solvents and hinder the electrospinning process [153,164,174].

From the above discussions, the conclusion reached is that for every parameter there is an intermediate optimum value that gives the best fibers. Furthermore, as all of these parameters are somewhat interrelated and interdependent, varying one can vary the previously obtained optimum value of another parameter [174–176]. Once the optimum

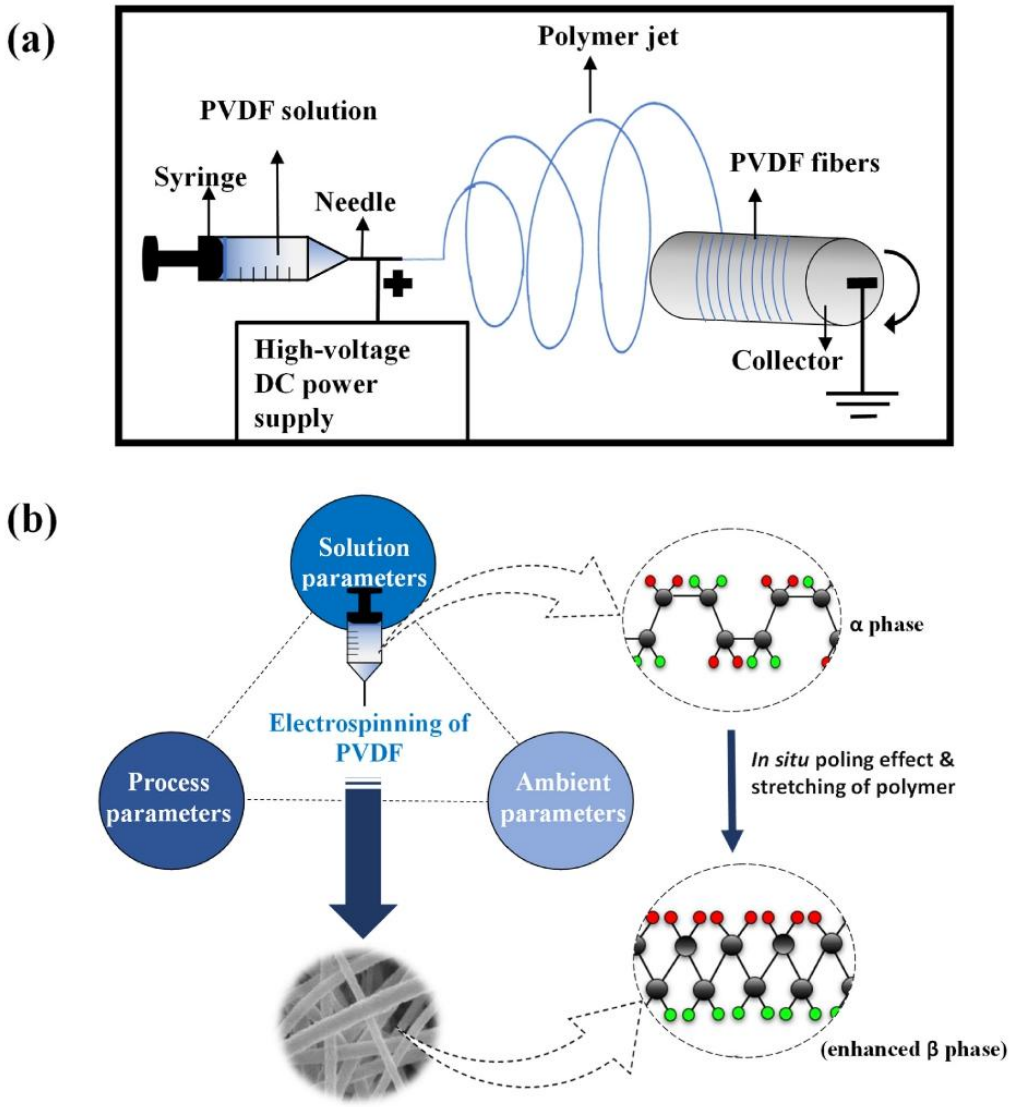

Fig. 3. Schematic representation of (a) the process of electrospinning of PVDF, and (b) the parameters which affect it along with the subsequent change in crystalline phase.

parameters have been found, electrospinning becomes a reliable way to produce PVDF fibers with a high electroactive phase fraction. Mechanical stretching and electrical poling are the most common methods to induce the β phase in PVDF. Electrospinning is the only technique that offers both of these methods within the process itself. The high voltage applied and the high drawing of the jet during electrospinning produce an *in situ* poling and stretching effect, and thereby induce preferred dipole orientation and all trans conformation in the electrospun PVDF fibers. The fraction of the β phase found in electrospun samples can be as high as 99% [177,178]. The electrospinning process of PVDF, the parameters which affect it, and the subsequent change in the crystalline phase are schematically shown in Fig. 3. After acknowledging the advantages of electrospinning for the manufacturing of electroactive PVDF nanofibers, the coming section of the review will present the recent developments and applications in which they can be of use.

3. Applications of electrospun PVDF- nanocomposites

The previous sections showed the interesting microcrystalline properties that can be achieved by PVDF fibers when the optimum electrospinning parameters are used. The next section will attempt to give an overview of the various application of such electrospun PVDF fibers.

3.1. Energy harvesting and sensing

PVDF is an excellent electroactive material with high sensitivity, flexibility, biocompatibility, and non-toxicity. Compared to other manufacturing processes of PVDF, electrospun nanofibers are reported to possess the highest β phase content, high surface area, and surface charge production. Hence, they are one of the most ideal candidates to harness the otherwise lost mechanical and thermal energy. The interest shown in research for such materials is made apparent by the great efforts to develop PVDF-based novel energy harvesting devices or self-powered sensors. The different energy harvesting mechanisms in PVDF-based devices can be explained as follows.

Under stress or other stimulations like change in temperature, deformation of the crystals, and rotation of dipoles occur within the crystalline phase of PVDF films. This forces a change in the dipole density of the film and causes the electric charges within the film to be out of equilibrium. Thus, the result is the variation of the electrostatic-induced charge density of the electrodes fixed on either side of the film, inducing a voltage and current flow in the external circuit. Once the stimulation is removed, the accumulated free charges flow back, resulting in a reverse electrical signal in the external circuit. When the external stimulation is completely removed, the device returns to its initial condition. The production of an electrical output by PVDF films in response to applied pressure forms the foundation of piezoelectric energy harvesting. Pyroelectric energy harvesting is based on the response of the PVDF films to temperature [179–184]. Because of its unique electroactive properties, electrospun PVDF is an effective dielectric material for triboelectric energy harvesting as well [185]. In triboelectric energy generation, it is the charge transfer due to contact electrification and electrostatic induction that is responsible for the production of the electrical output. This electrostatic induction arises from the friction of two different layers with different electro affinities, namely the positive triboelectric layer (losing electrons) and negative triboelectric layer (gaining electrons) which develop positive and negative charge respectively when subjected to pressure [185,186]. PVDF, especially in the β phase, can act as an excellent negative triboelectric layer that efficiently traps the electrons. This is made possible because of its high spontaneous polarization, high electronegativity, and high surface charge density. When the two triboelectric layers come in contact, they develop opposite charges and as they move away an electrical potential difference will begin to develop. This creates a flow of electrons from the electrode of the PVDF layer to the electrode of the positive triboelectric layer through an external circuit. As the separation between the layers increases, an electrostatic equilibrium is reached and the electron flow stops. When the two layers are again driven towards each other, the electrostatic equilibrium is again broken and the electrons flow back in the opposite direction, thus reducing the number of induced charges. Finally, all the induced charges are neutralized when the layers come in contact [187–189]. Interestingly, in PVDF-based devices, piezoelectric, pyroelectric, and triboelectric effects can act complementary to enhance the overall output performance and functionality of the device. This principle forms the basis of hybrid energy harvesting. For example, during the simultaneous application of pressure and heating, the piezoelectric output under the heated condition is observed to be higher due to thermal strain coupled with the piezoelectric effect. Similarly, the pyroelectric output improves upon increasing the stretching elongation of the device due to mechanical-strain-induced pyroelectric output [190]. Even when considering the application of external forces without heating, there still exists a complementary method to enhance the output of the devices through coupled mechanisms of piezoelectric and triboelectric energy harvesting. Indeed, when an external force is applied, the deformation of material can occur simultaneously with contact friction, thus allowing the complete exploitation of the applied mechanical energy. At first, when the triboelectric layers are brought toward each other, triboelectric charges develop due to interface friction. As the application of external force continues, a piezoelectric potential is also generated due to the deformation of the PVDF film. Then, there is a current flow in the circuit to balance the piezoelectric potential. As the external force is removed, the PVDF film recovers from compression and the piezoelectric potential disappears. With the triboelectric layers separating from each other, an internal triboelectric potential develops resulting in a current flow in the circuit [191]. Fig. 4 summarizes the principles of piezoelectric, pyroelectric, and triboelectric energy generation in PVDF-based devices. The following sections will discuss their architecture and applications.

3.1.1. Piezoelectric nanogenerators and sensors

The elemental structure of a piezoelectric nanogenerator (PENG) or sensor consists of four parts. The piezoelectric material is the active layer and is primarily responsible for the entire process of energy harvesting and sensing upon the application of pressure. The piezoelectric material is sandwiched between suitable electrodes connected to the external circuit. The entire PENG is wrapped in suitable materials like polydimethylsiloxane (PDMS) to protect it from damage from continuous use and exposure to different environments [192,193]. It is worth considering some of the recent PENGs, and innovations in their structure, output, and high-performance applications. The $CsPbBr_3$-PVDF PENG based on *in situ* growth of $CsPbBr_3$ nanocrystals in PVDF matrix fabricated by Chen *et al.* for mechanical energy harvesting and motion sensing is a relevant example [194]. They used a one-step technique in which the solutions containing $CsPbBr_3$ precursors and PVDF was electrospun to produce the nanocomposite fibers. The PENG gave a maximum piezoelectric output voltage of 103 V and a current density of 170 μAcm^{-2}. The fabrication of the flexible PENG, it's structure, cross-section, and energy harvesting during walking is schematically illustrated in Fig. 5. Sengupta *et al.* developed another motion sensor and PENG using PVDF−polycarbazole nanofibers which were suitable for biosensing and bioactuation [195]. The PENG generated an open-circuit voltage (V_{oc}) of 2V under a pressure of 0.24 MPa and had a stable response in the frequency range of 1 to 7 Hz. In the study conducted by Amith *et al.*, the addition of Cloisite-30B nanoclay into PVDF was found to strengthen the β phase and piezoelectric response of electrospun PVDF fibers. In this study, the authors reported the PVDF/Cloisite-30B nanofiber composite to produce an output voltage of 4.74 V when actuated at 1500 rpm [196]. Ramasamy *et al.* presented a rare result in which oleylamine functionalized boron nitride nanosheets (OLABN) incorporated PVDF nanofibres with a high fraction of ~92% of γ–phase

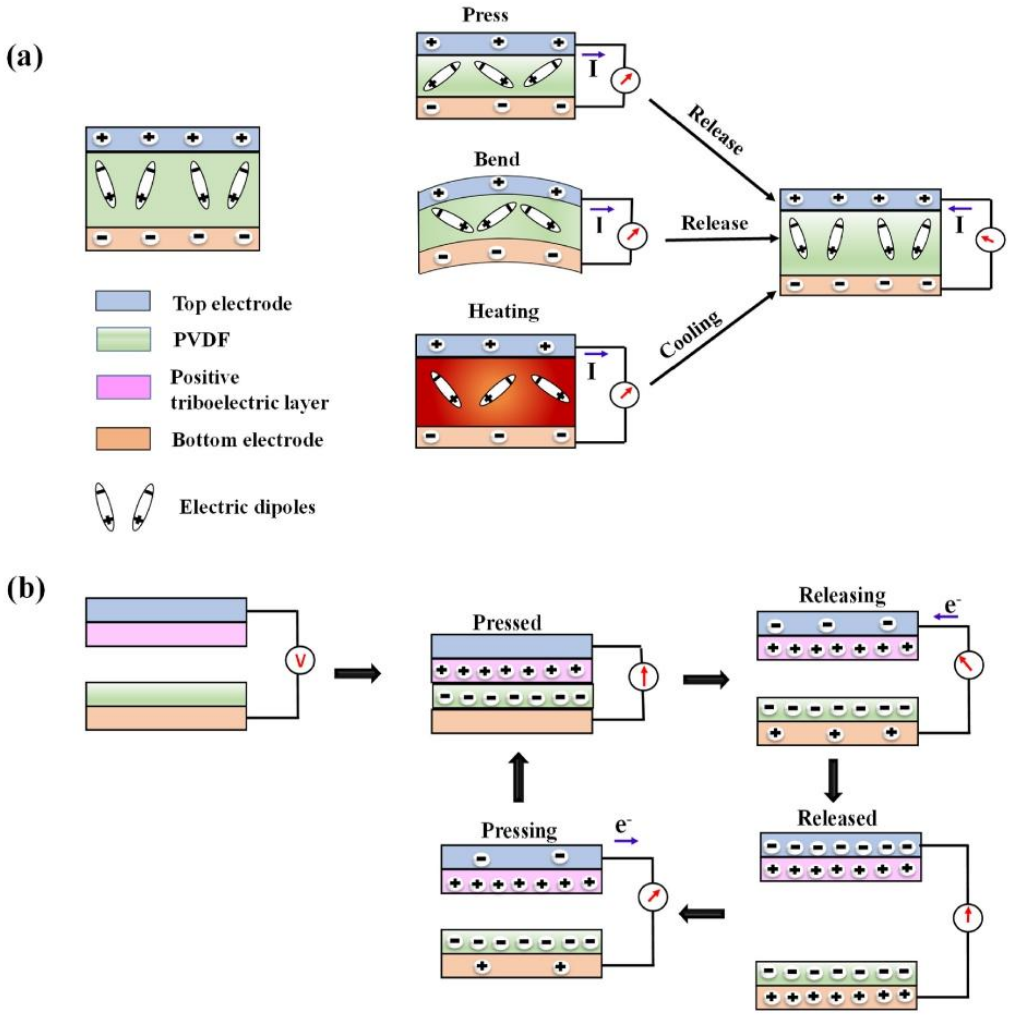

Fig. 4. Schematic representation of the principles of (a) piezoelectric, pyroelectric, and (b) triboelectric energy generation.

was used as the active material for energy harvesting and sensing [197]. The piezoelectric device developed from these fibers was able to detect a minimum force of 0.1 N and light up a 4V light-emitting diode (LED) upon finger tapping with the aid of a simple amplifier. A combination of $ZnSnO_3$–MoS_2 was used by Muduli *et al.* as fillers with PVDF to develop a PENG for biomechanical energy harvesting. Here, a 1 μF capacitor charged from the device was able to power a calculator with stability [198]. To explore the possibilities of another transition metal-based filler, Zhao *et al.* developed a highly sensitive pressure sensor based on flexible piezoelectric MXene/PVDF hybrid film [199]. They reported that with only 0.4 wt% MXene, the piezoelectric coefficient d_{33} of MXene/PVDF hybrid film reached values as high as 43 pC/N. The sensor gave a stable output for 10,000 s. A combination of $BiCl_3$ and ZnO was used by Zhang *et al.* as a filler to obtain PVDF/$BiCl_3$/ZnO composite fibers with a high β phase content of 92% [184]. The piezoelectric sensor developed from these fibers and simple aluminum foil electrodes gave a maximum V_{oc} of 3 V and 0.6 V for elbow and knee bending, and stretching between specific angles. This signals the applicability of the device as a wearable sensor for detecting vital signals such as breathing, heartbeats, and hand movements post-stroke or traumatic brain injury.

Shivalingappa *et al.* used silver nanoparticles as fillers with PVDF to fabricate a sensitive PENG [200], and Ongun *et al.* experimented with silver-doped zinc oxide nanoparticles [201]. The PENG of Shivalingappa *et al.* could trigger a burglar alarm when the pressure on the PENG was high enough to produce an output greater than 0.4 V. The device of Ongun's group had the potential to be used within flexible, portable electronic systems, and wearable gadgets. Similarly, Hasanzadeh *et al.* added ZnO nanoparticles along with graphene (graphene-ZnO nanocomposite) into PVDF fibers and found that an applied force of 1 N produced a peak-to-peak voltage (V_{pp}) of 840 mV. This was significantly higher than the outputs of the pristine PVDF and PVDF/ZnO nanofibers which were 640 mV and 710 mV respectively [202]. Another graphene-based filler incorporated PVDF nanofibres was developed using COOH-functionalized graphene nanosheet and talc nanosheet by Shetty *et al.* [203]. As they could obtain a power density of 1.72 μW/cm^2 when a pressure of 0.4 MPa was imparted, the authors suggested this material as a promising candidate for the fabrication of portable and flexible electronic devices. Electrospun PVDF films with Y-doped ZnO fillers and a very high F(β) of 98% were fabricated by Yi *et al.* thus combining the flexibility of PVDF and high piezoelectricity of Y-doped

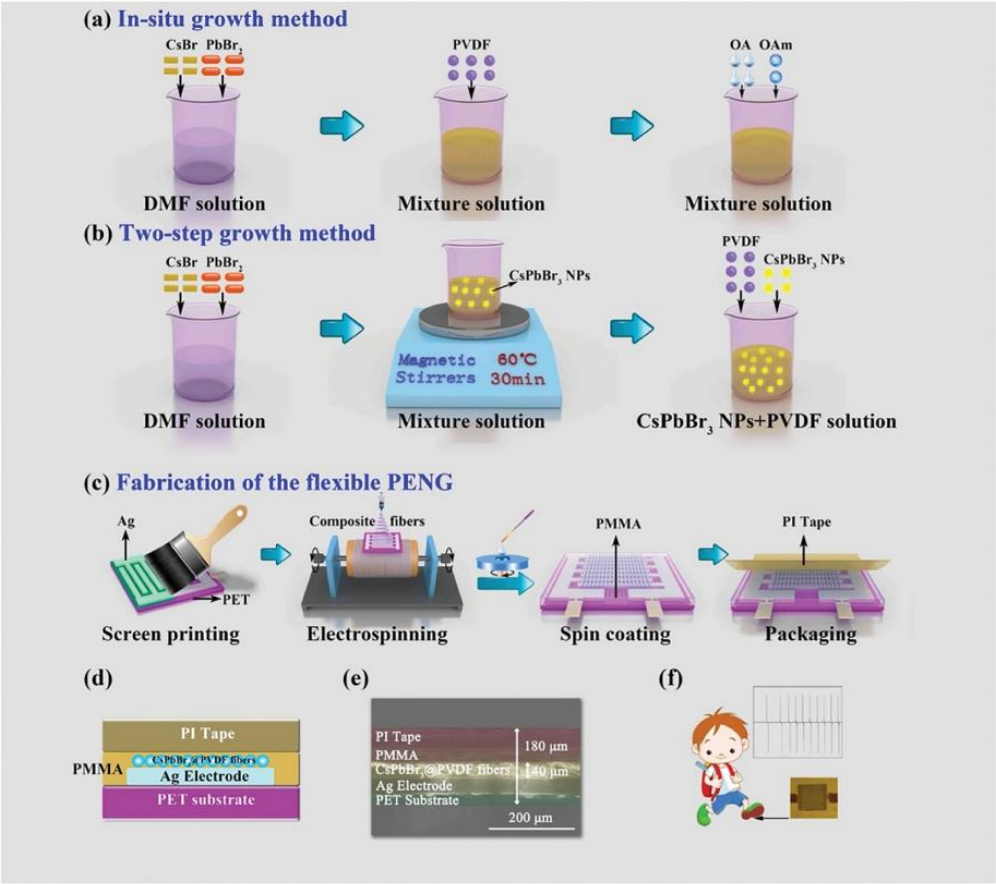

Fig. 5. a) Preparation of precursor solution of CsPbBr3@PVDF for *in situ* growth method. b) Preparation of precursor solution of CsPbBr3@PVDF for two-step growth method. c) Schematic diagram of the fabrication of the flexible PENG. d) Schematic diagram of the PENG structure. e) Cross section of the PENG based on in situ growth method. f) Display of energy collection during walking (reproduced with permission from Ref. [194]).

ZnO [204]. The PENG gave an output voltage of ~8 V under continuous punching for a trial lasting over 1100 s at 0.8 Hz. It could also charge a capacitor of 5 μF to ~2.8 V or ~3.7 V in 50 s by walking or running.

The possibility of using fillers derived from biological sources was explored by Ponnan *et al.* by using magnesiochromite nanocrystalline powder synthesized from egg shell membrane and incorporating it in PVDF nanofibers [205]. This PENG could provide stable output for over 750 cycles and could charge a 10 μF capacitor within 643 s. Exploring the possibilities of different fillers, and using a different electrospinning technique was done by Wang *et al.* [206]. In Wang's study, an all-organic and core-shell structured silk fibroin/PVDF nanofibers were fabricated using a coaxial electrospinning strategy. The ability of the device to generate distinct output voltage for different movements of the human body was used for the development of a sensor in a human-machine interactive interface. This was demonstrated by making a smart car move forward, backward, and turn around by punching, tapping, and bending respectively (Fig. 6.). A wearable piezoelectric device based on yarns and fabrics was woven by Xue *et al.* using a highly integrated PVDF/conductive nylon core-sheath structure [207]. In this study, a dense PVDF fibrous coating was electrospun on the outer surface of a conductive nylon yarn which functioned as one of the electrodes. The same nylon yarn was braided on top of the PVDF-coated nylon yarn via a 2D braiding technology to function as the second electrode. The output of the final piezoelectric yarn increased with the thickness of the PVDF layer. Bai *et al.* also used a distinct method by creating PVDF nanofiber array films via a combination of electrospinning and cutting methods [208]. The PVDF nanofiber films were stacked layer by layer along the same direction and compressed to get an oriented nanofiber bulk. It was then cut to obtain the PVDF nanofiber array film having dense vertical alignment as shown in Fig. 7. From the power output of two such parallelly connected PENG, 12 LEDs could be lit without storage devices.

A bit different from the conventional fabrication methods, Du *et al.* used a laminating method to develop multilayered porous composite fibers-based piezoelectric nanogenerators [209]. The laminating process was beneficial as it increased the possibility of stressing every fiber by reducing the porosity of the fiber film. For this, they layered fiber membranes of PZT incorporated PVDF fibers along the same direction and compressed them together. The output of the PENG was found to increase with the increase in thickness, and an output voltage as high as 92 V was obtained from a 500 μm thick film. Another example of innovative design is the piezo-organic e-skin sensor (POESS) fabricated by Maity *et al.* through an all-organic strategy. Here, metal-free, highly-conductive, flexible, and biocompatible spongy electrodes were used instead of conventional electrodes [210]. Such an organic electrode-piezoelectric stack was developed by polymerization of aniline monomer by vapor phase polymerization using $FeCl_3{\cdot}6H_2O$

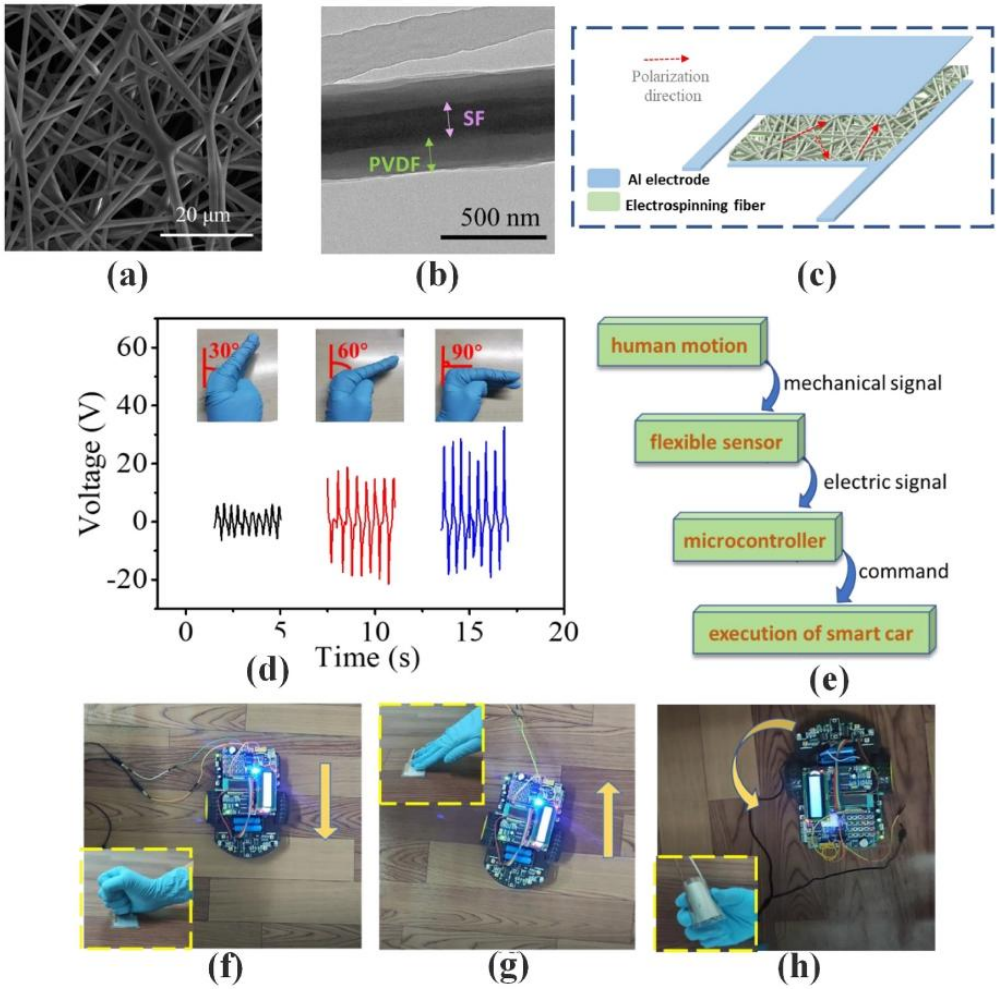

Fig. 6. (a) SEM image and (b) TEM image of SF/PVDF nanofibers. (c) Schematic diagram of the structure of the piezoelectric device based on SF/PVDF nanofibers. (d) The sensor attached on the hand bending at various angles and the corresponding piezoelectric responses. (e) The interacting process between human motion and a smart toy car. The smart toy car moved towards different directions when (f) punching, (g) tapping, and (h) bending motion were applied on the SF/PVDF piezoelectric sensor (reproduced with permission from Ref. [206]).

containing PVDF. The POESS was then attached to the human body for self-powered physiological signal monitoring such as wrist bending, neck stretching, throat movements, phonation recognition, and pulse measurement. An all-fiber piezoelectric nanogenerator (A-PNG) was designed by Mahanty *et al.* by using 0.5 wt% ZnO nanoparticles reinforced electrospun PVDF nanofibers as the active layer [211]. In this study, copper–nickel plate interlocked conducting micro-fiber-based polyester fabric was used as electrodes. Owing to its reliable piezoelectric response and skin conformable functionality, the A-PNG was attached to the throat, wrists, fingers, and knees for vocal cord movement monitoring, pulse monitoring, remote health care monitoring, sports activities, and related movements analysis respectively. The device was also used as a weight monitoring sensor which could give the weight of a person weighting between 45 and 80 kg. A core-shell type of PVDF yarn was developed by Li *et al.*, with a silver-plated nylon yarn as the core [212]. Li's group used TiO_2 as fillers and silver nanoparticles as an extra coating on top of the electrospun PVDF@TiO_2 nanofibers. An extra layer of PVDF nanofibers was electrospun onto this yarn to fix the silver nanoparticles. Finally, a plain weave fabric was made with nanofiber yarns through a traditional textile weaving technique. Here, the core layer of silver-plated nylon yarn acted as the inner electrode and the other electrode was a metal electrode clip clamped to the outer surface of the PVDF nanofiber film. The sensor was fabricated by encapsulating this yarn in PDMS and had good response behavior which increased with the increase of effective contact area and applied weight.

Similar to the advances made in manufacturing methods, researchers came up with advanced and novel applications for the different piezoelectric devices they fabricated. Yen *et al.* demonstrated that a dynamic soft sensing element made using $AgNO_3$/PVDF composite fibers could be used for accurate diagnosis and treatment [213]. The device could detect the tremors produced in the biceps muscles and was beneficial in detecting muscle tremors after high-intensity training to obtain information regarding the changes in the symptoms of fasciculation. Furthermore, Li *et al.* fabricated a wearable and implantable biomedical

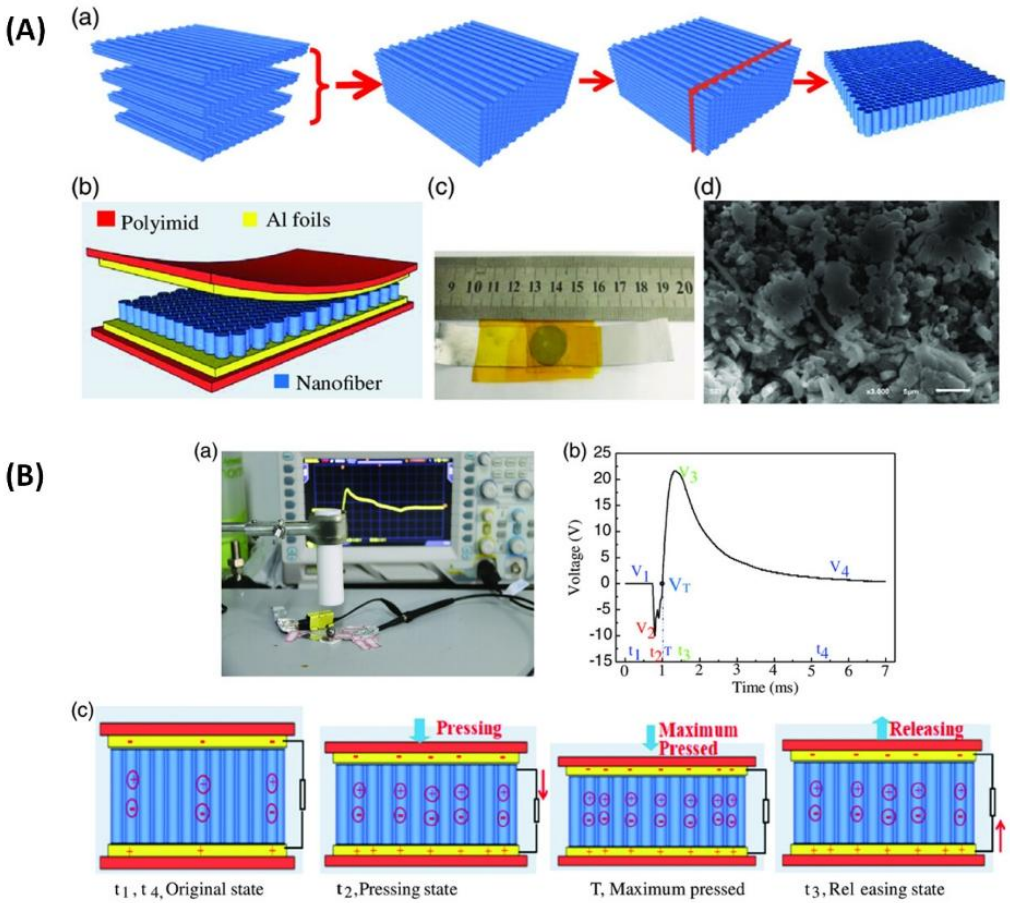

Fig. 7. (A) Processing and structure of PVDF nanofiber array film and nanogenerator. a) Schematic procedure of the preparation of the PVDF nanofiber array film. b, c) Schematic diagram and digital photograph of nanogenerator based on PVDF nanofiber array film. d) SEM image of PVDF nanofiber array film. (B) a) Digital photograph of the test system. b,c) Output voltage curve features of the piezoelectric nanogenerator based on the nanofiber array film with a thickness of 2.3 mm and schematic diagram of working mechanism during one impact cycle, respectively (reproduced with permission from Ref. [208]).

sensor from electrospun core/shell PVDF/dopamine nanofibers [214]. The device was attached to the diaphragm and around the femoral artery of mice and could indicate the inhibition of respiration and loosening of the peripheral arterial walls under the effect of anesthesia by a change in V_{pp}. Such a piezoelectric sensor offers great potential for the early assessment and prevention of cardiovascular diseases, respiratory disorders, and other pressure-related acute and chronic diseases. It could also be employed to harvest energy from biological deformations such as heartbeats and lung movements, and used to produce electrical stimulation for tissue repair and disease treatment (Fig. 8.). A PVDF-based piezoelectric device was also used as a human-machine interface in Zhao's study [215]. They fabricated a matrix motion sensor by arranging several small motion sensors from PVDF/ZnO hybrid material. The individual ones were used to detect various movements like finger and foot pressing. With the one with a two-dimensionally arranged set of devices, an NAO robot could be moved and turned according to the walking directions of a person.

Sources other than motion or mechanical deformation can be used to initiate the piezoelectric response of the PENGs. Demirci *et al.* studied the piezoelectric and magnetoelectric energy harvesting capability of a device fabricated from PVDF/$NiFe_2O_4$ fibers [216]. The device was found to be able to harvest the magnetic fields from the coil of a kettle. It generated a maximum output voltage of 17.45 mV and electrical power of 0.40 μW under a resistive load of 750 KΩ, at a low-level magnetic field frequency of 50 Hz. A novel PENG-sensor-photodetector was fabricated by Mondal *et al.* using a composite of all-inorganic cesium lead bromide ($CsPbBr_3$) perovskite rod and PVDF nanofiber [217]. The device is a potential vibration sensor for mobiles, air blower, and regular table fan with an output power of 4.24 mW and durability over 4 months. Similarly, Yang *et al.* used reduced graphene oxide incorporated PVDF fibers and developed a PENG for motion and air leakage detection that produced an output of 200 nA and 150 nA respectively [218]. A type of self-supporting smart air filter was developed by He *et al.* from electrospun PZT/PVDF nanofibers for the harvesting of wind energy along with air filtering [219]. The energy harvested was then used to inhibit bacterial growth. The energy harvester was designed to be a multifunctional device by sputtering a series of square gold particle layers over the fibers and using two metal meshes on either side as electrodes. The gold particle layer acted as a volatile organic compound sensing area in which resistance increases as cracks were formed. The formation of cracks is due to the swelling of the underlying PZT/PVDF fibers as they absorb ethanol vapors. The cracks were healed after the evaporation of ethanol and thus the conductivity of the sensing element was restored. Mousa *et al.* fabricated PVDF-cellulose nanocrystal

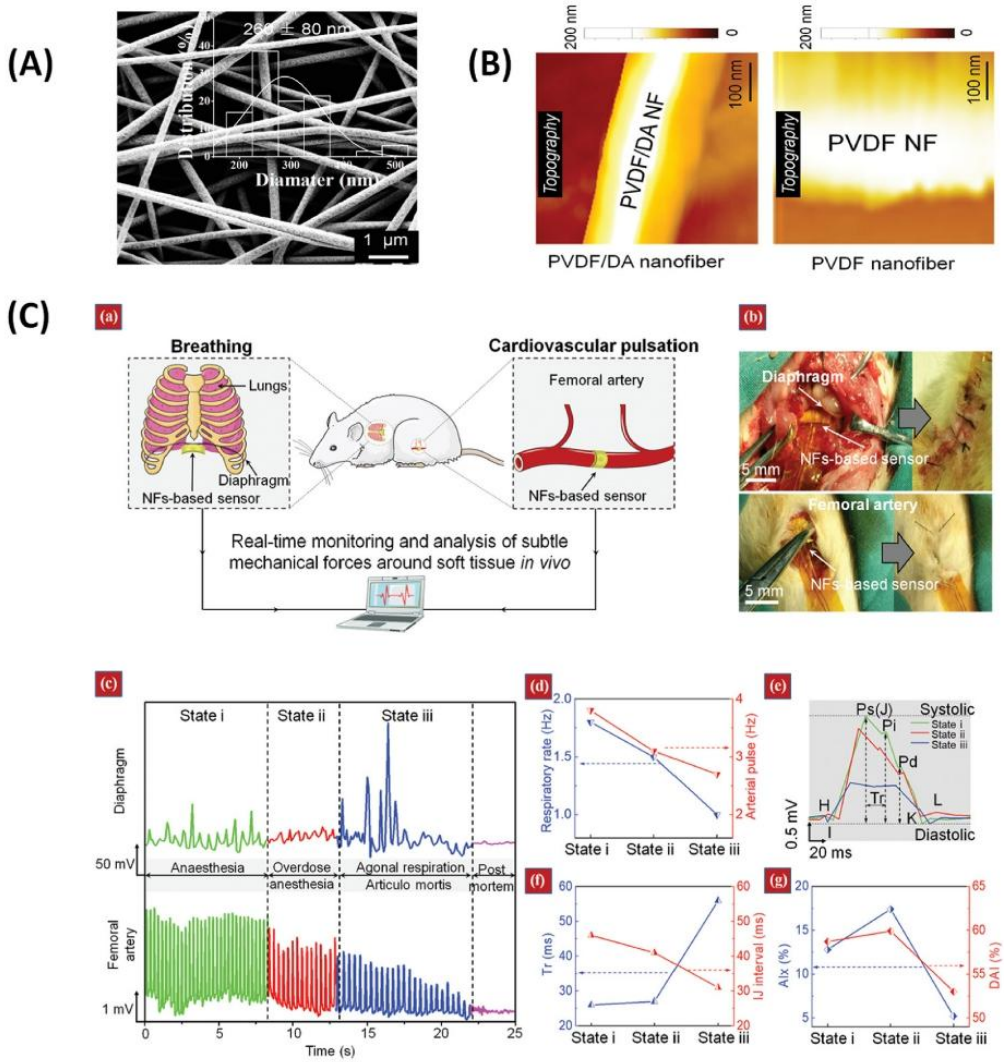

Fig. 8. (A) SEM image of PVDF/DA nanofibers (NFs) showing their uniform sizes with average diameters of 260 ± 80 nm. (B) Surface topography of a single PVDF/DA NF and pure PVDF NF. (C) In vivo applications of PVDF/DA NF-based sensors. a) Schematic of the PVDF/DA NF-based sensor implantation for recording subtle mechanical pressure changes *in vivo*. b) Surgical images of the implanted PVDF/DA NF-based sensors attached on the diaphragm membrane in the abdominal cavity (top) and onto the femoral artery (bottom). c) Piezoelectric voltage signals induced by diaphragm motions and blood pulsing when the mouse was at different physiological states. State i: anesthesia; state ii: overdose anesthesia; state ii: continuous overdose anesthesia (for diaphragm: agonal respiratory; for femoral artery: *articulo mortis*). d) Respiratory rate and arterial pulse of the mouse at different physiological states measured by a clinical vital signs monitor. e) Piezoelectric signals from femoral artery showing three typical BCG pulse waveforms of the Ps, Pi, and Pd. f) BCG values of IJ interval and Tr of a reflected wave from the hand periphery obtained from (e). g) Comparison of the femoral AIx and DAI among different physiological states, where AIx (%) was defined as (Ps − Pi)/Ps and DAI was defined as Pd/Ps (reproduced with permission from Ref. [214]).

membranes, that were used to make oil-wastewater separation and self-powered sensors [220]. With their higher water flux and oil rejection properties, they hold potential for future exploration, based on the energy harvesting from flowing droplets. Li *et al.* manufactured polyvinyl alcohol (PVA)-wrapped dopamine/polyvinylidene fluoride shell/core nanofibers and used them as a two-in-one humidity actuator-driven piezoelectric generator [221]. The ability of PVA to spontaneously form hydrogen bonds with water molecules under ambient humidity and anisotropical swelling allowed it to produce mechanical deformation within the PVDF fibers and thereby convert a change in humidity into electric power. Considering real-life applications, it was able to harvest energy from moisture changes in human breath, palm (based on its motion towards and away from the film) and also mental sweating. Thus, the device could be a candidate for human healthcare monitoring too. Another similar example is the study of Lu *et al.* [222]. They developed a PENG using 3D-Tb-modified (BaCa) (ZrTi)O_3 (BCZT)-PVDF core/shell nanofibrous membrane for microenergy harvesting from mechanical motion, acoustic waves and wind. The PENG could achieve 12–28 V as output voltage with wind speeds of 5 to 14 m/s. Hence, it holds the potential to be used as a commercial digital

temperature-humidity meter powered by wind energy.

Acoustic waves are another interesting source for stimulating the piezoelectric effect in PVDF nanofibers. Mahanty *et al.* designed a highly sensitive all-fiber acousto- and piezo-electric nanogenerator (AAPNG) with $MgCl_2{\cdot}6H_2O$ added PVDF nanofibers [223]. The AAPNG is a highly sensitive device that generated an open circuit output voltage of 2 and 3 V at sound pressure levels (SPL) of 80 and 120 dB respectively. Because of its improved sensitivity to SPL, the AAPNG could be used as a noise detector and possibly as a self-powering microphone for sound recording. Another motion monitor and acoustic energy harvester with high-potential electronic skin applications were developed by Roy *et al.* [224]. They used naphthylamine bridging a [Cd(II)-μ-I4] two-dimensional metal–organic framework-reinforced PVDF composite nanofibers mat to fabricate this flexible and sensitive composite piezoelectric nanogenerator. When the composite fibers were used for acoustic energy harvesting, the architecture of the device became slightly different from the conventional way. In this case, the nanofiber mat was sandwiched in between two samples of indium tin oxide coated on a poly(ethylene terephthalate) (PET) sheet, with one circular hole of 1 cm diameter cut on each PET film. The hole allowed nanofibers to directly experience the sound vibrations. The as-prepared acoustic nanogenerator gave an open-circuit voltage of 6 V at a sound wave frequency of 120 Hz and 110 dB SPL. A piezoelectric acoustic detector with a frequency resolution better than 0.1 Hz was developed by Xu *et al.* [225]. For this PVDF membrane, a soft pad and a metal plate were put in sequence on a metal and pushed into the grooves of a metal template. The PVDF film was then peeled off to obtain a wave-shaped nanofiber membrane. The device thus produced clear-cut and comparatively higher responses to sounds of different frequencies and SPL. Based on the above results and the fact that every human being's voice has a unique characteristic frequency spectrum, the potential of the device to recognize individuals, words, musical notes or animal sounds were demonstrated by human trials and sounds from a computer played via a loudspeaker.

3.1.2. Pyroelectric nanogenerators and sensors

The structure of a pyroelectric nanogenerator based on PVDF films is similar to that of a PENG. In this case, the film with high β phase content is expected to possess a high pyroelectric coefficient as well so that it responds well to changes in temperature. The electrodes and protective coatings are chosen in such a way that along with performing their normal functions, they contribute to the process of heat transfer to the active layer [226,227]. In this section, the different structures and methods used by researchers to maximize the pyroelectric output and to widen the practical applications of the device will be explored.

Wu *et al.* developed an infrared-driven non-contact pyroelectric generator based on electrospun tungsten oxide incorporated PVDF nanofibrous membrane ($PVDF/WO_{2.72}$) with improved Near Infrared (NIR) absorption and photothermal conversion ability [228]. They designed the generator using two types of electrodes to maximize the heat transfer and the pyroelectric output. Ni–Cu conductive fabric substrates were used as the bottom electrodes on which the PVDF nanofibers were directly electrospun. The top electrode was an L-shaped conductive carbon nanotube (CNT) sheet that partially covered the nanofibrous membrane, thus allowing maximum heat transfer (Fig. 9.). The as-prepared pyroelectric generator with 7 wt% $WO_{2.72}$ was subjected to NIR radiations, and the temperature rapidly increased to 107.1 °C after 60 s. Meanwhile, the maximum output voltage could reach 1.5 V and remained stable during multiple cycles (Fig. 10.). The outputs suggested that the device could also be used as an efficient temperature sensor. Employing cesium tungsten bronze ($Cs_{0.33}WO_3$) incorporated screen-printed serpentine electrodes (SRE) and $Cs_{0.33}WO_3$ incorporated PVDF nanofibers Gokana *et al.* developed a potential pyroelectric nanogenerator to harvest solar energy [229]. Compromising between the heat transfer rate and resistance of the electrode, and considering the pyroelectric output of the devices made, the SRE which covers 54% of the PVDF film was found to be a suitable electrode. The pyroelectric nanogenerator made from this electrode and 7 wt% of $Cs_{0.33}WO_3$ added PVDF films could power a liquid crystal display (LCD) and four light-emitting diodes through capacitor charging. Along with demonstrating the pyroelectric application of PVDF, the study demonstrates how the engineering of electrode structure plays a crucial role in the final output.

3.1.3. Triboelectric nanogenerators and sensors

Triboelectric nanogenerators (TENG) possess two active layers. As

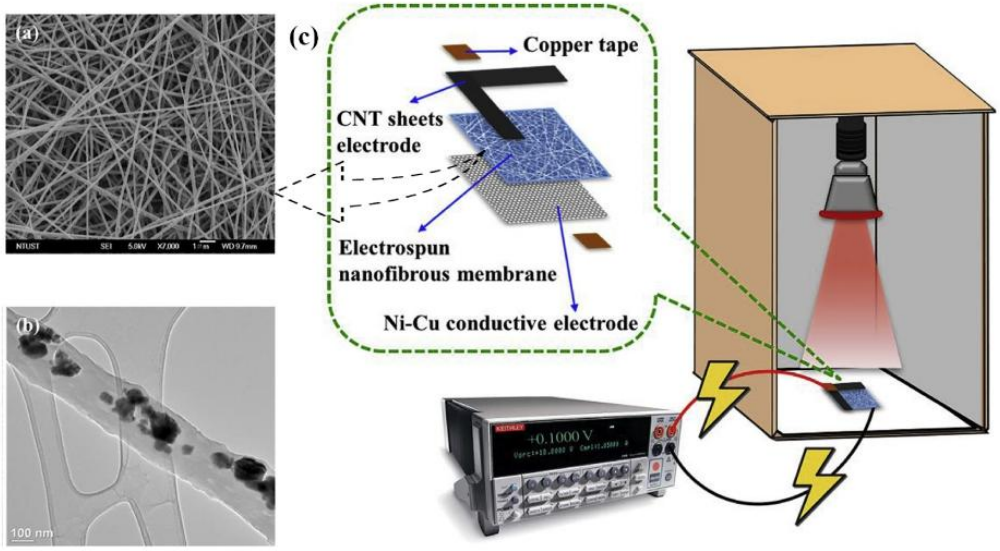

Fig. 9. (a) SEM and (b) TEM images of electrospun PVDF/WO2.72 nanofibrous membranes, (c) Schematic illustrations of pyroelectric measurement (reproduced with permission from Ref. [228]).

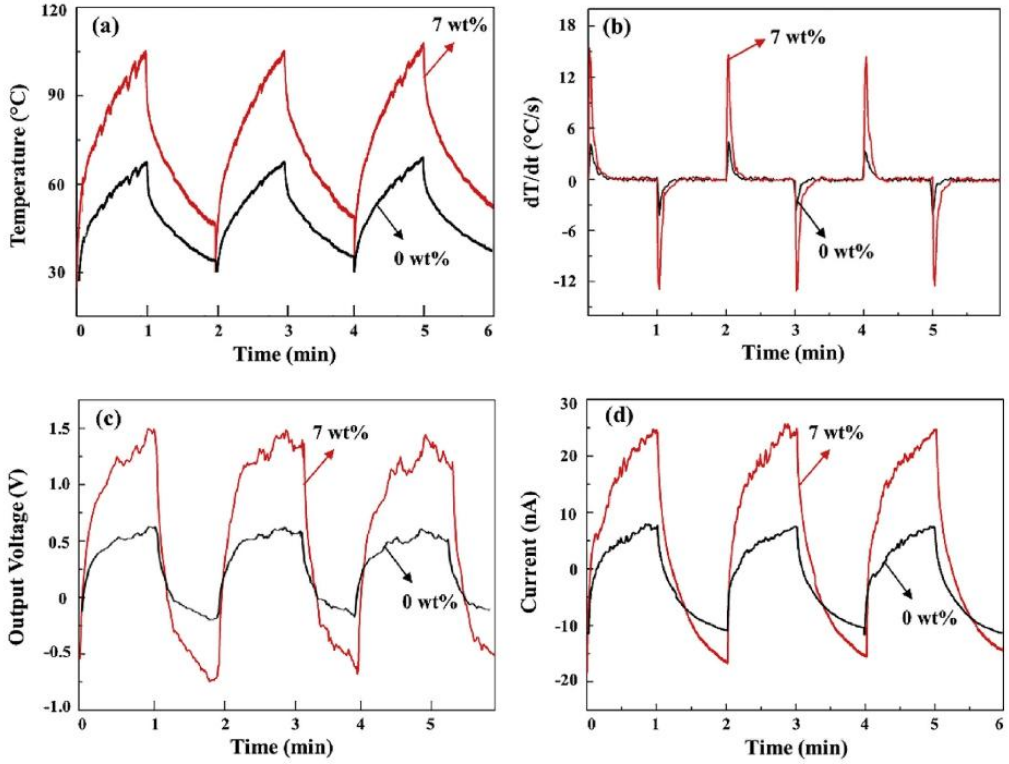

Fig. 10. (a) Temperature variation over time, (b) corresponding differential curve, (c) output voltage and (d) output current of $WO_{2.72}$-free PVDF and 7 wt% PVDF/$WO_{2.72}$ pyroelectric composites (reproduced with permission from Ref. [228]).

mentioned earlier, a PVDF nanofiber-based membrane acts as the triboelectric negative layer, and aluminum films, copper films, or nylon are commonly used as positive triboelectric layers. The separation between these active layers is maintained using spacers, binding yarns, or transition layers which are often made of polyimide (PI) films, Kapton films, etc. The electrodes and connection lead further to complete the TENG. There are four representative modes of operation of TENGs, among which the most common is the vertical separation mode. In this mode, the layer on which pressure is applied will come in contact with the other, and a transfer of charges occurs. As the pressure is released the layers attain the initial separation with the help of the spacers. In the lateral sliding mode, one triboelectric layer is made to slide over the other to produce charge separation. In the single-electrode mode charge transfer occurs as the surfaces of the triboelectric polymer fibers are brought to contact with the electrode. The fourth mode is the free-standing mode which is accomplished by arranging the triboelectric layers with electrodes attached to them underneath another frictional layer. The approaching and departing of the frictional layer from the electrodes build an unbalanced charge distribution resulting in the flow of electrons between the electrodes [230–234]. As the performance of TENGs strongly depends on surface properties, their fabrication should focus on improving the effective contact area and minimizing the change in surface properties with time under friction exposure and environmental conditions. Accordingly, great efforts have been made to develop robust TENGs. In this section of the review, some of the recent attempts in the case of PVDF-based TENGs will be explored, and the development of highly durable TENGs will be discussed.

Bhatta *et al.* proposed the use of MXene ($Ti_3C_2T_x$) functionalized PVDF composite nanofiber as a negative triboelectric layer for triboelectric energy harvesting performance [235]. An electrospun Nylon 6/6 nanofibrous membrane acted as the positive triboelectric membrane. The fabricated TENG-energy storage device could successfully power 120 commercial LEDS under gentle tapping. It could charge a 10 μF capacitor up to 2.25 V within 31 s and a 22 μF capacitor up to 2.25 V within 50 s to turn on a sports watch for 5 s and operate a hygrometer sensor, respectively. This device was further used as a self-powered foot motion sensor, which automatically controls the lights on the steps as one moves over the stair (Fig. 11.). Another PVDF-nylon TENG was developed by Sun *et al.* [236]. Herein they doped MoS_2/CNTs in PVDF to produce TENG that could give an open-circuit voltage reaching 300 V, and short-circuit current (I_{sc}) of ~11.5 μA when the thickness of PVDF nanofibers was 0.08 mm and MoS_2/CNT concentration was 0.3 wt%. It gave a V_{pp} of ~50 V, 90 V, and 100 V when worn while walking, or running. Similar to the above, the large difference in triboelectric polarity of PVDF and nylon membranes encouraged Li *et al.* to structure a wearable, flexible, and lightweight TENG from these [237]. By attaching the TENG to various keys of a keyboard, an output voltage of 8 V is obtained while typing and elbow bending produced 10 V.

Huang *et al.* developed an all-fiber-structured TENG as an energy harvester and self-powered human motion monitor [238]. Here, ethyl cellulose co-electrospun with polyamide 6 was used as the triboelectric positive material, and electrospun PVDF nanofibers with MXene sheet were used as the triboelectric negative material. This device could charge capacitors of varying capacitance and power 180 commercial LEDs. The motion monitoring ability of the TENG was confirmed from the output of the sensor detecting walking, hand clapping, and moving of arms. A TENG with ultrahigh outputs which reached 1502 V and

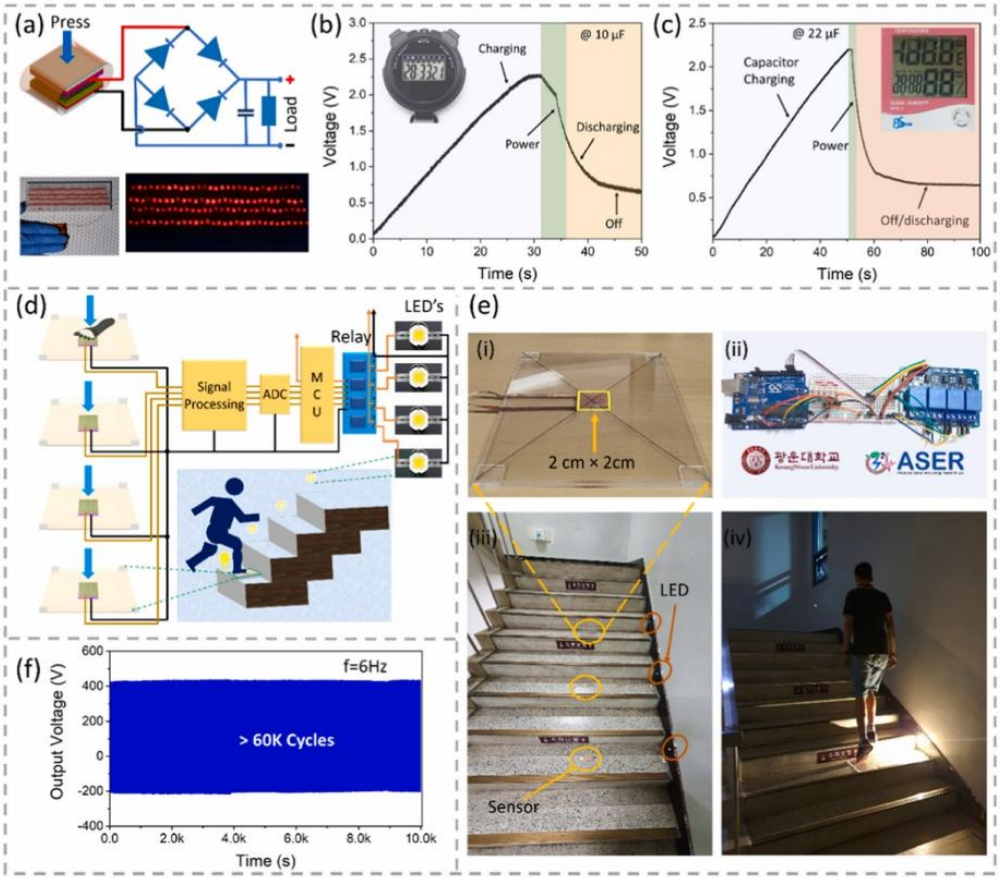

Fig. 11. Application and demonstrations of the TENG. (a) Schematic diagram of the TENG with rectifier circuit, photograph of more than 120 LEDs arranged in series connections, and photograph of the corresponding LEDs turned ON from the TENG upon simple hand tapping motion. (b) Charging and discharging characteristics curves of the capacitors utilized to operate a commercial sport watch (insert shows the turned ON condition hygrometer). (c) Charging and discharging characteristics curves of the capacitors utilized to operate a thermohygrometer sensor from the TENG under gentle hand tapping motion (insert shows the turned ON condition of thermohygrometer sensor) (d) Schematic illustration of the TENG utilized as a self-powered footstep motion sensor. (e) Photograph of (i) fabricated TENG utilized as self-powered foot motion sensor, (ii) sensor data processing and controlling circuitry, (iii) sensor and LED arrangements over the steps, and (iv), real-time step lights control application demonstration. (f) Durability test voltage waveform of TENG at 6 Hz input frequency. (reproduced with permission from Ref. [235]).

50.61 μA, was fabricated by Sun *et al.* [239]. For this, the friction layers were manufactured by growing triangular cone-structured polyaniline (PANI) nanofibers vertically on PI substrates and electrospinning PVDF on PI substrates. The micro/nanostructure obtained during electrospinning provided a rough surface which enhanced the generation of surface charges during the friction process. This TENG with stable output for over 50,000 cycles and 12,000 s at a frequency of 5Hz was later used to form self-powered electrostatic manipulation systems and to reciprocate the movement of macro-charged droplets. In a study conducted by Zhang *et al.*, an electrospun PVDF nanofibrous layer was put to aid the energy harvesting from a flexible triboelectric generator integrated with a high-efficiency energy storage unit [240]. This device gave a V_{oc} of 560 V and I_{sc} of 1.30 μA, respectively.

Busolo *et al.* focused on improving the robustness of the TENG along with improving its energy harvesting potential [241]. For this, a conducting CNT yarn electrode was placed as a rotating collector which was coated with PVDF fibers by electrospinning. For the energy harvesting study, the as-prepared yarn was cyclically tapped against a Nylon 6 film sputter-coated with gold on its non-contact side to form the vertical-separation TENG. Under a constant tapping of 10 N force and 2 Hz frequency, a maximum root-mean-square (RMS) power output of 72 nW at a 400M Ω resistance could be obtained. The ability of the triboelectric yarn (in single electrode mode) to generate voltage curves with distinct peaks, peak width, and peak amplitude portrays it as a wearable motion, haptic, and force sensor. Sun *et al.* developed a wearable, washable, and air-permeable TEN sensor which is also waterproof [242]. Electrospun PA66/MWCNT nanofiber film, conductive fabric electrode, and waterproof and breathable cotton fabric were sewn together to act as the triboelectric positive layer. Electrospun PVDF nanofiber film was sewn together to act as the waterproof, breathable fabric and the triboelectric negative layer. It could power 160 LEDs by itself and be combined with clothes to harvest the energy from hand, shoulder, or arm movement (49 V and 36 V, respectively). Tests revealed that the TENG has consistent output over 10,000 cycles of pressure stimulation and 2–6 h of washing. By weaving Si_3N_4 doped PVDF and polyurethane nanofiber core-spun yarns into a double-layer fabric, Tao *et al.* developed a flexible, wearable, washable, and highly durable TENG [243]. Herein they used a four-needle conjugated electrospinning

technique with copper fibers as the conductive core yarns. Later these yarns were woven into two plain fabrics using textile weaving technology and were sewn into a double-layer fabric by using nylon yarn. The output of the TENG depended on the fabric area and pressing frequency. The TENG was also successful in producing output signals with varying amplitudes and rates corresponding to the difference in the way of finger tapping. Thus, it was established that the TENG could clearly distinguish between various forces and frequencies and hence be used for human motion monitoring, intelligent textiles, etc. Adding to the list the highly durable TENGs, Cheng *et al.* developed a flexible, and self-healing ionic liquid elastomer-based triboelectric generator [244]. Herein, an electrospun PVDF/PU nanofibrous membrane was used as the triboelectric layer and was integrated on the CNTs-doped ionic liquid elastomer (ILC) electrodes by autonomous adhesion. This mechanical damage-resistance TENG with a stable output after five cutting-healing cycles is a promising wearable bioelectronic device for human healthcare detection and human-machine interaction.

In the framework of research during the Covid-19 pandemic, He *et al.* developed a respiration monitoring triboelectric nanogenerator (RM-TENG) The RM-TENG could be attached to a mask to be used as a convenient, smart, changeable, and self-powered mask filter [245]. It could successfully monitor respiratory parameters, such as respiratory rate (RR), inhalation time (t_{in}), exhalation time (t_{ex}), and their ratio (IER=t_{in}/t_{ex}) with good accuracy. Looking into the architecture of RM-TENG, polyacrylonitrile, and PVDF electrospun nanofiber mat functioned as the triboelectric layers, to which conductive aluminum fabrics (with and without holes) were attached as electrodes. A miniature printed circuit board was attached to collect and transmit the data. Fig. 12 Represents the signal wave forms and real-time RR and IER response of RM-TENG during walking and running when the mask was attached to RM-TENG. A novel approach in which a single self-powered device could simultaneously generate power from wave motion, sense, and wirelessly transmit wave information was put forward by Bhatta *et al.* [246]. The TENG had a composite nanofiber of 2D MXene/PVDF and

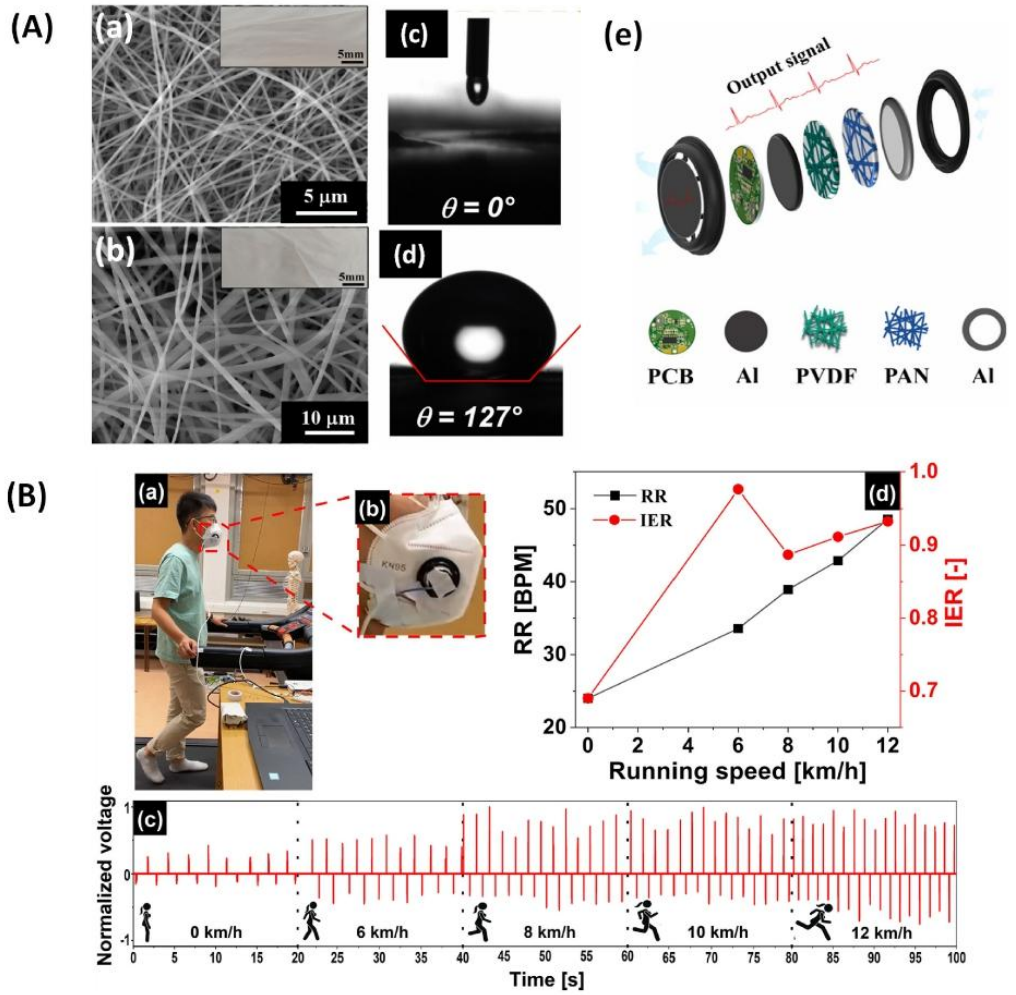

Fig. 12. (A) SEM image of PAN-NFM (insert is the photograph of the PAN-NFM); (b) SEM image of PVDF-NFM (insert is the photograph of the PVDF-NFM); (c) Water contact angle on flat PAN-NFM; (d) Water contact angle on flat PVDF-NFM. (e)Schematic illustration of the RM-TENG. (B) (a) Photo of the subject walking on the treadmill with a mask attached to the RM-TENG. (b) The enlarged mask attached to the RM-TENG. (c) The signal waveforms recorded by the RM-TENG after the subject walked/ran on the treadmill at various speeds. (d) The real-time RR and IER obtained from the RM-TENG after the subject walked/ran on the treadmill at various speeds (only 20 s of data recording for each test is displayed for the clear peaks and frequencies). (reproduced with permission from Ref. [245]).

Nylon 6/6 as the triboelectric layers and a custom-fabricated ferromagnetic composite film of iron-silicon chromium (FeSiCr)/PDMS attached on top of it. A magnetic ball within an ellipsoid body of the device rotated distinctly according to different wave parameters which caused actuation in the TENG, therefore producing an output that was characteristic of the wave. An entire Bluetooth signal processing circuitry was powered from a capacitor (1 F, 5.5 V) charged for 124.5 min to 4.1 V using the device. Continuous data transmission was possible from the Bluetooth circuitry for 31.25 s and stopped as the capacitor voltage dropped below 3.75 V. Apart from using TENG as sensors, Yang *et al.* used electrospun nylon-PVDF nanofiber-based TENG for water/oil (W/O) emulsion separation [247]. In this case, the TENG was used to charge parallel electrodes to produce an asymmetric alternating voltage output of 2500 V for W/O emulsion separation. Under the action of electric field force the demulsification, coalescence, and sedimentation of droplets occurred and visible free water appeared at the bottom of the container. After 30 min of being subjected to the asymmetric AC electric field powered by TENG, the moisture content reduced from 5 wt% to 0.15 wt% in the W/O emulsion. The separation efficiency increased with an increase in the output voltage of the TENG and working time. Furthermore, a sandwich-like TENG was designed to harvest wind energy and demonstrate W/O emulsion separation from natural energy sources. In this case, PVDF nanofibers served as the flexible vibration layer, and nylon nanofibers as the bound layer, an output voltage of 1400 V was produced at a triggering frequency of 28 Hz driven by the wind with a speed of 8 m/s. This was then used to power four parallel electrodes which produced an asymmetric AC electric field. After 30 min of use, the device was able to lower the moisture content in a 500 ml W/O emulsion from 10 wt% to 0.18 wt%. This high efficiency, along with the low cost and safety of the TENG qualifies it for industrial wastewater treatment.

3.1.4. Hybrid nanogenerators and sensors

Hybrid nanogenerators are devices that combine piezoelectric, pyroelectric, or triboelectric mechanisms for efficient and advanced energy harvesting and sensing applications. They are manufactured to maximize the output from both mechanisms without one suppressing the other [191,248]. A few of the recent attempts at developing such novel devices, their structure, and fascinating real-time applications are discussed in this section.

Mahanty *et al.* developed an interesting all-fiber pyro- and piezoelectric nanogenerator (PPNG) healthcare monitor and sensor [249]. Herein, MWCNT-incorporated electrospun PVDF nanofibers were used by them as the active layer along with an interlocked conducting micro-fiber-based electrode to fabricate this device. This PPNG, with an ultra-fast response time of ~10 m s, also had a high electrical throughput and produced an output voltage of ~35 V under repeated finger tapping. The PPNG was even capable of harvesting large temperature fluctuations of ~14.30 K as well as sensing thermal fluctuations as low as ~5.4 K. The device also exhibited different and characteristic responses for different biomechanical signals such as wrist and palm movements, pulse rate, or vocal cord vibrations. Thus, the PPNG could be used as a biomedical sensor capable of monitoring body temperature as well as body movements. This possibility was further demonstrated by integrating the PPNG with a Bluetooth module or Wi-Fi module connected to smartphones, for wireless healthcare monitoring. With a slightly more complex architecture, Wang *et al.* fabricated an all-in-one electronic skin textile for both temperature and pressure sensing [250]. The temperature sensing layer was made up of flexible thermal-resistance carbon nanofibers with localized graphitic structures while PVDF/ZnO nanofibrous membrane acted as the pressure sensing layer. The change in resistance as the temperature changes allowed the e-skin to detect temperature accurately. Practical pressure sensing applications were demonstrated by sensitive weight identification, finger touch pressing, and human carotid pulse capture. Expiratory air temperature monitoring depicted the potential of the e-skin in real-time temperature sensing. The sensor units could also be arranged as e-skin sensor arrays that can distinguish the contour of physical objects. It was finally able to track the real-time touch movements visually which could operate small robots, artificial prosthetics, etc.

Similarly, Ghosh *et al.* developed an all-organic stretchable energy harvester with electrodes made of a xylitol-added poly(3,4-ethylenedioxythiophene): poly(4-styrenesulfonate) film [190]. PANI-reinforced PVDF nanofibers were the piezo and pyro-active material and PDMS coating acted as the protective layer. The device produced maximum pyro- and piezoelectric power outputs of 3 $\mu W/m^2$ and 31 $\mu W/cm^2$ respectively under periodic thermal and mechanical oscillations. It was also attached to a philtrum to demonstrate its breath-sensing functionality and a peak-to-peak voltage of ~555 mV was obtained corresponding to the temperature fluctuation from 298 to 304 K during inhalation and exhalation. By producing a positive pyroelectric output peak as a hot object approached, and a negative pyroelectric output as it moved away (vice versa in the case of a cold object), the device demonstrated its purpose as a temperature sensor. It was also integrated into a smartphone to warrant the applicability of this sensor towards wireless human-machine interfacing point-of-care diagnostic devices (Fig. 13). Xia *et al.* developed a flexible, multi-site tactile and thermal sensor (MTTS) using PVDF nanofibers as the active material, etched copper wire polyimide film as the top electrode, and aluminum electrode array as the bottom one [251]. By arranging several of these sensors into a 2-D array the group successfully employed it for spatial mapping and recording of the 2-D motion trajectory of an object. The output voltage and current from each sensor of the array were recorded as the mapping of the external pressure and thermal stimulus from the object. The piezoelectric and pyroelectric components were extracted from the composite output through the mapping relationship between the signals. The simultaneous pressure and temperature mapping of the human palm and foot were performed using the device and the results showed very few errors from the actual pressure and temperature. The study demonstrated that integration of the MTTS with a wireless sensing system can have extraordinary potential in human behavior detection, disability aids, thermoelectric distribution detection, etc. In addition to the nucleation of the β phase, Li *et al.* explored the possibility of enhancing the piezoelectric and triboelectric effects in PVDF fibers through the addition of fillers [252]. In the study, by simply adding carbon-coated zinc oxide (ZnO@C) nanoparticles, they demonstrated that the piezoelectricity improved due to the nucleation of the β phase and the triboelectricity improved due to the shift in surface potential. The device made from 5% ZnO@C/PVDF nanofibers showed a very high output voltage of 37 V and 39 V as PENG and TENG respectively. It was then put to test as a motion sensor and was successful in producing characteristic outputs for different arm movements and also detecting even slight vibrations, with an output voltage of 0.1 V.

A piezo-tribo hybrid nanogenerator for efficient acoustic harvesting was fabricated by Yu *et al.* from nanoporous PVDF hollow fiber and PDMS valve (PHVAH) [253]. The hollow PVDF fibrous membrane was obtained by removing the polyethylene glycol (PEG) in the PVDF/PEG fiber prepared by coaxial electrospinning. Then, by immersing this membrane in the diluted PDMS, the PDMS valve structure which can mimic the eardrum could be formed between the hollow fibers. To facilitate the direct contact of sound waves with the fibers, iron meshes were placed on both sides of the membranes as electrodes. As the membrane deformed due to sound waves a piezoelectric output was generated along with a triboelectric output due to the rubbing of the PVDF hollow fibers with the PDMS valves and iron meshes (Fig. 14.). The optimum output of the acoustic harvester from the combined piezo and triboelectric effects was equal to 105.5 V under the sound stimulation of 117.6 dB and 150 Hz. PHVAH showed high sensitivity, wide frequency response (70 to 1500 Hz), stability, and flexibility and thus, could be used for real-time detection of sound changes and further harvesting of acoustic energy. In the study of Niu *et al.* on nylon-6/PVDF single-layer nanofibers, the device was fabricated so that it behaves like

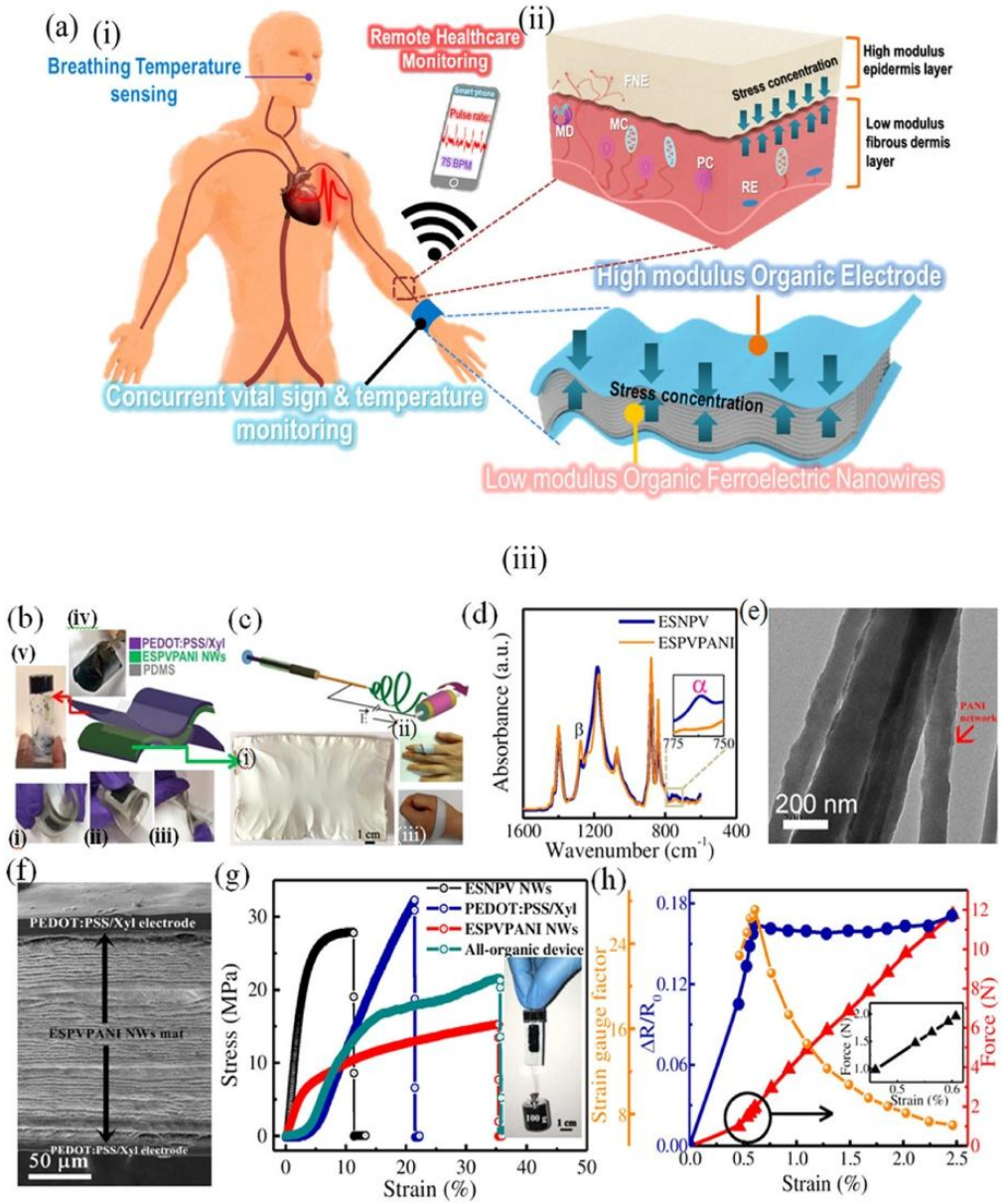

Fig. 13. a) Schematics of (i) wireless arterial pulse monitoring, (ii) epidermal–dermal layer of the human skin, and (iii) developed all-organic epidermal sensor. (b) Three-dimensional (3-D) design and optical images of the all-organic nanoharvester possessing bending (i), folding (ii), and twisting (iii) abilities and composed of (iv) flexible PEDOT:PSS/Xyl electrode manufactured from (v) the PEDOT:PSS/Xyl gel. (c) Schematic of electrospinning used for fabrication of (i) ESPVPANI nanowire mat possessing (ii) excellent flexibility and (iii) conformability to human skin, (d) Fourier transform infrared (FT-IR) spectra, (e) high-resolution transmission electron microscopy (HR-TEM) image, (f) cross-sectional field emission scanning electron microscopy (FE-SEM) image of the all-organic nanoharvester, (g) stress–strain curves, where the inset shows an optical image of the all-organic nanoharvester (without poly(dimethylsiloxane) (PDMS) encapsulation) loaded with a tensile force based on a hanging mass of 100 g, and (h) resistance change and corresponding strain gauge factor of the PEDOT:PSS/Xyl electrode under a range of compressive forces and strains. The inset shows the force versus strain graph up to 0.6% strain. (reproduced with permission from Ref. [190]).

an assembly of many small PENGs and TENGs [254]. Here, the small number of nylon-6 nanofibers incorporated into the PVDF fibrous matrix by co-electrospinning acted as a dopant to form macro dipoles. This improved the charge transport from the dielectric layer to the external electrodes and also caused an endogenous triboelectric effect with PVDF nanofibers. The device was completed with the addition of stainless-steel mesh electrodes and produced a peak voltage output of 201.4 V under a sound wave of frequency 230 Hz, 118 dB SPL. The practical application of the device was put to test by using it to charge batteries and capacitors, light LEDs, and power an electronic watch, and

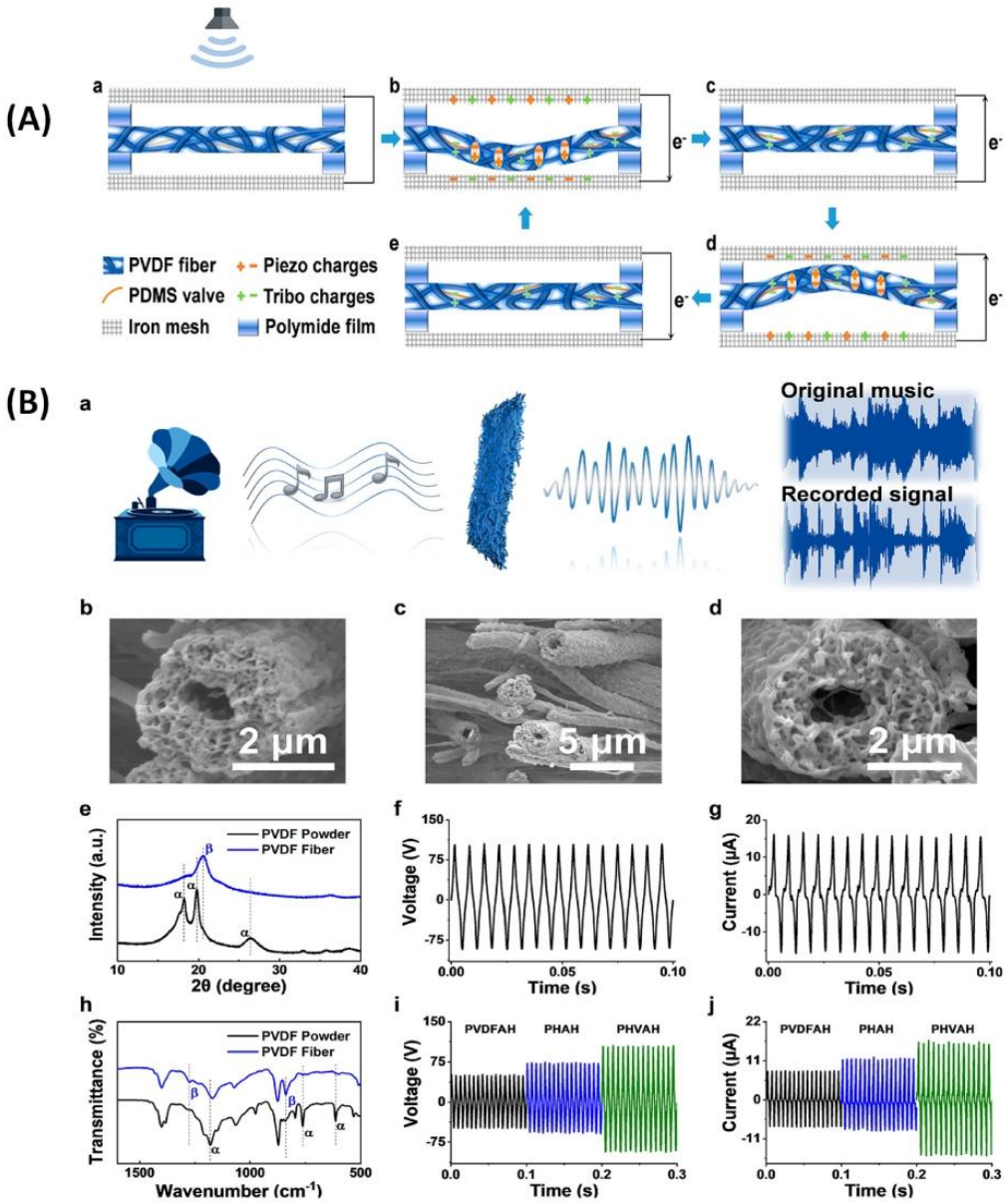

Fig. 14. (A)Structure illustration and mechanism diagram of PHVAH driven by sound: (a) Initial equilibrium state. (b) PVDF hollow fiber and polydimethylsiloxane valve (PHV) membrane deformed by sound waves. (c) Membrane recovers from the deformation. (d) PHV membrane deformed by sound waves in the opposite direction. (e) Membrane recovers from the deformation again. (B) (a) Schematic diagram of the realization from sound to electricity with the fabricated PHVAH. (b) Morphology of single PVDF hollow fiber (PH) fiber. (c) Morphology of PH fibers. (d) Morphology of PVDF fiber with PDMS valves. (e) X-ray diffraction (XRD) pictures of PVDF powder and PVDF fiber prepared by coaxial electrospinning. (f) Optimal output voltage of PHVAH under a sound stimulus of 117.6 dB and 150 Hz. (g) Optimal output current of PHVAH under a sound stimulus of 117.6 dB and 150 Hz. (h) Fourier-transform infrared spectra (FTIR) images of PVDF powder and PVDF fiber. (i) Output voltages of PVDF acoustic harvester (AH), PHAH, and PHVAH under a sound stimulus of 117.6 dB and 150 Hz. (j) Output currents of PVDFAH, PHAH, and PHVAH under a sound stimulus of 117.6 dB and 150 Hz. (reproduced with permission from Ref. [253]).

an electric torch. The charge of capacitors when the device was kept in a noisy workshop with a hammer sounds further justified its applicability.

Based on the above-mentioned research works it is clearly understood that electrospun PVDF films are high potential candidates for different types of nanogenerators and sensors. The study also reveals different types of fillers which contribute to the electroactive response of PVDF, the architecture, and a wide variety of non-conventional energy generation techniques.

3.2. Other applications

The applications of PVDF or electrospun PVDF nanofibers are not

limited to energy harvesting. Over time, both PVDF and electrospun PVDF nanofibers created their own space in several fields from material science to biology and medicine. Along with the intensive study on the polymer, great efforts are being taken to develop novel devices from it for various applications.

Because of the biocompatibility, non-degradable nature, and low fiber diameter of electrospun PVDF nanofibers, Klapstova *et al* used it as glaucoma drainage implants by mixing it with polyethyleneoxide (PEO) [255]. Meanwhile, Agueda *et al.* used PVDF nanofibers for renal tissue regeneration [256]. Along with biocompatibility, minimal cellular and tissue response, and chemical inertness, the possibility of producing uniform fibers with larger pore sizes was the reason for them to choose PVDF nanofibers. By soaking PVDF nanofibers in benzocaine and its complex with β-cyclodextrin (benzocaine-β-cyclodextrin or BNC:β-CD) Rajamohan *et al.* developed a drug delivery system of BNC and BNC:β-CD [257] (Fig. 15 (a).).

PVDF nanofibers are also extensively used for the fabrication of different filters. Because of their filtration efficiency, small pore size, and large surface-to-volume ratio, Victor *et al.* used PVDF-titanium nanotube fibers to develop an antibacterial filter media [258]. In the future, this filter could be used for filtration of other microbes, facemasks, and industrial-scale air filters. Wang *et al.* also used electrospun PVDF membrane to produce air filters that out-performed commercial masks by capturing up to 99.9% of coronavirus aerosols [259]. Pascariu *et al.* demonstrated that electrospun PVDF fibers with lanthanide (Ln) doped ZnO nanoparticles (Ln=Sm, La, Er) as fillers could be developed into membranes for adsorption and photocatalytic degradation of dyes and organic pollutants [260]. When put to test for the degradation of methylene blue (MB) and rhodamine B (RhB) the PVDF/ZnO: La membrane showed color removal efficiency of 96.33% and 93.36% respectively. By using ultrathin PVDF fibers with high surface area, smaller pores, and rough surface, Yang *et al.* developed a high-efficiency coalescence membrane [261]. The membrane, with poor oleophilicity under water, efficiently separated different types of emulsions which indicated its applicability to clean different oil wastewaters. A multi-functional fiber membrane for sewage treatment and desalination was developed by Tessema *et al.* from cesium tungsten oxide/graphitic carbon nitride ($Cs_{0.32}WO_3$@g-C_3N_4) hybrids doped PVDF nanofibers [262]. The multifunctionality of the membrane could be attributed to the hydrophobicity of PVDF. Organic dyes like 4-nitro phenol and tetracycline were also efficiently removed by the membrane making it a suitable candidate for practical waste water treatment in the future (Fig. 15 (b).).

Electrospun PVDF fibers, because of their electrochemical stability, mechanical strength, and flexibility can be used for battery applications [263]. A self-standing electrolyte membrane was created by Makhlooghiazad *et al.* from triisobutyl(methyl)phosphonium bis(fluorosulfonyl)imide ([P1i444][FSI]) OIPC mixed with 20 mol% of NaFSI or

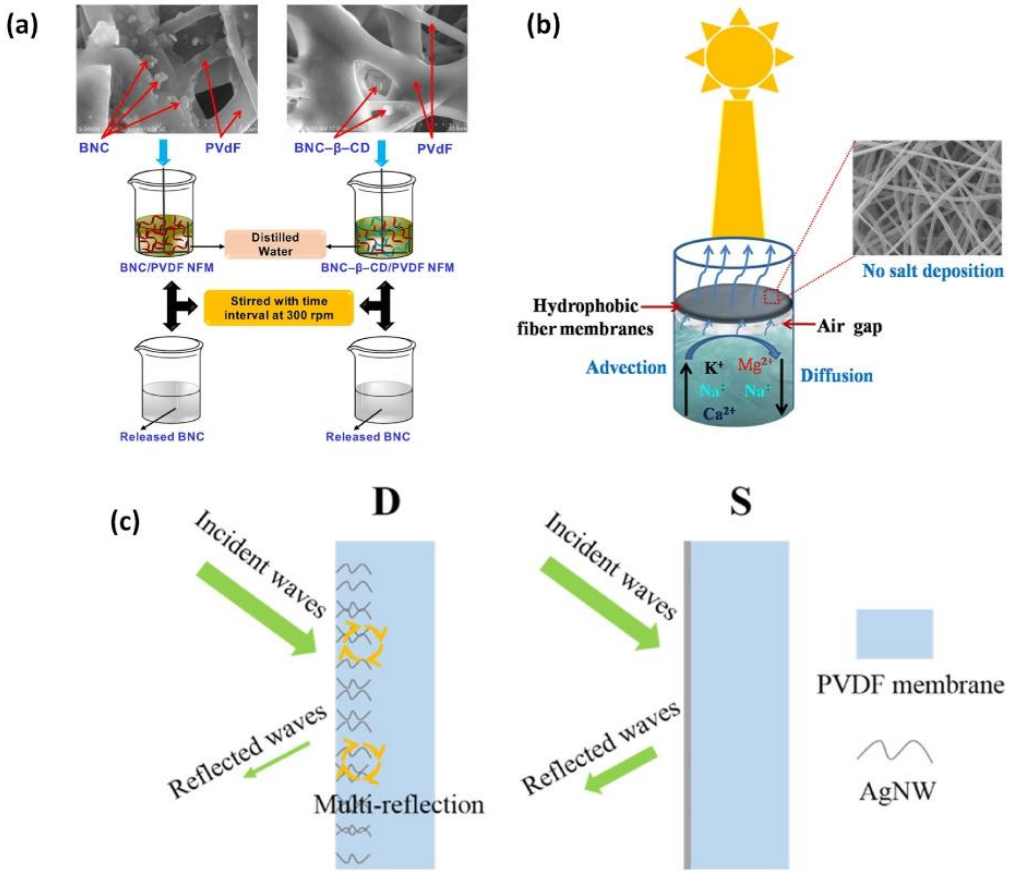

Fig. 15. (a) Schematic procedure for drug release from PVDF nanofibrous membranes (reproduced with permission from Ref. [257]), (b) Schematic illustration of salt resistance hydrophobic CS_xWO_3@g-C_3N_4/PVDF fiber membranes (reproduced with permission from Ref. [262]), Schematic electromagnetic interference shielding mechanisms for the dip-coated and spray-coated PVDF/AgNW hybrid membranes (reproduced with permission from Ref. [265])."

NaTFSI and combined with electrospun PVDF membranes. The PVDF nanofibers, along with providing structural support, interacted with NaTFSI-doped electrolytes and thus made them more conductive and superior to several other fiber-based electrolytes in Na metal batteries. Similarly, Barbosa *et al.* used electrospun PVDF fibers as separators for lithium-ion batteries [264]. In this case, the ionic conductivity of the PVDF fibers was enhanced by the addition of ionic liquids sharing the same anion, but different cations. By improving the electrical conductivity of PVDF nanofibers, it became suitable for electromagnetic interference (EMI) shielding. Qian *et al.* used electrospun porous PVDF nanofibers and developed an efficient lightweight EMI shielding membrane by dip-coating silver nanowires (AgNWs) onto it [265]. The AgNWs reached well into the pores of the PVDF fibers and increased the electrical conductivity of the fibers by forming 3D AgNW networks. This also resulted in the multiple reflections of the EM wave (Fig. 15 (c).). Ann Rose *et al.* also used electrospun PVDF fibers for EMI shielding [266]. Here they added graphene as the filler to improve electrical conductivity and by increasing its concentration, the EMI shielding property increased. Thus, PVDF can play an important role in reducing the growing radiation pollution as well.

4. Conclusions

PVDF is an excellent electroactive polymer, and one of the most studied polymers for the development of nanogenerators, wearable sensors, and many other applications. The elemental information about PVDF, and a wide variety of PVDF-based nanocomposites were discussed in the review. The process of electrospinning, its interest in film production, and the advantages of electrospun PVDF fibers were also explained. Following this, the review details how the different electrospinning parameters help to enhance the β phase, and thereby enhance the piezo-, pyro- and triboelectric performances of PVDF. The review then progresses into the recent developments of PVDF fiber-based devices in energy harvesting and sensing applications. This section highlighted the advances made to harvest the otherwise wasted mechanical and thermal energy. The innovations brought in the fabrication of different types of nanogenerators and their significance in real life as a renewable and green source of energy are discussed. Along with the conventional nanogenerators, the technological advances of hybrid nanogenerators are explored. These types of devices which could simultaneously harvest energy from multiple sources, sense various fluctuations in the surrounding environment, and also be integrated with wireless data transmitting devices are a true example of portable, multipurpose, and sustainable engineering. This review aims to highlight the potential of electrospun PVDF films to develop such functional devices and inspire their use as innovative sustainable sources of energy in the near future. Finally, a peek into the other possible applications of electrospun PVDF nanofibers like tissue regeneration, drug delivery, filtration, or EMI shielding is made to depict other possible uses of the material. Overall, the review is hoped to serve as a useful reference for the scientific community and to look forward to the possible commercialization of PVDF-based multifunctional devices.

Credit Author Statement

Sreelakshmi Moozhiyil Purushothaman: Investigation, methodology, writing- original draft review & editing, visualization

Maïté Fernandes Tronco: Investigation, methodology, writing-original draft and reviewing

Bicy Kottathodi: Visualization, formatting and editing

Isabelle Royaud: Supervision, Resources, reviewing and editing

Marc Ponçot: Supervision, Resources, reviewing and editing

Nandakumar Kalarikkal: Conceptualization, supervision and project administration, funding acquisition

Sabu Thomas: Resources, project administration

Didier Rouxel: Conceptualization, resources, supervision and project administration, funding acquisition

Declaration of competing interest

The authors declare that they have no known competing financial interests or personal relationships that could have appeared to influence the work reported in this paper.

Data availability

No data was used for the research described in the article.

Acknowledgments

The authors of the work would like to thank Indo-French Centre for the Promotion of Advanced Research/Centre Franco-Indien pour la Promotion de la Recherche Avancée (IFCPAR/CEFIPRA), French National Centre for Scientific Research (Centre national de la recherche scientifique, CNRS) and Lorraine University of Excellence for the support.

References

[1] J. Curie, P. Curie, Développement Par Compression de l'électricité Polaire Dans Les Cristaux Hémièdres à Faces Inclinées, Bull. Mineral. (1880) 90–93.
[2] K. Momeni, G.M. Odegard, R.S. Yassar, Nanocomposite electrical generator based on piezoelectric zinc oxide nanowires, J. Appl. Phys. 108 (2010), 114303.
[3] A. Koka, Z. Zhou, H. Tang, H.A. Sodano, Controlled synthesis of ultra-long vertically aligned BaTiO3 nanowire arrays for sensing and energy harvesting applications, Nanotechnology 25 (2014), 375603.
[4] G.L. Smith, J.S. Pulskamp, L.M. Sanchez, D.M. Potrepka, R.M. Proie, T.G. Ivanov, R.Q. Rudy, W.D. Nothwang, S.S. Bedair, C.D. Meyer, PZT-based piezoelectric MEMS technology, J. Am. Ceram. Soc. 95 (2012) 1777–1792.
[5] A.G. Kordlar, J. Koohsorkhi, E.T. Nejad, Barium titanate nanorods on micro-machined silicon substrate for performance enhancement of piezoelectric nanogenerators (NGs), Solid State Electron. 186 (2021), 108168, https://doi.org/10.1016/j.sse.2021.108168.
[6] M.-G. Kang, W.-S. Jung, C.-Y. Kang, S.-J. Yoon, Recent progress on PZT based piezoelectric energy harvesting technologies, Proc. Actuators; MDPI 5 (2016) 5.
[7] H. Kaczmarek, B. Królikowski, E. Klimiec, M. Chylińska, D. Bajer, Advances in the study of piezoelectric polymers, Russ. Chem. Rev. 88 (2019) 749.
[8] K.K. Sadasivuni, J.-J. Cabibihan, D. Ponnamma, M.A.S.A. Al-Maadeed, J. Kim, Biopolymer Composites in Electronics, Elsevier, 2016, 978-0-08-100974-1.
[9] B. Tandon, A. Magaz, R. Balint, J.J. Blaker, S.H. Cartmell, Electroactive biomaterials: vehicles for controlled delivery of therapeutic agents for drug delivery and tissue regeneration, Adv. Drug Deliv. Rev. 129 (2018) 148–168, https://doi.org/10.1016/j.addr.2017.12.012.
[10] T.D. Usher, K.R. Cousins, R. Zhang, S. Ducharme, The promise of piezoelectric polymers, Polym. Int. 67 (2018) 790–798, https://doi.org/10.1002/pi.5584.
[11] M. Smith, S. Kar-Narayan, Piezoelectric polymers: theory, challenges and opportunities, Int. Mater. Rev. 0 (2021) 1–24, https://doi.org/10.1080/09506608.2021.1915935.
[12] S.J. Lee, A.P. Arun, K.J. Kim, Piezoelectric properties of electrospun poly(l-lactic acid) nanofiber Web, Mater. Lett. 148 (2015) 58–62, https://doi.org/10.1016/j.matlet.2015.02.038.
[13] E. Fukada, Piezoelectricity of biopolymers, Biorheology 32 (1995) 593–609, https://doi.org/10.1016/0006-355X(95)00039-C.
[14] S.K. Karan, S. Maiti, A.K. Agrawal, A.K. Das, A. Maitra, S. Paria, A. Bera, R. Bera, L. Halder, A.K. Mishra, et al., Designing high energy conversion efficient bio-inspired vitamin assisted single-structured based self-powered piezoelectric/wind/acoustic multi-energy harvester with remarkable power density, Nano Energy 59 (2019) 169–183, https://doi.org/10.1016/j.nanoen.2019.02.031.
[15] A.J. Lovinger, Poly(Vinylidene fluoride), Dev. Crystalline Polymers—1 (1982) 195–273, https://doi.org/10.1007/978-94-009-7343-5_5.
[16] A.K. Nandi, L. Mandelkern, The influence of chain structure on the equilibrium melting temperature of poly(vinylidene fluoride), J. Polym. Sci. B Polym. Phys. 29 (1991) 1287–1297, https://doi.org/10.1002/POLB.1991.090291012.
[17] J. Joseph, M. Kumar, S. Tripathy, G.D.V.S. Kumar, S.G. Singh, S.R.K. Vaniari, A highly flexible tactile sensor with self-poled electrospun PVDF nanofiber, in: Proceedings of the 2018 IEEE SENSORS, October 2018, pp. 1–4.
[18] Y. Xin, C. Guo, X. Qi, H. Tian, X. Li, Q. Dai, S. Wang, C. Wang, Wearable and unconstrained systems based on PVDF sensors in physiological signals monitoring: a brief review, Ferroelectrics 500 (2016) 291–300, https://doi.org/10.1080/00150193.2016.1230440.
[19] Y. Xin, H. Sun, H. Tian, C. Guo, X. Li, S. Wang, C. Wang, The use of polyvinylidene fluoride (PVDF) films as sensors for vibration measurement: a brief review, Ferroelectrics 502 (2016) 28–42, https://doi.org/10.1080/00150193.2016.1232582.

[20] X. Wang, F. Sun, G. Yin, Y. Wang, B. Liu, M. Dong, Tactile-sensing based on flexible PVDF nanofibers via electrospinning: a review, Sensors 18 (2018), https://doi.org/10.3390/s18020330.

[21] P. Saxena, P. Shukla, A comprehensive review on fundamental properties and applications of poly(vinylidene fluoride) (PVDF), Adv. Compos. Hybrid Mater. 4 (2021) 8–26, https://doi.org/10.1007/s42114-021-00217-0.

[22] Z. He, F. Rault, M. Lewandowski, E. Mohsenzadeh, F. Salaün, Electrospun PVDF nanofibers for piezoelectric applications: a review of the influence of electrospinning parameters on the β phase and crystallinity enhancement, Polymers 13 (2021) 1–23, https://doi.org/10.3390/polym13020174.

[23] Y. Xin, J. Zhu, H. Sun, Y. Xu, T. Liu, C. Qian, A brief review on piezoelectric PVDF nanofibers prepared by electrospinning, Ferroelectrics 526 (2018) 140–151, https://doi.org/10.1080/00150193.2018.1456304.

[24] G. dong Kang, Y. ming Cao, Application and modification of poly(vinylidene fluoride) (PVDF) membranes - a review, J. Membr. Sci. 463 (2014) 145–165, https://doi.org/10.1016/j.memsci.2014.03.055.

[25] S. Lang, N. Muensit, Review of some lesser-known applications of piezoelectric and pyroelectric polymers, Appl. Phys. Mater. Sci. Process 85 (2006) 125–134, https://doi.org/10.1007/s00339-006-3688-8.

[26] A.J. Lovinger, Annealing of poly(vinylidene fluoride) and formation of a fifth phase, Macromolecules 15 (1982) 40–44, https://doi.org/10.1021/ma00229a008.

[27] W.W. Doll, J.B. Lando, Polymorphism of poly(vinylidene fluoride). III. The crystal structure of phase II, J. Macromol. Sci., Part B 4 (1970) 309–329, https://doi.org/10.1080/00222347008212505.

[28] A. Bachmann, J.B. Lando, A reexamination of the crystal structure of phase II of poly(vinylidene fluoride), Macromolecules 14 (1981) 40–46.

[29] A.J. Lovinger, H. Laboratories, M. Hill, Crystallization and morphology of melt-solidified poly, vinylidene fluoride 18 (1980) 793–809.

[30] L. Li, M. Zhang, M. Rong, W. Ruan, Studies on the transformation process of PVDF from α to β phase by stretching, RSC Adv. 4 (2013) 3938–3943, https://doi.org/10.1039/C3RA45134H.

[31] V. Sencadas, S. Lanceros-Mendéz, R. Gregorio Filho, D.L. Chinaglia, A.S. Pouzada, Influence of the processing conditions and corona poling on the morphology of β-PVDF, Proc. - Int. Symp. Electrets 2005 (2005) 161–164, https://doi.org/10.1109/ISE.2005.1612345.

[32] Ye, Y.; Jiang, Y.; Wu, Z.; Zeng, H.; Yang, Y.; Li, W. Characterization and Ferroelectric Properties of Electric Poled PVDF Films.

[33] J. Scheinbeim, C. Nakafuku, B.A. Newman, K.D. Pae, High-pressure crystallization of poly(vinylidene fluoride), J. Appl. Phys. 50 (2008) 4399, https://doi.org/10.1063/1.326429.

[34] J.Y. Lim, S. Kim, Y. Seo, Enhancement of β-phase in PVDF by electrospinning, AIP Conf. Proc. 1664 (2015), 070006, https://doi.org/10.1063/1.4918441.

[35] Y.R. Wang, J.M. Zheng, G.Y. Ren, P.H. Zhang, C. Xu, A flexible piezoelectric force sensor based on PVDF fabrics, Smart Mater. Struct. 20 (2011), 045009, https://doi.org/10.1088/0964-1726/20/4/045009.

[36] S.J. Kang, Y.J. Park, J. Sung, P.S. Jo, C. Park, K.J. Kim, B.O. Cho, Spin cast ferroelectric beta poly(vinylidene fluoride) thin films via rapid thermal annealing, Appl. Phys. Lett. 92 (2008), 012921, https://doi.org/10.1063/1.2830701.

[37] R. Hasegawa, Y. Takahashi, Y. Chatani, H.T. Adokoro, Crystal structures of three crystalline forms of poly(vinylidene fluoride), Polym. J. 3 (1972) 600–610, https://doi.org/10.1295/polymj.3.600.

[38] A. Biswas, K. Henkel, D. Schmeißer, D. Mandal, Comparison of the thermal stability of the α, β and γ phases in poly(vinylidene fluoride) based on in situ thermal fourier transform infrared spectroscopy, Phase Transitions 90 (2017) 1205–1213, https://doi.org/10.1080/01411594.2017.1337902.

[39] S.P. Muduli, S. Parida, S.K. Rout, S. Rajput, M. Kar, Effect of hot press temperature on β-phase, dielectric and ferroelectric properties of solvent casted poly(vinyledene fluoride) films, Mater. Res. Express 6 (2019), 095306, https://doi.org/10.1088/2053-1591/AB2D85.

[40] W.M. Prest, D.J. Luca, The Formation of the γ phase from the α and β polymorphs of polyvinylidene fluoride, J. Appl. Phys. 49 (2008) 5042, https://doi.org/10.1063/1.324439.

[41] F. He, J. Fan, S. Lau, Thermal, mechanical, and dielectric properties of graphite reinforced poly(vinylidene fluoride) composites, Polym. Test. 27 (2008) 964–970, https://doi.org/10.1016/J.POLYMERTESTING.2008.08.010.

[42] A. Samadi, S.M. Hosseini, M. Mohseni, Investigation of the electromagnetic microwaves absorption and piezoelectric properties of electrospun Fe3O4-GO/PVDF hybrid nanocomposites, Org. Electron. 59 (2018) 149–155, https://doi.org/10.1016/J.ORGEL.2018.04.037.

[43] G.T. Davis, J.E. McKinney, M.G. Broadhurst, S.C. Roth, Electric-field-induced phase changes in poly(vinylidene fluoride), J. Appl. Phys. 49 (2008) 4998, https://doi.org/10.1063/1.324446.

[44] A. Biswas, K. Henkel, D. Schmeißer, D. Mandal, Comparison of the Thermal Stability of the α, β and γ Phases in Poly(Vinylidene Fluoride) Based on in Situ Thermal Fourier Transform Infrared Spectroscopy, vol. 90, 2017, pp. 1205–1213, https://doi.org/10.1080/01411594.2017.1337902.

[45] D. Mandal, K.J. Kim, J.S. Lee, Simple synthesis of palladium nanoparticles, β-phase formation, and the control of chain and dipole orientations in palladium-doped poly(vinylidene fluoride) thin films, Langmuir 28 (2012) 10310–10317, https://doi.org/10.1021/LA300983X/SUPPL_FILE/LA300983X_SI_001.

[46] S. Ramasundaram, S. Yoon, K. Kim, C. Park, Preferential Formation of electroactive crystalline phases in poly(vinylidene fluoride)/organically modified silicate nanocomposites, J. Polym. Sci. Part B (2008), https://doi.org/10.1002/POLB.21550.

[47] S. Enomoto, Y. Kawai, M. Sugita, Infrared spectrum of poly(vinylidene fluoride), J. Polym. Sci. 2 Polym. Phys. 6 (1968) 861–869, https://doi.org/10.1002/POL.1968.160060506.

[48] R. Hasegawa, M. Kobayashi, H. Tadokoro, Molecular conformation and packing of poly(vinylidene fluoride). Stability of three crystalline forms and the effect of high pressure, Polym. J. 3 (1972) 591–599, https://doi.org/10.1295/polymj.3.591.

[49] A.A. Hussein, Preparation and characterization of electrical, morphological and topographic properties for advanced conductive PMMA/PVDF/PANI ternary blend for low percolation threshold devices, Int. J. Nanoelectron. Mater. 12 (2019).

[50] Y. Bormashenko, R. Pogreb, O. Stanevsky, E. Bormashenko, Vibrational spectrum of PVDF and its interpretation, Polym. Test. 23 (2004) 791–796, https://doi.org/10.1016/J.POLYMERTESTING.2004.04.001.

[51] P. Martins, A.C. Lopes, S. Lanceros-Mendez, Electroactive phases of poly (vinylidene fluoride): determination, processing and applications, Prog. Polym. Sci. 39 (2014) 683–706, https://doi.org/10.1016/J.PROGPOLYMSCI.2013.07.006.

[52] S. Garain, S. Jana, T.K. Sinha, D. Mandal, Design of in situ poled Ce3+-doped electrospun PVDF/graphene composite nanofibers for fabrication of nanopressure sensor and ultrasensitive acoustic nanogenerator, ACS Appl. Mater. Interfaces 8 (2016) 4532–4540, https://doi.org/10.1021/ACSAMI.5B11356/SUPPL_FILE/AM5B11356_SI_003.AVI.

[53] S. Jana, S. Garain, S. Sen, D. Mandal, The influence of hydrogen bonding on the dielectric constant and the piezoelectric energy harvesting performance of hydrated metal salt mediated PVDF films, Phys. Chem. Chem. Phys. 17 (2015) 17429–17436, https://doi.org/10.1039/C5CP01820J.

[54] K. Maity, B. Mahanty, T.K. Sinha, S. Garain, A. Biswas, S.K. Ghosh, S. Manna, S. K. Ray, D. Mandal, Two-dimensional piezoelectric MoS2-modulated nanogenerator and nanosensor made of poly(vinlydine fluoride) nanofiber webs for self-powered electronics and robotics, Energy Technol. 5 (2017) 234–243, https://doi.org/10.1002/ENTE.201600419.

[55] D. Mandal, K. Henkel, D. Schmeißer, The electroactive β-phase formation in poly (vinylidene fluoride) by gold nanoparticles doping, Mater. Lett. 73 (2012) 123–125, https://doi.org/10.1016/j.matlet.2011.11.117.

[56] A. Salimi, A.A. Yousefi, FTIR studies of β-phase crystal formation in stretched PVDF films, Polym. Test. 22 (2003) 699–704, https://doi.org/10.1016/S0142-9418(03)00003-5.

[57] S. Barrau, A. Ferri, A. Da Costa, J. Defebvin, S. Leroy, R. Desfeux, J.M. Lefebvre, Nanoscale investigations of α- and γ-crystal phases in PVDF-based nanocomposites, ACS Appl. Mater. Interfaces 10 (2018) 13092–13099, https://doi.org/10.1021/acsami.8b02172.

[58] Y. Bormashenko, R. Pogreb, O. Stanevsky, E. Bormashenko, Vibrational spectrum of PVDF and its interpretation, Polym. Test. 23 (2004) 791–796, https://doi.org/10.1016/J.POLYMERTESTING.2004.04.001.

[59] D. Yang, Y. Chen, β-Phase formation of poly(vinylidene fluoride) from the melt induced by quenching, J. Mater. Sci. Lett. 6 (1987) 599–603, https://doi.org/10.1007/BF01739296.

[60] J. Zheng, A. He, J. Li, C.C. Han, Polymorphism control of poly(vinylidene fluoride) through electrospinning, Macromol. Rapid Commun. 28 (2007) 2159–2162, https://doi.org/10.1002/MARC.200700544.

[61] W.A. Yee, M. Kotaki, Y. Liu, X. Lu, Morphology, polymorphism behavior and molecular orientation of electrospun poly(vinylidene fluoride) fibers, Polymer 48 (2007) 512–521, https://doi.org/10.1016/J.POLYMER.2006.11.036.

[62] J. Buckley, P. Cebe, D. Cherdack, J. Crawford, B.S. Ince, M. Jenkins, J. Pan, M. Reveley, N. Washington, N. Wolchover, Nanocomposites of poly(vinylidene fluoride) with organically modified silicate, Polymer 47 (2006) 2411–2422, https://doi.org/10.1016/J.POLYMER.2006.02.012.

[63] S. Manna, S.K. Batabyal, A.K. Nandi, Preparation and characterization of Silver−Poly(vinylidene fluoride) nanocomposites: formation of piezoelectric polymorph of poly(vinylidene fluoride), J. Phys. Chem. B 110 (2006) 12318–12326, https://doi.org/10.1021/JP061445Y.

[64] D. Mandal, K. Henkel, D. Schmeisser, Comment on "preparation and characterization of silver-poly(vinylidene fluoride) nanocomposites: formation of piezoelectric polymorph of poly(vinylidene fluoride).", J. Phys. Chem. B 115 (2011) 10567–10569, https://doi.org/10.1021/JP201335J/SUPPL_FILE/JP201335J_SI_001.PDF.

[65] S.K. Karan, D. Mandal, B.B. Khatua, Self-powered flexible Fe-doped RGO/PVDF nanocomposite: an excellent material for a piezoelectric energy harvester, Nanoscale 7 (2015) 10655–10666, https://doi.org/10.1039/C5NR02067K.

[66] X. Cai, T. Lei, D. Sun, L. Lin, A critical analysis of the α, β and γ phases in poly (vinylidene fluoride) using FTIR, RSC Adv. 7 (2017) 15382–15389, https://doi.org/10.1039/c7ra01267e.

[67] H. Shaik, S.N. Rachith, K.J. Rudresh, A.S. Sheik, K.H. Thulasi Raman, P. Kondaiah, G. Mohan Rao, Towards β-phase formation probability in spin coated PVDF thin films, J. Polym. Res. 24 (2017) 35, https://doi.org/10.1007/s10965-017-1191-x.

[68] P. Dhatarwal, R.J. Sengwa, Polymer compositional ratio-dependent morphology, crystallinity, dielectric dispersion, structural dynamics, and electrical conductivity of PVDF/PEO blend films, Macromol. Res. 27 (2019) 1009–1023, https://doi.org/10.1007/s13233-019-7142-0.

[69] Y.M. Song, Z.D. Zhao, W.X. Yu, B. Li, X.F. Chen, Morphological structures of poly (vinylidene fluoride)/montmorillonite nanocomposites, Sci. China, Ser. B: Chem. 50 (2007) 790–796, https://doi.org/10.1007/s11426-007-0079-8.

[70] T. Nishiyama, T. Sumihara, Y. Sasaki, E. Sato, M. Yamato, H. Horibe, Crystalline structure control of poly(vinylidene fluoride) films with the antisolvent addition method, Polym. J. 48 (2016) 1035–1038, https://doi.org/10.1038/pj.2016.62.
[71] C. Du, B.-K. Zhu, Y.-Y. Xu, Effects of stretching on crystalline phase structure and morphology of hard elastic PVDF fibers, J. Appl. Polym. Sci. 104 (2007) 2254–2259, https://doi.org/10.1002/app.25635.
[72] T. Lei, X. Cai, X. Wang, L. Yu, X. Hu, G. Zheng, W. Lv, L. Wang, D. Wu, D. Sun, et al., Spectroscopic evidence for a high fraction of ferroelectric phase induced in electrospun polyvinylidene fluoride fibers, RSC Adv. 3 (2013) 24952–24958, https://doi.org/10.1039/C3RA42622J.
[73] B. Dutta, E. Kar, N. Bose, S. Mukherjee, Significant enhancement of the electroactive β-phase of PVDF by incorporating hydrothermally synthesized copper oxide nanoparticles, RSC Adv. 5 (2015) 105422–105434, https://doi.org/10.1039/C5RA21903E.
[74] H. Horibe, Y. Hosokawa, H. Oshiro, Y. Sasaki, S. Takahashi, A. Kono, T. Nishiyama, T. Danno, Effect of heat-treatment temperature after polymer melt and blending ratio on the crystalline structure of PVDF in a PVDF/PMMA blend, Polym. J. 45 (2013) 1195–1201, https://doi.org/10.1038/pj.2013.53.
[75] H. Horibe, Y. Sasaki, H. Oshiro, Y. Hosokawa, A. Kono, S. Takahashi, T. Nishiyama, Quantification of the solvent evaporation rate during the production of three PVDF crystalline structure types by solvent casting, Polym. J. 46 (2014) 104–110, https://doi.org/10.1038/pj.2013.75.
[76] H. Kim, T. Fernando, M. Li, Y. Lin, T.-L.B. Tseng, Fabrication and characterization of 3D printed BaTiO3/PVDF nanocomposites, J. Compos. Mater. 52 (2018) 197–206, https://doi.org/10.1177/0021998317704709.
[77] K. Roy, S.K. Ghosh, A. Sultana, S. Garain, M. Xie, C.R. Bowen, K. Henkel, D. Schmeißer, D. Mandal, A self-powered wearable pressure sensor and pyroelectric breathing sensor based on GO interfaced PVDF nanofibers, ACS Appl. Nano Mater. 2 (2019) 2013–2025, https://doi.org/10.1021/acsanm.9b00033.
[78] K. Maity, S. Garain, K. Henkel, D. Schmeißer, D. Mandal, Self-powered human-health monitoring through aligned PVDF nanofibers interfaced skin-interactive piezoelectric sensor, ACS Appl. Polymer Mater. 2 (2020) 862–878, https://doi.org/10.1021/acsapm.9b00846.
[79] M.G. Broadhurst, G.T. Davis, Physical basis for piezoelectricity in PVDF, Ferroelectrics 60 (1984) 3–13, https://doi.org/10.1080/00150198408017504.
[80] S.M. Nakhmanson, M.B. Nardelli, J. Bernholc, Collective polarization effects in β-polyvinylidene fluoride and its copolymers with tri- and tetrafluoroethylene, Phys. Rev. B 72 (2005), 115210, https://doi.org/10.1103/PhysRevB.72.115210.
[81] S. Abdalla, A. Obaid, F.M. Al-Marzouki, Preparation and characterization of poly (vinylidene fluoride): a high dielectric performance nano-composite for electrical storage, Results Phys. 6 (2016) 617–626, https://doi.org/10.1016/j.rinp.2016.09.003.
[82] M.G. Broadhurst, G.T. Davis, J.E. McKinney, R.E. Collins, Piezoelectricity and pyroelectricity in polyvinylidene fluoride—a model, J. Appl. Phys. 49 (1978) 4992–4997, https://doi.org/10.1063/1.324445.
[83] R.G. Kepler, Piezoelectricity, pyroelectricity, and ferroelectricity in organic materials, Annu. Rev. Phys. Chem. 29 (1978) 497–518, https://doi.org/10.1146/annurev.pc.29.100178.002433.
[84] S.S. Bamji, K.J. Kao, M.M. Perlman, Piezoelectricity and pyroelectricity of polyvinylidene fluoride corona-poled at elevated temperature, J. Polym. Sci. Polym. Phys. Ed 18 (1980) 1945–1954, https://doi.org/10.1002/pol.1980.180180907.
[85] Eberle, G.; Eisenmenger, W. Thermal Depolarization of PVDF.
[86] A.B. da Silva, C. Wisniewski, J.V.A. Esteves, R. Gregorio, Effect of drawing on the dielectric properties and polarization of pressed solution cast β-PVDF films, J. Mater. Sci. 45 (2010) 4206–4215, https://doi.org/10.1007/s10853-010-4515-3.
[87] S. Kaur, A. Kumar, A.L. Sharma, D.P. Singh, Influence of annealing on dielectric and polarization behavior of PVDF thick films, J. Mater. Sci. Mater. Electron. 28 (2017) 8391–8396, https://doi.org/10.1007/s10854-017-6556-8.
[88] Electric energy storage properties of poly(vinylidene fluoride), Appl. Phys. Lett. 96 (2010), 192905, https://doi.org/10.1063/1.3428656.
[89] J. Li, Q. Meng, W. Li, Z. Zhang, Influence of crystalline properties on the dielectric and energy storage properties of poly(vinylidene fluoride), J. Appl. Polym. Sci. 122 (2011) 1659–1668, https://doi.org/10.1002/app.34020.
[90] J.G. Bergman, J.H. McFee, G.R. Crane, Pyroelectricity and optical second harmonic generation in polyvinylidene fluoride films, Appl. Phys. Lett. 18 (1971) 203–205, https://doi.org/10.1063/1.1653624.
[91] E. Fukada, T. Furukawa, Piezoelectricity and ferroelectricity in polyvinylidene fluoride, Ultrasonics 19 (1981) 31–39, https://doi.org/10.1016/0041-624X(81)90030-5.
[92] G. Pfister, M. Abkowitz, R.G. Crystal, Pyroelectricity in polyvinylidene fluoride, J. Appl. Phys. 44 (1973) 2064–2071, https://doi.org/10.1063/1.1662513.
[93] H. Kawai, The piezoelectricity of poly (vinylidene fluoride), Jpn. J. Appl. Phys. 8 (1969) 975–976, https://doi.org/10.1143/jjap.8.975.
[94] C. Wan, C.R. Bowen, Multiscale-structuring of polyvinylidene fluoride for energy harvesting: the impact of molecular-, micro- and macro-structure, J. Mater. Chem. 5 (2017) 3091–3128, https://doi.org/10.1039/C6TA09590A.
[95] R.A. Surmenev, T. Orlova, R.V. Chernozem, A.A. Ivanova, A. Bartasyte, S. Mathur, M.A. Surmeneva, Hybrid lead-free polymer-based nanocomposites with improved piezoelectric response for biomedical energy-harvesting applications: a review, Nano Energy 62 (2019) 475–506, https://doi.org/10.1016/j.nanoen.2019.04.090.
[96] R.A. Surmenev, R.V. Chernozem, I.O. Pariy, M.A. Surmeneva, A review on piezo- and pyroelectric responses of flexible nano- and micropatterned polymer surfaces for biomedical sensing and energy harvesting applications, Nano Energy 79 (2021), 105442, https://doi.org/10.1016/j.nanoen.2020.105442.
[97] Y.M. Yousry, K. Yao, S. Chen, W.H. Liew, S. Ramakrishna, Mechanisms for enhancing polarization orientation and piezoelectric parameters of PVDF nanofibers, Adv. Electron. Mater. 4 (2018), 1700562, https://doi.org/10.1002/aelm.201700562.
[98] R.W. Whatmore, Pyroelectric devices and materials, Rep. Prog. Phys. 49 (1999) 1335, https://doi.org/10.1088/0034-4885/49/12/002.
[99] D. DeRossi, A.S. DeReggi, M.G. Broadhurst, S.C. Roth, G.T. Davis, Method of evaluating the thermal stability of the pyroelectric properties of polyvinylidene fluoride: effects of poling temperature and field, J. Appl. Phys. 53 (1982) 6520–6525, https://doi.org/10.1063/1.330078.
[100] H.Z. Li, W.Z. Li, Y.J. Yang, H.L. Tai, X.S. Du, R.Y. Gao, S.Y. Li, Pyroelectric performances of 1-3 ferroelectric composites based on barium titanate nanowires/polyvinylidene fluoride, Ceram. Int. 44 (2018) 19254–19261, https://doi.org/10.1016/j.ceramint.2018.07.150.
[101] G. Prasad, P. Sathiyanathan, A.A. Prabu, K.J. Kim, Piezoelectric characteristics of electrospun PVDF as a function of phase-separation temperature and metal salt content, Macromol. Res. 25 (2017) 981–988, https://doi.org/10.1007/s13233-017-5127-4.
[102] P. Durga Prasad, J. Hemalatha, Dielectric and energy storage density studies in electrospun fiber mats of polyvinylidene fluoride (PVDF)/Zinc ferrite (ZnFe2O4) multiferroic composite, Phys. B Condens. Matter 573 (2019) 1–6, https://doi.org/10.1016/j.physb.2019.08.023.
[103] P.P. Dorneanu, C. Cojocaru, N. Olaru, P. Samoila, A. Airinei, L. Sacarescu, Electrospun PVDF fibers and a novel PVDF/CoFe2O4 fibrous composite as nanostructured sorbent materials for oil spill cleanup, Appl. Surf. Sci. 424 (2017) 389–396, https://doi.org/10.1016/j.apsusc.2017.01.177.
[104] S.M.N. Sultana, S.P. Pawar, M. Kamkar, U. Sundararaj, Tailoring MWCNT dispersion, blend morphology and EMI shielding properties by sequential mixing strategy in immiscible PS/PVDF blends, J. Electron. Mater. 49 (2020) 1588–1600, https://doi.org/10.1007/s11664-019-07371-8.
[105] J.E. Lee, Y.E. Shin, G.H. Lee, J. Kim, H. Ko, H.G. Chae, Polyvinylidene fluoride (PVDF)/Cellulose nanocrystal (CNC) nanocomposite fiber and triboelectric textile sensors, Compos. B Eng. 223 (2021), 109098, https://doi.org/10.1016/j.compositesb.2021.109098.
[106] S. Gopi, P. Balakrishnan, A. Pius, S. Thomas, Chitin nanowhisker (ChNW)-Functionalized electrospun PVDF membrane for enhanced removal of indigo carmine, Carbohydr. Polym. 165 (2017) 115–122, https://doi.org/10.1016/j.carbpol.2017.02.046.
[107] S. Boributh, A. Chanachai, R. Jiraratananon, Modification of PVDF membrane by chitosan solution for reducing protein, fouling 342 (2009) 97–104, https://doi.org/10.1016/j.memsci.2009.06.022.
[108] K. Roy, S. Jana, Z. Mallick, S.K. Ghosh, B. Dutta, S. Sarkar, C. Sinha, D. Mandal, Two-dimensional MOF modulated fiber nanogenerator for effective acoustoelectric conversion and human motion detection, Langmuir 37 (2021) 7107–7117, https://doi.org/10.1021/acs.langmuir.1c00700.
[109] S.M. Hosseini, A.A. Yousefi, Piezoelectric sensor based on electrospun PVDF-MWCNT-cloisite 30B hybrid nanocomposites, Org. Electron. 50 (2017) 121–129, https://doi.org/10.1016/j.orgel.2017.07.035.
[110] K. Deshmukh, M.B. Ahamed, R.R. Deshmukh, S.K.K. Pasha, K.K. Sadasivuni, D. Ponnamma, M.A.-A. AlMaadeed, Striking multiple synergies in novel three-phase fluoropolymer nanocomposites by combining titanium dioxide and graphene oxide as hybrid fillers, J. Mater. Sci. Mater. Electron. 28 (2017) 559–575, https://doi.org/10.1007/s10854-016-5559-1.
[111] O. Agboola, O.S.I. Fayomi, A. Ayodeji, A.O. Ayeni, E.E. Alagbe, S.E. Sanni, E. E. Okoro, L. Moropeng, R. Sadiku, K.W. Kupolati, et al., A review on polymer nanocomposites and their effective applications in membranes and adsorbents for water treatment and gas separation, Membranes 11 (2021) 139, https://doi.org/10.3390/membranes11020139.
[112] S. Thomas, R. Stephen, S. Bandyopadhyay, S. Thomas, Polymer nanocomposites: preparation, properties and applications, Rubber Fibers Plastics Int. 2 (2007) 49–56.
[113] S. Puggal, N. Dhall, N. Singh, M.A. Litt, Review on polymer nanocomposites: synthesis, characterization and mechanical prop, Indian J. Sci. Technol. 9 (2016), https://doi.org/10.17485/ijst/2016/v9i4/81100.
[114] F. Ram, T. Ambone, A. Sharma, R. Murugesan, D. Kajale, V. Borkar, S.F. Ali, P. K. Balu, G. Kumaraswamy, K. Shanmuganathan, Fluorinated nanocellulose-reinforced all-organic flexible ferroelectric nanocomposites for energy generation, J. Phys. Chem. C 122 (2018) 16540–16549, https://doi.org/10.1021/acs.jpcc.8b03470.
[115] S.K. Karan, R. Bera, S. Paria, A.K. Das, S. Maiti, A. Maitra, B.B. Khatua, An approach to design highly durable piezoelectric nanogenerator based on self-poled PVDF/AlO-rgo flexible nanocomposite with high power density and energy conversion efficiency, Adv. Energy Mater. 6 (2016), 1601016, https://doi.org/10.1002/aenm.201601016.
[116] J. Fu, Y. Hou, M. Zheng, M. Zhu, Comparative study of dielectric properties of the PVDF composites filled with spherical and rod-like BaTiO3 derived by molten salt synthesis method, J. Mater. Sci. 53 (2018) 7233–7248, https://doi.org/10.1007/s10853-018-2114-x.
[117] S.F. Mendes, C.M. Costa, C. Caparros, V. Sencadas, S. Lanceros-Méndez, Effect of filler size and concentration on the structure and properties of poly(vinylidene fluoride)/BaTiO3 nanocomposites, J. Mater. Sci. 47 (2012) 1378–1388, https://doi.org/10.1007/s10853-011-5916-7.
[118] P. Thakur, A. Kool, N.A. Hoque, B. Bagchi, F. Khatun, P. Biswas, D. Brahma, S. Roy, S. Banerjee, S. Das, Superior performances of in situ synthesized ZnO/

PVDF thin film based self-poled piezoelectric nanogenerator and self-charged photo-power bank with high durability, Nano Energy 44 (2018) 456–467, https://doi.org/10.1016/j.nanoen.2017.11.065.
[119] W. Zhou, J. Zuo, W. Ren, Thermal conductivity and dielectric properties of Al/PVDF composites, Compos. Appl. Sci. Manuf. 43 (2012) 658–664, https://doi.org/10.1016/j.compositesa.2011.11.024.
[120] R. Ram, V. Soni, D. Khastgir, Electrical and thermal conductivity of polyvinylidene fluoride (PVDF) – conducting carbon black (CCB) composites: validation of various theoretical models, Compos. B Eng. 185 (2020), 107748, https://doi.org/10.1016/j.compositesb.2020.107748.
[121] Dielectric Properties and Thermal Conductivity of PVDF Reinforced with Three Types of Zn Particles, ScienceDirect (2023). https://www.sciencedirect.com/science/article/abs/pii/S1359835X15003139?via%3Dihub.
[122] M. Pusty, P.M. Shirage, Insights and perspectives on graphene-PVDF based nanocomposite materials for harvesting mechanical energy, J. Alloys Compd. 904 (2022), 164060, https://doi.org/10.1016/j.jallcom.2022.164060.
[123] W. Yang, S. Yu, R. Sun, R. Du, Nano- and microsize effect of CCTO fillers on the dielectric behavior of CCTO/PVDF composites, Acta Mater. 59 (2011) 5593–5602, https://doi.org/10.1016/j.actamat.2011.05.034.
[124] A. Biswas, K. Henkel, D. Schmeißer, D. Mandal, Comparison of the Thermal Stability of the α, β and γ Phases in Poly(Vinylidene Fluoride) Based on in Situ Thermal Fourier Transform Infrared Spectroscopy, vol. 90, 2017, pp. 1205–1213, https://doi.org/10.1080/01411594.2017.1337902.
[125] A. Salimi, A.A. Yousefi, Conformational changes and phase transformation mechanisms in PVDF solution-cast films, J. Polym. Sci. B Polym. Phys. 42 (2004) 3487–3495, https://doi.org/10.1002/polb.20223.
[126] T. Nishiyama, T. Sumihara, E. Sato, H. Horibe, Effect of solvents on the crystal formation of poly(vinylidene fluoride) film prepared by a spin-coating process, Polym. J. 49 (2017) 319–325, https://doi.org/10.1038/pj.2016.116.
[127] D.M. Dhevi, A.A. Prabu, M. Pathak, K.J. Kim, Spin-coating temperature induced changes in ferroelectric crystallinity in polyvinylidene fluoride ultrathin films, Adv. Mater. Res. 584 (2012) 197–200. https://doi.org/10.4028/www.scientific.net/AMR.584.197.
[128] Y. Wang, M. Cakmak, J.L. White, Structure development in melt spinning poly (vinylidene fluoride) fibers and Tapes, J. Appl. Polym. Sci. 30 (1985) 2615–2632, https://doi.org/10.1002/app.1985.070300625.
[129] J.M. Samon, J.M. Schultz, B.S. Hsiao, S. Seifert, N. Stribeck, I. Gurke, C. Saw, Structure development during the melt spinning of polyethylene and poly (vinylidene fluoride) fibers by in situ synchrotron small- and wide-angle X-ray scattering techniques, Macromolecules 32 (1999) 8121–8132, https://doi.org/10.1021/ma9906332.
[130] Z.-X. Huang, M.-M. Wang, Y.-H. Feng, J.-P. Qu, β-Phase formation of polyvinylidene fluoride via hot pressing under cyclic pulsating pressure, Macromolecules 53 (2020) 8494–8501, https://doi.org/10.1021/acs.macromol.0c01609.
[131] Z. Liu, S. Li, J. Zhu, L. Mi, G. Zheng, Fabrication of β-phase-enriched PVDF sheets for self-powered piezoelectric sensing, ACS Appl. Mater. Interfaces 14 (2022) 11854–11863, https://doi.org/10.1021/acsami.2c01611.
[132] H. Kim, F. Torres, D. Villagran, C. Stewart, Y. Lin, T.-L.B. Tseng, 3D printing of BaTiO3/PVDF composites with electric in situ poling for pressure sensor applications, Macromol. Mater. Eng. 302 (2017), 1700229, https://doi.org/10.1002/mame.201700229.
[133] S. Bodkhe, P.S.M. Rajesh, F.P. Gosselin, D. Therriault, Simultaneous 3D printing and poling of PVDF and its nanocomposites, ACS Appl. Energy Mater. 1 (2018) 2474–2482, https://doi.org/10.1021/acsaem.7b00337.
[134] N. Bhardwaj, S.C. Kundu, Electrospinning: A fascinating fiber fabrication technique, Biotechnol. Adv. 28 (2010) 325–347, https://doi.org/10.1016/j.biotechadv.2010.01.004.
[135] B. Bera, Literature review on electrospinning process, A fascinating fiber fabrication technique 2 (2016) 14.
[136] J. Doshi, D.H. Reneker, Electrospinning process and applications of electrospun fibers, J. Electrost. 35 (1995) 151–160, https://doi.org/10.1016/0304-3886(95)00041-8.
[137] A.R. Unnithan, R.S. Arathyram, C.S. Kim, Electrospinning of polymers for tissue engineering, in: Nanotechnology Applications for Tissue Engineering, Elsevier, 2015, ISBN 978-0-323-32889-0, pp. 45–55.
[138] B. Robb, B. Lennox, 3 - the electrospinning process, conditions and control, in: L. A. Bosworth, S. Downes (Eds.), Electrospinning for Tissue Regeneration, Woodhead Publishing Series in Biomaterials, Woodhead Publishing, 2011, pp. 51–66, 978-1-84569-741-9.
[139] Z. Li, C. Wang, Effects of working parameters on electrospinning, in: Z. Li, C. Wang (Eds.), One-Dimensional Nanostructures: Electrospinning Technique and Unique Nanofibers, SpringerBriefs in Materials, Springer, Berlin, Heidelberg, 2013, pp. 15–28, 978-3-642-36427-3.
[140] B. Cramariuc, R. Cramariuc, R. Scarlet, L.R. Manea, I.G. Lupu, O. Cramariuc, Fiber diameter in electrospinning process, J. Electrost. 71 (2013) 189–198, https://doi.org/10.1016/j.elstat.2012.12.018.
[141] C. Wang, Y.-W. Cheng, C.-H. Hsu, H.-S. Chien, S.-Y. Tsou, How to manipulate the electrospinning jet with controlled properties to obtain uniform fibers with the smallest diameter?—a brief discussion of solution electrospinning process, J. Polym. Res. 18 (2011) 111–123, https://doi.org/10.1007/s10965-010-9397-1.
[142] C.L. Casper, J.S. Stephens, N.G. Tassi, D.B. Chase, J.F. Rabolt, Controlling surface morphology of electrospun polystyrene fibers: effect of humidity and molecular weight in the electrospinning process, Macromolecules 37 (2004) 573–578, https://doi.org/10.1021/ma0351975.
[143] R. Samatham, K.J. Kim, Electric current as a control variable in the electrospinning process, Polym. Eng. Sci. 46 (2006) 954–959, https://doi.org/10.1002/pen.20565.
[144] A.L. Yarin, S. Koombhongse, D.H. Reneker, Taylor cone and jetting from liquid droplets in electrospinning of nanofibers, J. Appl. Phys. 90 (2001) 4836–4846, https://doi.org/10.1063/1.1408260.
[145] A.K. Moghe, B.S. Gupta, Co-axial electrospinning for nanofiber structures: preparation and applications, Polym. Rev. 48 (2008) 353–377, https://doi.org/10.1080/15583720802022257.
[146] A. Varesano, R.A. Carletto, G. Mazzuchetti, Experimental investigations on the multi-jet electrospinning process, J. Mater. Process. Technol. 209 (2009) 5178–5185, https://doi.org/10.1016/j.jmatprotec.2009.03.003.
[147] M. Simonet, O.D. Schneider, P. Neuenschwander, W.J. Stark, Ultraporous 3D polymer meshes by low-temperature electrospinning: use of ice crystals as a removable void template, Polym. Eng. Sci. 47 (2007) 2020–2026, https://doi.org/10.1002/pen.20914.
[148] S.R. Givens, K.H. Gardner, J.F. Rabolt, D.B. Chase, High-temperature electrospinning of polyethylene microfibers from solution, Macromolecules 40 (2007) 608–610, https://doi.org/10.1021/ma062398a.
[149] G. Han, Y. Su, Y. Feng, N. Lu, Approaches for increasing the β-phase concentration of electrospun polyvinylidene fluoride (PVDF) nanofibers, ES Mater. Manufac. 6 (2019) 75–80.
[150] R. Fu, S. Chen, Y. Lin, Y. He, d Y. Gu, Preparation and piezoelectric investigation of electrospun polyvinylidene fluoride fibrous membrane, J. Nanosci. Nanotechnol. 16 (2016) 12337–12343, https://doi.org/10.1166/jnn.2016.13750.
[151] K. Magniez, C. De Lavigne, B.L. Fox, The effects of molecular weight and polymorphism on the fracture and thermo-mechanical properties of a carbon-fibre composite modified by electrospun poly (vinylidene fluoride) membranes, Polymer 51 (2010) 2585–2596, https://doi.org/10.1016/j.polymer.2010.04.021.
[152] B. Zaarour, L. Zhu, X. Jin, Controlling the surface structure, mechanical properties, crystallinity, and piezoelectric properties of electrospun PVDF nanofibers by maneuvering molecular weight, Soft Mater. 17 (2019) 181–189, https://doi.org/10.1080/1539445X.2019.1582542.
[153] Z. He, F. Rault, M. Lewandowski, E. Mohsenzadeh, F. Salaün, Electrospun PVDF nanofibers for piezoelectric applications: a review of the influence of electrospinning parameters on the β phase and crystallinity enhancement, Polymers 13 (2021) 1–23, https://doi.org/10.3390/polym13020174.
[154] H. Gade, S. Nikam, G.G. Chase, D.H. Reneker, Effect of electrospinning conditions on β-phase and surface charge potential of PVDF fibers, Polymer 228 (2021), 123902, https://doi.org/10.1016/j.polymer.2021.123902.
[155] A. Baji, Y.-W. Mai, Q. Li, Y. Liu, Electrospinning induced ferroelectricity in poly (vinylidene fluoride) fibers, Nanoscale 3 (2011) 3068–3071, https://doi.org/10.1039/C1NR10467E.
[156] L.M.M. Costa, R.E.S. Bretas, R. Gregorio, Effect of solution concentration on the electrospray/electrospinning transition and on the crystalline phase of PVDF, Mater. Sci. Appl. 1 (2010) 247–252, https://doi.org/10.4236/msa.2010.14036.
[157] J. Zheng, A. He, J. Li, C.C. Han, Polymorphism control of poly(vinylidene fluoride) through electrospinning, Macromol. Rapid Commun. 28 (2007) 2159–2162, https://doi.org/10.1002/MARC.200700544.
[158] R.K. Singh, S.W. Lye, J. Miao, Holistic investigation of the electrospinning parameters for high percentage of β-phase in PVDF nanofibers, Polymer 214 (2021), 123366, https://doi.org/10.1016/j.polymer.2020.123366.
[159] S. Gee, B. Johnson, A.L. Smith, Optimizing electrospinning parameters for piezoelectric PVDF nanofiber membranes, J. Membr. Sci. 563 (2018) 804–812, https://doi.org/10.1016/j.memsci.2018.06.050.
[160] S. Saha, V. Yauvana, S. Chakraborty, D. Sanyal, Synthesis and characterization of polyvinylidene-fluoride (PVDF) nanofiber for application as piezoelectric force sensor, Mater. Today: Proc. 18 (2019) 1450–1458, https://doi.org/10.1016/j.matpr.2019.06.613.
[161] H. Jiyong, Z. Yinda, Z. Hele, G. Yuanyuan, Y. Xudong, Mixed effect of main electrospinning parameters on the $\upbeta$-Phase crystallinity of electrospun PVDF nanofibers, Smart Mater. Struct. 26 (2017), 085019, https://doi.org/10.1088/1361-665X/aa7245.
[162] E. Ghafari, N. Lu, Self-polarized electrospun polyvinylidene fluoride (PVDF) nanofiber for sensing applications, Compos. B Eng. 160 (2019) 1–9, https://doi.org/10.1016/j.compositesb.2018.10.011.
[163] J.S. Andrew, D.R. Clarke, Effect of electrospinning on the ferroelectric phase content of polyvinylidene difluoride fibers, Langmuir 24 (2008) 670–672, https://doi.org/10.1021/la7035407.
[164] G. Kalimuldina, N. Turdakyn, I. Abay, A. Medeubayev, A. Nurpeissova, D. Adair, Z. Bakenov, A review of piezoelectric PVDF film by electrospinning and its applications, Sensors 20 (2020) 5214, https://doi.org/10.3390/s20185214.
[165] H. Shao, J. Fang, H. Wang, T. Lin, Effect of electrospinning parameters and polymer concentrations on mechanical-to-electrical energy conversion of randomly-oriented electrospun poly(vinylidene fluoride) nanofiber mats, RSC Adv. 5 (2015) 14345–14350, https://doi.org/10.1039/C4RA16360E.
[166] A.S. Motamedi, H. Mirzadeh, F. Hajiesmaeilbaigi, S. Bagheri-Khoulenjani, M. Shokrgozar, Effect of electrospinning parameters on morphological properties of PVDF nanofibrous scaffolds, Prog Biomater 6 (2017) 113–123, https://doi.org/10.1007/s40204-017-0071-0.
[167] B. Zaarour, L. Zhu, X. Jin, Maneuvering the secondary surface morphology of electrospun poly (vinylidene fluoride) nanofibers by controlling the processing parameters, Mater. Res. Express 7 (2019), 015008, https://doi.org/10.1088/2053-1591/ab582d.

[168] E. Ghafari, X. Jiang, N. Lu, Surface morphology and beta-phase formation of single polyvinylidene fluoride (PVDF) composite nanofibers, Adv. Compos. Hybrid Mater. 1 (2018) 332–340, https://doi.org/10.1007/s42114-017-0016-z.
[169] T. Lei, P. Zhu, X. Cai, L. Yang, F. Yang, Electrospinning of PVDF nanofibrous membranes with controllable crystalline phases, Appl. Phys. A 120 (2015) 5–10, https://doi.org/10.1007/s00339-015-9197-x.
[170] F. Huang, Q. Wei, J. Wang, Y. Cai, Y. Huang, Effect of temperature on structure, morphology and crystallinity of PVDF nanofibers via electrospinning, E-Polymers 8 (2008), https://doi.org/10.1515/epoly.2008.8.1.1758.
[171] S. Mohamadi, N. Sharifi-Sanjani, Crystallization of PVDF in graphene-filled electrospun PVDF/PMMA nanofibers processed at three different conditions, Fibers Polym. 17 (2016) 582–592.
[172] P.K. Szewczyk, D.P. Ura, U. Stachewicz, Humidity controlled mechanical properties of electrospun polyvinylidene fluoride (PVDF) fibers, Fibers 8 (2020) 65, https://doi.org/10.3390/fib8100065.
[173] B. Zaarour, L. Zhu, C. Huang, X. Jin, Controlling the secondary surface morphology of electrospun PVDF nanofibers by regulating the solvent and relative humidity, Nanoscale Res. Lett. 13 (2018) 285, https://doi.org/10.1186/s11671-018-2705-0.
[174] E.S. Cozza, O. Monticelli, E. Marsano, P. Cebe, On the electrospinning of PVDF: influence of the experimental conditions on the nanofiber properties, Polym. Int. 62 (2013) 41–48, https://doi.org/10.1002/pi.4314.
[175] Y. Xin, J. Zhu, H. Sun, Y. Xu, T. Liu, C. Qian, A brief review on piezoelectric PVDF nanofibers prepared by electrospinning, Ferroelectrics 526 (2018) 140–151, https://doi.org/10.1080/00150193.2018.1456304.
[176] K. Hwang, B. Kwon, H. Byun, Preparation of PVdF nanofiber membranes by electrospinning and their use as secondary battery separators, J. Membr. Sci. 378 (2011) 111–116, https://doi.org/10.1016/j.memsci.2011.06.005.
[177] T. Lei, L. Yu, G. Zheng, L. Wang, D. Wu, D. Sun, Electrospinning-induced preferred dipole orientation in PVDF fibers, J. Mater. Sci. 50 (2015) 4342–4347, https://doi.org/10.1007/s10853-015-8986-0.
[178] F. Mokhtari, M. Latifi, M. Shamshirsaz, Electrospinning/electrospray of polyvinylidene fluoride (PVDF): piezoelectric nanofibers, J. Text. Inst. (2015) 1–19, https://doi.org/10.1080/00405000.2015.1083300.
[179] A.G. Holmes-Siedle, P.D. Wilson, A.P. Verrall, PVdF: An electronically-active polymer for industry, Mater. Des. 4 (1983) 910–918, https://doi.org/10.1016/0261-3069(84)90003-7.
[180] P. Ueberschlag, PVDF piezoelectric polymer, Sens. Rev. 21 (2001) 118–126, https://doi.org/10.1108/02602280110388315.
[181] S. Wang, Y. Bai, T. Zhang, Chapter 1 - materials, systems, and devices for wearable bioelectronics, in: O. Parlak, A. Salleo, A. Turner (Eds.), Wearable Bioelectronics, Materials Today, Elsevier, 2020, pp. 1–48, 978-0-08-102407-2.
[182] S.B.I.X. Lang, Literature guide to pyroelectricity 1978-1979, Ferroelectrics 23 (1980) 133–160, https://doi.org/10.1080/00150198008018796.
[183] J. Zhao, F. Li, Z. Wang, P. Dong, G. Xia, K. Wang, Flexible PVDF nanogenerator-driven motion sensors for human body motion energy tracking and monitoring, J. Mater. Sci. Mater. Electron. 32 (2021) 14715–14727, https://doi.org/10.1007/s10854-021-06027-w.
[184] D. Zhang, X. Zhang, X. Li, H. Wang, X. Sang, G. Zhu, Enhanced piezoelectric performance of PVDF/BiCl 3/ZnO nanofiber-based piezoelectric nanogenerator, Eur. Polym. J. 166 (2022) 110956, https://doi.org/10.1016/j.eurpolymj.2021.110956.
[185] M.O. Shaikh, Y.-B. Huang, C.-C. Wang, C.-H. Chuang, Wearable woven triboelectric nanogenerator utilizing electrospun PVDF nanofibers for mechanical energy harvesting, Micromachines 10 (2019) 438, https://doi.org/10.3390/mi10070438.
[186] H.T. Baytekin, A.Z. Patashinski, M. Branicki, B. Baytekin, S. Soh, B. A. Grzybowski, The mosaic of surface charge in contact electrification, Science 333 (2011) 308–312, https://doi.org/10.1126/science.1201512.
[187] S. Cheon, H. Kang, H. Kim, Y. Son, J.Y. Lee, H.-J. Shin, S.-W. Kim, J.H. Cho, High-performance triboelectric nanogenerators based on electrospun polyvinylidene fluoride–silver nanowire composite nanofibers, Adv. Funct. Mater. 28 (2018), 1703778, https://doi.org/10.1002/adfm.201703778.
[188] T. Huang, C. Wang, H. Yu, H. Wang, Q. Zhang, M. Zhu, Human walking-driven wearable all-fiber triboelectric nanogenerator containing electrospun polyvinylidene fluoride piezoelectric nanofibers, Nano Energy 14 (2015) 226–235, https://doi.org/10.1016/j.nanoen.2015.01.038.
[189] Y. Zheng, L. Cheng, M. Yuan, Z. Wang, L. Zhang, Y. Qin, T. Jing, An electrospun nanowire-based triboelectric nanogenerator and its application in a fully self-powered UV detector, Nanoscale 6 (2014) 7842–7846, https://doi.org/10.1039/C4NR01934B.
[190] S.K. Ghosh, T.K. Sinha, M. Xie, C.R. Bowen, S. Garain, B. Mahanty, K. Roy, K. Henkel, D. Schmeißer, J.K. Kim, et al., Temperature-pressure hybrid sensing all-organic stretchable energy harvester, ACS Appl. Electron. Mater. 3 (2021) 248–259, https://doi.org/10.1021/acsaelm.0c00816.
[191] Y. Guo, X.-S. Zhang, Y. Wang, W. Gong, Q. Zhang, H. Wang, J. Brugger, All-fiber hybrid piezoelectric-enhanced triboelectric nanogenerator for wearable gesture monitoring, Nano Energy 48 (2018) 152–160, https://doi.org/10.1016/j.nanoen.2018.03.033.
[192] S.K. Ghosh, D. Mandal, Synergistically enhanced piezoelectric output in highly aligned 1D polymer nanofibers integrated all-fiber nanogenerator for wearable nano-tactile sensor, Nano Energy 53 (2018) 245–257, https://doi.org/10.1016/j.nanoen.2018.08.036.
[193] K. Maity, D. Mandal, All-organic high-performance piezoelectric nanogenerator with multilayer assembled electrospun nanofiber mats for self-powered multifunctional sensors, ACS Appl. Mater. Interfaces 10 (2018) 18257–18269, https://doi.org/10.1021/acsami.8b01862.
[194] H. Chen, L. Zhou, Z. Fang, S. Wang, T. Yang, L. Zhu, X. Hou, H. Wang, Z.L. Wang, Piezoelectric nanogenerator based on in situ growth all-inorganic CsPbBr3 perovskite nanocrystals in PVDF fibers with long-term stability, Adv. Funct. Mater. 31 (2021) 1–12, https://doi.org/10.1002/adfm.202011073.
[195] A. Sengupta, S. Das, S. Dasgupta, P. Sengupta, P. Datta, Flexible nanogenerator from electrospun PVDF-polycarbazole nanofiber membranes for human motion energy-harvesting device applications, ACS Biomater. Sci. Eng. 7 (2021) 1673–1685, https://doi.org/10.1021/acsbiomaterials.0c01730.
[196] V. Amith, R. Sridhar, A. Gangadhar, K.A. Vishnumurthy, Design and synthesis of PVDF-cloisite-30B nanocomposite fibers for energy harvesting applications, Surface. Interfac. 22 (2021), 100869, https://doi.org/10.1016/j.surfin.2020.100869.
[197] M. Sekkarapatti Ramasamy, A. Rahaman, B. Kim, Influence of oleylamine–functionalized boron nitride nanosheets on the crystalline phases, mechanical and piezoelectric properties of electrospun PVDF nanofibers, Compos. Sci. Technol. 203 (2021), 108570, https://doi.org/10.1016/j.compscitech.2020.108570.
[198] S.P. Muduli, S. Veeralingam, S. Badhulika, Interface induced high-performance piezoelectric nanogenerator based on a electrospun three-phase composite, Nano Fi Ber for Wearable Appl. (2021), https://doi.org/10.1021/acsaem.1c02371.
[199] Q. Zhao, L. Yang, Y. Ma, H. Huang, H. He, H. Ji, Z. Wang, J. Qiu, Highly sensitive, reliable and flexible pressure sensor based on piezoelectric PVDF hybrid film using MXene nanosheet reinforcement, J. Alloys Compd. 886 (2021), 161069, https://doi.org/10.1016/j.jallcom.2021.161069.
[200] R.T. Shivalingappa, H. Narayana, R. Narasimha, P. Purushothaman, P. Badiger, S. Savarn, U. Majumdar, G. Angadi, Development of poly (vinylidene fl uoride)/silver nanoparticle electrospun, Nano Fi Bre Mats for Energy Harvest. (2021), https://doi.org/10.1177/09673911211042005.
[201] M. Zeyrek Ongun, S. Oguzlar, U. Kartal, M. Yurddaskal, O. Cihanbegendi, Energy harvesting nanogenerators: electrospun β-PVDF nanofibers accompanying ZnO NPs and ZnO@Ag NPs, Solid State Sci. 122 (2021), 106772, https://doi.org/10.1016/j.solidstatesciences.2021.106772.
[202] M. Hasanzadeh, M.R. Ghahhari, S.M. Bidoki, Enhanced piezoelectric performance of PVDF-based electrospun nanofibers by utilizing in situ synthesized graphene-ZnO nanocomposites, J. Mater. Sci. Mater. Electron. (2021), https://doi.org/10.1007/s10854-021-06132-w.
[203] S. Shetty, A.M. Shanmugharaj, S. Anandhan, Physico-chemical and piezoelectric characterization of electroactive nanofabrics based on functionalized graphene/talc nanolayers/PVDF for energy harvesting, J. Polym. Res. 28 (2021) 419, https://doi.org/10.1007/s10965-021-02786-6.
[204] J. Yi, Y. Song, Z. Cao, C. Li, C. Xiong, Gram-scale Y-doped ZnO and PVDF electrospun film for piezoelectric nanogenerators, Compos. Sci. Technol. 215 (2021), 109011, https://doi.org/10.1016/j.compscitech.2021.109011.
[205] S. Ponnan, T.W. Schmidt, T. Li, H.B. Gunasekaran, X. Ke, Y. Huang, S. Mubarak, A. Anand Prabu, Z. Weng, L. Wu, Electrospun polyvinylidene fluoride-magnesiochromite nanofiber-based piezoelectric nanogenerator for energy harvesting applications, ACS Appl. Polymer Mater. 3 (2021) 4879–4888, https://doi.org/10.1021/acsapm.1c00627.
[206] S. Wang, K. Shi, B. Chai, S. Qiao, Z. Huang, P. Jiang, X. Huang, Core-shell structured silk fibroin/PVDF piezoelectric nanofibers for energy harvesting and self-powered sensing, Nano Mater. Sci. (2021), https://doi.org/10.1016/j.nanoms.2021.07.008.
[207] L. Xue, W. Fan, Y. Yu, K. Dong, C. Liu, Y. Sun, C. Zhang, W. Chen, R. Lei, K. Rong, et al., A novel strategy to fabricate core-sheath structure piezoelectric yarns for wearable energy harvesters, Adv. Fiber Mater. 3 (2021) 239–250, https://doi.org/10.1007/s42765-021-00081-z.
[208] Z. Bai, Y. Song, J. Peng, D. Chen, Y. Zhou, Y. Tao, S. Gu, J. Xu, Z. Deng, X. Yin, et al., Poly (vinylidene fluoride), nano fi ber array films with high strength for effective impact energy harvesting (2021) 1–8, https://doi.org/10.1002/ente.202100345.
[209] X. Du, Z. Zhou, Z. Zhang, L. Yao, Q. Zhang, H. Yang, Porous, multi-layered piezoelectric composites based on highly oriented PZT/PVDF electrospinning fibers for high-performance piezoelectric nanogenerators, J Adv Ceram 11 (2022) 331–344, https://doi.org/10.1007/s40145-021-0537-3.
[210] K. Maity, S. Garain, K. Henkel, D. Schmeißer, D. Mandal, Self-powered human-health monitoring through aligned PVDF nanofibers interfaced skin-interactive piezoelectric sensor, ACS Appl. Polymer Mater. 2 (2020) 862–878, https://doi.org/10.1021/acsapm.9b00846.
[211] B. Mahanty, S.K. Ghosh, S. Jana, Z. Mallick, S. Sarkar, D. Mandal, ZnO nanoparticle confined stress amplified all-fiber piezoelectric nanogenerator for self-powered healthcare monitoring, Sustain. Energy Fuels 5 (2021) 4389–4400, https://doi.org/10.1039/D1SE00444A.
[212] X.L.M.W.H. Peng, X. Zhang, Y. Ting, W.T. Li, C. Lou, J. Lin, Hierarchically Structured Polyvinylidene Fluoride Core-Shell Composite Yarn Based on Electrospinning Coating Method to Improve Piezoelectricity, 2022, pp. 1–11, https://doi.org/10.1002/pat.5613.
[213] C.-K. Yen, K. Dutt, Y.-S. Yao, W.-J. Wu, Y.-L. Shiue, C.-T. Pan, C.-W. Chen, W.-F. Chen, Development of flexible biceps tremors sensing chip of PVDF fibers with nano-silver particles by near-field electrospinning, Polymers 14 (2022) 331, https://doi.org/10.3390/polym14020331.
[214] T. Li, M. Qu, C. Carlos, L. Gu, F. Jin, T. Yuan, X. Wu, J. Xiao, T. Wang, W. Dong, et al., High-performance poly(vinylidene difluoride)/dopamine core/shell piezoelectric nanofiber and its application for biomedical sensors, Adv. Mater. 33 (2021), 2006093, https://doi.org/10.1002/adma.202006093.

[215] J. Zhao, F. Li, Z. Wang, P. Dong, G. Xia, K. Wang, Flexible PVDF nanogenerator-driven motion sensors for human body motion energy tracking and monitoring, J. Mater. Sci. Mater. Electron. 32 (2021) 14715–14727, https://doi.org/10.1007/s10854-021-06027-w.
[216] D. Demirci, M. Koç, S. Aktürk, Piezoelectric and magnetoelectric properties of PVDF/NiFe 2 O 4 based electrospun nanofibers for flexible piezoelectric nanogenerators, 36, 2022, pp. 143–159, https://doi.org/10.1016/j.cap.2022.01.013.
[217] S. Mondal, T. Paul, S. Maiti, B.K. Das, K.K. Chattopadhyay, Human motion interactive mechanical energy harvester based on all inorganic perovskite-PVDF, Nano Energy 74 (2020) 104870, https://doi.org/10.1016/j.nanoen.2020.104870.
[218] J. Yang, Y. Zhang, Y. Li, Z. Wang, W. Wang, Q. An, W. Tong, Piezoelectric nanogenerators based on graphene oxide/PVDF electrospun nanofiber with enhanced performances by in-situ reduction, Mater. Today Commun. 26 (2021), https://doi.org/10.1016/j.mtcomm.2020.101629.
[219] W. He, Y. Guo, Y.B. Zhao, F. Jiang, J. Schmitt, Y. Yue, J. Liu, J. Cao, J. Wang, Self-supporting smart air filters based on PZT/PVDF electrospun nanofiber composite membrane, Chem. Eng. J. 423 (2021), 130247, https://doi.org/10.1016/j.cej.2021.130247.
[220] H.M. Mousa, H.S. Fahmy, R. Abouzeid, G.T. Abdel-Jaber, W.Y. Ali, Polyvinylidene fluoride-cellulose nanocrystals hybrid nanofiber membrane for energy harvesting and oil-water separation applications, Mater. Lett. 306 (2022), 130965, https://doi.org/10.1016/j.matlet.2021.130965.
[221] T. Li, F. Jin, M. Qu, F. Yang, J. Zhang, T. Yuan, W. Dong, J. Zheng, T. Wang, Z.-Q. Feng, Power generation from moisture fluctuations using polyvinyl alcohol-wrapped dopamine/polyvinylidene difluoride nanofibers, Small 17 (2021), 2102550, https://doi.org/10.1002/smll.202102550.
[222] H. Lu, J. Zhang, L. Yang, Y. Zhang, Y. Wu, H. Zheng, Enhanced output performance of piezoelectric nanogenerators by Tb-modified (BaCa)(ZrTi)O3 and 3D core/shell structure design with PVDF composite spinning for microenergy harvesting, ACS Appl. Mater. Interfaces 14 (2022) 12243–12256, https://doi.org/10.1021/acsami.1c23946.
[223] B. Mahanty, S.K. Ghosh, S. Jana, K. Roy, S. Sarkar, D. Mandal, All-fiber acousto-electric energy harvester from magnesium salt-modulated PVDF nanofiber, Sustain. Energy Fuels 5 (2021) 1003–1013, https://doi.org/10.1039/d0se01185a.
[224] K. Roy, S. Jana, Z. Mallick, S.K. Ghosh, B. Dutta, S. Sarkar, C. Sinha, D. Mandal, Two-dimensional MOF modulated fiber nanogenerator for effective acoustoelectric conversion and human motion detection, Langmuir 37 (2021) 7107–7117, https://doi.org/10.1021/acs.langmuir.1c00700.
[225] F. Xu, J. Yang, R. Dong, H. Jiang, C. Wang, W. Liu, Z. Jiang, Wave - shaped piezoelectric nanofiber membrane nanogenerator for acoustic detection and recognition, Adv. Fiber Mater. 3 (2021) 368–380, https://doi.org/10.1007/s42765-021-00095-7.
[226] H. Li, C.S.L. Koh, Y.H. Lee, Y. Zhang, G.C. Phan-Quang, C. Zhu, Z. Liu, Z. Chen, H. Y.F. Sim, C.L. Lay, et al., A wearable solar-thermal-pyroelectric harvester: achieving high power output using modified RGO-PEI and polarized PVDF, Nano Energy 73 (2020), 104723, https://doi.org/10.1016/j.nanoen.2020.104723.
[227] Q. Leng, L. Chen, H. Guo, J. Liu, G. Liu, C. Hu, Y. Xi, Harvesting heat energy from hot/cold water with a pyroelectric generator, J. Mater. Chem. 2 (2014) 11940–11947, https://doi.org/10.1039/C4TA01782J.
[228] C.M. Wu, M.H. Chou, T.F. Chala, Y. Shimamura, R. ichi Murakami, Infrared-driven poly(vinylidene difluoride)/tungsten oxide pyroelectric generator for non-contact energy harvesting, Compos. Sci. Technol. 178 (2019) 26–32, https://doi.org/10.1016/j.compscitech.2019.05.004.
[229] M.R. Gokana, C.-M. Wu, K.G. Motora, J.Y. Qi, W.-T. Yen, Effects of patterned electrode on near infrared light-triggered cesium tungsten bronze/poly (Vinylidene)Fluoride nanocomposite-based pyroelectric nanogenerator for energy harvesting, J. Power Sources 536 (2022), 231524, https://doi.org/10.1016/j.jpowsour.2022.231524.
[230] J.P. Lee, J.W. Lee, J.M. Baik, The progress of PVDF as a functional material for triboelectric nanogenerators and self-powered sensors, Micromachines 9 (2018) 532, https://doi.org/10.3390/mi9100532.
[231] M.O. Shaikh, Y.-B. Huang, C.-C. Wang, C.-H. Chuang, Wearable woven triboelectric nanogenerator utilizing electrospun PVDF nanofibers for mechanical energy harvesting, Micromachines 10 (2019) 438, https://doi.org/10.3390/mi10070438.
[232] S. Cheon, H. Kang, H. Kim, Y. Son, J.Y. Lee, H.-J. Shin, S.-W. Kim, J.H. Cho, High-performance triboelectric nanogenerators based on electrospun polyvinylidene fluoride–silver nanowire composite nanofibers, Adv. Funct. Mater. 28 (2018), 1703778, https://doi.org/10.1002/adfm.201703778.
[233] Y. Zheng, L. Cheng, M. Yuan, Z. Wang, L. Zhang, Y. Qin, T. Jing, An electrospun nanowire-based triboelectric nanogenerator and its application in a fully self-powered UV detector, Nanoscale 6 (2014) 7842–7846, https://doi.org/10.1039/C4NR01934B.
[234] F. Chen, Y. Wu, Z. Ding, X. Xia, S. Li, H. Zheng, C. Diao, G. Yue, Y. Zi, A novel triboelectric nanogenerator based on electrospun polyvinylidene fluoride nanofibers for effective acoustic energy harvesting and self-powered multifunctional sensing, Nano Energy 56 (2019) 241–251, https://doi.org/10.1016/j.nanoen.2018.11.041.
[235] T. Bhatta, P. Maharjan, H. Cho, C. Park, S.H. Yoon, S. Sharma, M. Salauddin, M. T. Rahman, S.S. Rana, J.Y. Park, High-performance triboelectric nanogenerator based on MXene functionalized polyvinylidene fluoride composite nanofibers, Nano Energy 81 (2021), 105670, https://doi.org/10.1016/j.nanoen.2020.105670.
[236] C. Sun, G. Zu, Y. Wei, X. Song, X. Yang, Flexible Triboelectric Nanogenerators Based on Electrospun Poly (Vinylidene Fl Uoride) with MoS 2/Carbon Nanotube Composite Nano Fi Bers, 2022, https://doi.org/10.1021/acs.langmuir.1c02785.
[237] W. Li, D. Sengupta, Y. Pei, A. Giri, P. Kottapalli, Wearable nanofiber-based triboelectric nanogenerator for body motion energy harvesting, 2021, pp. 18–21.
[238] J. Huang, Y. Hao, M. Zhao, W. Li, F. Huang, Q. Wei, All-fiber-structured triboelectric nanogenerator via one-pot electrospinning for self-powered wearable sensors, ACS Appl. Mater. Interfaces 13 (2021) 24774–24784, https://doi.org/10.1021/acsami.1c03894.
[239] X. Sun, Y. Feng, B. Wang, Y. Liu, Z. Wu, D. Yang, Y. Zheng, J. Peng, M. Feng, D. Wang, A new method for the electrostatic manipulation of droplet movement by triboelectric nanogenerator, Nano Energy 86 (2021), 106115, https://doi.org/10.1016/j.nanoen.2021.106115.
[240] Q. Zhang, J. Mu, J. Mu, X. Yang, S. Zhang, X. Han, Y. Zhao, Y. You, J. Yu, X. Chou, A design of flexible triboelectric generator integrated with high-efficiency energy storage unit, Energy Technol. 9 (2021), 2000962, https://doi.org/10.1002/ente.202000962.
[241] T. Busolo, P.K. Szewczyk, M. Nair, U. Stachewicz, S. Kar-Narayan, Triboelectric yarns with electrospun functional polymer coatings for highly durable and washable smart textile applications, ACS Appl. Mater. Interfaces 13 (2021) 16876–16886, https://doi.org/10.1021/acsami.1c00983.
[242] N. Sun, G. Wang, H. Zhao, Y. Cai, J. Li, G. Li, Nano energy waterproof , breathable and washable triboelectric nanogenerator based on electrospun nanofiber films for wearable electronics, Nano Energy 90 (2021) 106639, https://doi.org/10.1016/j.nanoen.2021.106639.
[243] X. Tao, Y. Zhou, K. Qi, C. Guo, Y. Dai, J. He, Z. Dai, Journal of colloid and interface science wearable textile triboelectric generator based on nanofiber core-spun yarn coupled with electret effect, J. Colloid Interface Sci. 608 (2022) 2339–2346, https://doi.org/10.1016/j.jcis.2021.10.151.
[244] Y. Cheng, W. Zhu, X. Lu, C. Wang, Mechanically robust, stretchable, autonomously adhesive, and environmentally tolerant triboelectric electronic skin for self-powered healthcare monitoring and tactile sensing, Nano Energy 102 (2022), 107636, https://doi.org/10.1016/j.nanoen.2022.107636.
[245] H. He, J. Guo, B. Illés, A. Géczy, B. Istók, V. Hliva, D. Török, J.G. Kovács, I. Harmati, K. Molnár, Monitoring multi-respiratory indices via a smart nanofibrous mask filter based on a triboelectric nanogenerator, Nano Energy 89 (2021), 106418, https://doi.org/10.1016/j.nanoen.2021.106418.
[246] T. Bhatta, P. Maharjan, K. Shrestha, S. Lee, M.T. Rahman, S.M.S. Rana, S. Sharma, C. Park, S.H. Yoon, J.Y. Park, A hybrid self-powered arbitrary wave motion sensing system for real-time wireless marine environment monitoring application, 2102460, 2022, pp. 1–14, https://doi.org/10.1002/aenm.202102460.
[247] D. Yang, Y. Feng, B. Wang, Y. Liu, Y. Zheng, X. Sun, J. Peng, M. Feng, D. Wang, Nano energy an asymmetric AC electric field of triboelectric nanogenerator for efficient water/oil emulsion separation, Nano Energy 90 (2021) 106641, https://doi.org/10.1016/j.nanoen.2021.106641.
[248] A. Sultana, S.K. Ghosh, MdM. Alam, P. Sadhukhan, K. Roy, M. Xie, C.R. Bowen, S. Sarkar, S. Das, T.R. Middya, et al., Methylammonium lead iodide incorporated poly(vinylidene fluoride) nanofibers for flexible piezoelectric–pyroelectric nanogenerator, ACS Appl. Mater. Interfaces 11 (2019) 27279–27287, https://doi.org/10.1021/acsami.9b04812.
[249] B. Mahanty, S.K. Ghosh, K. Maity, K. Roy, S. Sarkar, D. Mandal, All-fiber pyro- and piezo-electric nanogenerator for IoT based self-powered health-care monitoring, Mater. Adv. 2 (2021) 4370–4379, https://doi.org/10.1039/d1ma00131k.
[250] Y. Wang, M. Zhu, X. Wei, J. Yu, Z. Li, B. Ding, A dual-mode electronic skin textile for pressure and temperature sensing, Chem. Eng. J. 425 (2021), 130599, https://doi.org/10.1016/j.cej.2021.130599.
[251] G. Xia, Y. Huang, F. Li, L. Wang, J. Pang, L. Li, K. Wang, A thermally flexible and multi-site tactile sensor for remote 3D dynamic sensing imaging, Front. Chem. Sci. Eng. 14 (2020) 1039–1051, https://doi.org/10.1007/s11705-019-1901-5.
[252] X. Li, D. Ji, B. Yu, R. Ghosh, J. He, X. Qin, S. Ramakrishna, Boosting piezoelectric and triboelectric effects of PVDF nanofiber through carbon-coated piezoelectric nanoparticles for highly sensitive wearable sensors, Chem. Eng. J. 426 (2021), 130345, https://doi.org/10.1016/j.cej.2021.130345.
[253] Z. Yu, M. Chen, Y. Wang, J. Zheng, Y. Zhang, H. Zhou, D. Li, Nanoporous PVDF hollow fiber employed piezo-tribo nanogenerator for effective acoustic harvesting, ACS Appl. Mater. Interfaces 13 (2021) 26981–26988, https://doi.org/10.1021/acsami.1c04489.
[254] H. Niu, H. Zhou, H. Shao, H. Wang, X. Ding, R. Bai, T. Lin, Nano energy energy generation from airborne noise : improving electrical outputs of single-layer polyvinylidene difluoride nanofiber membranes by incorporating a small number of nylon-6 nanofibers, Nano Energy 90 (2021) 106618, https://doi.org/10.1016/j.nanoen.2021.106618.
[255] A. Klapstova, J. Horakova, M. Tunak, A. Shynkarenko, J. Erben, J. Hlavata, P. Bulir, J. Chvojka, A PVDF electrospun antifibrotic composite for use as a glaucoma drainage implant, Mater. Sci. Eng. C 119 (2021), 111637, https://doi.org/10.1016/j.msec.2020.111637.
[256] J.R.S. Agueda, J. Madrid, J.M. Mondragon, J. Lim, A. Tan, I. Wang, N. Duguran, A. Bondoc, Synthesis and characterization of electrospun polyvinylidene fluoride-based (PVDF) scaffolds for renal bioengineering, J. Phys.: Conf. Ser. 2071 (2021), 012005, https://doi.org/10.1088/1742-6596/2071/1/012005.
[257] R. Rajamohan, M. Sillanpää, A. Subramania, Electrospun polyvinylidene fluoride nanofibrous mats as the carrier for drug delivery system of benzocaine and its complex with β-cyclodextrin, J. Mol. Liq. 341 (2021), 117411, https://doi.org/10.1016/j.molliq.2021.117411.

[258] F.S. Victor, V. Kugarajah, M. Bangaru, S. Ranjan, S. Dharmalingam, Electrospun nanofibers of polyvinylidene fluoride incorporated with titanium nanotubes for purifying air with bacterial contamination, Environ. Sci. Pollut. Res. 28 (2021) 37520–37533, https://doi.org/10.1007/s11356-021-13202-3.
[259] Shuai, D. Development of Electrospun Nanofibrous Filters for Controlling Coronavirus Aerosols. vol. 17.
[260] P. Pascariu, C. Cojocaru, P. Samoila, N. Olaru, A. Bele, A. Airinei, Novel electrospun membranes based on PVDF fibers embedding lanthanide doped ZnO for adsorption and photocatalytic degradation of dye organic pollutants, Mater. Res. Bull. 141 (2021), 111376, https://doi.org/10.1016/j.materresbull.2021.111376.
[261] Y. Yang, L. Li, Q. Zhang, W. Chen, S. Lin, Z. Wang, W. Li, Enhanced coalescence separation of oil-in-water emulsions using electrospun PVDF nanofibers, Chin. J. Chem. Eng. 38 (2021) 76–83, https://doi.org/10.1016/j.cjche.2020.08.037.
[262] A.A. Tessema, C.-M. Wu, K.G. Motora, S. Naseem, Highly-efficient and salt-resistant CsxWO3@g-C3N4/PVDF fiber membranes for interfacial water evaporation, desalination, and sewage treatment, Compos. Sci. Technol. 211 (2021), 108865, https://doi.org/10.1016/j.compscitech.2021.108865.
[263] K. Bicy, A.B. Gueye, D. Rouxel, N. Kalarikkal, S. Thomas, Lithium-ion battery separators based on electrospun PVDF: a review, Surface. Interfac. 31 (2022), 101977, https://doi.org/10.1016/j.surfin.2022.101977.
[264] J.C. Barbosa, D.M. Correia, R. Gonçalves, V. de Zea Bermudez, M.M. Silva, S. Lanceros-Mendez, C.M. Costa, Enhanced ionic conductivity in poly(vinylidene fluoride) electrospun separator membranes blended with different ionic liquids for lithium ion batteries, J. Colloid Interface Sci. 582 (2021) 376–386, https://doi.org/10.1016/j.jcis.2020.08.046.
[265] J. Qian, Z.-M. Zhang, R.-Y. Bao, Z.-Y. Liu, M.-B. Yang, W. Yang, Lightweight poly (vinylidene fluoride)/silver nanowires hybrid membrane with different conductive network structure for electromagnetic interference shielding, Polym. Compos. 42 (2021) 522–531, https://doi.org/10.1002/pc.25844.
[266] A. Rose, P.A. F, P.K. S Mural, A.M. Chandran, A Carbon Doped Electrospun Nano Fibre for Effective Emi Shielding, Social Science Research Network, Rochester, NY, 2021.



Sreelakshmi Moozhiyil Purushothaman obtained her MS.c.in Physics in 2021 from School of pure and applied physics, Mahatma Gandhi University, Kerala, India. She subsequently started her Ph.D. at Insitut Jean Lamour, University of Lorraine, Nancy, France, under the supervision of Prof. Didier Rouxel and Prof. Isabelle Royaud. Her research works focuses on the elaboration and microstructure-property relations studies of polymer nanocomposites and the development of polymer-based nanogenerators and sensors.



Maïté Fernandes Tronco is a doctoral student at Institut Jean Lamour, University of Lorraine, Nancy, France. Under the guidance of Prof. Didier Rouxel and Dr. Marc Ponçot she studies piezoelectric polymers, polymer-nanocomposites, their microstructure, properties and their potential in energy harvesting and sensing. She had completed her degree in Materials Engineering from École Européenne d'Ingénieurs en Génie des Matériaux (EEIGM), Nancy, France.



Bicy Kottathodi obtained her Ph.D from Mahatma Gandhi University, Kerala, India in 2020. The doctoral research work focused on the fabrication of microporous polymer nanocomposite membranes for lithium ion battery separator application. She received junior research fellowship in Chemistry from Council of Scientific and Industrial Research (CSIR), India in 2013. Her research interests are, polymer blends and nanocomposites, lithium-ion battery, piezoelectric polymers, energy harvesting and storage, biopolymers etc. She has participated several national and international conferences and worked at Institute Jean Lamour, University of Lorraine, Nancy France, as a part of her PhD. Currently she is working as a teacher.



Isabelle Royaud who is a University lecturer in Polymer physics and Polymer science since 1990 joined the University of Lorraine in 2011 after beginning her career in the University of Lyon. She has obtained her PhD in Polymer Properties from University of Southampton – UK on "Conformation and crystallinity in Polymers: A study using novel Raman techniques" in 1989 then she has obtained her HDR on "Study of the influence of ageing on molecular mobility of polymers", (University of Lyon 1/IMP-Engineering of Polymer Material) in 2000. From 2011 and up to now, she is a Professor at University of Lorraine (EEIGM: European School of Material Science and Engineering, Nancy, France) and a Researcher at Institut Jean Lamour UMR CNRS 7198 (Nancy, France). She is a specialist of relationship architecture/morphology/dielectric, viscoelastic and vibrational properties of polymers. Her scientific production is composed of 81 Publications, 2 book chapters, 1 patent, 13 invited lectures in International Conferences, 180 Communications; 89 oral (International Conferences: 50); 91 posters (International Conferences: 62), and 18 invited seminars. Her research activities deal with the following subjects:

- Polymer physic properties for synthetic polymers and biopolymers.
- Relations between architecture/morphology and mechanical, electrical, vibrational properties of polymer and multimaterials.
- Influence of ageing and morphology on molecular mobility and relaxational phenomena in polymer materials.
- Molecular mobility at the interfaces of nanostructured systems.
- in situ monitoring of plastic deformation in polymers at different scales using vibrational techniques, videometric tensile test, synchrotron radiation and broadband dielectric analysis.



Marc Ponçot obtained his PhD in 2009 at the Institut National Polytechnique de Lorraine as part of a CIFRE grant with AcelorMital on the development and characterization of metal/polymer composites for the automotive sector. In 2011, he was appointed Associate Professor at the Ecole Nationale Supérieure des Mines de Nancy, University of Lorraine. He carries out his research at the Institut Jean Lamour within the Physics, Mechanics and Plasticity team in the field of polymers and composites, elaboration-microstructure-property relations. Since 2019, he has received his Habilitation à Diriger les Recherches (HDR).



Nandakumar Kalarikkal received his Ph. D in Semiconductor Physics from Cochin University of Science & Technology, Kerala, India. In 1994, he joined the School of Pure and Applied Physics, Mahatma Gandhi University, Kerala, India as a Lecturer and at present is a Senior Professor at the school. Prof. Kalarikkal also functioned as the Director of the School of Pure and Applied Physics and the International and Inter University Centre for Nanoscience and Nanotechnology, at Mahatma Gandhi University. His presence among the academic community is strengthened by the various other recognitions he received, which include Professor@Lorraine, University of Lorraine, Nancy, France, CNRS Professor, Institute of Light Matter, Claud-Bernard Lyon University, Lyon, France, Visiting Professor, Stockholm University, Sweden, Guest Scientist, Leibniz-Institut fur Polymerforschung Dresden, Germany, and Visiting Fellow, Jawaharlal Nehru Centre for Advanced Scientific Research, Bangalore, India The research activities of his group are highly interdisciplinary in nature to address issues related to Energy, Water, Food, Health and Environment securities in including the syntheses, characterization, and applications of various Nanomaterials, LASER Plasma, Ion irradiation effects on various novel materials and phase transitions. Through various national and international projects, he could contribute to scientific research by co-authoring more than 260 publications, 16 book chapters, and editing 32 books. He has an h-index of 50 with more than 8500 citations. Recently, he was awarded the Fulbright-Nehru Academic and Professional Excellence Fellowship.



Sabu Thomas is the Vice-Chancellor of Mahatma Gandhi University, Kottayam, Kerala, India. He is also a Professor of Polymer Science and Engineering at the School of Chemical Sciences, and also the Director of School of Energy Materials and the founder Director of International and Inter-University Centre for Nanoscience and Nanotechnology, Mahatma Gandhi University. He obtained in Ph. D in Polymer Science and Engineering in 1987, Indian Institute of Technology, Kharagpur, India. His research interests include polymer nanocomposites, polymer blends, fiber filled polymer composites, polymer nanocomposites for electronic applications, green bionanotechnological and nanobiomedical sciences, dual porous nanocomposite scaffolds for tissue engineering, recyclability and reuse of waste plastics and rubbers, etc. Prof. Thomas has authored around 1200 peer reviewed publications, edited and co-authored 150 books and holds four patents. Furthermore, he has received a number of national and international awards, including Docteur Honoris Causa from University of Southern Brittany, and University of Lorraine, France, Fellowship of the Royal Society of Chemistry, MRSI award, CRSI award, the Distinguished Professorship award form Josef Stefan Institute, Slovenia, Kairali Life time Research Award 2021 b y Kerala Government and was also honoured as the Foreign Fellow of the European Academy of Sciences (EurASc). The H index of Professor Thomas is 132 and has a citations of more than 83,000.



Didier Rouxel was born in Lyon, France, in 1965. He received the Engineer degree from the École Supérieure des Sciences et Techniques de l'Ingénieur de Nancy, Nancy, France, and the Ph. D. degree in material sciences and engineering from the University of Nancy I, Nancy, France, in 1993. Since 2013, he has been the Leader of the "Micro and NanoSystems" Group of the Institut Jean Lamour, Nancy, France. He is currently a Full Professor of the University of Lorraine, Lorraine, France, and the Institut Jean Lamour of Nancy, Nancy, France. His research interests include physical chemistry of surfaces and thin films, quasicrystal surfaces, and more recently on Brillouin spectroscopy for elastic properties of polymeric materials, polymer nanocomposites, nanomaterials and piezoelectric materials. Prof. Rouxel has been involved in the spectroscopic analysis of inorganics and is vastly experienced in the analysis of polymer nanocomposite systems by almost all spectroscopic techniques. His current areas of interest include the development of electrospun polymer nanocomposite materials and of micro-devices based on piezoelectric polymers, for example acoustic microsensor for surgery, energy harvesting device, etc. He has written more than 150 publications, including more than 100 in international journals, 14 book chapters, 8 books edited and more than 200 communications.

Chapter 2: Elaboration and characterisation of the nanocomposites

1. Materials of the study

The aim of this section is to present the different materials that were necessary for the elaboration of the studied films, including the components of the neat PVDF films and added nanofillers.

1.1. Polyvinylidene fluoride (PVDF)

PVDF was purchased in powder form from Thermo Fisher Scientific (referenced as 044080.36). The average molecular weight is indicated to range from 250000 to 450000 g/mol.

1.2. Cellulose nanocrystals (CNC)

The cellulose nanocrystals (CNC) were purchased from Nanografi in powder form (referenced as SKU NG01NC0101), and used as purchased. The technical properties displayed on the Nanografi website give an average particle size of 10-20 nm wide and 300-900 nm length, a crystallinity ratio of cellulose of 92% (determined by X-Ray Diffraction - XRD), and a decomposition temperature of 349°C (determined by thermogravimetric analysis - TGA in N_2).

Complementary dynamic light scattering (DLS) analyses were performed to characterise the actual particle size of the cellulose nanocrystals, considering possible aggregates and agglomerates. Aqueous solution of concentration under 1 mg/mL was prepared, then stirred for 30 minutes for the first measurement. A second measurement was performed after one minute of supplementary sonication using a sonoprobe. The measurements were performed using a VASCO granulometer from Cordouan Technologies, with Pade Laplace algorithm. The real and imaginary values of the refractive index selected for the analysis were n=1.490 and k=0.002 [121].

Table 1: DLS results on CNC after 30 minutes of stirring and after sonication.

	Size (nm)	Intensity	Decay Rate.	Diffusion Coeff. (m^2/s)
After stirring	82	0.3	3176	60E-013
	372	0.6	699	13E-013
After sonication	60	0.3	4339	82E-013
	252	0.7	1030	19E-013

As presented in Table 1, the initial measurement after 30 minutes of stirring gave two main population sizes, of 82 and 372 nm. After sonication the sizes logically decrease towards 60 and 252 nm. While the smaller population size fits the characteristics of primary nanoparticles, the bigger population could represent agglomerates of cellulose nanocrystals that change into smaller aggregates after sonication.

1.3. Quasicrystals (QC)

The quasicrystals (QC) used in this work were previously synthesised at Institut Jean Lamour [122]. They are present in powder form, and used as obtained. They are formed of aluminium, copper, iron and boron ($Al_{59}Cu_{25.5}Fe_{12.5}B_3$, icosahedral phase). Similarly to the CNC particles, DLS measurements were performed on the QC powder, after realisation of an aqueous solution on concentration under 1 mg/mL. The same experimental protocol was applied, only this time the used values of real and imaginary values of the refractive index selected for the analysis were n=1.1 and k=0.3 [123].

Table 2: DLS results on QC after 30 minutes of stirring and after sonication.

	Size (nm)	Intensity	Decay Rate.	Diffusion Coeff. (m^2/s)
After stirring	607	0.9	428	81E-014
After sonication	606	0.9	429	81E-014

After the initial stirring, the measurement displayed in Table 2 show one main population of particles, of size 607 nm. This size does not decrease with sonication, which suggests that this is the nominal particle size.

The graphs corresponding to the DSL measurements performed on CNC and QC materials can be consulted in the Appendices (see p.i).

1.4. Solvents

The same solvents were used for the elaboration of the PVDF solutions used for solvent casting and electrospinning. N,N-Dimethylformamide (DMF) (referenced as 33120-M) and acetone (referenced as 32201-M) were both purchased from Sigma Aldrich. The boiling point of DMF is located at 153°C, while that of acetone is located around 56°C [124,125]

2. Elaboration of the nanocomposites

2.1. Solvent casting

The basic principle of solvent casting is fairly simple. It consists in preparing a polymeric solution, then cast it into a recipient, then let the solvent evaporate to retrieve a thin film. In this work, a 150 g/L PVDF solution was prepared by dissolving 1.5 g of PVDF powder into a mix of acetone and DMF in a sealed 10 mL vial. To achieve the dissolution of PVDF in the solvent mix, continuous magnetic stirring at 50°C for 3h followed by continuous magnetic stirring at room temperature overnight was used. The obtained viscous polymeric solution was then casted into a glass Petri dish, and left lo evaporate under a fume hood at ambient temperature.

A preliminary study aiming at finding the DMF:Acetone ratio allowing to obtain a thin, flexible and transparent film of PVDF was conducted. Various DMF:Acetone ratios were studied, from 5:5 to 1:9.



Figure 1: Solvent casted films with various DMF:Acetone ratio. From left to right: 5:5, 4:6, 3:7, 2:8, 1:9.

From Figure 1, the results of the study show that with low acetone content the films appear less homogeneous and rigid, with a brownish coloration. With the increased acetone content, the films appear more homogeneous, more flexible and transparent. In the following works, the solvent casted films studied were prepared from a 150 g/L PVDF, obtained from the dissolution of 1.5 g of PVDF powder into a 10 mL mix of DMF and acetone, with ratio 1:9.

2.2. Study of electrospinning parameters on pristine PVDF fibres

In order to produce electrospun fibres of good quality, optimisation of the various electrospinning parameters was performed. As a reminder, many parameters influence the outcome of the electrospinning process. They can be classified in three categories: solution parameters (polymer used and its concentration in the solution, type of solvent and solvent ratio in case of mix), process parameters (applied voltage, tip-to-collector distance, flow-rate, collector choice), and ambient parameters (humidity, temperature) [58–64,126]. A special unit was bought at the end of the PhD to control the humidity and temperature of the process, but the lack of time did not allow to implement it on time for this work. Hence, all the produced fibres were elaborated in ambient temperature and humidity, with little control over the possible variations.

In order to optimise the process, 150 g/L and 160 g/L polymeric solutions were prepared by dissolving 1.5 or 1.6 g of PVDF powder in a 10 mL mix of acetone and DMF, in a sealed 10 mL vial. Similarly to the elaboration of the solution for solvent casting, to achieve the dissolution of PVDF in the solvent mix, continuous magnetic stirring at 50°C for 3h followed by continuous magnetic stirring at room temperature overnight is advised. Two types of 10 mL solvent mixes with different DMF:Acetone (D:A) ratio were used to produce two categories of fibres, using a 3:7 DMF:Acetone ratio, and using a 4:6 DMF:Acetone ratio. Moreover, several process parameters were tested, with variating applied voltage (AV), flow rate (FR) and tip-to-collector distance (TCD). The range of values tested in this optimisation study was inspired by previous results from the literature [58–61,63,64,78–80,91–94,127–133] . A summary of the 20 different combinations studied is given in Table 3. Conclusions of this study are presented in the next chapter.

Table 3: Pristine PVDF fibres electrospinning parameters for optimisation study.

Sample name	Solution parameters	Electrospinning parameters
ES15WT37DA 10_08_15	150 g/L PVDF in 10mL 3:7 D:A	AV: 10 kV, FR: 0.8 mL/h, TCD: 15 cm
ES15WT37DA 12_08_15	150 g/L PVDF in 10mL 3:7 D:A	AV: 12 kV, FR: 0.8 mL/h, TCD: 15 cm
ES15WT37DA 15_08_15	150 g/L PVDF in 10mL 3:7 D:A	AV: 15 kV, FR: 0.8 mL/h, TCD: 15 cm
ES15WT37DA 13_1_12	150 g/L PVDF in 10mL 3:7 D:A	AV: 13 kV, FR: 1 mL/h, TCD: 12 cm
ES15WT37DA 13_12_12	150 g/L PVDF in 10mL 3:7 D:A	AV: 13 kV, FR: 1.2 mL/h, TCD: 12 cm
ES15WT46DA 10_08_15	150 g/L PVDF in 10mL 4:6 D:A	AV: 10 kV, FR: 0.8 mL/h, TCD: 15 cm
ES15WT46DA 12_08_15	150 g/L PVDF in 10mL 4:6 D:A	AV: 12 kV, FR: 0.8 mL/h, TCD: 15 cm
ES15WT46DA 15_08_15	150 g/L PVDF in 10mL 4:6 D:A	AV: 15 kV, FR: 0.8 mL/h, TCD: 15 cm
ES15WT46DA 13_1_12	150 g/L PVDF in 10mL 4:6 D:A	AV: 13 kV, FR: 1 mL/h, TCD: 12 cm
ES15WT46DA 13_12_12	150 g/L PVDF in 10mL 4:6 D:A	AV: 13 kV, FR: 1.2 mL/h, TCD: 12 cm
ES16WT37DA 10_08_15	160 g/L PVDF in 10mL 3:7 D:A	AV: 10 kV, FR: 0.8 mL/h, TCD: 15 cm
ES16WT37DA 12_08_15	160 g/L PVDF in 10mL 3:7 D:A	AV: 12 kV, FR: 0.8 mL/h, TCD: 15 cm
ES16WT37DA 15_08_15	160 g/L PVDF in 10mL 3:7 D:A	AV: 15 kV, FR: 0.8 mL/h, TCD: 15 cm
ES16WT37DA 13_1_12	160 g/L PVDF in 10mL 3:7 D:A	AV: 13 kV, FR: 1 mL/h, TCD: 12 cm
ES16WT37DA 13_12_12	160 g/L PVDF in 10mL 3:7 D:A	AV: 13 kV, FR: 1.2 mL/h, TCD: 12 cm
ES16WT46DA 10_08_15	160 g/L PVDF in 10mL 4:6 D:A	AV: 10 kV, FR: 0.8 mL/h, TCD: 15 cm
ES16WT46DA 12_08_15	160 g/L PVDF in 10mL 4:6 D:A	AV: 12 kV, FR: 0.8 mL/h, TCD: 15 cm
ES16WT46DA 15_08_15	160 g/L PVDF in 10mL 4:6 D:A	AV: 15 kV, FR: 0.8 mL/h, TCD: 15 cm
ES16WT46DA 13_1_12	160 g/L PVDF in 10mL 4:6 D:A	AV: 13 kV, FR: 1 mL/h, TCD: 12 cm
ES16WT46DA 13_12_12	160 g/L PVDF in 10mL 4:6 D:A	AV: 13 kV, FR: 1.2 mL/h, TCD: 12 cm

Concerning the electrospinning setup, a needle of diameter 0.6 mm was used, and the selected collector was a plate wrapped in aluminium foil. A schematic representation of the electrospinning setup is displayed in Figure 2.

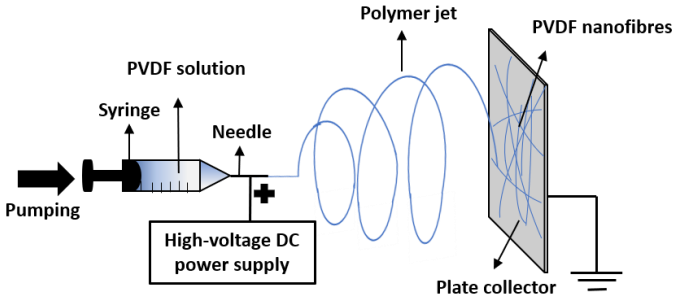

Figure 2: Schematic representation of the electrospinning setup [134].

2.3. Electrospinning of nanocomposites

150 g/L polymeric solutions were prepared by dissolving 1.5 g of PVDF powder in a 10 mL mix of acetone and DMF, with a ratio 3:7 DMF:Acetone. Once again, to achieve the dissolution of PVDF in the solvent mix, continuous magnetic stirring at 50°C for 3h was performed. The appropriate filler weight fraction (1, 2, 3, 4, 5 wt/wt% respectively to PVDF weight fraction) is then added, followed by continuous magnetic stirring at room temperature overnight. To improve dispersion, the solution containing the fillers is submitted to ultrasonic bath for 30 minutes. The process parameters selected after the optimization study were an applied voltage of 13 kV, flow rate of 1 mL/h, and tip-to-collector distance of 12 cm. The sample names and respective filler content are given in Table 4.

Table 4: PVDF-based nanocomposites fibres.

Material name	Material and filler content
PVDF/CNC0	Pristine PVDF fibres
CNC1	1 wt.% CNC
CNC2	2 wt.% CNC
CNC3	3 wt.% CNC
CNC4	4 wt.% CNC
CNC5	5 wt.% CNC
QC1	1 wt.% QC
QC2	2 wt.% QC
QC3	3 wt.% QC
QC5	5 wt.% QC

3. Experimental characterisation techniques

This section aims at presenting the instruments and experimental techniques employed to thoroughly characterise the PVDF fibres and nanocomposites. A brief presentation of the technique along the instrument and analysis details is provided.

3.1. Differential scanning calorimetry (DSC)

Differential scanning calorimetry (DSC) enables to characterise polymers and composites thermal transitions by the analysis of thermal flux variations associated to said transitions. The main observable transitions by DSC on polymer materials are glass transition, physical relaxations, crystallisation, melting, crosslinking and degradation.

During the analysis, two pans are simultaneously heated, one being an empty pan serving as reference, and the other being the pan containing the material to be analysed. Typically, the sample weights between 5 and 15 mg. Measuring the difference of power necessary to match the temperature of the reference and analysed pans allows

to retrieve the heat absorbed (endothermic process) or released (exothermic process) during the different transitions, and study the sample microstructure. The analysis output is typically a visualisation of the heat flow (in W/g) as a function of temperature, called a thermogram [135].

In the frame of this thesis, DSC analyses were performed on a Q200 calorimeter from TA Instruments. The configuration of this instrument has both sample pans, made of aluminium, located in the same oven. Calibration was performed using an indium sample. All measurements were performed under a nitrogen flow of 50 mL/min, a neutral atmosphere preventing oxidation phenomena. Different protocols were implemented depending on the study goals.

Determination of the crystallinity was obtained by submitting the materials to a heating cycle from 100 to 200°C at a heating rate of 10°C/min. To study more in depth the effect of the thermomechanical history of the nanofibres, the samples were submitted to three cycles, heating-cooling-heating from 25 to 200°C at the same heating rate of 10°C/min. While the first heating allows to study the microstructure of the material influenced by its thermal and mechanical history, which is of considerable impact in the case of electrospun materials, the second heating allows studying the standard thermal behaviour of a material after controlled cooling from the melt.

The DSC thermograms were analysed using the TA Universal Analysis software. Melting temperatures (T_m) were determined at the maximum of the endothermic peaks. Determination of the crystallinity ratio χ_c is calculated from the melting enthalpy (ΔH_m), obtained by the integration of the heat flow curve segment corresponding to the melt endotherm, and from the standard value of the melting enthalpy of a 100% crystalline material ($\Delta H°_m$). The crystallinity ratio is then given by the following

Equation 1:

$$\chi_C = \frac{\Delta H_m}{\Delta H_m^0}$$

Equation 1

where $\Delta H°_m$ is 104.6 J/g [136–142].

All values in the manuscript are given as an average of three trials, the uncertainties correspond to the largest deviation observed in the series of samples tested.

3.2. Wide-angle X-ray scattering (WAXS)

Wide-angle X-ray scattering (WAXS) is a non-destructive characterisation technique allowing to study the semi-crystalline microstructure of polymers. WAXS is based on the interaction of an X-rays beam with the studied sample, with the particularity of scanning large diffraction angles (2θ>1°), characterised by an elastic scattering. As WAXS enables the analysis of elements down to the nanometre size, which is the order of magnitude of the d-spacing size of unit cells in crystalline polymers, hence making this technique suitable for the determination the crystallinity ratio and the crystalline phases identification of such materials.

When an X-rays beam of wavelength λ encounters a family of crystalline planes of Miller indexes (hkl), separated by inter-reticular distance d_{hkl}, at an incident angle of θ, diffraction occurs when the planes are in Bragg's position. Two conditions must then be verified: Bragg's law (Equation 2), illustrated by Figure 3 , and structural factors that are not zero.

$$n\lambda = 2\, d_{hkl}\, sin\theta$$

Equation 2

where n is the diffraction order.

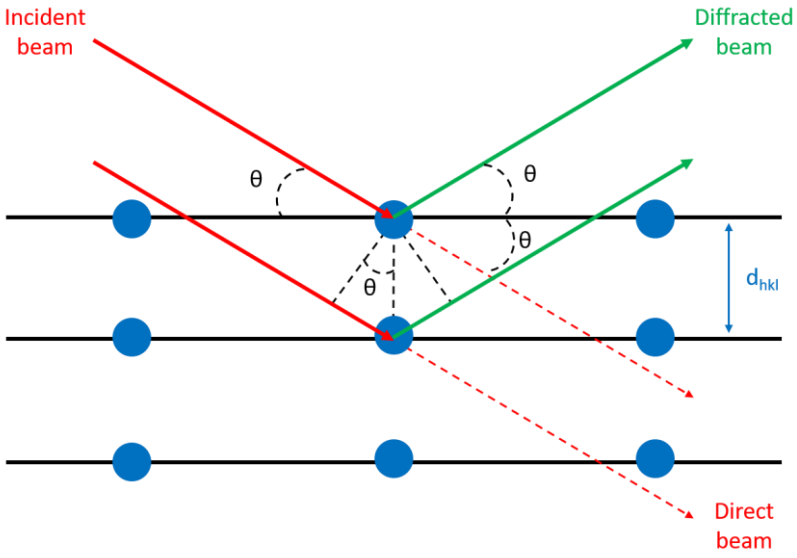

Figure 3: X-ray diffraction from a family of reticular planes inside a crystalline lattice [143].

In the case of PVDF, the three main crystalline phases are α, β and γ. In the α phase, polymer chains are arranged in a monoclinic (or pseudo-orthorhombic) unit cell. In the β phase, the chains are arranged in an orthorhombic unit cell. In the γ phase, the chains are arranged in a monoclinic unit cell. To allow the identification of the crystalline phases present in a PVDF sample, Table 5 provides the association of phase, planes and corresponding 2θ value (for copper irradiation, lambda = 0.154nm). This table was built by calculating values of 2θ from Equation 3 and Equation 4, and compiling phase identification results from the literature [22,144–150].

$$2\theta = 2 * \sin^{-1}\left[\left(\frac{\lambda^2}{4}\left[\frac{h^2}{a^2}+\frac{k^2}{b^2}+\frac{l^2}{c^2}\right]\right)^{1/2}\right]$$

Equation 3

$$2\theta = 2 * \sin^{-1}\left[\left(\frac{\lambda^2}{4\sin^2\beta}\left[\frac{h^2}{a^2} + \frac{k^2\sin^2\beta}{b^2} + \frac{l^2}{c^2} - \frac{2hl\cos\beta}{ac}\right]\right)^{1/2}\right]$$

Equation 4

Table 5: Correspondence of PVDF crystalline phases with corresponding planes and 2ϑ value [22,144–150].

Phase and corresponding lattice parameter [22]	**Plane**	**2θ (Cu Kα)**
α Monoclinic / pseudo-orthorhombic a=4.96 Å b=9.64 Å c=4.62 Å β=90°	(100)	17.86
	(020)	18.38
	(110)	20.11
	(120)	25.74
	(021)	26.7
	(121)	32.31
	(130)	33.18
	(200)	36.18
	(002)	38.94
β Orthorhombic a=8.58 Å b=4.91 Å c=2.56 Å	(200)	20.68
	(110)	20.82
	(020)	36.56
	(101)	36.59
	(120)	38.08
	(201)	41.01
	(111)	41.08
	(221)	56.09
γ Monoclinic a=4.96 Å b=9.67 Å c=9.20 Å β=93°	(020)	18.33
	(002)	19.3
	(110)	20.12
	(101)	20.78
	(022)	26.74
	(200)	36.23
	(211)	39.23

However, in practice, some values of 2θ are so close that it becomes nearly impossible to distinguish. As such, XRD is used in this work mainly to calculate the crystalline ratio of the studies materials. For the analyse of WAXS diffractograms, deconvolution is preceded by the definition of a baseline based on the slope of a Gaussian curve and a normalisation of the spectra by their total integrated intensity, in order to standardise the spectra and make comparisons possible. The diffractograms are treated using Fityk (open-source software) [151] to subtract the baseline and deconvolute the amorphous halo from the crystalline peaks, as illustrated by Figure 4.

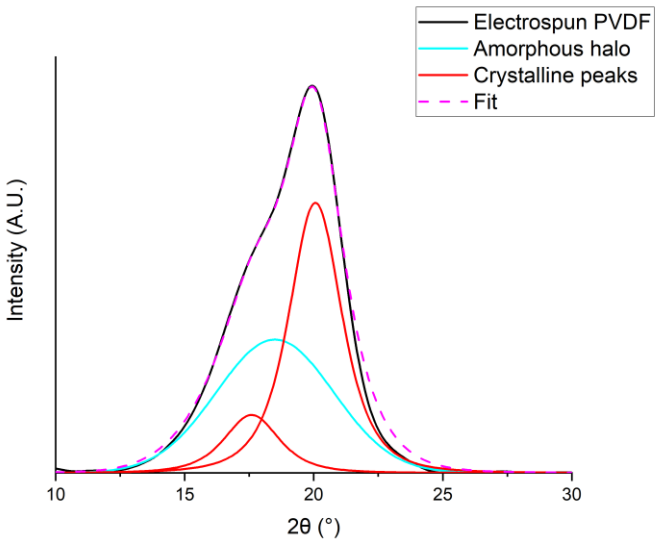

Figure 4: Deconvolution of a typical WAXS diffractogram of an electrospun PVDF sample.

In line with the work of YE. L. Gal'perin *et al*.[152], a Gaussian curve representative of the amorphous halo is centred around 2θ=18.40°. In the case of electrospun fibres, the presence of two bands is generally expected. The main band centred around 2θ=20.50° could represent either the (200) and (110) planes of the β phase, or the (110) and (101) planes of the γ phase. A shoulder located around 2θ=18.40° may correspond to the (020) planes of the α or γ phases.

Once the fit of the peaks is obtained, the crystallinity ratio can easily be obtained by the following Equation 5:

$$F_c = \frac{\sum A_{cr}}{\sum A_{cr} + \sum A_{am}}$$

Equation 5

where ΣA_{cr} is the sum of all the crystalline peaks areas, and ΣA_{am} the area of the amorphous halo.

All values in the manuscript are given as an average of three trials, the uncertainties correspond to the largest deviation observed in the series of samples tested.

For this thesis, WAXS analyses of the different PVDF samples were performed on an APEX2 diffractometer from Brucker. The anode employed is made of molybdenum, and the corresponding used wavelength is that of molybdenum K_α (energy of 17.5 keV and λ = 0.071 nm). The presented 2θ diffractograms are converted to correspond to the Cu K_α wavelength. The sample-detector distance is 59.5 mm (with a slight variation due to the sample thickness).

3.3. FTIR

Fourier transform infrared spectroscopy (FTIR) is widely used in characterisation of polymer materials, as it allows accessing various type of information concerning the chemical structure of the material, as well as its crystallinity. Like any absorption spectroscopy, the principle is to submit the sample to a light source, in this case infrared (IR) radiation, which will be selectively absorbed by the material. As the different molecules in the material are vibrating in different modes, depending on the type of bond, atomic weight, spatial arrangement of the atoms in the studied molecule, they will absorb IR light at different frequencies. Contrary to the first IR spectrometer that

needed to scan individually each frequency of the IR light individually, which was a time costly process with an important noise component, FTIR allows to scan multiple frequencies simultaneously with the use of an interferometer. In order to retrieve the IR spectra used for analysis and interpretation, the data must be submitted to Fourier transform, which gives its name to the technique [153,154].

In the scope of this thesis, FTIR characterisation was performed on a Nicolet 6700 Spectrometer from Thermo Fisher Scientific, in ATR mode with a diamond crystal. The analyses were set to 64 accumulations on a wavelength range going from 400 to 4000 cm^{-1}, with a resolution of 4 cm^{-1}. For comparison purposes, all presented FTIR spectra are normalised by total intensity.

In the case of PVDF, though some contradictory results in bands assignation have been published over the years, a notable review work from Cai *et al.* [155] intended to propose a definitive identification method of α, β and γ phase. Based on their work and additional complementary sources [138,156–160], Table 6 lists the FTIR bands of PVDF in the range 400 to 1500 cm^{-1} (the most intense region containing most characteristic bands) along with the associated phase and vibrational mode.

Table 6: FTIR band assignation for phase identification in PVDF [138,155–160].

Band location (cm^{-1})	**Associated phase**	**Associated vibrational modes**
410	α	CF_2 rocking, CF_2 bending
431	γ	
445	β	
473	β	CF_2 wagging
482	γ	
489	α	CCC bending, CF_2 bending, CF_2 wagging, CF_2 rocking
510	β γ	CF_2 bending, CCC bending
532	α	CF_2 bending, CCC bending, CF_2 rocking
614	α	CF_2 bending, CF_2 wagging
763	α	CF_2 wagging, CCC bending
776	γ	CH_2 rocking
795	α	CH_2 rocking
811	γ	CH_2 wagging
830	γ	
840	β γ	CH_2 rocking, CF_2 stretching
854	α	CH_2 rocking, CC stretching
881	α β γ	CF_2 stretching, CH_2 twisting, CC stretching
975	α	CH_2 twisting, CF_2 stretching
1070	α β γ	CC stretching, CH_2 wagging, CF_2 wagging, CF_2 stretching CF_2 stretching, CC stretching
1149	α	CF_2 stretching, CC stretching, CC stretching, CH_2 twisting
1176	α β γ	CF_2 stretching, CC stretching, CF_2 stretching, CF_2 stretching, CF_2 bending
1209	α	CF_2 stretching, CF_2 rocking
1234	γ	CF out of plane deformation
1275	β	CH_2 rocking, CF_2 rocking, CF_2 stretching
1383	α	CH_2 wagging, CC stretching
1401	α β γ	CH_2 wagging, stretching
1423	α	CH_2 bending
1429	γ	
1431	β	CH_2 bending

Figure 5 illustrates the phase attributions in the 400-1500 cm^{-1} region of various PVDF samples.

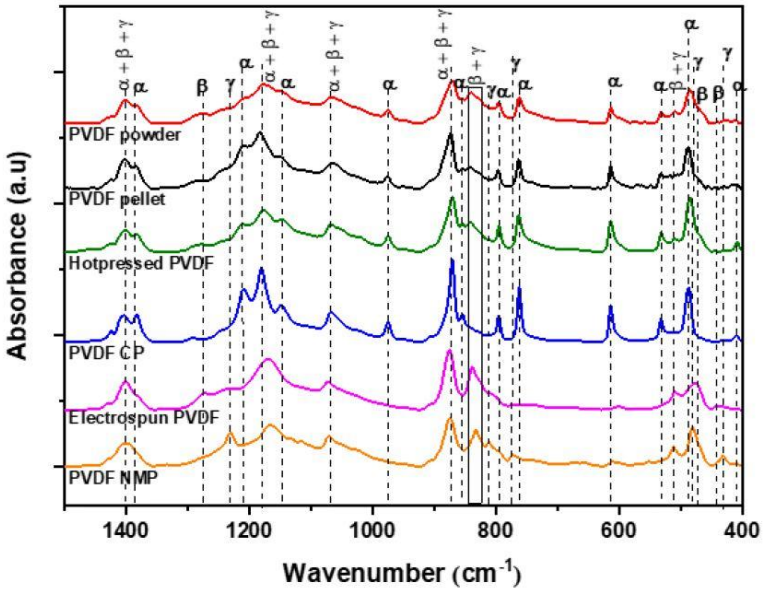

Figure 5: FTIR spectra of PVDF films prepared by various methods. PVDF CP and PVDF NMP are solvent casted samples prepared with cyclopentanone and NMP as solvents respectively [134].

Considering the 650-950 cm^{-1} region has the strongest contribution for all three main phases of PVDF, it has been chosen as the representative region of the FTIR spectra for comparison [134]. The normalisation by total intensity method was selected as no identified band is independent from crystallinity ratio and phase distribution within a sample.

3.4. Raman spectroscopy

Similarly to infrared spectroscopy, Raman spectroscopy is a technique that allows the study of the vibrational spectrum of molecules. The two techniques are complementary, as some bonds that are inactive in IR will respond very well in Raman, and conversely. The technique is based on the Raman effect, where the light passing through a material, resulting in a modified frequency, is compared to the incident beam. Among the various information that can be retrieved from a Raman spectrum, each band can be characterised by its position, which is linked to the associated vibration mode, and intensity, which is proportional to the number of molecules contributing to the signal. Hence, Raman spectroscopy allows the identification of the chemical composition of a polymer material, as well as the study of its microstructure [153,161].

For this thesis, two different Raman spectrometers have been used. The first one is a RXNI-785nm spectrometer from Kaiser Optical Systems, operating with a wavelength of 785 nm, and a power of 400 mW. As the probe is connected to the apparatus by optical fibres, is allows some remote sensing away from the apparatus body. This feature, combined with a probe head adapted to the used DSC setup, allowed coupled studies and the acquisition of Raman spectra as a function of temperature in an *in situ* setup. The second spectrometer is the LabRAM HR from Horiba. The employed laser was again a 785 nm laser, with a power of 14.5 mW. The particularity of this spectrometer is the coupling with a confocal microscope, allowing the precise focalisation of the laser at the sample surface. For this thesis, a x100IR lens was employed. This particular setup allowed “local” Raman analyses on identified electrospun fibres. For comparison purposes, all presented Raman spectra are normalised by total intensity.

From previous literature works [158,162–166], characteristic Raman bands of PVDF have been attributed to the main crystalline phases of PVDF, thus making this technique suitable for phase identification and quantification. Table 7 lists the Raman bands of PVDF in the range 400 to 1500 cm^{-1} along with the associated phase and vibrational mode.

Table 7: Characteristic Raman Bands of PVDF, with associated crystalline phase and vibration mode [158,162–166].

Band location (cm^{-1})	Associated phase	Associated vibrational modes
410	α	CF_2 rocking
484	α	CF_2 scissoring, CF_2 wagging
510	β	CF_2 scissoring
533	α	CF_2 scissoring
609	α	CF_2 scissoring, CCC scissoring
763	α	CF_2 scissoring, CCC scissoring
797	α	CH_2 rocking
811	γ	CH_2 rocking
840	strong for β	CH_2 rocking, CF_2 antisymmetric stretching
873	α	CC symmetric stretching, CCC scissoring
881	α β γ	CC symmetric stretching, CF_2 symmetric stretching,
973	α	CH_2 twisting
1055	α	CF_2 symmetric stretching, CH_2 wagging
1070	α β γ	CC antisymmetric stretching, CF_2 wagging, CH_2 wagging
1144	α	CC antisymmetric stretching, CF_2 symmetric stretching
1196	α	CF_2 antisymmetric stretching, CH_2 wagging
1278	α β γ	CF_2 symmetric stretching, CC symmetric stretching, CCC scissoring,
1291	α	CF_2 antisymmetric stretching, CF_2 rocking
1401	α β γ	CH_2 scissoring, CH_2 wagging, CC antisymmetric stretching,
1426	α	CH_2 scissoring, CH_2 wagging
1430	α β γ	CH_2 scissoring, CH_2 wagging

Figure 6 illustrates the phase attributions in the 400-1000 cm^{-1} region of various PVDF samples.

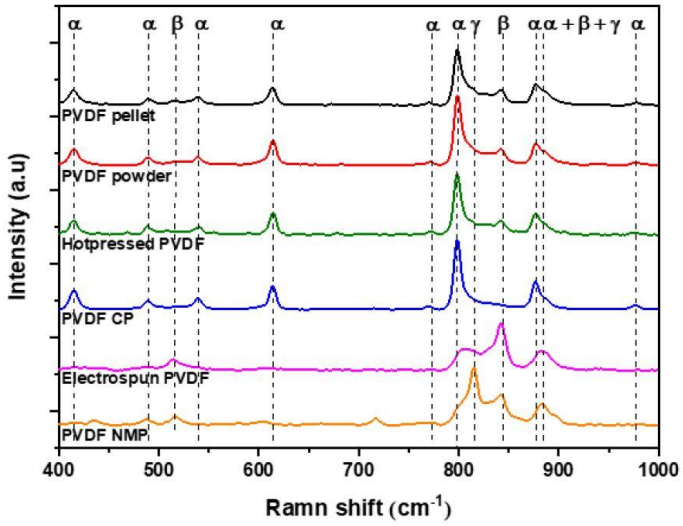

Figure 6: Raman spectra of PVDF samples prepared by different methods. PVDF CP and PVDF NMP are solvent casted samples prepared with cyclopentanone and NMP as solvents respectively [134].

Inspired by the work of Chapron *et al*. [162], and considering the 780-920 cm^{-1} region has the strongest contribution for all three main phases of PVDF, it has been chosen as the representative region of the Raman spectra for comparison and calculations [134].

After setting the baseline, all spectra were normalised by total intensity. This solution was adopted as no identified band is independent from the sample crystallinity ratio or phase distribution. Deconvolution of the spectra was performed using the Fityk software [151], the details of the procedure are discussed in the following chapter. Once performed, the calculation of the crystallinity ratio (Equation 6) and respective crystalline phase fractions (Equation 7, 8 and 9) is relatively simple:

$$F_c = \frac{\sum A_{cr}}{\sum A_{cr} + \sum A_{am}}$$

Equation 6

$$F_\alpha = \frac{\sum A_\alpha}{\sum A_\alpha + A_\beta + \sum A_\gamma}$$

Equation 7

$$F_\beta = \frac{\sum A_\beta}{\sum A_\alpha + A_\beta + \sum A_\gamma}$$

Equation 8

$$F_\gamma = \frac{\sum A_\gamma}{\sum A_\alpha + A_\beta + \sum A_\gamma}$$

Equation 9

where ΣA_{cr} corresponds to the sum of the areas of all crystalline bands, ΣA_{am} corresponds to the sum of the areas of all amorphous bands, ΣA_α corresponds to the sum of the areas of all bands associated to α phase, ΣA_γ corresponds to the sum of the areas of all bands associated to γ phase, and A_β the area of the band associated with β phase.

All values in the manuscript are given as an average of three trials, the uncertainties correspond to the largest deviation observed in the series of samples tested.

3.5. TGA

Thermogravimetric analysis (TGA) involves the measurement of the mass variation of a studied sample as a function of temperature. It is generally used to characterise the thermal behaviour and chemical composition of materials. In this thesis, the analyses were performed on a Setsys Evolution 1750 analyser from Setaram, on samples weighting approximately 5 to 15 mg, in an alumina crucible. The sample is submitted to an air flux of 20 mL/min, and heated from 20 to 800°C at a heating rate of 10 °C/min. The use of TGA in the scope of this thesis was mainly the verification of remaining solvent in the evaporated materials, solvent casted films and electrospun nanofibres.

3.6. Brillouin spectroscopy

Brillouin spectrometry was used to characterize the mechanical properties of individual fibres. This light spectroscopy is a non-destructive, non-contact light scattering technique. By providing information of the acoustic wave velocity in materials, it allows to reach its elastic constants. If it is used to characterize mechanical properties of crystalline single crystals [167,168] or thin films [169–171], it is particularly well suited for the study of soft materials, like oligomers [172,173], polymers [174–176] and polymer nanocomposites [177–180], due to the important opto-mechanical coupling in these materials.

In Brillouin spectroscopy, the interaction between the photons from the incident laser beam, and the acoustic phonons within the material, occur at hypersonic frequencies (about 1 to 100 GHz, which approximately corresponds to acoustic wavelengths between 180 nm to few µm). This interaction causes frequency shifts (f) of the scattered light. As photons and phonons follow the conservative laws usual in inelastic scattering processes, conservation of energy involves the frequencies of the incident and scattered light, and frequency of the acoustic wave (Equation 10), and conservation of momentum involves the light and acoustic wave vectors (Equation 11):

$$\hbar\omega_s = \hbar\omega_i \pm \hbar\Omega$$

Equation 10

$$\hbar k_s = \hbar k_i \pm \hbar q$$

Equation 11

Where ω_i and ω_s are the angular frequencies of the incident and scattered photons, k the wavevectors of the incident and scattered photons, Ω the angular frequency of the photons, and q the wavevector of the photons.

By assuming negligible energy transfer between photons and phonons, and from Equation 10 and Equation 11, the relation between the sound velocity v, the acoustic phonon frequency f and the acoustic wave vector q can be calculated (Equation 12):

$$v = \frac{2\pi f}{q} = \frac{\lambda_0 f}{2n\,sin\left(\frac{\theta_i}{2}\right)}$$

Equation 12

where λ_0 is the laser wavelength, and θ_i the angle between the incident and scattered vectors, respectively $\overrightarrow{k_i}$ and $\overrightarrow{k_s}$.

Then, knowing the material mass density ρ, the elastic modulus of an isotropic material can be easily calculated (Equation 13):

$$c(\vec{q}) = \rho v^2(\vec{q})$$

Equation 13

The Brillouin scattering measurements were performed using a Spectra Physics laser (power of 200 mW and wavelength 532 nm) with a narrow spectral bandwidth and a very fine stable power. A modified Olympus BX51 microscope with an objective x50 was used to perform micro-Brillouin spectroscopy. The received power level on the sample was approximately 30mW. The laser beam through the optical path allowed a measurement of

average diameter of about 2 µm. The measurements were made at room temperature and the studied sample was not heated by the beam. The intensity of the spectral distribution was analysed by a Fabry–Perot (2 × 3 tandem pass) brand Table Stable (Switzerland), the Tandem Fabry–Perot Interferometer TFP-1. The opto-electronic conversion was carried out by a photomultiplier and the spectrum was accumulated on a multichannel analyser (MCA- Ghost). The whole system was controlled by computer to increase the stability of the optical path. The mirrors of the Fabry-Perot interferometer were settled with a gap of 3 mm between them. The scanning amplitude used was 300 nm. Due to the use of the microscope, the configuration of the optical path was that of backscattering. The micro-Brillouin in backscattering configuration is presented in Figure 7.

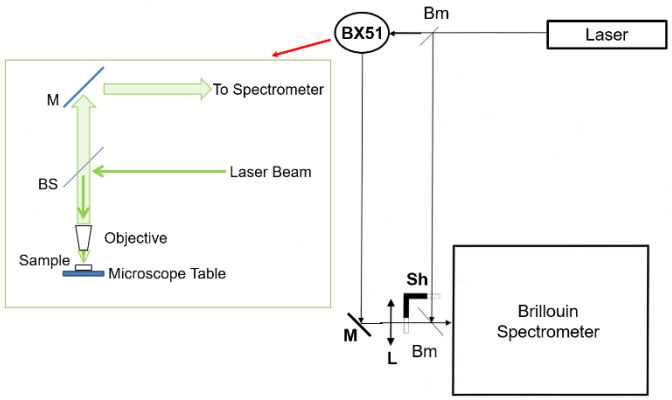

Figure 7: Micro-Brillouin setup [171].

The micro-Brillouin measurements in temperature were carried out using two different setups. In Nancy, a HFS600E-PB4/PB2 System from LINKAM Scientific was employed. The liquid nitrogen circulation system was a LNP95 connected to a T95 System Controller, allowing to set the temperature parameter for the tests. Various acquisitions ranging from -50 to 110°C were performed. In Madrid, temperature-dependent measurements were conducted inside a low-temperature optical cryostat (Optistat from Oxford Instruments) using liquid nitrogen as coolant, which allowed to explore lower ranges of temperatures down to -75°C, and in a home-made furnace with an optical window, in vacuum if necessary, and allowing a temperature range between 8°C to 450°C.

3.7. SEM

Scanning electron microscopy (SEM) was performed using a Gemini SEM 500 from Zeiss equipped with a high-resolution detector (Inlens). The tests were conducted under high vacuum and low applied tension of 1kV. The secondary electrons imaging was used to investigate the surface of the produced fibres, and explore the possible surface roughness difference between the different fibre types.

3.8. DMA

The dynamic mechanical analysis (DMA) allows studying the viscoelasticity properties of a material. During the test, the sample is submitted to an oscillatory solicitation at small deformations, with variating frequency, as a function of temperature. It is one of the major techniques to study the glass transition relaxation of polymers.

The variables measured during a test are the strain, resulting stress and phase shift angle δ, allowing to calculate the modulus of the material using Hooke's law (Equation 14):

$$|E^*| = \frac{\sigma_A}{\varepsilon_A}$$

Equation 14

where $\sigma_{A\ is}$ the amplitude of the applied stress and ε_A the amplitude of the strain.

This complex modulus E* is composed of two parts, E' being relative to the rigidity of the material, due to its elastic behaviour, and E'' being relative to the amount of dissipated energy due to the viscous behaviour of the material. The relations between the different variables can be written as follows (Equation 15, 16 and 17):

$$E^* = E' + iE'' = E'(1 + i\ tan\delta)$$

Equation 15

$$E' = |E^*|\ cos\delta$$

Equation 16

$$E'' = |E^*|\ sin\delta$$

Equation 17

where tanδ is the loss factor, which is a measure of the dissipated energy by damping relatively to the elastic energy, and depends on the applied frequency of the DMA test.

The setup used during this thesis is a DMA 242C apparatus from NIETZCH in traction mode. The study in temperature ranges from -80 to 120°C (which is low enough to avoid melting of the sample) at a heating rate of 2K/min. The studied frequencies were 0.1, 1, 10 and 20 Hz for the solvent casted sample, and 1 Hz on the electrospun sample. The analysed samples were in both cases band cut from the films, of dimensions 40x6 mm.

3.9. Electric characterisation and energy harvesting

The nanogenerators are formed of four different parts: the electrospun scaffold, covered on both sides with P-shaped aluminium electrodes, the connection wires, and the PET encapsulation layer. Seven device types were fabricated from electrospun fibres with various cellulose nanocrystals (CNC) or Al-Cu-Fe-B quasicrystals (QC). Table 8 summarises the composition of the different devices.

Table 8: Name and composition of the devices.

Device name	Material and filler content
PVDF	Pristine electrospun PVDF fibres
CNC1	Electrospun PVDF fibres + 1 wt% CNC
CNC3	Electrospun PVDF fibres + 3 wt% CNC
CNC5	Electrospun PVDF fibres + 5 wt% CNC
QC1	Electrospun PVDF fibres + 1 wt% QC
QC3	Electrospun PVDF fibres + 3 wt% QC
QC5	Electrospun PVDF fibres + 5 wt% QC

To make the devices, two PET rectangles of dimensions 5x4.5 cm are cut to make the protective layer. With double-sided tape, a P-shaped electrode made from aluminium foil is pasted on each PET layer. The connective wires are inserted at the bottom of the electrodes and secured with aluminium foil. Then, a 3x3 cm square of electrospun

scaffold is placed on the square part of one of the electrodes. The two PET layers are then reunited, with the PVDF scaffold in-between the two aluminium electrodes. The two halves are assembled using double-sided tape. Some pictures illustrating the process are presented in Figure 8.

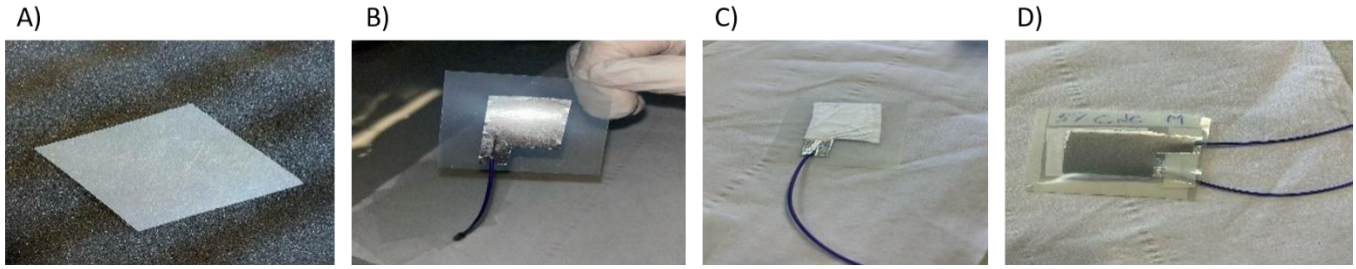

Figure 8: Preparation steps of the PVDF devices A) the PET layer, B) the P-shaped electrode with the connecting wire, C) addition of the electrospun scaffold, D) the finished device.

In this configuration, the electrodes are pressed but not glued against the mat fibres. When the device is deployed, it is therefore possible, even probable, that there will be some slippage and friction of the electrodes on the fibres, inducing a triboelectric effect in the overall response.

Measurements of the output voltage and currents of the nanogenerator devices has been carried out using an instrumented tapping test setup realised at Institut Jean Lamour. The setup includes a rammer responsible for the strike movement. The applied force is controlled through to addition of six weights of 400 g each. The applied frequency of the tapping test can be controller either via a potentiometer, or using a software interface developed on PyCharm. Observation of the output voltage and current was performed using a Keithley DMM6500 digital multimeter. The development of the custom-built tapping test system in further developed in Chapter 5, and a functional diagram is provided along with a photograph of the machine in Figure 9.

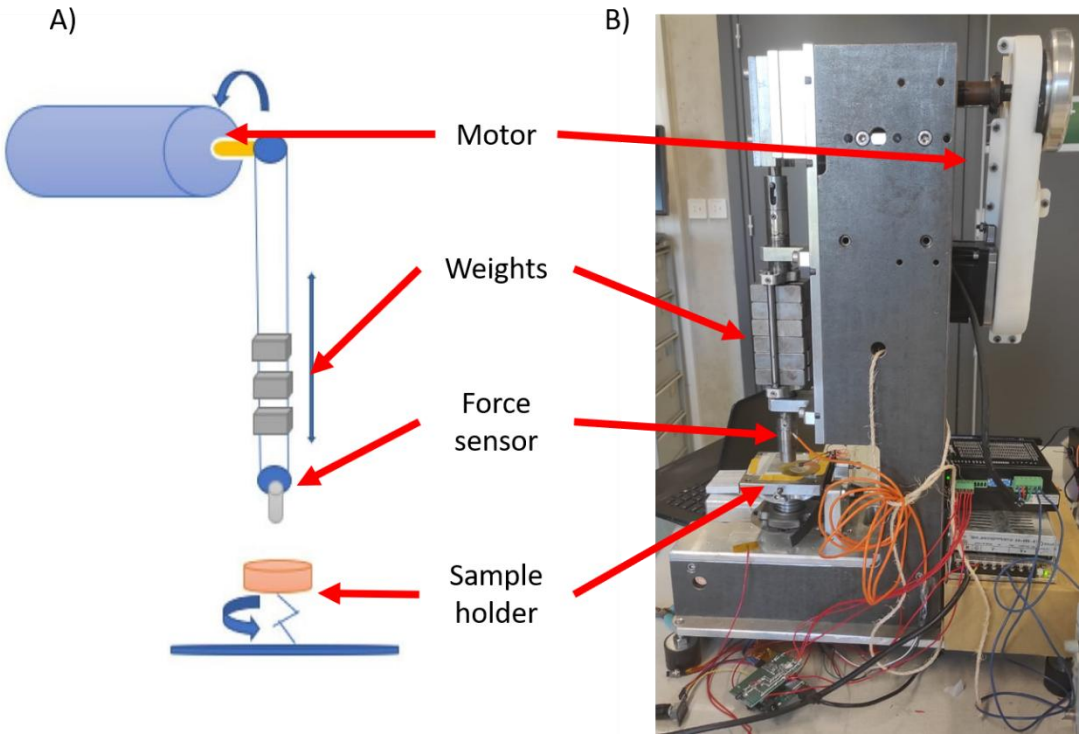

Figure 9: A) Functional diagram and B) photograph of the tapping test bench.

Chapter 3: Crystalline characterisation of the electrospun fibres and influence of nanofillers addition

1. Introduction

While electrospinning is recognised as a promising method to produce PVDF with high electroactive fractions, it is important to keep in mind that the outcome of the electrospinning process is influenced by numerous parameters. Producing satisfying fibres generally involves a preliminary work of parameter optimisation. Once this first step in successfully completed, further improvement of the fibre properties can be achieved by the addition of fillers. Given the scope of the thesis, the first goal of filler addition is to improve the fraction of electroactive phases, especially the β phase, to enhance the electroactive properties and energy harvesting capacity of the PVDF scaffolds. Moreover, depending on the nature of the filler, mechanical strength, thermal stability and other additional improvements can be made compared to the pristine fibres.

After electrospinning pristine fibres with a variety of electrospinning parameters, characterisation of the fibres is necessary to determine which set of parameters allows the production of the best fibres in terms of electric response. Several points have been considered to make the selections. First, the crystalline properties such as crystallinity ratio and phase fraction were studied. While the use of DSC, WAXS and FTIR correspond to a characterisation protocol usually employed in polymer and polymer-based composites, in the frame of this thesis a new Raman criterion is proposed, aiming at identifying and quantifying the crystalline phases of PVDF.

In this chapter, the development of the Raman criterion is first detailed, then applied on the pristine electrospun fibres. Characterisation results from DSC, WAXS, FTIR and SEM are added and compared to Raman results to obtain a reliable overview of the fibres crystallinity and select the optimal set of electrospinning parameters. Using the selected set of parameters, nanocomposites fibres are then elaborated and studied employing the same characterisation routine, providing an insight about the influence of the addition of two nanofiller types: cellulose nanocrystals (CNC) and Al-Cu-Fe-B quasicrystals (QC).

2. New proposal for a Raman criterion for identification and quantification of PVDF crystalline phases

Usually, WAXS and FTIR are considered as the go-to techniques for the characterisation of the different crystalline phases in PVDF, which is the main use that will be considered in the scope of this thesis. From the author's experience, and based on previous works exploring the use of Raman spectroscopy for phase quantification in polymers [162,164,181–185], the idea of building a reliable criterion based on the technique emerged. Though early works used to rely on the intensities of a few bands, characteristics of specific phases of PVDF, this method is mainly adapted to compare materials with similar properties. To gain more in-depth understanding of the polymeric materials, the approach based on the areas of the characteristic bands is considered to be more appropriate.

The main inspiration for the work presented in this chapter is an article previously published in ACS Applied Polymer Materials by members of the IJL team:

Quantifying the crystalline polymorphism in PVDF: comparative criteria using DSC, WAXS, FT-IR, and Raman spectroscopy. Sreelakshmi Moozhiyil Purushothaman, ***Maïté Fernandes Tronco****, Marc Ponçot, Chitralekha C.S, Nathanael Guigo, Marc Malfois, Nandakumar Kalarikkal, Sabu Thomas, Isabelle Royaud, and Didier Rouxel. ACS Applied Polymer Materials, 2024, vol. 6, no 14, p. 8291-8305. DOI: 10.1021/acsapm.4c01157*

2.1. Crystalline phase identification using Raman spectroscopy

Even though Raman acquisitions were obtained from 400 to 1500 cm^{-1}, the studied region in this thesis is reduced to the 780-920 cm^{-1} range, as it contains characteristic bands from the three main phases of PVDF, namely α, β and γ.

Figure 10 presents the Raman spectra of three representative materials. For comparison purposes, all presented Raman spectra are normalised by total intensity. The pristine electrospun fibres are the typical example of a material with very high electroactive phase fraction, and little to no α phase. A PVDF solvent casted sample was also tested, presenting some amount of electroactive phase, but with a visible portion of α phase. On the contrary, after a heating cycle to 200°C, the solvent casted sample cooled from the melt will preferentially crystallise in α phase, with a reduced amount of electroactive phase present.

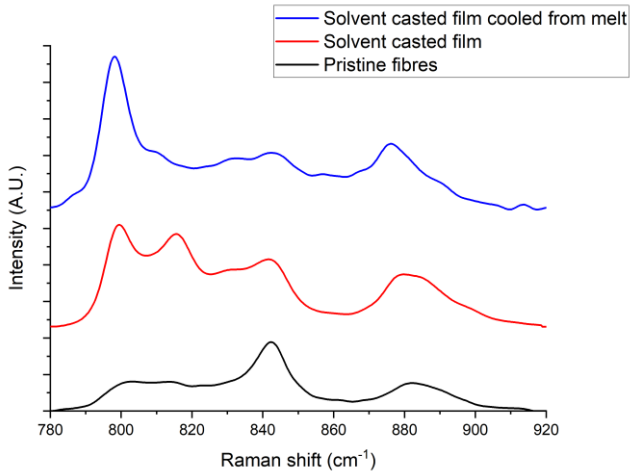

Figure 10: Raman spectra of pristine PVDF electrospun fibres (black), and a PVDF solvent casted sample before (red), and after (blue) a heating ramp to 200°C.

Initially, the characteristic bands of the electroactive phases are visible. In the electrospun sample, the more prominent band, at 842 cm^{-1}, is distinctive of the β phase. Then, the bands at 813 and 830 cm^{-1}, that are present in the form of shoulders, are attributed to the γ phase. The last band which appears very broad and centred around 882 cm^{-1} cannot be attributed to a specific crystalline phase as it is systematically present (it accounts for α, β and γ). Hence, it must be taken into account for the calculation of the crystallinity ratio.

In solvent casted samples, additional bands present at 799 and 874 cm^{-1} indicate the presence of α phase. After heating to 200°C and cooling, the spectrum presents a totally different appearance. If a residual band seems still present at 842 cm^{-1}, the prominent band is located this time at 799 cm^{-1}. Completed by another band very visible at 874 cm^{-1}, they are strong indication of the presence of a high α phase fraction in the sample. As previously presented, the band centred around 883 cm^{-1} is still present.

2.2. Calculation of the crystallinity ratio and determination of the different phase fractions

The basics of the phase quantification methods is similar to the proposal made in the article published in ACS Applied Polymer Materials [134]. First, the molten PVDF spectrum is deconvoluted using Gaussian curves to represent the contribution of the amorphous phase of the semi-crystalline sample. Attempts have been made of quick quenching some melt to obtain a fully amorphous PVDF sample. However, the resulting samples would systematically present a high amount of crystallisation due to the α phase formation. Thus, the molten material

had to be studied as the approaching equivalent of a fully amorphous material. Once the deconvolution of the amorphous contribution is done, the study of the semi-crystalline materials can be carried out. In addition to the amorphous curves, Pearson 7 [134] curves are added to represent the usual bands characteristic of the three main crystalline bands of PVDF.

The approach previously used for the deconvolution of the amorphous spectrum was mathematical, which means that the main goal was to obtain a fit as close as possible to the original curve. As a result, the amorphous contribution was modelled using eight Gaussian curves, of which three do not have any physical attribution. The novel approach intends to limit the number of curves to a minimum of physically identifiable bands. The new deconvolution of the spectrum corresponding to the melt is illustrated in Figure 11.

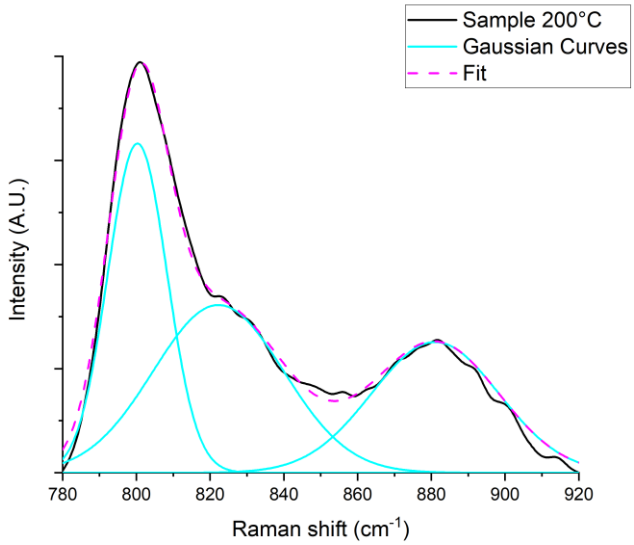

Figure 11: Deconvolution of the Raman spectrum of molten PVDF.

In this version, with only three Gaussian curves, the fit of the Raman spectrum taken at 200°C remains satisfactory. Identification of the known Raman band is provided in Chapter 2, along with the reference articles. The first Gaussian curve located at 800 cm^{-1} can easily be identified to the known band at 795 cm^{-1} associated with CH_2 rocking, characteristic of the α phase in the crystallised samples. Similarly, the third Gaussian curve located at 881 cm^{-1} can be identified to the band at 881 cm^{-1} associated with CF_2 symmetric stretching, CH_2 in phase twisting and CC out of phase symmetric stretching, which is associated with all three crystalline phases. The second band, located at 822 cm^{-1} is slightly more difficult to identify, as it does not directly correspond to an existing identified band. However, two known bands are located at 811 and 840 cm^{-1}. The first one is associated to CH_2 out of plane wag and γ phase, and the second to CH_2 rocking and CF_2 antisymmetric stretching and β phase. An additional shoulder located at 830 cm^{-1} present in samples with high γ phase has also been identified [134]. Hence, it was suggested that the band located at 822 cm^{-1} in the melt goes to crystallise into β or γ phase when the elaborating conditions are met. Upon cooling, the amorphous phase is set in the material. Thus, the area ratios calculated between the three Gaussian bands in the molten state can be kept in the fitting of all spectra [181]. The fixed area ratios are indicated in Table 9.

Table 9: Area ratios between the Gaussian bands.

Gaussian band position (± 5 cm^{-1})	800	822	881
Area ratio	1	1.12	0.85

With the fit of the melt, the Raman spectra of semi-crystalline samples can be analysed. The three samples previously used in the identification section were analysed by applying the complete routine. The resulting fits are presented in Figure 12.

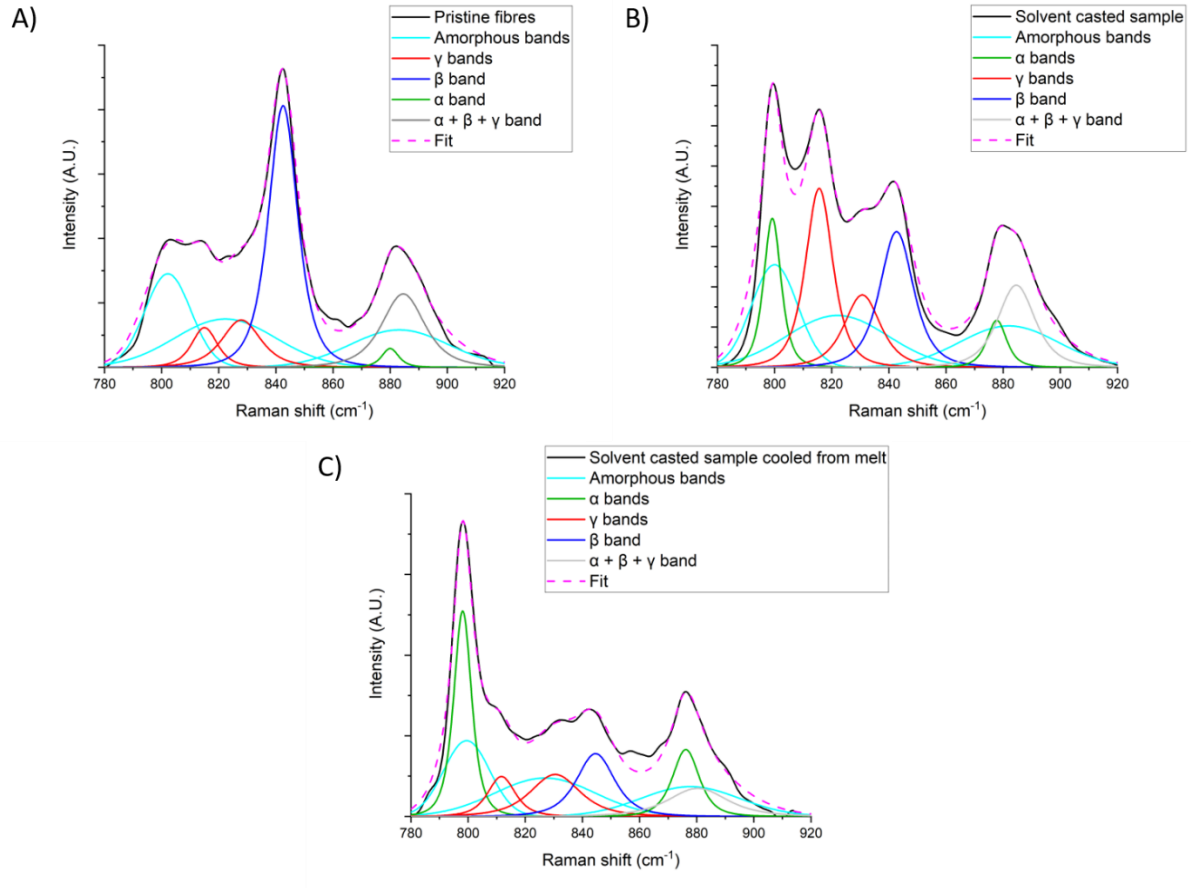

Figure 12: Raman Spectra of A) pristine electrospun fibres and B) solvent casted PVDF sample and C) solvent casted sample cooled from melt.

It is now possible to calculate the crystallinity ratios, and the fractions of the three main phases of PVDF present in the two samples. The results of these calculations are presented in Table 10, along with the crystallinity ratios obtained by DSC on the same samples.

Table 10: Calculated values of crystallinity ratio and phase fraction using Raman spectroscopy and DSC.

	Pristine fibres	**Solvent casted sample**	**Solvent casted sample cooled from melt**	
Crystallinity ratio by DSC (χ_c %)	46	43	38	± 5%
Crystallinity ratio by Raman (χ_c %)	55	52	42	± 3%
α fraction (F_α %)	2	23	50	± 2%
β fraction (F_β %)	71	29	22	± 5%
γ fraction (F_γ %)	27	48	29	± 5%

The obtained values are representative of the differences between the samples. The electrospun fibres show a negligible α phase fraction, with over 98% of electroactive phases fraction combined. The prevalent phase is the β phase, with a β/γ proportion of 71/27 approximately. The solvent casted sample possesses all three crystalline phases in substantial proportions, but the lack of mechanical stretching is illustrated by the much lower β phase

fraction. After melting and recrystallisation of the sample, the α phase becomes dominant and the proportion of electroactive phases is further reduced.

The deconvolution proposed allows to take into account a wide range of crystalline phase fractions, and obtain a numerical value for these phase proportions within a sample. However, the values of the crystallinity ratio obtained from the Raman spectra were always higher than the values obtained by DSC, with a consistent 20% increase. The Raman criterion proposed in this section will then be used and compared to the values of crystallinity ratio or/and phase fractions obtained from DSC and WAXS.

3. Optimisation of the electrospinning process: a study to optimise the parameters

Given the wide range of parameters that influence the outcome of electrospinning, a study was conducted to understand the influence of the PVDF weight percentage in solution, the solvent ratio, the applied voltage (AV), the flow rate (FR) and the tip-to-collector distance (TCD). The range of values tested in this optimisation study was chosen accordingly to previous results from the literature [58–61,63,64,78,80,91,92,94,127–133,186,187]. Unfortunately, it has not been possible to control the temperature and humidity so fibre elaboration was submitted to climate variations. From the different tested combinations of parameters, 20 samples were electrospun, and the detail is summarised in Table 11.

Table 11: Pristine PVDF fibres electrospinning parameters for optimisation study.

Sample name	Solution parameters	Electrospinning parameters
ES15WT37DA 10_08_15	150g/L PVDF in 10mL 3:7 D:A	AV: 10kV, FR: 0.8 mL/h, TCD: 15cm
ES15WT37DA 12_08_15	150g/L PVDF in 10mL 3:7 D:A	AV: 12kV, FR: 0.8 mL/h, TCD: 15cm
ES15WT37DA 15_08_15	150g/L PVDF in 10mL 3:7 D:A	AV: 15kV, FR: 0.8 mL/h, TCD: 15cm
ES15WT37DA 13_1_12	150g/L PVDF in 10mL 3:7 D:A	AV: 13kV, FR: 1 mL/h, TCD: 12cm
ES15WT37DA 13_12_12	150g/L PVDF in 10mL 3:7 D:A	AV: 13kV, FR: 1.2 mL/h, TCD: 12cm
ES15WT46DA 10_08_15	150g/L PVDF in 10mL 4:6 D:A	AV: 10kV, FR: 0.8 mL/h, TCD: 15cm
ES15WT46DA 12_08_15	150g/L PVDF in 10mL 4:6 D:A	AV: 12kV, FR: 0.8 mL/h, TCD: 15cm
ES15WT46DA 15_08_15	150g/L PVDF in 10mL 4:6 D:A	AV: 15kV, FR: 0.8 mL/h, TCD: 15cm
ES15WT46DA 13_1_12	150g/L PVDF in 10mL 4:6 D:A	AV: 13kV, FR: 1 mL/h, TCD: 12cm
ES15WT46DA 13_12_12	150g/L PVDF in 10mL 4:6 D:A	AV: 13kV, FR: 1.2 mL/h, TCD: 12cm
ES16WT37DA 10_08_15	160g/L PVDF in 10mL 3:7 D:A	AV: 10kV, FR: 0.8 mL/h, TCD: 15cm
ES16WT37DA 12_08_15	160g/L PVDF in 10mL 3:7 D:A	AV: 12kV, FR: 0.8 mL/h, TCD: 15cm
ES16WT37DA 15_08_15	160g/L PVDF in 10mL 3:7 D:A	AV: 15kV, FR: 0.8 mL/h, TCD: 15cm
ES16WT37DA 13_1_12	160g/L PVDF in 10mL 3:7 D:A	AV: 13kV, FR: 1 mL/h, TCD: 12cm
ES16WT37DA 13_12_12	160g/L PVDF in 10mL 3:7 D:A	AV: 13kV, FR: 1.2 mL/h, TCD: 12cm
ES16WT46DA 10_08_15	160g/L PVDF in 10mL 4:6 D:A	AV: 10kV, FR: 0.8 mL/h, TCD: 15cm
ES16WT46DA 12_08_15	160g/L PVDF in 10mL 4:6 D:A	AV: 12kV, FR: 0.8 mL/h, TCD: 15cm
ES16WT46DA 15_08_15	160g/L PVDF in 10mL 4:6 D:A	AV: 15kV, FR: 0.8 mL/h, TCD: 15cm
ES16WT46DA 13_1_12	160g/L PVDF in 10mL 4:6 D:A	AV: 13kV, FR: 1 mL/h, TCD: 12cm
ES16WT46DA 13_12_12	160g/L PVDF in 10mL 4:6 D:A	AV: 13kV, FR: 1.2 mL/h, TCD: 12cm

The targeted applications of the fibres are oriented towards the elaboration of energy harvesting devices. Hence, the main criterion for the selection of fibres is the high percentage of electroactive phases, and especially that of β phase. The aim of this section is to use different characterisation methods to have a fine comprehension of the PVDF microstructure processed in electrospun fibres, and compare the results obtained from the various methods.

3.1. Phase identification and qualitative analysis from FTIR spectra

Even though phase quantification is possible from FTIR spectra, it was chosen to focus more on Raman spectroscopy and restrict the study of FTIR spectra to the qualitative aspect in this thesis. The development of a new FTIR criterion, similar to the one proposed for Raman analysis, constitutes an appealing perspective for this work.

3.1.1. Influence of the solvent ratio

The choice of solvent, and the ratio in the case of a solvent mix is an important part of the electrospinning process. The ratio of the DMF:Acetone solvent can possibly affect the fibres properties. As the boiling point of acetone is significantly lower than DMF (26°C compared to 153°C), a higher acetone ratio would lead to quicker evaporation of the solvent during electrospinning. From previous works, it is known that lower evaporation rates tend to favour the formation of β phase, while high rates favour α phase [72,75]. However, using DMF only can lead to incomplete drying of the fibres, and an excess of acetone could lead to a solvent evaporation so quick that the solution will dry at the needle tip and clog it [69,74,188]. Two different solvent ratio were tested, 3:7 and 4:6 DMF/acetone, as they often appear as preferred ratio from previous works [75,76,187]. The comparison of materials elaborated with these two ratios is presented in Figure 13.

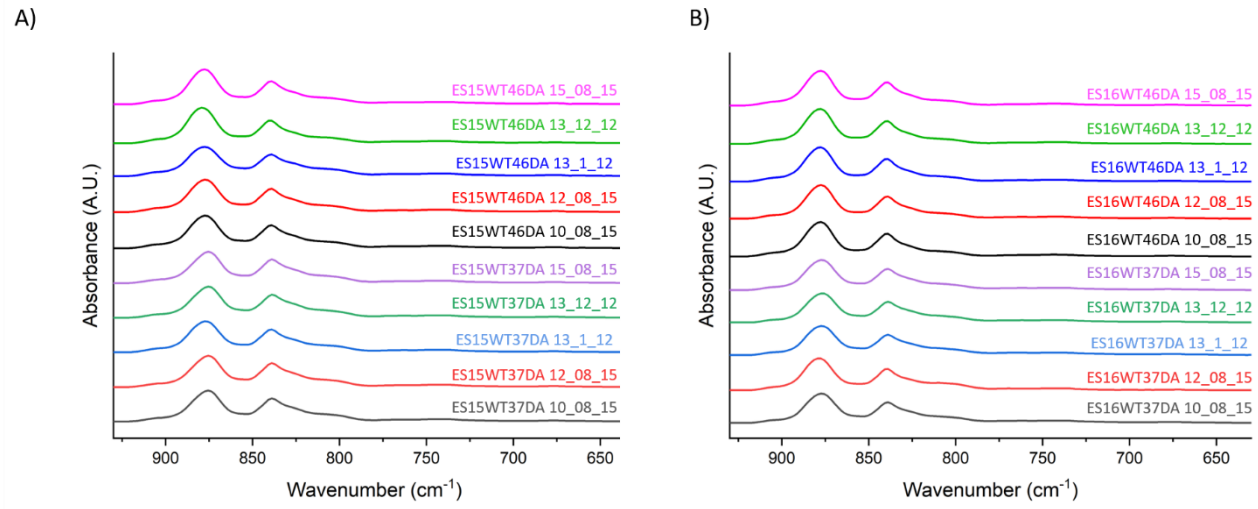

Figure 13: Comparison between 3:7 and 4:6 DMF/acetone ratio for A) 15wt% PVDF and B) 16wt% PVDF in solution.

From Figure 13, it is very clear that all sample present a very intense band at 840 cm^{-1}, which is representative of β phase. This would give a hint that a majority of β phase is present in the samples, which is the main goal of using electrospinning. The shoulder located at around 830 cm^{-1} indicates that some amount of γ phase is also present in the sample. The presence of α phase in the samples is demonstrated by the shoulder visible around 800 cm^{-1}. The differences in intensity of the three characteristic bands previously mentioned can be considered quite low from a sample to another, which could mean that the different samples have in fact a similar distribution in the proportion of the different crystalline phases. It is especially difficult to make a distinction in the case of sample elaborated with 15wt% of PVDF in solution, while in the case of samples with 16wt% of PVDF the 4:6 DMF ratio seems to slightly promote the formation of the β phase over that of γ phase.

3.1.2. Influence of the weight percentage of PVDF in solution

The difference of the weight percentage of PVDF in the polymeric solution is another key factor of electrospinning. Typically, the amount of polymer in solution will be a factor that controls the viscosity of the solution. With higher

viscosity, the jet will tend to stretch more under the applied voltage, which promotes the formation of β phase. However, an excessive viscosity will make the solution harder to stretch, and decrease the electroactive phase content [69–71]. It can also cause clogging at the needle tip, which hinders the electrospinning process. Two different values have been tested, 15 and 16wt% of PVDF in solution. The comparison of materials elaborated with these two values is presented in Figure 14.

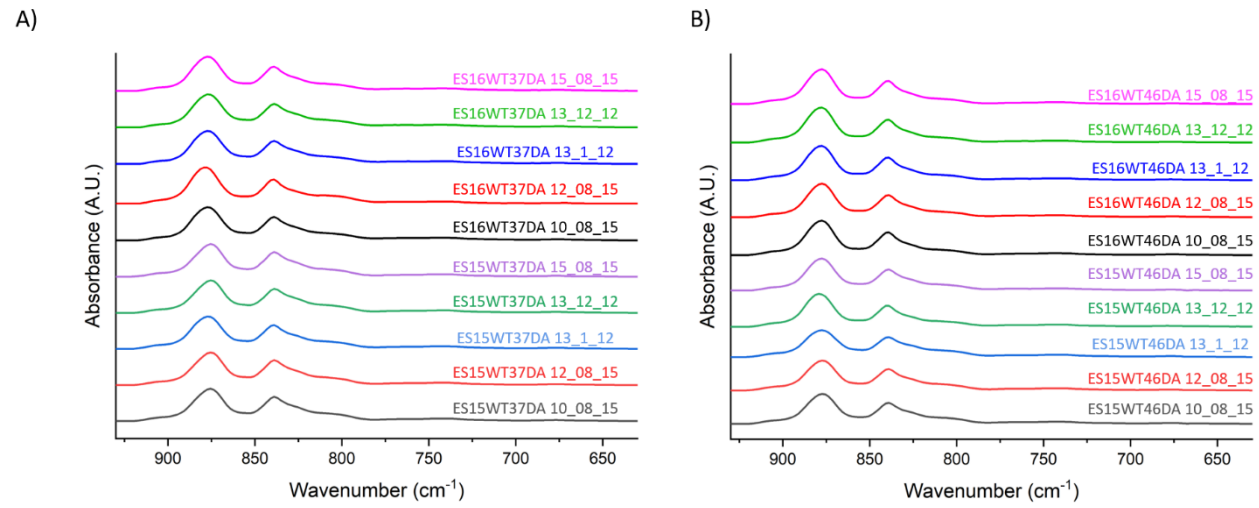

Figure 14: Comparison between 15wt% and 16wt% PVDF in solution for A) 3:7 and B) 4:6 DMF/acetone ratio.

From Figure 14, all samples present a very intense β band at 840 cm^{-1}. The shoulder located at around 830 cm^{-1} confirms the presence of γ. The presence of α phase in the samples is demonstrated by the shoulder visible around 800 cm^{-1}. It seems that the percentage of PVDF in solution has very little effect on the materials crystallinity, especially for fibres produced with a 3:7 DMF:Acetone ratio. Indeed, the various curves seem to superpose almost perfectly. In the case of fibres produced with a 4:6 DMF:Acetone ratio, a higher PVDF content seems to slightly promote β phase over γ, as it leads to a higher intensity of the 840 cm^{-1} band, and a slight decrease of the 830 cm^{-1} shoulder. Moreover, some height disparities can be observed for the 881 cm^{-1} band, which is a common crystalline band for α, β and γ phases. It could indicate some variations in the overall crystallinity ratio of the materials, with materials produced with a higher PVDF content presenting an increased crystalline fraction.

Overall, the variations observed from height intensities of the characteristic bands of the crystalline phases of PVDF are relatively small. All samples present a very intense band indicative of the β phase, with some amount of α and γ phase, which appear as shoulders. From the different comparisons, it could seem that fibres elaborated with a 16wt% PVDF content and a 4:6 DMF:Acetone ratio present in average a higher crystallinity ratio, and a slightly improved β/γ phase ratio. However, a more reliable assessment of the total crystallinity phase fractions is needed, which was made possible by the use of complementary characterisation methods.

3.2. Crystallinity ratio from DSC thermograms

DSC analysis is a precious tool to study the thermal response of polymer samples and their crystallinity ratio [135]. The first testing procedure used was a three-cycles study: one heating ramp from -80 to 200°C, cooling down to

-80°C, and a second heating up to 200°C. The corresponding thermograms for one of the electrospun samples (ES CNC0) are presented in Figure 15.

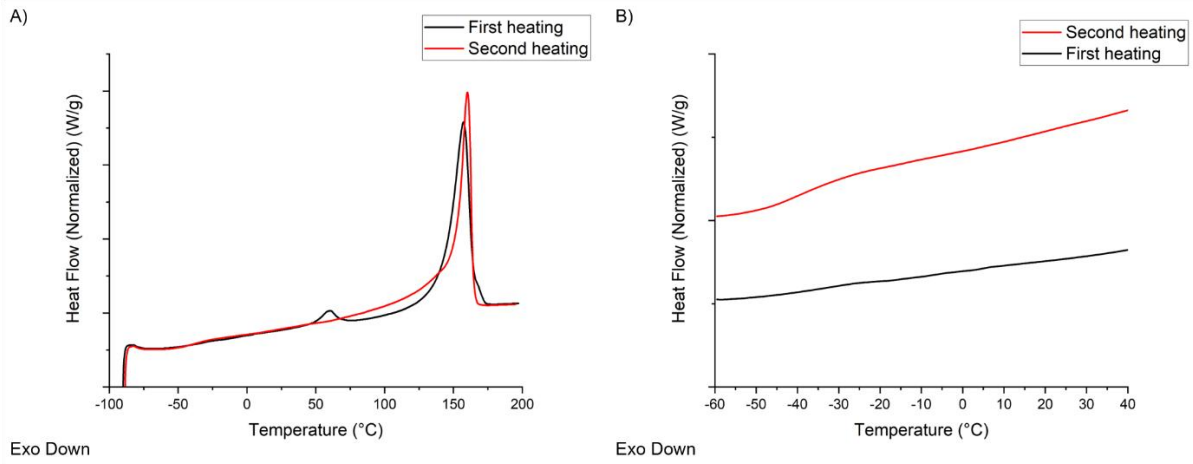

Figure 15: Typical DSC thermograms of electrospun fibres A) full heating cycles B) zoom on the glass transition.

Three thermal events can be observed. The glass transition is visible around -35°C, for both heating cycles. A small endotherm is present around 60°C in the first heating thermogram, but not in the second. An in-depth investigation about the nature of this peak is proposed in the following chapter. It is worth noting that the crystalline fraction represented by this peak is very small compared to the main melting endotherm (respective enthalpies of 3 and 52 J/g). Thus, it will not be considered in the calculations of total crystallinity. After cooling from the melt, the total crystallinity goes slightly down (from 50 to 44%). Moreover, the peak appears slimmer, which indicates a more uniform distribution of crystallites sizes, and melting temperature shifts to a higher temperature, going from 157 to 160°C.

The main use of DSC for this section was the calculation of the crystallinity ratio. Knowing that PVDF usually melts around 160°C, and given the large number of samples to be studied, calculations were made from single heating cycles from 50 to 200°C. It is worth noting that the thermograms of all samples look very similar, as visible in Figure 16. The calculated crystallinity ratios (χ_c) and the recorded melting temperatures (T_m) are given in Table 12.

Table 12: Calculated crystallinity ratio values and melting temperatures obtained from DSC analyses.

	χ_c (± 5%)	**T_m (± 1°C)**		**χ_c (± 5%)**	**T_m (± 1°C)**
ES15WT37DA 10_08_15	45	157	ES15WT46DA 10_08_15	44	158
ES15WT37DA 12_08_15	46	157	ES15WT46DA 12_08_15	47	158
ES15WT37DA 15_08_15	47	157	ES15WT46DA 15_08_15	48	158
ES15WT37DA 13_1_12	46	158	ES15WT46DA 13_1_12	47	157
ES15WT37DA 13_12_12	44	158	ES15WT46DA 13_12_12	45	158
	χ_c (± 5%)	**T_m (± 1°C)**		**χ_c (± 5%)**	**T_m (± 1°C)**
ES16WT37DA 10_08_15	49	156	ES16WT46DA 10_08_15	46	157
ES16WT37DA 12_08_15	47	157	ES16WT46DA 12_08_15	47	157
ES16WT37DA 15_08_15	47	157	ES16WT46DA 15_08_15	47	157
ES16WT37DA 13_1_12	49	159	ES16WT46DA 13_1_12	45	157
ES16WT37DA 13_12_12	47	157	ES16WT46DA 13_12_12	47	157

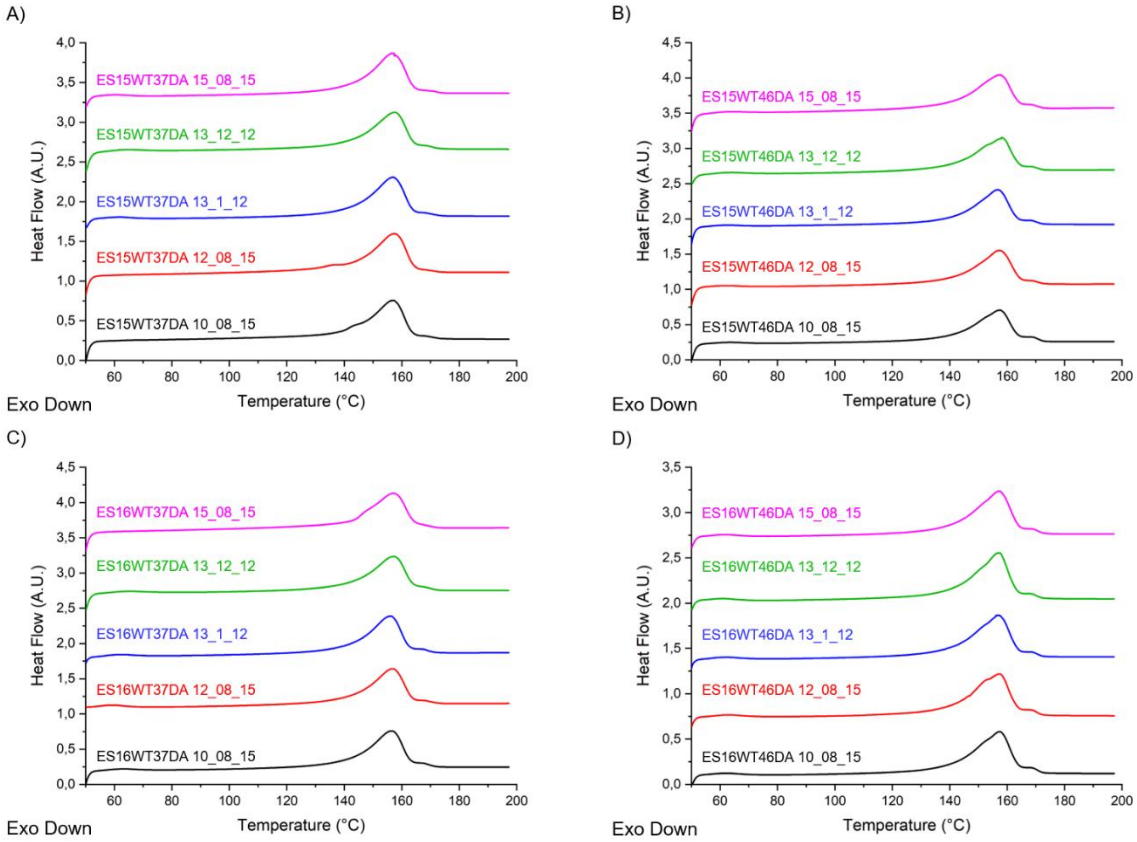

Figure 16: Thermograms of PVDF fibres elaborated with various electrospinning parameters: A) 15 wt.% PVDF – 3:7 D:A, B) 15 wt.% PVDF – 4:6 D:A, C) 16 wt.% PVDF – 3:7 D:A and D) 16 wt.% PVDF – 4:6 D:A.

Table 12 shows that as all samples melt around 158°C, and the calculated crystallinity ratio remains close to 46%. Hence, the variation of electrospinning parameters does not influence the thermal response of the material. The observed differences in melting temperatures and crystallinity ratio between samples is not significative, as it lies within the standard deviation observed in measurements from the same sample.

3.3. Crystallinity ratio from WAXS diffractograms

WAXS is one of the main characterisation technique to identify and quantify the different crystalline phases in polymer materials [155]. As mentioned in Chapter 2, due to the close values of planes belonging to different crystalline phases of PVDF, it is not possible to properly isolate the contributions from each phase. Then, it is preferable for WAXS be used to get a first idea of the phases present in the samples, as well as calculating the crystallinity ratio (see p.39).

The WAXS diffractograms of the different electrospun fibres is displayed in Figure 17. In order to standardise the spectra and make comparisons possible, the diffractograms are normalised by their total integrated intensity.

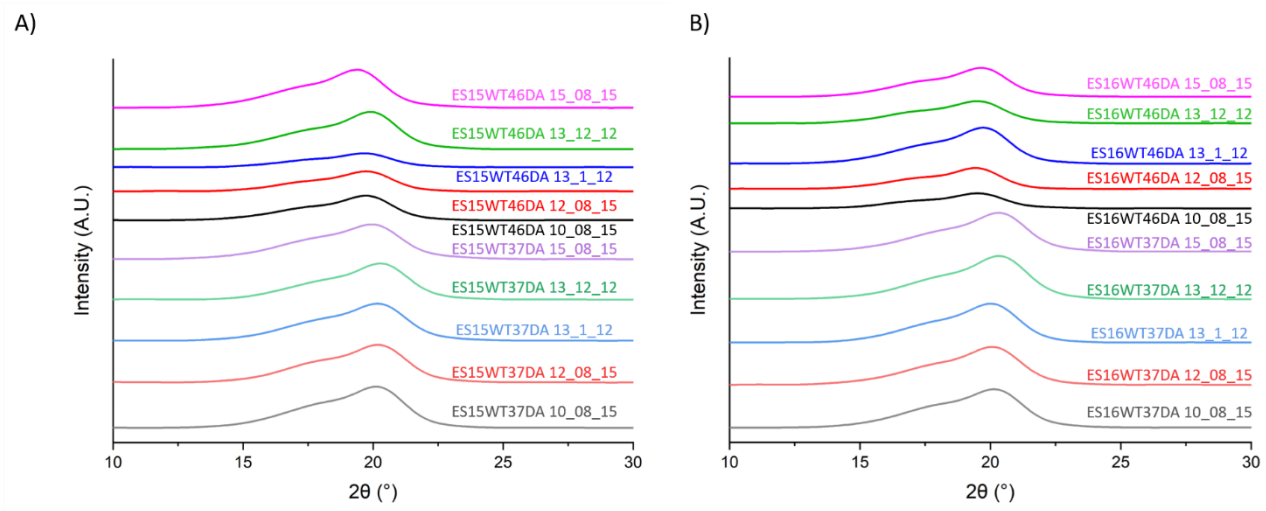

Figure 17: WAXS diffractograms of the electrospun fibres elaborated with: A) 15 wt.% PVDF and B) 16 wt.% PVDF in solution.

The diffractograms presented in Figure 17 show strong resemblance in shape. They are composed of a main band centred around 2θ = 20.50° that could represent either the (200) and (110) planes of the β phase, or the (110) and (101) planes of the γ phase, and a shoulder located around 2θ = 18.40° that may correspond to the (020) planes of the α or γ phases. The contribution of the β/γ band is visibly more important than the α/γ band, which demonstrates the high fraction of electroactive phases in the samples. The calculated crystallinity ratios from the diffractograms are presented in Table 13.

Table 13: Calculated crystallinity ratio values from WAXS diffractograms. (Introduce some evaluation of the precision on the values measured and calculated)

	χ_c (± 5%)		**χ_c (± 5%)**
ES15WT37DA 10_08_15	56	ES15WT46DA 10_08_15	57
ES15WT37DA 12_08_15	56	ES15WT46DA 12_08_15	57
ES15WT37DA 15_08_15	57	ES15WT46DA 15_08_15	56
ES15WT37DA 13_1_12	56	ES15WT46DA 13_1_12	56
ES15WT37DA 13_12_12	56	ES15WT46DA 13_12_12	56
	χ_c (± 5%)		**χ_c (± 5%)**
ES16WT37DA 10_08_15	57	ES16WT46DA 10_08_15	56
ES16WT37DA 12_08_15	57	ES16WT46DA 12_08_15	56
ES16WT37DA 15_08_15	57	ES16WT46DA 15_08_15	57
ES16WT37DA 13_1_12	57	ES16WT46DA 13_1_12	56
ES16WT37DA 13_12_12	57	ES16WT46DA 13_12_12	57

Table 13 shows that all samples present the same crystallinity ratio, to within 1% difference. The values of crystallinity ratio obtained from WAXS are different from the ones obtained from DSC, with a reproduced difference of 20%. It should be noted that the crystallinity ratio measured by DSC corresponds to a mass ratio, while the one obtained from WAXS is volumetric. The relation between the two values is given by:

$$\chi_m = \frac{\rho_c}{\rho_s}\,\chi_v$$

Where χ_m is the mass ratio, χ_v the volumetric ratio, ρ_c the density of the fully crystalline component, ρ_s the density of the sample.

From this relation one would expect the values of crystallinity ratio obtained from DSC to be higher than the ones obtained from WAXS. However, given the porous nature of electrospun mats, and experimental errors stemming from both characterisation techniques, the correlation is made more difficult.

From DSC analysis, χ_c was estimated to be close to 46% in average for all the samples, from WAXS it is closer to 57%. The difference between DSC and WAXS results is comparable to the difference previously highlighted between DSC and Raman spectroscopy results. However, the highlighted trend and conclusions are the same for both techniques: the different sets of parameters tested do not induce a change in the calculated crystallinity ratio from a sample to another.

3.4. Phase identification, crystallinity ratio and phase fraction from Raman spectra

As previously stated, Raman spectroscopy has proven to be a powerful tool, combining the possibilities of phase identification, determination of the crystallinity ratio, and determination of the phase fraction of the three main crystalline phases of PVDF, namely α, β and γ. Figure 18 presents the Raman spectra of the different electrospun fibres samples.

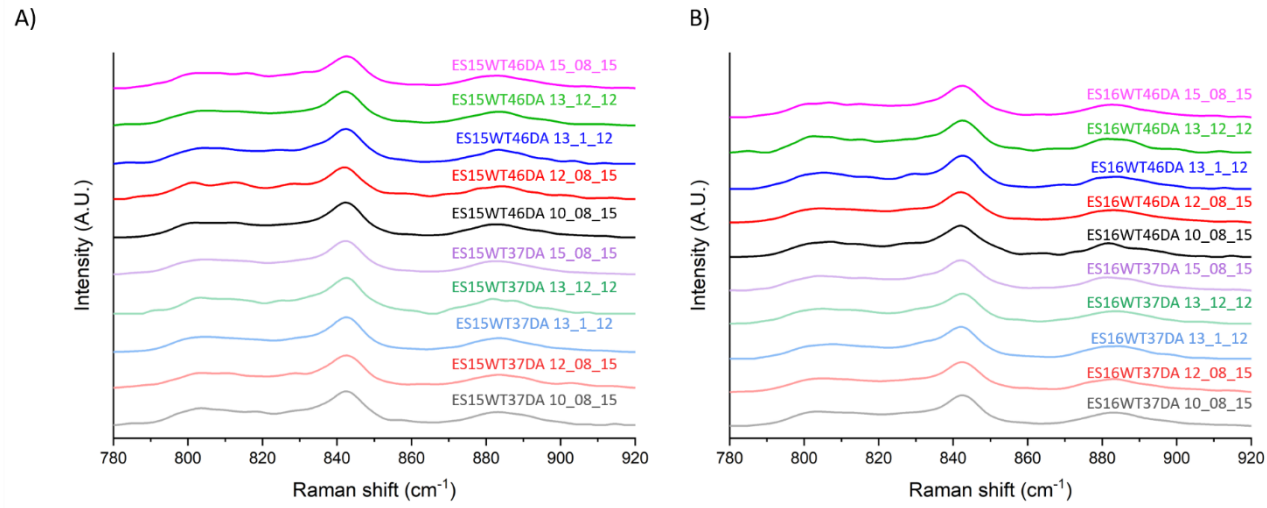

Figure 18: Raman spectra of the electrospun fibres elaborated with: A) 15 wt.% PVDF and B) 16 wt.% PVDF in solution.

The most prominent band located at 840 cm^{-1} is associated to CH_2 rocking and CF_2 antisymmetric stretching. It is the band representative of the β phase, which demonstrates a high fraction of this phase in the samples. The band at 881 cm^{-1} is associated with CF_2 symmetric stretching, CH_2 in phase twisting and CC out of phase symmetric stretching. This band cannot be attributed to a specific crystalline band, but is important for the crystallinity ratio calculations. The deconvolution allows to highlight the contribution of the γ phase with the presence of two bands: the one at 813 cm^{-1} is associated to CH_2 out of plane wag, and the second is located at 830 cm^{-1}. A small amount of α phase is also probable dur to the presence a shoulder around 875 cm^{-1}. Calculations of the crystallinity ratio and crystalline phase fractions were performed following the method detailed previously. The results are compiled in

Table 14.

Table 14: Calculated crystallinity ratio and crystalline phase fractions values from Raman spectra.

	χ_c (%)	α (%)	β (%)	γ (%)
ES15WT37DA 10_08_15	51	3	68	29
ES15WT37DA 12_08_15	51	2	72	26
ES15WT37DA 15_08_15	51	2	68	30
ES15WT37DA 13_1_12	52	2	75	23
ES15WT37DA 13_12_12	53	3	67	30
	χ_c (%)	**α (%)**	**β (%)**	**γ (%)**
ES15WT46DA 10_08_15	53	2	69	29
ES15WT46DA 12_08_15	52	3	64	34
ES15WT46DA 15_08_15	51	2	67	31
ES15WT46DA 13_1_12	53	2	73	26
ES15WT46DA 13_12_12	52	2	69	30
	χ_c (%)	**α (%)**	**β (%)**	**γ (%)**
ES16WT37DA 10_08_15	52	3	68	29
ES16WT37DA 12_08_15	52	1	73	25
ES16WT37DA 15_08_15	51	4	65	31
ES16WT37DA 13_1_12	52	2	70	28
ES16WT37DA 13_12_12	51	2	62	36
	χ_c (%)	**α (%)**	**β (%)**	**γ (%)**
ES16WT46DA 10_08_15	52	4	70	27
ES16WT46DA 12_08_15	52	2	71	28
ES16WT46DA 15_08_15	52	3	69	28
ES16WT46DA 13_1_12	52	2	74	24
ES16WT46DA 13_12_12	52	3	65	32

In agreement with the calculations from the previous techniques, the crystallinity ratios remain almost unchanged across all samples, with an average value of 52%. The calculated fraction of α phase is also very low in all samples, remaining under 5%, with a value of 2% in average. The proportion of β and γ is roughly 70 and 30% respectively, although some trends can be highlighted.

Generally speaking, the samples elaborated with the process parameters of AV=13 kV, FR=1mL/h and TCD=12cm (13_1_12) display the higher β phase fraction (73% in average), the highest achieved value being 75% with the ES15WT37DA 13_1_12 sample. Samples elaborated with AC=12 kV, FR=0,8mL/h and TCD=15 (12_08_15) also give very good β fraction (70% in average). The samples elaborated AV=13 kV, FR=1.2mL/h and TCD=12cm (13_12_12) have the lowest β phase fraction (66%).

It has been documented that, with higher flow rate, the fibre diameter tends to increase, with sometimes beads formation, and simultaneously the β phase fraction is reduced [60,64,78,189]. The use of the lowest and highest applied voltage, 10 kV and 15kV also seems to reduce the β phase fraction. Usually, the β phase fraction increases with the applied voltage, but excessive applied voltage causes the apparition of beading and breakage of the fibres, thus impacting negatively the β phase formation [64,78,80,132,187].

Overall, the best sample in terms of electroactive and especially β phase fractions is the ES15WT37DA 13_1_12 sample. As the first tests of fillers addition appeared successful (production of a mat without much needle clogging, satisfactory mechanical behaviour when handled by hand), this set of parameters was selected for the production of the composite fibres with addition of cellulose nanocrystals or Al-Cu-Fe-B quasicrystals.

Maximising the β phase fraction, the most electroactive phase of PVDF, is essential to ensure the best electric performances of the devices fabricated from the electrospun fibres, and make them suitable for sensor and energy harvesting applications.

3.5. Additional characterisation from optical microscopy

In parallel of the study focused on the semi-crystalline microstructure of the materials, optical microscopy studies were performed to look at the shape of the fibres elaborated by electrospinning. A non-optimal choice of process parameters can lead to the apparition of several structural defects such as beading, or apparition of flat areas, heterogeneous matter distribution (alternation porous and dense areas) or heterogeneities in the fibres diameter distribution [190]. Some optical micrographs of electrospun scaffolds are given in Figure 19.

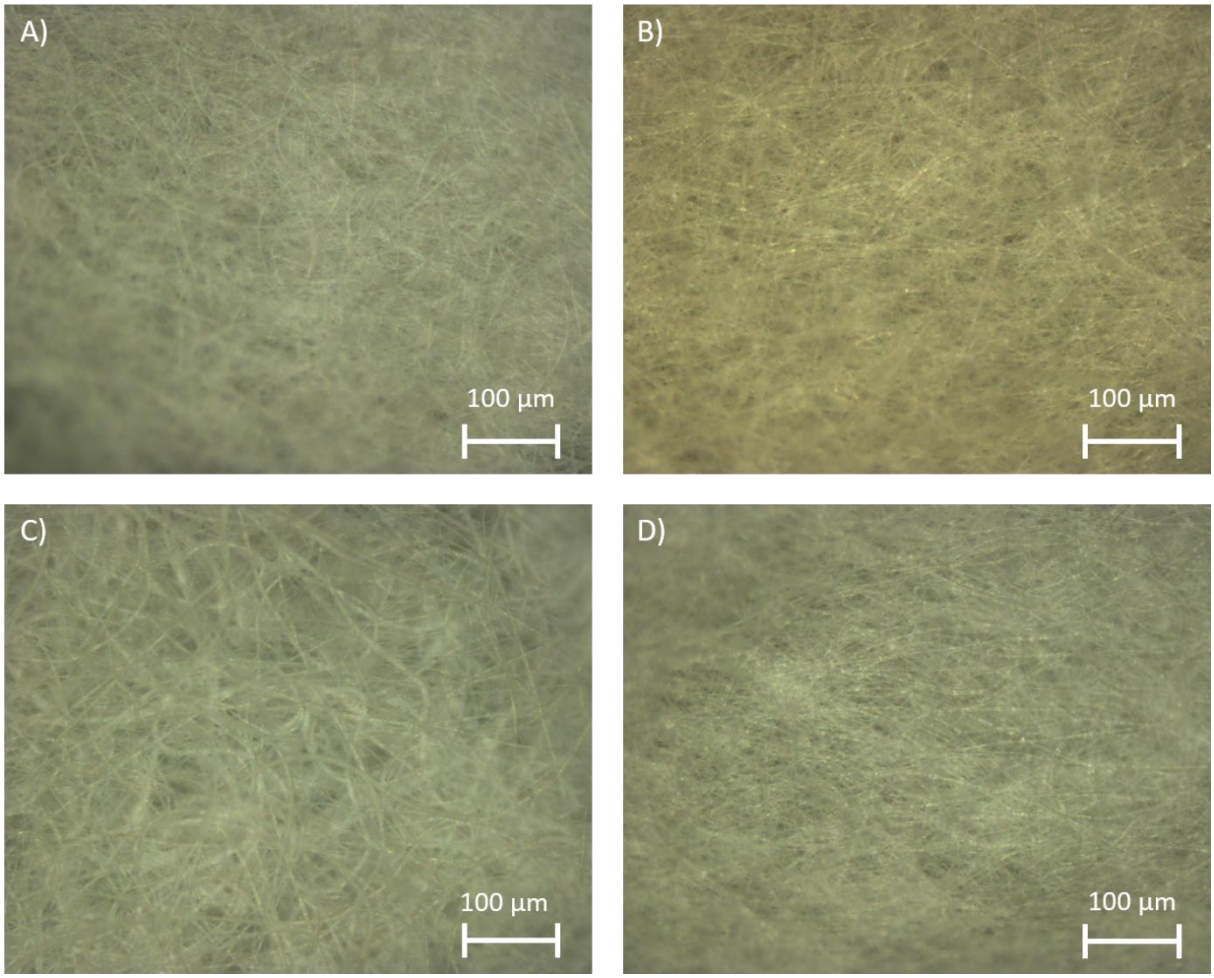

Figure 19: Optical micrographs of some electrospun fibres, A) ES15WT46DA 12_08_15, B) ES15WT37DA 13_1_12, C) ES16WT46DA 12_08_15 and D) ES16WT37DA 12_08_15.

From optical microscopy, most of the fibre scaffolds obtained with process parameters AV=13 kV, FR=1 mL/h and TCD=12cm (13_1_12) and AV=12 kV, FR=0,8 mL/h and TCD=15 cm (12_08_15) appear rather thin and uniform, like in the picture presented in Figure 19.

However, some parameter sets produced fibres with very visible defects. The most striking example is given by fibres produced with a flow rate of 1.2 mL/h (the highest tested value). As visible in Figure 20, very thick fibres can be observed, along with numerous beads. The important number of defects can explain the lowest β phase fraction of these fibres. Defects are regions where the materials are much less stretched compared to the usual thin fibres, and stretching is one of the main parameters that allow beta phase formation.

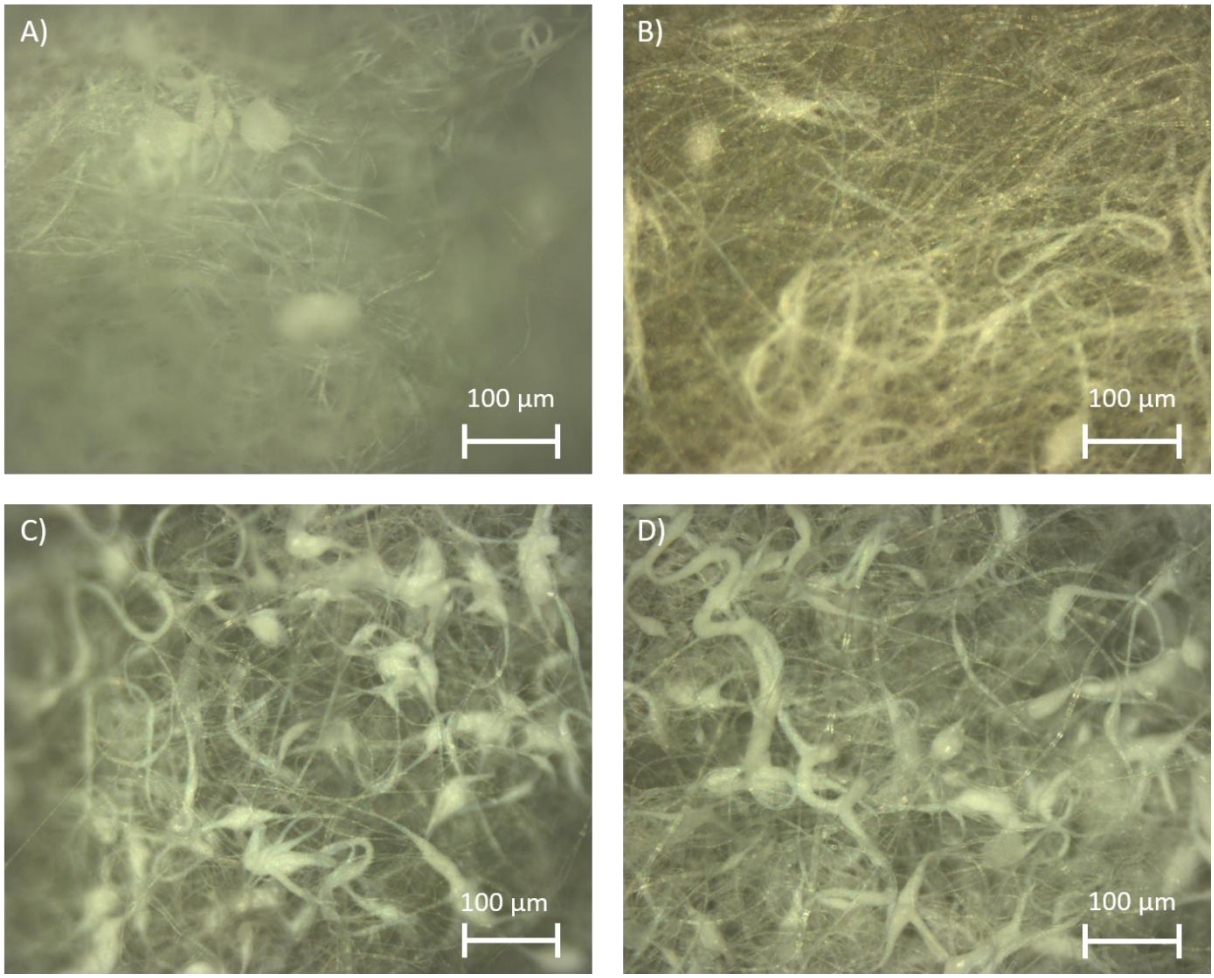

Figure 20: Fibres elaborated with a FR of 1.2 mL/h: A) ES15WT46DA 13_12_12, B) ES15WT37DA 13_12_12, C) and D) ES16WT37DA 13_12_12 .

The same kind of defects, although less prominent, have been observed in fibres elaborated with 10 or 15 kV of applied voltage, which is also in line with the Raman results (see next paragraph). Some examples are provided in Figure 21.

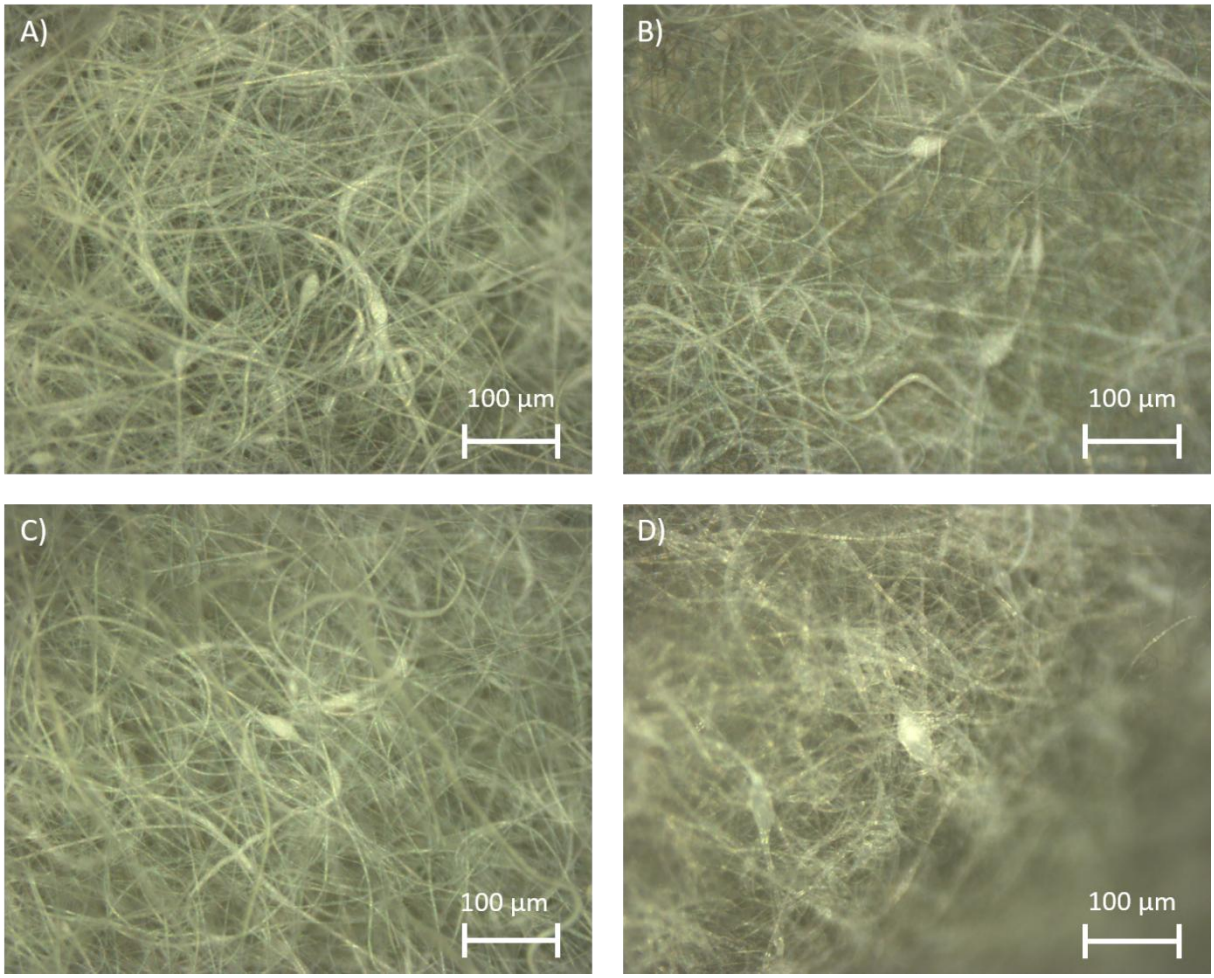

Figure 21: Fibres elaborated with an AP of 10 or 15 kV: A) ES15WT46DA 10_08_15, B) ES15WT46DA 15_08_15, C) ES16WT46DA 10_08_15 and D) ES16WT37DA 10_08_15.

Further discussion regarding the surface topology of the fibres is provided in Chapter 4, using micrographs obtaining by scanning electron microscopy.

4. Raman study of local crystallinity ratio and phase fraction within a sample

As highlighted by the presented micrographs, electrospun samples can present variations of fibre diameter, and defects. To investigate the impact of these defects on the fibre crystallinity, and ultimately the possible electric performances of the fibre mat, local Raman studies were conducted on a LabRAM HR from Horiba. The coupling with a confocal microscope allows precise localisation of the analysed part of the sample. The analyses were performed on three samples: ES15WT37DA 10_08_15, ES16WT46DA 10_08_15 and ES16WT37DA 10_08_15. Images (in the visible range with a dedicated camera) of the fibres taken before the Raman spectra acquisition are provided in Figure 22.

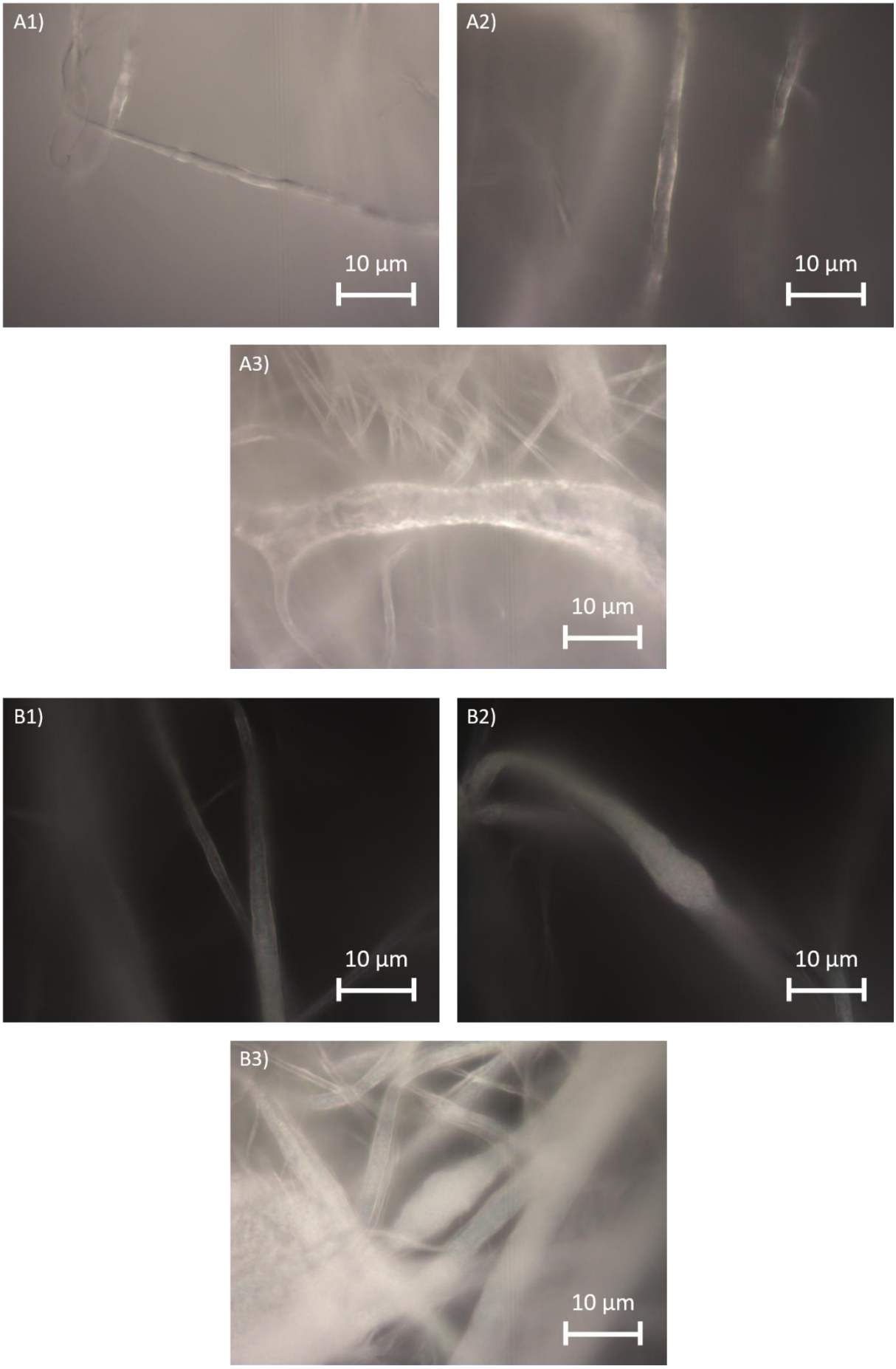
A1)
10 µm
A2)
10 µm
A3)
10 µm
B1)
10 µm
B2)
10 µm
B3)
10 µm

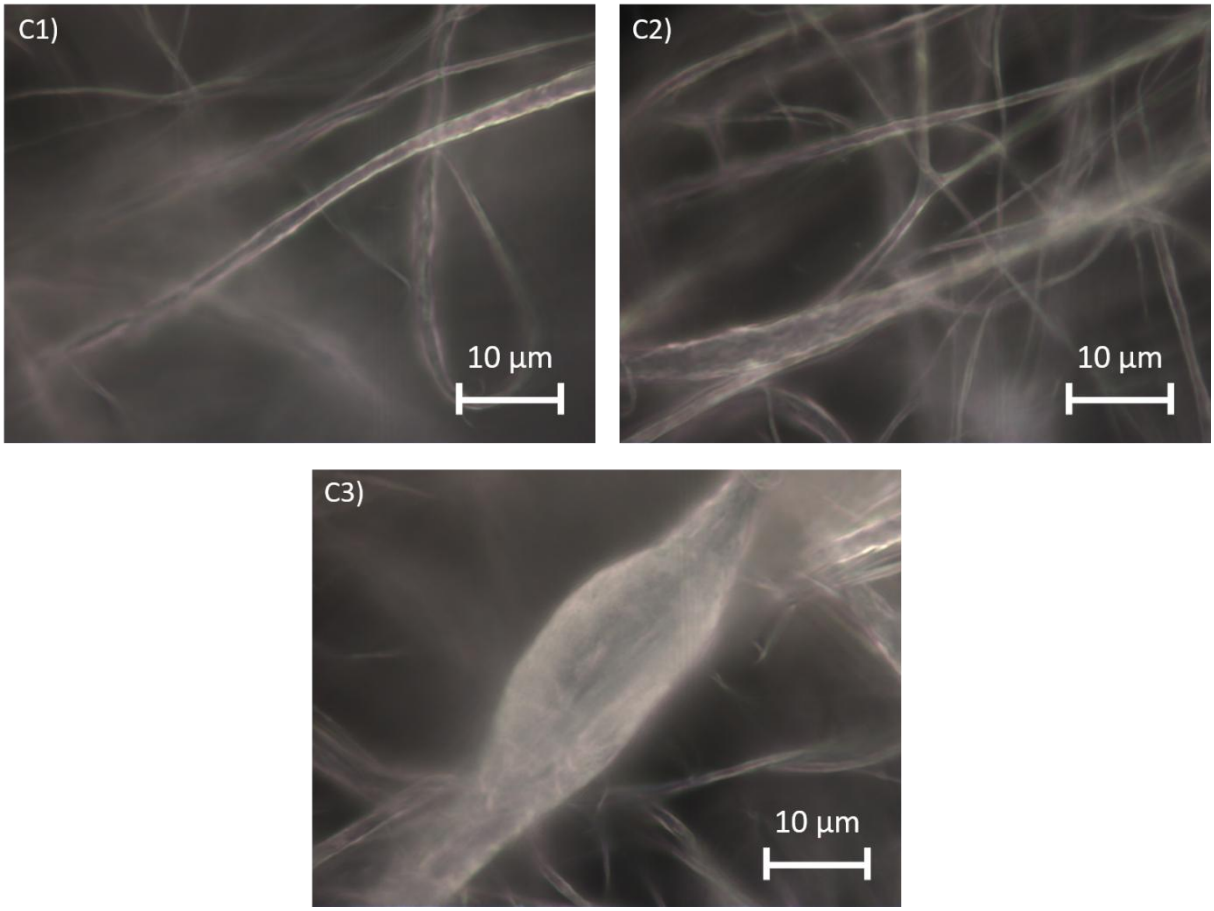

Figure 22: Visible camera observation of where the Local Raman characterisation of the electrospun fibres were conducted: A1), A2) and A3 ES15WT37DA 10_08_15, B1), B2) and B3 are from ES16WT46DA 10_08_15, C1), C2) and C3) are from ES16WT37DA 10_08_15.

For each sample, three types of fibres have been selected: 1) a "thin" fibre, 2) a "thicker" fibre, and 3) an agglomerate or bead. The results of crystallinity ratio and crystalline phase fractions obtained from the Raman spectra are summarised in Table 15.

Table 15: Crystallinity ratio and crystalline phase fractions from local Raman characterisation.

ES15WT37DA 10_08_15				
Corresponding image	χ_c (%)	α (%)	β (%)	γ (%)
A1	46	5	72	23
A2	43	7	71	22
A3	45	6	66	28
ES16WT46DA 10_08_15				
Corresponding image	χ_c (%)	α (%)	β (%)	γ (%)
B1	46	5	78	17
B2	45	7	67	26
B3	45	6	54	40
ES16WT37DA 10_08_15				
Corresponding image	χ_c (%)	α (%)	β (%)	γ (%)
C1	43	7	82	12
C2	46	7	73	20
C3	42	8	65	27

Like in the case of “bulk” Raman characterisation on fibre scaffolds, the crystallinity ratio and α phase content remain very similar for all fibres. Nevertheless, the differences in β/γ phase ratio can vary drastically from one fibre to another within the same sample. The most striking example is given by the ES16WT46DA 10_08_15, where the β phase fraction goes down from 78 to 54%, while the γ phase fraction goes up from 17 to 40%. These results clearly demonstrate the impact large and numerous defects can have on the β/γ phases fractions. Indeed, the presence of defects imply a reduced stretching effect applied to the fibre during the electrospinning process. As stretching is the main governing factor of β phase formation, the result is a reduced β fraction. It also explains why a sample like ES15WT37DA 13_1_12, which appears to contain a low amount of beads or fused fibres from optical microscopy and SEM imaging, would present one of the highest β phase fraction.

5. Study of the electrospun nanocomposites: effect of the filler addition on the fibre crystallinity

In addition to the optimisation of electrospinning parameters, various properties of the produced fibres can be tuned with the addition of fillers. The addition of cellulose in PVDF films and fibres is expected to enhance the β phase fraction, due to the presence of hydroxyl groups able to form hydrogen bonds with the fluorine atoms of PVDF, that might promote the β phase formation. Improvement of the tensile strength is also reported [37,101–106]. Nevertheless, a study from Bai *et al.* (2012) found that, in electrospun fibres, the electrospinning process is the main promotor of β phase, with little contribution of the added cellulose [191]. In the case of Al-Cu-Fe-B quasicrystals addition in PVDF, very few studies can be found. Two articles published by Venkatesh *et al*. highlight the role of quasicrystals addition in obtaining composites with a very high dielectric constant 50[166,167].

Overall, the best sample in terms of electroactive and especially β phase fractions is the ES15WT37DA 13_1_12 sample. As the first tests of fillers addition appeared successful (production of a mat without much needle clogging, satisfactory mechanical behaviour when handled by hand), this set of parameters was selected for the production of the composite fibres with addition of cellulose nanocrystals or Al-Cu-Fe-B quasicrystals.

Hence, composite electrospun fibres with addition of 1 to 5wt% of cellulose nanocrystals (CNC) or Al-Cu-Fe-B quasicrystals (QC) were elaborated to study the impact of fillers addition on the crystallinity of the PVDF fibres, using the same routine previously described for the characterisation of pristine PVDF fibres. The samples bear the name of the filler used followed by the weight fraction value, i.e. CNC1 is the name of the fibres elaborated with addition of 1wt% CNC. The pristine fibres without filler addition are noted PVDF.

5.1. Phase identification and qualitative analysis from FTIR spectra

The FTIR spectra of the fibres elaborated with the addition of CNC or QC filler are presented in Figure 23. For comparison purposes, all presented Raman spectra are normalised by total intensity.

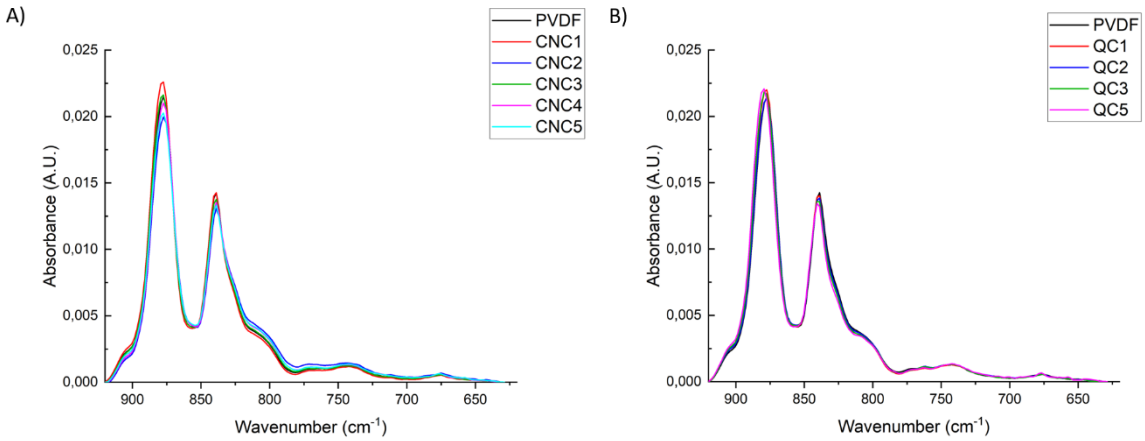

Figure 23 : FTIR spectra of: A) CNC and B) QC composite fibres.

All spectra look almost identical to the one of the pristine PVDF fibres. As previously described, the spectra present a very intense band at 840 cm^{-1}, which is representative of β phase, and a shoulder located around 830 cm^{-1} which is representative of the γ phase. The presence of α phase in the samples is also demonstrated by the shoulder visible around 800 cm^{-1}. As the intensities of the three mentioned bands are almost equal for all samples, it appears that the addition of both filler types has little impact on the materials crystallinity and repartition of the crystalline phase fractions. However, this means that the composite fibres should present a very high proportion of electroactive phases, with a majority of β phase, like the pristine fibres.

5.2. Crystallinity ratio from DSC thermograms

Similarly to the previous DSC study on pristine fibres, calculations were made from heating cycles from 50 to 200°C. Once again, the thermograms of all samples look alike, as visible in Figure 24. The calculated crystallinity ratio (χ_c) and measured melting temperature (T_m) are given in Table 16.

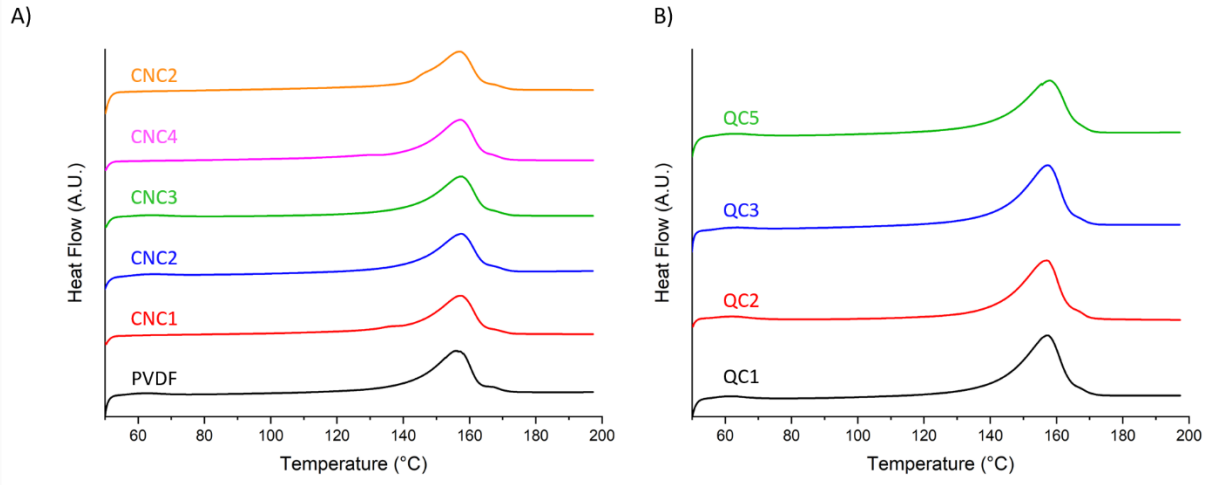

Figure 24: DSC thermograms of the fibres composite with addition of A) CNC and B) QC.

Table 16: Calculation of the crystallinity ratio of the fibres with addition of CNC and QC.

	χ_c (± 5%)	T_m (± 1°C)		χ_c (± 5%)	T_m (± 1°C)
PVDF	49	156			
CNC1	45	157	QC1	48	157
CNC2	46	157	QC2	46	157
CNC3	47	157	QC3	47	157
CNC4	46	157			
CNC5	46	156	QC5	47	157

Like what was observed with the variation of electrospinning parameters (see p. 57), the addition of fillers does not influence the thermal response of the material, as all samples melt around 157°C. Moreover, the calculated crystallinity ratio remains close to 47%. The difference between samples is not significative, as it lies within the standard deviation of the DSC instrument (±5%).

5.3. Phase identification and crystallinity ratio from WAXS diffractograms

The WAXS diffractograms of all the composite samples are presented in Figure 25.

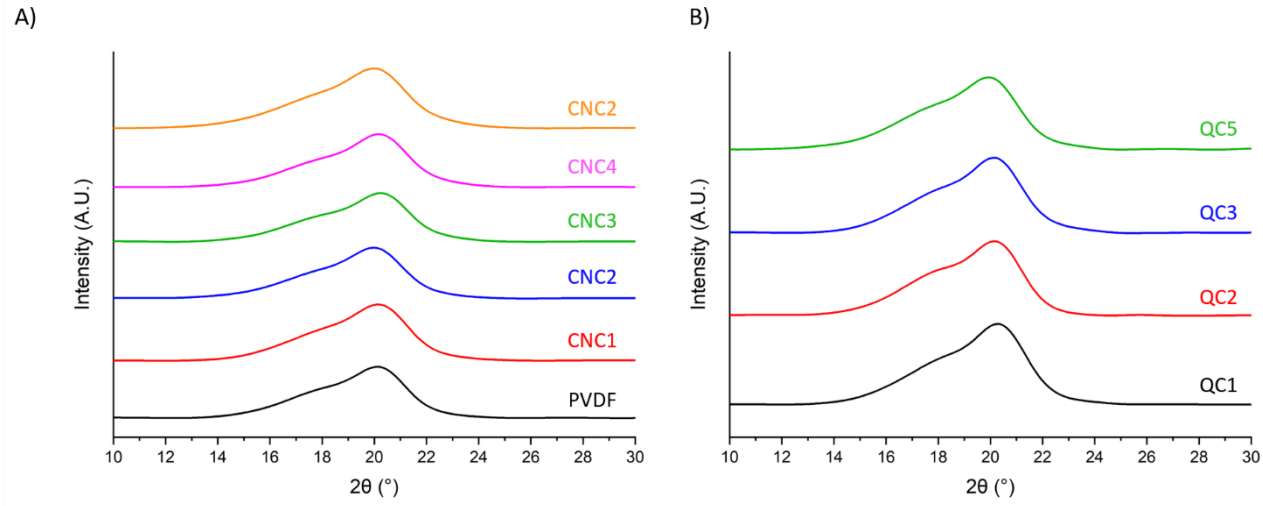

Figure 25: WAXS diffractograms of the composite fibres with A) CNC and B) QC addition.

In the case of composite fibres, two bands are observed. As described for pristine fibres (see p.59), the main band centred around 2θ=20.50° represents either the (200) and (110) planes of the β phase, or the (110) and (101) planes of the γ phase. The shoulder located around 2θ=18.40° corresponds to the (020) planes of the α or γ phases. The contribution of the β/γ band is visibly more important than the α/γ band, which shows once again the high fraction of electroactive phases in all the samples, as they present almost identical diffractograms. Following the same deconvolution method previously detailed, the calculated values of crystallinity ratio from WAXS diffractograms were calculated for the composite fibres. The results are presented in

Table 17.

Table 17: Crystallinity ratios of the composite fibres with CNC and QC addition calculated from WAXS diffractograms.

	χ_c (± 5%)		χ_c (± 5%)
PVDF	57		
CNC1	57	QC1	57
CNC2	56	QC2	56
CNC3	57	QC3	57
CNC4	56		
CNC5	57	QC5	56

The values of crystallinity ratio obtained from WAXS are different from the ones obtained from DSC, with a difference of 20%. From DSC analysis, χ_c was estimated to be close to 47% in average for all the samples, from WAXS it is closer to 57%. However, the conclusion of the analyses remains the same: the crystallinity of all composites is almost similar to that of the pristine fibres.

5.4. Phase identification, crystallinity ratio and phase fraction obtained from Raman spectra

The Raman spectra of all the composite samples are presented Figure 26.

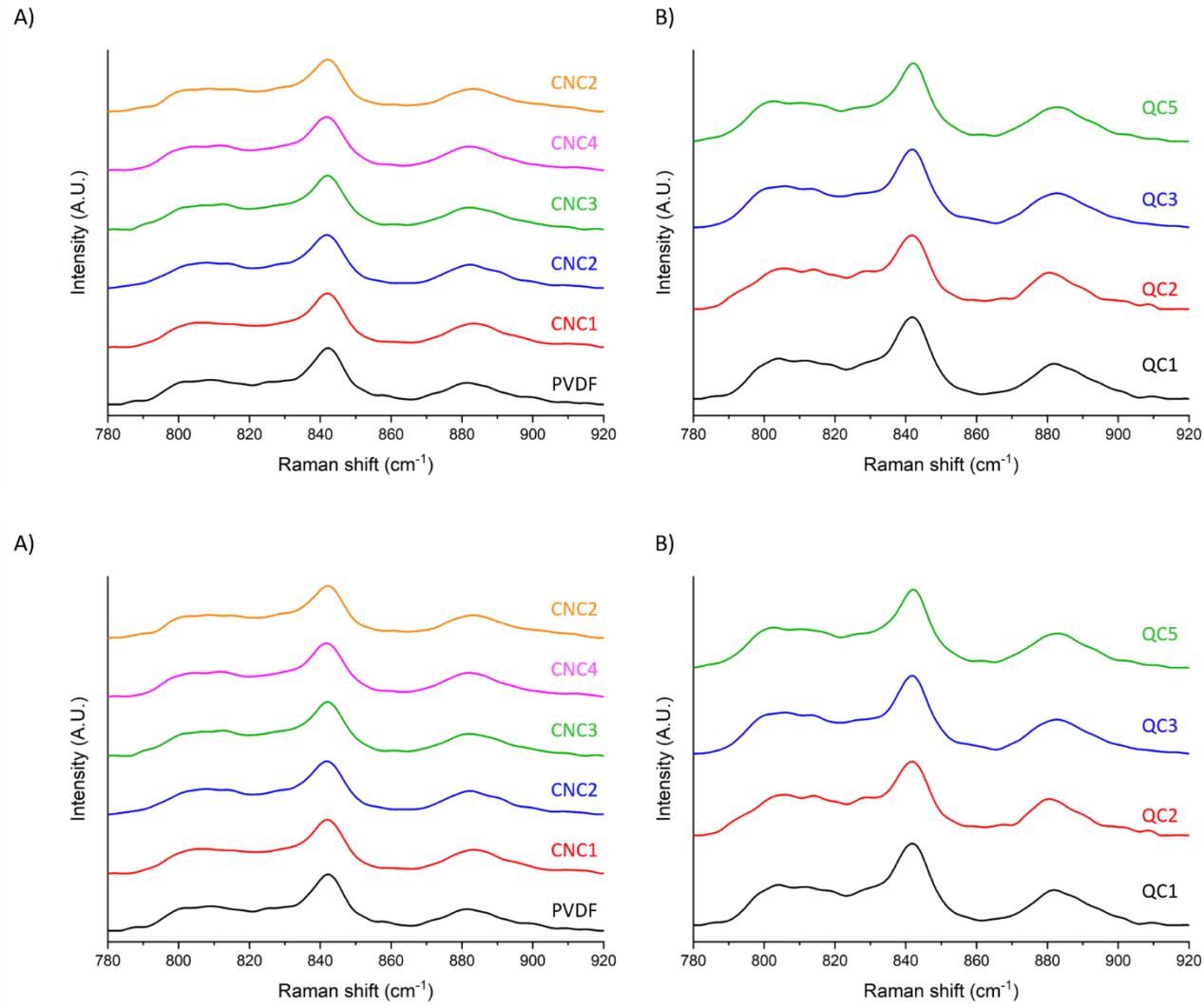

Figure 26: Raman spectra of the composite fibres with A) CNC and B) QC addition.

The composite fibres show spectra very similar to the ones of pristine fibres. The most prominent band located at 840 cm^{-1}, representative of the β phase, demonstrates a high fraction of this phase in the samples. The band at 881 cm^{-1} cannot be attributed to a specific crystalline phase, but is necessary for the crystallinity ratio calculations. The deconvolution allows to see the contribution of the γ phase with the presence of two bands: one at 813 cm^{-1} and one at 830 cm^{-1}. A small amount of α phase is also probable due to the presence a shoulder around 875 cm^{-1}. After the deconvolution, the crystalline ratio and crystalline phase fraction are calculated, and the results are compiled in Table 18.

Table 18: Crystallinity ratio and crystalline phase fractions from Raman characterisation of the composite fibres.

	χ_c (± 3%)	**α (±2%)**	**β (±5%)**	**γ (±5%)**
PVDF	51	4	71	25
CNC1	52	3	68	28
CNC2	51	3	70	27
CNC3	51	3	66	32
CNC4	52	3	66	31
CNC5	50	3	72	26
	χ_c (± 3%)	**α (±2%)**	**β (±5%)**	**γ (±5%)**
QC1	52	3	68	29
QC2	51	3	66	31
QC3	52	3	66	31
QC5	50	4	65	31

Very akin to what was observed in calculations from the previous techniques, the crystallinity ratios remain almost unchanged across all samples, with an average value of 51%. The calculated fraction of α phase is also very low in all samples, remaining under 5%, with a value 3% in average. The proportion of β and γ is roughly 70 and 30% respectively. If the composite fibres tend to have a slightly lower β/γ ratio compared to the pristine fibres, no trend can be highlighted with the increase of the filler content.

6. Conclusion

A routine characterisation allowing to put in perspective crystallinity ratio results from DSC, WAXS, FTIR and Raman spectroscopy is detailed. A new Raman criterion for the quantification of the crystalline phases fraction of the three main crystalline phases of PVDF is proposed. In this proposal, the fit of the amorphous contribution of the Raman spectra is realised using a reduced number of Gaussian curves possessing a physical identification reported in the literature.

This routine is first applied on pristine electrospun PVDF fibres to test the influence of various parameters on the electrospinning result: the PVDF weight percentage in solution, the solvent ratio, the applied voltage (AV), the flow rate (FR) and the tip-to-collector distance (TCD). The results from all characterisation techniques show that the crystallinity ratio of the sample is very little influenced by these parameters compared to the electrospinning stretching itself which is the main parameter coming from this original process.

If the calculated crystalline phase fractions using the Raman criterion give a very low amount of α phase in the fibres (lower than 5%), and a proportion of β and γ of roughly 70 and 30% respectively, some differences have been observed among the samples. The ES15WT37DA 13_1_12 sample present 75% of β phase fraction, which is the highest observed value among the tested samples, hence why the associated set of parameters (15wt% PVDF, 3:7 DMF:Acetone ratio, AV=13 kV, FR=1mL/h and TCD=12cm) was selected for the elaboration of the composite fibres. On the contrary, sample elaborated with the highest flow rate present the lowest amount of β phase (66%). The use of the lowest and highest applied voltage, 10 kV and 15kV also seems to reduce the β phase fraction. The

presence of a higher number of important defects within the fibres, like beading, electrospraying or fibre agglomeration, observed in optical microscopy, illustrates the relation between defects and reduced electroactive phase formation. Moreover, a localised Raman study on single fibres showed that within the same sample, fibres that present defects also present a visibly reduced β phase fraction compared to the expected thin, homogeneous fibres.

The addition of 1 to 5 wt.% of cellulose nanocrystals (CNC) and Al-Cu-Fe-B (QC) was expected to improve the formation of β phase in the fibres. However, all techniques showed that the crystallinity ratio which is already very high by the electrospinning process does not increase significantly compared to the pristine fibres when fillers are added. From Raman spectroscopy studies, it even seems that the addition of the fillers slightly reduces the β phase fraction (from 71 to 66% approximately). Nonetheless, no clear trend has been observed concerning the impact of the increase of the filler addition on the crystallinity ratio of fibres.

Chapter 4: Brillouin spectroscopy studies on single electrospun PVDF fibres

1. Introduction

The semi-crystalline microstructural characterisation of the electrospun PVDF-based fibres gives a precious overview of the potential electroactive performances of devices made of these materials. However, in order to guarantee all their properties in use, some mechanical strength and resistance to mechanical solicitations is also required. It is generally admitted that the elastic modulus, which is dependent on the formulation and microstructure of the samples, is a valuable data to monitor the mechanical properties of materials. Yet, usual mechanical techniques are difficult to implement in the case of electrospun scaffolds, as the randomly oriented fibres composing the mat are torn apart by tests involving stretching, like in the case of tensile test.

Hence, the use of a non-contact characterisation technique was privileged. Brillouin spectroscopy is a light-scattering technique used to determine the variation of the elastic modulus in transparent materials. The use of micro-Brillouin, or Brillouin spectroscopy coupled with an optical microscope, has already been seen in studies of fibrous materials like collagen [194], spider silk [195,196], silk fibroin [197] and cellulose [198]. Nevertheless, to the best of our knowledge the study presented in this chapter constitutes the first micro-Brillouin spectroscopy study on electrospun PVDF fibres.

Micro-Brillouin spectroscopy at room temperature allowed us to investigate the difference that the DMF:Acetone ratio can make on the elastic response of electrospun fibres. This result demonstrates the suitability and efficiency of the Brillouin spectroscopy, as none of the characterisation techniques previously employed to investigate the semi-crystalline microstructure of the fibres could allow to find differences between fibres based on the solvents ratios employed. Moreover, a study was performed on nanocomposites fibres to investigate how fillers addition could impact the mechanical properties of the fibres. Finally, by studying the evolution of mechanical properties of the fibres as a function of temperature, an unexpected elastic behaviour is observed and discussed.

2. Pristine PVDF nanofibres with different proportions of acetone and DMF solvents

For this section, the study focused on the electrospun fibres obtained from the two types of polymeric solutions with different DMF:Acetone (D:A) ratio, and different electrospinning process parameters. Variations of the applied voltage (AV), flow rate (FR) and tip-to-collector distance (TCD) were made to study the influence of said parameters on the nanofibres produced, as mentioned in Chapter 3 (see p.55). Fibres grouped under the Type A denomination were obtained using a 3:7 DMF:Acetone solvent ratio, while Type B fibres were obtained using a 4:6 solvent ratio. A recap of the samples names and associated parameters is provided in Table 19.

Table 19: Electrospinning parameters for the elaboration of the PVDF fibres.

	Material	Solution parameters	Electrospinning parameters
Type A	ES15WT37DA 10_08_15	150g/L PVDF in 10mL 3:7 D:A	AV: 10kV, FR: 0.8 mL/h, TCD: 15cm
	ES15WT37DA 13_1_12	150g/L PVDF in 10mL 3:7 D:A	AV: 13kV, FR: 1 mL/h, TCD: 12cm
	ES16WT37DA 10_08_15	160g/L PVDF in 10mL 3:7 D:A	AV: 10kV, FR: 0.8 mL/h, TCD: 15cm
	ES16WT37DA 13_1_12	160g/L PVDF in 10mL 3:7 D:A	AV: 13kV, FR: 1 mL/h, TCD: 12cm
Type B	ES15WT46DA 10_08_15	150g/L PVDF in 10mL 4:6 D:A	AV: 10kV, FR: 0.8 mL/h, TCD: 15cm
	ES15WT46DA 13_1_12	150g/L PVDF in 10mL 4:6 D:A	AV: 13kV, FR: 1 mL/h, TCD: 12cm
	ES16WT46DA 10_08_15	160g/L PVDF in 10mL 4:6 D:A	AV: 10kV, FR: 0.8 mL/h, TCD: 15cm
	ES15WT46DA 13_1_12	160g/L PVDF in 10mL 4:6 D:A	AV: 13kV, FR: 1 mL/h, TCD: 12cm

Representative optical micrographs of both fibre types are presented in Figure 27.

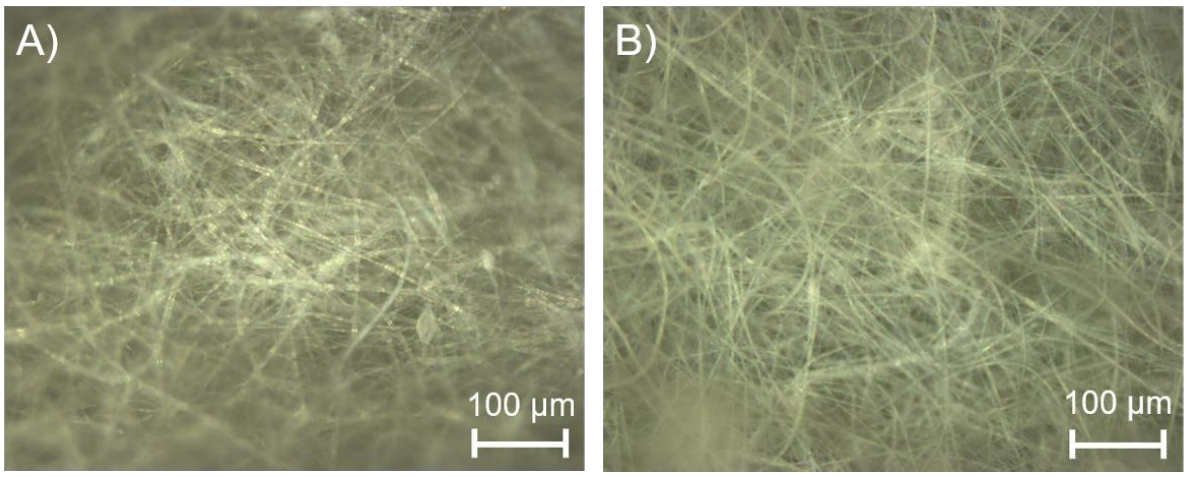

Figure 27: Optical micrographs of A) Type A fibres and B) Type B fibres.

This section is focused on the study of electrospun fibres obtained from the two types of polymeric solutions with different DMF:Acetone (D:A) ratios, and different electrospinning process parameters (see Table 19 for the parameters details of each type of fibres).

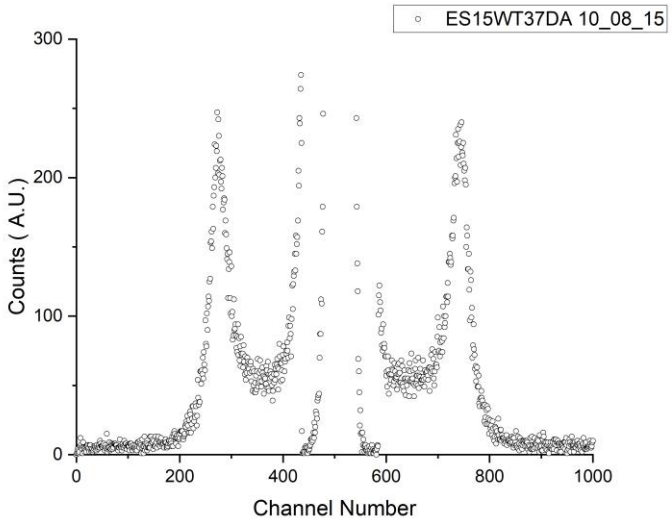

Figure 28: Typical Brillouin spectrum of Type A fibres.

As shown in Figure 28, Type A fibres showed very well resolved peaks. This was the case for the four tested samples of Type A. For better accuracy, Counts vs Channel number graphs were used to determine the position in channel number of the peaks on each side of the Rayleigh scattering central peak, then converted into acoustic phonon frequencies. Fitting of the peaks was performed by creating a "Poly Voigt" fit function which is a mix of a pseudo-Voigt function with a polynomial function of the 3rd order. An example of a typical Type A Brillouin spectrum after fitting using this function is presented in Figure 29.

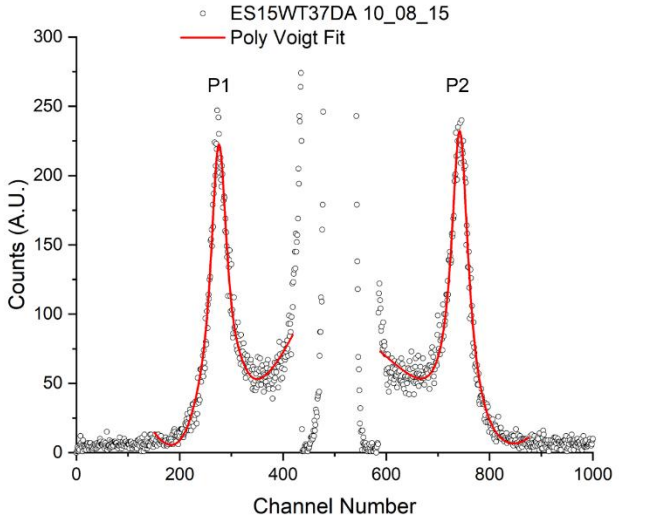

Figure 29: Example of fit on the Type A fibre spectrum.

Once an optimized fit of the peaks is obtained, the peak frequencies are retrieved using the following Equation 18:

$$F = \frac{P2 - P1}{2} * SA * calibration\ coeff$$

Equation 18

with P1 and P2 being the peak position in channel number (as shown in Figure 29), SA the scanning amplitude in nanometres, and the calibration coefficient being in GHz/canal/nm.

The Brillouin peak frequency have then been translated into the corresponding elastic constant value. The c_{11} constant is obtained from the peak frequency using the following Equation 19:

$$c_{11} = \rho\, v^2 = \rho \left(\frac{\lambda_0 f}{2n}\right)^2$$

Equation 19

with n=1.42 [199], λ_0= 532x10^{-9} nm and ρ=1.78g/cm^3 [200].

The elastic constant determined on electrospun fibres is necessarily c_{11}, as the measurement is conducted perpendicularly to the longitudinal direction of the fibre.

After fitting the spectra of the different Type A samples, calculations gave a peak frequency falling around 12.5GHz in average, which corresponds to an average c_{11} value of 9.8 GPa. The measurement results for the four tested samples in given in Table 20.

Table 20: Calculated peak frequencies and corresponding c_{11} values for Type A fibres.

Material	**ES15WT37DA 10_08_15**	**ES15WT37DA 13_1_12**	**ES16WT37DA 10_08_15**	**ES16WT37DA 13_1_12 01**
Frequency (GHz)	12.7	12.4	12.4	12.6
c_{11} (GPa)	10.1	9.7	9.6	9.9

It is important to note that a dispersion in the obtained values exist among the different fibres from the same sample. A complementary test campaign on four different fibres from the ES15WT37DA 13_1_12 scaffold gave an average peak frequency of 12.6 GHz, with a standard deviation of 0.2 GHz. Hence, it is possible to estimate that the variation of frequency between the four Type A sample in not significant.

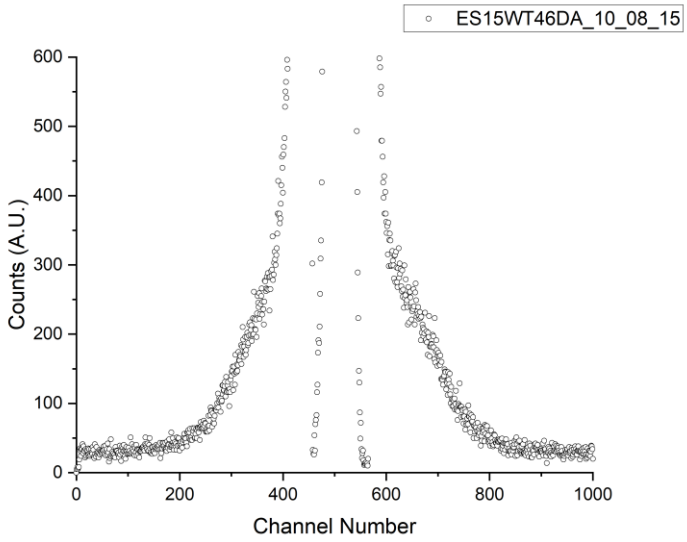

Figure 30: Typical Brillouin spectrum of Type B fibres.

Very surprisingly, the Brillouin spectra of Type B, shown in Figure 30, appeared very different from that of Type A fibres. Indeed, instead of defined peaks that disappear, Type B fibres only show a shoulder in the Rayleigh diffusion peak. This shoulder on each side results of an addition between the Rayleigh incident diffusion peak and a smaller, and wider peak. Due to the change of peak shape, which makes the fit more difficult to obtain, the Brillouin frequency was determined using a new fit method, presented in Figure 31.

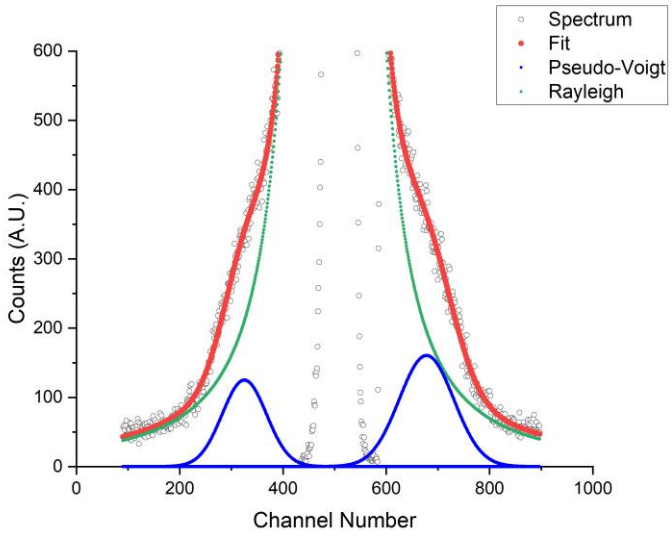

Figure 31 : Example of a Type B Brillouin spectrum fit.

The obtained results after fit for the two Type B samples are given in Table 21. It is then possible to observe a clear shift of the peaks towards lower values, closer to the frequency of the Rayleigh central line.

Table 21: Calculated peak frequencies and corresponding c_{11} values for Type B fibres.

Material	ES15WT46DA 10_08_15	ES15WT46DA 13_1_12	ES16WT46DA 10_08_15	ES16WT46DA 13_1_12
Frequency (GHz)	9.4	6.8	9.0	9.3
c_{11} (GPa)	5.5	2.9	5.1	5.5

The major differences that can be highlighted between Type A and Type B fibre Brillouin spectra are the shape and position of the peaks. They are sharp and well resolved in the case of Type A fibres, whereas Type B fibres exhibit larger peaks, with a shift in frequency toward that of the Rayleigh scattering, from 12 to 9 GHz approximately. As the typical standard deviation in the frequency values lies around 0.5 GHz for those fits, the shift can be considered significant. In the case of the ES15WT46DA 13_1_12 sample, the spectrum quality was affected by an important level of noise, making the fit more difficult to obtain. The obtained frequency was then determined with a much bigger error on the value. However, the obtained value is significantly lower than 12 GHz.

The reasons behind this much unexpected difference are not straightforward to explain, but there are a number of possible interpretations, such as:

- microstructural differences between the two types of fibres, in particular in terms of crystallinity ratios, lamellar thicknesses and crystalline phases fractions
- the presence of some remaining trapped solvent,
- a morphological difference between the fibres, in particular the surface morphology

2.1. Hypothesis of microstructural differences

A usual and effective way to analyse the semi-crystalline microstructure of PVDF is Raman spectroscopy, as previously exposed in Chapter 3 (see p.51). This technique allows in particular the determination of the crystallinity ratio (χc), as well as the fraction of the crystalline phases amongst the three main crystalline phases usually observed in PVDF, namely α, β and γ. The Raman results for the different samples are displayed in Table 22.

Table 22: Crystallinity ratio (xc) and fraction in the crystalline phase of the three main crystalline phases observed in PVDF, α, β and γ, as measured by Raman spectroscopy.

	Material	χ_c (± 3%)	α (±2%)	β (±5%)	γ (±5%)
Type A	ES15WT37DA 10_08_15	50	2	77	21
	ES15WT37DA 13_1_12	50	2	78	20
	ES16WT37DA 10_08_15	50	2	75	24
	ES16WT37DA 13_1_12	51	2	77	22
Type B	ES15WT46DA 10_08_15	51	2	73	26
	ES15WT46DA 13_1_12	51	2	78	21
	ES16WT46DA 10_08_15	51	2	75	24
	ES16WT46DA 13_1_12	51	2	76	22

When comparing Type A and Type B fibres elaborated with the same set of electrospinning parameters (same PVDF content in solution, same applied voltage, same flow rate, and same tip-to-collector distance), no significative variation can be observed. For all samples the crystallinity ratio remains close to 50%, with almost no α crystalline phase, and the distribution of electroactive phases for β and γ is about 80/20. Thus, the hypothesis of a significant crystalline difference explaining the discrepancy observed in Brillouin spectroscopy between Type A and Type B fibres cannot be verified.

In the same manner, we can notice that the variation of the other electrospinning parameters explored in this study did not affect much the produced fibres crystallinity ratio and phase fractions. All fibres exhibit a very dominant electroactive phases fractions, meaning that the optimisation of electrospinning was very successful. Typically, electrospun fibres with high electroactive phases fractions make excellent candidates for a number of applications, including sensing and energy harvesting devices.

2.2. Hypothesis of trapped solvent

The only critical parameter that differentiates Type A and Type B fibres is the DMF:Acetone ratio in the polymeric solution used for electrospinning. Type B fibres were produced from a solution containing more DMF, which is much slower to evaporate compared to acetone. Indeed, the boiling point of DMF is located at 153°C, while that of acetone is around 56°C. A possibility would be that some remaining DMF could stay trapped after electrospinning in Type B fibres. To check this hypothesis, TGA analysis was performed on both type of fibres, and the analysis results are displayed in Figure 32.

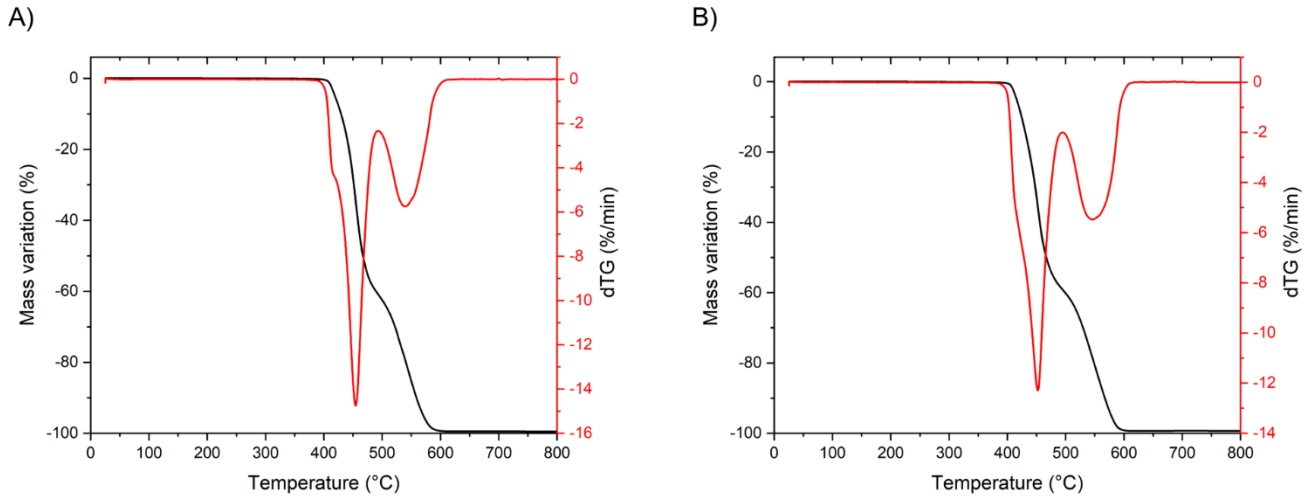

Figure 32: TGA analysis of A) Type A fibres, and B) Type B fibres.

The presence of remaining DMF in the fibres would appear on TGA thermographs by a mass loss located around 153°C. However, such variation could not be observed in either of the fibre types.

The combination of results from Raman and TGA allowed to prove that there are no major chemical differences between the two types of fibres. Thus, this conclusion leads to think that the difference between the two types of fibres could be stemmed from a topographic origin.

2.3. Hypothesis of a topographic difference

The clear frequency shift of the peaks towards lower values, observed when the solvent mixture is richer in DMF, expresses a reduction in elastic moduli.

The first hint at a difference of topographic nature of the fibres could be found in the optical micrographs presented in Figure 27. Indeed, the Type A fibres appear very shiny and transparent, while Type B fibres look more matte and opaquer. However, optical microscopy is not powerful enough to study the surface of the fibres. A difference in the roughness of the two types of fibres could lead to different light scattering behaviour, hence why it was necessary to move to SEM to explore in more depth the possible change in surface roughness between Type A and Type B fibres. Two SEM micrographs corresponding to each fibre type are presented in Figure 33.

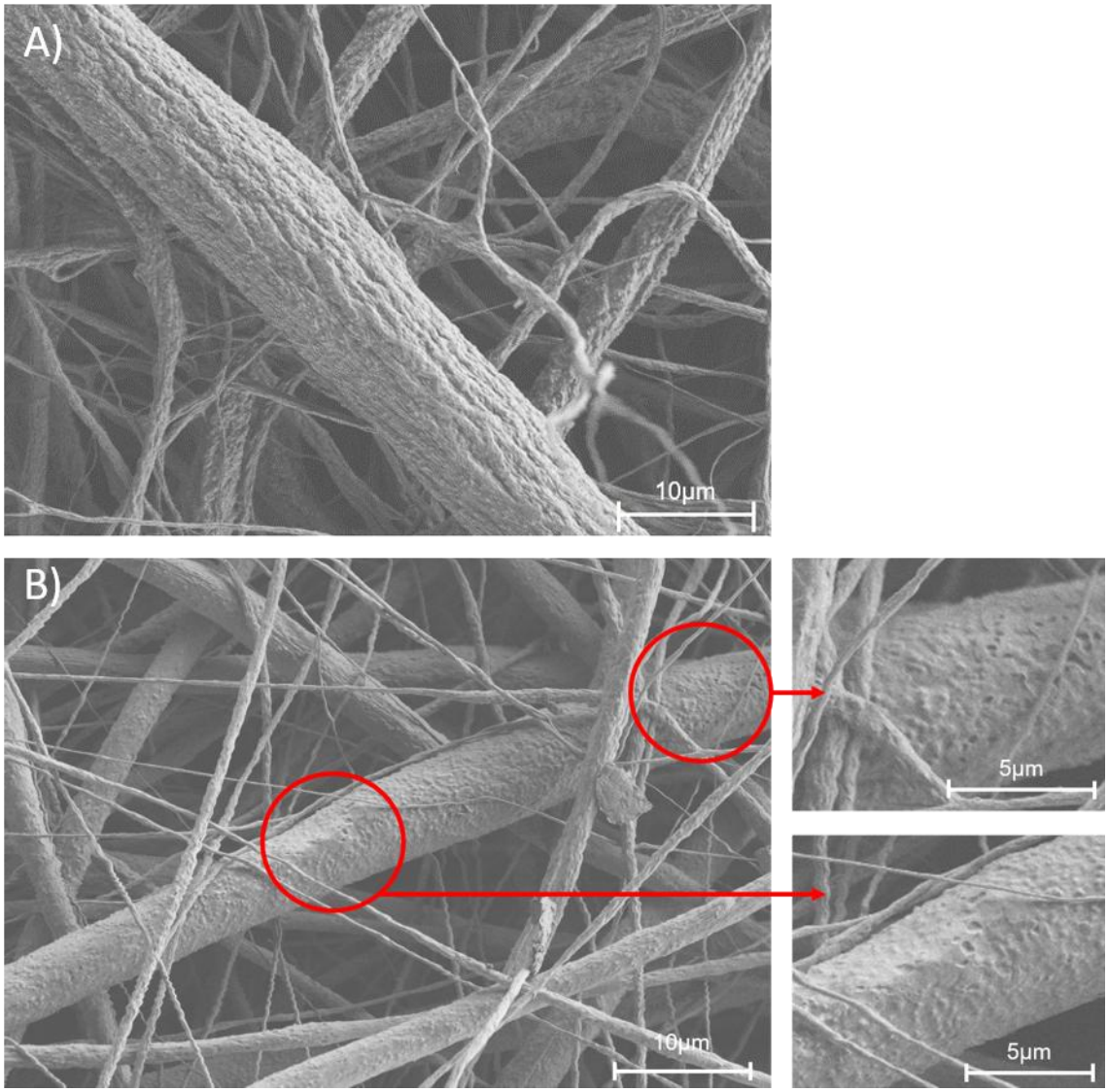

Figure 33: SEM micrographs of A) Type A and B) Type B fibres.

These SEM micrographs clearly show that both fibres types do not present the same surface when different solvent ratios are used. Type A fibres look like tree bark, with wide groves. But at this scale, the roughness of the fibres did not cause much perturbation in micro-Brillouin, as they did not prevent the acquisition of good quality spectra. In the case of Type B fibres, the surface looks smoother, but exhibits a large number of smaller bumps and holes, which can explain the more matte appearance of the fibres in optical microscopy but not the loss of elastic properties observed.

It is well known that in Brillouin spectroscopy, artefacts at the surface can cause issues in the collection of the scattered light. These issues can be of different natures. In case of surface rugosity, the light transmission can be degraded. Another issue can by the lack of propagation of the acoustic wave vector. In both cases, the shape of the spectrum can be altered.

The Brillouin spectroscopy integrates over at least 1 μm^3 of matter. The presence of meso-porosities in volume inside the fibre, of the order of range of the acoustic wave vector size at 180 nm could explain the decrease in optical properties. Indeed, if the porosity is of this order of magnitude, the acoustic phonon will diffuse: this is a classical opto-elastic coupling problem. Surface roughness can produce very well-defined peaks, as observed for

the type A samples, whereas internal porosity in the order of magnitude of the acoustic wavelength prevents the propagation of acoustic phonons.

A difference in PVDF sample surface porosities has already been studied on solvent-casted polymer film by Gregorio *et al*. in 2008 [201]. This study focused on the casting of PVDF-DMF solutions at temperatures variating from 60 to 140°C, and comparison with other solvents like NMP and HMPA. A conclusion reached from SEM micrographs at the surface of films casted at various temperatures was that sample porosity appeared proportional to the solvent boiling point. Hence, solvents like DMF with high boiling points and low evaporation rates lead to samples exhibiting a higher porosity. To translate this conclusion to the case of our two fibres types, it seems that Types B fibres, which were elaborated with a higher content of DMF, would indeed be more prone to exhibit porosities.

It has also been documented in the literature that a variation in the microstructure can modify the shape of the Brillouin spectrum [202], like for example a variation in the Brillouin peaks asymmetry [203]. These issues appear particularly significant in the case of defects reaching sizes in the order of magnitude of the wave vector. In the literature, the observed change in spectra shape has already been documented by Pierno *et al*. [204]. In non-sintered PTFE films, the constituent particles are estimated to be close to 200 nm, which is also the approximate probed spatial scale. The closer we get to this particular size of particles, the larger the Brillouin peak appears. Eventually, the Brillouin peak goes extinct when reaching the acoustic wave vector. This effect implies that this particular type of mesostructure is found everywhere in the scattering volume.

To translate these observations to the case of electrospun fibres, the presence of multiple holes in Type B fibres in the size of the acoustic wave vector approximately would lead to the confinement of the propagation mode of the acoustic waves, thus explaining the change in spectrum shape. Moreover, the multiplicity of small holes within the fibres could also explain the shift towards lower frequencies, which can by correlated to a lower elastic constant.

3. Nanocomposite electrospun fibres with addition of cellulose nanocrystals (CNC) and Al-Cu-Fe-B quasicrystals (QC)

For this section, the studied samples are electrospun fibres elaborated with the following parameters:

- 150g/L PVDF,
- 3:7 DMF:Acetone ratio in 10 mL solution,
- AV: 13kV, FR: 1 mL/h,
- TCD: 15cm
- Addition of 1 to 5wt% CNC or QC.

The samples bear the name of the filler used followed by the weight fraction value, i.e. CNC1 is the name of the fibres elaborated with addition of 1wt% CNC.

The acquisition and the fit of the Brillouin spectra follow the same methodology applied in the previous fibres on Type A fibres. Five acquisitions were realised on each CNC sample. The calculated c_{11} values obtained from the different trials are plotted in Figure 34, along with the average for each sample.

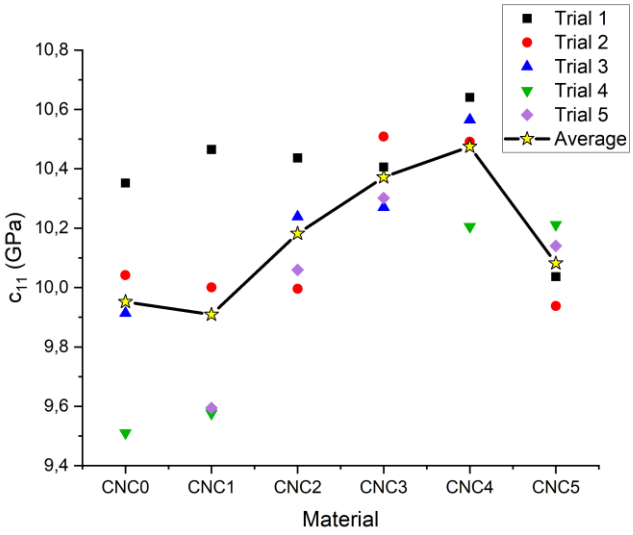

Figure 34: Calculated c_{11} values for the CNC samples, with sample average result.

The average value across five repetitions shows the typical behaviour observed in composites: the c_{11} values increases with the fillers content, from 9.9 GPa (CNC0) to 10.5 GPa (CNC4), then decreases to 10.1 GPa for CNC5. As CNC possess a higher stiffness than PVDF [191,205], it is expected that CNC addition improves the overall value of c_{11} value for the nanocomposite. However, above a certain filler content, aggregation of the fillers tends to happen, thus creating heterogeneities and defects in the fibre microstructure [206]. Nevertheless, this result needs to be treated with caution. Indeed, the variation of c_{11} values for a single sample is quite important, especially for lower CNC contents, and largely exceeds the variations from sample to sample. As mentioned in Chapter 3 (see p.66), the semi-crystalline microstructure of fibres studied locally by Raman spectroscopy can sometimes differ more depending on the fibre picked from the same sample rather than differences inherent to the studied sample. Overall, the addition of a few percent by mass of CNC has a slight reinforcement effect on the electrospun fibres compared to the results that were obtained from the electrospinning process alone, despite the disparities of c_{11} values observed within the same sample.

A similar study was planned on QC samples, but proved to be much more challenging. Indeed, it was not possible to get usable Brillouin spectra close to the QC particles. A first attempt focused on a region where a QC cluster was clearly visible. Four measures were taken gradually closer to the QC aggregate, as pictured in Figure 35.

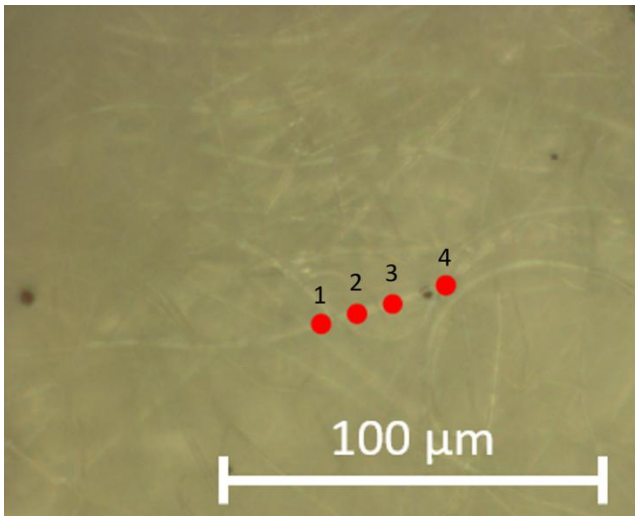

Figure 35: Measures taken gradually closer to a QC cluster.

The corresponding Brillouin spectra, along with the calculated frequency of the Brillouin peaks are presented in Figure 36.

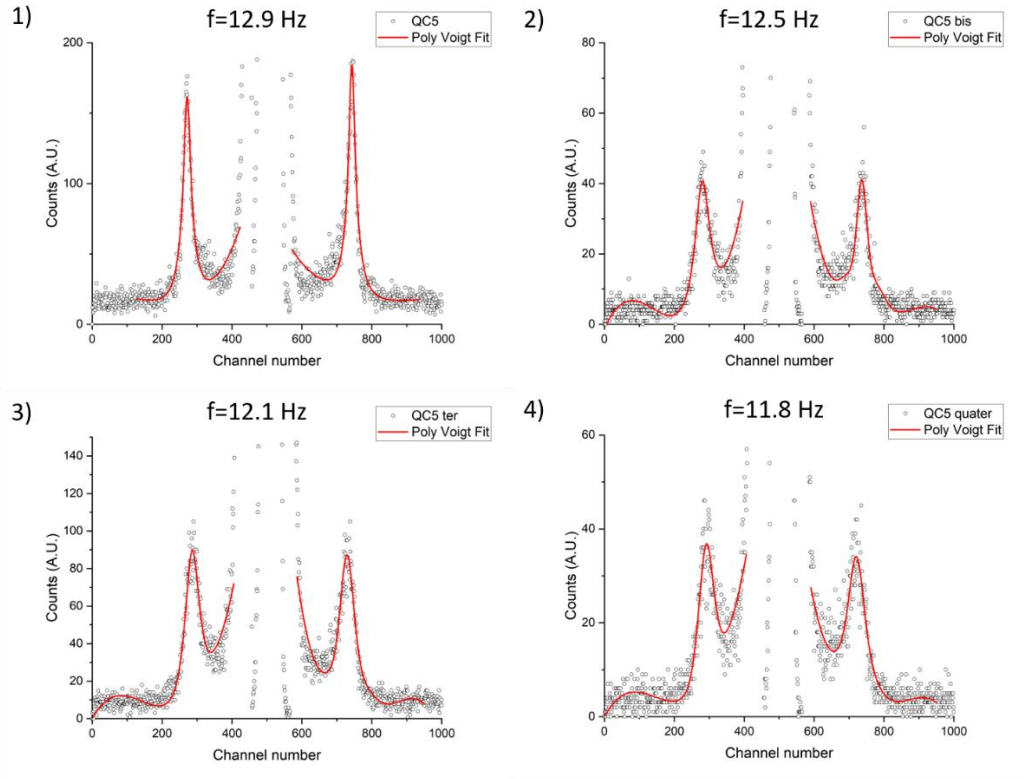

Figure 36: Fit and calculated Brillouin peak frequency gradually closer to the QC cluster (numerotation 1-4 corresponds to the points illustrated in Figure 35).

The closer the measure is to the QC cluster, the lower the frequency of the Brillouin peak gets, dropping from 12.9 to 11.8 GHz. The c_{11} value is proportional to the square of the frequency; it means that the fibre progressively softens as the measure spot gets closer to the cluster. A possible explanation is that when getting closer to a QC particle, the PVDF matrix of the fibre heats up due to the thermal absorption of the laser light by the QC particle, which is very opaque and notoriously poor thermal conductor [122]. Due to the diameter of the laser spot, this spot affects the particle even if it is not centred on it, and possibly heat the opaque QC particle even when the defined measure point is slightly to the side. In this case the softening of the fibres overshadows the considered reinforcement of the material by the QC particles.

In summary, the study on CNC-nanocomposite fibres showed that addition of some percent of CNC has a slight reinforcement effect on the electrospun fibres compared to pristine PVDF electrospun fibres, although disparities in c_{11} values were observed within the same sample. On fibres with QC, the study near large particles leads to a softening of the polymer matrix, interpreted as a heating effect of the particles by the laser, and masking a possible reinforcement effect.

4. Brillouin scattering study in temperature: evidence of an elastic anomaly

This second study focused on the thermal evolution (between -50 and 110°C) of the mechanical properties determined by Brillouin spectroscopy of an electrospun fibre, in order to detect possible structural changes.

The material chosen to perform this study was the 3:7 DMF:Acetone scaffold (Type A fibre) since it presents better Brillouin scattering response thanks to a more adaptable topological surface aspect in comparison to fibres elaborated with a solvent ratio of 4:6, as previously discussed.

An optical micrograph showing the laser focused on a single fibre before the acquisition of the point at -50°C is displayed in Figure 37. The incident laser is strongly attenuated in order to avoid blinding the camera installed on the micro-Brillouin microscope, and find an accurate focus of the laser on the fibre.

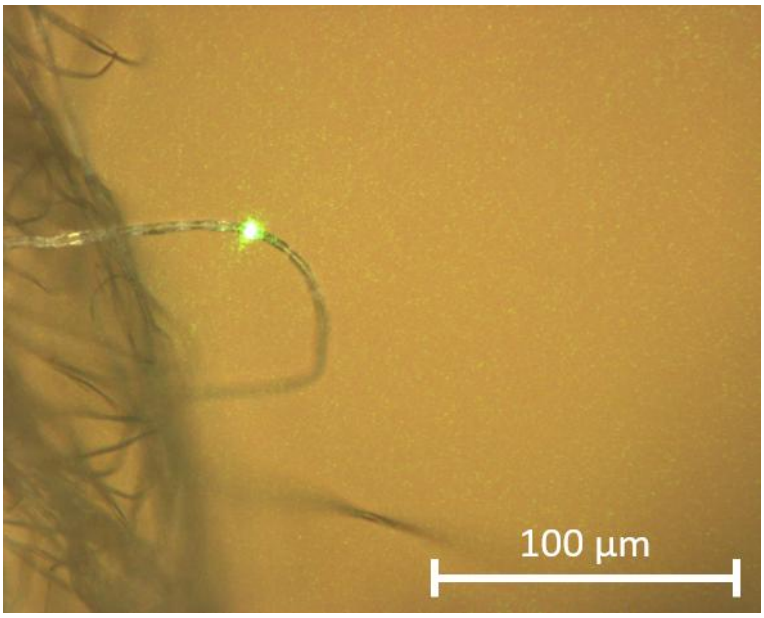

Figure 37: Optical micrograph showing the laser focused on a single Type A fibre.

Two examples of experimental spectra resulting from acquisition at different temperatures are presented in Figure 38. Between 0 and 110°C, a very visible shift of the peak frequency can be observed towards lower values with the increase in temperature.

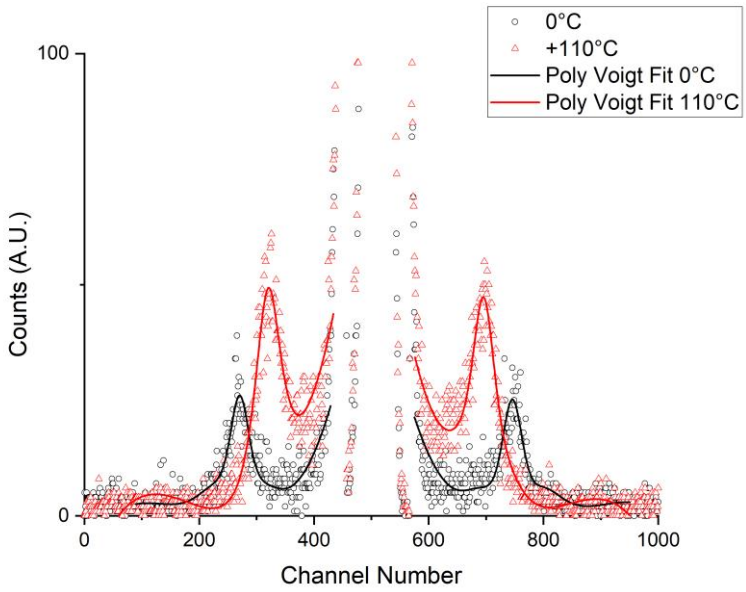

Figure 38: Experimental spectra acquired at 0 and 110°C on a single PVDF fibre.

Once the fit is achieved, as shown in Figure 38, the frequency position of the peaks allows to calculate the elastic constant c_{11} for each temperature according to Equation 19. In Figure 39, the obtained c_{11} values as a function of temperature are plotted.

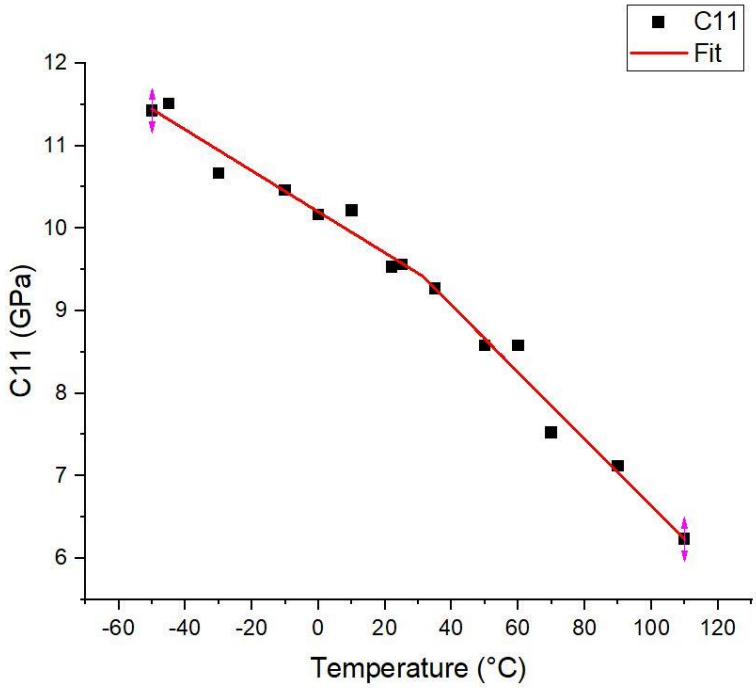

Figure 39: Evolution of the calculated c_{11} as a function of temperature.

From Figure 39, a linear decrease in the elastic constant c_{11} as a function of temperature can be observed, with an abrupt change in slope at a temperature close to 31°C. The slope of the first segment is determined to be 0.02 GPa/°C, and the slope of the second segment is 0.04 GPa/°C. The function used to fit the results is given by Equation 20. Note that for this difficult experiment, the relatively small number of experimental points over a wide temperature range leads to significant uncertainty in the fit: ±13°C.

$$P1 - P2 * x + (P3 + P2) * 0.5 * (ABS(x - P4) + x - P4)$$

Equation 20

with P1 the values for x=0, P2 the value of the first slope, P3 the value of the second slope, and P4 the position of the slope change. ABS is a function returning the absolute value.

Then, in order to determine if this result was specific to the fibre elaboration using electrospinning, a similar experiment was conducted on a mechanically stretched PVDF plain film sample. Here, Brillouin spectra were obtained every 2°C from 15°C to 100°C. The evolution of the frequency of acoustic phonons is presented in Figure 40.

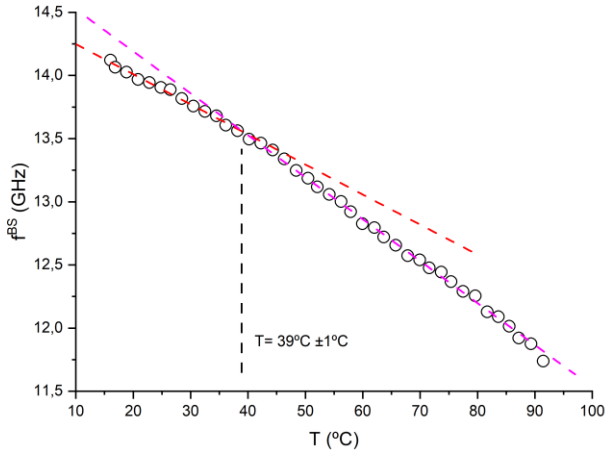

Figure 40: Brillouin study of an oriented solvent-casted sample at high temperatures.

In that case, very similarly to what was observed in the electrospun fibres, a change of slope located around 39°C (± 1°C) is visible on the oriented material. The important number of experimental points around the slope change helped to significantly reduce the error on the determination of the temperature at which said slope change happens (±1°C compared to ± 13°C in the previous experiment). The slope of the first segment is determined to be 0.02 GPa/°C, and the slope of the second segment is 0.03 GPa/°C.

This change of mechanical behaviour, which could be attributed to various physical phenomenon, will be discussed in the next sections.

4.1. Differentiation with the glass transition (Tg)

The change of slope observed at +31°C is very characteristic of what is typically observed in Brillouin spectroscopy in the case of a polymer which passes through its glass temperature transition, enlightening the change of physical state of the amorphous phase from vitreous to rubbery [179,207–213]. However, regardless the processing technique (solvent casting, hot pressed plate, electrospinning), the glass transition of the manufactured PVDF samples lies always around -36°C, as illustrated by Figure 41 [214] that presents the DSC thermograms of such materials.

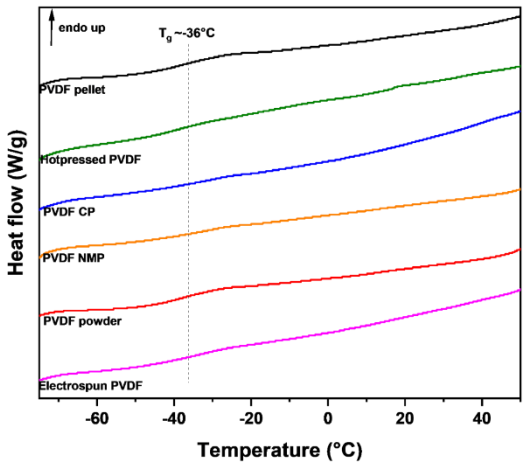

Figure 41: DSC determination of the glass transition of PVDF for various processing methods [214].

To prove the classical glass transition can be differentiated from the elastic anomaly detected at +31°C by Brillouin scattering, an additional test at lower temperatures was conducted on a solvent casted PVDF sample. In this experiment, an Oxford continuous flow cryostat was used in order to explore lower temperatures from -73 to 13 °C. The resulting graph is presented in Figure 42.

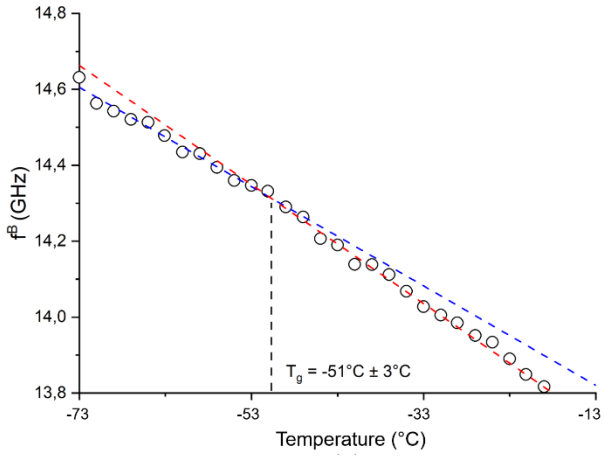

Figure 42: Study of c_{11} as a function of temperature in the lower range (-73 to 13°C).

From Figure 42, a very faint slope change around -51°C is observed and could be attributed to T_g. As expected, the T_g observed by Brillouin spectroscopy lies lower than the T_g determined from DSC. It is a measurement in quasi-static mode, while a heating ramp of 10°C/min is used in DSC.

It is worth mentioning that Brillouin spectroscopy usually allows to decorrelate static and dynamic glass transitions, as illustrated by Figure 43. On the one hand, the quasi-static T_g obtained with Brillouin spectroscopy from a slope change can be compared to the values obtained from other techniques, such as DSC or DMA (at low frequencies). Indeed, at the measurement frequency in Brillouin, in the tens of GHz range, matter is like dynamically "frozen". The imposed frequencies are so high that the molecules cannot follow the imposed excitation, and the measures are then considered to take place in a quasi-static setup. On the other hand, it is well known that the dynamical glass transition temperature is shifted towards higher temperatures when the studied sample is submitted to higher frequencies. This is the case of the dynamic T_g, which is obtained by locating a maximum value of the acoustic attenuation.

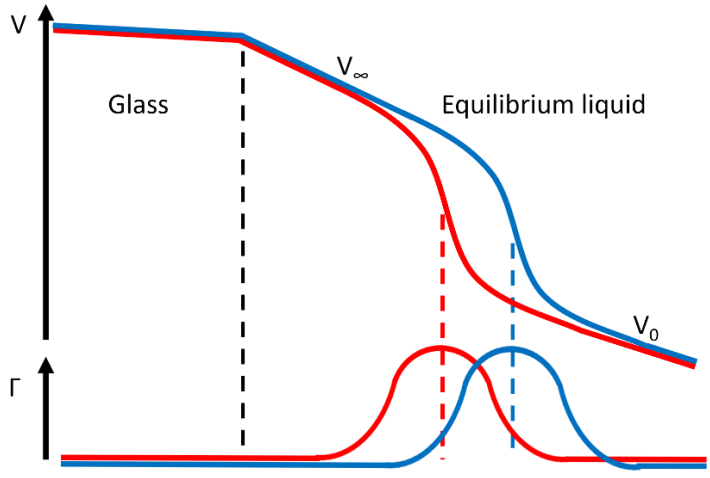

Figure 43: Static and dynamic properties determined at acoustic frequencies [215].

The study of the acoustic attenuation presented in Figure 44, it is obtained by reporting the values of the half width at half maximum of the Brillouin peaks. The acoustic attenuation decreases with decreasing temperature until it reaches the value of quasi-static T_g, where it stabilises. However, no maximum of the attenuation, that would correspond to the dynamic T_g, can be observed, even at 27°C.

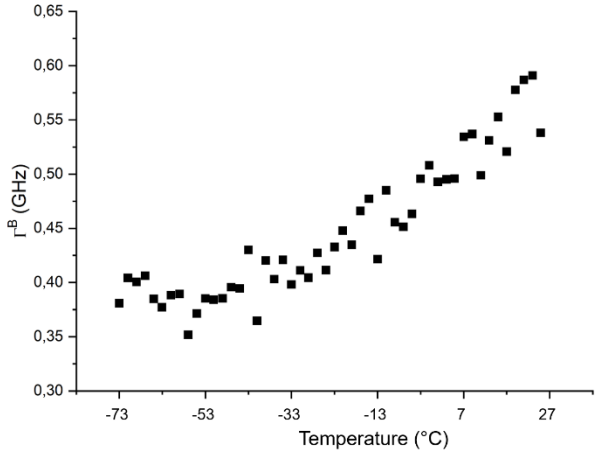

Figure 44: Acoustic attenuation in the lower temperature range (-73 to 27°C).

The combination of results from DSC and Brillouin spectroscopy shows proofs that the T_g of PVDF is located around -40°C. Therefore, the elastic anomaly located at around 31°C cannot be attributed to the glass transition phenomena.

4.2. DMA and DSC analyses

As the observed elastic anomaly cannot be related to T_g, it is necessary to search whether another type of transition can be observed in PVDF around 30°C. Preliminary DMA studies on a PVDF solvent casted film further confirm the T_g of PVDF used in this study to be around -45 to -40°C. In Figure 45 another transition is also visible at higher temperature, with a peak in tan δ visible around 30 to 60°C, depending on the frequency (ranging from 0.1 to 10 Hz).

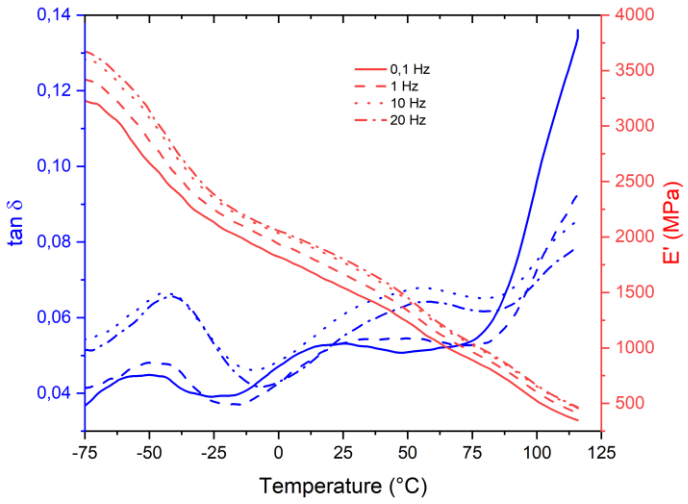

Figure 45: Evolution of E' and tan δ as a function of temperature in DMA analysis of a solvent casted PVDF film.

Figure 46 illustrates the mechanical behaviour of an electrospun PVDF sample at a frequency of 1 Hz. The two transitions previously observed on the solvent casted sample are also present. From Figure 46, T_g would be located around -50°C, and the second transition around 80°C.

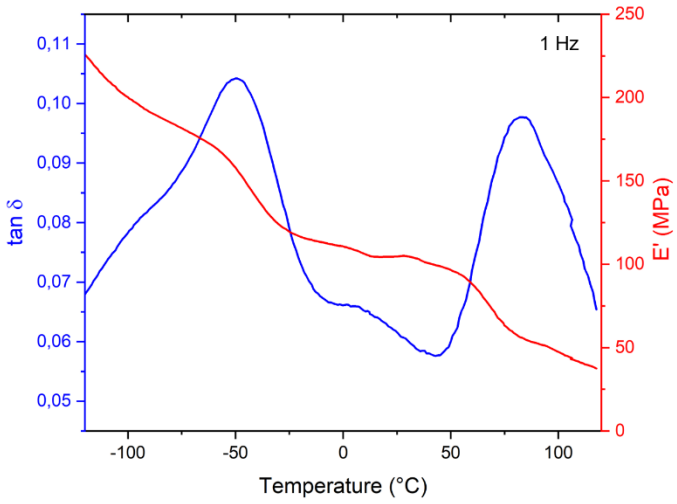

Figure 46: Evolution of E' and tan δ as a function of temperature in DMA analysis of an electrospun PVDF film

However, it is important to bear in mind that the presented results are not representative of single fibres individually, but depict the behaviour of the whole fibre mat, with the possibility of fibres breaking, slipping, and the influence of the very high porosity between the fibres.

DMA can be considered as one of the main techniques to investigate T_g. The glass transition can clearly be separated from a second transition, located at positive temperature, that needs to be identified. As such, DSC studies have been conducted on both electrospun fibres and solvent casted samples. The resulting thermograms are presented in Figure 47.

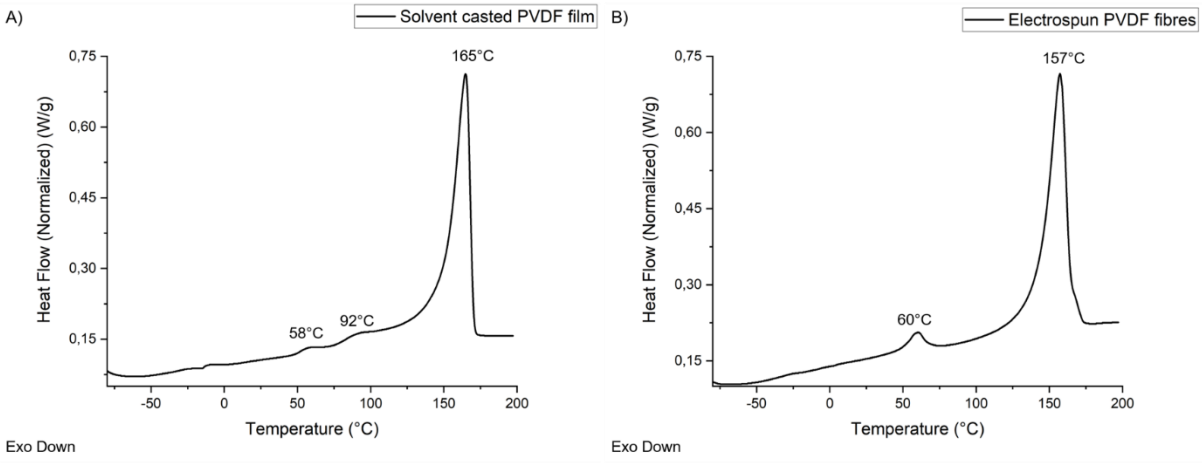

Figure 47: DSC heating ramp at 10°C/min of A) Solvent casted PVDF and B) Electrospun PVDF fibres.

Both DSC thermograms show the presence of small endotherms located before the major endotherm at 160°C, corresponding to the melting of main PVDF crystals. In the case of the solvent casted film, two peaks are located at 58 and 92°C. This is coherent with the DMA result, which showed a transition in a large range of temperature from 20 to 90°C, with several points of inflexion visible in the E' curves. In the case of electrospun fibres, only one

peak is observed in DSC at 60°C. It can once again be approached to the large transition centred around 60°C in DMA. Moreover, the possibility of remaining solvent present in the electrospun fibres has been overruled by the results obtained in Figure 32. In this TGA experiment that was conducted before the DSC, when the fibres were more recently electrospun, no weight loss that could have corresponded to solvent evaporation can be observed between 0 and 350°C.

The second transition visible both in DSC and DMA needs to be elucidated, as well as the possible correspondence between this DMA transition, and the slope change observed in Brillouin spectroscopy.

4.3. Discussion

In their DMA study of poled and unpoled PVDF, Sencadas *et al*. [216] noted that, in addition to the presence of Tg around -30°C, a new relaxation can be seen above 30°C. This process, which is generally labelled α_c is associated with motions in the material crystalline fraction, and can be observed in other flexible semicrystalline polymers. Moreover, in a dielectric study of PVDF, Rekik *et al*. [217] confirmed the presence of a maximum of the imaginary part of the dielectric modulus (M'') around 30°C also attributed to α_c relaxation that usually happens between 0 and 150°C. The relaxations within the crystalline phase are attributed in this study to defects in the crystal, such as "chain loops at the lamellar surface, chain rotations and twisting within the interior of the crystals, discontinuities defects". Interestingly, in a study using thermostimulated current spectroscopy (TSC), Teyssedre *et al.* [218] showed that the presence of an α_c peak occurs both in α and β phase of PVDF, but appears with a greater magnitude in β PVDF, thus not being specific to the presence of β phase. Discussing the nature of this transition, also observed in DSC in the form of an endotherm located around 60°C, the authors propose that it is linked to the reorganisation of disordered regions in the crystallites, and more specifically at the lamellae surfaces. In another DSC study from Leonard *et al.* [219], they found several transitions in addition to the main melting peak. The first one is denominated as lower glass transition, located around 233K (-40°C). Then, they mentioned an upper glass transition between 303 and 333K (30-60°C), that they attribute to the amorphous-crystalline interphase. Above 333K, other transitions are attributed to pre-melting movements.

It is well known that there are individual changes in molecular orientation/order without any change in crystalline structure that give variations in the evolution of elastic properties with temperature very similar in Brillouin spectroscopy to the variation observed during a glass transition. These transitions are known as orientational glass transitions in orientational disorder crystals (ODCs) [220–222]. Thus, the transition observed at 31°C could correspond to a reorientation/ reorganisation/ disorganisation in the crystalline region of PVDF mechanically oriented which would appear in Brillouin spectroscopy very similar to the behaviour of an orientational glass transition.

The possibility to observe a second-order transition in Brillouin spectroscopy has already been explored. In their study, Mitchell *et al.* [211] have presented a thermal study of PMMA using Brillouin spectroscopy. A change of slope at 101°C is attributed to the glass transition of PMMA, which is correlated to DSC results. A second change of slope around 45°C is labelled as second order discontinuity, and labelled as the β transition of PMMA.

From the DSC thermograms, the presence of a peak at 60°C suggests that a melting phenomenon is occurring. In a DSC study of PVDF, Yang *et al.* [223] observed a weak melting peak at 68°C that they attribute to poor secondary α crystals that were formed during the biaxial orientation of their film. In the case of our study, the melting of the secondary α crystals is visible in DSC around 60°C, but has not been observed in Brillouin. A plausible explanation would be that the fraction of α crystals represent much less matter compared to the crystalline involved in the behaviour of the elastic anomaly. The melt could also be overshadowed by the anomaly.

4.4. Conclusion

The study in temperature of the mechanical properties of electrospun PVDF fibres by micro-Brillouin revealed an unexpected elastic anomaly. The evolution of c_{11} values as a function of temperature showed show a clear change of slope at a determined temperature of 31°C, that resembles the usual behaviour observed for a glass transition. However, further experiments and data from the literature prove that the glass transition of PVDF is located around -40°C. The most plausible hypothesis is that this elastic anomaly can be interpreted as a reorientation at the amorphous-crystalline interphase in mechanically oriented materials. This transition precedes the melting of imperfect α crystals happening around 60°C, occurring below the melting temperature of PVDF around 160°C.

5. Influence of mechanical stretching and temperature cycles on the Brillouin response

To gain further knowledge about the thermomechanical behaviour of PVDF, an additional Brillouin studies was conducted at higher temperatures on a PVDF solvent casted sample. It was interesting to test whether a non-oriented standard PVDF sample would show the same thermoelastic behaviour as mechanically stretched oriented materials.

After the heating (at 120°C) of a non-oriented sample which was originally brown, the investigated region was observed discoloured and turned white. The last section of this chapter covers this change of colour. The following discussion will cover only Brillouin results obtained from the white region of the sample, in order to remove this supplementary factor from the study.

Two additional successive heating cycles until 90°C were investigated by Brillouin spectroscopy. The obtained results are presented in Figure 48.

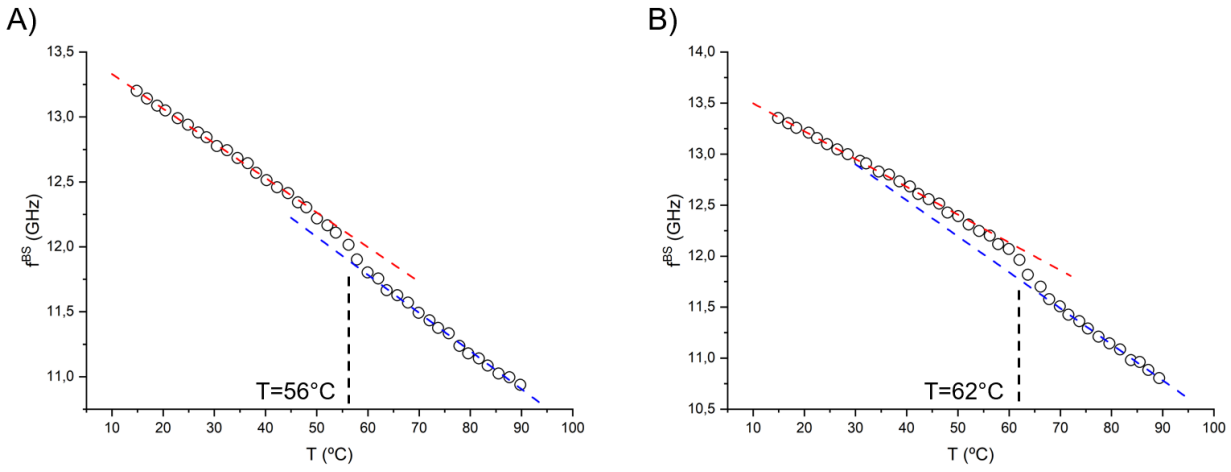

Figure 48: A) Second and C) Third heating cycles to 90°C on non-oriented PVDF.

From each heating cycle, it is visible that an elastic anomaly can be observed in Brillouin spectroscopy even in the case of a non-oriented material. However, instead of the slope change previously observed in the oriented film and the fibres, which are mechanically stretched during the electrospinning process, this time a step-like anomaly appears. The characteristic temperature of the step evolves to higher temperatures with the repetition of the heating cycles, moving from 56°C to 62°C approximately.

In order to shed light on the change of position of the step with temperature, it was also studied via DSC. Instead of reaching the melting temperature of PVDF like in previous studies, PVDF fibres were heated to 90°C at a 10°C/min rate, then cooled, and heated again to 200°C at a 10°C/min. A repetition of this study was performed on

a second electrospun sample from the same material, this time heating to 110°C during the first heating cycle. The two resulting thermograms are presented in Figure 49.

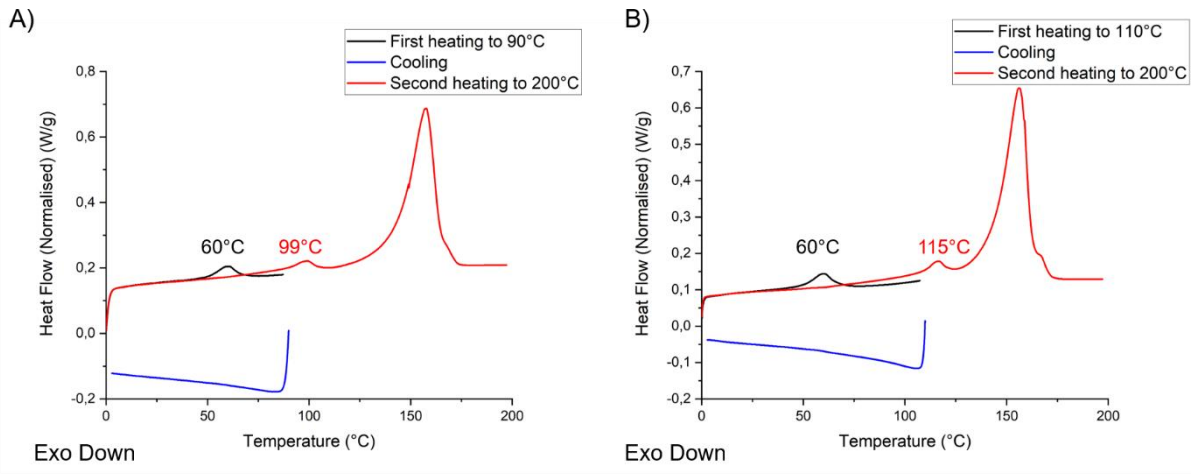

Figure 49: DSC thermograms of the fibres heated to A) 90 and B) 110°C before full melting cycle.

From the presented thermograms, it appears that during the first heating ramp, an endotherm appears around 60°C. During the cooling ramp, no exotherm is observed in either of the studies. Then, during the second heating ramp, the position of the endotherm seems to depend on the heating temperature that was first reached during the previous ramp. Indeed, after a heating to 90°C, the endotherm will be located around 99°C, while it moves 115°C after heating to 110°C.

This DSC study was repeated on the same solvent-casted sample used for the Brillouin study with repeated heating cycles. The sample was heated from 20°C to 90°C at a 10°C/min rate, cooled to 20°C, heated from 20°C to 110°C at a 10°C/min rate, cooled to 20°C, then finally heated from 20°C to 200°C at a 10°C/min rate. The reached temperature at the end of each heating or cooling cycle was maintained for 5 minutes. The resulting thermogram is presented in Figure 50.

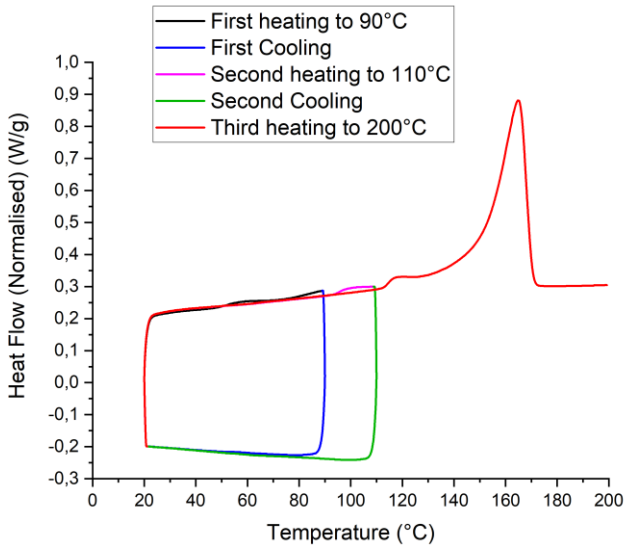

Figure 50: Thermogram of the solvent-casted film submitted to three heating/cooling cycles.

Very similarly to the study on electrospun fibres, the endotherm visible at 60°C during the first heating ramp to 90°C moves to higher temperatures with each heating cycle, going up to 100°C during the heating ramp to 110°C, then finally to 118°C during the heating ramp to 200°C. It is worth noting that during the first heating ramp, it seems that a second small endotherm located around 85°C appears, but cannot be fully studied as the ramp stops at 90°C. It has already been observed in the previous section (see Figure 47). During the following heating ramps, only one smaller endotherm appears before the malting peak located at 165°C.

As stated in the previous section, in mechanically oriented materials like the electrospun fibres, the elastic anomaly has been interpreted as a reorientation at the amorphous-crystalline interphase happening around 30°C. In the non-oriented material, this particular change is not observed, illustrating that the phenomenon occurring in the different types of samples is different. Rather, the sample presents a step-like Brillouin anomaly around 60°C, which resembles a phase transition, and appears at higher temperatures when the sample is submitted to heating cycles that do not entirely melt the sample. DSC analyses have identified the presence of small endotherms usually around 60°C caused by the melting of small α crystals. They also shift towards higher temperatures when the sample is submitted to heating cycles without reaching complete melting.

In this non-oriented solvent-casted sample, the amount of β phase (usually created by mechanical drawing) is around 30% (see p.52), compared to the 75% usually obtained in fibres for example. It is then possible that the contribution of the reorientation at the amorphous-crystalline interphase is largely reduced compared to a very oriented sample, and that the melting of imperfect α phase crystals makes a more prominent contribution in the observed elastic anomaly, thus explaining the change of slope taking a S shape rather than a simple slope change.

6. Unexplained behaviour: discoloration of the sample

After the repetition of the heating cycles, a discoloration in the analysed region of the sample (PVDF non-oriented) that was simultaneously heated and submitted to the laser beam was detected, as illustrated in Figure 51.

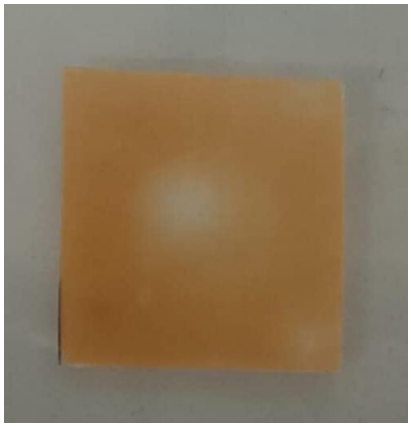

Figure 51: Discoloration on the PVDF film submitted to heating and laser beam.

The initial brown colour could stem from the presence of solvent that did not completely evaporate during the drying phase of the film. Indeed, Figure 52 shows the TGA analysis performed on a solvent casted membrane.

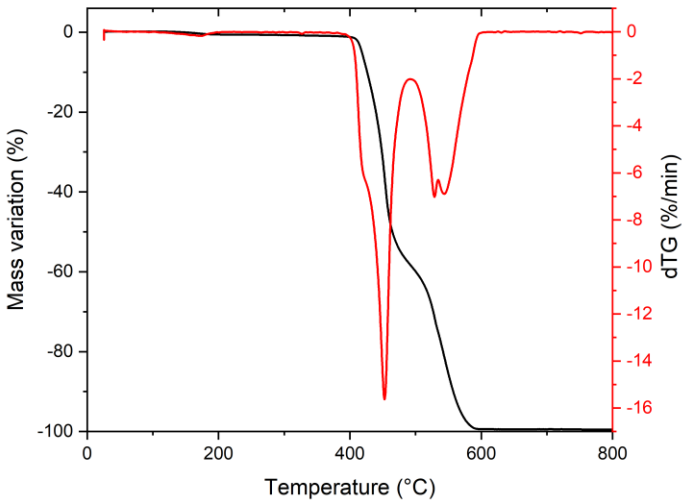

Figure 52: TGA analysis of a solvent casted film.

A bump located around 150°C in the dTG curve demonstrates a mass variation in the temperature region where solvent evaporation is expected, thus showing the possibility of trapped solvent that was remaining in the membrane.

To understand the origin of this discoloration, additional studies were performed on both the brown region, which is the initial colour of the sample, and the white region that was discoloured after Brillouin experiments. First, two Raman spectra were taken using a 532 nm laser in each region, a few minutes apart. This laser has the same wavelength as the laser used for Brillouin spectroscopy. The resulting Raman spectra are presented in Figure 53.

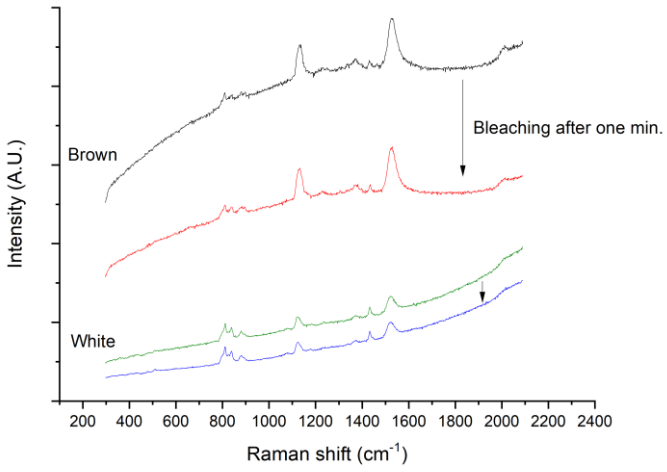

Figure 53: Raman spectra taken in the brown region and discoloured white region of the sample.

In both regions, the first spectrum taken exhibits an intense background baseline, but the shape is different. After waiting a few minutes (same dull time for both), a second spectrum is taken. For both regions the intensity of this background baseline is reduced, although the intensity gap is much more important in the brown region, revealing an important effect of laser bleaching. This behaviour has not been previously detected during the routine characterisation studies on fibres, conducted using a 785 nm laser. After removing the baseline from the original spectra, the resulting curves are presented in Figure 54.

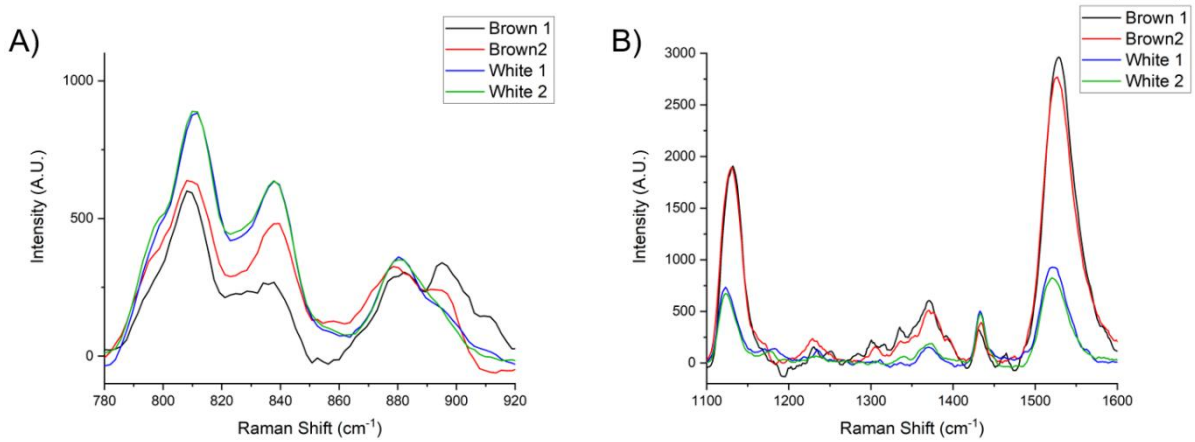

Figure 54: Comparison on the spectra after definition of a baseline in A) the 780-920 cm^{-1} and B) the 1100-1600 cm^{-1} regions.

Looking at the 780-920 cm^{-1} range, it is visible that both regions exhibit intense band located at 830 and 840 cm^{-1}, respectively corresponding to the γ and β phase of PVDF. However, in the spectra corresponding to the white region, the intensity of the two bands is visibly greater compared to the spectra taken in the brown region. Even though it is generally less studied, the 1100-1600 cm^{-1} region gives complementary information. The band located around 1144 cm^{-1} is attributed to the α phase, even though its asymmetric shape suggests a convolution of several bands. While the γ and β bands seem to grow in the white region compared to the brown one, this α band intensity is reduced by more than half its size. Thus, it is possible that the exposure to the laser beam, in addition to providing extra solvent evaporation and removing the brown colour associated with the presence of solvent, promotes the electroactive phases formation, to the detriment of the α phase.

Moreover, Brillouin spectroscopy results seem to confirm this tendency. Two measurements were taken in two different locations in both the brown and the white region. In the white region, one spectrum was taken close to the centre of the region, and one further from the centre. The results of the Brillouin peak frequency are presented in Figure 55.

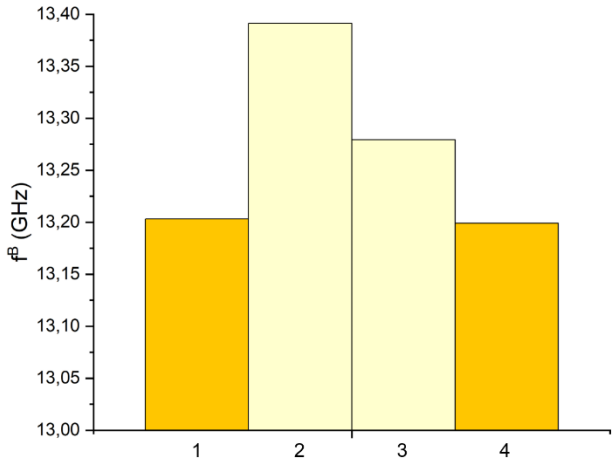

Figure 55: Brillouin frequency measured in the brown (1 and 4) and the white (2: centre and 3: off-centre) region of the sample.

In the brown region, both calculated frequencies are equal to f^B = 13.20 GHz (case 1 and 4). In the white region, the frequency measured at the centre gives f^B = 13.39 GHz, and the other one 13.28 GHz.

A similar trend was observed by submitting the brown region of the sample to a low laser power of 3mW, using a x10 objective on the micro-Brillouin, at room temperature. The resulting frequency shift is presented in Figure 56.

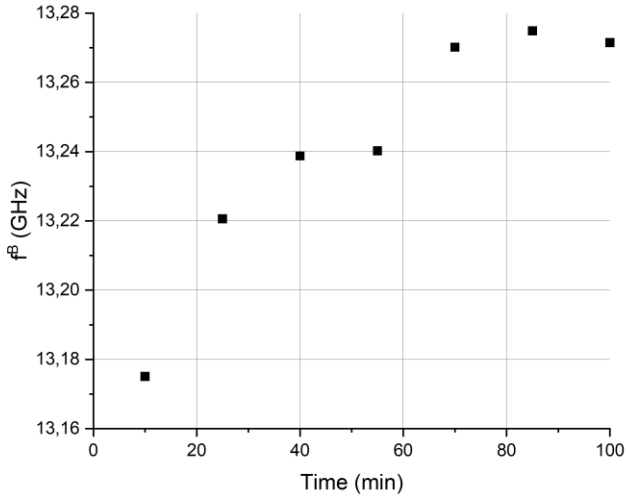

Figure 56: Resulting Brillouin frequency shift due to laser exposure with a power of 3mW.

Even though no discoloration could be obtained within the time frame of the experiment, it is visible that with prolongated exposure to the laser, the Brillouin frequency value gradually increases, going up from 13.18 to 13.28 GHz. Moreover, no heating effect has been observed during this experiment

Thus, with exposure to a 532 nm laser, the value of the Brillouin frequency increases. This value being proportional to the c_{11} constant, the increasing stiffness with laser exposure would be consistent with the hypothesis of an increased proportion of the electroactive phases. Indeed, is has been demonstrated that a growing amount of β phase in a sample contributes to stiffing the sample and improving overall mechanical properties [224]. Thus, it would appear that a different crystallisation of the sample is realised under exposure to a green laser (532 nm). This has not been previously observed using the 785 nm laser beam, of lower energy. However, the exact phenomenon behind the discoloration of the sample is not fully explained. Further studies on the chemical nature of both regions would be necessary to gain in in-depth understanding of the laser effect on the material.

7. Conclusion

The studies presented in this chapter constitute the first time that isolated electrospun PVDF fibres were mechanically characterised by Brillouin microscopy.

The influence of solvent during electrospinning was studied. Between fibres processed with different DMF:Acetone ratios, strong differences in mechanical properties obtained by Brillouin spectroscopy are highlighted, whereas the Raman and TGA characterisations do not detect any difference. This strong variation in mechanical properties (from 12.5 to 9 GHz, a 20% drop in frequency corresponding to a 40% drop in elastic modulus) is attributed to the presence of mesoporosities in the fibre volume, caused by the difference in solvent evaporation speed.

A study on composite electrospun fibres with addition on cellulose nanocrystals (CNC) and Al-Cu-Fe-B quasicrystals (QC) was also realised. Overall, the addition of some percent of CNC has a slight effect reinforcement effect on the electrospun fibres compared to the results that were obtained from the electrospinning process alone, despite the disparities of c_{11} values observed within the same sample. Concerning the electrospun fibres with QC, analysis near the particles shows a drop in elastic properties, interpreted as local heating by the laser in the vicinity of the QC

particles, due to their low thermal conductivity. This softening effect of the PVDF fibre matrix overshadows the possible reinforcement effect of the material by QC addition.

Furthermore, an unexpected elastic anomaly was evidenced, by exploring the evolution with temperature of the mechanical properties of electrospun fibres. Micro-Brillouin spectra show a clear change of slope in the variation of the elastic constant c_{11} with temperature, similar to what can be observed for a glass transition, at a determined temperature of 31°C. This temperature does not correspond to the usual glass transition temperature of PVDF, located as described in literature around -40°C. The hypothesis defended in this chapter is that this elastic anomaly can be interpreted as a reorientation/ reorganisation/ disorganisation at the amorphous-crystalline interphase, located around 30°C in electrospun fibres. This transition precedes the melting of imperfect α crystals happening around 60°C, and ultimately the melting of PVDF at around 160°C.

A complementary Brillouin study on a solvent-casted sample shows that a different elastic anomaly can be observed in non-mechanically oriented materials, but takes a S shape instead of a simple slope change, which hints at a phase transition. This event, initially observed around 60°C, shifts toward higher temperatures with thermal treatments that remain below the melt temperature of PVDF. In line with the previous conclusions, it is interpreted as the melting of α crystals. The absence of the simple slope change located at 30°C in non-mechanically oriented materials highlights the fact that the elastic anomaly associated with reorientations at the amorphous-crystalline interphase is exclusive to mechanically oriented materials.

The last study also highlighted a phenomenon of discoloration due to the exposure to the Brillouin 532 nm laser. Along with the colour change, usually associated with removing of trapped solvent, complementary Raman and Brillouin studies seem to indicate that the exposure to laser contributes to the promotion of the electroactive crystalline phases over α phase. The Raman vibrational bands usually attributed to β and γ become more intense while that of α decrease in intensity in the discoloured zone, and higher β phase fraction is known to stiffen the material. This result is in line with Brillouin measurements, that shows an increase of the Brillouin frequency with laser exposure. However, further characterisation studies are still needed to fully understand the origin of the discoloration happening in the solvent casted sample.

Chapter 5: Electric characterisation and energy harvesting performances of the electrospun PVDF-nanocomposites fibre mats

1. Introduction

After having fabricated and performed chemical, morphological, structural and mechanical characterisation on the PVDF electrospun scaffolds, we are moving on to the topic of their electric characterisation, and potential applications.

In this chapter, we will first review some testing setups used by various research teams from the literature. As we saw that usual testing methods are difficult to apply to electrospun materials, and to perform controlled and reproducible characterisation, it became necessary to develop our own testing bench. Hence, the next part follows the realisation of a tapping test machine here at Institut Jean Lamour. It covers the design, manufacturing, implementation and electronic command of the machine.

Using this setup, output voltage and current values were obtained for the different PVDF-nanocomposite scaffolds, pristine and with addition of 1-5% of cellulose nanocrystals (CNC) and Al-Cu-Fe-B quasicrystals (QC). A comparison with the performance of a PZT buzzer is also provided. These results allow us to select the best candidate from among our devices, with which we implemented the applications.

Then, we focus on how to optimize and exploit the energy harvesting achieved. To this end, we explore the different ways to handle the generated voltage and current peaks to store the energy and release it in a form useful for everyday low-power applications. We present a comparative study of the three main energy harvesting electronic boards available on the market and argue our choice for the next steps. With the chosen card, called EM300, we show the optimization of the total stored energy as a function of the load impedance.

In the final part of this chapter, we plan a complete sensor system and the transmission of sensor information via a Bluetooth system powered by energy harvested using our devices. First, using the same materials developed in this study, we demonstrate the development of an "arterial pulse sensor" application, mounted in a dedicated test bench to demonstrate perfect detection of the simulated pulse and accurate obtention of the blood rate. Second, we demonstrate the development of the Bluetooth system, reprogrammed specifically for this application. The overall project is not yet fully achieved, but we present the detailed schematic, with most of the building blocks completed and validated.

This chapter especially benefited from the precious help of students in M1/M2 project or M2 training from the Master EEA-CIM (”Capteurs intelligents et micro-nanotechnologies”) that I co-supervised during the three years of my PhD.

2. Piezoelectric characterisation of a PVDF film: state of the art

We first present a brief state-of-the-art review on the subject to frame our work and identify areas where our efforts should be focused.

2.1. Measurement of the piezoelectric coefficient (d33)

The piezoelectric coefficient in the longitudinal or out-of-plane direction, often written as d_{33}, is an important parameter to evaluate the properties of a piezoelectric material [225]. The usual characterisation method is the Berlincourt meter [226,227], mostly used in the case of the d_{33} measurement of bulk materials [228]. This simple testing method is composed of metallic jaws holding the plane piezoelectric in a fixed position, to which an alternating force is applied. The generated electric force is then analysed [229–231]. A schematic diagram of the test principle is shown in Figure 57.

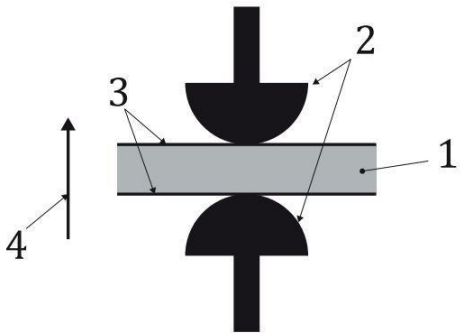

Figure 57: Schematic diagram of a Berlincourt meter with 1) specimen, 2) probe, 3) electrode, 4) polarisation direction [231].

A high d_{33} constant in piezoelectric materials has a significant effect on the performance and application on the fabricated devices, as it describes the material efficiency to convert mechanical energy into electrical energy (and conversely). It is particularly significant for transducers and sensors working in longitudinal mode [232].

If some teams managed to directly use the d_{33} meter on electrospun fibres, such as Mani et *al.* [233], this type of characterisation is particularly difficult to manage in practice, because the horizontal arrangement and random distribution of fibres generally leads to a zero value of d_{33}. Hence, we will explore in the following paragraphs alternative methods to assess the piezoelectric response of electrospun PVDF fibres.

2.2. Tapping test

The tapping test involves a cyclic “press-and-release” applied force on the test material that creates a slight deformation in the material. Many research teams have used human body movements to generate the striking force, such as finger tapping, hand tapping or foot tapping. Pictures corresponding to different testing setups are presented in Figure 58.

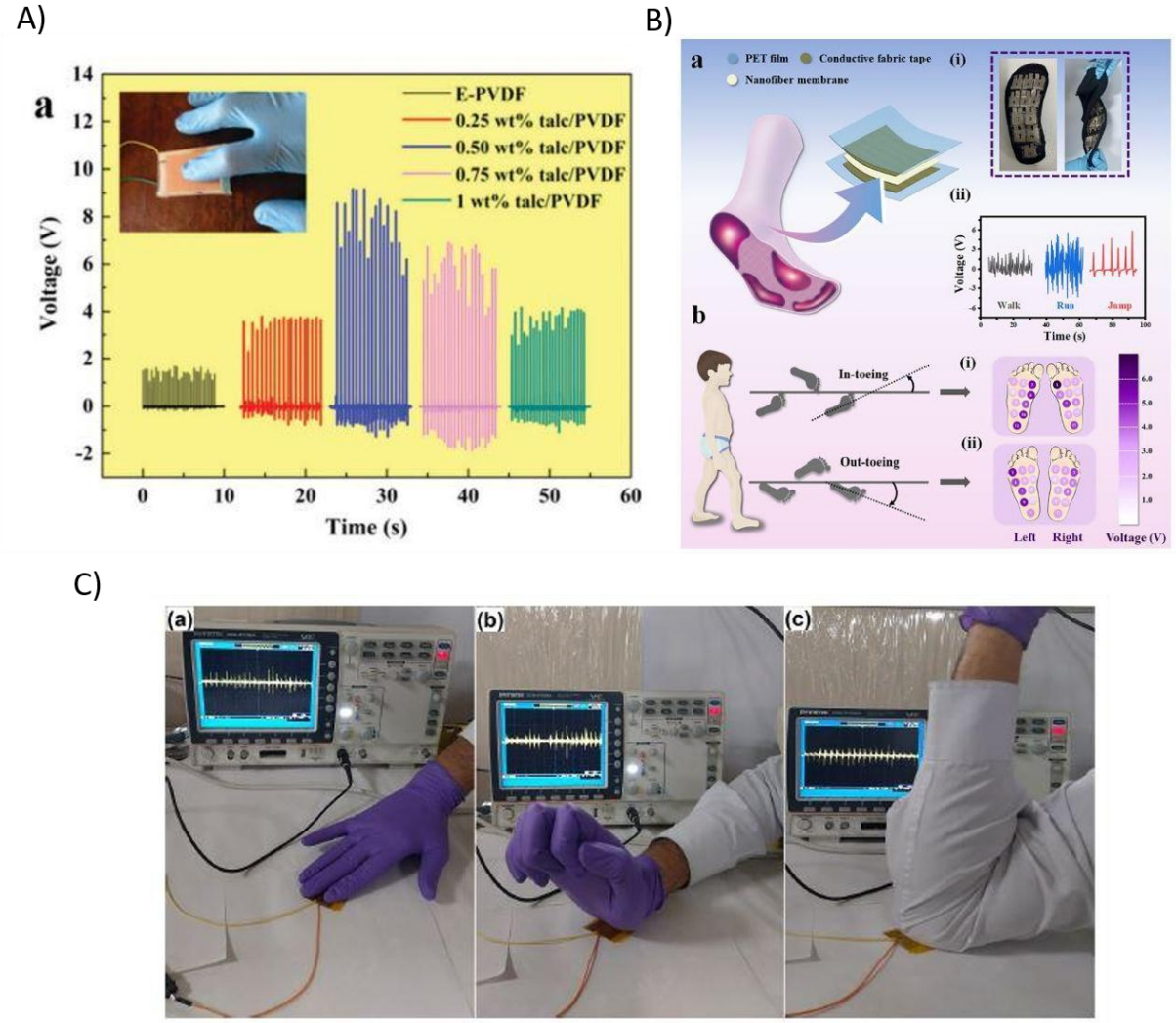

Figure 58: Tapping test from human motion: A) Finger tapping [234], B) Foot tapping [235], C) Palm, wrist and elbow tapping [236].

However, in these presented setups, crucial parameters such as contact surface, frequency and applied force might be challenging to assess precisely. A change in said parameters has a significant impact on the tested device response. In order to improve the reproducibility of tests, mechanical tapping systems have also started to appear in papers.

For example, Sadeque *et al*. [237] studied triboelectric nanogenerators made of thermally drawn PVDF fibres filled with graphene nanoplatelets. The unusual device making process involved making a graphene-filled PVDF film using the solvent casting method. Then, the film is rolled over a carbon paste electrode previously moulded into a cylindrical shape. The resulting assembly is then coated with a sacrificial polycarbonate sacrificial layer, annealed in vacuum, and submitted to thermal fibre draw to get tens of meters of fibre. The PC layer is finally dissolved to obtain the graphene-integrated PVDF fibre. To carry the electrical characterisation of the devices, the team has designed a custom-made tapping device, coupled with an oscilloscope and current preamplifier to carry the

electrical characterisation of their triboelectric nanogenerators devices. An illustration of the setup is provided in Figure 59.

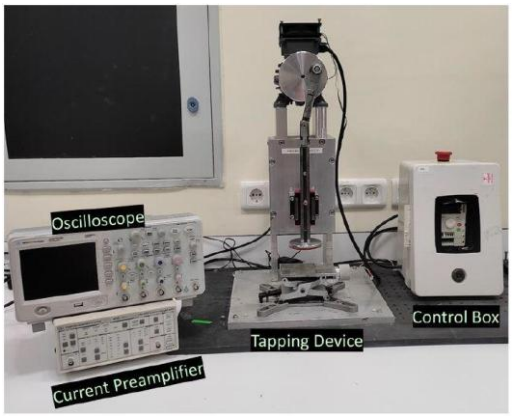

Figure 59: Custom made tapping test setup [237].

Different test parameter sets are employed to study their influence on both the output voltage (V_{OC}) and current (I_{OC}). With a set frequency of 5 Hz, by varying the contact length between the fibre and testing device from 1 to 4 cm V_{OC} increased from 10.2 to 23.2 V. Similarly, I_{OC} increased from 11.6 µA to 23.6µA by increasing the contact length from 1 to 4 cm. These results are expected, as an increase in the contact area leads to an increase of the amount of transferred charges, and thus an increased charge density [238]. Conversely, the effect of the contact frequency was studied while fixing the contact length to 3 cm. Here, by increasing the frequency from 1 to 7 Hz, V_{OC} increased from 7.6 to 24 V, reaching an IOC of 26.4 µA at 7 Hz. With a high contact frequency keeps a high surface charge density, by reducing the possibility of charge decay. The graphs corresponding to the previously mentioned tests are shown in Figure 60.

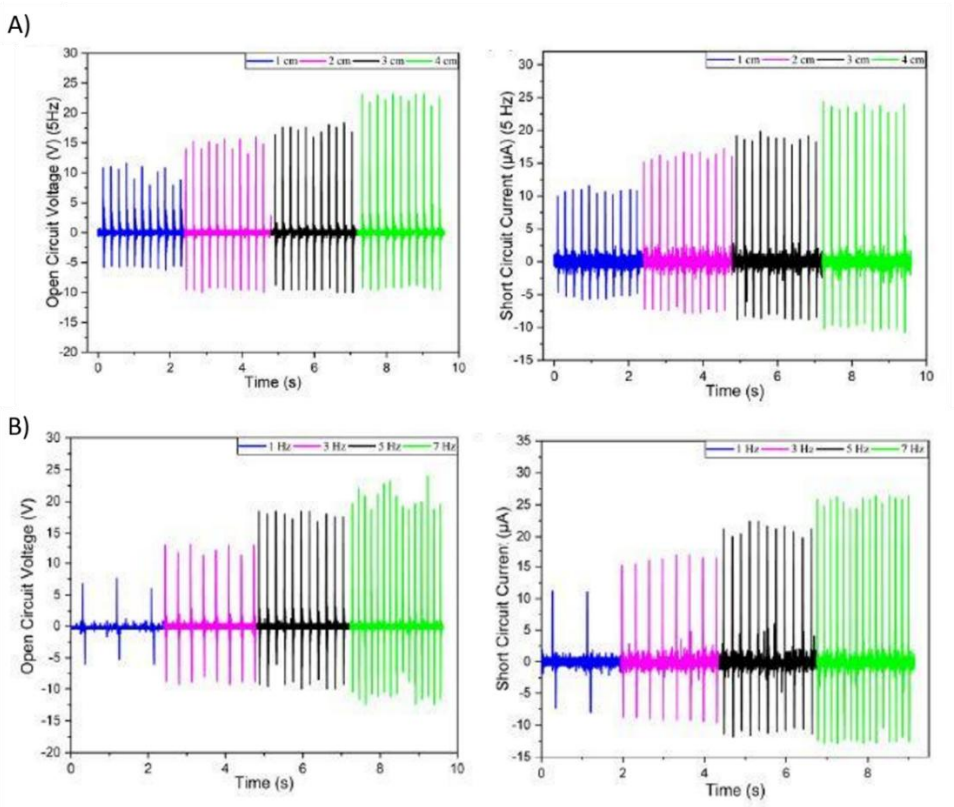

Figure 60: Effect of A) the contact area and B) the contact frequency on the output voltage and current [237].

Another example of setup was used by Akbarinedjad *et al.* [239] to determine the role of triboelectricity in the signal output from piezoelectric nanogenerators tested in different modes, including tapping. A schematic illustration and a picture of the actual testing setup are presented in Figure 61.

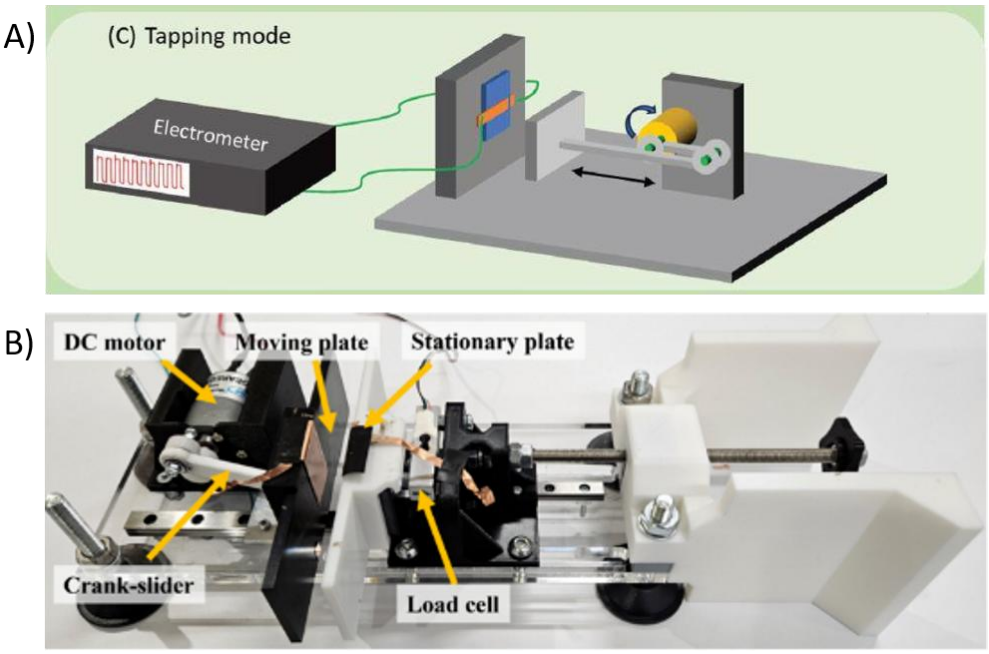

Figure 61: A) Schematic representation and B) photograph of the tapping test setup [239].

Interestingly, the authors showed that all tested materials of the study, including non-poled PVDF, thermally depoled PVDF, poled PVDF and Teflon, showed peak-to-peak open-circuit voltage of 4 V when submitted to a tapping 10 N force at a 3.5 Hz frequency. With some non-piezoelectric materials on the list, the results likely show that the primary contribution to the measured output voltage is in fact triboelectricity, rather than piezoelectricity. A complementary study using the same materials also demonstrated the positive effect of PDMS encapsulation on the output voltage compared to the non-encapsulated devices. As an example, PDMS-encapsulated PVDF displayed an output voltage of 9.4 V, compared to the 4.6 V produced by the same non-encapsulated material. The graphs corresponding to the two studies are displayed in Figure 62.

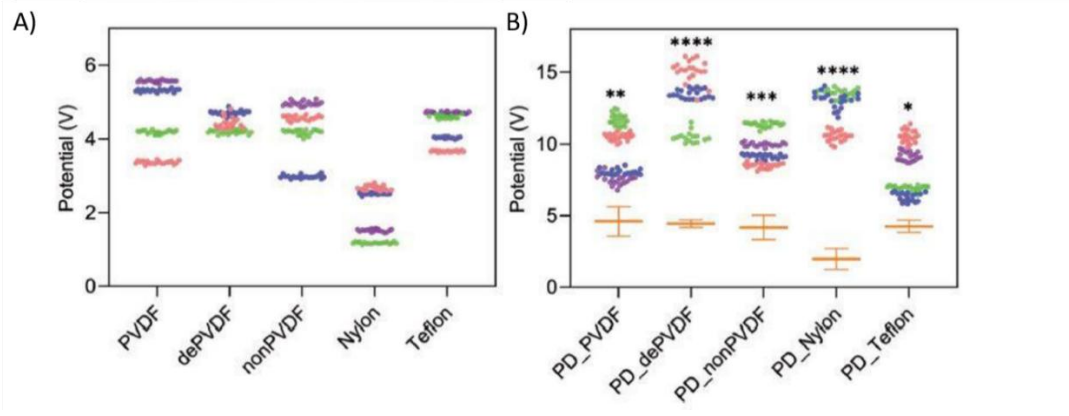

Figure 62: Peak-to-peak open-circuit voltage of A) non-encapsulated and B) PDMS-encapsulated devices made of poled PVDF, depoled PVDF, non-poled PVDF, Nylon and Teflon [239].

In their paper , Sun *et al.* [240] studied electrospun PVDF-TrFE fibres filled with zinc oxide (ZnO), adding functionalised multiwalled carbon nanotubes (F-MWCNT) to enhance the dispersion of ZnO into the PVDF matrix.

Using a horizontal testing setup connected to an oscilloscope, they were able to record the open-circuit voltage as a response to a varying applied force on their devices. The setup and test results are displayed in Figure 63.

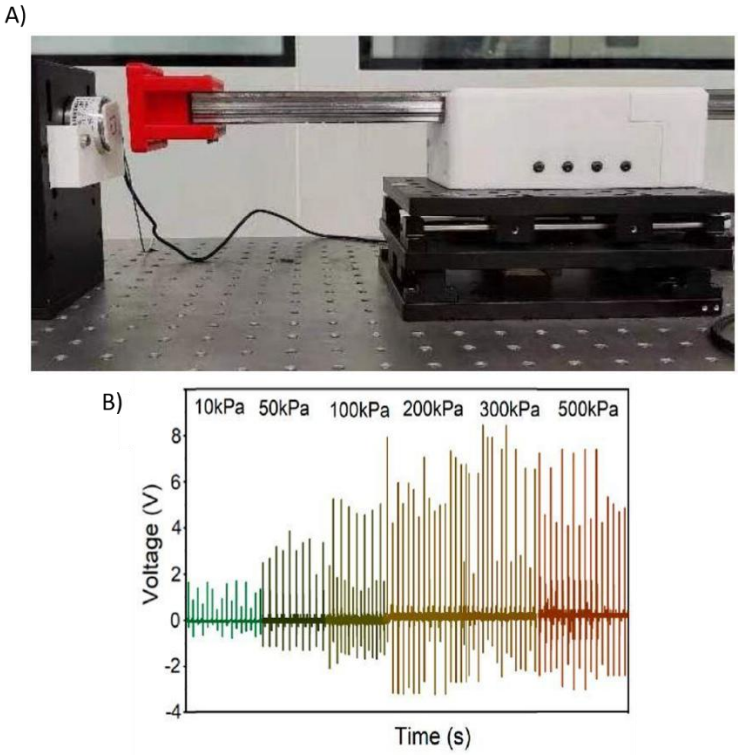

Figure 63: A) Electrical testing setup and B) open-circuit voltage of the device as a function of the applied load [240].

According to this test, the open-circuit voltage first increases with the applied load, with a maximum of 8.2 V obtained at 300 kPa. The proposed explanation for the decrease observed at 500 kPa is the deterioration of the structure of the electrospun scaffold due to the high load.

2.3. Bending test

In addition to the tapping test, bending tests can be useful for replicating a large array of human bodily movements. Again, some research teams resorted to “handmade” testing of their devices, either by simple bending like Yang et *al*. [241], or by directly using the various bending movements of the human body, such as Li et *al*. [242]. In their paper, they successfully used their devices to monitor the motion of various hand, arm, leg and foot joints. The previously described tests are illustrated in Figure 64.

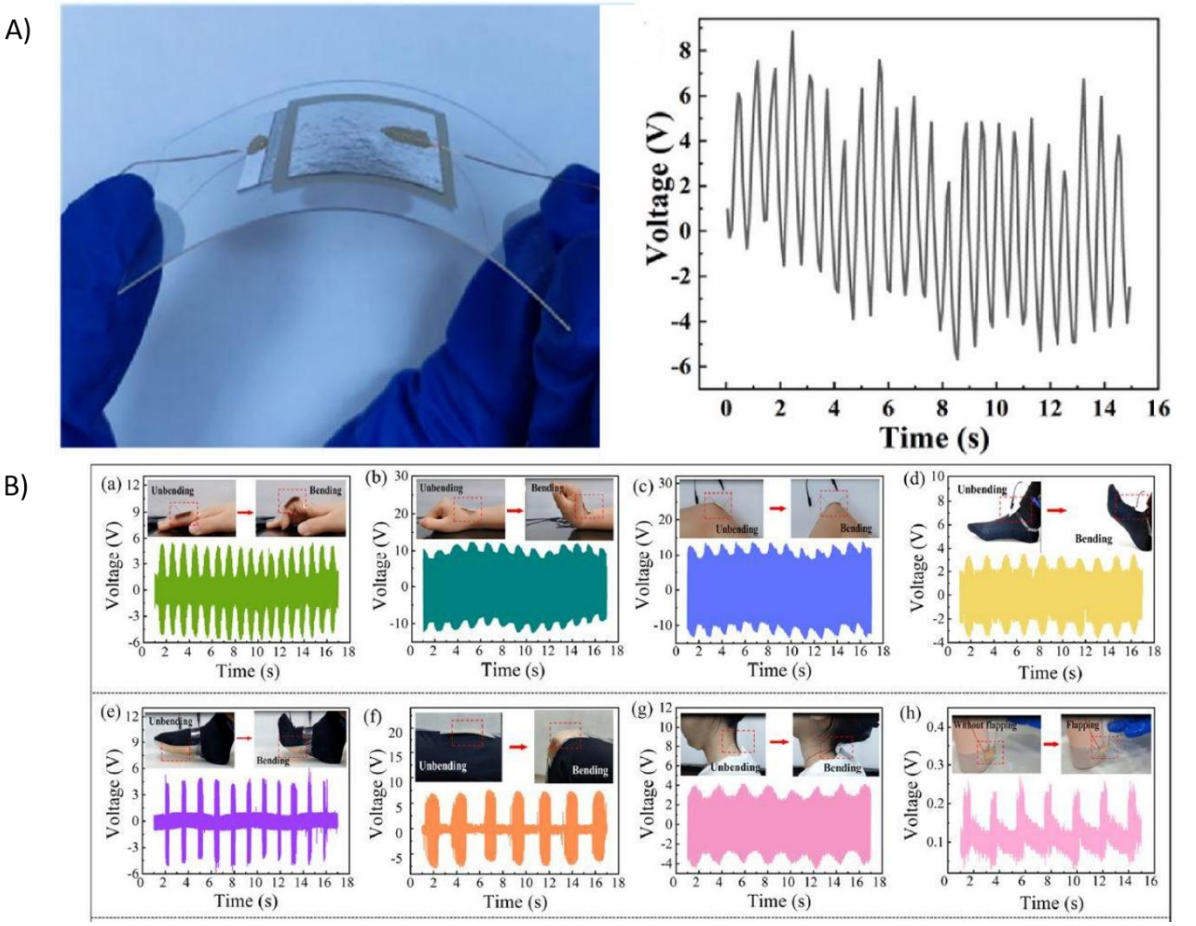

Figure 64: A) Simple bending of a piezoelectric PVDF-based device and output voltage [241] and B) Output voltages of a PVDF-based membrane for monitoring the motions of body joints a) finger, b) wrist, c) elbow, d) ankle, e) toe, f) knee, g) cervical joint of hum and h) water flapping *[242]*.

As such tests lack the precise definition and repeatability, automated test setups have been developed. For example, Deng *et al.* [243] used a horizontal bending test to characterize their PVDF/ZnO nanofibers based bending motion sensor. In their tests, they measured the open circuit voltage and short-circuit current produced by the tested devices as a function of the bending angle, showing the clear dependence of the electrical responses with the bending angle. The test setup and results are displayed in Figure 65.

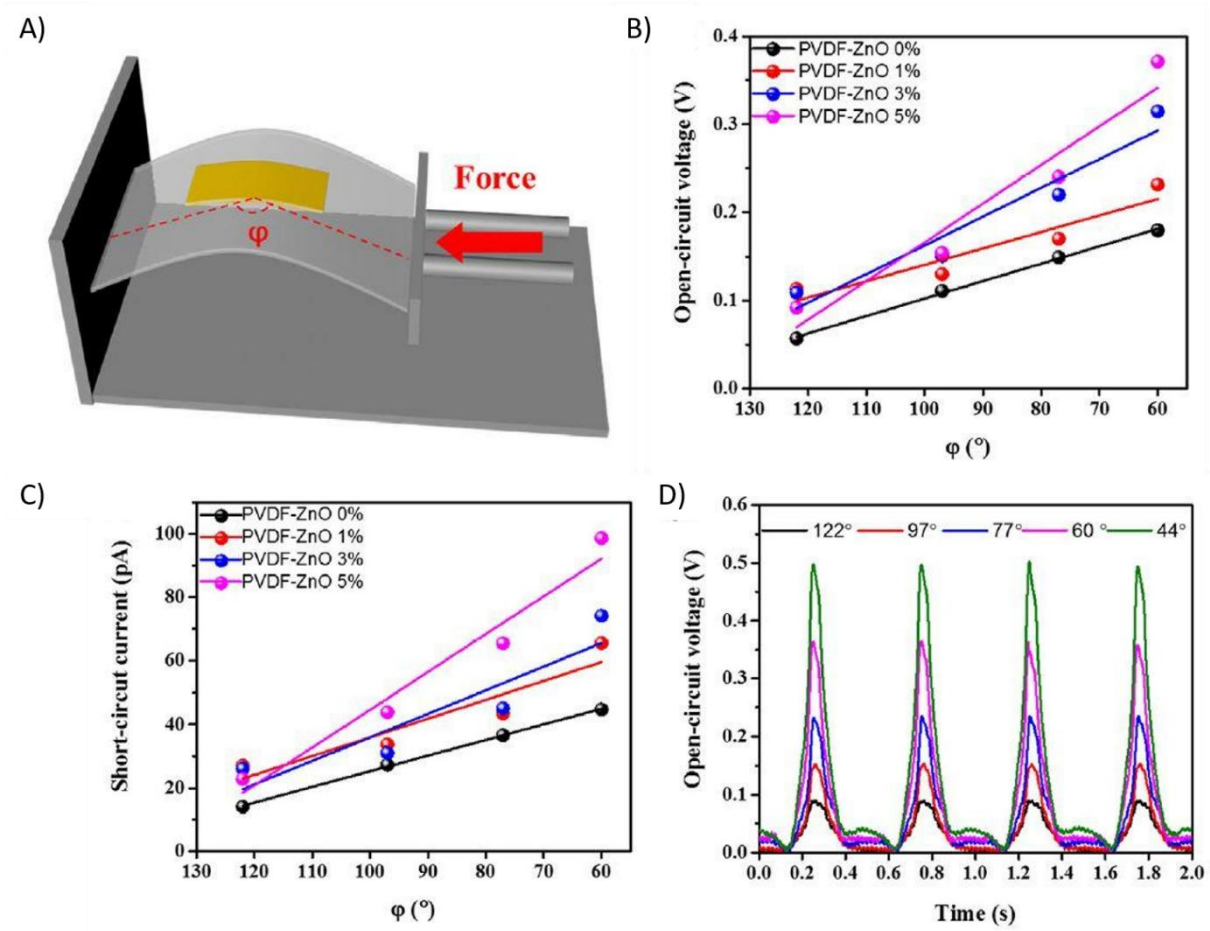

Figure 65: A) Schematic illustration of the bending test, dependence of B) the open-circuit voltage and C) the short-circuit current on the bending angle, and D) an enlarged view showing the dependence of the open-circuit voltage on the bending angle [243].

From the various examples presented previously, it appears clearly that the characterisation of the energy harvesting of PVDF-based devices requires an instrumented testing bench. Indeed, "handmade" tests do not allow to measure and repeat the test conditions, because of the various parameters that influence the response of the devices. The key parameters that must be controlled in order to allow the repeatability of tests are: controlled thickness and contact surface/analysed surface of the samples, control of the applied frequency of solicitation, control of the force applied on the samples.

3. Development of a testing bench in tapping mode

The previous state-of-the-art section has proven the necessity of using a reliable and instrumented setup to test the electrical properties of our electrospun devices. In this section, we present the design, manufacturing and use of our own tapping test bench. The goal was to be able to set different applied forces, modulate the tapping frequency, while ensuring the repeatability of the test. Ultimately, instrumentation is crucial to retrieve the output signals (voltage and current) produced by the tested devices.

3.1. Design

The technical specifications of the tapping test bench aimed at meeting several needs. As seen previously, the response of tested devices widely depends on the contact surface, applied force and frequency of the stimulations. In the case of a tapping test, in means that the testing setup should meet the following requirements:

- The machine should be able to apply a cyclic press-and-release motion to the tested device.

- The applied force should be variable to test the response of the device to increased load, and possibly detect a maximum force over which the sample starts to deteriorate. Moreover, precise determination of the applied load at each cycle allows to ensure the reproductivity of the tests. Usually, the applied force ranges between a few MPa to hundreds of MPa.

- The frequency of the applied force should also be variable. In our case, we are targeting frequency ranging from under 1 to 10 Hz

- The sample holder should be able to hold in place the device across the variating force and frequency applied to ensure the contact surface between the test machine and the sample remains the same. This is particularly crucial for durability tests involving a large amount of testing cycles.

- Instrumentation of the testing bench is another key point, as testing analysing the output voltage and currents are necessary to correctly size the energy harvesting circuits, and corresponding applications

The global architecture of a pestle-like machine includes the structure and organisation of the mechanical and electronic components of the setup designed to strike objects or surfaces. This architecture is usually composed of several interconnected elements such as:

- The rammer: central element of the system, responsible for the impact or striking movement. In our system, it will be mechanically operated.

- The driving system: generates the force necessary for the rammer to strike. It may include motors, hydraulic cylinders, springs or other propulsion mechanisms. In our case, the rammer is activated by transforming a continuous rotational movement of the motor into a reciprocating translation movement, using a flat cam.

- The sensors: integrated sensors can be added to control various parameters like speed, force or position of the rammer. The acquired data can be then used to optimise the operation of the system, and ensure reproducibility of the tests.

- The controller: in automated and semi-automated systems the controller is needed to regulate the movement of the rammer, monitor the sensors or make real-time decisions.

- User interface (UI): in interactive systems, UI are integrated to allow operators to control the different actions of the system. They can take the form of buttons, touch screens, voice commands etc.

- Power: the system requires a power source to operate. In this case, an external electrical power supply was chosen.

A functional diagram illustrating the main parts of the test machine and a photograph of the realised machine are provided in Figure 66.

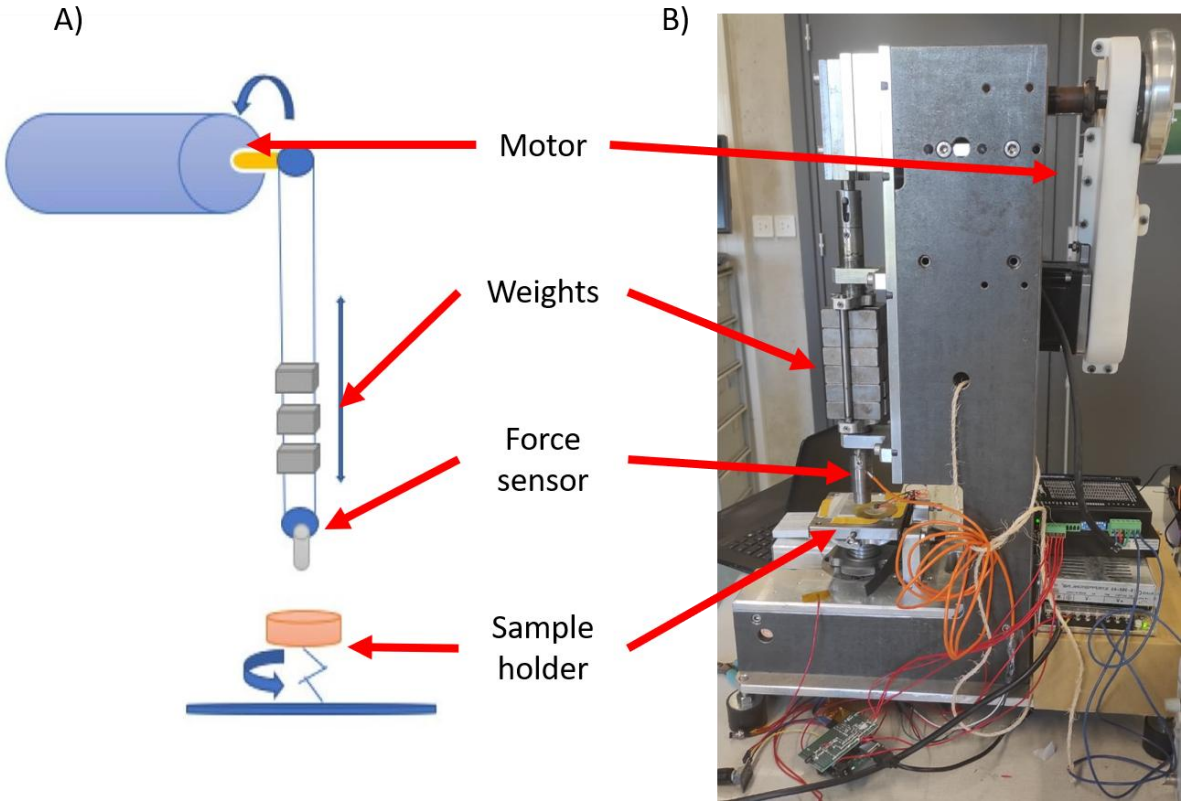

Figure 66: A) Functional diagram and B) photograph of the tapping test bench.

3.2. Manufacturing and implementation

The development of the tapping test setup was carried out by computed aided design (CAD) on Solidworks, allowing the full design and troubleshooting of the machine before the production. The whole test setup was realised at the mechanical workshop of Institut Jean Lamour, with the major help of Emmanuel Vatoux. This section will present some of the technical choices that were made to realise the machine. SolidWorks assembly diagrams are provided in the appendices (see p.iii).

The practical solution adopted for the control of the applied force is the manual addition 1 to 6 weights of 400 g each. With the addition of the rammer and column used to hold the weights in place, it is crucial to correctly seize the motor that will drive to assembly to perform the strokes. As an example, the first iteration of the machine did not allow to add the weights and maintain a steady frequency as the motor torque was way too low. An in-depth study of the system allowed us to find a new motor, the NEMA 34 (34HE59-6004 model from Stepperonline). This stepper motor offers a high torque, up to 12Nm, which is ideal for actioning high weights. Another interesting aspect is the 1,8° step angle (± 5%) allowing precise positioning, as well as adaptation to micro-step operation mode. An illustration of the motor is provided in **Erreur ! Source du renvoi introuvable.**. The motor datasheet is included in the appendices (see p. vi).

The selected driver paired with the NEMA 34 motor is a stepper DM860T driver from Stepperonline. It uses a digital signal processor (DSP) algorithm offering a smooth and reliable operation. With an anti-resonance asset, the driver is able to provide an optimal couple, with reduced instability. Its micro-step resolution can go up to 40000, and maximum input impulsion frequency goes up to a maximum of 200 kHz. An illustration of the driver in provided in **Erreur ! Source du renvoi introuvable.**. The datasheet of the DM860T is provided in the appendices (see p. vi).

To power the motor, a S-350-60 switching power supply from Stepperonline was selected. It was especially designed to work with stepping motors like the NEMA 34. Its main characteristics are an output power of 350 W, output voltage of 60 V DC, and an output current of 5.9 A.

To monitor the force applied to the sample during the test time duration, the force sensor selected is the DYMH-103. Its signal is collected with a circuit board based on an HX711 24 bits analogue-to-digital converter (ADC). Its role is to convert the analogue signals from strain gauges or load cells to digital signals, and can communicate with an Arduino via two electric wires. A photograph of the force sensor mounted on the rammer is provided in Figure 67. The wiring and sensor calibration process are presented in the appendices (see p.viii).

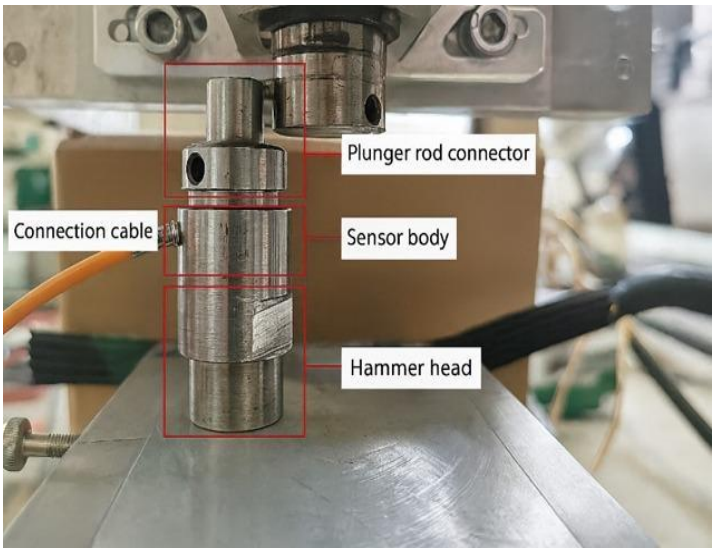

Figure 67: The force sensor mounted on the tapping test setup.

3.3. Electronic control system

The electronic control system is described in detail in the Appendices (see p.viii) . The developed solution allows controlling the motor speed and adjusting the parameters by two approaches: either manually via a potentiometer or via a software interface, which also allows monitoring the force applied to the tested sample.

As a result, two types of user interfaces were developed: one using physical components, and the other with a software approach using Python. The appendix details the pushbutton and encoder parameters, as well as the development of the graphical user interface, which was carried out using PyCharm, a free software based on Python.

3.4.Validation of the test bench

In this section, we will use the tapping test setup on two types of test materials: a PZT buzzer, known to give very strong piezoelectric responses, and one of our PVDF nanogenerators. The direct observation at the device output using a Keithley DMM6500 digital multimeter will allow to estimate the voltage and current output delivered by the devices.

3.4.1. Parasitic effect of motor induction on current measurements

The tapping test bench went through a few iterations, one of the major issues was that the initial motor did not have the adequate power to be able to lift the pestle with the different weight, and reach a 10 Hz solicitation frequency. After the change to the Nema 34 motor, we carried out a series of measurements with the PZT and

PVDF samples and obtained non-coherent results. In particular, we got very high current peaks as shown in Figure 68, where we can see peaks of over 200 µA for PZT, peaks of 60 µA for PVDF, and also an excessively high DC component delivered by the two samples, which does not reflect the physics of the sources.

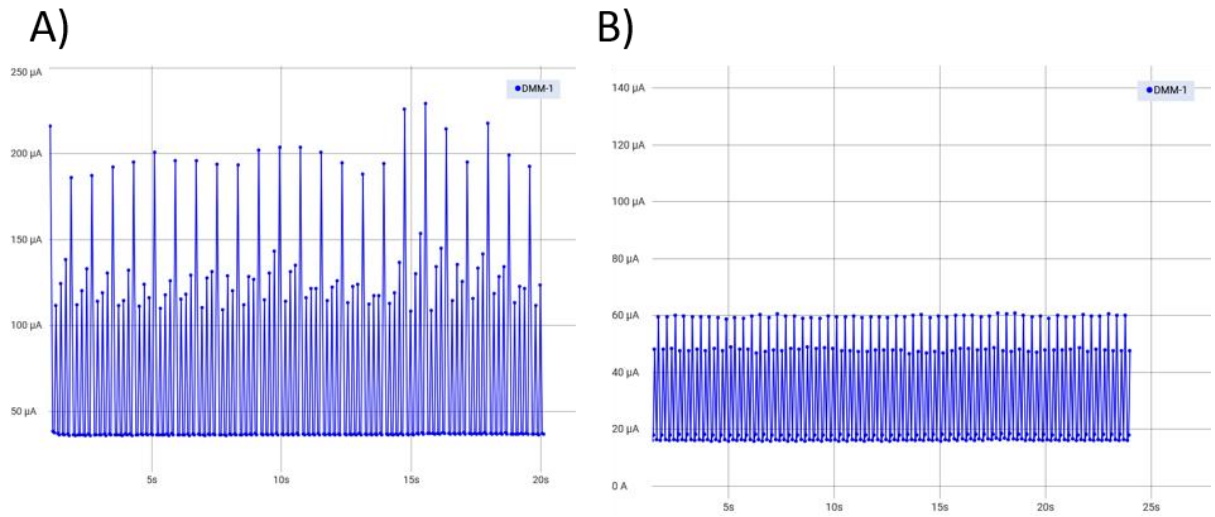

Figure 68: Short-circuit current of A) PZT, B) PVDF.

Given that the motor casing is made of metal, and connected to the metallic chassis of the machine, we assumed that the electromagnetic induction of the motor coils generates a parasitic voltage throughout the chassis and the sample holder. To confirm this, we measured the induced voltage on the chassis with an electrostatic voltmeter and observed a parasitic voltage of 22 V as shown in Figure 69 A).

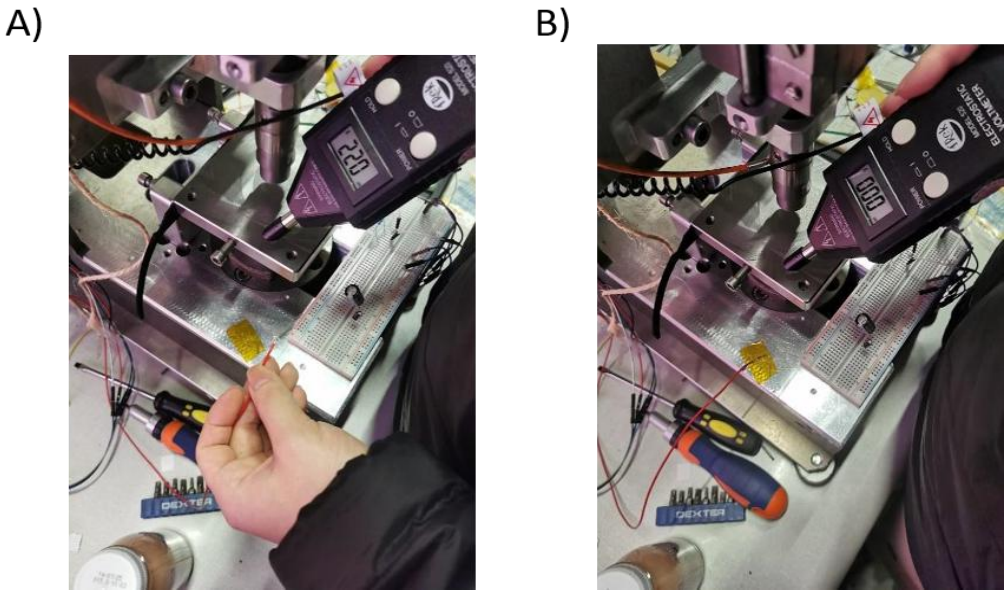

Figure 69: Measurement of motor-induced voltage A) without chassis connected to earth and B) with chassis connected to earth.

To overcome this problem, we decided to connect the chassis to earth in order to eliminate the induced component of the voltage. After connecting the chassis to earth, we can see on the electrostatic voltmeter pictured in Figure 69 B) that the chassis voltage is zero. We then have acquired a new set of measurements with this new configuration.

As we can see in Figure 70, the DC component has almost disappeared, and the peak heights of 80 µA for PZT and 5 µA for PVDF are much more consistent with the expected values.

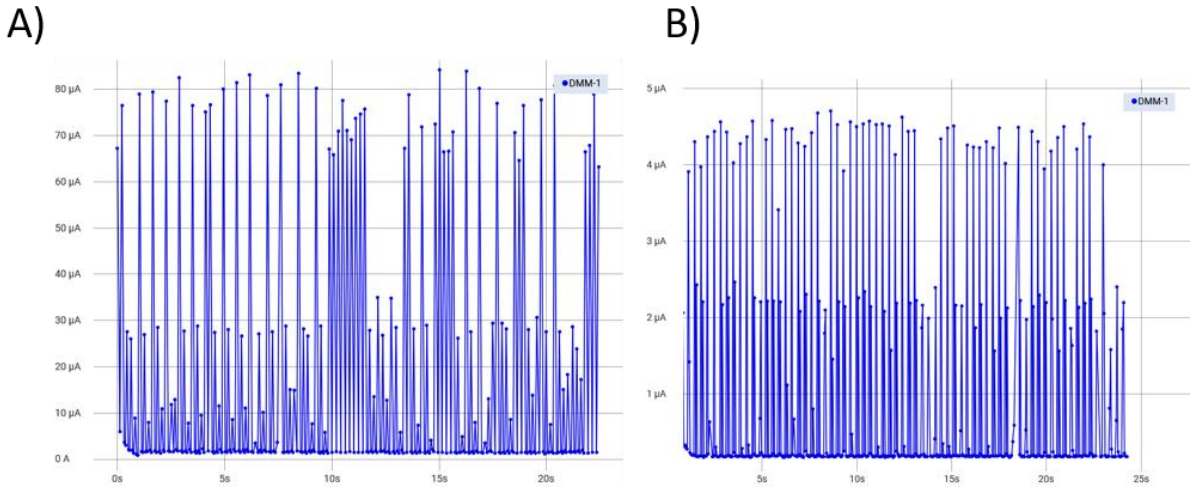

Figure 70: Short-circuit current of A) PZT, B) PVDF.

The mandatory calibration steps of the electrostatic voltmeter used in this part are given in the appendices (Force sensor wiring and calibration steps).

3.4.2. Frequency variation of the solicitation

In order to validate the frequency variation of the pestle, we carried out a series of measurements on a PZT sample, with the aim of observing the impact of the frequency on the voltage signal spectrum. Calculation of the frequency of the two signals gives a frequency of 3.4 Hz (17 peaks over 5 seconds) for Figure 71 A) at a set frequency of 3 Hz, and a frequency of 6 Hz (30 peaks over 5 seconds) for Figure 71 B), at a set frequency of 6 Hz. These results validate the test bench ability to generate mechanical excitations at variable frequencies, and demonstrate the consistency between the programmed frequency and the measured frequency. The slight difference observed at 3 Hz can be attributed to minor variations in the control of the motor at low frequency.

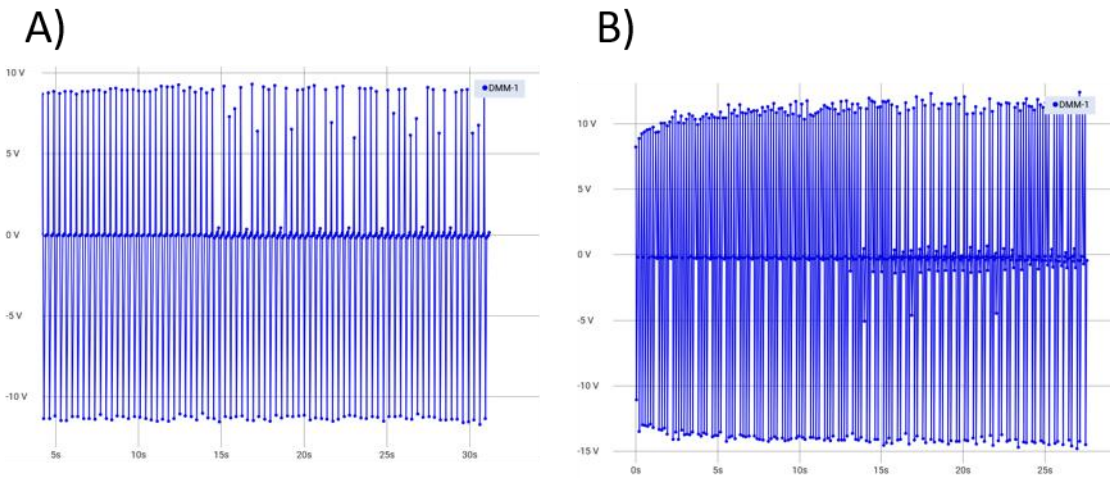

Figure 71: Voltage measurements for two different frequencies A) 3 Hz and B) 6 Hz.

An additional test was carried on a different PZT buzzer by variating the tapping frequency from 1 to 5 Hz without stopping the data acquisition. The results, presented in Figure 72, show the increased density of peaks corresponding to the increased tapping solicitation frequency. Moreover, steps in the intensity values of output voltage appear with each frequency increment. With increased tapping speed, it seems that the tapping force applied to the sample is also increased. Hence, most comparisons between samples were carried out in the continuation of the study at the same tapping frequency of 5 Hz to ensure reproducibility.

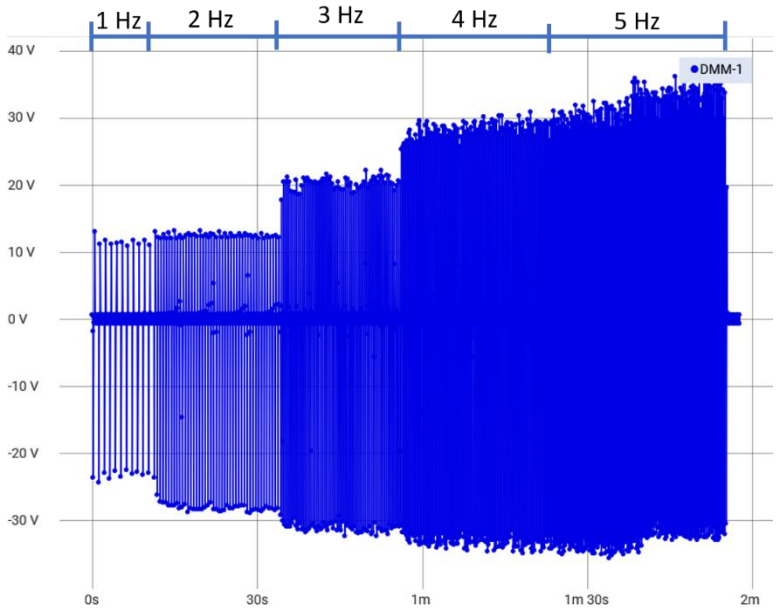

Figure 72: Voltage measurement on a PZT buzzer with variating frequency from 1 to 5 Hz.

Testing the current output response is also necessary. The PZT buzzer was subjected to tapping at a frequency of 1Hz, illustrated by Figure 73 A), and a tapping frequency of 5 Hz, illustrated by Figure 73 B). It is clearly visible from the two graphs that the tapping frequency of 1 Hz produces 1 peak per second, while 5 peaks are visible within the same timeframe for a solicitation of 5 Hz. As previously mentioned, the intensity of the peaks is increased with the tapping frequency, which confirms that the tapping force is also increasing.

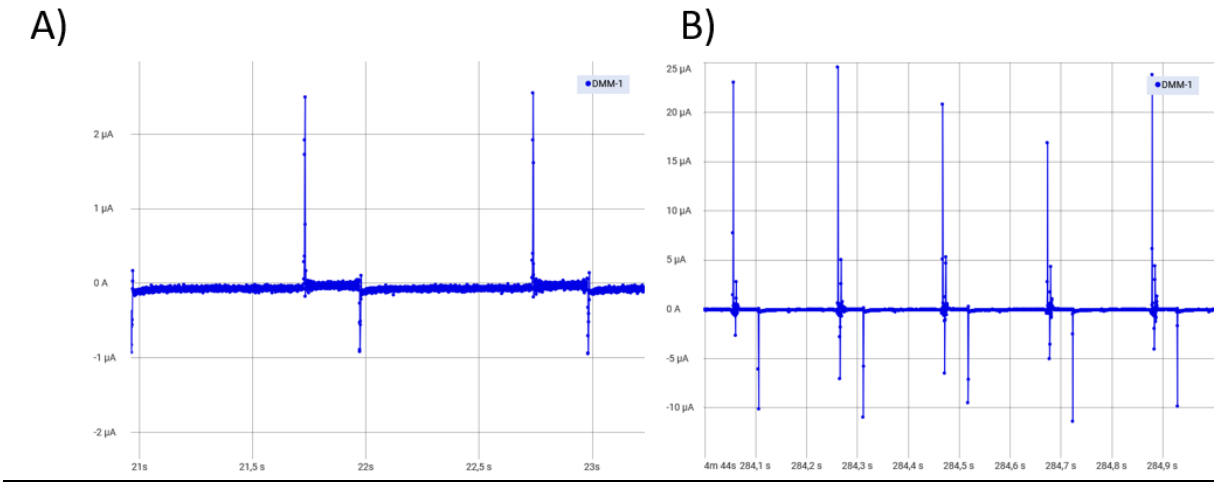

Figure 73: Current measurements for two different frequencies A) 1 Hz and B) 5 Hz.

4. Testing of the electrospun PVDF sensors: influence of the filler addition

We present here the initial results obtained on devices made from the series of samples studied in the previous chapters, with different nanoparticle contents.

4.1. Elaboration process of the electrospun PVDF based devices

The devices are formed of four different parts: the electrospun scaffold, covered on both sides with P-shaped aluminium electrodes, the connection wires, and the PET encapsulation layer. Seven device types were fabricated from electrospun fibres with various cellulose nanocrystals (CNC) or Al-Cu-Fe-B quasicrystals (QC). Table 23 summarises the composition of the different devices.

Table 23: Name and composition of the devices.

Device name	Material and filler content
PVDF	Pristine electrospun PVDF fibres
CNC1	Electrospun PVDF fibres + 1 wt.% CNC
CNC3	Electrospun PVDF fibres + 3 wt.% CNC
CNC5	Electrospun PVDF fibres + 5 wt.% CNC
QC1	Electrospun PVDF fibres + 1 wt.% QC
QC3	Electrospun PVDF fibres + 3 wt.% QC
QC5	Electrospun PVDF fibres + 5 wt.% QC

The elaboration steps are described in detail in Chapter 2. Some pictures illustrating the elaboration process and the finished device are presented in Figure 74.

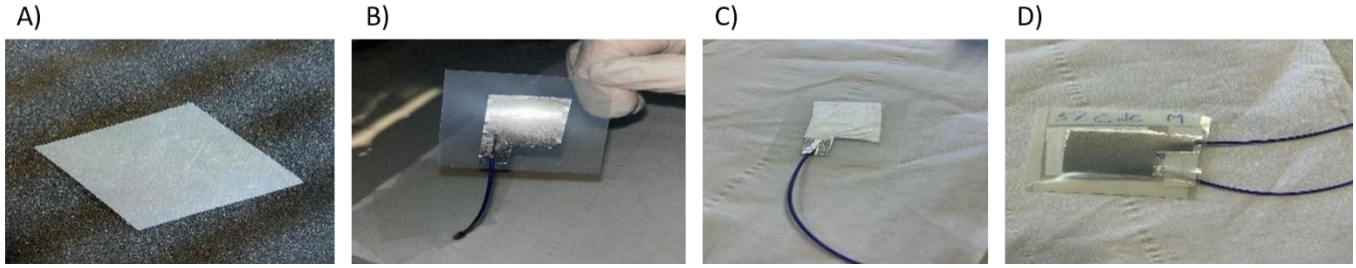

Figure 74: Preparation steps of the PVDF devices A) the PET layer, B) the P-shaped electrode with the connecting wire, C) addition of the electrospun scaffold, D) the finished device.

4.2. Testing of the devices: voltage and current outputs

The electrical characterization of PVDF-based nanogenerator devices was performed using a Keithley DMM6500 configured in Digitize mode. The measurements were managed through the KickStart software interface, which allowed precise control of the acquisition settings. The voltage signal was digitized over a 100 V range with a high input impedance of 10 MΩ, ensuring accurate measurement of small signals without loading effects. For current measurements, the Digitize Current function was set to a 100 µA range, which is well-suited to capture the low currents typically produced by PVDF under mechanical excitation. The sample rate was configured at 5000 samples per second (5 kSa/s), offering sufficient temporal resolution to record the transient voltage and current peaks generated at frequencies between 1 and 5 Hz. The tests were conducted with all the weights placed on the machine, which represents 4 kg in total, with the pestle weight added. The trigger mode was set to Immediate, enabling the measurements to begin without any external delay, and the acquisition was set to continue

indefinitely until manually stopped. These settings collectively ensured a faithful and comprehensive capture of the transient signals produced by the PVDF nanogenerators during mechanical tapping or dynamic loading tests.

The aim of this section is to evaluate the performance of different PVDF-based devices. The study included pure PVDF films as well as PVDF composites incorporating varying concentrations of functional additives. As said, samples were prepared with cellulose nanocrystals (CNC) at concentrations of 1%, 3%, and 5%, and with quasi-crystals (QC) at the same concentration levels. The objective was to investigate how these additives influence the electric response of the device, particularly in terms of energy (voltage and current peaks) generated during dynamic mechanical stress. By analysing and comparing the electrical outputs of these different material configurations, the study aims to identify the most efficient compositions for energy harvesting applications.

4.2.1. Pure PVDF electrospun fibres

The PVDF device was characterised under mechanical tapping at frequencies ranging from 1 to 5 Hz, with all the six weights (400 g each) placed on the machine.

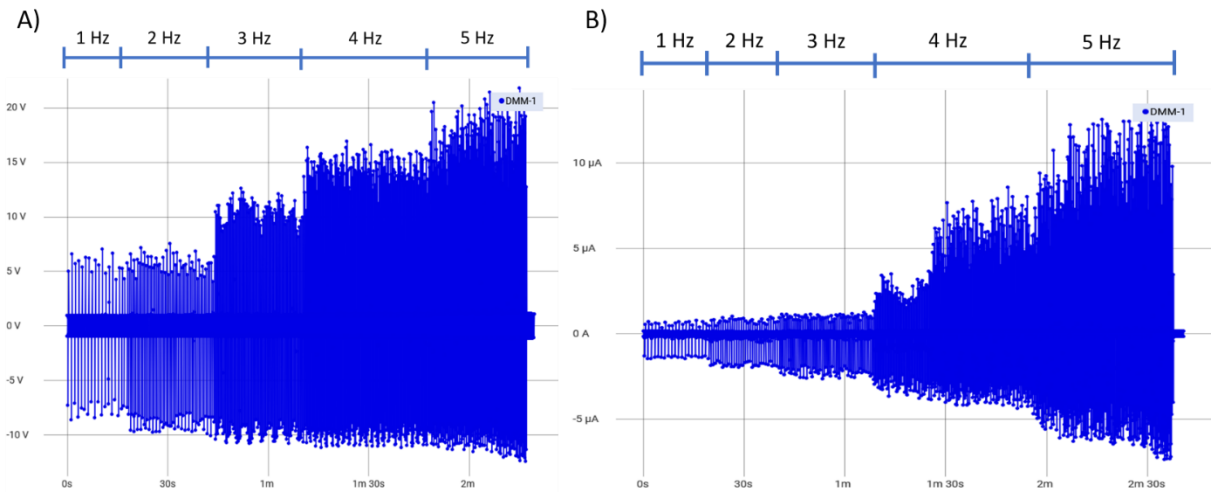

Figure 75: A) Voltage and B) Current waveform of the pure PVDF nanogenerator under mechanical excitations from 1 to 5 Hz.

Figure 75 shows the voltage and current responses of the PVDF devices submitted to tapping with increased frequency, from 1 to 5 Hz. Both signals exhibit a general increase in peak amplitude as the excitation frequency rises, demonstrating the frequency-dependent behaviour of the electric signal. At 5 Hz, voltage peaks reach values up to approximately +20 V in the positive direction and down to about –15 V in the negative direction, resulting in a peak-to-peak voltage of roughly 35 V. Similarly, the current signal shows peaks of approximately +10 µA and –7 µA at 5 Hz, yielding a peak-to-peak current of around 17 µA.

As mentioned, it was chosen to compare the performances of the different devices at a frequency of 5 Hz, as the tapping force is also increased with the frequency, it is the configuration that gives the best output amplitude.

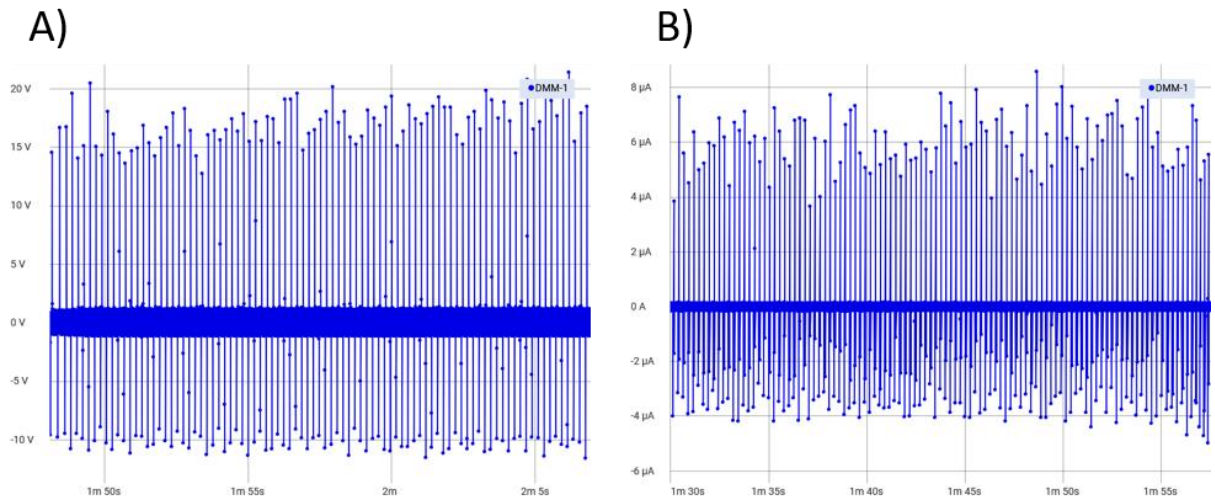

Figure 76: Zoomed view on the 5 Hz solicitation portion of A) Voltage and B) Current waveform of the pure PVDF nanogenerators.

Zoomed views at 5 Hz presented in Figure 76 reveal that the voltage and current waveforms are generally periodic but exhibit noticeable asymmetry between positive and negative peaks. This asymmetry suggests an uneven charge generation during mechanical loading and unloading cycles, which may be attributed to intrinsic properties of the PVDF material, such as preferential dipole alignment or mechanical anisotropy.

Nevertheless, the results confirm that pure PVDF is capable of generating significant electric output under dynamic mechanical excitation. The observed increase in signal amplitude with frequency indicates improved energy conversion efficiency at higher tapping rates.

4.2.2. PVDF fibres with addition of 1-5% CNC

The nanocomposite electrospun fibres were tested in the same way as the pure PVDF fibres. The response to the increased frequency is very similar in its shape to the response observed for the pure PVDF sample. In this section, and the following concerning QC nanocomposites, only the responses to mechanical solicitation at 5 Hz will be included. The complete curves can be found in the Appendices (see p. xvii).

The PVDF-nanocomposites incorporating CNC at concentrations of 1wt%, 3wt%, and 5wt% exhibited significant enhancements in response compared to pure PVDF, as shown in Figure 77. The CNC1 sample demonstrated a positive current peak of approximately +20 µA and a negative peak around –10 µA, resulting in a peak-to-peak current (I_{pp}) of about 30 µA. The voltage response reached +25 V and –15 V, yielding a peak-to-peak voltage (V_{pp}) of roughly 40 V. The signal was stable and well-defined, indicating effective energy transduction and good reproducibility under mechanical excitation at 5 Hz.

With the CNC3 sample, electrical output increased substantially, with current peaks reaching approximately +55 µA, and a peak-to-peak voltage of about 45 V (+20 V/–25 V). However, this enhancement in signal magnitude came at the cost of reduced stability, as the waveforms became more irregular and less reproducible across cycles.

The CNC5 sample achieved the highest output levels, with positive current peaks around +60 µA and a peak-to-peak voltage of 60 V (+30 V/–30 V). Importantly, in addition to its high electrical performance, the signals remained relatively stable and periodic, making the 5% CNC composite a strong candidate for practical energy harvesting applications.

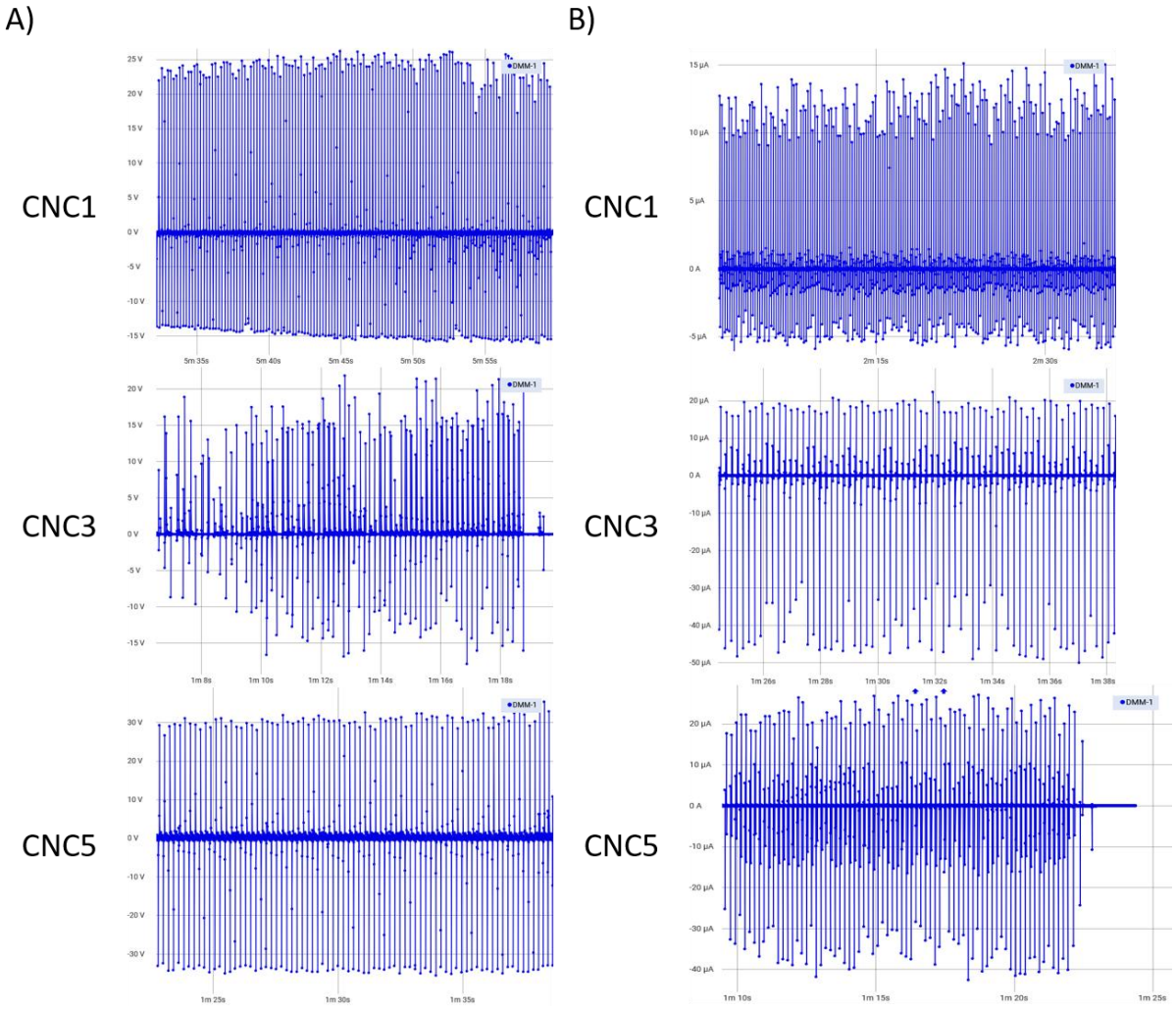

Figure 77: A) Voltage and B) Current waveform of the PVDF-CNC devices under mechanical excitations at 5 Hz.

Therefore, these results presented Figure 77 indicate that increasing CNC concentration enhances the response of the PVDF matrix. The CNC5 composite appears to show the best performances, achieving higher output amplitudes with good signal regularity, making it a promising candidate for energy harvesting applications.

4.2.3. PVDF fibres with addition of 1-5% QC

Similarly to CNC addition, incorporating QC at concentrations of 1wt%, 3wt%, and 5wt% in the electrospun fibres demonstrated significant improvements in response compared to pure PVDF, as shown in Figure 78.

The QC1 sample showed a positive current peak of approximately +25 µA and a negative peak around –10 µA, yielding a peak-to-peak current of about 35 µA. Its voltage response reached with a peak-to-peak voltage of roughly 30 V (+25 V / –5 V). This composition exhibited excellent signal stability and clarity, making it well-suited for consistent energy harvesting applications.

The QC3 composite achieved higher electrical outputs, with current peaks reaching 45 µA peak-to-peak (+20 µA and –25 µA) and 55 V peak-to-peak (+30 V and –25 V). However, these stronger signals were accompanied by increased irregularity and variability in waveform shape, indicating lower reproducibility and potential challenges for practical use.

In contrast, the QC5 composite displayed a more balanced performance, with a peak-to-peak current of about 40 µA (+30 µA / –10 µA) and a peak-to-peak voltage of approximately 35 V (+15 V and –20 V). While moderate

asymmetry and minor fluctuations were still observed, the QC5 composite provided a good compromise between signal amplitude and stability.

Overall, incorporating QC into PVDF significantly enhances electrical output, but the choice of concentration critically affects signal stability. The QC1 composite appears optimal for applications requiring reliable, stable operation, while higher concentrations yield greater electrical output but at the expense of signal regularity.

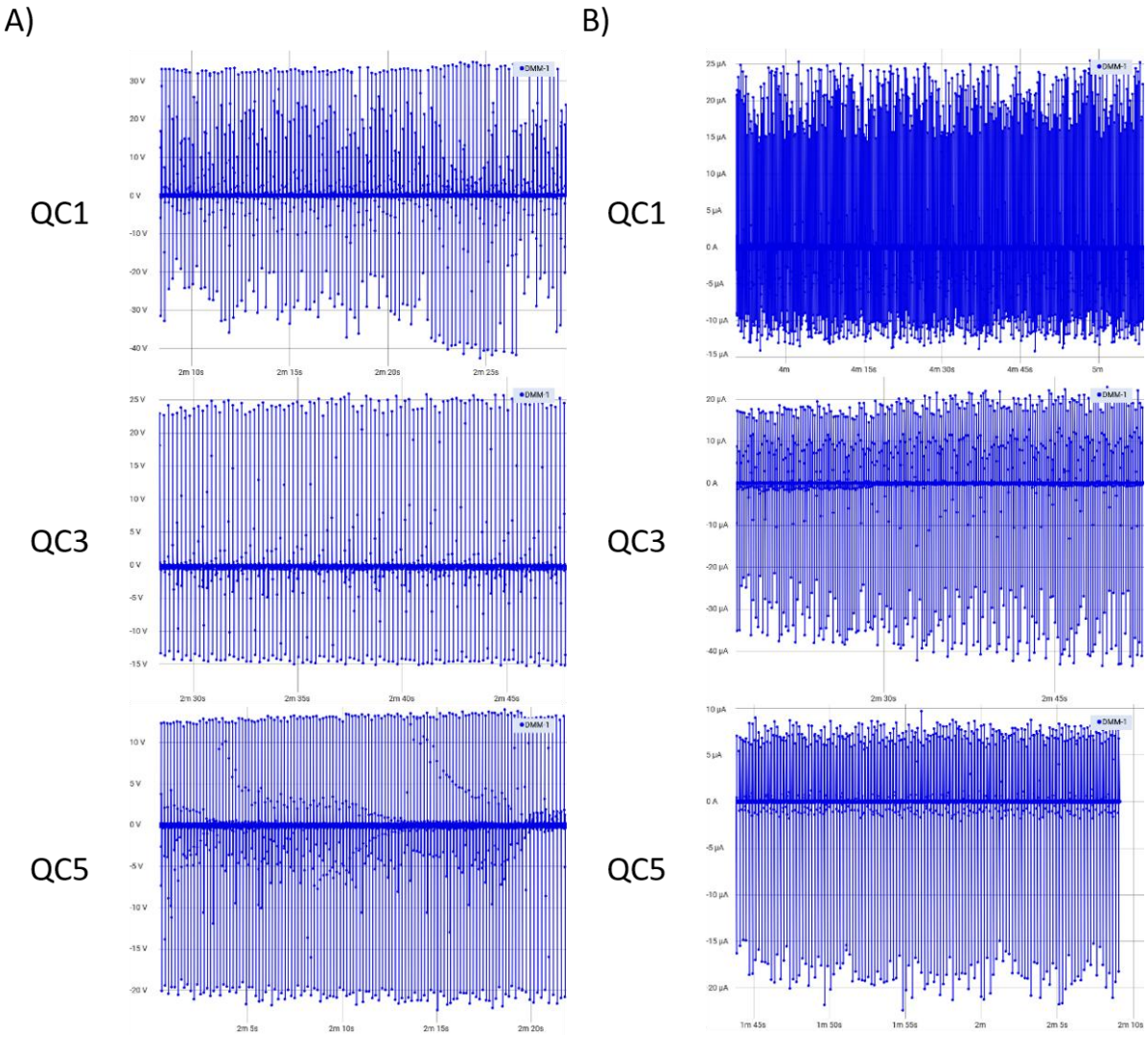

Figure 78: A) Voltage and B) Current waveform of the PVDF-QC devices under mechanical excitations at 5 Hz.

4.2.4. Conclusion and selection of the best sample

Table 24 provides a summary of the different results obtained from the testing of the PVDF, PVDF-CNC and PVDF-QC devices in tapping mode (5 Hz and 4 kg).

Table 24: Comparative table of the PVDF-Based Nanogenerators electric performances.

Material	+ Voltage (V)	– Voltage (V)	V_{pp} (V)	+ Current (µA)	– Current (µA)	I_{pp} (µA)	Signal Stability
PVDF	+20	–15	35	+10	–7	17	Good
CNC1	+25	–15	40	+20	–10	30	Good
CNC3	+20	–25	45	+30	–25	55	Low (unstable signals)
CNC5	+30	–30	60	+30	–30	60	Good
QC1	+25	–5	30	+25	–10	35	Excellent
QC3	+30	–25	55	+20	–25	45	Low (irregular signals)
QC5	+15	–20	35	+30	–10	40	Good, slight residual asymmetry

The experimental results confirm that PVDF-based nanogenerators exhibit measurable electric responses under dynamic mechanical excitation. Pure PVDF generates moderate voltage and current outputs with good stability, forming a reliable baseline material.

Compared to composite PVDF materials containing CNC or QC additives, the electrical output of pure PVDF remains moderate, underscoring the potential advantages of using fillers to enhance electric performance. Adding CNC or QC fillers significantly improves the electrical performance of PVDF, increasing both voltage and current peaks. However, higher filler concentrations can introduce signal instability and asymmetry. The PVDF-CNC composites demonstrated the highest overall amplitudes, with the CNC5 sample achieving strong signals while maintaining good stability. Meanwhile, PVDF-QC composites offered excellent signal clarity at lower concentrations but showed increased irregularities at higher levels.

Overall, these findings indicate that material optimization—particularly in selecting filler type and concentration—is essential for developing efficient and reliable energy harvesting devices based on PVDF nanogenerators. The sample selected for the following application section is the CNC5 nanocomposite.

4.3. Electrical response analysis under applied loads

In this experimental study, we analysed the electrical response of the PVDF nanogenerator under applied mechanical loads of 1.6 kg, 2.4 kg, 3.2 kg, and 4 kg. For each mass, the frequency was increased from 1 to 5 Hz, and voltage waveforms were recorded using the Keithley DMM6500 and KickStart software. The corresponding curves are presented in Figure 79.

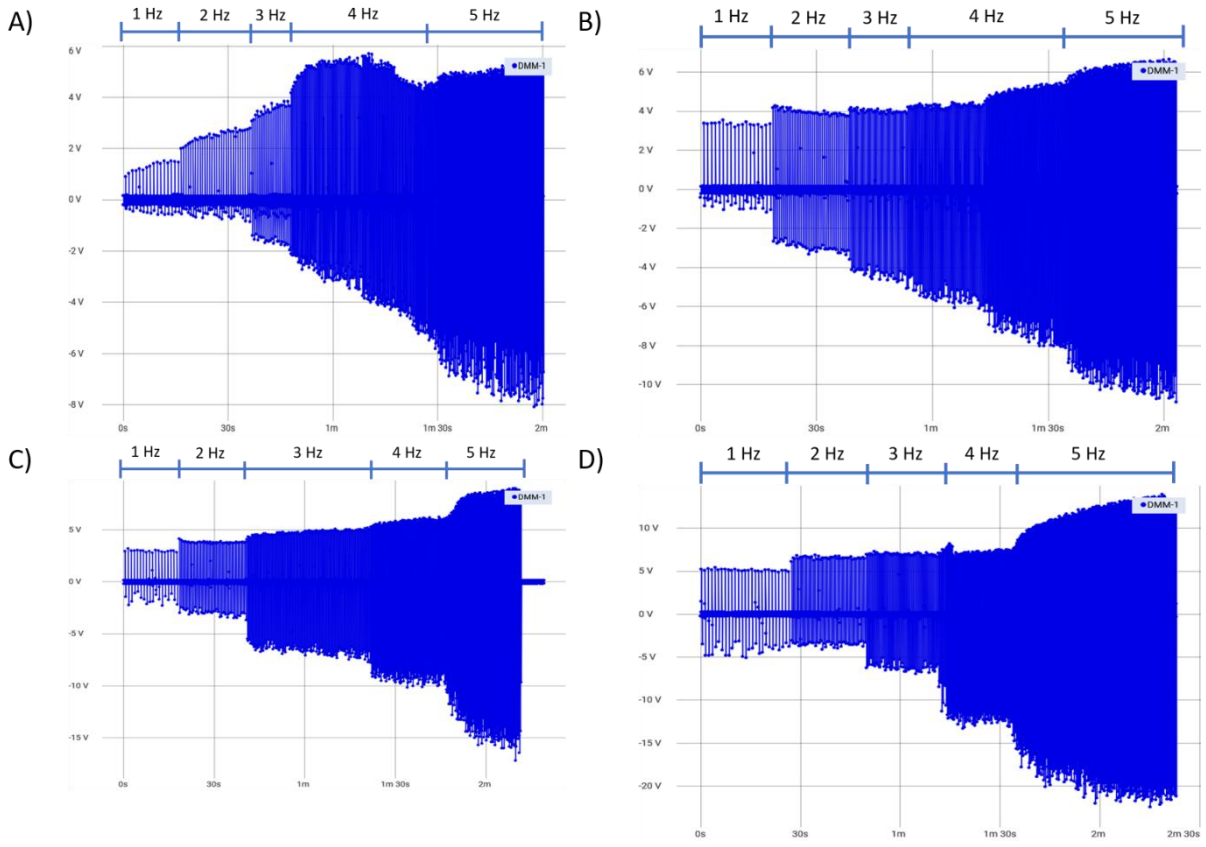

Figure 79: Voltage waveforms generated by the PVDF nanogenerator under increasing mechanical loads: A) 1.6 kg, B) 2.4 kg, C) 3.2 kg, D) 4.0 kg.

From the measurements, we observed that the peak voltage (V_{peak}) generated by the PVDF nanogenerator increases with the applied force and the piezoelectric properties of the material. The experimental observations made based on Figure 79 give the following values:

- For F = 19.6 N (2 kg), $V_{peak} \approx 6$ V
- For F = 24.5 N (2.5 kg), $V_{peak} \approx 8$ to 10 V
- For F = 29.4 N (3 kg), $V_{peak} \approx 12$ to 15 V
- For F = 34.3 N (3.5 kg), $V_{peak} \approx 15$ to 18 V
- For F = 39.2 N (4 kg), $V_{peak} \approx 20$ to 22 V

From those results, it is visible that higher loads result in greater deformation of the PVDF material and thus in stronger signals. This demonstrates a clear positive correlation between mechanical force and electrical output.

4.4. Validation of the PVDF nanogenerator using a full-bridge rectifier

To experimentally validate the energy-harvesting capability of the PVDF nanogenerator, a simple circuit was implemented, based on a full-wave diode bridge, a capacitor and a red LED (see Figure 80) . This setup is a widely used and intuitive method to demonstrate the ability of a nanogenerator to power a real electronic load.

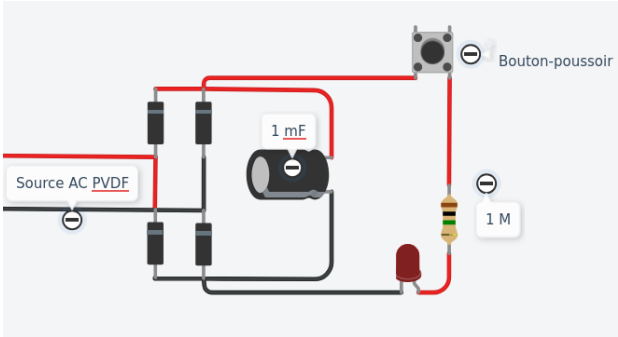

Figure 80: Energy harvesting and discharge circuit using a PVDF nanogenerator.

In this configuration, the AC output of the PVDF nanogenerator under mechanical excitation is connected to a full-bridge rectifier built using four 1N4007 diodes. The rectified signal is then directly applied to a red LED. The choice of a full-wave rectifier allows the system to utilize both the positive and negative voltage peaks generated during mechanical excitation, effectively doubling the frequency of rectified pulses.

It is important to note that the 1N4007 diodes exhibit a forward voltage drop of approximately 525 mV each. Since two diodes conduct simultaneously in each half-cycle, the total voltage drop across the bridge is roughly 1.05 V.

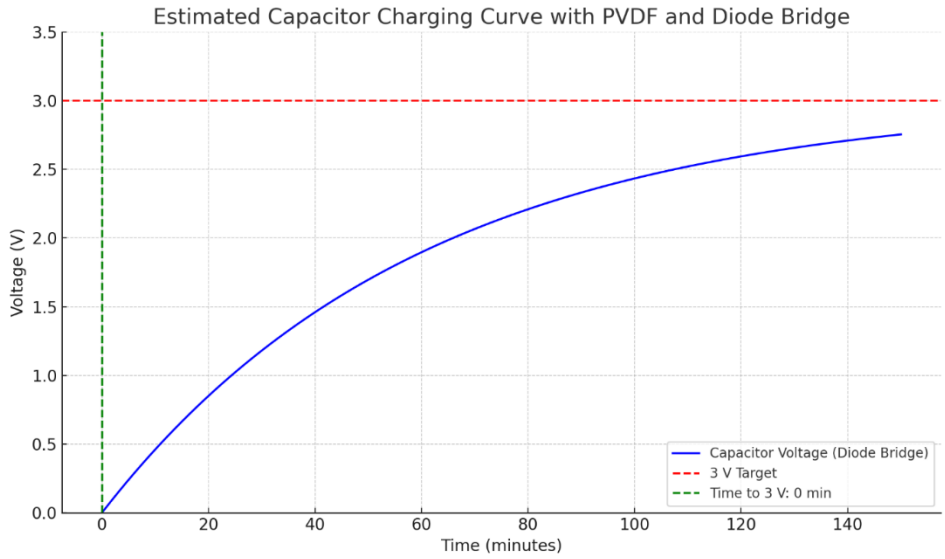

Figure 81: Estimated capacitor charging curve with PVDF and diode bridge.

Figure 81 shows the charging curve of a capacitor powered by a PVDF-based nanogenerator connected to a full-wave bridge rectifier - estimated from real data obtained using a DMM6500 in digitize mode during charging experiments, under mechanical excitation (4 kg tapping at 2 Hz). The voltage across the capacitor follows a typical exponential behaviour, gradually increasing to approximately 2.7 V after 150 minutes. This curve illustrates the limited efficiency of passive rectification when using nanogenerators like PVDF: the capacitor fails to reach 3 V even after prolonged excitation, due to the voltage drop across the diodes and the inherently low current output of PVDF. Despite this, the exponential shape of the charging curve is preserved, reflecting the typical RC charging behaviour of the system. After 150 min of charge, the stored energy allowed to light a red LED for about 3 seconds.

These results demonstrate that a PVDF nanogenerator, even when connected to a simple full-wave diode bridge, can charge a capacitor slowly over time. However, non-regulated voltage, high diode losses and slow accumulation severely limit the practical efficiency of this method. Additionally, most applications require a regulated power

supply (e.g. 3V), which requires an integrated voltage regulator. For more effective and usable power output, dedicated energy harvesting circuits are necessary.

5. Energy harvesting electronic circuits and optimisation

Energy recovery from piezoelectric sources can be achieved using recovery circuits that store the electrical energy supplied by the transducer.

The composition of the components of these circuits can vary according to the type of application. As the piezoelectric source behaves as a high-impedance AC voltage source, it is necessary to rectify this voltage so that it can be used for applications requiring a DC power supply. Some applications also require a regulated power supply to operate nominally. It is important to note that as the power generated by the piezoelectric transducer is generally low, the choice of components for the recovery circuits is crucial. This includes sizing the rectifier, filter and energy storage elements to optimise the efficiency and performance of the energy recovery system. This approach makes it possible to cover a wide range of potential applications while taking account of the constraints associated with the low power of piezoelectric sources.

5.1. Comparison of commercially available energy harvesting circuits

While it is still common for research papers to demonstrate the energy harvesting possibilities of their nanogenerator devices using a simple bridge rectifier coupled to a capacitor, steps towards circuit optimisation to enhance the energy harvesting efficiency have led to the development of several commercial electronic circuits. Among the commercially available solutions we have selected three systems: LTC3588-1 from Analog Devices, AEM30330 from E-Pease and EH300 from Advanced Linear devices. The aim of this part is to present them, and select the best suited one for our targeted applications.

5.1.1. LTC3588-1 (Analog Devices)

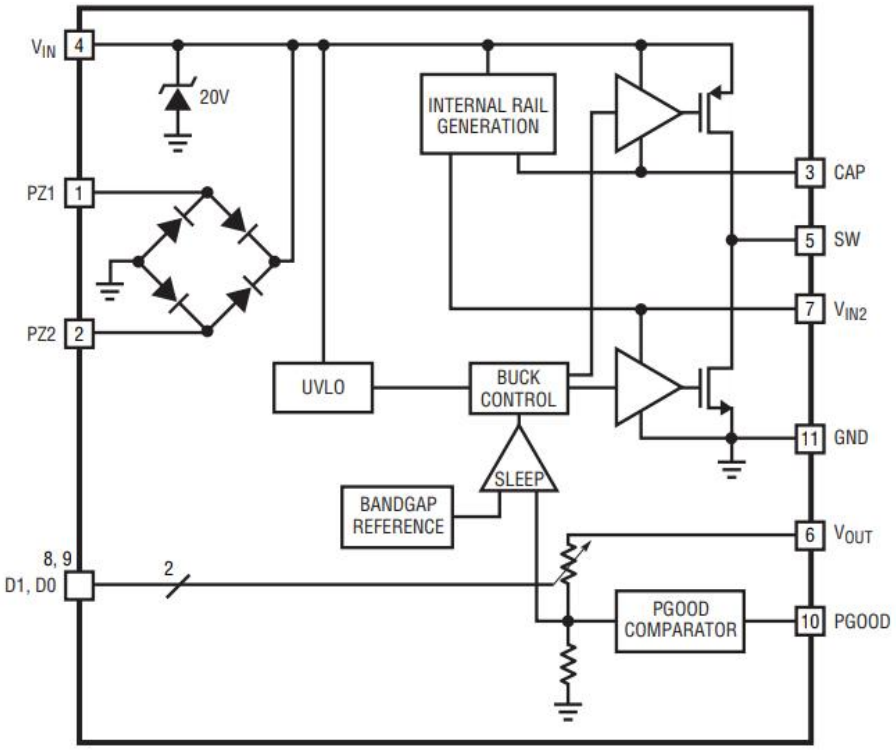

Figure 82: Internal Functional Block Diagram of the LTC3588-1 piezoelectric energy harvesting power supply.

As shown in Figure 82, this solution is an integrated circuit dedicated to energy harvesting from high impedance sources, such as piezoelectric transducers. It integrates a low-loss bridge rectifier, a high-efficiency buck regulator and a protective shunt limiting the input voltage to 20 V. It operates by accumulating energy in an external storage capacitor (C2), which then feeds the Buck converter to generate a regulated voltage of 1.8 V, 2.5 V, 3.3 V or 3.6 V, depending on the load requirements. This circuit is integrated into the DC1459A evaluation board, which facilitates its operation by providing the necessary components for its operation, including an external storage capacitor (C2) and a configuration for testing different output voltages [244,245]. The system architecture is designed as follows:

- Low loss bridge rectifier: The circuit incorporates an internal Graetz rectifier to convert AC energy from a piezoelectric device into a usable DC voltage. This bridge rectifier has a low voltage drop (~400 mV at 10 µA), minimising losses and optimising the energy recovered. A protection shunt is built in to limit the input voltage to 20 V, avoiding any risk of overvoltage that could damage the circuit.

- External storage capacitor (C2): After going through the rectifier, the input voltage is stored in the C2 capacitor which serves as an intermediary source for the buck converter

- Step-down voltage regulator (Buck Converter): When the voltage in C2 reaches a set threshold, the buck converter is activated to convert the stored energy into a regulated voltage of 1.8, 2.5, 3.3 or 3.6V depending on the needs. This converter operates in hysteretic mode, charging the output in pulses, and optimising energy efficiency. It can supply a current up to 100 mA, provided the stored energy is sufficient.

- Power management: When the output voltage reaches the set threshold, the buck converter goes into sleep mode, reducing the consummation to a few nA. In case of energy consumption causing the voltage to go below the set sleep threshold, the Buck converter is reactivated and starts drawing in C2 again. This cyclical operation mode maximises the use of a weak and intermittent energy source.

- Undervoltage lockout (UVLO): Undervoltage Lockout (UVLO) is a protection mechanism in the LTC3588-1 that prevents the Buck regulator from operating when the input voltage is too low to ensure stable conversion. This mechanism is based on two thresholds:

    - UVLO Rising (activation): When the input voltage (VIN) reaches 4.04 V at typical and 4.30 V at maximum, the Buck Converter activates and starts to regulate the output voltage (VOUT).

    - UVLO Falling (deactivation): If VIN falls below 2.87 V typical and 2.66 V minimum, the Buck deactivates to prevent unstable operation.

For an output regulated to 1.8 V, buck operation is conditioned by these thresholds. As long as VIN remains below 4.04 V, the buck remains inactive and VOUT is zero. When VIN reaches 4.04 V, the buck starts up and attempts to stabilise the output voltage. However, if the energy stored in capacitor C2 is insufficient and VIN drops below 2.87 V, the Buck cuts out immediately and VOUT collapses. It does not restart until VIN returns above the activation threshold.

We carried a test with the DC1459A board, a commercial card integrating the LTC3588 and allowing the testing of this component, using an electrospun PVDF-based device as the power source. This device produces 9V and 34µA as outputs after a full bridge rectifier. During the test, we observed that the C2 voltage could reach 11V, but the VOUT output remained at a few millivolts. Normally, the Buck should be started, as VIN is over the UVLO rising threshold set at 4.04 for a 1.8V output. Here, C2 stays charged at 11V without triggering the energy conversion. The probable explanation for this stem from the high impedance of our PVDF entrance power source, which is limiting the LTC3588-1 ability to extract a sufficient current to start the Buck converter. Even if the voltage meets

the requirement to make it work, the current might be too low to provide the needed power to activate the Buck converter, thus explaining why the output voltage remains almost null. In short, our device does not provide sufficient current to trigger the operation of this energy recovery card.

5.1.2. AEM30330

The AEM 30330 is an energy management circuit designed to recover energy from very low power sources. It incorporates a high-efficiency buck-boost converter and a set of energy management circuits for optimised conversion to power low-consumption electronic devices. It works by accumulating energy in a supercapacitor or battery, which is then used to power the converter to generate a regulated voltage of 1.2 V, 1.8 V or 2.5 V, depending on the needs of the application [246,247].

The AEM 30330 operates with an input voltage of between 100 mV and 4.5 V. However, piezoelectric nanogenerators often generate AC voltages of up to several tens of volts, which is well beyond the range supported by the AEM30330. Without proper adaptation, these high voltages can damage the circuit. Preliminary rectification and regulation are therefore essential to make these sources compatible. An evaluation board that directly integrates a diode bridge for rectification and a Zener diode (5.1 V) for overvoltage protection is commercially available for the AEM30330. This board allows the AEM30330 to be tested without having to design an external protection circuit, simplifying its integration with alternative sources such as piezoelectric PVDF [247].

The AEM30330 is designed to extract and condition energy from high-impedance, low-current sources. It has an input capable of handling low input voltages, as previously mentioned, optimising energy recovery from intermittent sources. Once collected, the energy is stored in a supercapacitor (e.g. 4700 µF) or an intermediate battery before being supplied to the load. The AEM30330 provides precise control of storage through a number of configurable thresholds that determine the minimum and maximum voltage levels allowed. These levels can be adjusted via external resistors to suit the specific constraints of the application.

To optimise system autonomy, the AEM30330 has two integrated power management modes:

- Sleep Mode: When the output voltage reaches the target level and the load does not require additional current, the circuit goes into sleep mode to minimise consumption.
- Wake-Up Mode: If the load is consuming power and the output voltage drops below a predefined threshold, the inverter automatically reactivates and supplies power to the load.

5.1.3. EH300

The EH300 module is a solution for managing and converting energy from various sources, such as piezoelectric generators, micro-generators or photovoltaic cells. It stores the energy recovered and supplies it in the form of a regulated voltage of 1.8 V to 3.6 V, providing a stable power supply for low-power electronic devices [248]. The EH300 is designed to operate with a wide range of input voltages, from 0 V to ±500, AC or DC, and can handle input currents from 200 nA to 400 mA. This flexibility means it is compatible with a variety of power sources, whether DC, AC or pulsed.

The EH300 module stores energy from the input source in a bank of internal capacitors. It operates using hysteretic control to switch between two voltage thresholds:

- VL (minimum voltage, 1.8 V): threshold below which the power supply is deactivated to prevent excessive discharge.

- VH (maximum voltage, 3.5 V): threshold at which energy is released to supply the load.

After evaluation and experimental testing of the three commercial energy harvesting modules, namely LTC3588-1, AEM30330, and EH300, the EH300 module offers the best performance and system compatibility for our specific application based on PVDF nanogenerators. The main characteristic of each module is summarised in Table 25.

Table 25: Comparison of the energy management modules.

	LTC3588	**AEM30330**	**EH300**
Converter type	Buck	Buck-boost	Threshold regulation
Input voltage (V_{in})	Up to 20 V	100 mV to 4.5 V	Up to 500 V
Energy storage	Capacitor	Supercapacitor/battery	Capacitor/battery
MPPT (power optimisation)	None	Yes, customisable	None
Standby power consumption	450 to 950 nA	875 nA (VSTO = 3.7 V, VLOAD = 2.5 V)	Always active (dynamic consumption)
Power consumption in use	Up to 250 µA	Tens of µA	
Energetic efficiency	50 to 80 % depending on the charge	Up to 80%	Depends on the stored and available energy (~80 %)
Typical applications	Piezoelectric energy harvesting	IoT, autonomous sensors, solar or vibration energy harvesting	Powering of low consumption circuits, high voltage sources
Constraints	Variable performance	Input voltage limited to 4.5 V: necessary to add an external regulation for higher input sources	No standby mode
Activation current threshold	Not specified – failed to trigger with low-current (PVDF or PZT) source	Low (µA range)	Very low (nA range)

While the LTC3588-1 is a compact and efficient solution in theory, its activation current threshold is incompatible with the very high impedance and low current output. In practice, even though the harvested voltage exceeded the UVLO threshold, the circuit failed to trigger energy conversion, confirming its limited applicability for our system.

The AEM30330 presents better adaptability to low-voltage sources and offers robust power management features including sleep and wake-up modes. However, its restricted input voltage range (maximum of 4.5 V) necessitates the addition of external protection when interfacing with high-voltage AC signals. This adds complexity, volume, and potentially reduces overall efficiency.

In contrast, the EH300 was specifically designed to operate across a very wide input range (up to ±500 V AC or DC), This is particularly beneficial for intermittent energy sources like PVDF nanogenerators, where energy is accumulated over time and must be released precisely to power downstream electronics such as BLE transmitters. Moreover, the EH300's low activation current requirements, its stability in handling pulsed or AC signals, and its minimal external component dependency simplify integration and increase the system's robustness

Based on our experimental results, the EH300 module was selected as the optimal energy management solution for integrating with our PVDF-based nanogenerator and low-power wireless communication system. The EH300 card has two versions with different storage elements, the EH300A and the EH300 itself.

5.1.4. Experimental Comparison: EH300, EH300A, and passive diode bridge circuit

To evaluate the performance of various energy harvesting circuits, a series of experimental tests were conducted using a PZT piezoelectric disc as the mechanical-to-electrical energy source. The tests compared three different circuits: a traditional diode bridge (passive circuit), the EH300 module, and the EH300A version.

5.1.4.1. Reference: Passive Diode Bridge

In the first experiment, the AC voltage generated by the PZT was rectified using a simple diode bridge (passive configuration), without any regulation or power control circuitry. The rectified output was used to charge a 47-mF supercapacitor. The device was subjected to periodic mechanical stimuli for 90 minutes, at the end of which the capacitor voltage reached 3 V. While functional, this result highlights the limitations of passive circuits: energy is transferred slowly, without optimization, and significant losses occur due to the forward voltage drop across the diodes.

5.1.4.2. Test with EH300 (1000 µF)

The same PZT source was then connected to the EH300 energy harvesting module, which includes with a 1000 µF storage capacitor. The experiment yielded the following results:

Full charge time (0 V → 3.6 V): approximately 10 minutes

Partial recharge time (1.8 V → 3.6 V, regulation cycle): 4 minutes

These results demonstrate a clear gain in efficiency compared to the passive diode bridge, primarily due to the EH300's threshold management and optimized energy storage strategy prior to load activation.

5.1.4.3. Test with EH300A (2 × 3300 µF)

Finally, an updated and optimized version of the circuit, the EH300A, was tested under similar conditions. The EH300A includes two 3300 µF capacitors. The results were as follows:

Full charge time (0 V → 3.6 V): 60 minutes

Partial recharge time (1.8 V → 3.6 V): 20 minutes

5.1.5. Final choice of energy harvesting circuit

Despite the promising performance of the EH300A, the final implementation of our application relies on the EH300 module, which proved to be the most suitable compromise between simplicity, efficiency, and stability for our energy harvesting setup. The EH300 effectively manages the charge/discharge cycles, utilizing the energy from the PVDF nanogenerator to reach the 3.6 V threshold and deliver power down to 1.8 V, thereby ensuring a reliable energy supply to low-consumption loads, the EH300 remains more appropriate for our current design, particularly due to its faster start-up and straightforward integration.

5.2. Energy Storage Experiment

A complementary series of experiments was conducted to evaluate the actual efficiency of energy transfer to a capacitive load, using the commercial EH300 energy harvesting circuit. They were performed on a PZT buzzer and a CNC5 device, the PZT buzzer being used for testing and fine-tuning our electronic energy harvesting system. Its results are then compared with those of the devices developed in this study.

The options for energy harvesting circuit and final choice will be detailed in the following section. The aim was to measure the charging speed of an internal capacitor driven by the generators.

5.2.1. Slope of the charging speed of capacitor

To observe the rate of voltage increase over time, and compare the amount of energy stored in the capacitor at different excitation frequencies, the samples were submitted to mechanical excitation using the tapping system operating at controlled frequencies ranging from 1 to 5 Hz, with an increase of frequency every 30 seconds. The voltage across the capacitor was measured using the DMM6500 digital multimetre.

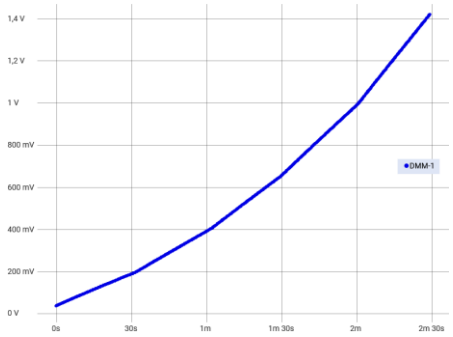

Figure 83: Example of capacitor charge (from PZT buzzer). Each change in slope corresponds to a 1 Hz increment in the tapping frequency, here from 1 Hz to 5 Hz.

Figure 83 shows the capacitor voltage profile measured, the piezoelectric energy source (here PZT buzzer), being connected to the EH300 energy harvesting circuit. The voltage across the capacitor rises progressively as mechanical excitations are applied via the tapping system. Notably, the slope of the voltage curve increases significantly when the tapping frequency is raised from low values up to 5 Hz, indicating a higher energy transfer rate from the piezoelectric generator to the storage capacitor.

At a tapping frequency of 5 Hz, the capacitor voltage reaches its saturation level rapidly compared to lower frequencies. The linear portion of the curve suggests that, within this range, the harvested energy per pulse remains relatively constant, while the total accumulated energy depends mainly on the number of mechanical impacts per unit time.

Unexpectedly, the PVDF nanogenerator containing 5% cellulose nanocrystals (CNC5) exhibits a different behaviour from the PZT buzzer. As shown in Figure 84 the capacitor voltage increases linearly during the mechanical excitation. However, the slope decreases when the tapping frequency increases (after 2 Hz), that is to say that at a frequency of 5 Hz, the voltage achieved over a given period is significantly lower than that obtained at 1 Hz. We can observe a reduced efficiency of energy transfer at higher excitation frequencies.

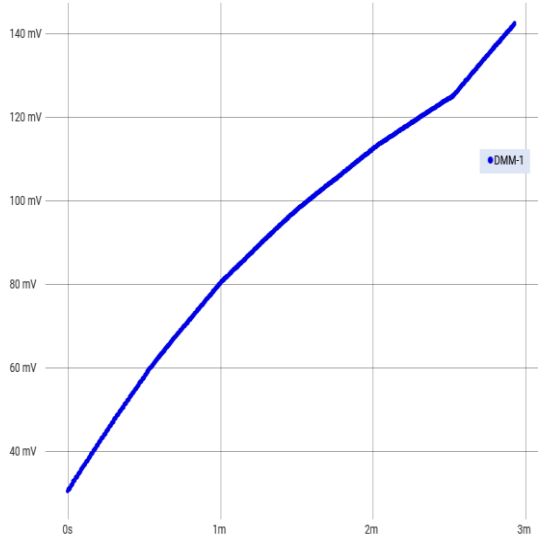

Figure 84: Capacitor charge from a CNC5 nanogenerator. Each 30s, a 1 Hz increment in the tapping frequency is applied, from 1 Hz to 5 Hz, and then back to 1 Hz.

To further confirm this phenomenon, the experimental protocol included returning to the initial frequency of 1 Hz after reaching 5 Hz, which resulted in the voltage curve recovering its initial slope, thereby confirming that the reduced charging performance at higher frequencies is reversible and frequency-dependent rather than caused by irreversible fatigue or degradation. Nonetheless, we can see that charge collection is more efficient at 1 Hz or 2 Hz than at higher frequencies.

This behaviour suggests that the CNC nanogenerators may possess limitations in charge transfer kinetics, possibly due to its higher internal impedance or slower mechanical relaxation dynamics compared to ceramic-based piezoelectric materials like PZT. We did not find an explanation for this phenomenon in our study. Anyway, these results subsequently led us to work with CNC5 at 2 Hz.

5.3. Optimising power output from the electroactive source

It is essential to know the maximum power that the source can supply for a given load, in order to be able to define our energy recovery application. We carried out a series of measurements of the voltage at the terminals of the source, loaded by an impedance ranging from short-circuit to open circuit. Since the source voltage is highly variable, we decided to collect its root-mean-square (RMS) value in order to minimise measurement errors.

5.3.1. PZT buzzer

Figure 85 shows the evolution of RMS power, current and voltage as a function of the load connected across the PZT source. As expected, the optimum power is in the microwatt range, which is 50 times smaller than the power of PZT. In addition, the optimum load for PVDF of approximately 10 MΩ is greater than for PZT, which was around 1 MΩ.

We can observe that the maximum power obtained is around 50 µW, for an optimum load of 1 to 2 MΩ. Piezoelectric materials are known to have a high output impedance, which leads to the delivery of maximum power for high load impedances, typically from 1 MΩ. Given our previous measurements, we know that PVDF provides a lower current than PZT, which entails that the optimum impedance will be greater for PVDF.

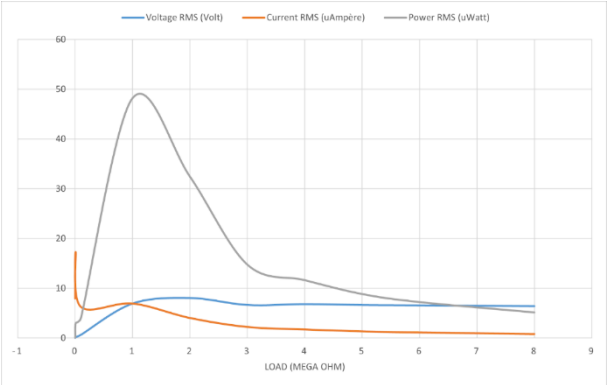

Figure 85: Evolution of the PZT RMS power, voltage and current as a function of the load.

5.3.2. CNC5 device

Figure 86 shows the evolution of RMS power, current and voltage as a function of the load connected across the PZT source. As expected, the optimum power is in the microwatt range, which is 50 times smaller than the power of PZT. In addition, the optimum load for PVDF of approximately 10 MΩ is greater than for PZT, which was around 1 MΩ.

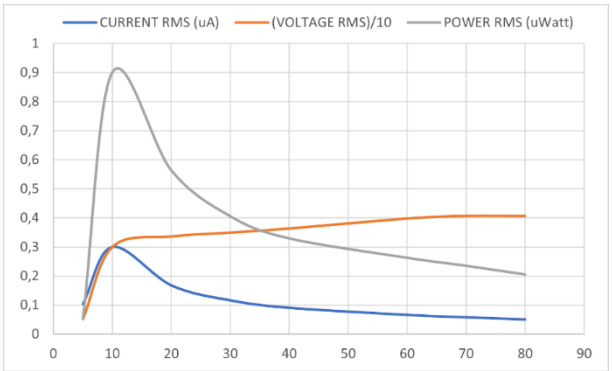

Figure 86: Evolution of the PVDF RMS power, voltage and current as a function of the load.

6. Data transmission from a sensor: a low-power application for the PVDF devices

The application selected to demonstrate the capacity of the CNC5 device as a sensor, but also as an energy harvesting nanogenerator is the transmission of a pulse signal via Bluetooth. This particular application can be divided in various subparts, detailed in the next sections:

1. Energy harvesting: using the tapping test bench, an electrospun CNC5 device, is impacted to generate the charges that are harvested.

2. Storage section: in this section the EH300 receives the energy produced by the piezoelectric device, then stores it before powering the Bluetooth Low Energy (BLE) module

3. Sensor section: the targeted application aims at simulating the circulation of blood through an artery. A PVDF deformation sensor implanted in an artery should make it possible to monitor its physiological behaviour following stimulation of the system. A peristaltic pump mimics the heart, and the sensor is mounted on a tube to mimic the artery.

4. Bluetooth section: this module, which is powered by the output of the EH300, ensures data transmission.

A schematic representation of the application is given in Figure 87 just below.

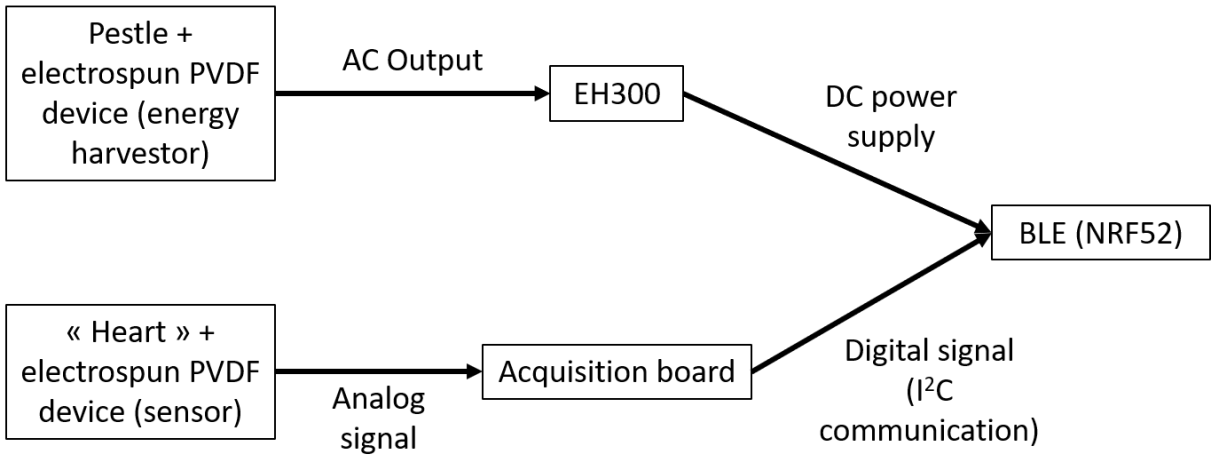

Figure 87: A schematic representation of the heart pulse sensing application.

6.1. PVDF as energy harvesting nanogenerator

The aim of this step is to demonstrate the capability of a PVDF-based nanogenerator to harvest mechanical energy and store it in the 1000 µF capacitor of an EH300 energy harvesting module, with enough energy to drive a real load such as a red LED. This experiment (Figure 88) provides a first practical proof-of-concept for the potential use of flexible nanogenerators in low-power autonomous systems.

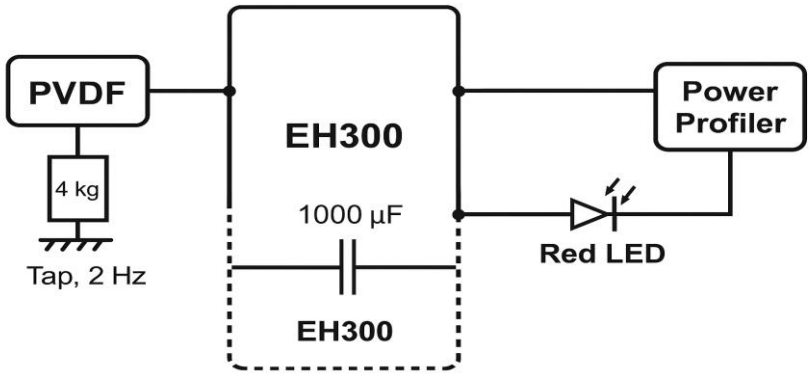

Figure 88: Schematic diagram of the experimental setup.

To maximize energy transfer, the tapping area was increased to a 4 cm radius, and the PVDF film was subjected to a controlled mechanical excitation of 4 kg at 2 Hz. The harvested energy was accumulated in the EH300 capacitor until the voltage reached approximately 3.6 V, at which point a red LED was connected as a demonstration load, as illustrated by Figure 88.

To monitor the energy consumption and discharge profile, we inserted into the circuit a Nordic Power Profiler Kit II (PPK II), which measures instantaneous current and energy delivered to the load. The Power Profiler software provided a clear visualization of the LED discharge behaviour and allows confirming the energy transfer efficiency of the system. Figure 89 summarizes the different curves and elements which are detailed below.

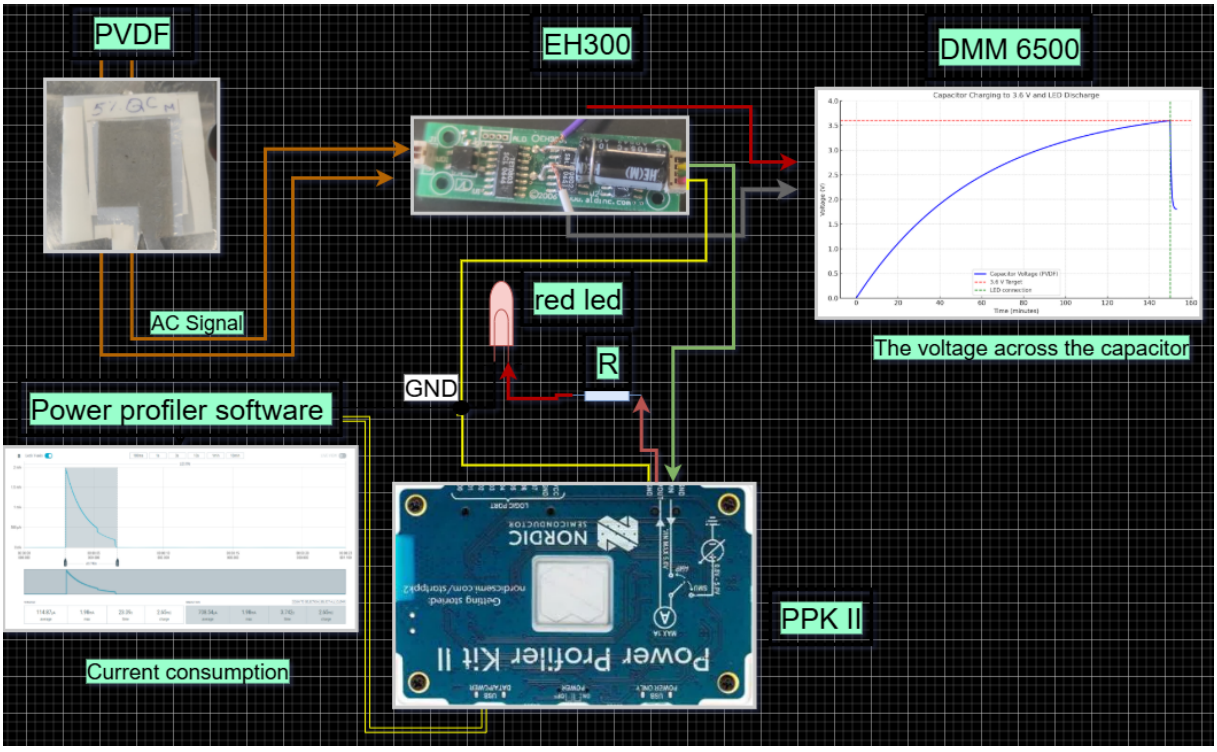

Figure 89: Experimental setup for the PVDF-based energy harvesting test.

6.1.1. Charging of the EH300 capacitor

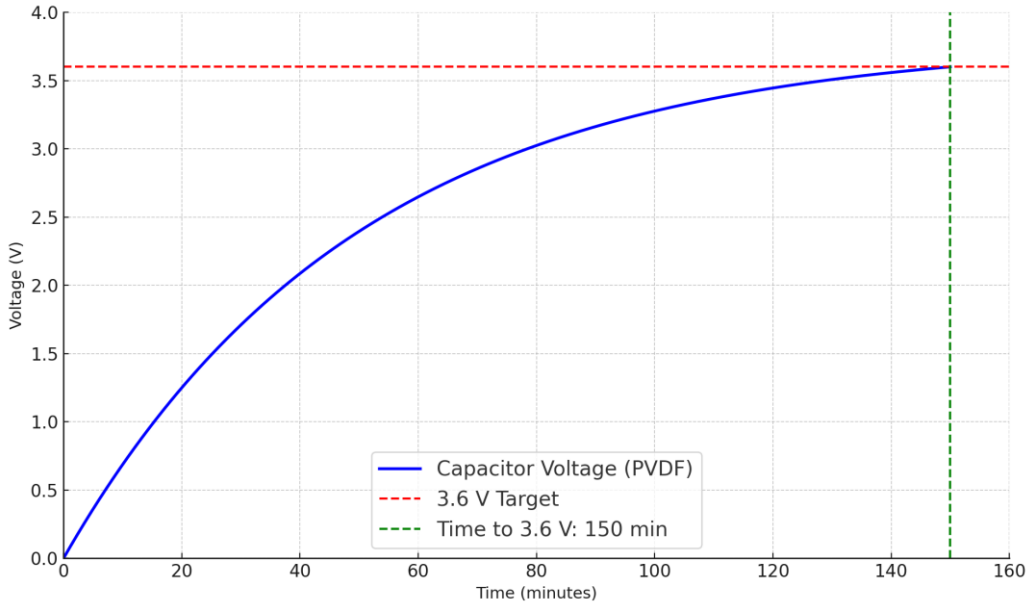

Figure 90: Charging profile of the 1000 µF capacitor obtained from experimental data recorded by the DMM 6500.

Figure 90 shows the charging profile of the 1000 µF capacitor in the EH300 circuit when powered by the PVDF nanogenerator under a tapping excitation of 4 kg at 2 Hz. The voltage rises progressively with a characteristic exponential RC behaviour, reaching approximately 3.6 V after ~150 minutes. The total stored energy is given by Equation 21 :

$$E = \frac{1}{2} \times C \times V^2 = \frac{1}{2} \times 1000 \cdot 10^{-6} \times 3.6^2 = 6.48\, mJ$$

This result indicates that the energy harvested by the PVDF device is sufficient to fill the capacitor to a usable level >5 mJ.

6.1.2. Discharge into a LED load

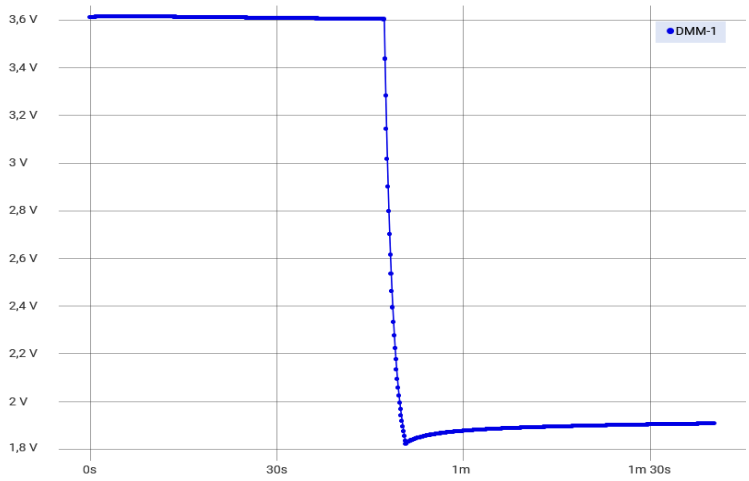

Figure 91: Voltage drop of the 1000 µF capacitor measured by the DMM 6500 during discharge into the LED load.

Figure 91 shows a voltage drop, observed at around 150 minutes, which corresponds to the connection of the red LED load. This sharp decrease reflects the discharge of the capacitor through the LED, confirming that the stored energy can power a small electronic component.

In practice, as soon as 3.6 V is reached, the EH300 circuit automatically triggers its output, allowing the stored energy to be delivered to the load until the voltage drops to 1.8 V, after which the capacitor starts charging again. The LED discharge profile provides clear evidence of actual energy delivery, reinforcing the feasibility of PVDF-based energy harvesting for small electronic loads.

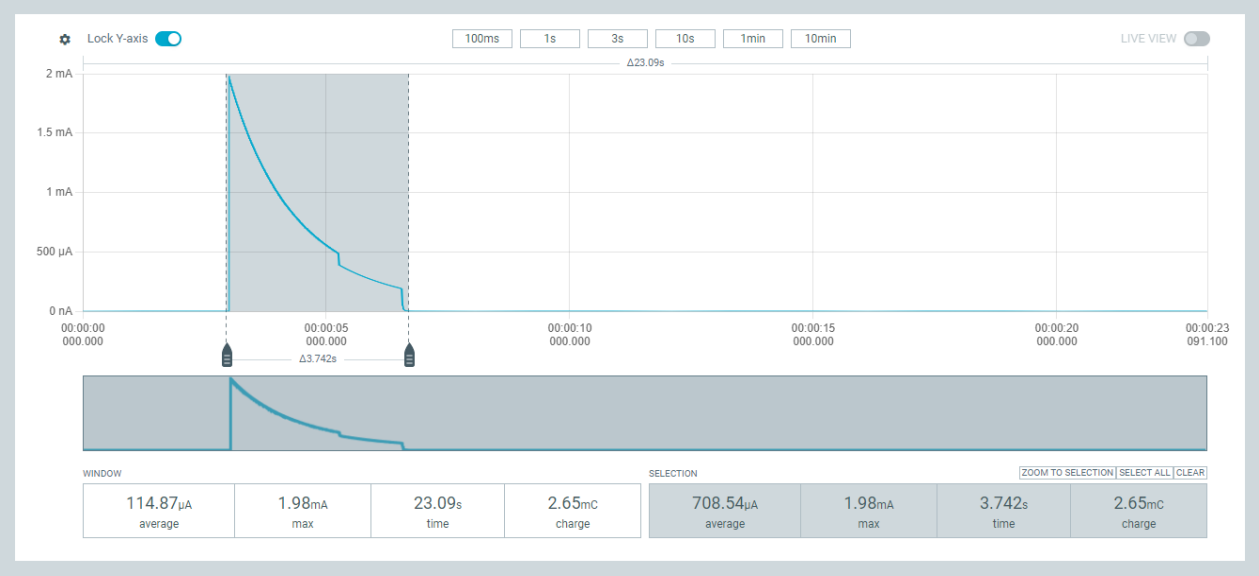

Figure 92: Current profile during the discharge of the 1000 µF capacitor into the LED, measured with the Power Profiler Kit II (PPK II).

A more precise study of the energy delivered was enabled by the use of a dedicated energy management and measurement module: Nordic Power Profiler Kit (PPK) II. The Nordic PPK II was connected to the red LED through

to measure the discharge profile and the energy delivery in the LED. The corresponding curve is displayed in Figure 45. Several key parameters can be extracted from the discharge profile:

- At the beginning, the maximum current drawn by the LED reach almost 2mA (1.98 mA).
- Discharge duration: 3.742 seconds, representing the total time the LED remained powered in this configuration (when the voltage drops from 3.6V to 1.8V)
- Average current: 708.54 µA, reflecting the sustained current throughout the discharge.

The total charge transferred to the LED is calculated by integrating the current over the discharge time, resulting in approximately 2.65 mC. This short but sharp current pulse shows that the energy accumulated by the PVDF nanogenerator and stored in the EH300's capacitor can effectively drive a small electronic component, by periodically sending a pulse, for example to send information from a sensor.

6.1.3. Conclusion of the experiment

The results of this experiment confirm that a PVDF-based nanogenerator is capable of harvesting mechanical energy and storing it in a capacitor sufficiently to power light loads such as a red LED. This demonstrates the feasibility of using PVDF nanogenerators for low-power autonomous applications, especially where intermittent energy pulses are acceptable.

From this proof of concept, several perspectives emerge:

- Enhancing energy harvesting performance through mechanical optimization (e.g., improving tapping force) and advanced energy management circuits for better conversion efficiency.
- Integration with low-power wireless systems, such as Bluetooth Low Energy (BLE) modules, where the harvested energy could extend battery life or even achieve battery-free operation in specific use cases.

6.2. Pulse sensor on an artery

In this section, we used the same materials developed in this study to realise a "blood pulse sensor", and to demonstrate the development of an arterial pulse sensor application. The mats were covered up and down by soft electrodes, connected to thin wires to collect electrical charges, and tightly wrapped around flexible tube simulating human artery, a Tygon R-3603 tube (internal diameter 3mm, external diameter 6mm, 1.5 thickness). This artery equipped with its sensor was mounted in a dedicated test bench to demonstrate perfect detection of the simulated pulse and accurate obtention of the blood rate.

A peristaltic pump (ISMATEC ISM 444 B (BVP)) generated a pulsed flow of water through a tube, similarly to the way the heart would generate a blood pulse. The pressure variations induced by the flow in the tube and consequently in the PVDF mat generate electrical signals that are acquired using an oscilloscope. The Qtiplot software was then used to analyse the time and frequency signals, filter the signals, and apply Fast Fourier Transform (FFT). By varying the pump's flow rate, we were able to observe the sensor's response over a range of physiological heart rates. A diagram of the test bench is shown in Figure 93.

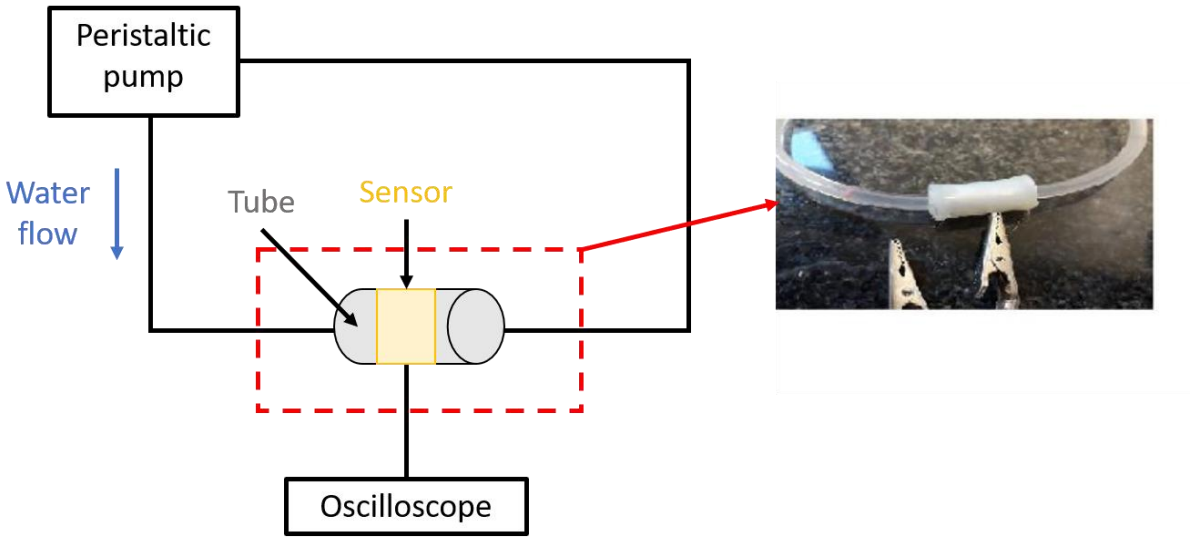

Figure 93: Schematic representation of the pulse test bench.

6.2.1. First case: Human being at rest

We can estimate the heartbeat frequency for a healthy human being at rest to be approximately 80 beats per minute, which corresponds to a frequency of 1.33 Hz. We will therefore measure the voltage across the transducer and analyse its frequency spectrum. To ensure that all the results are referenced to the same value, we took a no-load measurement of the voltage at the terminals of the oscilloscope probe. The results of this first measurement are displayed in Figure 94.

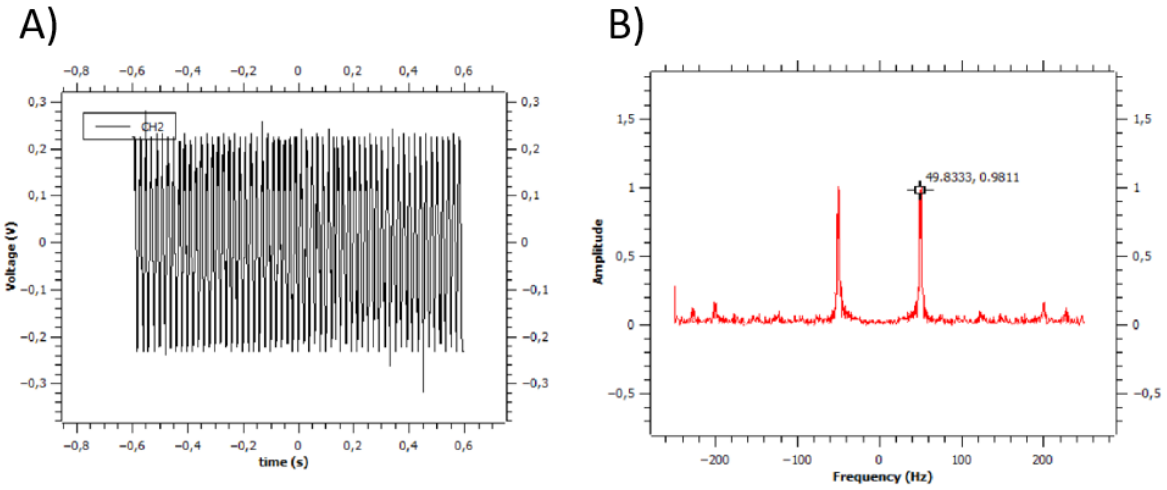

Figure 94: A) No-load voltage of the oscilloscope probe (b) spectrum of the observed signal obtained after FFT.

With no load, a noise is visible around 50 Hz. Our target measurement range is between 1-10 Hz. The signal obtained by the oscilloscope will therefore have to be filtered at a frequency below 50 Hz.

Upon imposing a water flow pulsion of 1.33 Hz, the measured results are displayed in Figure 95.

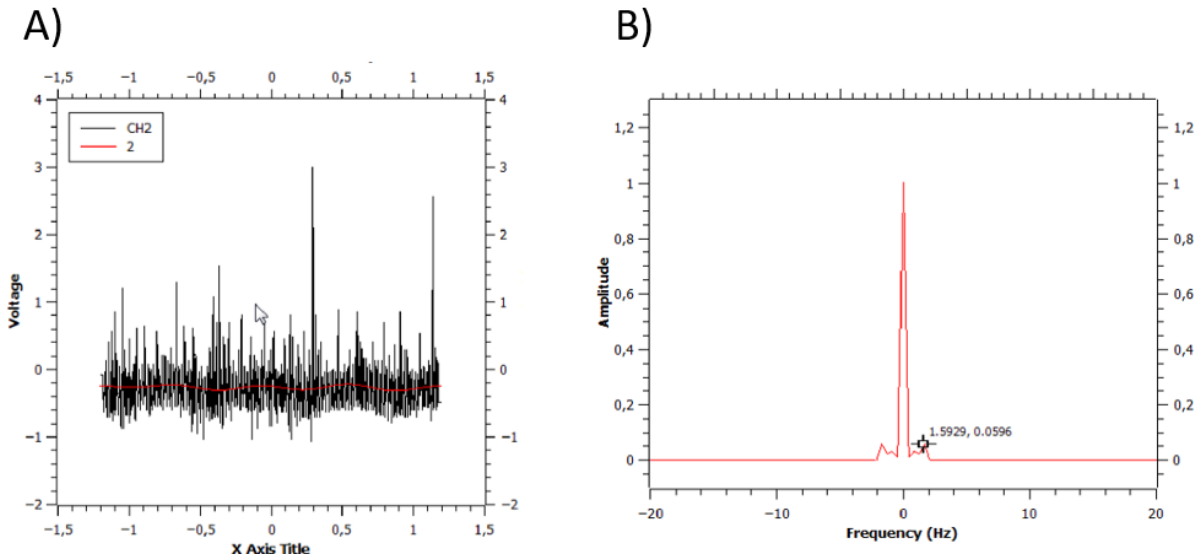

Figure 95: A) voltage at the sample terminals in black, voltage filtered at a frequency of 5 Hz in red, B) spectrum of the signal filtered at 5 Hz after FFT.

Figure 95 B) represents the spectrum of the measured signal filtered at 5 Hz, where we can see a harmonic at a frequency of 1.59 Hz, which we consider close to the frequency of the water flow in the pipe imposed by the peristaltic pump. The sample can therefore detect the pressure variations imposed by the pump.

6.2.2. Second case: Human being after a great effort

We can estimate the heartbeat frequency for a healthy human after a great effort to be approximately 200 beats per minute, which corresponds to a frequency of 3.33 Hz. This time we chose to filter the signal at 10 Hz to observe only the peak of interest. The observed frequency at 3.41 Hz in Figure 96 B) is very close to the frequency of the water flow in the pipe, imposed by the peristaltic pump, which is 3.33 Hz. As before, we can see that the sample is able to detect the pressure variations imposed by the pump.

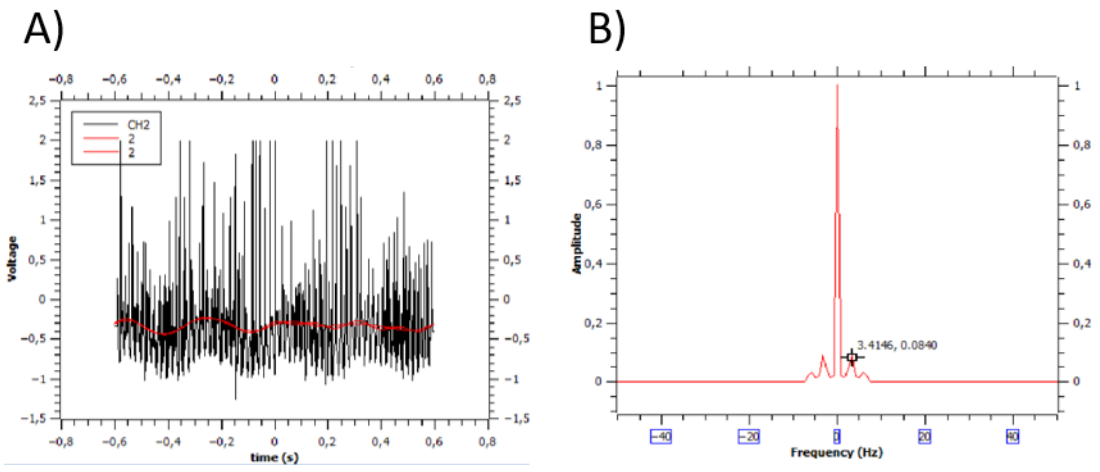

Figure 96: A) voltage at the sample terminals in black, voltage filtered at a frequency of 10 Hz in red, B) spectrum of the signal filtered at 10 Hz after FFT.

6.2.3. Third case: Laboratory rat after adrenaline injection

The beat frequency for a laboratory rat after injection of adrenaline corresponds to approximately 400 beats per minute, which translates to a frequency of 6.67 Hz. This time we chose to filter the signal at 20 Hz to observe only the peak of interest. The observed frequency at 6.73 Hz in Figure 97 B) is again very close to the frequency of the water flow in the pipe, which is 6.67 Hz. The intensity of the peak being higher in this case, it seems that the sensor accuracy improves at higher frequencies.

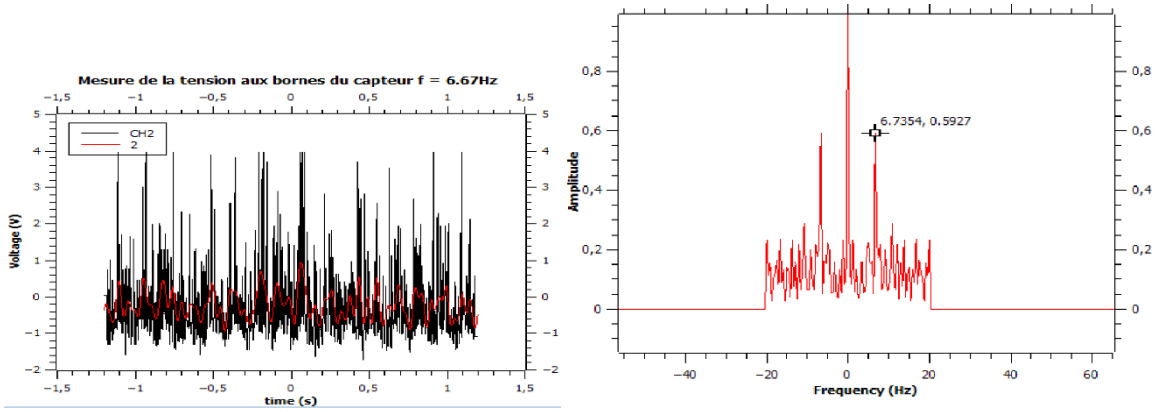

Figure 97: A) voltage at the sample terminals in black, voltage filtered at a frequency of 20 Hz in red, B) spectrum of the signal filtered at 20 Hz after FFT.

6.2.4. Conclusion

The PVDF sensor successfully detects pressure pulses across physiological frequencies, demonstrating its potential for biomedical monitoring. Small frequency shifts and the need for tailored signal filtering highlight challenges for practical use. Overall, the sensor shows promise for integration into low-power, wireless health monitoring systems, provided further optimization of signal processing and system integration are completed.

6.3. Powering and sending data via Bluetooth

Assuming that the processing of the previous sensor information is done, we have a digital value to transmit wirelessly to a terminal. It is the role of this section to define the Bluetooth equipment allowing this last step to be carried out, to move into more practical and integrated applications.

The developed system combines a PVDF nanogenerator, an EH300 power management circuit, and a Bluetooth Low Energy (BLE) communication module based on Nordic Semiconductor's nRF52840 System-on-Chip (SoC). A schematic representation of the system is provided in Figure 98.

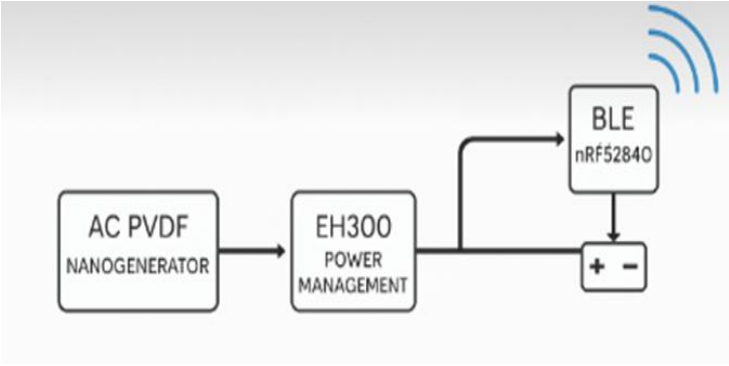

Figure 98: Powering of the BLE module with a CNC5 device.

In this architecture, the electrospun PVDF nanogenerator harvests energy from mechanical deformations such as vibrations, bending, or tapping. This energy is conditioned and regulated by the EH300, which stores it in a supercapacitor and supports power delivery to the BLE module. While the system includes a battery of 1000µF to guarantee stability, the harvested energy significantly reduces the reliance on the battery, extending its operational lifetime by supplementing power during active phases. When enough energy is accumulated, the nRF52840 wakes from deep sleep, samples predefined sensor inputs, and transmits data wirelessly using BLE 5.3. This hybrid energy model ensures that the battery is only minimally discharged during standby and communication events, supporting long-term deployment with reduced maintenance.

6.3.1. Wireless Communication via Bluetooth Low Energy (BLE)

Bluetooth Low Energy (BLE) was chosen as the wireless communication protocol because of its very low power consumption, appropriate range for short-range communication, and broad compatibility with widely used devices like smartphones and BLE gateways. These features render BLE highly suitable for low-power embedded systems, particularly those using energy harvesting techniques or small rechargeable battery supplies.

For BLE communication, the system uses either an nRF52832 or nRF52840 microcontroller from Nordic Semiconductor. These chips have a 64 MHz ARM Cortex-M4F processor, a BLE 5.x compliant radio, and various peripherals like analog-to-digital converters (ADC), real-time clocks (RTC), and various communication interfaces (like SPI and I²C). Their low energy consumption and versatile configuration make them a good choice for infrequent; low-duty-cycle uses like ours. The firmware is still being implemented in C using Nordic's nRF5 SDK (v17.1.0) and SoftDevice S140 BLE stack, the current progress state of the work is presented in Appendices (see p. xix).

6.3.2. Theoretical assessment of the system capacity to power the BLE module

As a first proof of concept for wireless communication, we implemented a minimal BLE transmission scenario where the system sends a 4-byte notification using a custom BLE characteristic.

The EH300 energy management module integrates a 1000 µF supercapacitor, which stores energy and powers the BLE module once the voltage reaches a defined high threshold (V_{high} = 3.6 V) and stops discharging when it reaches a low threshold (V_{low} = 1.8 V). The total usable energy between these voltage limits is calculated using Equation 22:

$$E = \frac{1}{2} \times C \times \left({V_{high}}^2 - {V_{low}}^2\right) = \frac{1}{2} \times 1000 \cdot 10^{-6} \times (3.6^2 - 1.8^2) = 4.9\, mJ$$

Equation 22

During use, a single BLE transmission cycle involves two energy phases:

1) Microcontroller wake-up and BLE stack initialization (E_{boot})

2) BLE transmission (TX + RX) (E_{tx})

TX stands for Transmit: the device is sending data wirelessly; RX stands for Receive: the device is receiving data wirelessly.

The values used for the following theoretical BLE power consumption estimations are based on the nRF52840 datasheet [249], the official Power Profiler tool from Nordic Semiconductor [250], and the Bluetooth Core Specification [251]. The datasheets specify the required voltage and current to power the device (3 V and ≈5–7

mA), wake-up durations (≈150 ms), and advertising event durations (≈3.5–5 ms). They are all in line with the manufacturer's documentation and verified simulation outputs.

1) For microcontroller wake-up and BLE stack initialization, the datasheet gives a consumption of 150 ms at 7 mA. The corresponding energy required is given by Equation 23:

$$E_{boot} = I \times V \times t = 0.007 \times 3 \times 0.15 = 3.15\, mJ$$

Equation 23

2) For BLE transmission (TX + RX), the consumption corresponds to 5 ms at 5 mA. The corresponding energy required is given by Equation 24.

$$E_{tx} = I \times V \times t = 0.005 \times 3 \times 0.005 = 75\ \mu J$$

Equation 24

The total energy required per cycle is therefore given by Equation 25:

$$E_{total} = E_{boot} + E_{tx} = 3.2\, mJ$$

Equation 25

At each cycle, of 150 min in our example with CNC5, we therefore have a charge of the capacitor in the EH300, which allows 4.9 mJ to be collected, then the sending of information, from a sensor for example, assuming the awakening of the microcontroller, the initialization of the BLE and the transmission itself, which consume in total 3.2 mJ. This result confirms that the combination of the energy harvesting circuit EH300 and with the Bluetooth module nRF52840 enables periodic BLE communication powered by harvested energy, without external battery usage. In hybrid configurations (with a backup battery), the harvested energy significantly extends the battery life by reducing the need for frequent recharges. This experimental scenario validates the core objective of the study: demonstrating that low-frequency, energy-autonomous BLE sensing is technically feasible using a PVDF nanogenerator, even under tight energy constraints.

7. Conclusion:

This chapter has thoroughly explored the electric characterization and energy harvesting capabilities of electrospun PVDF-based nanogenerators, incorporating both cellulose nanocrystals (CNC) and Al-Cu-Fe-B quasicrystals (QC) as fillers.

After reviewing the existing possibilities from previous research works, and identifying the limitations of conventional piezoelectric testing methods when applied to fibrous, electrospun materials, it was decided to build a fully instrumented tapping test setup, and use it to test the power producing capacity of the nanogenerators fabricated from PVDF electrospun fibres. This custom-built setup enabled precise control of key testing parameters such as frequency, applied force, and contact area, ensuring reproducible and accurate electrical measurements.

Using this system, a comparative study was conducted on pristine PVDF samples and those doped with various concentrations (1%, 3%, and 5%) of CNC and QC fillers. From output voltage and current curves, it was possible to prove the proportional response of the devices to increased tapping frequency and force, and compare the performances of the materials with several filler content. The results demonstrated a clear enhancement in both voltage and current outputs with increasing filler content compared to pure PVDF fibres. Especially, the CNC5 device achieved the highest output performance while maintaining good signal stability, reaching 60V of peak-to-

peak voltage, and 60µA of peak-to-peak current. In contrast, higher QC concentrations led to improved amplitudes but introduced instability and signal irregularities, highlighting the trade-offs between performance and reliability.

The investigation further extended into practical applications by integrating the PVDF-based devices into energy harvesting circuits. Among three commercial energy harvesting modules evaluated—LTC3588-1, AEM30330, and EH300—the EH300 proved to be the most compatible and effective for PVDF-based nanogenerators, thanks to its wide input voltage range, low activation current, and robust handling of intermittent inputs.

Experimental demonstrations validated the ability of the CNC5 device to charge capacitors, power LEDs, and drive low-power electronics such as wireless modules. The application elected to demonstrate a realistic use of the CNC5 device is a pulse sensor completed with a data transmission system. While it was not possible during the time frame of the PhD to implement the complete system, tests showed its suitability as a physiological sensor in a simulated artery system, where it could detect pressure variations induced by a peristaltic pump mimicking a heartbeat, and as a power source by charging a capacitor using a commercial energy harvesting circuit, the EH300, thus proving its dual role in sensing and energy harvesting.

In conclusion, this chapter has established that electrospun PVDF nanogenerators, particularly with 5% CNC, offer a promising platform for flexible, lightweight, and multifunctional energy harvesting devices. These findings open the door for further development in self-powered wearable sensors and biomedical devices. Future work may involve optimizing the mechanical excitation interface, integrating advanced rectification and storage strategies, and exploring long-term stability under real-world conditions.

This material paves the way for the development of IoT applications and self-powered sensor systems, where energy harvesting can significantly increase battery lifespan or even eliminate the need for batteries in ultra-low-power devices. Future work should focus on improving the mechanical-to-electrical conversion efficiency, integrating advanced power management electronics, and combining the PVDF nanogenerator with low-energy communication modules (e.g., BLE) to achieve fully autonomous and battery-free IoT platforms.

Conclusion

Due to the growing concerns about energy consumption and environmental impact of electronic devices, alternatives to batteries have become a huge topic of interest. For low power applications, energy harvesting through electroactive polymer based nanogenerators is one of the regarded routes. Among such polymers, Polyvinylidene fluoride (PVDF) is the most widely studied, good electro-mechanical coupling properties, high chemical stability, flexibility and biocompatibility. Fundamental knowledge concerning PVDF, the use of electrospinning to produce PVDF-based electroactive scaffolds and possible applications is provided in the first part of this thesis.

One of the major challenges regarding PVDF, and its ability for energy harvesting and sensing applications, is the presence of a high amount of its electroactive phases, and especially the β crystalline phase. The α phase is the most thermodynamically stable crystalline phase, and is naturally obtained from the melt with a trans-gauche-trans-gauche conformation, which makes it non-electroactive. The β phase has a zigzag all-trans conformation which allows it to possess the highest electric dipole moment of all PVDF crystalline phases. Generally speaking, the obtention of high amounts of β phase in a sample is achieved through the combination of mechanical stretching and poling. Among the elaboration methods of PVDF films, electrospinning is a particularly promising innovative technique, as it possesses the advantage of combining the high stretching and *in situ* poling stages.

In order the precisely characterise the crystalline phase fractions of the produced PVDF samples, a multi-technique approach has been developed, involving DSC, WAXS, FTIR and Raman spectroscopy. DSC and WAXS were mainly used for precise determination of the crystallinity ratio of the samples, while FTIR and Raman spectroscopy are better suited for phase identification. Additionally, a new Raman criterion for the precise quantification of the α, β and γ phase fractions was proposed, using a curve deconvolution approach. By using a reduced number of identified Gaussian curves to model the amorphous contribution to the Raman spectra of samples, and a cumulative approach to the crystalline phase quantification, the method offers a reliable and accessible quantification tool that can be applied to PVDF samples with very different crystalline forms distribution.

With the characterisation routine established, a careful study of the influence of several electrospinning parameters was presented. While some differences in the calculated values of the crystallinity ratio from the different techniques are present, the highlighted trends remain the same. Crystallinity ratio is very little influenced by the different sets of parameters (~50%), comparing to the effect of stretching coming from the electrospinning technique. Moreover, all produced fibres showed a negligible amount of crystalline α phase (<5%), and a proportion of β to γ crystalline phase of roughly 70/30%. However, higher solution flow rate, and an applied voltage either too low or to high have been demonstrated to lower the ratio of β/γ phase fractions, by causing the apparitions of defects that could be observed in optical microscopy (beading, electrospraying, merged fibres). A localised Raman study on single fibres showed that within the same sample, fibres that present defects also present a visibly reduced β phase fraction compared to the expected thin, homogeneous fibres. Hence, the study justified the choice of the set of parameters (15wt% PVDF, 3:7 DMF:Acetone ratio, AV=13 kV, FR=1mL/h and TCD=12cm), which gave the highest β phase fraction of all samples (75%).

This set of parameters has then been used to produced nanocomposite PVDF-based electrospun fibres, with addition of 1 to 5 wt.% of cellulose nanocrystals (CNC) and Al-Cu-Fe-B quasicrystals (QC). Filler addition was expected to further promote the nucleation of the crystalline β phase, and improve the mechanical strength and thermal stability of the materials. Nevertheless, all characterisation techniques showed that no clear improvement could be obtained compared to the pristine PVDF fibres, as the crystallinity ratios and electroactive phase fractions were already very high.

For the first time, micro-Brillouin spectroscopy was used for the mechanical characterisation of isolated PVDF electrospun fibres. While other techniques like Raman spectroscopy or TGA did not detect variations between fibres elaborated by electrospinning with different DMF:Acetone ratios, the Brillouin response was strikingly different. The strong variation of mechanical properties observed, a drop from 12.5 GHz to 9 GHz between fibres elaborated with a 3:7 DMF:Acetone ratio compared to the fibres elaborated with a 4:6 DMF:Acetone ratio, was attributed to the presence of mesoporosities within the fibres, originating from the difference in solvent evaporation speed.

A study on composite electrospun fibres with addition on cellulose nanocrystals (CNC) and Al-Cu-Fe-B quasicrystals (QC) was also realised. Overall, the addition of some percent of CNC has a slight effect reinforcement effect on the electrospun fibres compared to the results that were obtained from the electrospinning process alone, despite the disparities of c_{11} values observed within the same sample. Analyses near the QC particles shows a drop in elastic properties, which could be explained by a local heating from the laser in the vicinity of the QC particles, due to their low thermal conductivity. This softening effect of the PVDF fibre matrix overshadows the possible reinforcement effect of the material by QC addition.

Another important result was obtained by exploring the evolution as a function of temperature of the mechanical properties of electrospun PVDF fibres. An unexpected elastic anomaly has been highlighted, in the form of a change of slope in the variation of the elastic constant c_{11} with temperature at a determined temperature of 31°C. The proposed explanation is that this elastic anomaly can be interpreted as a reorientation/ reorganisation/ disorganisation at the amorphous-crystalline interphase, located around 30°C in electrospun fibres. This transition precedes the melting of imperfect α crystals happening around 60°C, and ultimately the melting of PVDF at around 160°C. In the case of PVDF samples that were not submitted to mechanical stretching, the melting of the α crystals is the only event that can be observed in Brillouin spectroscopy. The absence of the simple slope change located at 30°C in non-mechanically oriented materials highlights the fact that the elastic anomaly associated with reorientations at the amorphous-crystalline interphase is exclusive to mechanically oriented materials.

A complementary study on a solvent-casted material as brought to light a discoloration phenomenon caused by exposure to the 532 nm used in Brillouin spectroscopy studies. From Raman spectroscopy, it appears that the sample submitted to the laser exhibit a growing proportion of β and γ crystalline phases, while simultaneously displaying lower amounts of α phase. Brillouin spectroscopy measurements show that with laser exposure, the Brillouin frequency increases. This result is in line with the hypothesis that exposure to the 532 nm laser promotes the formation of the electroactive phases of PVDF, as the presence of β phase contributes to stiffen the samples.

After the thorough chemical, morphological, structural and mechanical characterisation performed on the PVDF electrospun scaffolds, the electric outputs of the materials were evaluated using a tapping-test bench conceived in the lab. The custom-made machine is instrumented with a Keithley DMM6500 digital multimeter allowing the measurement of output currents and voltages during the tests. Using this setup, it was possible to test the performances of the PVDF-composite fibres, and ensure its sensitivity to applied force and frequency changes. Among the tested materials, the CNC5 sample achieved the highest output performance while maintaining good signal stability, reaching 60 V of peak-to-peak voltage, and 60 µA of peak-to-peak current. After selecting an appropriate energy harvesting board, the EH300, a demonstrator application was proposed. A peristaltic pump was used to mimic a heartbeat, and a CNC5 device was mounted on a tube representing an artery to function as a heart pulse sensor. The sensor showed sensitivity to varying pulse frequencies corresponding to increasing levels of physical activity. A separate CNC5 device was used to harvest energy from mechanical tapping to charge the EH300 capacitor. A Bluetooth data transmission system powered by the PVDF nanogenerator is currently under development to complete the application. The PVDF device proved its practical ability to function both as a sensor,

and as a mechanical energy harvesting nanogenerator, showing a potential for integration into low-power, wireless health monitoring systems.

Perspectives

Due to the large number of topics covered in this thesis, some possibilities arise regarding further investigation that could not be covered during the time frame of the PhD.

Regarding the electrospinning process, interrogations are rising concerning the effect of the applied voltage on the polymeric solution during the jet travel from the needle tip to the collector. It is possible that the *in situ* polling effect does not play a prominent role on the electric response of the elaborated fibres, and that the major contribution of the techniques lies in the stretching effect. An additional challenging but very promising experiment would be to implement *in situ* WAXS and Raman spectroscopy during the electrospinning process, to assess the evolution of crystalline phase formation and orientation along the jet travel. Moreover, all fibres presented in this work were elaborated using a static plane collector. As the implementation of a rotating collector could add extra stretching to the fibres and induce fibre alignment in the scaffolds, it would be interesting to study the effect of the drum rotation speed on the electrospun mats. The ambient parameters are also known to have a strong impact on the electrospinning output. As an illustration, the optimised parameters proposed by our colleagues in MGU in India, where the climate is significantly hotter and more humid compared to Nancy, do not work in IJL. A control unit was bought for the IJL setup, but could not be installed during the time frame of this work to perform a systematic study of the effect of ambient temperature and humidity. In the case of composite fibres, adding a functionalisation step could help with the filler surface-PVDF matrix interaction.

As the thesis is oriented towards the use of electrospun PVDF materials for energy harvesting applications, the presence of a high proportion of electroactive phases is mandatory. While important progress could be achieved regarding multi-curve deconvolution of the Raman spectra and WAXS diffractograms, some improvements towards the accuracy of the methods could still be achieved. Testing of the proposed methods on a more diverse set of samples elaborated with varying processing methods could be of use. Obtaining a similar criterion for the deconvolution of FTIR spectra, focusing on a reduced number of physically identified amorphous curves would also constitute an interesting addition. An advanced use of the WAXS diffractograms can also be envisioned by developing its use for phase identification, and the quantification of the macromolecular orientation of samples depending of the elaboration method (through calculations of Herman's factor). An aspect that could not be explored in this work is the *in situ* characterisation of the materials with temperature. Such coupled studies of DSC with FTIR, Raman spectroscopy and WAXS could allow an in-depth exploration of the crystalline evolutions of PVDF with temperature by conducting kinetic monitoring of crystallisation studies. *In situ* setups could also include the monitoring of the semi-crystalline microstructure of samples during tensile tests, and the investigation of the effect of controlled mechanical stretching on PVDF. Complementary *post mortem* studies could also be performed using Brillouin spectroscopy. To achieve these goals, the implementation of multivariate analysis could constitute a compelling to observe trends on a large number of datasets associated with *in situ* studies. Additional mechanical investigation could be oriented towards the use of DMA and perhaps micro-traction on single fibres, and comparison with Brillouin spectroscopy results.

Concerning the electroactive properties of PVDF and possible related applications, experimental work has shown the importance of the sample preparation method on the final output of the fabricated devices. Hence, some further developments are envisioned, such as testing various encapsulating options to extend the duration of use of the devices, staking extra electrospun layers to intent increasing the produced output voltages and currents, perform an additional Corona poling step on the electrospun fibres, and improve the design of the electrodes to improve the produced charge transfer. Some adjustments are still necessary to optimise the custom-built tapping system. Ideas include a better control of the applied force or the inclusion of the force sensor data into a regulation loop. Lastly, the development of a real-time signal processing program of the pulse sensor voltage signals coupled

with the finalisation of the BLE code would allow to complete the data transmission application powered from PVDF nanogenerators.

Résumé en français de la thèse

Face aux préoccupations croissantes concernant la consommation d'énergie et l'impact environnemental des appareils électroniques, les alternatives aux batteries suscitent un vif intérêt. Pour les applications basse consommation, la récupération d'énergie par nanogénérateurs à base de polymères électroactifs est une voie envisagée. Parmi ces polymères, le polyfluorure de vinylidène (PVDF) est le plus étudié, offrant de bonnes propriétés de couplage électromécanique, une stabilité chimique élevée, une grande flexibilité et une biocompatibilité. La première partie de cette thèse présente des connaissances fondamentales sur le PVDF (Figure 1) et la technique choisie dans cette étude pour produire des structures électroactives à base de PVDF : l'électrofilage (Figure 2).

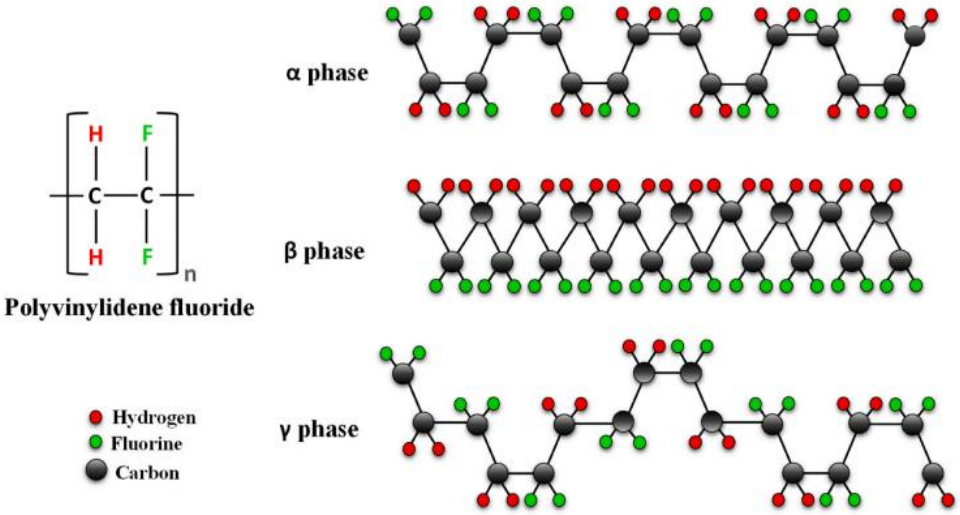

Figure 1 : Représentation schématique des phases α, β et γ du PVDF [252].

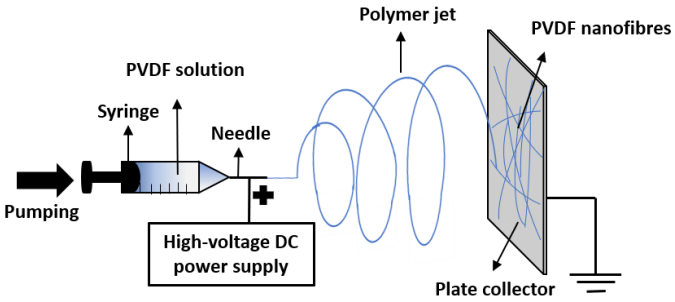

Figure 2 : Schéma du dispositif d'électrofilage.

L'un des principaux défis liés à l'utilisation du PVDF pour ses applications de récupération d'énergie et de détection réside dans la présence en son sein d'une proportion importante de phases électroactives, notamment de la phase cristalline ferroélectrique β. Afin de caractériser précisément les fractions de phase cristalline des échantillons de PVDF produits, une approche multi-techniques a été développée, impliquant la DSC, la WAXS, la FTIR et la spectroscopie Raman.

La DSC et la WAXS ont principalement été utilisées pour déterminer avec précision le taux de cristallinité des échantillons, tandis que nous avons montré que la FTIR et la spectroscopie Raman sont plus adaptées à l'identification des phases.

Un apport important de notre étude a été le développement d'un nouveau critère Raman pour la quantification précise des fractions de phase α, β et γ, par déconvolution des spectres Raman. En utilisant un nombre réduit de courbes gaussiennes identifiées pour modéliser la contribution amorphe aux spectres Raman des échantillons, et une approche cumulative pour la quantification de la phase cristalline, nous avons montré que cette méthode offre un outil de quantification fiable et accessible, applicable à des échantillons de PVDF et de composites à base PVDF, présentant des distributions cristallines très variées (Figure 3).

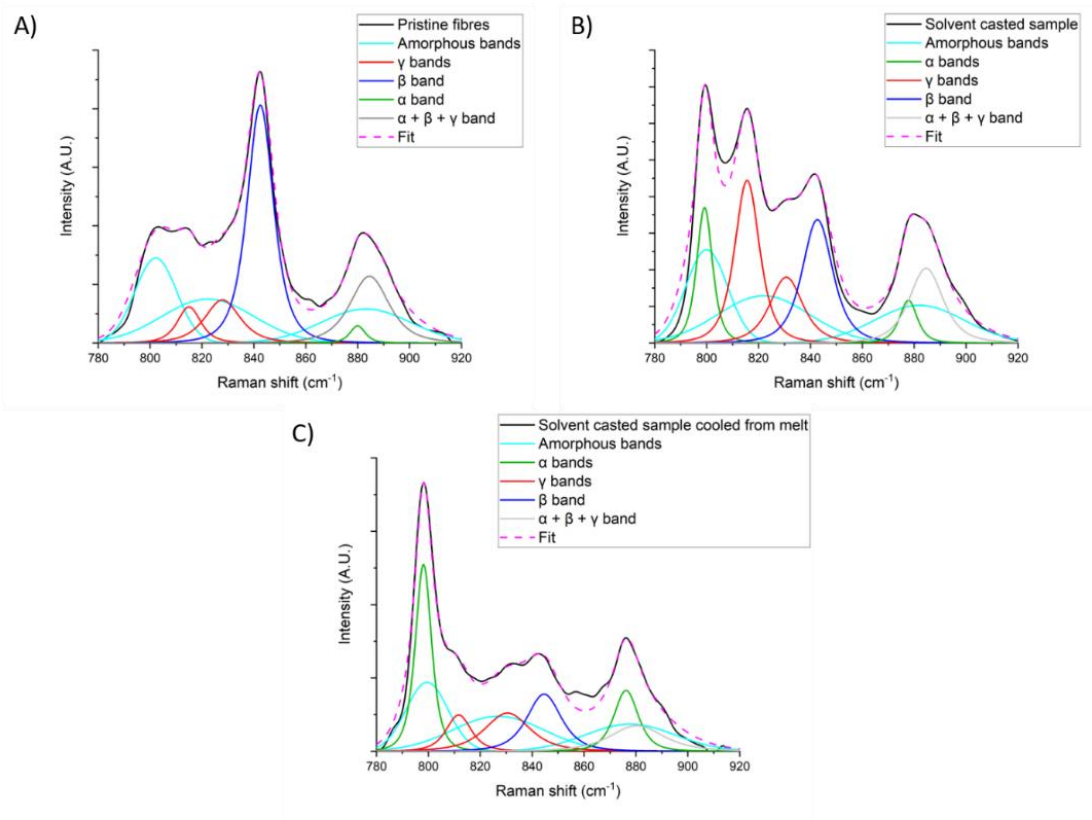

Figure 3 : Spectres Raman de A) fibres électrofilées vierges ; B) échantillon de PVDF obtenu par solvent casting et C) échantillon de PVDF obtenu par solvent casting refroidi à partir de la masse fondue.

Une fois ce protocole de caractérisation établi, une étude approfondie de l'influence de plusieurs paramètres d'électrofilage a été réalisée. Cette étude a mis en évidence que toutes les fibres produites par électrofilage présentent dans leur partie cristalline une très forte proportion de phases électroactives β et γ (phase α cristalline <5 %). Le taux de cristallinité global est également très peu influencé par la variation des différents ensembles de paramètres (~50 %). Une proportion de phase cristalline β/γ d'environ 70/30 % est souvent observée, mais nous avons montré qu'un débit de solution trop élevé et une tension appliquée trop faible ou trop élevée diminuaient le rapport des fractions de phase β/γ, provoquant l'apparition de défauts observables en microscopie optique (de type perlage, électropulvérisation, fibres fusionnées, Figure 4). Grâce à cette étude, nous avons établi le jeu de paramètres optimal pour obtenir la fraction de phase β la plus élevée de tous les échantillons (75 %) : 15 % en poids de PVDF, rapport DMF:acétone 3:7, tension appliquée = 13 kV, débit de la solution = 1 ml/h et distance entre l'aiguille et le collecteur = 12 cm.

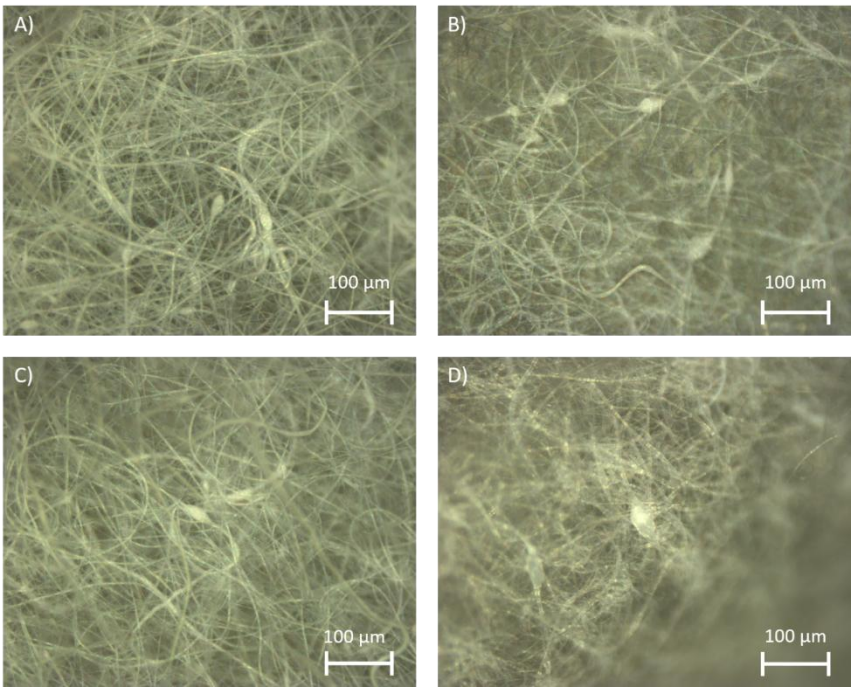

Figure 4 : Exemples de fibres élaborées selon différents paramètres d'électrofilage. On peut observer la présence de perles dans chaque cas.

Cet ensemble de paramètres a ensuite été utilisé pour produire des fibres électrofilées nanocomposites à base de PVDF, avec l'ajout de 1 à 5 % en poids de nanocristaux de cellulose (CNC) et de quasicristaux d'Al-Cu-Fe-B (QC). Un effet possible de l'ajout de charge était d'accroitre encore davantage la nucléation de la phase β cristalline. Néanmoins, le taux de cristallinité et les fractions de phase électroactives étant déjà très élevés, les différentes techniques de caractérisation n'ont pu démontrer une amélioration nette par rapport aux fibres PVDF vierges.

Dans cette thèse, la caractérisation mécanique de fibres isolées de PVDF a été réalisée avec succès pour la première fois par spectroscopie micro-Brillouin (Figure 6 et 7).

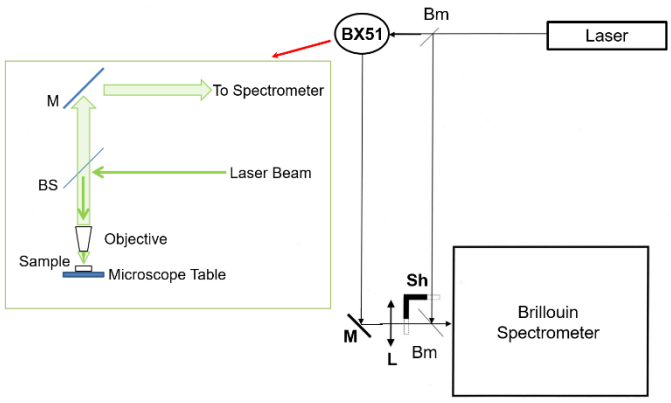

Figure 6 : Représentation schématique du banc optique Brillouin [171].

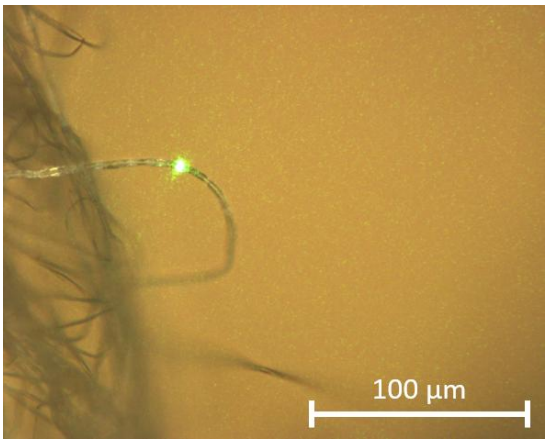

Figure 7 : Micrographie optique à un grossissement x50 montrant le laser focalisé sur une seule fibre.

Parmi les principaux paramètres d'électrofilage se trouve le rapport de solvants, DMF et acétone, utilisés pour mettre le PVDF en solution dans la seringue d'injection. Alors que d'autres techniques comme la spectroscopie Raman ou l'ATG n'avaient détecté aucun changement significatif entre les fibres élaborées par électrofilage avec différents rapports DMF:acétone, la réponse obtenue en spectrométrie Brillouin est remarquablement différente. Une forte variation des propriétés mécaniques a été observée : une chute de 12,5 GHz à 9 GHz, qui correspond à une variation de c_{11} 10 à 5 GPa, entre les fibres élaborées avec un rapport DMF:acétone de 3:7 (Figure 8) par rapport aux fibres élaborées avec un rapport DMF:acétone de 4:6 (Figure 9). Cette variation est attribuée à la présence de mésoporosités au sein des fibres, en lien direct avec les différences de vitesse d'évaporation des solvants. Elle conduit aussi à une variation d'aspect de surface observable en microscopie électronique à balayage (Figure 10).

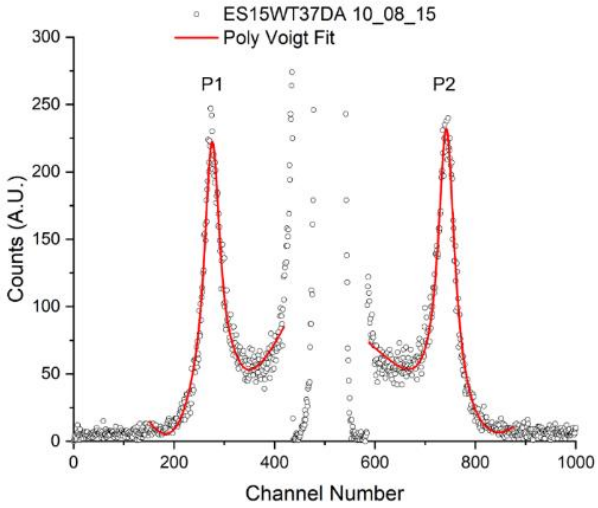

Figure 8 : Exemple de spectre Brillouin sur les fibres élaborées avec un rapport DMF:acétone de 3:7.

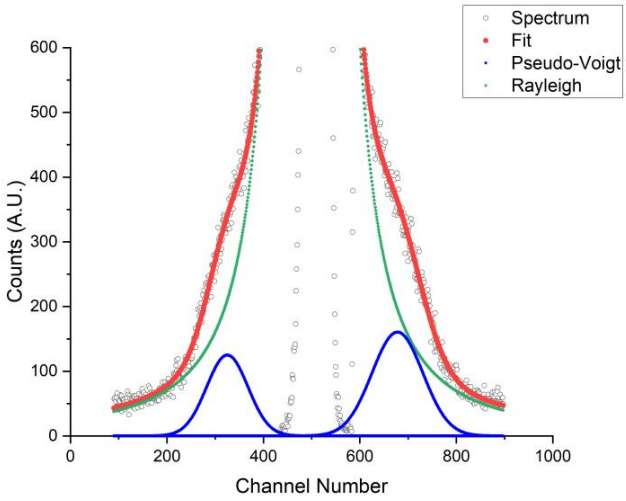

Figure 9 : Exemple de spectre Brillouin sur les fibres élaborées avec un rapport DMF:acétone de 4:6.

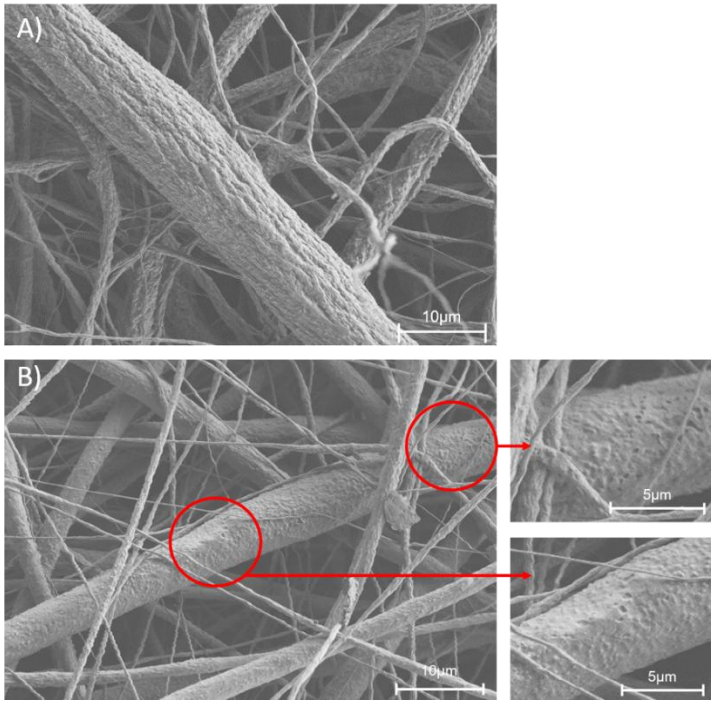

Figure 10 : Images de microscopie électronique à balayage sur A) fibres élaborées avec un rapport DMF:acétone de 3 :7 ; B) fibres élaborées avec un rapport DMF:acétone de 4:6.

Une étude menée sur des fibres composites CNC a confirmé les résultats obtenus à partir des méthodes de caractérisation précédentes, montrant que l'ajout de CNC a un impact négligeable sur le taux de cristallinité et les valeurs c_{11} des fibres composites par rapport aux résultats obtenus à partir du seul processus d'électrofilage. Il n'a pas été possible de reproduire la même étude sur des fibres avec QC. En raison de la faible conductivité thermique des agrégats de QC, le chauffage et le ramollissement consécutif de la matrice fibreuse en PVDF pourraient masquer l'effet de renforcement possible de l'ajout de QC, ce qui pourrait rendre impossible la mesure par spectroscopie Brillouin de la valeur c_{11} des fibres composites PVDF-QC.

Un autre résultat important a été obtenu en explorant l'évolution en fonction de la température des propriétés mécaniques des fibres de PVDF électrofilées. Une anomalie élastique inattendue a été mise en évidence, sous la forme d'un changement de pente dans la variation de la constante élastique c_{11} avec la température à une température déterminée de 31 °C (Figure 11).

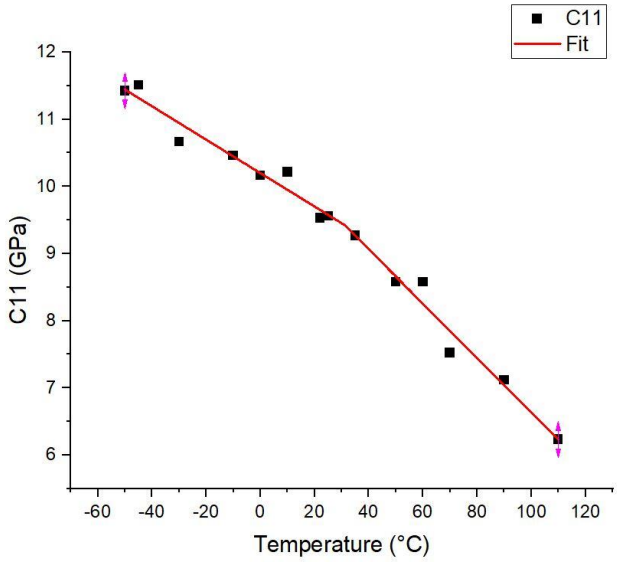

Figure 11 : Evolution de la constante élastique c_{11} calculée, en fonction de la température.

L'explication proposée est que cette anomalie élastique peut être interprétée comme une réorientation/réorganisation/désorganisation à l'interface amorphe-cristalline, située autour de 30 °C dans les fibres électrofilées. Cette transition précède la fusion des cristaux α imparfaits qui se produit autour de 60 °C, et finalement la fusion du PVDF autour de 160 °C. Dans le cas des échantillons de PVDF qui n'ont pas été soumis à un étirement mécanique, la fusion des cristaux α est le seul événement observable en spectroscopie Brillouin. L'absence du simple changement de pente situé à 30 °C dans les matériaux non orientés mécaniquement souligne le fait que l'anomalie élastique associée aux réorientations à l'interface amorphe-cristalline est exclusive aux matériaux orientés mécaniquement. Une étude complémentaire sur un échantillon obtenu par solvent casting, impliquant des analyses de spectroscopie Raman et Brillouin, suggère par ailleurs la possibilité que l'exposition à un laser vert de 532 nm puisse favoriser la croissance de la phase β.

Après la caractérisation chimique, morphologique, structurelle et mécanique approfondie des matrices électrofilées en PVDF, des dispositifs de test ont été réalisés avec les différents matériaux électrofilés, sous forme de mats (Figure 12). Puis les performances électriques des dispositifs ont été évaluées à l'aide d'un banc d'essai de battement périodique conçu et réalisé au laboratoire dans le cadre de cette thèse (Figure 13). La pression périodique de la tige sur l'échantillon PVDF permet de générer des charges électriques récoltées via les électrodes du dispositif.

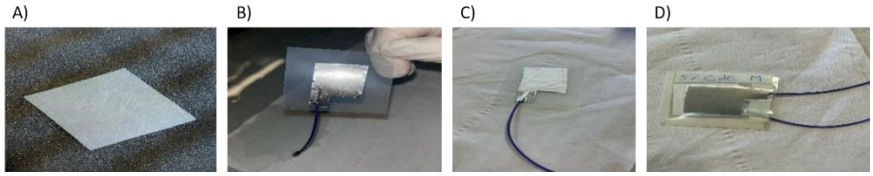

Figure 12 : Étapes de préparation des dispositifs PVDF A) la couche PET, B) l'électrode en forme de P avec le fil de connexion, C) ajout du mat électrofilé, D) le dispositif fini.

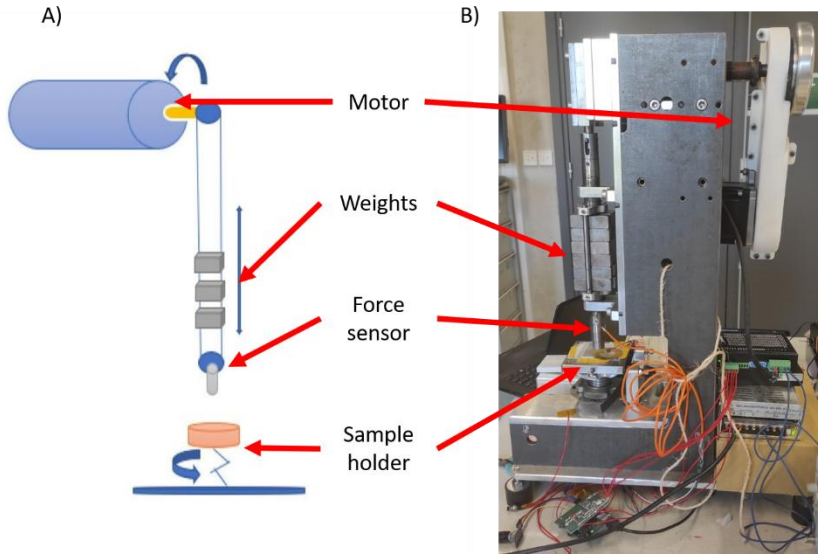

Figure 13 : A) Schéma fonctionnel et B) photographie du banc d'essai de battement périodique.

Ce dispositif a permis de tester les performances des fibres PVDF pures et nanocomposites, et d'évaluer leur sensibilité aux forces mécaniques appliquées et aux variations de fréquence de battement.

Parmi les dispositifs testés, le dispositif avec le PVDF chargé en nanocristaux de cellulose à 5% a obtenu les performances de sortie les plus élevées, tout en maintenant une bonne stabilité du signal, atteignant 60 V de tension crête à crête et 60 µA de courant crête à crête.

Après avoir sélectionné une carte de récupération d'énergie appropriée, l'EH300, une application de démonstration du dispositif a été proposée (Figure 14).

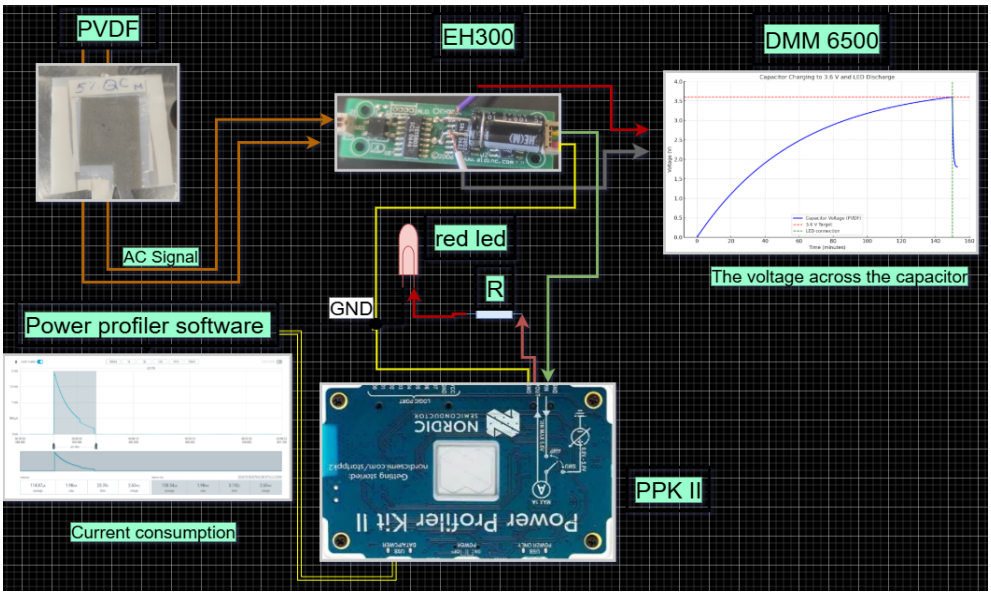

Figure 14 : Configuration expérimentale pour le test de récupération d'énergie à base de PVDF.

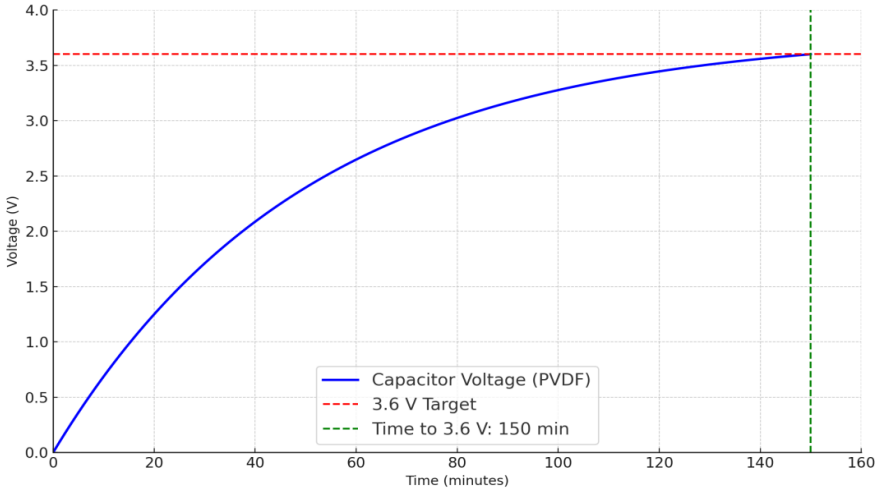

Figure 40 : Profil de charge du condensateur de 1000 µF de l'EH300 par le dispositif en fibres PVDF soumis à une pression périodique de 4 kg à 2 Hz.

Nous avons démontré la capacité pratique du PVDF à fonctionner à la fois comme capteur d'impulsions et comme nanogénérateur de récupération d'énergie mécanique, démontrant ainsi son potentiel d'intégration par exemple dans des systèmes de surveillance de la santé sans fil à faible consommation.

References

[1] H. Habibzadeh, K. Dinesh, O. Rajabi Shishvan, A. Boggio-Dandry, G. Sharma, T. Soyata, A Survey of Healthcare Internet of Things (HIoT): A Clinical Perspective, IEEE Internet Things J. 7 (2020) 53–71. https://doi.org/10.1109/JIOT.2019.2946359.

[2] D. N. Perkins, M.-N. Brune Drisse, T. Nxele, P. D. Sly, E-Waste: A Global Hazard, Annals of Global Health 80 (2014) 286. https://doi.org/10.1016/j.aogh.2014.10.001.

[3] E.M. Melchor-Martínez, R. Macias-Garbett, A. Malacara-Becerra, H.M.N. Iqbal, J.E. Sosa-Hernández, R. Parra-Saldívar, Environmental impact of emerging contaminants from battery waste: A mini review, Case Studies in Chemical and Environmental Engineering 3 (2021) 100104. https://doi.org/10.1016/j.cscee.2021.100104.

[4] L. Xiao, B. Yin, Z. Geng, J. Li, R. Jia, K. Zhang, Flexible wearable devices based on self-powered energy supply, Nano Energy 142 (2025) 111157. https://doi.org/10.1016/j.nanoen.2025.111157.

[5] N. Hossein Motlagh, M. Mohammadrezaei, J. Hunt, B. Zakeri, Internet of Things (IoT) and the Energy Sector, Energies 13 (2020) 494. https://doi.org/10.3390/en13020494.

[6] M. Dachyar, T.Y.M. Zagloel, L.R. Saragih, Knowledge growth and development: internet of things (IoT) research, 2006–2018, Heliyon 5 (2019) e02264. https://doi.org/10.1016/j.heliyon.2019.e02264.

[7] M. Yang, K. Peng, Z. Li, Y. Gao, Q. Tian, Z. Zhou, Y. Chen, Recent progress in flexible materials for wearable devices for body function and athletic performance monitoring, Chemical Engineering Journal 505 (2025) 159659. https://doi.org/10.1016/j.cej.2025.159659.

[8] J. Wang, M.K. Lim, C. Wang, M.-L. Tseng, The evolution of the Internet of Things (IoT) over the past 20 years, Computers & Industrial Engineering 155 (2021) 107174. https://doi.org/10.1016/j.cie.2021.107174.

[9] J.H. Nord, A. Koohang, J. Paliszkiewicz, The Internet of Things: Review and theoretical framework, Expert Systems with Applications 133 (2019) 97–108. https://doi.org/10.1016/j.eswa.2019.05.014.

[10] N. Sezer, M. Koç, A comprehensive review on the state-of-the-art of piezoelectric energy harvesting, Nano Energy 80 (2021) 105567. https://doi.org/10.1016/j.nanoen.2020.105567.

[11] S. Chalasani, J.M. Conrad, A Survey of Energy Harvesting Sources for Embedded Systems, (n.d.).

[12] A. Ali, H. Shaukat, H. Elahi, S. Taimur, M.Q. Manan, W.A. Altabey, S.A. Kouritem, M. Noori, Advancements in energy harvesting techniques for sustainable IoT devices, Results in Engineering 26 (2025) 104820. https://doi.org/10.1016/j.rineng.2025.104820.

[13] M.-L. Ku, W. Li, Y. Chen, Advances in Energy Harvesting Communications: Past, Present, and Future Challenges, (n.d.).

[14] C. Xu, Y. Song, M. Han, H. Zhang, Portable and wearable self-powered systems based on emerging energy harvesting technology, Microsyst Nanoeng 7 (2021) 25. https://doi.org/10.1038/s41378-021-00248-z.

[15] S. Bauer, F. Bauer, 6 Piezoelectric Polymers and Their Applications, (n.d.).

[16] K.S. Ramadan, D. Sameoto, S. Evoy, A review of piezoelectric polymers as functional materials for electromechanical transducers, Smart Mater. Struct. 23 (2014) 033001. https://doi.org/10.1088/0964-1726/23/3/033001.

[17] S. Mishra, L. Unnikrishnan, S.K. Nayak, S. Mohanty, Advances in Piezoelectric Polymer Composites for Energy Harvesting Applications: A Systematic Review, Macromol. Mater. Eng. 304 (2019) 1800463. https://doi.org/10.1002/mame.201800463.

[18] M. Ali, M.J. Bathaei, E. Istif, S.N.H. Karimi, L. Beker, Biodegradable Piezoelectric Polymers: Recent Advancements in Materials and Applications, Adv Healthcare Materials 12 (2023) 2300318. https://doi.org/10.1002/adhm.202300318.

[19] K.K. Sappati, S. Bhadra, Piezoelectric Polymer and Paper Substrates: A Review, Sensors 18 (2018) 3605. https://doi.org/10.3390/s18113605.

[20] Z. Wu, X. Ding, X. Chen, J. Chen, X. Chang, Z. Liu, L. Song, J. Huang, Y. Zhu, Recent progress of polymer-based piezoelectric nanogenerators, Adv Compos Hybrid Mater 8 (2025) 225. https://doi.org/10.1007/s42114-025-01225-0.

[21] E. Fukada, M. Date, T. Ochiai, S. Koyama, Y. Sasaki, Piezoelectricity in polyurethane films induced by electrostriction and bias electric field, in: 10th International Symposium on Electrets (ISE 10). Proceedings

(Cat. No.99 CH36256), IEEE, Athens, Greece, 1999: pp. 655–658. https://doi.org/10.1109/ISE.1999.832131.
[22] D.C. Bassett, ed., Developments in Crystalline Polymers—1, Springer Netherlands, Dordrecht, 1982. https://doi.org/10.1007/978-94-009-7343-5.
[23] M.G. Broadhurst, G.T. Davis, Physical basis for piezoelectricity in PVDF, Ferroelectrics 60 (1984) 3–13. https://doi.org/10.1080/00150198408017504.
[24] A. Salimi, A.A. Yousefi, Conformational changes and phase transformation mechanisms in PVDF solution-cast films, J. Polym. Sci. B Polym. Phys. 42 (2004) 3487–3495. https://doi.org/10.1002/polb.20223.
[25] V. Sencadas, R. Gregorio, S. Lanceros-Méndez, α to β Phase Transformation and Microestructural Changes of PVDF Films Induced by Uniaxial Stretch, Journal of Macromolecular Science, Part B 48 (2009) 514–525. https://doi.org/10.1080/00222340902837527.
[26] J.L. Lutkenhaus, K. McEnnis, A. Serghei, T.P. Russell, Confinement Effects on Crystallization and Curie Transitions of Poly(vinylidene fluoride- *co* -trifluoroethylene), Macromolecules 43 (2010) 3844–3850. https://doi.org/10.1021/ma100166a.
[27] V. R. P., D.V. Khakhar, A. Misra, Studies on α to β phase transformations in mechanically deformed PVDF films, J. Appl. Polym. Sci. (2010) n/a-n/a. https://doi.org/10.1002/app.32218.
[28] M. Li, I. Katsouras, C. Piliego, G. Glasser, I. Lieberwirth, P.W.M. Blom, D.M. de Leeuw, Controlling the microstructure of poly(vinylidene-fluoride) (PVDF) thin films for microelectronics, J. Mater. Chem. C 1 (2013) 7695. https://doi.org/10.1039/c3tc31774a.
[29] L. Li, M. Zhang, M. Rong, W. Ruan, Studies on the transformation process of PVDF from α to β phase by stretching, RSC Adv. 4 (2014) 3938–3943. https://doi.org/10.1039/C3RA45134H.
[30] P. Saxena, P. Shukla, A comprehensive review on fundamental properties and applications of poly(vinylidene fluoride) (PVDF), Adv Compos Hybrid Mater 4 (2021) 8–26. https://doi.org/10.1007/s42114-021-00217-0.
[31] S. Sukumaran, S. Chatbouri, D. Rouxel, E. Tisserand, F. Thiebaud, T. Ben Zineb, Recent advances in flexible PVDF based piezoelectric polymer devices for energy harvesting applications, Journal of Intelligent Material Systems and Structures 32 (2021) 746–780. https://doi.org/10.1177/1045389X20966058.
[32] A.S. Motamedi, H. Mirzadeh, F. Hajiesmaeilbaigi, S. Bagheri-Khoulenjani, M. Shokrgozar, Effect of electrospinning parameters on morphological properties of PVDF nanofibrous scaffolds, Prog Biomater 6 (2017) 113–123. https://doi.org/10.1007/s40204-017-0071-0.
[33] J. Stanger, N. Tucker, M. Staiger, Electrospinning, Rapra Technology, Shawbury, 2006.
[34] P. Filip, J. Zelenkova, P. Peer, Electrospinning of a Copolymer PVDF-co-HFP Solved in DMF/Acetone: Explicit Relations among Viscosity, Polymer Concentration, DMF/Acetone Ratio and Mean Nanofiber Diameter, (2021).
[35] S. Agarwal, M. Burgard, A. Greiner, J. Wendorff, Electrospinning: A Practical Guide to Nanofibers, De Gruyter, 2016. https://doi.org/10.1515/9783110333510.
[36] T. Pardy, R. Joemaa, F. Ender, T. Rang, K. Hegedus, D. Balogh-Weiser, Polymer Nanofiber Deposition in Lab-on-a-Chip Devices By Electrospinning, in: 2020 17th Biennial Baltic Electronics Conference (BEC), IEEE, Tallinn, Estonia, 2020: pp. 1–4. https://doi.org/10.1109/BEC49624.2020.9277494.
[37] S. Bodkhe, P.S.M. Rajesh, S. Kamle, V. Verma, Beta-phase enhancement in polyvinylidene fluoride through filler addition: comparing cellulose with carbon nanotubes and clay, J Polym Res 21 (2014) 434. https://doi.org/10.1007/s10965-014-0434-3.
[38] P. Thakur, A. Kool, B. Bagchi, S. Das, P. Nandy, Enhancement of β phase crystallization and dielectric behavior of kaolinite/halloysite modified poly(vinylidene fluoride) thin films, Applied Clay Science 99 (2014) 149–159. https://doi.org/10.1016/j.clay.2014.06.025.
[39] B. Ma, J. Yang, Q. Sun, W. Jakpa, X. Hou, Y. Yang, Influence of cellulose/[Bmim]Cl solution on the properties of fabricated NIPS PVDF membranes, J Mater Sci 52 (2017) 9946–9957. https://doi.org/10.1007/s10853-017-1150-2.
[40] F. Ram, T. Ambone, A. Sharma, R. Murugesan, D. Kajale, V. Borkar, S.F. Ali, P.K. Balu, G. Kumaraswamy, K. Shanmuganathan, Fluorinated Nanocellulose-Reinforced All-Organic Flexible Ferroelectric Nanocomposites for Energy Generation, J. Phys. Chem. C 122 (2018) 16540–16549. https://doi.org/10.1021/acs.jpcc.8b03470.
[41] F. Ram, A. Gudadhe, T. Vijayakanth, S. Aherrao, V. Borkar, R. Boomishankar, K. Shanmuganathan, Nanocellulose Reinforced Flexible Composite Nanogenerators with Enhanced Vibrational Energy

Harvesting and Sensing Properties, ACS Appl. Polym. Mater. 2 (2020) 2550–2562. https://doi.org/10.1021/acsapm.0c00158.
[42] Y. Wu, Y. Ma, H. Zheng, S. Ramakrishna, Piezoelectric materials for flexible and wearable electronics: A review, Materials & Design 211 (2021) 110164. https://doi.org/10.1016/j.matdes.2021.110164.
[43] Md. Ataur Rahman, G.-S. Chung, Synthesis of PVDF-graphene nanocomposites and their properties, Journal of Alloys and Compounds 581 (2013) 724–730. https://doi.org/10.1016/j.jallcom.2013.07.118.
[44] X. Wang, F. Sun, G. Yin, Y. Wang, B. Liu, M. Dong, Tactile-Sensing Based on Flexible PVDF Nanofibers via Electrospinning: A Review, Sensors 18 (2018) 330. https://doi.org/10.3390/s18020330.
[45] R.C. Twiney, Novel piezoelectric materials, Adv. Mater. 4 (1992) 819–822. https://doi.org/10.1002/adma.19920041213.
[46] H.M.G. Correia, M.M.D. Ramos, Quantum modelling of poly(vinylidene fluoride), Computational Materials Science 33 (2005) 224–229. https://doi.org/10.1016/j.commatsci.2004.12.040.
[47] Y. Feng, C. Peng, Q. Deng, Y. Li, J. Hu, Q. Wu, Annealing and Stretching Induced High Energy Storage Properties in All-Organic Composite Dielectric Films, Materials 11 (2018) 2279. https://doi.org/10.3390/ma11112279.
[48] K. Jurczuk, A. Galeski, M. Mackey, A. Hiltner, E. Baer, Orientation of PVDF α and γ crystals in nanolayered films, Colloid Polym Sci 293 (2015) 1289–1297. https://doi.org/10.1007/s00396-015-3542-7.
[49] M.P. Silva, V. Sencadas, G. Botelho, A.V. Machado, A.G. Rolo, J.G. Rocha, S. Lanceros-Mendez, α- and γ-PVDF: Crystallization kinetics, microstructural variations and thermal behaviour, Materials Chemistry and Physics 122 (2010) 87–92. https://doi.org/10.1016/j.matchemphys.2010.02.067.
[50] H. Wang, X. Yang, Y. Zhao, C. Yan, S. Wang, H. Yang, X. Wang, J.M. Schultz, Preparation of gamma-PVDF with controlled orientation and insight into phase transformation, Polymer 123 (2017) 282–289. https://doi.org/10.1016/j.polymer.2017.07.004.
[51] H. Horibe, Y. Sasaki, H. Oshiro, Y. Hosokawa, A. Kono, S. Takahashi, T. Nishiyama, Quantification of the solvent evaporation rate during the production of three PVDF crystalline structure types by solvent casting, Polym J 46 (2014) 104–110. https://doi.org/10.1038/pj.2013.75.
[52] P.K. Mahato, A. Seal, S. Garain, S. Sen, Effect of fabrication technique on the crystalline phase and electrical properties of PVDF films, Materials Science-Poland 33 (2015) 157–162. https://doi.org/10.1515/msp-2015-0020.
[53] M. Yasar, P. Hassett, N. Murphy, A. Ivankovic, β Phase Optimization of Solvent Cast PVDF as a Function of the Processing Method and Additive Content, ACS Omega 9 (2024) 26020–26029. https://doi.org/10.1021/acsomega.4c01221.
[54] A. Biswas, K. Henkel, D. Schmeißer, D. Mandal, Comparison of the thermal stability of the α, β and γ phases in poly(vinylidene fluoride) based on *in situ* thermal Fourier transform infrared spectroscopy, Phase Transitions (2017) 1–9. https://doi.org/10.1080/01411594.2017.1337902.
[55] K. Pilla, M. Neergat, K.N. Jonnalagadda, Strain and temperature induced phase changes in SPIN-COATED PVDF thin films, Journal of Polymer Science 61 (2023) 1082–1096. https://doi.org/10.1002/pol.20220688.
[56] Z. Yin, B. Tian, Q. Zhu, C. Duan, Characterization and Application of PVDF and Its Copolymer Films Prepared by Spin-Coating and Langmuir–Blodgett Method, Polymers 11 (2019) 2033. https://doi.org/10.3390/polym11122033.
[57] T. Nishiyama, T. Sumihara, E. Sato, H. Horibe, Effect of solvents on the crystal formation of poly(vinylidene fluoride) film prepared by a spin-coating process, Polym J 49 (2017) 319–325. https://doi.org/10.1038/pj.2016.116.
[58] L.M.M. Costa, R.E.S. Bretas, R. Gregorio, Effect of Solution Concentration on the Electrospray/Electrospinning Transition and on the Crystalline Phase of PVDF, MSA 01 (2010) 247–252. https://doi.org/10.4236/msa.2010.14036.
[59] E.S. Cozza, O. Monticelli, E. Marsano, P. Cebe, On the electrospinning of PVDF: influence of the experimental conditions on the nanofiber properties: Electrospinning of poly(vinylidene fluoride), Polym. Int. 62 (2013) 41–48. https://doi.org/10.1002/pi.4314.
[60] G. Kalimuldina, N. Turdakyn, I. Abay, A. Medeubayev, A. Nurpeissova, D. Adair, Z. Bakenov, A Review of Piezoelectric PVDF Film by Electrospinning and Its Applications, Sensors 20 (2020) 5214. https://doi.org/10.3390/s20185214.

[61] A.M. Al-Dhahebi, M.S.M. Saheed, M. Mustapha, Effects of solution concentration on the synthesis of polyvinylidene fluoride (PVDF) electrospun nanofibers, Materials Today: Proceedings (2021) S2214785321044837. https://doi.org/10.1016/j.matpr.2021.06.128.
[62] R.K. Singh, S.W. Lye, J. Miao, Measurement of impact characteristics in a string using electrospun PVDF nanofibers strain sensors, Sensors and Actuators A: Physical 303 (2020) 111841. https://doi.org/10.1016/j.sna.2020.111841.
[63] H.M. Venkatesan, A.P. Arun, High-performance triboelectric nanogenerators based on Ag-doped ZnO loaded electrospun PVDF nanofiber mats for energy harvesting and healthcare monitoring, Sci Rep 15 (2025). https://doi.org/10.1038/s41598-025-87148-8.
[64] Z. He, F. Rault, M. Lewandowski, E. Mohsenzadeh, F. Salaün, Electrospun PVDF Nanofibers for Piezoelectric Applications: A Review of the Influence of Electrospinning Parameters on the β Phase and Crystallinity Enhancement, Polymers 13 (2021) 174. https://doi.org/10.3390/polym13020174.
[65] Lyles School of Civil Engineering, Sustainable Materials and Renewable Technology (SMART) Lab, Purdue University, USA, G. Han, Y. Su, Lyles School of Civil Engineering, Sustainable Materials and Renewable Technology (SMART) Lab, Purdue University, USA, Y. Feng, Lyles School of Civil Engineering, Sustainable Materials and Renewable Technology (SMART) Lab, Purdue University, USA, N. Lu, Lyles School of Civil Engineering, Sustainable Materials and Renewable Technology (SMART) Lab, Purdue University, USA, School of Materials Engineering, Purdue University, USA, Center for intelligent infrastructure, Purdue University, USA, Approaches for Increasing the β-phase Concentration of Electrospun Polyvinylidene Fluoride (PVDF) Nanofibers, ES Mater.Manuf. (2019). https://doi.org/10.30919/esmm5f612.
[66] R. Fu, S. Chen, Y. Lin, Y. He, d Y. Gu, Preparation and Piezoelectric Investigation of Electrospun Polyvinylidene Fluoride Fibrous Membrane, J Nanosci Nanotechnol 16 (2016) 12337–12343. https://doi.org/10.1166/jnn.2016.13750.
[67] K. Magniez, C. De Lavigne, B.L. Fox, The effects of molecular weight and polymorphism on the fracture and thermo-mechanical properties of a carbon-fibre composite modified by electrospun poly (vinylidene fluoride) membranes, Polymer 51 (2010) 2585–2596. https://doi.org/10.1016/j.polymer.2010.04.021.
[68] B. Zaarour, L. Zhu, X. Jin, Controlling the surface structure, mechanical properties, crystallinity, and piezoelectric properties of electrospun PVDF nanofibers by maneuvering molecular weight, Soft Materials 17 (2019) 181–189. https://doi.org/10.1080/1539445X.2019.1582542.
[69] Z. He, F. Rault, M. Lewandowski, E. Mohsenzadeh, F. Salaün, Electrospun PVDF Nanofibers for Piezoelectric Applications: A Review of the Influence of Electrospinning Parameters on the β Phase and Crystallinity Enhancement, Polymers 13 (2021) 174. https://doi.org/10.3390/polym13020174.
[70] H. Gade, S. Nikam, G.G. Chase, D.H. Reneker, Effect of electrospinning conditions on β-phase and surface charge potential of PVDF fibers, Polymer 228 (2021) 123902. https://doi.org/10.1016/j.polymer.2021.123902.
[71] A. Baji, Y.-W. Mai, Q. Li, Y. Liu, Electrospinning induced ferroelectricity in poly(vinylidene fluoride) fibers, Nanoscale 3 (2011) 3068. https://doi.org/10.1039/c1nr10467e.
[72] L.M.M. Costa, R.E.S. Bretas, R. Gregorio, Effect of Solution Concentration on the Electrospray/Electrospinning Transition and on the Crystalline Phase of PVDF, MSA 01 (2010) 247–252. https://doi.org/10.4236/msa.2010.14036.
[73] R.K. Singh, S.W. Lye, J. Miao, Measurement of impact characteristics in a string using electrospun PVDF nanofibers strain sensors, Sensors and Actuators A: Physical 303 (2020) 111841. https://doi.org/10.1016/j.sna.2020.111841.
[74] J. Zheng, A. He, J. Li, C.C. Han, Polymorphism Control of Poly(vinylidene fluoride) through Electrospinning, Macromol. Rapid Commun. 28 (2007) 2159–2162. https://doi.org/10.1002/marc.200700544.
[75] S. Gee, B. Johnson, A.L. Smith, Optimizing electrospinning parameters for piezoelectric PVDF nanofiber membranes, Journal of Membrane Science 563 (2018) 804–812. https://doi.org/10.1016/j.memsci.2018.06.050.
[76] S. Saha, V. Yauvana, S. Chakraborty, D. Sanyal, Synthesis and Characterization of Polyvinylidene-fluoride (PVDF) Nanofiber for Application as Piezoelectric Force Sensor, Materials Today: Proceedings 18 (2019) 1450–1458. https://doi.org/10.1016/j.matpr.2019.06.613.
[77] H. Jiyong, Z. Yinda, Z. Hele, G. Yuanyuan, Y. Xudong, Mixed effect of main electrospinning parameters on the *β* -phase crystallinity of electrospun PVDF nanofibers, Smart Mater. Struct. 26 (2017) 085019. https://doi.org/10.1088/1361-665X/aa7245.

[78] H. Gade, S. Nikam, G.G. Chase, D.H. Reneker, Effect of electrospinning conditions on β-phase and surface charge potential of PVDF fibers, Polymer 228 (2021) 123902. https://doi.org/10.1016/j.polymer.2021.123902.
[79] H. Jiyong, Z. Yinda, Z. Hele, G. Yuanyuan, Y. Xudong, Mixed effect of main electrospinning parameters on the *β* -phase crystallinity of electrospun PVDF nanofibers, Smart Mater. Struct. 26 (2017) 085019. https://doi.org/10.1088/1361-665X/aa7245.
[80] E. Ghafari, N. Lu, Self-polarized electrospun polyvinylidene fluoride (PVDF) nanofiber for sensing applications, Composites Part B: Engineering 160 (2019) 1–9. https://doi.org/10.1016/j.compositesb.2018.10.011.
[81] T. Lei, L. Yu, G. Zheng, L. Wang, D. Wu, D. Sun, Electrospinning-induced preferred dipole orientation in PVDF fibers, J Mater Sci 50 (2015) 4342–4347. https://doi.org/10.1007/s10853-015-8986-0.
[82] A. Kumar, V. Gupta, P. Malik, S. Ram, D. Mandal, Electrospun polarity-controlled molecular orientation for synergistic performance of an artifact-free piezoelectric anisotropic sensor, Mater. Horiz. 11 (2024) 4424–4437. https://doi.org/10.1039/D4MH00540F.
[83] Y.M. Yousry, K. Yao, A.M. Mohamed, W.H. Liew, S. Chen, S. Ramakrishna, Theoretical Model and Outstanding Performance from Constructive Piezoelectric and Triboelectric Mechanism in Electrospun PVDF Fiber Film, Adv Funct Materials 30 (2020) 1910592. https://doi.org/10.1002/adfm.201910592.
[84] L. Persano, C. Dagdeviren, Y. Su, Y. Zhang, S. Girardo, D. Pisignano, Y. Huang, J.A. Rogers, High performance piezoelectric devices based on aligned arrays of nanofibers of poly(vinylidenefluoride-co-trifluoroethylene), Nat Commun 4 (2013) 1633. https://doi.org/10.1038/ncomms2639.
[85] H. Yu, T. Huang, M. Lu, M. Mao, Q. Zhang, H. Wang, Enhanced power output of an electrospun PVDF/MWCNTs-based nanogenerator by tuning its conductivity, Nanotechnology 24 (2013) 405401. https://doi.org/10.1088/0957-4484/24/40/405401.
[86] J. Fang, X. Wang, T. Lin, Electrical power generator from randomly oriented electrospun poly(vinylidene fluoride) nanofibre membranes, J. Mater. Chem. 21 (2011) 11088. https://doi.org/10.1039/c1jm11445j.
[87] B.J. Hansen, Y. Liu, R. Yang, Z.L. Wang, Hybrid Nanogenerator for Concurrently Harvesting Biomechanical and Biochemical Energy, ACS Nano 4 (2010) 3647–3652. https://doi.org/10.1021/nn100845b.
[88] D. Farrar, K. Ren, D. Cheng, S. Kim, W. Moon, W.L. Wilson, J.E. West, S.M. Yu, Permanent Polarity and Piezoelectricity of Electrospun α -Helical Poly(α -Amino Acid) Fibers, Advanced Materials 23 (2011) 3954–3958. https://doi.org/10.1002/adma.201101733.
[89] M. Zaccaria, D. Fabiani, A. Zucchelli, J. Belcari, O. Bocchi, T. Cramer, B. Fraboni, Electret behavior of electrospun PVdF-based polymers, in: 2016 IEEE Conference on Electrical Insulation and Dielectric Phenomena (CEIDP), IEEE, Toronto, ON, Canada, 2016: pp. 137–140. https://doi.org/10.1109/CEIDP.2016.7785653.
[90] D. Lolla, M. Lolla, A. Abutaleb, H. Shin, D. Reneker, G. Chase, Fabrication, Polarization of Electrospun Polyvinylidene Fluoride Electret Fibers and Effect on Capturing Nanoscale Solid Aerosols, Materials 9 (2016) 671. https://doi.org/10.3390/ma9080671.
[91] H. Shao, J. Fang, H. Wang, T. Lin, Effect of electrospinning parameters and polymer concentrations on mechanical-to-electrical energy conversion of randomly-oriented electrospun poly(vinylidene fluoride) nanofiber mats, RSC Adv. 5 (2015) 14345–14350. https://doi.org/10.1039/C4RA16360E.
[92] A.S. Motamedi, H. Mirzadeh, F. Hajiesmaeilbaigi, S. Bagheri-Khoulenjani, M. Shokrgozar, Effect of electrospinning parameters on morphological properties of PVDF nanofibrous scaffolds, Prog Biomater 6 (2017) 113–123. https://doi.org/10.1007/s40204-017-0071-0.
[93] B. Zaarour, W. Zhang, L. Zhu, X.Y. Jin, C. Huang, Maneuvering surface structures of polyvinylidene fluoride nanofibers by controlling solvent systems and polymer concentration, Textile Research Journal 89 (2019) 2406–2422. https://doi.org/10.1177/0040517518792748.
[94] E. Ghafari, X. Jiang, N. Lu, Surface morphology and beta-phase formation of single polyvinylidene fluoride (PVDF) composite nanofibers, Adv Compos Hybrid Mater 1 (2018) 332–340. https://doi.org/10.1007/s42114-017-0016-z.
[95] E.S. Cozza, O. Monticelli, E. Marsano, P. Cebe, On the electrospinning of PVDF: influence of the experimental conditions on the nanofiber properties: Electrospinning of poly(vinylidene fluoride), Polym. Int. 62 (2013) 41–48. https://doi.org/10.1002/pi.4314.

[96] F. Huang, Q. Wei, J. Wang, Y. Cai, Y. Huang, Effect of temperature on structure, morphology and crystallinity of PVDF nanofibers via electrospinning, E-Polymers 8 (2008). https://doi.org/10.1515/epoly.2008.8.1.1758.
[97] S. Mohamadi, N. Sharifi-Sanjani, Crystallization of PVDF in graphene-filled electrospun PVDF/PMMA nanofibers processed at three different conditions, Fibers Polym 17 (2016) 582–592. https://doi.org/10.1007/s12221-016-5038-6.
[98] P. Szewczyk, D. Ura, U. Stachewicz, Humidity Controlled Mechanical Properties of Electrospun Polyvinylidene Fluoride (PVDF) Fibers, Fibers 8 (2020) 65. https://doi.org/10.3390/fib8100065.
[99] B. Zaarour, L. Zhu, C. Huang, X. Jin, Controlling the Secondary Surface Morphology of Electrospun PVDF Nanofibers by Regulating the Solvent and Relative Humidity, Nanoscale Res Lett 13 (2018) 285. https://doi.org/10.1186/s11671-018-2705-0.
[100] Y. Xin, J. Zhu, H. Sun, Y. Xu, T. Liu, C. Qian, A brief review on piezoelectric PVDF nanofibers prepared by electrospinning, Ferroelectrics 526 (2018) 140–151. https://doi.org/10.1080/00150193.2018.1456304.
[101] S. Ponnan, C.L. C S, M.S. Reza, S. Moozhiyil Purushothaman, M. Fernandes-tronco, M. Poncot, H. Kim, S. Thomas, I. Royaud, D. Rouxel, N. Kalarikkal, Bi-filler Interacted β-Phase Enhancement in Polyvinylidene Fluoride Composited with Cellulose Nanocrystals and Nickel Ferrite: A Multifunctional Energy Harvester and Sleep Monitoring Sensor, ACS Appl. Electron. Mater. 6 (2024) 4963–4976. https://doi.org/10.1021/acsaelm.4c00519.
[102] L. Pan, Y. Wang, Q. Jin, Z. Hu, Z. Zhou, M. Zhu, Self-poled PVDF/recycled cellulose composite fibers utilizing cellulose nanocrystals to induce PVDF β-phase formation through wet-spinning as a flexible fabric piezoelectric sensor, Chemical Engineering Journal 479 (2024) 147742. https://doi.org/10.1016/j.cej.2023.147742.
[103] J.-E. Lee, Y.-E. Shin, G.-H. Lee, J. Kim, H. Ko, H.G. Chae, Polyvinylidene fluoride (PVDF)/cellulose nanocrystal (CNC) nanocomposite fiber and triboelectric textile sensors, Composites Part B: Engineering 223 (2021) 109098. https://doi.org/10.1016/j.compositesb.2021.109098.
[104] J. Chen, J. Fan, M. Livojevic, M. Gupta, T. Tang, C. Ayranci, Enhancing piezoelectric properties of PVDF-HFP composite nanofibers with cellulose nanocrystals, Materials Today Communications 39 (2024) 108872. https://doi.org/10.1016/j.mtcomm.2024.108872.
[105] H. Bai, X. Wang, Y. Zhou, L. Zhang, Preparation and characterization of poly(vinylidene fluoride) composite membranes blended with nano-crystalline cellulose, Progress in Natural Science: Materials International 22 (2012) 250–257. https://doi.org/10.1016/j.pnsc.2012.04.011.
[106] P.S.M. Rajesh, S. Bodkhe, S. Kamle, V. Verma, Enhancing beta-phase in PVDF through physicochemical modification of cellulose, Electron. Mater. Lett. 10 (2014) 315–319. https://doi.org/10.1007/s13391-013-3083-5.
[107] M.F.H. Abd El-Kader, N.S. Awwad, H.A. Ibrahium, M.K. Ahmed, Graphene oxide fillers through polymeric blends of PVC/PVDF using laser ablation technique: electrical behavior, cell viability, and thermal stability, Journal of Materials Research and Technology 13 (2021) 1878–1886. https://doi.org/10.1016/j.jmrt.2021.05.024.
[108] S. Begum, H. Ullah, I. Ahmed, Y. Zhan, A. Kausar, M.A. Aleem, S. Ahmad, Investigation of morphology, crystallinity, thermal stability, piezoelectricity and conductivity of PVDF nanocomposites reinforced with epoxy functionalized MWCNTs, Composites Science and Technology 211 (2021) 108841. https://doi.org/10.1016/j.compscitech.2021.108841.
[109] R. Ram, V. Soni, D. Khastgir, Electrical and thermal conductivity of polyvinylidene fluoride (PVDF) – Conducting Carbon Black (CCB) composites: Validation of various theoretical models, Composites Part B: Engineering 185 (2020) 107748. https://doi.org/10.1016/j.compositesb.2020.107748.
[110] J.A. Puértolas, J.F. García-García, F.J. Pascual, J.M. González-Domínguez, M.T. Martínez, A. Ansón-Casaos, Dielectric behavior and electrical conductivity of PVDF filled with functionalized single-walled carbon nanotubes, Composites Science and Technology 152 (2017) 263–274. https://doi.org/10.1016/j.compscitech.2017.09.016.
[111] I.S. Elashmawi, Effect of LiCl filler on the structure and morphology of PVDF films, Materials Chemistry and Physics 107 (2008) 96–100. https://doi.org/10.1016/j.matchemphys.2007.06.045.
[112] J. Chen, H. Lu, J. Yang, Y. Wang, X. Zheng, C. Zhang, G. Yuan, Effect of organoclay on morphology and electrical conductivity of PC/PVDF/CNT blend composites, Composites Science and Technology 94 (2014) 30–38. https://doi.org/10.1016/j.compscitech.2014.01.010.

[113] W. Zhou, J. Zuo, W. Ren, Thermal conductivity and dielectric properties of Al/PVDF composites, Composites Part A: Applied Science and Manufacturing 43 (2012) 658–664. https://doi.org/10.1016/j.compositesa.2011.11.024.
[114] Y. Li, Z. Wang, M. Kong, Z. Yi, Improved thermal conductivity and breakdown strength of PVDF‐based composites by improving the dispersion of BN, High Voltage 7 (2022) 595–605. https://doi.org/10.1049/hve2.12150.
[115] B. Wang, X. Yin, D. Peng, Y. Zhang, W. Wu, X. Gu, B. Na, R. Lv, H. Liu, Highly thermally conductive PVDF-based ternary dielectric composites via engineering hybrid filler networks, Composites Part B: Engineering 191 (2020) 107978. https://doi.org/10.1016/j.compositesb.2020.107978.
[116] S.K. Karan, A.K. Das, R. Bera, S. Paria, A. Maitra, N.K. Shrivastava, B.B. Khatua, Effect of γ-PVDF on enhanced thermal conductivity and dielectric property of Fe-rGO incorporated PVDF based flexible nanocomposite film for efficient thermal management and energy storage applications, RSC Adv. 6 (2016) 37773–37783. https://doi.org/10.1039/C6RA04365H.
[117] G. Yi, J. Li, L.C. Henderson, W. Lei, L. Du, S. Zhao, Enhancing Thermal Conductivity of Polyvinylidene Fluoride Composites by Carbon Fiber: Length Effect of the Filler, Polymers 14 (2022) 4599. https://doi.org/10.3390/polym14214599.
[118] P. Durga Prasad, J. Hemalatha, Dielectric and energy storage density studies in electrospun fiber mats of polyvinylidene fluoride (PVDF)/zinc ferrite (ZnFe2O4) multiferroic composite, Physica B: Condensed Matter 573 (2019) 1–6. https://doi.org/10.1016/j.physb.2019.08.023.
[119] B. Martin, E. Dantras, A. Lonjon, L. Laffont, C. Lacabanne, Fabrication of Nickel NanoChains/PVDF Nanocomposites and Their Electrical/Magnetic Properties, Physica Status Solidi (a) 216 (2019) 1900158. https://doi.org/10.1002/pssa.201900158.
[120] B. Martin, E. Dantras, A. Lonjon, C. Lacabanne, L. Laffont, Magnetoelectric coupling in PVDF/Nano $NaNbO_3$ /NanoNi composites: Influence of Ni particles aspect ratio, IEEE Trans. Dielect. Electr. Insul. 27 (2020) 1381–1386. https://doi.org/10.1109/TDEI.2020.008432.
[121] I. Niskanen, T. Suopajärvi, H. Liimatainen, T. Fabritius, R. Heikkilä, G. Thungström, Determining the complex refractive index of cellulose nanocrystals by combination of Beer-Lambert and immersion matching methods, Journal of Quantitative Spectroscopy and Radiative Transfer 235 (2019) 1–6. https://doi.org/10.1016/j.jqsrt.2019.06.023.
[122] S. Kenzari, D. Bonina, J. Marie Dubois, V. Fournée, Complex metallic alloys as new materials for additive manufacturing, Science and Technology of Advanced Materials 15 (2014) 024802. https://doi.org/10.1088/1468-6996/15/2/024802.
[123] T. Eisenhammer, A. Mahr, A. Haugeneder, W. Assmann, Selective absorbers based on AlCuFe thin films, Solar Energy Materials and Solar Cells 46 (1997) 53–65. https://doi.org/10.1016/S0927-0248(96)00097-9.
[124] D. Mana Kialengila, K. Wolfs, J. Bugalama, A. Van Schepdael, E. Adams, Full evaporation headspace gas chromatography for sensitive determination of high boiling point volatile organic compounds in low boiling matrices, Journal of Chromatography A 1315 (2013) 167–175. https://doi.org/10.1016/j.chroma.2013.09.058.
[125] R.F. Remler, The Solvent Properties of Acetone., (n.d.).
[126] S. Kenzari, D. Bonina, J. Marie Dubois, V. Fournée, Complex metallic alloys as new materials for additive manufacturing, Science and Technology of Advanced Materials 15 (2014) 024802. https://doi.org/10.1088/1468-6996/15/2/024802.
[127] B. Zaarour, L. Zhu, X. Jin, Controlling the surface structure, mechanical properties, crystallinity, and piezoelectric properties of electrospun PVDF nanofibers by maneuvering molecular weight, Soft Materials 17 (2019) 181–189. https://doi.org/10.1080/1539445X.2019.1582542.
[128] R.K. Singh, S.W. Lye, J. Miao, Holistic investigation of the electrospinning parameters for high percentage of β-phase in PVDF nanofibers, Polymer 214 (2021) 123366. https://doi.org/10.1016/j.polymer.2020.123366.
[129] K. Magniez, C. De Lavigne, B.L. Fox, The effects of molecular weight and polymorphism on the fracture and thermo-mechanical properties of a carbon-fibre composite modified by electrospun poly (vinylidene fluoride) membranes, Polymer 51 (2010) 2585–2596. https://doi.org/10.1016/j.polymer.2010.04.021.
[130] A. Baji, Y.-W. Mai, Q. Li, Y. Liu, Electrospinning induced ferroelectricity in poly(vinylidene fluoride) fibers, Nanoscale 3 (2011) 3068. https://doi.org/10.1039/c1nr10467e.

[131] J. Zheng, A. He, J. Li, C.C. Han, Polymorphism Control of Poly(vinylidene fluoride) through Electrospinning, Macromol. Rapid Commun. 28 (2007) 2159–2162. https://doi.org/10.1002/marc.200700544.
[132] S. Gee, B. Johnson, A.L. Smith, Optimizing electrospinning parameters for piezoelectric PVDF nanofiber membranes, Journal of Membrane Science 563 (2018) 804–812. https://doi.org/10.1016/j.memsci.2018.06.050.
[133] S. Saha, V. Yauvana, S. Chakraborty, D. Sanyal, Synthesis and Characterization of Polyvinylidene-fluoride (PVDF) Nanofiber for Application as Piezoelectric Force Sensor, Materials Today: Proceedings 18 (2019) 1450–1458. https://doi.org/10.1016/j.matpr.2019.06.613.
[134] S.M. Purushothaman, M.F. Tronco, M. Ponçot, C. C.S, N. Guigo, M. Malfois, N. Kalarikkal, S. Thomas, I. Royaud, D. Rouxel, Quantifying the Crystalline Polymorphism in PVDF: Comparative Criteria Using DSC, WAXS, FT-IR, and Raman Spectroscopy, ACS Appl. Polym. Mater. 6 (2024) 8291–8305. https://doi.org/10.1021/acsapm.4c01157.
[135] J. Grenet, B. Legendre, Analyse calorimétrique différentielle à balayage (DSC), Techniques d'analyse (2010). https://doi.org/10.51257/a-v1-p1205.
[136] G. Rui, E. Allahyarov, R. Li, P.L. Taylor, L. Zhu, Hard-to-soft transition-enhanced piezoelectricity in poly(vinylidene fluoride) *via* relaxor-like secondary crystals activated by high-power ultrasonication, Mater. Horiz. 9 (2022) 1992–1998. https://doi.org/10.1039/D2MH00442A.
[137] S.J. Kang, Y.J. Park, J.Y. Hwang, H.J. Jeong, J.S. Lee, K.J. Kim, H.-C. Kim, J. Huh, C. Park, Localized Pressure-Induced Ferroelectric Pattern Arrays of Semicrystalline Poly(vinylidene fluoride) by Microimprinting, Adv. Mater. 19 (2007) 581–586. https://doi.org/10.1002/adma.200601474.
[138] S. Lanceros-Méndez, J.F. Mano, A.M. Costa, V.H. Schmidt, FTIR AND DSC STUDIES OF MECHANICALLY DEFORMED β-PVDF FILMS, Journal of Macromolecular Science, Part B 40 (2001) 517–527. https://doi.org/10.1081/MB-100106174.
[139] G. Teyssedre, A. Bernes, C. Lacabanne, Influence of the crystalline phase on the molecular mobility of PVDF, J. Polym. Sci. B Polym. Phys. 31 (1993) 2027–2034. https://doi.org/10.1002/polb.1993.090311316.
[140] A. Gradys, P. Sajkiewicz, Determination of the melting enthalpy of β phase of poly(vinylidene fluoride), E-Polymers 13 (2013). https://doi.org/10.1515/epoly-2013-0119.
[141] G. Mago, D.M. Kalyon, F.T. Fisher, Membranes of Polyvinylidene Fluoride and PVDF Nanocomposites with Carbon Nanotubes via Immersion Precipitation, Journal of Nanomaterials 2008 (2008) 759825. https://doi.org/10.1155/2008/759825.
[142] N. Meng, X. Zhu, R. Mao, M.J. Reece, E. Bilotti, Nanoscale interfacial electroactivity in PVDF/PVDF-TrFE blended films with enhanced dielectric and ferroelectric properties, J. Mater. Chem. C 5 (2017) 3296–3305. https://doi.org/10.1039/C7TC00162B.
[143] B. Jouffrey, R.A. Portier, Diffraction dans les métaux et alliages : conditions de diffraction, Étude et propriétés des métaux (2007). https://doi.org/10.51257/a-v1-m4126.
[144] F.S. Navarro Oliva, S.N. Murthy, L. Lenglet, A. Ospina, S. Weigand, F. Bedoui, In-situ WAXS and SAXS microstructural investigation of Poly(vinylidene fluoride)- Fe3O4 coaxial-electrospun nanocomposites under thermal and mechanical loading: Nanoparticles size effects on fibers molecular orientation, mechanical properties and crystalline polymorphs, Polymer 308 (2024) 127406. https://doi.org/10.1016/j.polymer.2024.127406.
[145] C. Du, B.-K. Zhu, Y.-Y. Xu, Effects of stretching on crystalline phase structure and morphology of hard elastic PVDF fibers, J. Appl. Polym. Sci. 104 (2007) 2254–2259. https://doi.org/10.1002/app.25635.
[146] Z. Ye, J. Yi, Y. Zhang, C. Xiong, Ultra-drawn PVDF piezoelectric film for linear and large-range pressure sensing, Reactive and Functional Polymers 208 (2025) 106159. https://doi.org/10.1016/j.reactfunctpolym.2025.106159.
[147] S.L. Moffitt, S. Uličná, S.-S. Jhang, P.-C. Pan, M. Owen-Bellini, P. Hacke, M.D. Kempe, J. Tracy, K.R. Choudhury, L.T. Schelhas, X. Gu, PVDF-based backsheet cracking: Mapping in situ phase evolution by X-ray scattering, Solar Energy Materials and Solar Cells 282 (2025) 113355. https://doi.org/10.1016/j.solmat.2024.113355.
[148] A.K. Maurya, E. Mias, J. Schoeller, I.E. Collings, R.M. Rossi, A. Dommann, A. Neels, Understanding multiscale structure–property correlations in PVDF-HFP electrospun fiber membranes by SAXS and WAXS, Nanoscale Adv. 4 (2022) 491–501. https://doi.org/10.1039/D1NA00503K.

[149] J. Defebvin, S. Barrau, G. Stoclet, C. Rochas, J.-M. Lefebvre, In situ SAXS/WAXS investigation of the structural evolution of poly(vinylidene fluoride) upon uniaxial stretching, Polymer 84 (2016) 148–157. https://doi.org/10.1016/j.polymer.2015.12.041.
[150] S. Barrau, A. Ferri, A. Da Costa, J. Defebvin, S. Leroy, R. Desfeux, J.-M. Lefebvre, Nanoscale Investigations of α- and γ-Crystal Phases in PVDF-Based Nanocomposites, ACS Appl. Mater. Interfaces 10 (2018) 13092–13099. https://doi.org/10.1021/acsami.8b02172.
[151] M. Wojdyr, *Fityk* : a general-purpose peak fitting program, J Appl Crystallogr 43 (2010) 1126–1128. https://doi.org/10.1107/S0021889810030499.
[152] Ye.L. Gal'perin, B.P. Kosmynin, V.K. Smirnov, Determination of the crystallinity of polyvinylidene fluoride, Polymer Science U.S.S.R. 12 (1970) 2133–2139. https://doi.org/10.1016/0032-3950(70)90133-4.
[153] J.-L. Gardette, Caractérisation des polymères par spectrométrie optique, (1996).
[154] B. Humbert, J.-Y. Mevellec, J. Grausem, M. Dossot, C. Carteret, Spectrométrie d'absorption dans l'infrarouge, Techniques d'analyse (2012). https://doi.org/10.51257/a-v1-p2850.
[155] X. Cai, T. Lei, D. Sun, L. Lin, A critical analysis of the α, β and γ phases in poly(vinylidene fluoride) using FTIR, RSC Adv. 7 (2017) 15382–15389. https://doi.org/10.1039/C7RA01267E.
[156] Ye. Bormashenko, R. Pogreb, O. Stanevsky, Ed. Bormashenko, Vibrational spectrum of PVDF and its interpretation, Polymer Testing 23 (2004) 791–796. https://doi.org/10.1016/j.polymertesting.2004.04.001.
[157] A. Salimi, A.A. Yousefi, Analysis Method: FTIR studies of β-phase crystal formation in stretched PVDF films, Polymer Testing 22 (2003) 699–704. https://doi.org/10.1016/S0142-9418(03)00003-5.
[158] T. Boccaccio, A. Bottino, G. Capannelli, P. Piaggio, Characterization of PVDF membranes by vibrational spectroscopy, Journal of Membrane Science 210 (2002) 315–329. https://doi.org/10.1016/S0376-7388(02)00407-6.
[159] E. Benedetti, S. Catanorchi, A. D'Alessio, G. Moggi, P. Vergamini, M. Pracella, F. Ciardelli, FTIR-Microspectroscopy andDSC Studies of Poly(vinylidene fluoride), Polym. Int. 41 (1996) 35–41. https://doi.org/10.1002/(SICI)1097-0126(199609)41:1%253C35::AID-PI579%253E3.0.CO;2-T.
[160] T. Greeshma, R. Balaji, S. Jayakumar, PVDF Phase Formation and Its Influence on Electrical and Structural Properties of PZT-PVDF Composites, Ferroelectrics Letters Section 40 (2013) 41–55. https://doi.org/10.1080/07315171.2013.814460.
[161] J. Barbillat, D. Bougeard, G. Buntinx, M. Delhaye, P. Dhamelincourt, F. Fillaux, Spectrométrie Raman, (1999).
[162] D. Chapron, F. Rault, A. Talbourdet, G. Lemort, C. Cochrane, P. Bourson, E. Devaux, C. Campagne, In-situ Raman monitoring of the poly(vinylidene fluoride) crystalline structure during a melt-spinning process, J Raman Spectrosc 52 (2021) 1073–1079. https://doi.org/10.1002/jrs.6081.
[163] A. Arrigoni, L. Brambilla, C. Bertarelli, G. Serra, M. Tommasini, C. Castiglioni, P(VDF-TrFE) nanofibers: structure of the ferroelectric and paraelectric phases through IR and Raman spectroscopies, RSC Adv. 10 (2020) 37779–37796. https://doi.org/10.1039/D0RA05478J.
[164] M.T. Riosbaas, K.J. Loh, G. O'Bryan, B.R. Loyola, In situ phase change characterization of PVDF thin films using Raman spectroscopy, in: J.P. Lynch, K.-W. Wang, H. Sohn (Eds.), San Diego, California, USA, 2014: p. 90610Z. https://doi.org/10.1117/12.2045430.
[165] H. Wang, X. Yang, Y. Zhao, C. Yan, S. Wang, H. Yang, X. Wang, J.M. Schultz, Preparation of gamma-PVDF with controlled orientation and insight into phase transformation, Polymer 123 (2017) 282–289. https://doi.org/10.1016/j.polymer.2017.07.004.
[166] B. Mattsson, H. Ericson, L.M. Torell, F. Sundholm, Micro-Raman investigations of PVDF-based proton-conducting membranes, J. Polym. Sci. A Polym. Chem. 37 (1999) 3317–3327. https://doi.org/10.1002/(SICI)1099-0518(19990815)37:16%253C3317::AID-POLA30%253E3.0.CO;2-%2523.
[167] M.E. Hakiki, J. Eschbach, D. Rouxel, B. Vincent, J.K. Krüger, O. Elmazria, P. Alnot, Elastic and Piezoelectric Constants of Potassium Niobate Studied by Brillouin Spectroscopy, (n.d.).
[168] B. Vincent, Imaging of microwave-induced acoustic fields in LiNbO3 by high-performance Brillouin microscopy.pdf, (n.d.).
[169] Jiménez Riobóo, Brillouin scattering determination of the surface acoustic wave velocity in InxGa1−xN A probe into the.pdf, (2012).

[170] Jiménez Riobóo, Hypersonic characterization of sound propagation velocity in AlxGa1-xN thin films.pdf, (2002).
[171] R.J.J. Riobóo, M. Desco, V. Gómez-Gaviro, Impact of optical tissue clearing on the Brillouin signal from biological tissue samples, (n.d.).
[172] J.K. Krüger, U. Müller, R. Bactavatchalou, J. Mainka, C. Gilow, W. Possart, A. Tschöpe, P. Alnot, D. Rouxel, R. Sanctuary, B. Wetzel, The generalized Cauchy relation as an universal property of the amorphous state, JOURNAL DE PHYSIQUE IV (n.d.).
[173] R. Bactavatchalou, The generalized Cauchy relation a probe for local structure in materials with isotropic symmetry.pdf, (n.d.).
[174] A. Létoffé, Resilience improvement of an isotactic polypropylene-g-maleic anhydride by crosslinking using polyether triamine agents, (2019).
[175] J. Streque, D. Rouxel, A. Talbi, M. Thomassey, B. Vincent, LOW TEMPERATURE VARIATION OF ACOUSTIC VELOCITY IN PDMS FOR HIGH FREQUENCY APPLICATIONS, (n.d.).
[176] J. Krüger, Brillouin spectroscopy and its application to polymers, in: Optical Techniques to Characterize Polymer Systems, Elsevier Amsterdam, 1989.
[177] D. Rouxel, Brillouin Spectroscopy of Polymer Nanocomposites, in: Spectroscopy of Polymer Nanocomposites, Elsevier, n.d.
[178] R. Hadji, V.S. Nguyen, B. Vincent, D. Rouxel, F. Bauer, Preparation and Characterization of P(VDF-TrFE)/Al2O3 Nanocomposite, 59 (2012).
[179] J. Eschbach, D. Rouxel, B. Vincent, Y. Mugnier, C. Galez, R.L. Dantec, P. Bourson, J.K. Krüger, O. Elmazria, P. Alnot, Development and characterization of nanocomposite materials, Materials Science and Engineering C (2007).
[180] B. Vigolo, B. Vincent, J. Eschbach, P. Bourson, J.-F. Mareche, E. McRae, A. Dahoun, D. Rouxel, Multiscale Characterization of Single-Walled Carbon Nanotube/Polymer Composites by Coupling Raman and Brillouin Spectroscopy, Polymer Composites (n.d.).
[181] K.B. Hafsia, M. Ponçot, D. Chapron, I. Royaud, A. Dahoun, P. Bourson, A novel approach to study the isothermal and non-isothermal crystallization kinetics of Poly(Ethylene Terephthalate) by Raman spectroscopy, J Polym Res 23 (2016) 93. https://doi.org/10.1007/s10965-016-0984-7.
[182] F. Rault, D. Chapron, A. Talbourdet, C. Cochrane, G. Lemort, E. Devaux, C. Campagne, P. Bourson, INTEREST OF IN SITU-RAMAN SPECTROSCOPY IN THE OPTIMIZATION OF PIEZOELECTRIC FIBERS FOR THE DEVELOPMENT OF ENERGY HARVESTERS, (2019).
[183] J. Martin, M. Ponçot, P. Bourson, A. Dahoun, J. Hiver, Study of the crystalline phase orientation in uniaxially stretched polypropylene by Raman spectroscopy: Validation and use of a time‐resolved measurement method, Polymer Engineering & Sci 51 (2011) 1607–1616. https://doi.org/10.1002/pen.21944.
[184] M. Bouita, J. Tinnes, P. Bourson, M. Malfois, M. Ponçot, A new Raman spectroscopy‐based method for monitoring the crystallinity ratio of polyethylene terephthalate, J Raman Spectroscopy 54 (2023) 225–232. https://doi.org/10.1002/jrs.6473.
[185] M. Veitmann, D. Chapron, S. Bizet, S. Devisme, J. Guilment, I. Royaud, M. Poncot, P. Bourson, Thermal behavior of PVDF/PMMA blends by differential scanning calorimetry and vibrational spectroscopies (Raman and Fourier-Transform Infrared), Polymer Testing 48 (2015) 120–124. https://doi.org/10.1016/j.polymertesting.2015.10.004.
[186] B. Zaarour, L. Zhu, X. Jin, Maneuvering the secondary surface morphology of electrospun poly (vinylidene fluoride) nanofibers by controlling the processing parameters, Mater. Res. Express 7 (2020) 015008. https://doi.org/10.1088/2053-1591/ab582d.
[187] H. Jiyong, Z. Yinda, Z. Hele, G. Yuanyuan, Y. Xudong, Mixed effect of main electrospinning parameters on the *β* -phase crystallinity of electrospun PVDF nanofibers, Smart Mater. Struct. 26 (2017) 085019. https://doi.org/10.1088/1361-665X/aa7245.
[188] R.K. Singh, S.W. Lye, J. Miao, Holistic investigation of the electrospinning parameters for high percentage of β-phase in PVDF nanofibers, Polymer 214 (2021) 123366. https://doi.org/10.1016/j.polymer.2020.123366.
[189] A.A. Budiarto, S.S. Syed Bakar, S. Saad, S. Yahud, Investigation on the Effect of Electrospinning Parameters: Voltage and Flow Rate on PVDF Fiber, in: M.A.A. Mohd Salleh, D.S. Che Halin, K. Abdul Razak, M.I.I. Ramli (Eds.), Proceedings of the Green Materials and Electronic Packaging Interconnect Technology Symposium,

Springer Nature Singapore, Singapore, 2023: pp. 757–765. https://doi.org/10.1007/978-981-19-9267-4_74.
[190] M. Borrotti, E. Lanzarone, F. Manganini, S. Ortelli, A. Pievatolo, C. Tonetti, Defect minimization and feature control in electrospinning through design of experiments, J of Applied Polymer Sci 134 (2017) app.44740. https://doi.org/10.1002/app.44740.
[191] A.A. Issa, M. Al-Maadeed, A.S. Luyt, M. Mrlik, M.K. Hassan, Investigation of the physico-mechanical properties of electrospun PVDF/cellulose (nano)fibers, J of Applied Polymer Sci 133 (2016). https://doi.org/10.1002/app.43594.
[192] Ch. Venkatesh, V.V. Rao, Annealing effect on the dielectric response of novel polymer/nano-quasicrystalline composites, in: Bikaner, Rajasthan, India, 2013: pp. 879–880. https://doi.org/10.1063/1.4810509.
[193] Ch. Venkatesh, V. Srinivas, M. Panda, V.V. Rao, Dielectric response in novel polyvinylidene fluoride/nanoquasicrystalline composites, Solid State Communications 150 (2010) 893–896. https://doi.org/10.1016/j.ssc.2010.01.047.
[194] S. Cusack, A. Miller, Determination of the Elastic Constants of Collagen by Brillouin Light Scattering, (n.d.).
[195] D. Schneider, N. Gomopoulos, C.Y. Koh, P. Papadopoulos, F. Kremer, E.L. Thomas, G. Fytas, Nonlinear control of high-frequency phonons in spider silk, NATURE MATERIALS (n.d.).
[196] Z. Wang, Y. Cang, F. Kremer, E.L. Thomas, G. Fytas, Determination of the Complete Elasticity of Nephila pilipes Spider Silk, (2020).
[197] N. Korakas, Photo-elasticity of silk fibroin harnessing whispering gallery modes, Scientific Reports (2023).
[198] K. Elsayad, Mechanical Properties of cellulose fibers measured by Brillouin spectroscopy, (2020).
[199] J.G. Speight, N.A. Lange, Lange's handbook of chemistry, 16ème édition, McGraw-Hill, 2005.
[200] R. Dallaev, T. Pisarenko, D. Sobola, F. Orudzhev, S. Ramazanov, T. Trčka, Brief Review of PVDF Properties and Applications Potential, (2022).
[201] R. Gregorio, D.S. Borges, Effect of crystallization rate on the formation of the polymorphs of solution cast poly(vinylidene fluoride), (2008).
[202] B.A. Young, Discriminating the Interaction Anisotropy in Polymorphs Using Powder Brillouin Light Scattering, Journal of Pharmaceutical Sciences (2022).
[203] S. Corezzi, A simple analysis of Brillouin spectra from opaque liquids and its application to aqueous suspensions of poly-N-isopropylacrylamide microgel particles, Journal of Molecular Liquids (2018).
[204] M. Pierno, C.S. Casari, R. Piazza, C.E. Bottani, Structural evolution of crystalline polymer latex films: Propagating and confined acoustic modes, (2025).
[205] B.S. Lalia, E. Guillen, H.A. Arafat, R. Hashaikeh, Nanocrystalline cellulose reinforced PVDF-HFP membranes for membrane distillation application, Desalination 332 (2014) 134–141. https://doi.org/10.1016/j.desal.2013.10.030.
[206] J.-E. Lee, Y.-E. Shin, G.-H. Lee, J. Kim, H. Ko, H.G. Chae, Polyvinylidene fluoride (PVDF)/cellulose nanocrystal (CNC) nanocomposite fiber and triboelectric textile sensors, Composites Part B: Engineering 223 (2021) 109098. https://doi.org/10.1016/j.compositesb.2021.109098.
[207] G.D. Patterson, T. Nishi, T.T. Wang, Brillouin Scattering from Poly(vinylidene fluoride)-Poly(methyl methacrylate) Mixtures, Macromolecules 9 (1976) 603–605. https://doi.org/10.1021/ma60052a014.
[208] S. Kojima, 100th Anniversary of Brillouin Scattering: Impact on Materials Science, (2022).
[209] Y. Ike, S. Kojima, Brillouin scattering study of polymer dynamics, Materials Science and Engineering: A 442 (2006) 383–386. https://doi.org/10.1016/j.msea.2006.03.114.
[210] E.A. Friedman, A.J. Ritger, R.D. Andrews, Brillouin Scattering Near the Glass Transition of Polymethyl Methacrylate □, (2025).
[211] S. Mitchell, J.E. Guillet, Brillouin scattering in amorphous polymeric solids, (n.d.).
[212] J.K. Krüger, R. Roberts, H.-G. Unruh, K.-P. Frühauf, J. Helwig, H.E. Müser, A reinvestigation of the hypersonic properties and the specific heat of PMMA around the quasi-static glass transition, in: W. Wilke (Ed.), Frontiers in Polymer Science, Steinkopff, Darmstadt, 1985: pp. 77–85. https://doi.org/10.1007/BFb0114018.
[213] J.K. Kruger, K.-P. Bohn, R. Jimenez, J. Schreiber, On the existence of an intrinsic glass transition in a fragile liquid: polyvinylacetate, Colloid Polym Sci 274 (1996) 490–495. https://doi.org/10.1007/BF00652473.
[214] S. Moozhiyil Purushothaman, Bio-filler-interfaced electrospun PVDF-nanomultiferroic hybrid nanogenerator for energy harvesting and sensing applications, (2025).

[215] J.K. Krüger, Brillouin Spectroscopy and its Application to Polymers, in: Optical Techniques to Characterize Polymer Systems, Elsevier, Amsterdam, 1989: pp. 429–534.
[216] V. Sencadas, S. Lanceros-Méndez, J.F. Mano, Characterization of poled and non-poled ℕ-PVDF films using thermal analysis techniques, Thermochimica Acta (2004).
[217] H. Rekik, Dielectric relaxation behaviour in semi-crystalline polyvinylidene fluoride (PVDF)/TiO2 nanocomposites, Part B (2013).
[218] G. Teyssedre, A. Bernes, C. Lacabanne, Influence of the crystalline phase on the molecular mobility of PVDF, J. Polym. Sci. B Polym. Phys. 31 (1993) 2027–2034. https://doi.org/10.1002/polb.1993.090311316.
[219] C. Leonard, J.L. Halary, L. Monnerie, F. Micheron, DSC studies on the transitions in poly(vinylidenefluoride) and some related copolymers, Polymer Bulletin 11 (1984). https://doi.org/10.1007/bf00258030.
[220] R.J. Jimenez-Rioboo, M.A. Ramos, Brillouin-spectroscopy experiments on polymorphic ethanol, Philosophical Magazine (n.d.).
[221] J. Kruger, J. Schreiber, R. Jimenez-Rioboo, K.-P. Bohn, F. Smutny, M. Kubat, J. Petzelt, J. Hrabovska-Bradshaw, S. Kamba, J. Legrand, Unconventional orientational glass transitions in symmetrical difluorotetrachloroethane, 6 (n.d.). https://doi.org/10.1088/0953-8984/6/35/006.
[222] R.J.J. Rioboo, Elastic anomalies and orientational glass transition in Na(CN)xCl1−x mixed crystals. A Brillouin spectroscopic study, The European Physical Journal B (n.d.).
[223] L. Yang, J. Ho, E. Allahyarov, R. Mu, L. Zhu, Semicrystalline Structure–Dielectric Property Relationship and Electrical Conduction in a Biaxially Oriented Poly(vinylidene fluoride) Film under High Electric Fields and High Temperatures, ACS Appl. Mater. Interfaces 7 (2015) 19894–19905. https://doi.org/10.1021/acsami.5b02944.
[224] A.M. Abd El-Aziz, M. Afifi, Influence the β-PVDF phase on structural and elastic properties of PVDF/PLZT composites, Materials Science and Engineering: B 301 (2024) 117152. https://doi.org/10.1016/j.mseb.2023.117152.
[225] X. Mo, Piezoelectrets for wearable energy harvesters and sensors, Nano Energy (2019).
[226] D. Berlincourt, H. Jaffe, L.R. Shiozawa, Electroelastic Properties of the Sulfides, Selenides, and Tellurides of Zinc and Cadmium, (n.d.).
[227] D. Berlincourt, H. Jaffe, Elastic and Piezoelectric Coefficients of Single-Crystal Barium Titanate, (n.d.).
[228] M.H. Malakooti, H.A. Sodano, Noncontact and simultaneous measurement of the d33 and d31 piezoelectric strain coefficients, Appl. Phys. Lett. (2025).
[229] J. Erhart, L. Burianová, What is really measured on a d33-meter, Journal of the European Ceramic Society Volume 21 (2001) Pages 1413-1415. https://www.sciencedirect.com/science/article/pii/S0955221901000309.
[230] ANSI/IEEE Std 176-1987 An American National Standard IEEE Standard on Piezoelectricity, (n.d.).
[231] ISO 19622:2018 Fine ceramics (advanced ceramics, advanced technical ceramics) — Test method for piezoelectric constant d33 of piezoelectric ceramics by direct quasi-static method, (n.d.). https://www.iso.org/fr/standard/65515.html.
[232] H. Longbiao, F. Xiujuan, K. Triantafillos, N. Feng, Z. Bo, COMPARISON BETWEEN METHODS FOR THE MEASURE- MENT OF THE D33 CONSTANT OF PIEZOELECTRIC MATE-, (2018).
[233] S. Mani, A. Kasi, T. Nagamalai, V.A. Subramani, A. Natarajan, A.H. Seikh, M. Krishnan, S.K. Ramachandran, Enhancement of piezoelectric responses of electrospun PVDF nanofibers through mechanical stretching and annealing process, Materials Science (2024).
[234] S. Shetty, Development of a new flexible nanogenerator from electrospun nanofabric based on PVDF/talc nanosheet composites, Soft Matter (2020).
[235] Z. Gong, Flexible PVDF/SiC/FeCl3 nanofiber membrane generators with synergistically enhanced piezoelectricity, Nano Energy (2024).
[236] M. Kumar, Piezoelectric performance enhancement of electrospun functionally graded PVDF/BaTiO3 based flexible nanogenerators, Materials Research Bulletin (2024).
[237] S.B. Sadeque, M. Rahman, M. Hasan, M. Ordu, Graphene Nanoplatelet Integrated Thermally Drawn PVDF Triboelectric Nanocomposite Fibers for Extreme Environmental Conditions, (2024).
[238] S. Mishra, Effect of surface and contact points modification on the output performance of triboelectric nanogenerator, Nano Energy (2022).

[239] A. Akbarinejad, H. Fiedler, J. Nguyen, Z. Li, D.A. Gito, P.C. Sherrell, A.V. Ellis, K. Aw, J. Malmstrom, Stretching, Tapping, or Compressing–What Role Does Triboelectricity Play in the Signal Output from Piezoelectric Nanogenerators?, (2024).
[240] W. Sun, H. Liu, Z. Guo, A. Li, C. Gao, C. Lu, W. Zhou, J. Zhang, Y. Liu, Functionalized Multiwalled Carbon Nanotubes Improve Piezoelectric and Biological Performances of the PVDF–TrFE/ZnO Electrospun Fiber Film, (2024).
[241] X. Yang, Efficient energy harvesting enabled by large-area piezoelectric PVDF-based composite film enhanced by carbon nanotubes, Ceramics International (2024).
[242] W.-M. Li, Enhanced flexoelectric and piezoelectric pairing of bent polyvinylidene fluoride (PVDF) membrane with two-dimensional (2D) stannic sulfide-bismuth oxychloride (SnS2-BiOCl) heterojunction, Nano Energy (2024).
[243] W. Deng, Cowpea-structured PVDF/ZnO nanofibers based flexible self-powered piezoelectric bending motion sensor towards remote control of gestures, Nano Energy (2019).
[244] LTC3588-1 Datasheet, (n.d.). https://www.analog.com/media/en/technical-documentation/data-sheets/35881fc.pdf.
[245] Quick Start Guide LTC3588EMSE-1 LTC3588EMSE-2, (n.d.). https://www.analog.com/media/en/technical-documentation/user-guides/dc1459b.pdf.
[246] AEM30330 Datasheet, (n.d.). https://e-peas.com/documents/AEM30330/UG-AEM30330_QFN40_EVK.pdf.
[247] AEM30330 Evaluation Board User Guide, (n.d.). https://www.mouser.com/pdfDocs/User-Guide-AEM30330-v10-1.pdf?srsltid=AfmBOoo30pJJbkaQBNMY4vOpMxWRNe4rS1niFtCbEkeLbMiz3pyCRznx.
[248] EH300 Datasheet, (n.d.). https://www.aldinc.com/pdf/EH300.pdf.
[249] nRF52840 Datasheet, (n.d.). https://docs.nordicsemi.com/bundle/ps_nrf52840/page/keyfeatures_html5.html.
[250] Online Power Profiler for Bluetooth LE, Devzone Nordic Semiconductor (n.d.). https://devzone.nordicsemi.com/power/w/opp/2/online-power-profiler-for-bluetooth-le (accessed August 10, 2025).
[251] Power Management Module, Nordic Semiconductor (n.d.). https://docs.nordicsemi.com/bundle/ncs-latest/page/nrf/applications/nrf_desktop/doc/power_manager.html (accessed August 18, 2025).
[252] S.M. Purushothaman, M.F. Tronco, B. Kottathodi, I. Royaud, M. Ponçot, N. Kalarikkal, S. Thomas, D. Rouxel, A review on electrospun PVDF-based nanocomposites: Recent trends and developments in energy harvesting and sensing applications, Polymer 283 (2023) 126179. https://doi.org/10.1016/j.polymer.2023.126179.
[253] 34HE59-6004S Full Datasheet, (n.d.). https://www.omc-stepperonline.com/fr/e-serie-nema-34-moteur-pas-a-pas-bipolar-1-8deg-12-0-nm-1699-68oz-in-6-0a-86x86x151-5mm-4-fils-34he59-6004s?search=34HE59-6004S.
[254] 34HE59-6004S Torque Curve, (n.d.). https://www.omc-stepperonline.com/fr/e-serie-nema-34-moteur-pas-a-pas-bipolar-1-8deg-12-0-nm-1699-68oz-in-6-0a-86x86x151-5mm-4-fils-34he59-6004s?search=34HE59-6004S.
[255] DM860T User Manual V3, (n.d.). https://www.omc-stepperonline.com/fr/pilote-pas-a-pas-numerique-2-4-7-2a-18-80vac-ou-24-110vdc-pour-moteur-nema-34-dm860t.
[256] P.-Y. Rochat, PWM : Modulation de Largeur d'Impulsion, (n.d.). https://pyrochat.github.io/mooc-led/cours/303/pwm.html.

Appendices

1) Annex 1 : DLS results

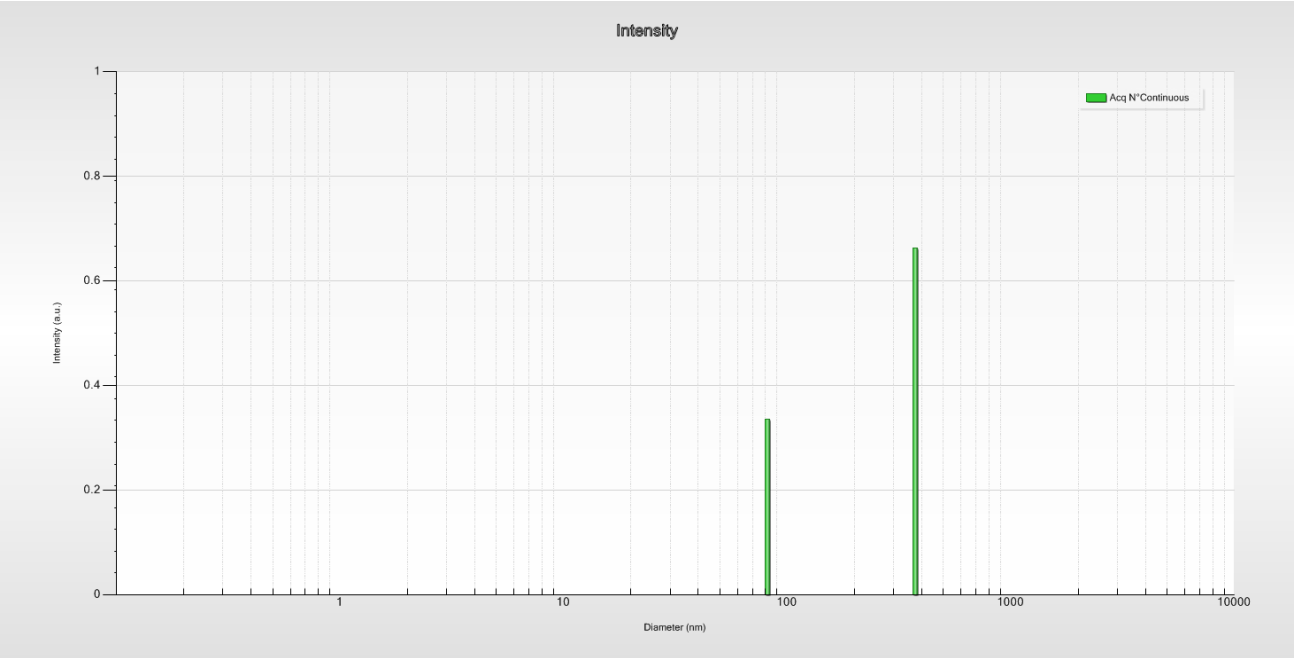

Figure 99: DLS results on CNC after 30 minutes of stirring.

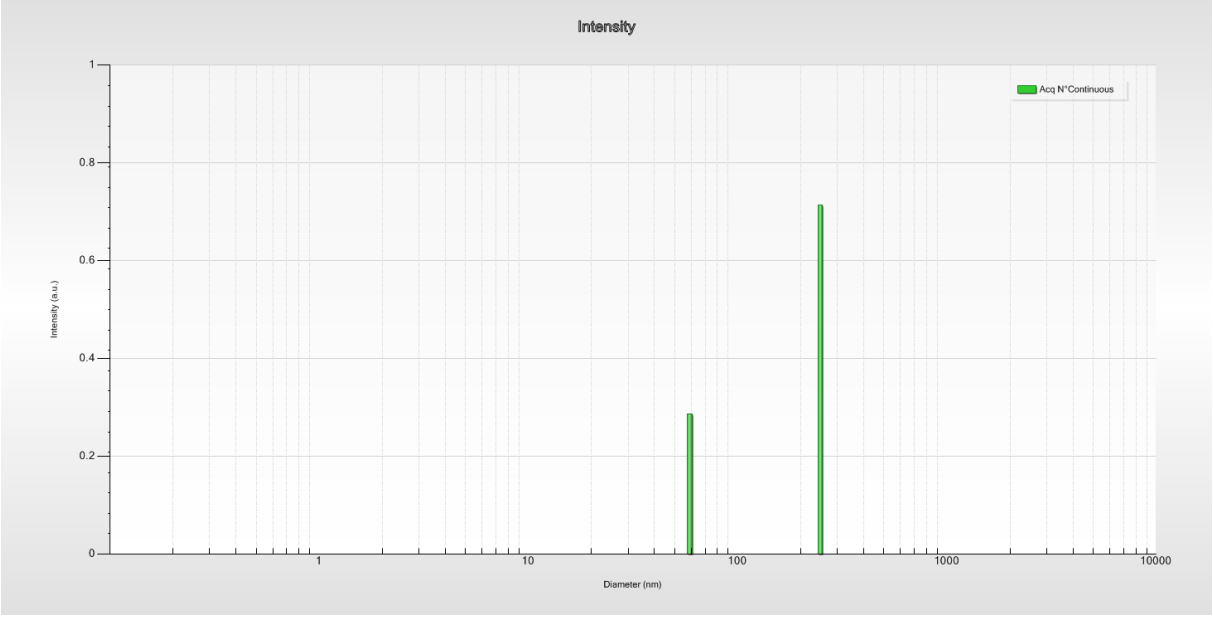

Figure 100: DLS results on CNC after sonication.

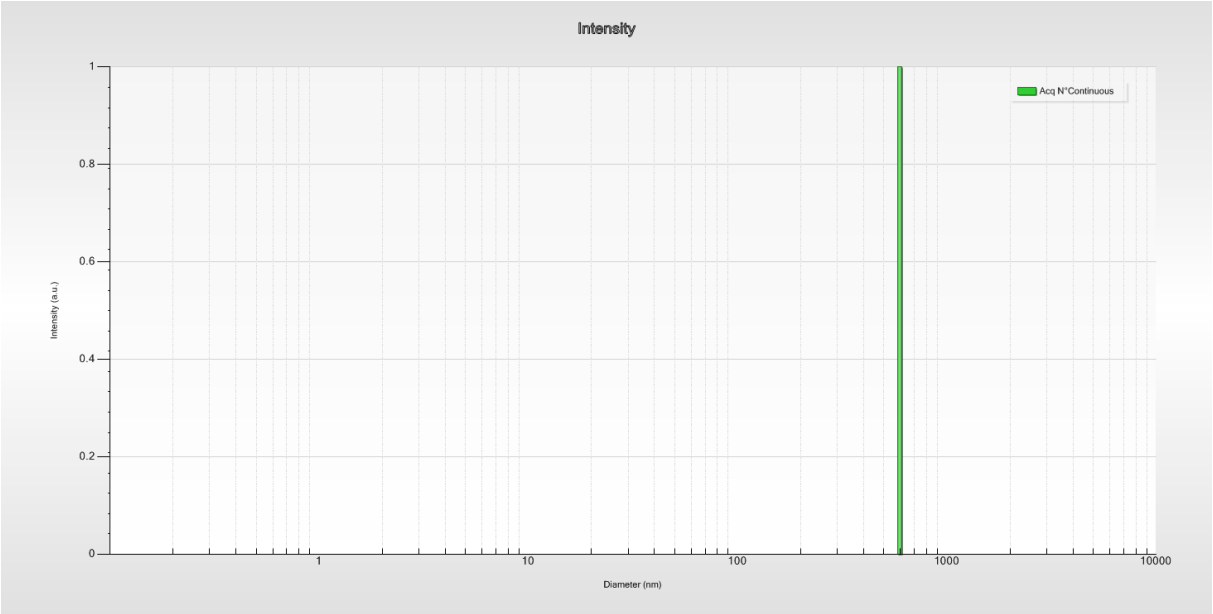

Figure 101: DLS results on QC after 30 minutes of stirring.

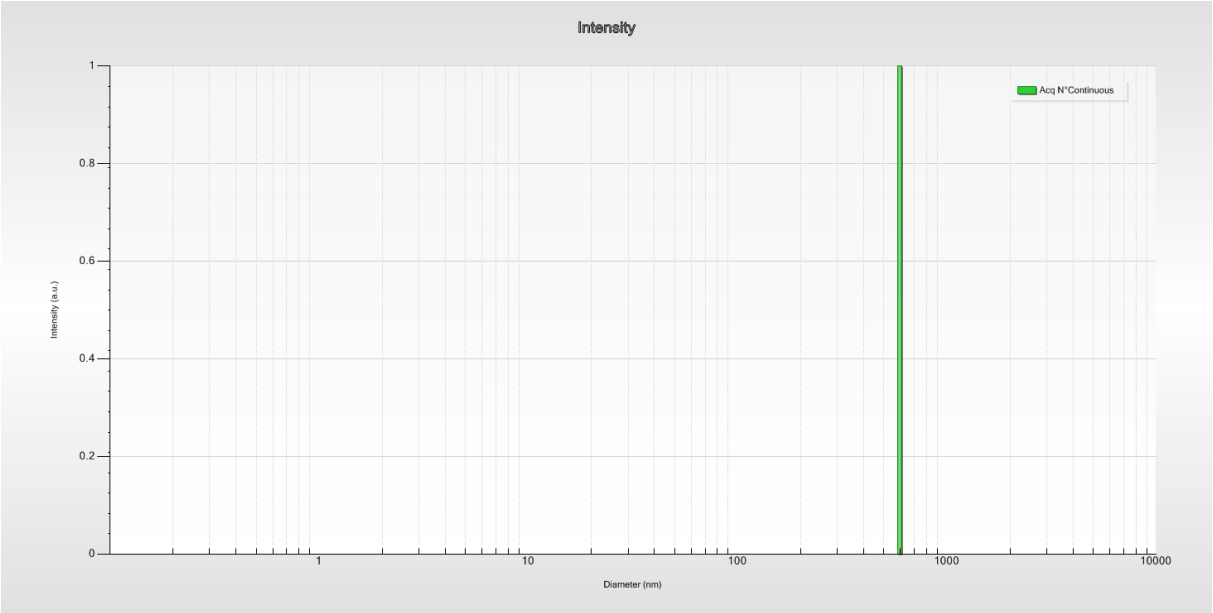

Figure 102: DLS results on QC after sonication.

2) Annex 2: SolidWorks assembly diagrams

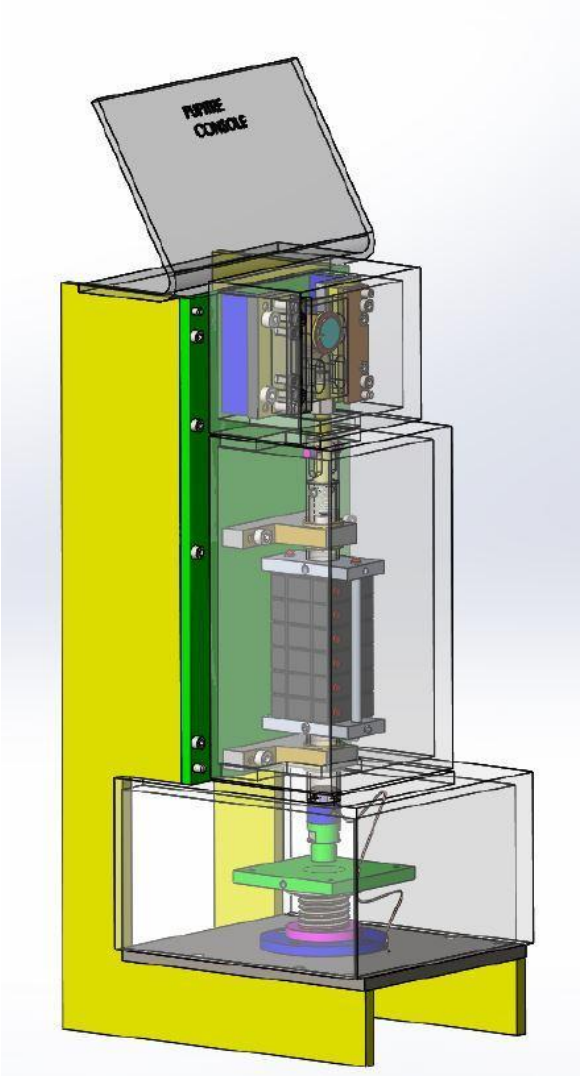

Figure 103: Overview of the tapping test machine.

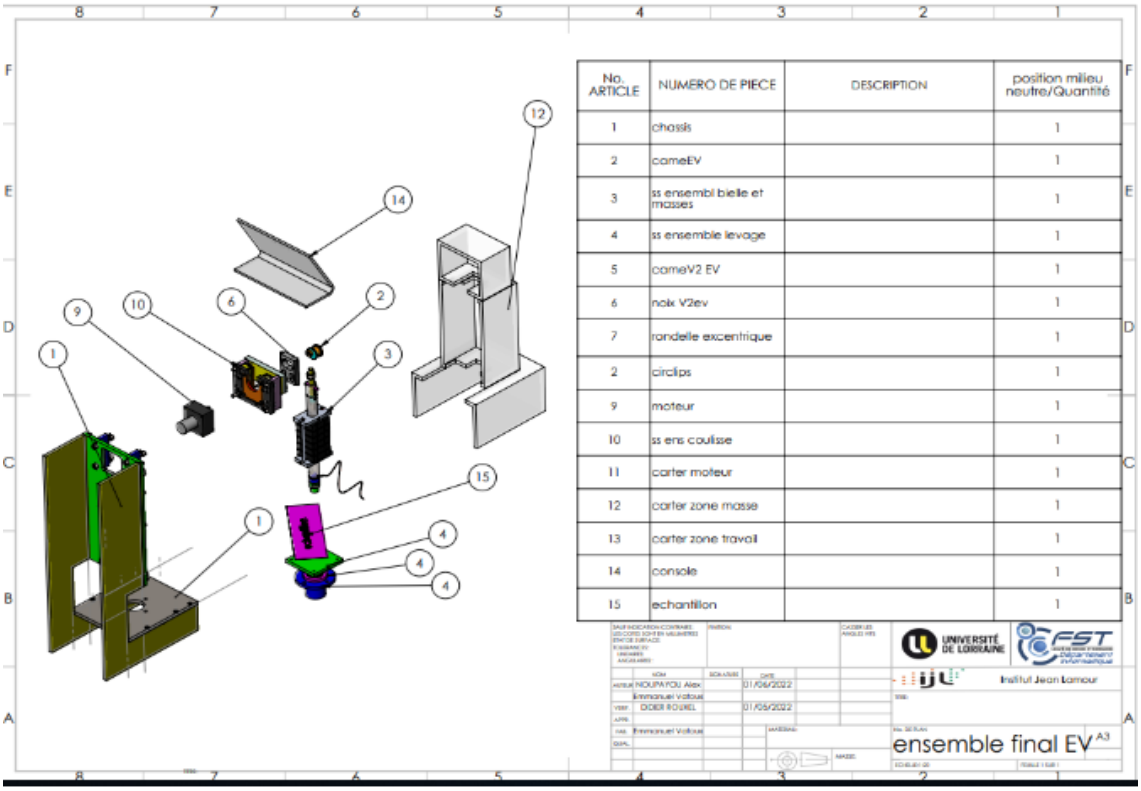

No. ARTICLE	NUMERO DE PIECE	DESCRIPTION	position milieu neutre/Quantité
1	chassis		1
2	cameEV		1
3	ss ensembl bielle et masses		1
4	ss ensemble levage		1
5	cameV2 EV		1
6	noix V2ev		1
7	rondelle excentrique		1
2	circlips		1
9	moteur		1
10	ss ens coulisse		1
11	carter moteur		1
12	carter zone masse		1
13	carter zone travail		1
14	console		1
15	echantillon		1

UNIVERSITÉ DE LORRAINE — FST — Institut Jean Lamour

ensemble final EV A3

Figure 104: Exploded view of the tapping test machine.

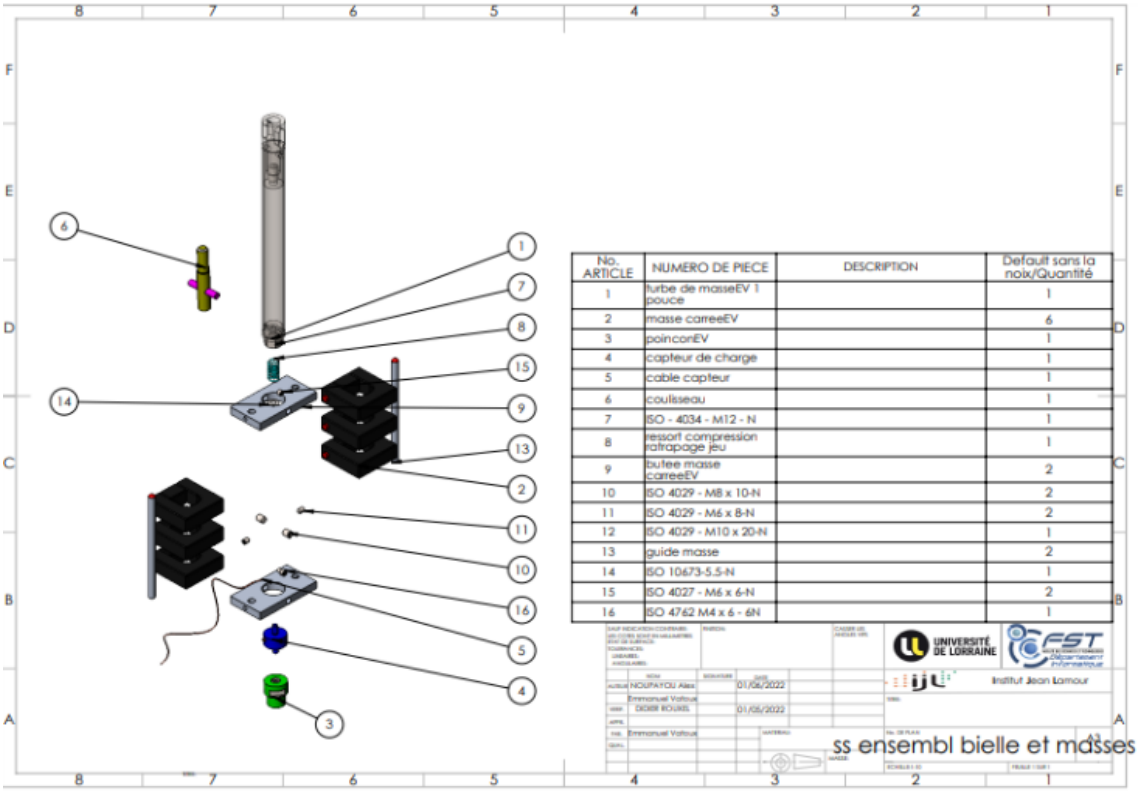

No. ARTICLE	NUMERO DE PIECE	DESCRIPTION	Default sans la noix/Quantité
1	turbe de masseEV 1 pouce		1
2	masse carreeEV		6
3	poinconEV		1
4	capteur de charge		1
5	cable capteur		1
6	coulisseau		1
7	ISO - 4034 - M12 - N		1
8	ressort compression ratrapage jeu		1
9	butee masse carreeEV		2
10	ISO 4029 - M8 x 10-N		2
11	ISO 4029 - M6 x 8-N		2
12	ISO 4029 - M10 x 20-N		1
13	guide masse		2
14	ISO 10673-5.5-N		1
15	ISO 4027 - M6 x 6-N		2
16	ISO 4762 M4 x 6 - 6N		1

UNIVERSITÉ DE LORRAINE — FST — Institut Jean Lamour

ss ensembl bielle et masses A3

Figure 105: Connecting rod and weights assembly.

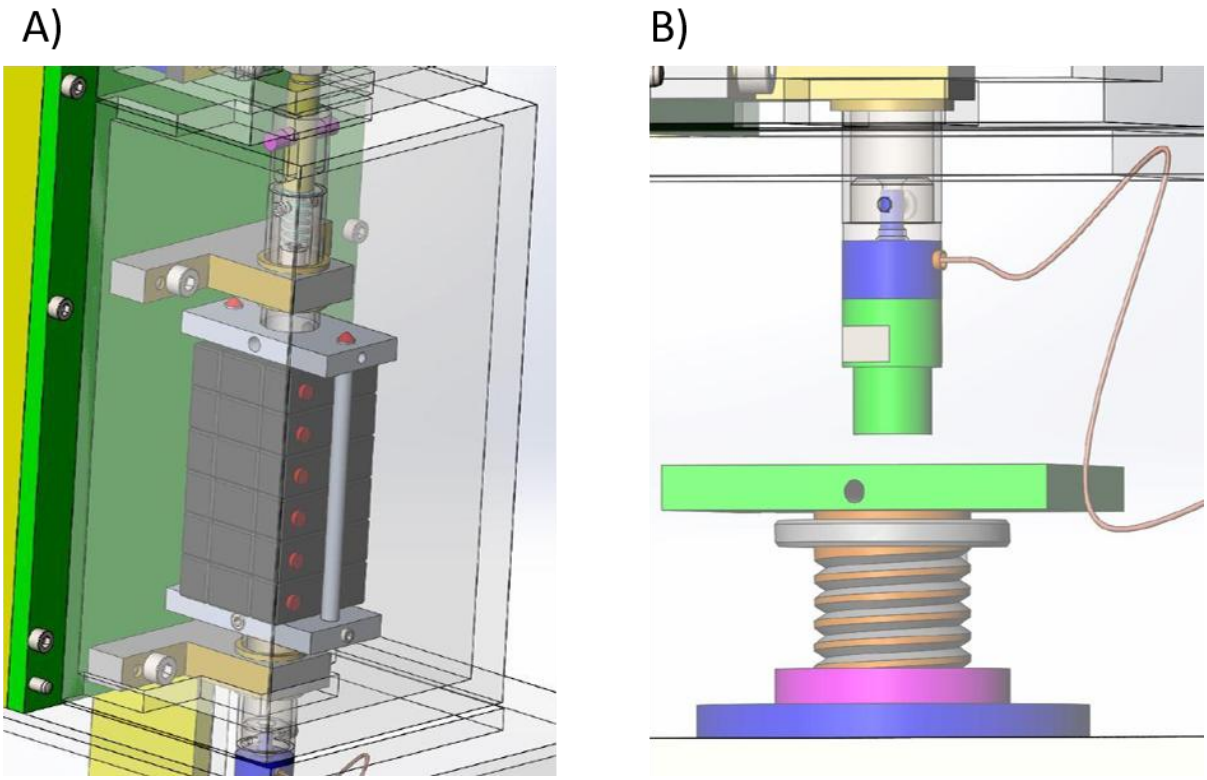

Figure 106: Zoomed view of A) the removable weights and B) the cell force and sample holder.

3) Annex 3: Datasheets

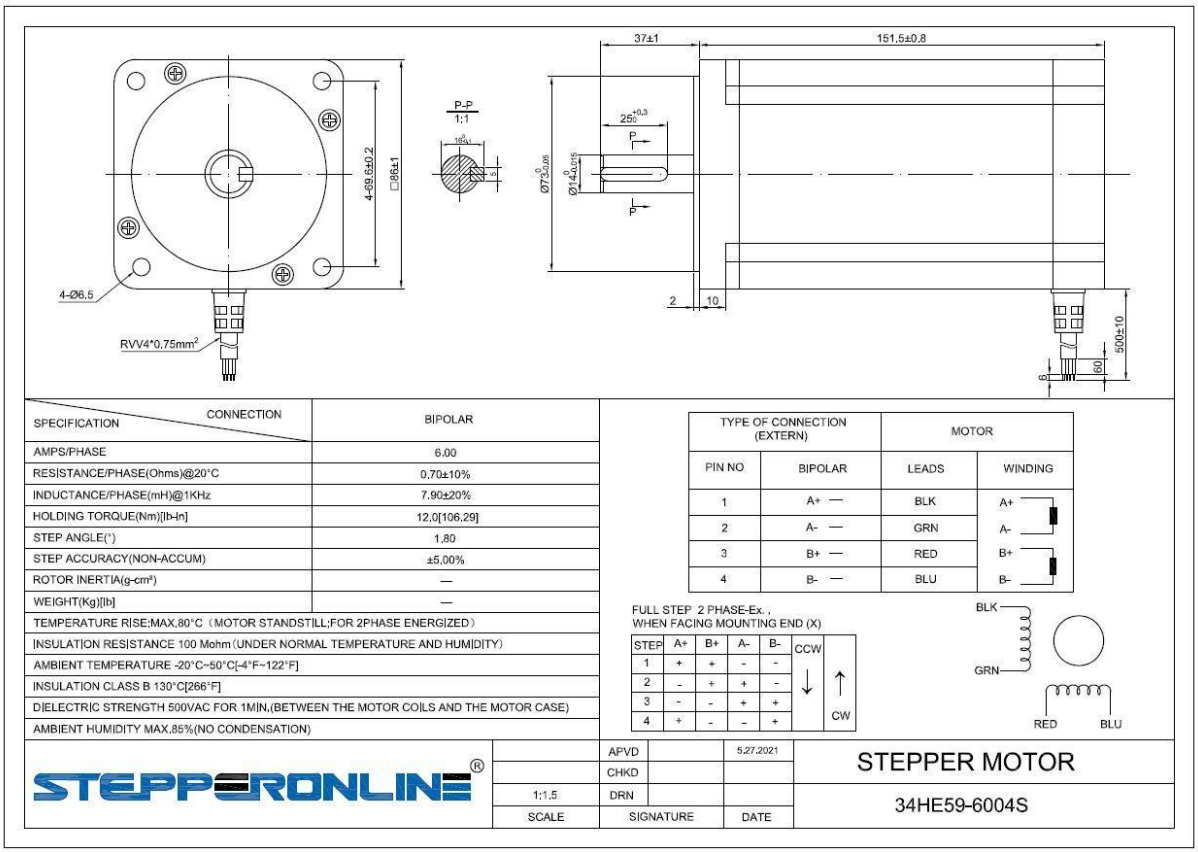

SPECIFICATION / CONNECTION	BIPOLAR
AMPS/PHASE	6.00
RESISTANCE/PHASE(Ohms)@20°C	0.70±10%
INDUCTANCE/PHASE(mH)@1KHz	7.90±20%
HOLDING TORQUE(Nm)[lb-in]	12.0[106.29]
STEP ANGLE(°)	1.80
STEP ACCURACY(NON-ACCUM)	±5.00%
ROTOR INERTIA(g-cm²)	—
WEIGHT(Kg)[lb]	—
TEMPERATURE RISE:MAX.80°C（MOTOR STANDSTILL;FOR 2PHASE ENERGIZED）	
INSULATION RESISTANCE 100 Mohm (UNDER NORMAL TEMPERATURE AND HUMIDITY)	
AMBIENT TEMPERATURE -20°C~50°C[-4°F~122°F]	
INSULATION CLASS B 130°C[266°F]	
DIELECTRIC STRENGTH 500VAC FOR 1MIN.(BETWEEN THE MOTOR COILS AND THE MOTOR CASE)	
AMBIENT HUMIDITY MAX.85%(NO CONDENSATION)	

TYPE OF CONNECTION (EXTERN)		MOTOR	
PIN NO	BIPOLAR	LEADS	WINDING
1	A+	BLK	A+
2	A-	GRN	A-
3	B+	RED	B+
4	B-	BLU	B-

FULL STEP 2 PHASE-Ex. ,
WHEN FACING MOUNTING END (X)

STEP	A+	B+	A-	B-
1	+	+	-	-
2	-	+	+	-
3	-	-	+	+
4	+	-	-	+

CCW ↓ ↑ CW

STEPPERONLINE®

	APVD		5.27.2021
	CHKD		
1:1.5	DRN		
SCALE	SIGNATURE		DATE

STEPPER MOTOR

34HE59-6004S

Figure 107: NEMA 34 stepper motor datasheet [253].

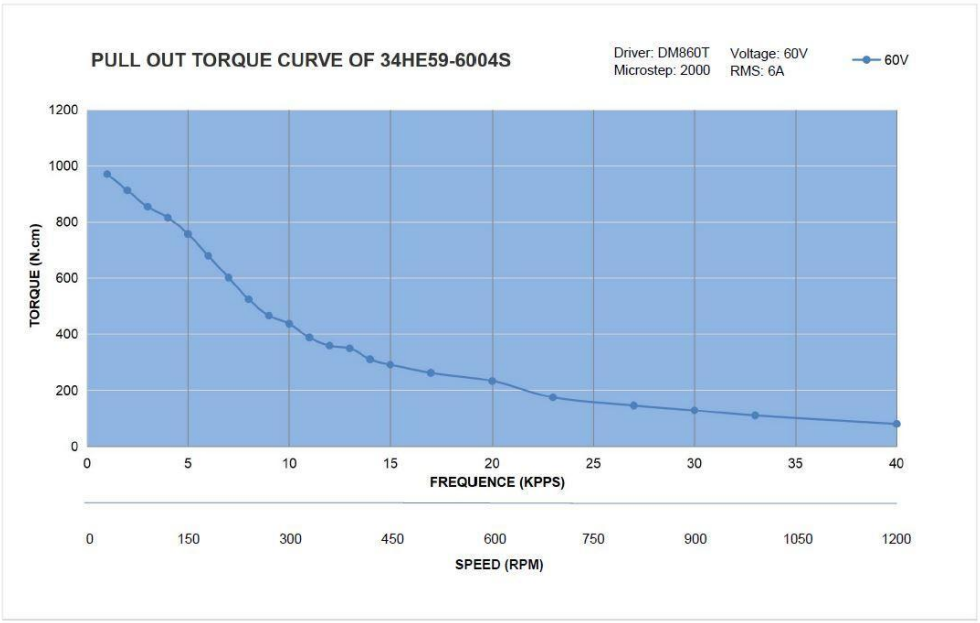

Figure 108 : Full torque curve of the NEMA 34 motor [254].

1. Features

- Step & direction (PUL/DIR) or CW/CCW (double pulse) control set by SW9
- Input voltage 18-80VAC or 24-110VDC (recommended 20-70VAC or 30-100VDC)
- 200 KHz max pulse input frequency
- 8 output current settings of 2.4-7.2A via DIP Switches SW1-SW3
- Idle current reduction to 50% or 90% selection via SW4
- 16 microstep resolutions of 400-51,200 via DIP switches SW5-SW8
- Control command smoothing for reducing motor vibration set by SW10
- Auto-tuning to match wide-range NEMA 23, 24, 34 and 42 stepper motors
- Anti-Resonance for optimal torque, extra smooth motion, low motor heating and noise
- Optically isolated inputs with 5V or 24V
- Fault and Brake outputs
- Over-voltage and over-current protections

2. Specifications

2.1 Electrical Specifications

Parameters	DM860T(V3.0)			
	Min	Typical	Max	Unit
Output Current	2.4	-	7.2	A
Supply Voltage	18 24	20 - 70 30 - 100	80 110	VAC VDC
Logic signal current	7	10	16	mA
Pulse input frequency	0	-	200	kHz
Minimal Pulse Width	2.5	-	-	μS
Minimal Direction Setup	5.0	-	-	μS
Isolation resistance	500			MΩ

2.2 Environment

Cooling	Natural Cooling or Forced cooling	
Operating Environment	Environment	Avoid dust, oil fog and corrosive gases
	Humidity	40%RH—90%RH
	Operating Temperature	0°C — 40°C (32°F - 109°F)
	Vibration	10-50Hz / 0.15mm
Storage Temperature	-20°C — 65°C (-4°F - 149°F)	
Weight	Approx. 510g (1.13 lbs)	

Figure 109 : DM860T driver datasheet [255].

4) Annex 4: Electronic control system

To control the motor speed, two approaches have been developed: we wanted the operator to be able to set the test parameters either via a potentiometer or using a software interface. The last option would also give the option to monitor the applied force on the tested sample. This section is mainly based on the work carried out by Jungfeng Tan (junfeng.tan6@etu.univ-lorraine.fr), one of the EEA-CIM master students who I supervised during my PhD.

Motor speed control

The first step is to power and use the DM860T driver, which is fully digital, to control the motor. The DM860T datasheet gives the definition of the driver pins, presented in Table 26.

3.1 P1 - Control Connector

PIN	Details
PUL+ (CW+)	Pulse and Direction Connection: **(1)** Optically isolated, high level 4.5-5V or 24V, low voltage 0-0.5V
PUL- (CW-)	**(2)** Maximum 200 KHz input frequency **(3)** The width of PUL signal is at least 2.5μs, duty cycle is recommended 50%
DIR+ (CCW+)	**(4)** Single pulse (step & direction) or double pulse (CW/CCW) is set by DIP Switch SW9 **(5)** DIR signal requires advance PUL signal minimum 5 μs in single pulse mode
DIR- (CCW-)	**(6)** The factory setting of control signal voltage is 24V, must need to set S2 (figure 2) if it is 5V
ENA+	Enable Connection: (default no connection) **(1)** Optically isolated, differential. **(2)** Disable the drive by 4.5- 24V input connection; enable the drive by 0-0.5V connection
ENA-	**(3)** ENA signal requires advance DIR signal minimum 5μs in single pulse mode **(4)** Enable time to be at least 200ms

Table 26: Pin definition of the DM860T [255].

PUL pins deal with the impulse signal input. As the PUL signal width must be at least 2.5 μs, it limits the input signal frequency to 200 KHz. A comparator is located at the PUL input to compare the PUL+ and – signals. As the high-level detection range for PUL+ ranges from 4.5 to 5V, and low-level detection for PUL- ranges from 0 to 0.5 V, PUL- must be connected to a reference voltage, usually ground (GND). PUL+ must be connected to a pulse signal output, like an Arduino microcontroller, which has a voltage amplitude ranging from 0 to 5 V. The DIR pins control the direction of the motor rotation. There is also a comparator in the DIR output, and for a clockwise rotation DIR- must be connected to GND and DIR+ to +5 V. For a counter-clockwise rotation, DIR- must be connected to 0 V. If the rotation direction does not need to be modified, DIR+ can be connected either to GND or +5 V of the power source. If it needs to be modified, DIR+ can be connected to the signal output of the Arduino. The ENA pins are used to activate or deactivate the motor. By default, if both ENA pins are connected to GND the motor is activated, and deactivated if ENA+ is connected to +5 V. The current going from the driver to the motor is used to stop the motor when it is activated but stopped (no impulse signal input). To avoid energy losses and extend the durability of the motor, we connected ENA+ to an Arduino output, to control the activation or deactivation of the motor.

Microsteps are used to enhance the precision, fluidity and motor noise reduction in stepper motors. However, the motor torque is reduced. Instead of working with full steps, the division into micro-steps allows finer and smoother movements from the motor. According to the microstep resolution configurations presented in Table 27, the motor rotates by an angle of 1.8° for each received impulsion, meaning that for a full step rotation the needed number of impulsions equals to 360/1.8 = 200 impulsions. In the case of a 2 microstep, the angle for an impulsion is divided by 2, resulting in a number of impulsions for a full rotation equal to 360/(1.8/2) = 400.

7.1 Microstep Resolution Configurations

Microstep resolution is set by SW5, 6, 7, 8 of the DIP switches as shown in the following table.

Microstep	Steps/rev.(for 1.8°motor)	SW5	SW6	SW7	SW8
2	400	ON	ON	ON	ON
4	800	OFF	ON	ON	ON
8	1600	ON	OFF	ON	ON
16	3200	OFF	OFF	ON	ON
32	6400	ON	ON	OFF	ON
64	12800	OFF	ON	OFF	ON
128	25600	ON	OFF	OFF	ON
256	51200	OFF	OFF	OFF	ON
5	1000	ON	ON	ON	OFF
10	2000	OFF	ON	ON	OFF
20	4000	ON	OFF	ON	OFF
25	5000	OFF	OFF	ON	OFF
40	8000	ON	ON	OFF	OFF
50	10000	OFF	ON	OFF	OFF
100	20000	ON	OFF	OFF	OFF
200	40000	OFF	OFF	OFF	OFF

Table 27: Microstep resolution configurations of the DM860T [255].

An impulse signal has two states: high or low, as represented in Figure 110.

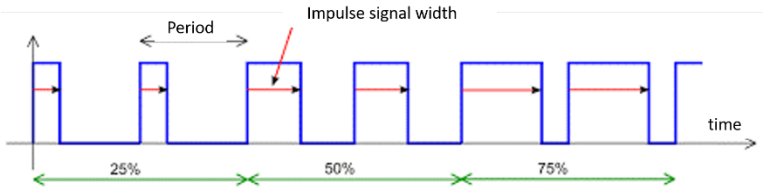

Figure 110: Representation of an impulse signal [256].

In our case, we use a duty cycle of 50% to ensure the precision of each step. The pulse width depends on the impulse signal frequency, it is half the period given by Equation 26:

$$T\ (\mu s) = \frac{1000000\ (\mu m)}{Frequency\ \times Microstep}$$

Equation 26

In practice, when the motor is not loaded, a microstep resolution of 2 causes a motor torque too high, making the motor vibrate and unable to work. Hence, to ensure a smooth start of the motor and enhance its performances, we chose a microstep resolution of 1600. It is necessary to ensure that the microstep resolution corresponds to the DIP selector switch located behind the driver.

Our impulse signal will be generated by an Arduino, then sent to the driver via the PUL+ pin, as explained earlier in this section.



Figure 111: The Arduino Uno.

The chosen hardware to generate the impulse signal is an Arduino Uno Card, one of the most popular cards, ideal to get started with Arduino, illustrated by Figure 111. It is simple and economical, based on an ATmega328 microcontroller clocked at 16 MHz. This section aims at presenting the general structure of the code, the extensive code lines being presented in the following Appendices section (see p.xix).

The part of the program in charge of generating the impulse signal is based on the 16 bits Timer1 integrated to Arduino. This efficient route allows to generate the impulse signal corresponding to a 10 Hz frequency for the motor. To operate this timer, several items are involved such as the processor frequency (16 MHz), the control registers (TCCR1x), the frequency divider, the counter (TCNTx) and the comparison registers (OCRx). Timer1 is configured using the TCCR1A and TCCR1B registers. These two control registers play distinct roles. On the one hand, TCCR1A is mainly used for pulse width modulation (PWM) to adjust the duty cycle, but cannot be used to divide the main frequency. TCCR1B, on the other hand, is used to generate a pulse signal using CTC (Clear Timer on Compare Match) mode, which enables the stepper motor to be controlled. CTC mode allows the counter to reset automatically when it reaches a specific value stored in OCR1A. This reset is accompanied by an inversion of the level of the pulse signal output pin, generating a stable signal. This means that during a cycle, two inversions will occur as a cycle involves two edges: a rising edge and a falling edge.

The TNCTx counter is a 16 bits counter, meaning that its counting ranges from 0 to 65535. In a case where the counting would go over this range, a counting error would occur. To avoid this kind of situation, it is possible to use a frequency divider. The critical OCR1A threshold is obtained using the main frequency of the microcontroller, which is equal to 16 MHz, and the impulse frequency. The OCR1A threshold is given by Equation 27.

$$OCR1A\ threshold = \frac{microcontroller\ frequency}{2\ \times impulse\ frequency}$$

Equation 27

We chose for our stepper motor a 1600 microstep by revolution resolution. Hence, for a 1 Hz speed (1 revolution by second), the impulse frequency must be 1600. Our range of use is located between 1 and 10 Hz, giving the following OCRA thresholds for the limit values:

$$OCR1A\ threshold\ (1Hz) = \frac{16 \cdot 10^6}{2\ \times 1600\ \times 1} = 5000$$

$$OCR1A\ threshold\ (10Hz) = \frac{16 \cdot 10^6}{2\ \times 1600\ \times 10} = 500$$

The previous calculations allow us to ensure that the OCR1A thresholds lie within the working range of the counter for our frequencies of use. Hence, the use of a frequency divider is not needed for Timer1. To check that our program was indeed able to generate an impulse signal corresponding to the targeted operating frequency of the motor, we connected an oscilloscope to the Arduino. The results, presented in Figure 112, confirm that the output after the timer use is precise. For a motor rotation of 1 Hz the corresponding impulse signal is indeed 1600 Hz, and for a 10 Hz setpoint, it is 16000 Hz.

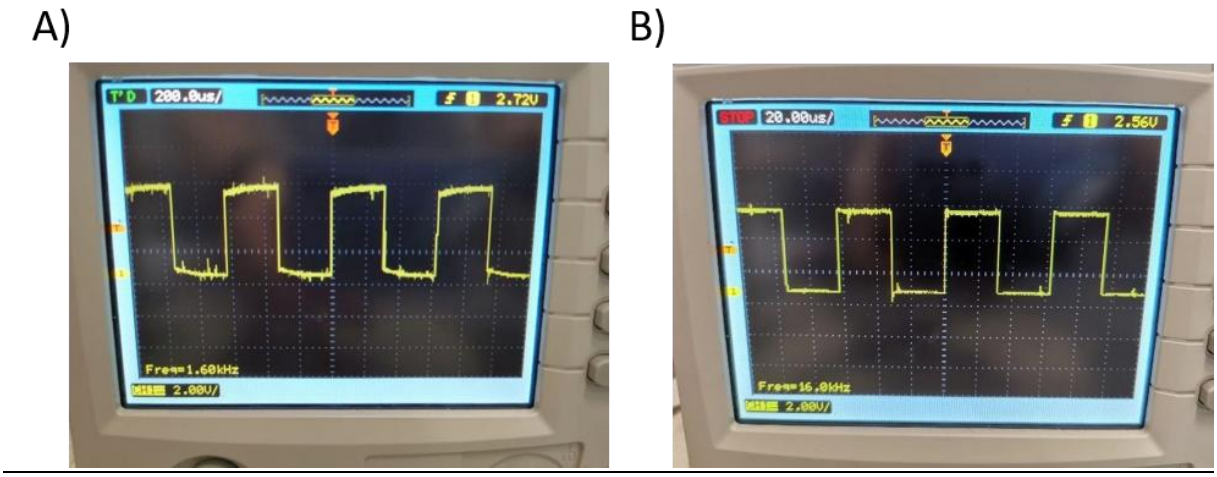

Figure 112: Impulse signal generated for a motor rotation at A) 1 Hz, B) 10 Hz.

The different steps presented allowed to modify the force applied on the sample by adding or removing six 400 g weight, and the applied tapping frequency by setting the motor and driver parameters. The addition of a force captor will allow the real-time monitoring of the force applied during the test. The complete wiring system including the Arduino, force sensor and driver is presented in Figure 113.

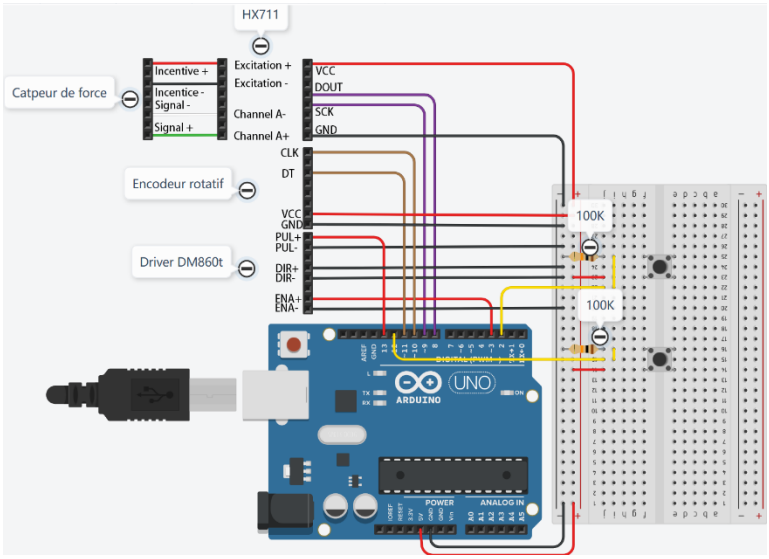

Figure 113: Complete schematic wiring diagram of the tapping test bench.

Force sensor wiring and calibration steps

The DYMH-103 force captor has four wires which have to be connected to a circuit board based on an HX711 to collect the signal. The wiring and pin definition of this circuit is presented in the following picture.

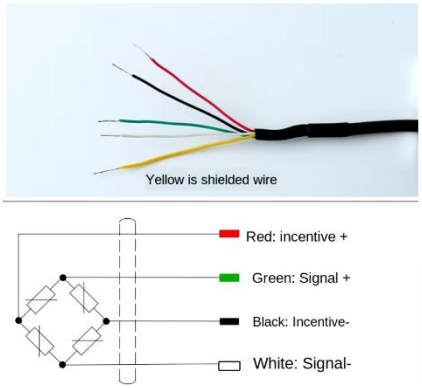

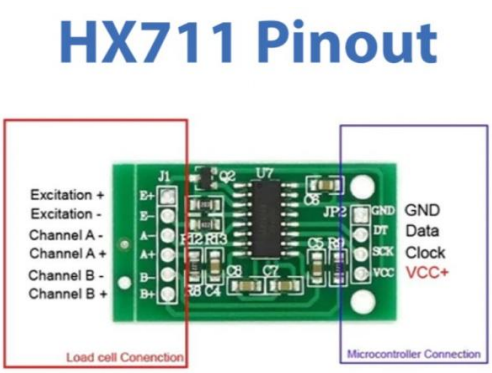

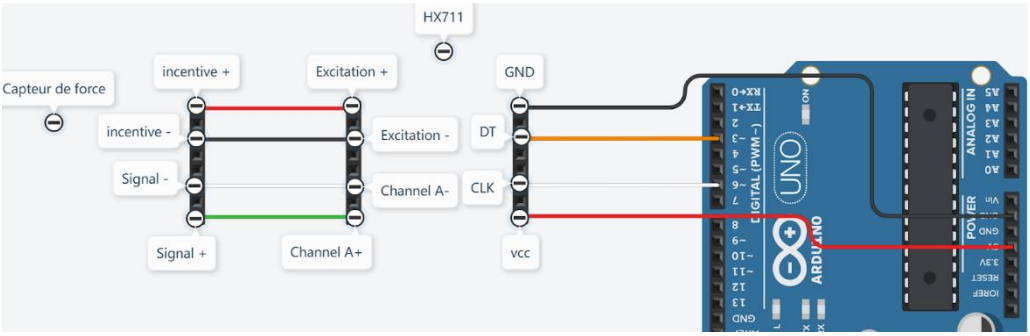

As many factors in the test environment can have an influence on the sensor output data, it is needed to calibrate the HX711. The main goal of the calibration is to find the scale factor, meaning the conversion ratio between the ADC reading and the actual weight to measure. We introduced the HX711 library to Arduino to simplify the program.

By accessing the support file for the HX711 function, we can find the specific steps for calibrating the sensor, including: tare, place a known weight, calculate the scale factor and finally test the calibration result.

In practice, we started by calling the function

scale.tare(); // return to zero

for the tare. The HX711 reading should be close to 0 at this point.

Then, we placed a 2kg weight on the loadcell, and read the ADC value from the HX711 by using:

long reading = scale.get_units(10);

Serial.print("Raw Reading: ’);

Serial.println(reading);

The scale factor calculation is made using the following formula : $Scale\ factor = \frac{reading - tare}{weight}$. We put this value in scale_factor variable.

Then we used the function

scale.set_scale(scale_factor);

in the code to apply the scale factor.

Finally, we averaged 10 reading using

scale.get_units(10);

Thanks to this series of operations, our scale factor is finally set at 2.25.

The fourth step in calibrating the sensor is to test the readings. In general, the output of a pressure sensor fluctuates due to various interfering factors such as temperature, humidity and the stability of the power supply. Therefore, in common applications of pressure sensors, it is common practice to take the average of the measured before displaying this average as the final reading. However, in our project, the motor runs at a frequency of 1 to 10 Hz. In order to ensure real-time synchronisation between the sensor readings and the movement of the motor, we chose not to use the averaging algorithm. As a result, the value measured by the sensor will be displayed directly without any additional processing.

Push button and encoder setting

The on/off switch for the motor command is a push button, so we need to take into account the two states of the button (up and down), and set a counter that increments when the button is pushed. If we directly code an increment to the counter when the button is in up position, the incrementation will not remain 1 for a long press, instead it will continue to increment until the button is released. To ensure that we get one increment for one push and reduce the processor use, we introduced the Elimination Buffeting of Keystroke function. It is performed by comparing the current state of the button with the previous state of the button. When the Arduino detects that the button is pressed (high level), which means the current state of the button is different from its previous state and the button is in high level, the button counter increments by one. If the remainder of the counter divided by two equals 0, the motor stops; if it equals 1, the motor starts. Finally, we need to synchronise the state of the motor, by replacing the previous state of the motor becomes by the current state of the motor. In addition, when the button is released, the Arduino detects a low level, which initiates a new state comparison of the button; however no code was defined for the button at low level. At the end, the state of the button is updated as not pressed, so in low state. The wiring of the button is presented in the following picture.

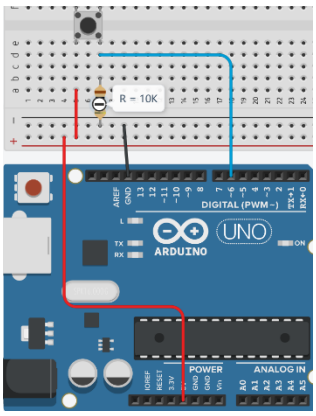

An incremental rotary encoder is used to physically change the motor frequency. The encoder is an electromechanical sensor that measures the rotation of an axis and translates this rotation into a series of electrical signals, enabling the position or speed of this axis to be tracked.

By definition, the encoder (as shown in the following picture) has two outputs: data (DT) and clock (CLK). When the encoder rotates clockwise, the CLK signal is 90° ahead of DT (phase shift), whereas when the encoder rotates anti-clockwise, the CLK signal is 90° behind DT.

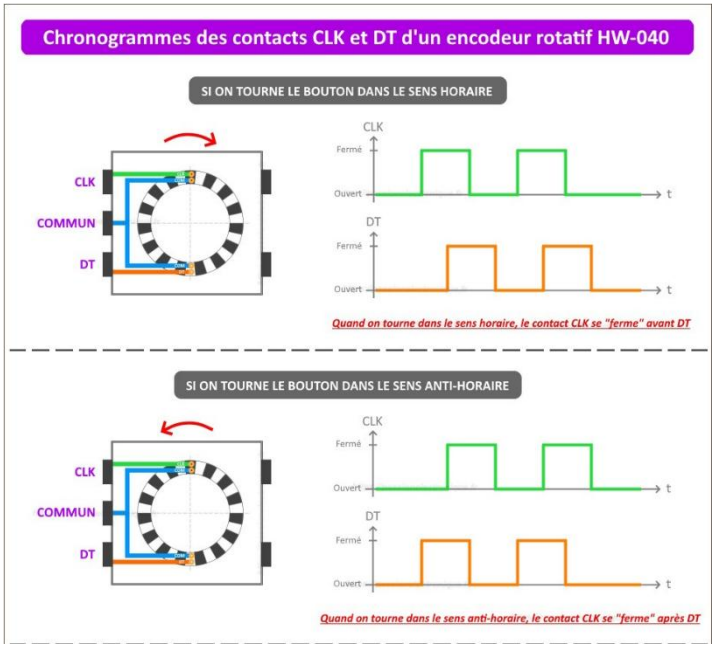

In the program, we need to detect and compare the signal levels of the DT and CLK inputs, then update their states in real time. If CLK is high and DT is low, this means that the rotary encoder is turning clockwise, in which case the frequency variable will be incremented by +1. Conversely, if DT is high and CLK is low, the rotary encoder rotates counter-clockwise, and the frequency variable must be decremented by 1. The wiring of the rotary encoder is presented in the following picture.

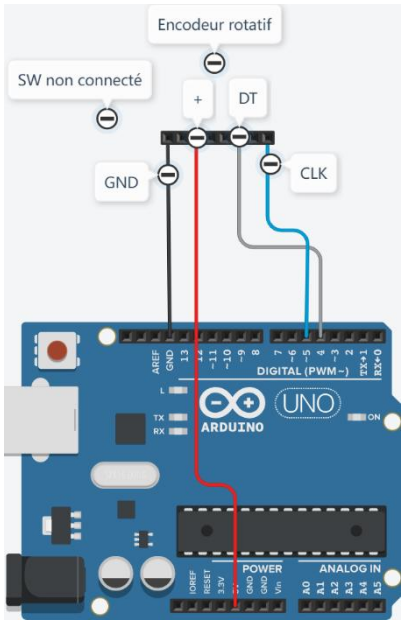

Creation of the user interface (UI)

As previously mentioned, two UI types have been developed: one using physical components, and one software approach using Python. This section will only present the later, the push button and encoder setting are developed

in the appendices. The graphical UI development was realised on PyCharm, a free software based on Python. It allows quite easily to create a graphical UI (with the tkinter library), plot curves (matplotlib library), configure a serial connection between an Arduino and a PC (serial library), and acquire Arduino data (threading library).

Before starting to code, one must first design the program operating logic. First of all, as the program is meant to be potentially operated on various computers, each one having a different serial port that will be connected to the Arduino. Hence, before starting the main program, the user must first select the Arduino serial port and test the connection. The selected port will then be registered and used in the main program. The main program is meant to operate all the needed actions to conduct the piezoelectric test using the tapping test bench. This includes the start/stop motor button, the test frequency setting in real time, the force captor zeroing option, the applied force on the sample displayed in real time, the maximum set force, the scrolling force graph, the number of points per second on the scrolling graph (indicated by the sampling frequency), the zooming option for the scrolling graph, and buttons to save the data , access user instructions and exit the program. The sequence diagram for running the graphical window is shown in Figure 114.

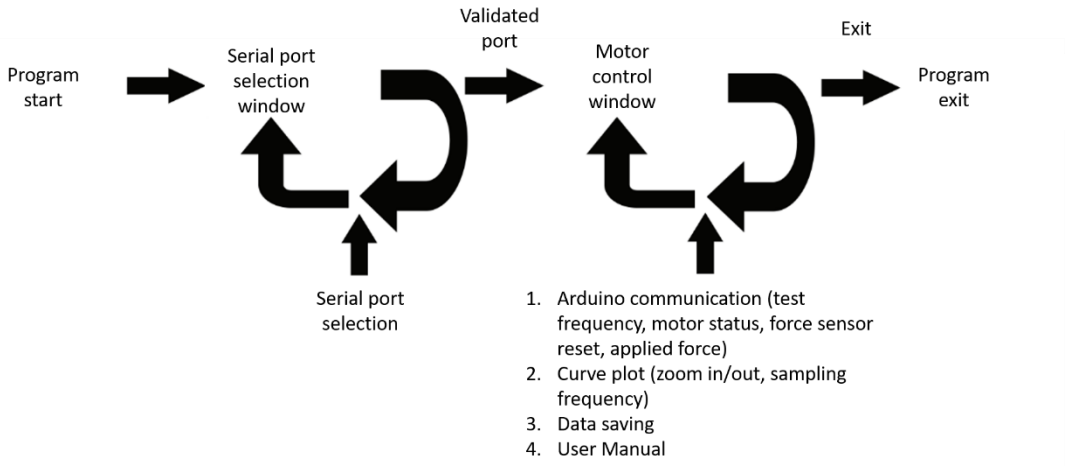

Figure 114: Graphical diagram of the program execution sequence.

The first window to appear when the program is started is then the serial port selection, shown in Figure 115. It contains a drop-list to select the serial port, with a Test button to test the correct connection with the Arduino, and a User Manuel ("Mode d'emploi") button leading to the README file and some labels to indicate the operation status and guide the user. Upon validation of the serial port, a second window will appear to properly operate the test, shown in Figure 116.

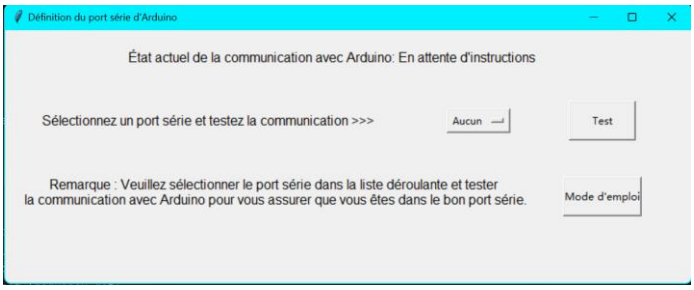

Figure 115: Serial port selection.

This window is designed to set the test frequency and the sampling frequency. It also allows to monitor in real time the actual tapping frequency and applied force on the sample during the test. After the test, the option to save the graph of the applied force as a function of time is given.

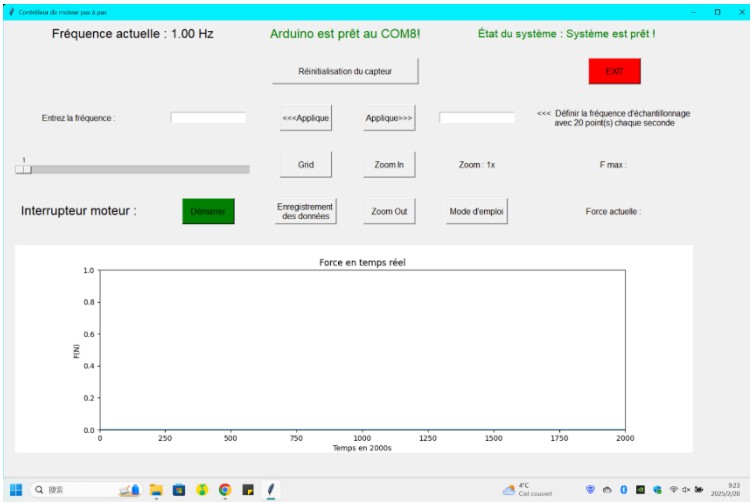

Figure 116: The test setting window.

5) Annex 5: Electrical Response of PVDF-Based Nanogenerators with CNC and QC filler addition

This section summarizes the electrical performance of PVDF nanogenerators doped with 1 %, 3 %, and 5 % of cellulose nanocrystals (CNC) and quasicrystals (QC). Voltage and current responses were measured under mechanical excitation from 1 Hz to 5 Hz.

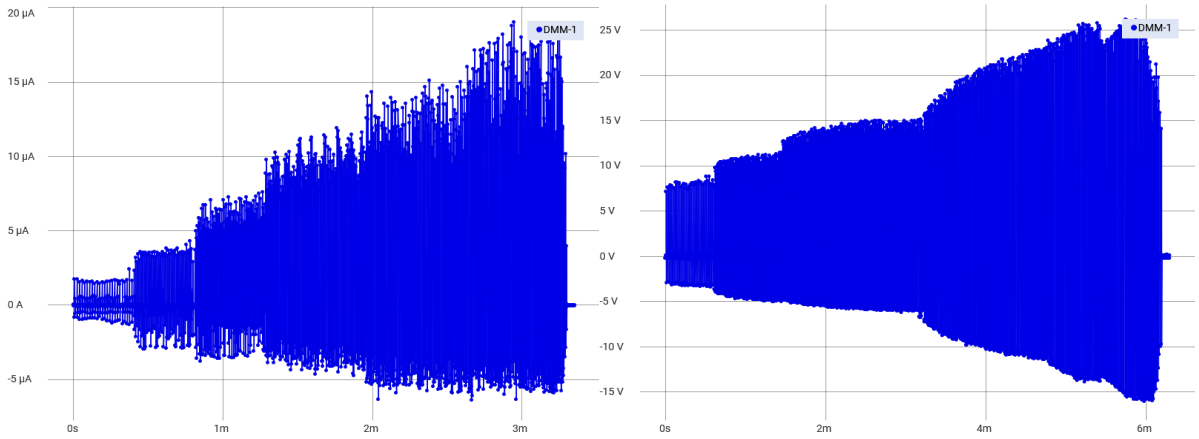

Figure 117: Voltage and current responses of CNC1 under mechanical excitation from 1 to 5 Hz.

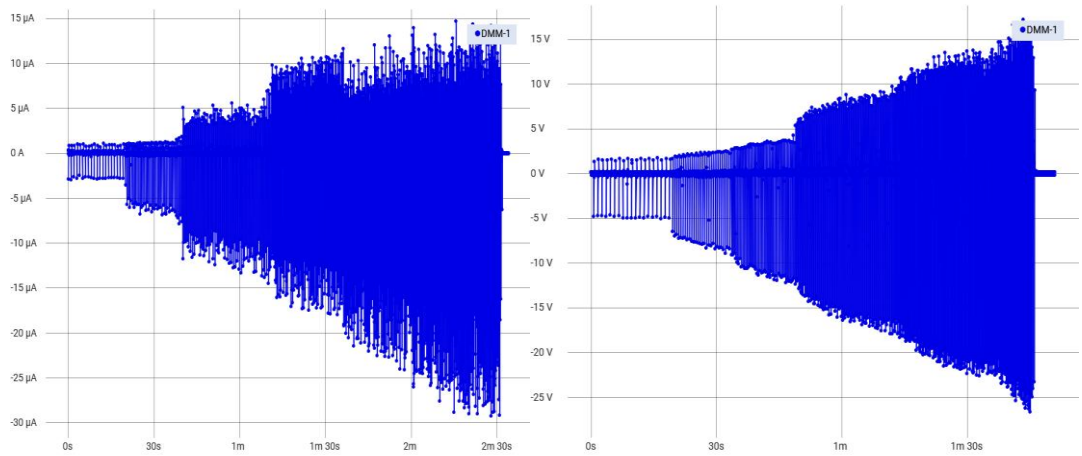

Figure 118: Voltage and current responses of CNC3 under mechanical excitation from 1 to 5 Hz.

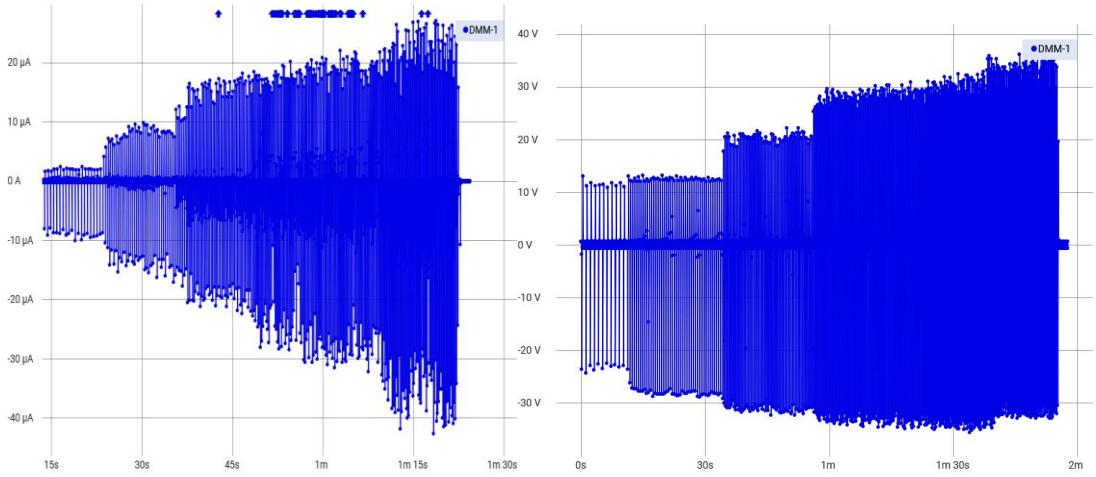

Figure 119: Voltage and current responses of CNC5 under mechanical excitation from 1 to 5 Hz.

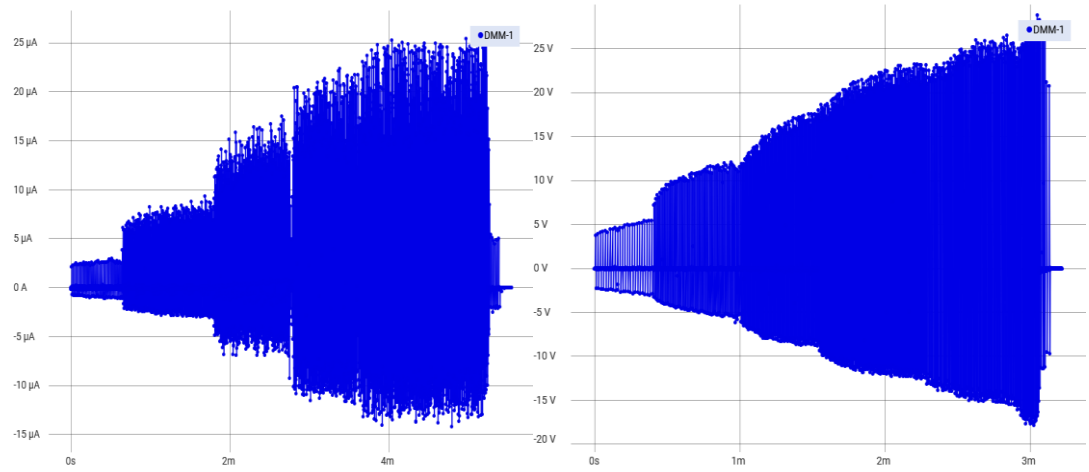

Figure 120: Voltage and current responses of QC1 under mechanical excitation from 1 to 5 Hz.

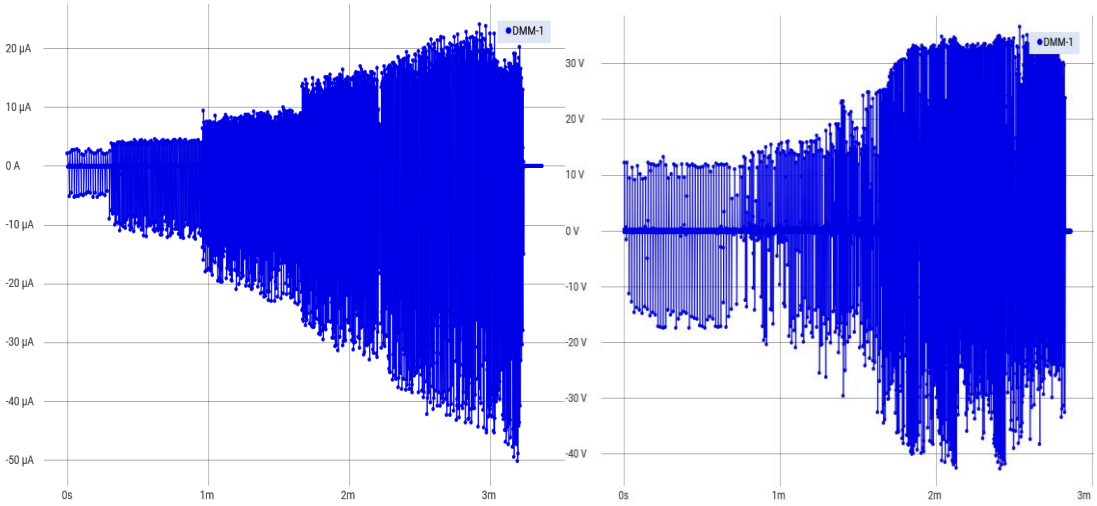

Figure 121: Voltage and current responses of QC3 under mechanical excitation from 1 to 5 Hz.

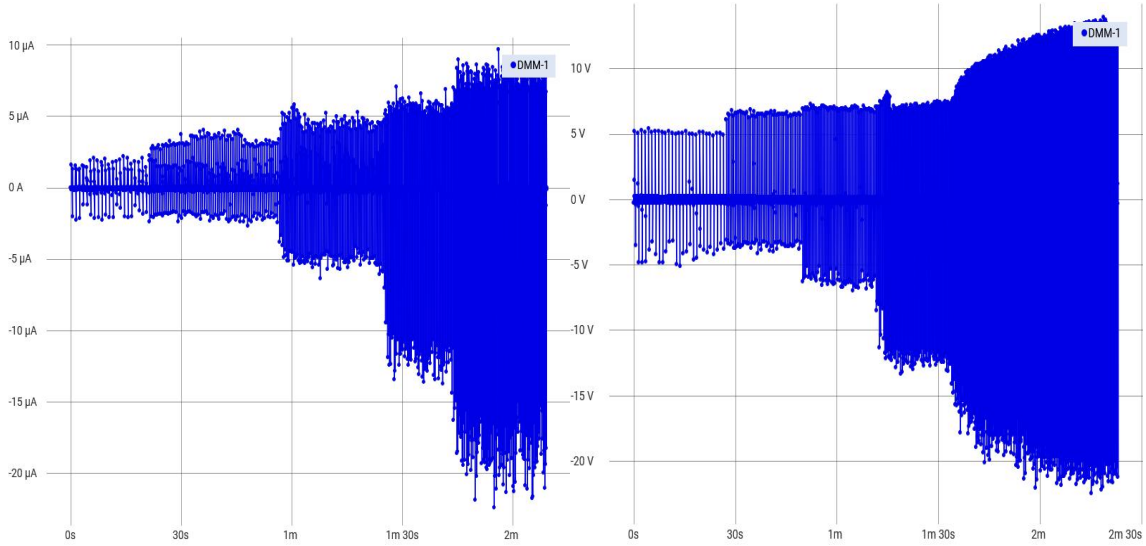

Figure 122: Voltage and current responses of QC5 under mechanical excitation from 1 to 5 Hz.

6) Annex 6: Code

Arduino code

```
#include "HX711.h" // librarie HX711

#define DOUT  8 // HX711 DOUT est connecté au broche 8

#define SCK   9 // HX711 SCK est connecté au broche 9

HX711 scale; // changement du nom d'appel de HX711


const short int ONOFF = 12; // bouton ON OFF à port 12

const short int DT = 11; // encodeur DT à port 11

const short int CLK = 10; // encodeur CLK à port 10

const short int ENA = 3; // driver ENA à port 3

const short int SLOW = 2; // Appuyez longuement sur le bouton pour faire tourner le moteur est à port 2


short int button_counter = 0; // compteur du bouton ONOFF

short int Max_frequency = 10; // fréqeuce max

short int stepresolution = 1600; // résolution du driver

float frequencyIncrement = 0.1; // incrément de la fréquence

float actual_frequency = 1.0; // fréquence actuel

float frequency = 1.0; // fréquence cible

float lastfrequency = frequency; // état de la fréquence pour réduire l'utilisation du processeur

float force = 0.0; // initialisation de la force

float scale_factor = 2.25; // facteur HX711

byte currentStateencoder = false; // état actuel de l'encodeur

byte lastStateencoder = false; // état précédent de l'encodeur

byte currentStatebutton = false; // état actuel du bouton

byte lastStatebutton = false; // état précédent du bouton

byte motor_state = false; // état du moteur

byte lastmotor_bytestate = motor_state; // état précédent du moteur

byte motor_running = false; // état de tourne du moteur

unsigned long previousMillis = 0; // temps de la fonction Millis précédent
```

```
const long interval = 12; // delay d'exécution de la fonction Millis par rapport au 1/80
// la fréquence d’échantillonnage de HX711

void setup() {
  Serial.begin(115200); // définition du débit en baud
  DDRB |= (1 << PB5); // Pin 13 pour le signal d'impulsion en sortie
  PORTB &= ~(1 << PB5); // port 13 en niveau bas
  pinMode(ONOFF,INPUT); // Pin bouton ONOFF en entrée
  pinMode(DT,INPUT); // Pin DT en entrée
  pinMode(CLK,INPUT); // Pin CLK en entrée
  pinMode(ENA,OUTPUT); // Pin ENA en sortie
  pinMode(SLOW,INPUT); // Pin SLOW en entrée
  lastStateencoder = digitalRead(CLK); // actualisation de l'état de l'encodeur
  scale.begin(DOUT, SCK); // initialisation HX711
  scale.set_scale(scale_factor);// applique le facteur d’echelle
  delay(100); // attende 100ms
  scale.tare(); // mettre en 0 le capteur de force
  setStepFrequency(1.0); // appliquer la fréqeunce initialle au timer1
}

void loop() {
  currentStatebutton = digitalRead(ONOFF); // lecture de l'état du bouton ONOFF
  currentStateencoder = digitalRead(CLK); // lecture de l'état de l'encodeur
  encoder_state_detection(); // fonction de la détection de l'encodeur
  bottom_state_detection(); // fonction de la détection du bouton
  reception(); // fonction pour le lecture des information de l'ordinateur
  run_motor(); // fonction de gestion du moteur
  slowmove(); // fonction pour tourner le moteur en bas vitesse
  unsigned long currentMillis = millis(); // lecture du temps actuel
  if (currentMillis - previousMillis >= interval) { // si le temps est passé de 12ms qu'avant
```

```
    // arduino va envoyer la force à l'ordinateur
    // la fonction Millis ne bloquera pas la fonction principale
      previousMillis = currentMillis; // actualiser le temps
      send_force(); // envoie la force
   }
}


 // fonction de gestion du moteur
void run_motor()
{
  if(motor_state == true)// si l'état du moteur est 1, démarrage du moteur
  {
   digitalWrite(ENA,LOW); // activer le moteur
   if(motor_running == false) actual_frequency = 1.0; // initialisation de la fréquence
   motor_running = true; // actualisation de l'état de tourne du moteur
   if (actual_frequency < frequency) { // accélération du moteur à la fréquence cible
     for (actual_frequency;actual_frequency <= frequency;actual_frequency+=frequencyIncrement)
     {
       setStepFrequency(actual_frequency*stepresolution);
       delay(30);
       }
     if (actual_frequency > frequency) actual_frequency = frequency;
   } else if (actual_frequency > frequency) { // décélération à la fréquence cible
     for (actual_frequency;actual_frequency >= frequency;actual_frequency-=frequencyIncrement)
     {
       setStepFrequency(actual_frequency*stepresolution);
       delay(30);
       }
     if (actual_frequency < frequency) actual_frequency = frequency;
   }
```

```
    setStepFrequency(actual_frequency*stepresolution);
  }
  else // sinon l'arrêt du moteur
  {
    if (motor_running == true)
    {
      if (actual_frequency > 2.0) { // décélération du moteur jusqu'à l'arrêt
      for (actual_frequency;actual_frequency >= 1.0;actual_frequency-=frequencyIncrement)
      {
        setStepFrequency(actual_frequency*stepresolution);
        delay(20);
        }
      if (actual_frequency < frequency)
      {
        motor_running = false;
        actual_frequency = 2.0;
        }
      }
    }
    stopTimer1(); // arrêt du timer
    motor_running = false;
    actual_frequency = 1.0;
    digitalWrite(ENA,HIGH); // désactiver le moteur
  }
}


// Fonction Timer1 en mode CTC configuré TCCR1B
void setStepFrequency(long frequency1)
{
  long timerCount = (16000000 / (2  * frequency1)) - 1;
```

```
  TCCR1A = 0;//on utilise le registre TCCR1B, donc TCCR1A est déactivé
  TCCR1B = (1 << WGM12) | (1 << CS10);//configuration TCCR1B en mode CTC,pas de division en fréquence
  OCR1A = timerCount;// actualiser le seuil du compteur
  TIMSK1 |= (1 << OCIE1A);//Activer la comparaison de correspondance A pour l'interruption du compteur 1
  //Lorsque le temporisateur TCNT1 compte jusqu'à la valeur de OCR1A, l'interruption TIMER1_COMPA_vect est déclenchée.
}

//Interrupt Service Routine, (ISR）
//à chaque interrupt, le niveau de sortie est basculé
ISR(TIMER1_COMPA_vect) {
  PORTB ^= (1 << PB5);
}

//Arrêtez complètement le compteur 1 et effacez l'état associé
void stopTimer1() {
  TIMSK1 &= ~(1 << OCIE1A);//Désactiver la comparaison de correspondance A pour l'interruption du minuteur 1
  TCCR1B = 0; //Arrêter la minuterie 1
  TCNT1 = 0; //Effacer le compteur du Timer 1
  PORTB &= ~(1 << PB5);//Assurez-vous que le PB5 (D13) génère un niveau bas
}

 // fonction de lecture de l'ordinateur
void reception()
{
  if(frequency != lastfrequency || motor_state != lastmotor_bytestate || Serial.available() > 0)
   // cette focntion if sert à réduire l'utilisation du processeur
  {
    if(Serial.available() > 0)
    {
       String message = Serial.readStringUntil('\n');
```

```
if(message.startsWith("ON"))
{
 motor_state = true;
 button_counter ++;
 Serial.print("motorstate: ");
 Serial.println(motor_state);
 }
else if(message.startsWith("OFF"))
{
 motor_state = false;
 button_counter ++;
 Serial.print("motorstate: ");
 Serial.println(motor_state);
 Serial.print("force: ");
 Serial.println(0);
 }
else if(message.startsWith("Fre"))
{
 String fre = message.substring(message.indexOf(':') + 1);
 fre.trim();
 frequency = fre.toFloat();
 Serial.print("frequency: ");
 Serial.println(frequency);
}
else if(message.startsWith("test"))
{
  for(int i = 0;i<=5;i++)
  {
   Serial.println("v");
   delay(50);
   }
```

```
        }
        else if(message.startsWith("Reset"))
        {
          button_counter = 0;
          scale.begin(DOUT, SCK);
          delay(100);
          scale.tare();
          Serial.println("Resetdone");
          }
      }
    lastfrequency = frequency;
    lastmotor_bytestate = motor_state;
    Serial.print("motorstate: ");
    Serial.println(motor_state);
    Serial.print("frequency: ");
    Serial.println(frequency);
    }
  }


 // fonction d'envie de la force
void send_force()
{
  if(scale.is_ready() && motor_state == true)
  {
    float weight = scale.get_units(1);
    force = (weight/1000.0) * 9.8;
    Serial.print("force: ");
    Serial.println(force);
    }
}
```

```
 // fonction de la détection de l'encodeur
void encoder_state_detection()
{
  if(currentStateencoder != lastStateencoder)
  {
    if(digitalRead(DT) != currentStateencoder)
    {
     if(frequency < Max_frequency)
     {
      frequency += 0.5;
     }
     }
     else
     {
      if(frequency > 1)
      {
        frequency -= 0.5;
       }
      }
    }
  lastStateencoder = currentStateencoder;
  }


 // fonction de la détection du bouton
void bottom_state_detection()
{
  if(currentStatebutton != lastStatebutton)
  {
    if(currentStatebutton == HIGH)
```

```
    {
      button_counter ++;
      if(button_counter % 2 == 0)
      {
        motor_state = false;
        Serial.print("force: ");
        Serial.println(0);
        }
        else
        {
          motor_state = true;
         }
      }
    }
  lastStatebutton = currentStatebutton;
  }


 // fonction pour tourner le moteur en bas vitesse
void slowmove()
{
  if(motor_state == false)
  {
    if(digitalRead(SLOW)==HIGH)
    {
      digitalWrite(ENA,LOW);
      digitalWrite(13, HIGH);
      delayMicroseconds(1000);
      digitalWrite(13, LOW);
      delayMicroseconds(1000);
    }
```

```
  else
  {
    digitalWrite(ENA,HIGH);
  }
 }
}
```

```
from collections import deque
import serial.tools.list_ports # Répertorier les périphériques série disponibles dans le système actuel
import tkinter as tk # Importer la librairie Tkinter
import threading #librairie multithread
from matplotlib.backends.backend_tkagg import FigureCanvasTkAgg
#I ntégration de graphiques Matplotlib dans une interface graphique Tkinter
from matplotlib.figure import Figure # import la figure pour le courbe
from tkinter import messagebox # Boîte de message contextuelle
from tkinter import StringVar # Stocker et gérer les données de chaîne de liste déroulante
from tkinter import filedialog # boîte de dialogue de fichier
import os # Obtenir le répertoire du fichier README
import sys # Obtenez le chemin et déterminez si le fichier peut être exécuté

fonte_police = "Arial" # Style de police
taille_de_police = 12 # taille de la police

#La fenêtre pour la définition la port série d'Arduino
def fenetre_de_selection_arduino_com():
        global fonte_police,taille_de_police
        fenetre_chois_com = tk.Tk() # Création de la fenêtre
        fenetre_chois_com.title("Définition du port série d'Arduino")# le titre de la fenêtre
        fenetre_chois_com.geometry("820x300")# la taille de la fenêtre

        def list_serial_ports():# fonction pour obtenir les ports séries valables
        ports = serial.tools.list_ports.comports()# ports est une liste pour tous les ports série sur ordinateur
        available_ports = [port.device for port in ports]# available_ports est une list pour les ports valables
        return available_ports # retourner la liste

        ports_detected = list_serial_ports()
        # ports_detected fait référence à la fonction et obtient la valeur renvoyée par la fonction
        selected_option = StringVar()
        # selected_option est la valeur sélectionnée par la list déroulant actuel, la valeur par défaut est Aucun
        selected_option.set('Aucun')

        def test_de_connexion(): #Fonction pour tester la connection
        if selected_option.get() == "Aucun" : # si la list n'est pas sélectionné
        messagebox.showinfo("Erreur", "Choisissez un port série")
        else:
       button_test_connection.configure(state="disabled")# Rendre les boutons et les
        # listes déroulantes non sélectionnables pour empêcher les utilisateurs d'en faire trop
        dropdown.config(state="disabled")
        com = selected_option.get() # passer la valeur sélectionné à com
        try:# Test de connection
        ser = serial.Serial(com, 115200, timeout=2)
        #Établir une connexion sur le port série à un débit de 19 200 bauds
        label_communication_state.config(text = f"État de communication actuel avec Arduino au '{com}' est : Envoi")
        fenetre_chois_com.after(2000, test_connection_avec_arduino, ser, com)
        #Attendez 2 secondes puis lire la réponse de l'arduino
        except serial.SerialException as e:
        #Si la connexion échoue, une erreur s'affiche
        label_communication_state.config(text = f"État de communication actuel avec Arduino au '{com}' est : Échouer")
          button_test_connection.configure(state="normal")
        dropdown.config(state="normal")

        #Fonction pour l'écriture vers Arduino
        def test_connection_avec_arduino(ser,com):
        ser.write("test".encode('utf-8'))#l'envoie du message test
        response = ser.readline().decode('utf-8').strip()#lire la réponse d'arduino
        if response.startswith("v"):#si la réponse est V, passant à la fenêtre principal
```

```
        ser.close()
        fenetre_chois_com.destroy()
        fenetre_principale(com)
        else:#Si non affiche d'erreur
        label_communication_state.config(text = f"État de communication actuel avec Arduino au '{com}' est : Échouer")
       button_test_connection.configure(state = "normal")
        dropdown.config(state = "normal")
        ser.close()#Fermeture du port série

        def get_base_path():#Obtenire la répertoire du programme pour chercher le fichier README
        if getattr(sys, 'frozen', False):
        return os.path.dirname(sys.executable)
        else:
        return os.path.dirname(os.path.abspath(__file__))

        def show_help():#L'ouvrage du fichier README
        file_path = os.path.join(get_base_path(), "README.txt")
        try:
        os.startfile(file_path)
        except FileNotFoundError:#Si le fichier n'a pas trouvé, affichage d'erreur
        messagebox.showerror(f"Erreur",f"Impossible de trouver le fichier Readme.txt")
        except Exception as e:
        messagebox.showerror(f"Erreur",f"Impossible de trouver le fichier Readme.txt {e}")

        #Liste déroulant pour choisir les ports séries
        dropdown = tk.OptionMenu(fenetre_chois_com, selected_option, *ports_detected)

        #Définition du bouton test
        button_test_connection = tk.Button(fenetre_chois_com, text="Test", command=test_de_connexion, width=10,
height=2)

        #Définition du bouton help
        button_help = tk.Button(fenetre_chois_com, text="Mode d'emploi", command=show_help, width=12, height=2)

        #Définition de l'étiquette de la liste déroulant
        label_com_dropdown = tk.Label(fenetre_chois_com, text="Sélectionnez un port série et testez la communication
>>>",font=(fonte_police, taille_de_police))

        #Définition de notice
        label_notice = tk.Label(fenetre_chois_com, text="Remarque : Veuillez sélectionner le port série dans la liste
déroulante et tester \n"
                                "la communication avec Arduino pour vous assurer que vous êtes dans le bon port
série.\n",font=(fonte_police, taille_de_police))

        #Définition de l'état de la communication
        label_communication_state = tk.Label(fenetre_chois_com, text="État actuel de la communication avec Arduino: En
attente d'instructions",font=(fonte_police, taille_de_police))

        #Emplacement des mudoles
        label_communication_state.grid( row=0, column=0, columnspan=3,padx=1, pady=20)
        label_com_dropdown.grid(        row=1, column=0, padx=20, pady=20)
        dropdown.grid(          row=1, column=1, padx=20, pady=20)
        button_test_connection.grid(        row=1, column=2, padx=20, pady=20)
        label_notice.grid(          row=2, column=0,rowspan = 2, columnspan=2, padx=20, pady=20)
        button_help.grid(           row=2, column=2, padx=20, pady=20)

        fenetre_chois_com.mainloop()#boucle principal de la premier fenêtre

 #La fenêtre principale
 def fenetre_principale(porte):
        #Appel du fonte et la taille de police en global#
```

```
    global fonte_police, taille_de_police

    #Définition des variables#
    frequency_max = 10 #Fréqeunce maximum#
    frequency_min = 1 #Fréquence minimum#
    state_motor = 0 #l'état du moteur
    frequency = 1 #fréquence actuel
    force = 0 #Force appliqué
    f_max = 0 #Force maximum
    force_data = [] #matrice pour stocker les forces mesurées
    time_data = [] #matrice pour stocker le temps à chaque échantillonage
    sampling_frequency = 2000 #fréqeunce d'échantillonage
    x_data = list(range(sampling_frequency)) #définition de la longueur de la matrice
    y_data = deque([0] * sampling_frequency, maxlen=sampling_frequency) #définition de la longueur de la matrice
    show_grid_state = 0 #l'état du grid
    magnification = 1 #le taux d'amplification
    reset_value = 0 #variable pour le reset du capteur

    #Création de la fenêtre
window = tk.Tk()
    width = window.winfo_screenwidth()
    height = window.winfo_screenheight()
    window.geometry(f"{width}x{height}+0+0")
    window.title("Contrôleur de moteur pas à pas")

    #Création de la figure pour l'affichage de la courbe des forces
    fig = Figure(figsize=(13, 4), dpi=100) #la taille de la figure
    ax = fig.add_subplot(111)
    ax.set_title("Force en temps réel") #TItre de la figure
    ax.set_xlabel(f"Temps en {len(x_data)}s") #label de l'axe x
    ax.set_ylabel("F(N)") #label de l'axe y
    ax.set_xlim(0, len(x_data)) #définir la limite de l'axe x
    ax.set_ylim(0, max(y_data) + 1) #définition de la limite de l'axe y
    line, = ax.plot(x_data, list(y_data)) #définition la base des données de la courbe
    canvas = FigureCanvasTkAgg(fig, master=window) #définition le zone d'affichage
    ser = serial.Serial(porte, 115200, timeout=1) # l'ouvrage de la communication série

    # focntion de compteur au début de l'affichage de la fenêtre principal
    def countdown(n):
    label_counter.config(text=f"Arduino sera prêt dans : {n}s")
    if n >= 1:  # les commandes sont indisponible avant le compteur attaindre à 1
    window.after(1000, countdown, n - 1)
    button_set_frequency.config(state="disabled")
    button_onoff.config(state="disabled")
    button_save_data.config(state="disabled")
    button_set_sampling.config(state="disabled")
    button_reset_sensor.config(state="disabled")
    button_show_grid.config(state="disabled")
    button_zoom_in.config(state="disabled")
    button_zoom_out.config(state="disabled")
    button_help.config(state="disabled")
    scale.config(state="disabled")
    show_infor("En attente de la configuration d'Arduino")
    else:  # si le compteir est terminé, les commandes sont diponible
    label_counter.config(text=f"Arduino est prêt au {porte}!", font=(fonte_police, 18), fg="green")
    button_set_frequency.config(state="normal")
    button_onoff.config(state="normal")
    button_save_data.config(state="normal")
    button_set_sampling.config(state="normal")
    button_reset_sensor.config(state="normal")
    button_show_grid.config(state="normal")
```

```
button_zoom_in.config(state="normal")
button_zoom_out.config(state="normal")
button_help.config(state="normal")
scale.config(state="normal")
show_infor("Réinitialisation du capteur")
ser.write(f"Reset: {10}".encode())  # reset du capteur

#lire les données d'Arduino
def read_from_arduino():
nonlocal frequency,state_motor,force,f_max,x_data,y_data
while True:
#lire d'aborde les données puis les traiter à partie de l'étiquette au début des données
read = ser.readline().decode('utf-8').strip()

#si les données commence par frequency, donc actualiser la fréquence
if read.startswith("frequency:"):
frequency = read.split(":")[1].strip()
scale.set(frequency)
  label_actual_frequency.configure(text=f"Fréquence actuelle : {frequency} Hz")

#Si les données commence par motostate, donc le démarrage ou l'arrêt du moteur
elif read.startswith("motorstate:"):
state_motor = int(read.split(":")[1].strip())
if state_motor == 0:
      button_onoff.configure(text="Démarrer", bg="green")
elif state_motor == 1:
      button_onoff.configure(text="Arrêter", bg="red")

#si les données commence par force, actualisation de la force et la force max
elif read.startswith("force:"):
force = float(read.split(":")[1].strip())
label_force.configure(text=f"Force actuelle : {force} N")
if f_max < force:
            f_max = force
  label_force_max.configure(text=f"F max : {f_max}")

#si les données commence par Resetdone, le reset du capteur est terminé
elif read.startswith("Resetdone"):
show_infor("La réinitialisation du capteur est terminée!")
window.after(1000, show_infor, "Système est prêt !")

#Fonction pour actualiser et envoyer l'état du bouton
def send_onoff():
nonlocal state_motor,force,f_max,x_data,y_data,reset_value,force_data,time_data
if state_motor == 0:
force_data.clear()
time_data.clear()
reset_data()
ser.write(b'ON\n')#lorsque le démarrage, le graphe s'initialiser
else:
ser.write(b'OFF\n')  # l'arrête du moteur
time_data = [i * (100/sampling_frequency) for i in range(len(force_data))]
show_infor("Moteur arrêté")
window.after(2000, show_infor, "Système est prêt !")
ser.write(f"Reset: {reset_value}".encode())

#Fonction pour définir et envoyer la fréquence à Arduino
def set_frequency():
frequency_get = check_integer(entry_frequency.get()) #envoie à la detection d'entier
if not frequency_get: #si l'entrée n'est pas entier
entry_frequency.delete(0, tk.END)
```

```
            elif int(frequency_get) < 1: #si l'entrée est négatif
            messagebox.showinfo("Erreur", "Valeur ne peut pas être 0 !")
            entry_frequency.delete(0, tk.END)
            else: #si l'entrée est validé
            frequency_get = entry_frequency.get()
           if frequency_min <= int(frequency_get) <= frequency_max: #si la fréquence entrée n'est pas hors de la limite
            ser.write(f"Fre: {frequency_get}".encode())
            entry_frequency.delete(0, tk.END)
            show_infor("Frequence est appliqué !")
            window.after(2000, show_infor, "Système est prêt !")
            else: # sinon affiche l'erreur
            messagebox.showinfo("Erreur", f"La fréquence doit être comprise entre {frequency_min} et {frequency_max} !")
            entry_frequency.delete(0, tk.END)

            #Fonction pour actualiser la valeur dans entry set_frequency lorsqu'on jouer sur le bar déroulant
            def on_scale_change(value):
            entry_frequency.delete(0, tk.END)
            entry_frequency.insert(0, f"{value}")
            set_frequency()

            #Re-initialiser le capteur
            def reset_sensor():
            nonlocal f_max,force,x_data,y_data,force,reset_value
            show_infor("Réinitialisation du capteur")
            # le reset du capteur réinitialiser quand même le graphe
            ser.write(f"Reset".encode())
            reset_data()

            #fonction pour actualiser le graphe
            def update_plot():
            nonlocal x_data, y_data, sampling_frequency, force
            y_data.append(force) #la matrice primaire prend la valeur de force et le mettre en fin de la matrice
            if state_motor == 1:
            force_data.append(force)
            line.set_ydata(y_data) #définision de la base de données
            ax.set_ylim(min(y_data) , max(y_data) + 1) #définition de la limite de l'axe y
            ax.set_xlabel(f"Temps en {100 / magnification}s")
            canvas.draw() #dessine la courbe
            label_magnification.config(text=f"Zoom : {magnification}x")
            window.after(int(1000*100 / sampling_frequency), update_plot) #affichage en fonction de la fréqeunce
d'échantillonage

            #fonction pour définire la fréquence d'échantillonage
            def set_sampling_frequency():
            nonlocal sampling_frequency,f_max,x_data,y_data,force
            entry_read = check_integer(entry_sampling_frequency.get()) #envoie à la detection d'entier
            if not entry_read: #si l'entrée n'est pas entier
            entry_sampling_frequency.delete(0, tk.END)
            elif int(entry_read) < 1: #si l'entrée est négatif
            messagebox.showinfo("Erreur", "Valeur ne peut pas être 0 !")
           entry_sampling_frequency.delete(0, tk.END)
            else: #si l'entrée est validé, le graphe est initialisé
            sampling_frequency = int(entry_read)*100
            entry_sampling_frequency.delete(0, tk.END)
            reset_data()
            ax.set_xlabel(f"Temps en {len(x_data)}s")
            label_sampling.config(text=f"<<<  Définir la fréquence d'échantillonnage \navec {int(sampling_frequency/100)} point(s)
chaque seconde")
            #zoom_out()
            show_infor("la fréquence d'échantillonnage est appliqué !")
            window.after(1000,show_infor,"Système est prêt!") #affichage de l'état du système
```

```
        #Fonction pour zoomer
        def zoom_in():
        nonlocal x_data,y_data,magnification
        x_min, x_max = ax.get_xlim()
        current_x_length = x_max - x_min
        if current_x_length <= 100:
        return
        magnification = magnification + 1.5
        new_width = (x_max - x_min) / magnification
        new_x_min = x_max - new_width
        new_x_max = x_max
        ax.set_xlim(new_x_min, new_x_max)

        #Fonction pour dézoomer
        def zoom_out():
        nonlocal x_data,magnification
        magnification = 1
        ax.set_xlim(0, len(x_data))

        #Fonction pour enregistrement des données
        def save_data():
        nonlocal force_data,time_data
        # apparaîte la fenêtre pour choisir la répertoir du fichier
        save_path = filedialog.asksaveasfilename(title="Sélection du Répertoire",defaultextension=".txt",filetypes=[("Text
files","*.txt"),("All files","*.*")])
        show_infor("Enregistrement des données")
        if save_path: #une fois la répertoir est choisi, le fichier des données va généré
        with open(save_path, "w") as file:
        file.write("time(s)\tForce(N)\n")
        for time_in_data, force_in_data in zip(time_data,force_data):
                file.write(f"{time_in_data}\t{force_in_data}\n")
        messagebox.showinfo("Enregistrement","Enregistré avec succès")
        window.after(1000, show_infor, "Système est prêt!")
        force_data.clear()
        time_data.clear()
        reset_data()
        else:
        messagebox.showerror("Erreur", "Répertoire illégal")

        #Fonction pour afficher ou enlever le grid
        def show_grid():
        nonlocal show_grid_state
        if show_grid_state == 0:
        ax.grid(True)
        show_grid_state =1
        show_infor("Grid ON")
        window.after(1000, show_infor, "Système est prêt!")
        elif show_grid_state == 1:
        ax.grid(False)
        show_grid_state = 0
        show_infor("Grid OFF")
        window.after(1000, show_infor, "Système est prêt!")
         else:
        messagebox.showerror("Show Grid","Erreur inattendue")

        #Obtenire la répertoire du programme pour chercher le fichier README
        def get_base_path():
        if getattr(sys, 'frozen', False):
        return os.path.dirname(sys.executable)
```

```
        else:
        return os.path.dirname(os.path.abspath(__file__))

        # L'ouvrage du fichier README
        def show_help():
        file_path = os.path.join(get_base_path(), "README.txt")
        try:
        os.startfile(file_path)
       show_infor("README est ouvert !")
        window.after(1000, show_infor, "Système est prêt!")
        except FileNotFoundError:
        messagebox.showerror(f"Erreur",f"Impossible de trouver Readme.txt")
        except Exception as e:
        messagebox.showerror(f"Erreur",f"Impossible de trouver Readme.txt {e}")

        # Fonction spécialisé pour l'affichage des information du système
        def show_infor(message):
        label_windows_information.config(text=f"État du système : {message}")

        #Fonction pour vérifié l'entrée est entier
        def check_integer(data):
        user_input = data
        try:
        int(user_input)
        return user_input
        except ValueError:
        messagebox.showerror("Erreur", "Veuillez saisir un nombre entier !")
        return ""

        # Fonction pour réinitialiser les data
        def reset_data():
        nonlocal sampling_frequency, f_max, x_data, y_data, force, magnification
        force = 0
        f_max = 0
        magnification = 1
        x_data = list(range(sampling_frequency))
        y_data = deque([0] * sampling_frequency, maxlen=sampling_frequency)
        ax.set_xlim(0, len(x_data))
        line.set_data(x_data, list(y_data))

        # Fonction pour quitter le programme
        def exit_program():
        nonlocal ser
        if ser.is_open:
        ser.close()
        window.quit()
        window.destroy()

        #Définition des modules
        #Partie label
        label_counter = tk.Label(window, text="Arduino sera prêt dans : ", font=(fonte_police, 18),fg="red")
        label_actual_frequency = tk.Label(window, text="Fréquence actuelle : 1 Hz", font=(fonte_police, 18))
        label_state_motor = tk.Label(window, text="Interrupteur moteur :", font=(fonte_police, 18))
        label_entre_frequency = tk.Label(window, text="Entrez la fréquence :", font=(fonte_police, taille_de_police))
        label_force = tk.Label(window, text="Force actuelle : ",font=(fonte_police, taille_de_police))
        label_force_max = tk.Label(window, text="F max : ",font=(fonte_police, taille_de_police))
        label_sampling = tk.Label(window, text="<<<  Définir la fréquence d'échantillonnage \navec 20 point(s) chaque
seconde",font=(fonte_police, taille_de_police))
        label_magnification = tk.Label(window, text="Zoom : 1x",font=(fonte_police, taille_de_police))
        label_windows_information = tk.Label(window, text="État du système : ", font=(fonte_police, 16),fg = "green")
```

```
        #Partie bouton
        button_set_frequency = tk.Button(window, text="<<<Applique", command=set_frequency, width=10, height=2
,font=(fonte_police, taille_de_police))
        button_onoff = tk.Button(window, text="Démarrer", command=send_onoff, width=10, height=2, bg="green"
,font=(fonte_police, taille_de_police))
        button_save_data = tk.Button(window, text="Enregistrement \ndes données", command=save_data, width=12,
height=2 ,font=(fonte_police, taille_de_police))
        button_set_sampling = tk.Button(window, text="Applique>>>", command=set_sampling_frequency, width=10,
height=2 ,font=(fonte_police, taille_de_police))
        button_reset_sensor = tk.Button(window, text="Réinitialisation du capteur",command=reset_sensor, width=30,
height=2 ,font=(fonte_police, taille_de_police))
        button_zoom_in = tk.Button(window, text="Zoom In",command=zoom_in, width=10, height=2 ,font=(fonte_police,
taille_de_police))
        button_zoom_out = tk.Button(window, text="Zoom Out", command=zoom_out, width=10, height=2 ,font=(fonte_police,
taille_de_police))
        button_show_grid = tk.Button(window, text="Grid", command=show_grid, width=10, height=2 ,font=(fonte_police,
taille_de_police))
        button_help = tk.Button(window, text="Mode d'emploi", command = show_help, width=12, height=2
,font=(fonte_police, taille_de_police))
        bouton_exit = tk.Button(window, text="EXIT", command = exit_program, width=12, height=2 ,font=(fonte_police,
taille_de_police),bg = "red")

        #Partie entry
        entry_frequency = tk.Entry(window)
        entry_sampling_frequency = tk.Entry(window)

        #Scale
        scale = tk.Scale(window, from_=frequency_min, to=frequency_max, orient='horizontal',
command=on_scale_change,length=450)

        # emplacement des modules
        label_actual_frequency.grid(        row=0, column=0, columnspan=2, padx=1, pady=10)
        label_counter.grid(         row=0, column=2, columnspan=2, padx=1, pady=10)
        label_windows_information.grid( row=0, column=4, columnspan=2, padx=1, pady=10)
        button_reset_sensor.grid(           row=1, column=2, columnspan=2,padx=20, pady=20)
        bouton_exit.grid(           row=1, column=5, padx=20, pady=20)
        label_entre_frequency.grid(         row=2, column=0, padx=20, pady=20)
        entry_frequency.grid(       row=2, column=1, padx=20, pady=20)
        button_set_frequency.grid(          row=2, column=2, padx=20, pady=20)
        button_set_sampling.grid(           row=2, column=3, padx=20, pady=20)
        entry_sampling_frequency.grid(  row=2, column=4, padx=20, pady=20)
        label_sampling.grid(        row=2, column=5, padx=20, pady=20)
        scale.grid(                 row=3, column=0, columnspan=2, padx=20, pady=20)
        button_show_grid.grid(              row=3, column=2, padx=20, pady=20)
        button_zoom_in.grid(        row=3, column=3, padx=20, pady=20)
        label_magnification.grid(   row=3, column=4, padx=20, pady=20)
        label_force_max.grid(       row=3, column=5, padx=20, pady=20)
        button_save_data.grid(              row=4, column=2, padx=20, pady=20)
        label_state_motor.grid(     row=4, column=0, padx=20, pady=20)
        button_onoff.grid(          row=4, column=1, padx=20, pady=20)
        button_zoom_out.grid(               row=4, column=3, padx=20, pady=20)
        button_help.grid(           row=4, column=4, padx=20, pady=20)
        label_force.grid(           row=4, column=5, padx=20, pady=20)
        canvas.get_tk_widget().grid(        row=5, column=0, rowspan=3, columnspan=6, padx=20, pady=20)

        update_plot() #actualiser la figure de la courbe
        threading.Thread(target=read_from_arduino, daemon=True).start() #Démarrage du processus read from arduino
        countdown(2) #Démarrage du compteur
        window.mainloop() #boucle principal de la deuxième fenêtre

fenetre_de_selection_arduino_com() #Démarrage de la fenêtre de la sélection du port série
```

Objective

This section presents the implementation of a low-power BLE application that periodically broadcasts a custom payload using the nRF52840 SoC.
The primary goal is to evaluate whether the energy harvested by a PVDF-based nanogenerator is sufficient to power the system long enough to initialize the BLE stack and transmit data.
To validate this concept under controlled conditions, a wake-up period of 10 minutes was selected arbitrarily for testing purposes.
This interval can be later adjusted depending on the actual amount of harvested energy and power requirements.

Overview of Operation

The application configures the RTC2 peripheral to generate an interrupt every 600 seconds (10 minutes).
Upon each interrupt, the system wakes from sleep mode and sends a BLE advertising packet containing a single byte of application data (0xAB).
The advertising is performed in non-connectable, non-scannable mode, with a short duration to conserve energy.
After advertising, the system returns to low-power mode, awaiting the next RTC interrupt.

Code Explanation

The application consists of five main functional blocks:

a) RTC2 Initialization

```
NRF_RTC2->PRESCALER = 327;

NRF_RTC2->CC[0] = 60000;

...

NRF_RTC2->TASKS_START = 1;
```

- The RTC2 runs at 32.768 kHz, divided by (327 + 1), giving a 100 Hz counter (10 ms resolution).
- The compare register is set to trigger every 60000 ticks (10 minutes).
- When the event triggers, the RTC interrupt handler starts BLE advertising.

b) RTC2 Interrupt Handler

```
void RTC2_IRQHandler(void) {

  if (NRF_RTC2->EVENTS_COMPARE[0]) {

    NRF_RTC2->EVENTS_COMPARE[0] = 0;

    ...
```

```
      sd_ble_gap_adv_start(m_adv_handle, APP_BLE_CONN_CFG_TAG);
    }
}
```

- Clears the interrupt flag.
- Reschedules the next interrupt.
- Triggers BLE advertising.

c) BLE Stack Initialization

```
nrf_sdh_enable_request();
nrf_sdh_ble_default_cfg_set(APP_BLE_CONN_CFG_TAG, &ram_start);
nrf_sdh_ble_enable(&ram_start);
```

- Enables the SoftDevice.
- Configures BLE parameters (e.g., link count, RAM allocation).

d) BLE Advertising Configuration

```
ble_advdata_manuf_data_t manuf_data = {
    .company_identifier = 0xFFFF,
    .data.p_data = &TX_DATA_BYTE,
    .data.size = 1
};
...
sd_ble_gap_adv_set_configure(&m_adv_handle, &adv_data_config, &adv_params);
```

- Configures a manufacturer-specific BLE advertising payload.
- The payload contains a single byte: 0xAB.
- Advertising uses the GAP non-connectable mode, with no scan response and low duty cycle.

e) Low-Power Sleep Mode

```
while (true) {
    sd_app_evt_wait();
}
```

- The system enters sleep mode using the SoftDevice's event-wait function.
- It wakes only upon RTC2 interrupt.

Energy Efficiency Considerations

- The use of RTC2 ensures precise timing with ultra-low power consumption during standby.
- BLE advertising is configured to use minimal transmission duration.
- The internal DC-DC converter is enabled to further reduce power usage (NRF_POWER->DCDCEN = 1).
- No UART, logging, or debugging features are enabled in this configuration.

Summary

This implementation demonstrates an efficient strategy to achieve long-term low-power BLE communication. By combining RTC-based wake-up with minimal BLE advertising, the system conserves energy while still transmitting periodic information.
Such a pattern is ideal for energy harvesting applications, remote sensors, and beacon-type devices.

The project also includes provisions for over-the-air firmware update via USB (DFU mode). Although the full update process is not yet finalized, the firmware packaging step using nrfutil is currently under development. While the application has been compiled successfully and the .hex file is ready, the creation of a DFU-compatible .zip package has encountered compatibility issues, particularly related to SoftDevice identifiers and Python environment dependencies.
Nevertheless, all tools required for this process have been installed and tested, and the method is well understood. This step will be finalized once the technical environment is fully stabilized.

Code

```
#include <stdint.h>

#include <stdbool.h>

#include <string.h>



#include "nrfx.h"

#include "nrf.h"

#include "nrf_rtc.h"

#include "nrf_soc.h"

#include "nrf_sdh.h"

#include "nrf_sdh_ble.h"
```

```
#include "ble_gap.h"
#include "ble_types.h"
#include "ble_srv_common.h"
#include "ble_advdata.h"
#include "nrf_pwr_mgmt.h"
#include "app_error.h"



#define RTC2_PRESCALER        327        // 32.768kHz / (327+1) = 100Hz
#define RTC_COMPARE_COUNT     60000      // 100 Hz * 600 = 10 minutes
#define BLE_ADV_INTERVAL      1600       // 1600 * 0.625 ms = 1 sec
#define ADV_DURATION_UNITS    60         // 60 * 10 ms = 0.6 sec
#define DEVICE_NAME           "BLE-RF"
#define COMPANY_ID            0xFFFF
#define TX_DATA_BYTE          0xAB
#define APP_BLE_CONN_CFG_TAG  1

static uint8_t m_adv_handle = BLE_GAP_ADV_SET_HANDLE_NOT_SET;
static uint8_t m_enc_advdata[BLE_GAP_ADV_SET_DATA_SIZE_MAX] = {0};
static ble_gap_adv_params_t m_adv_params;

// ==== RTC2 INIT ====
static void rtc2_init(void) {
    NRF_RTC2->PRESCALER = RTC2_PRESCALER;
    NRF_RTC2->CC[0] = RTC_COMPARE_COUNT;
    NRF_RTC2->EVTENSET = RTC_EVTEN_COMPARE0_Msk;
```

```
    NRF_RTC2->INTENSET = RTC_INTENSET_COMPARE0_Msk;
    NVIC_EnableIRQ(RTC2_IRQn);
    NRF_RTC2->TASKS_START = 1;
}

// ==== RTC2 Handler ====
void RTC2_IRQHandler(void) {
    if (NRF_RTC2->EVENTS_COMPARE[0]) {
        NRF_RTC2->EVENTS_COMPARE[0] = 0;

        // Gestion du débordement 24 bits
        uint32_t next_cc = NRF_RTC2->CC[0] + RTC_COMPARE_COUNT;
        if (next_cc > 0xFFFFFF) {
            NRF_RTC2->TASKS_CLEAR = 1;
            NRF_RTC2->CC[0] = RTC_COMPARE_COUNT;
        } else {
            NRF_RTC2->CC[0] = next_cc;
        }

        // Démarre l'advertising BLE
        (void)sd_ble_gap_adv_start(m_adv_handle, APP_BLE_CONN_CFG_TAG);
    }
}

// ==== BLE Stack ====
static void ble_stack_init(void) {
    ret_code_t err_code;
```

```
    err_code = nrf_sdh_enable_request();
    APP_ERROR_CHECK(err_code);

    uint32_t ram_start = 0;
    err_code = nrf_sdh_ble_default_cfg_set(APP_BLE_CONN_CFG_TAG, &ram_start);
    APP_ERROR_CHECK(err_code);
    err_code = nrf_sdh_ble_enable(&ram_start);
    APP_ERROR_CHECK(err_code);
}

// ==== BLE Advertising ====
static void advertising_init(void) {
    ret_code_t err_code;

    uint8_t adv_data_byte[1] = { TX_DATA_BYTE };

    ble_advdata_manuf_data_t manuf_data = {
        .company_identifier = COMPANY_ID,
        .data.p_data = adv_data_byte,
        .data.size = sizeof(adv_data_byte)
    };

    ble_advdata_t advdata = {0};
    advdata.name_type = BLE_ADVDATA_NO_NAME;
    advdata.flags = BLE_GAP_ADV_FLAGS_LE_ONLY_GENERAL_DISC_MODE;
    advdata.p_manuf_specific_data = &manuf_data;
```

```
  ble_gap_adv_data_t adv_data_config = {
    .adv_data = {
      .p_data = m_enc_advdata,
      .len = sizeof(m_enc_advdata)
    },
    .scan_rsp_data = { .p_data = NULL, .len = 0 }
  };

  err_code = ble_advdata_encode(&advdata, m_enc_advdata, &adv_data_config.adv_data.len);
  APP_ERROR_CHECK(err_code);

  m_adv_params = (ble_gap_adv_params_t){
    .properties.type = BLE_GAP_ADV_TYPE_NONCONNECTABLE_NONSCANNABLE_UNDIRECTED,
    .p_peer_addr = NULL,
    .interval = BLE_ADV_INTERVAL,
    .duration = ADV_DURATION_UNITS, // 1.6 sec
    .filter_policy = BLE_GAP_ADV_FP_ANY,
    .primary_phy = BLE_GAP_PHY_1MBPS
  };

  err_code = sd_ble_gap_adv_set_configure(&m_adv_handle, &adv_data_config, &m_adv_params);
  APP_ERROR_CHECK(err_code);
}

// ==== Power management ====
static void power_management_init(void) {
  ret_code_t err_code = nrf_pwr_mgmt_init();
```

```
    APP_ERROR_CHECK(err_code);
}


// ==== MAIN ====
int main(void) {
    NRF_POWER->DCDCEN = 1; // Active régulateur DCDC pour économie


    ble_stack_init();
    advertising_init();
    rtc2_init();
    power_management_init();


    while (true) {
        sd_app_evt_wait(); // Ultra-basse consommation
    }
}
```